Talanta

The International Journal of Pure and Applied Analytical Chemistry

Publication information: *Talanta* (ISSN 0039-9140). For 2007, volumes 71–73 are scheduled for publication. Subscription prices are available upon request from the Publisher or from the Regional Sales Office nearest you or from this journal's website (http://www.elsevier.com/locate/talanta). Further information is available on this journal and other Elsevier products through Elsevier's website: (http://www.elsevier.com). Subscriptions are accepted on a prepaid basis only and are entered on a calendar year basis. Issues are sent by standard mail (surface within Europe, air delivery outside Europe). Priority rates are available upon request. Claims for missing issues should be made within six months of the date of dispatch.

Orders, claims, and journal enquiries: please contact the Customer Service Department at the Regional Sales Office nearest you:
Orlando: Elsevier, Customer Service Department, 6277 Sea Harbor Drive, Orlando, FL 32887-480 USA; phone: (+1) (877) 8397126 [toll free number for US customers], or (+1) (407) 3454020 [customers outside US]; fax: (+1) (407) 3631354; e-mail: usjcs@elsevier.com
Amsterdam: Elsevier, Customer Service Department, PO Box 211, 1000 AE Amsterdam, The Netherlands; phone: (+31) (20) 4853757; fax: (+31) (20) 4853432; e-mail: nlinfo-f@elsevier.com
Tokyo: Elsevier, Customer Service Department, 4F Higashi-Azabu, 1-Chome Bldg, 1-9-15 Higashi-Azabu, Minato-ku, Tokyo 106-0044, Japan; phone: (+81) (3) 5561 5037; fax: (+81) (3) 5561 5047; e-mail: jp.info@elsevier.com
Singapore: Elsevier, Customer Service Department, 3 Killiney Road, #08-01 Winsland House I, Singapore 239519; phone: (+65) 63490222; fax: (+65) 67331510; e-mail: asiainfo@elsevier.com

USA mailing notice: *Talanta* (ISSN 0039-9140) is published monthly by Elsevier B.V. (P.O. Box 211, 1000 AE Amsterdam, The Netherlands). Annual subscription price in the USA US$ 3,818 (valid in North, Central and South America), including air speed delivery. Application to mail at periodical postage rate is paid at Rathway, NJ and additional mailing offices.
USA POSTMASTER: Send address changes to *Talanta*, Publications Expediting Inc., 200 Meacham Avenue, Elmont, NY 11003.
AIRFREIGHT AND MAILING in the USA by Publications Expediting Inc., 200 Meacham Avenue, Elmont, NY 11003.

Available online at www.sciencedirect.com
ScienceDirect
Talanta 73 (2007) 546–552
Talanta
www.elsevier.com/locate/talanta

Determination of aluminium in water samples by adsorptive cathodic stripping voltammetry in the presence of pyrogallol red and a quaternary ammonium salt

Verónica Arancibia*, Carolina Muñoz

Departamento de Química Inorgánica, Facultad de Química, Pontificia Universidad Católica de Chile, Vicuña Mackenna 4860, Santiago, Chile

Received 27 December 2006; received in revised form 14 April 2007; accepted 15 April 2007
Available online 22 April 2007

Abstract

A fast, sensitive and selective method for the determination of aluminium based on the reaction of the metal with pyrogallol red (PR) in the presence of tetrabutylammonium tetrafluoroborate (TBATFB) to form an $Al(PR)_3x9TBATFB$ complex which is adsorbed on the mercury electrode is presented. Under these conditions complexation of aluminium is rapid and no waiting period or heating of the sample is required. The reduction current of the accumulated complex is measured by scanning the potential in the cathodic direction. The variation of peak current with pH, adsorption time, adsorption potential, ligand and quaternary ammonium salt concentration, and some instrumental parameters, such as stirring rate in the accumulation stage, and step amplitude, pulse amplitude and step duration while obtaining the square wave voltamperograms were optimized. The best experimental parameters were pH 8.5, (NH_4Ac–NH_3 buffer), $C_{PR} = 25\ \mu mol\ L^{-1}$, C_{TBATFB} over $75\ \mu mol\ L^{-1}$, $t_{ads} = 60$ s, and $E_{ads} = -0.60$ V versus Ag/AgCl. A linear response is observed over the 0.0–30.0 $\mu g\ L^{-1}$ concentration range, with a detection limit of 1.0 $\mu g\ L^{-1}$. Reproducibility for 9.0 $\mu g\ L^{-1}$ aluminium solution was 2.3% ($n = 6$). Synthetic sea water and sea water reference material CRM-SW were used for validation measurements. Aluminium in urine samples of a volunteer who ingested 800 mg of $Al(OH)_3$ was analyzed.

Keywords: Adsorptive cathodic stripping voltammetry; Aluminium; Pyrogallol red; Tetrabutylammonium tetrafluoroborate; Sea water; Urine samples

1. Introduction

Aluminium occurs ubiquitously in the environment, in the form of salts and oxides. Aluminun is not an essential element in humans, and it has been linked with a number of disorders in man including Alzheimer's disease, Parkinson's dementia and osteomalacia. However, the potential contribution of aluminium in Alzheimer's disease and related disorders is not resolved. Some studies have found an increase of this element in the brain [1–4], whereas others have not [5–8]. On the other hand, several epidemiological studies have associated aluminium in drinking water with the incidence of Alzheimer's disease [9–13]; other studies have not found significant associations with similar levels of aluminium concentration [14–17]. On the other hand, the bioavailability of aluminium from water and foods is low. Studies of the relative bioavailability of aluminium naturally present in aluminium treated dinking water were determined in healthy volunteers with normal renal function who consumed 1.6 L per day with 140 $\mu g\ L^{-1}$ aluminium. The bioavailability of aluminium from this treated water was 0.37%, similar to that form food (0.28–0.64%) [18].

Aluminium exhibits a complex chemistry in natural waters. Solution pH and the presence of fluoride, silicon, iron and natural chelating agents in the water may all influence the speciation of aluminium and consequently its bioavailability. Trivalent Al^{3+} and the hydrolyzed ions $Al(OH)^{2+}$ and $Al(OH)_2{}^{+}$ represent the species of principal concern, with organically bound Al and polymeric forms considered far less toxic [19].

Sensitive, selective and accurate methods are required for the determination of aluminium in biological and environmental matrices. Electroanalytical techniques have important advantages that include speed, high selectivity and sensitivity, low detection limit, relative simplicity, and low equipment cost compared to other techniques. Of these electroanalytical methods, stripping voltammetry is the most sensitivity one because it has a preconcentration step on the electrode surface prior to

* Corresponding author.
E-mail address: darancim@puc.cl (V. Arancibia).

0039-9140/$ – see front matter © 2007 Elsevier B.V. All rights reserved.
doi:10.1016/j.talanta.2007.04.009

Table 1
List of the adsorptive stripping voltammetric methods have been reported for determination of aluminium

Method	Ligand	pH	Linear range	Detection limit	Refs.
DPSV	Solochrome violet RS	4.5	0–30 $\mu g\,L^{-1}$	0.15 $\mu g\,L^{-1}$	[20]
LSV	Solochrome violet RS	5.2	1×10^{-8}–8×10^{-7} mol L^{-1}	5.1×10^{-9} mol L^{-1}	[21]
		8.5	1×10^{-8}–1×10^{-6} mol L^{-1}	3.8×10^{-9} mol L^{-1}	
DPAdSV	Solochrome violet	4.5		1.4 $\mu g\,L^{-1}$	[22]
	Palatine chrome black 6B	7.0		69.0 $\mu g\,L^{-1}$	
	Chromazul S	7.0		35.5 $\mu g\,L^{-1}$	
	Erochrome black T	4.5		49.2 $\mu g\,L^{-1}$	
AdCSV	Solochrome violet RS	8.8		4.5×10^{-9} mol L^{-1}	[23]
DPAdSV	DASA	7.1–7.3		1 n mol L^{-1}	[24]
AdCSV	DASA	7.1	0.8–30 $\mu g\,L^{-1}$	0.8 $\mu g\,L^{-1}$	[25]
AdCSV	Cupferron	7.0		30 ng L^{-1}	[26]
AdCSV	Alizarin S	8.2	2.5×10^{-8}–3.5×10^{-7} mol L^{-1}	2.5×10^{-8} mol L^{-1}	[27]
AdCSV	Morin	7.0	1–15 $\mu g\,L^{-1}$	0.11 $\mu g\,L^{-1}$	[28]
FSDPV	Arsenazo III	3.6	0–6×10^{-6} mol L^{-1}	3.7×10^{-8} mol L^{-1}	[29]
LSV	Norepinephrine	8.5	4×10^{-6}–4×10^{-5} mol L^{-1}	1.8×10^{-6} mol L^{-1}	[31]
SWAdSV	Cupferron	4.5	0.5–5.0 $\mu g\,L^{-1}$ (240 s) 1–10 $\mu g\,L^{-1}$ (120 s) 2–20 $\mu g\,L^{-1}$ (60 s)	0.5 $\mu g\,L^{-1}$	[32]

recording the voltammogram. The accumulation of metal ions can occur by electrolysis (anodic stripping voltammetry, ASV) or by adsorption (adsorptive stripping voltammetry, AdSV) after complexation with a surface active ligand. The quantitation of aluminium by ASV is difficult because it is reduced at −1.75 V versus Ag/AgCl, close to hydrogen evolution. The presence of a ligand which forms a complex with aluminium displaces the potential to more positive values due to adsorption of the complex on the working electrode. AdSV is more sensitive than ASV, but the concentration range for its application is more limited because the surface area of the electrode is saturated and many ligands are adsorbed, competing with the complex. There are few reports on the application of adsorptive cathodic stripping voltammetry for the determination of aluminium; they use solochrome violet RS [20–23], 1,2-dihydroxy-anthraquinone-3-sulphonic acid (DASA) [24,25], cupferron [26], alizarin S [27], morin [28], arsenazo III [29], calmagite [30], and norepinephrine [31] with hanging mercury drop or mercury film electrodes, and recently cupferron [32] with bismuth film electrodes (Table 1). A good detection limit was obtained with solochrome violet RS, but it was necessary to heat the sample solution for 10 min at 90 °C to ensure quantitative complexation [20–22]. On the other hand, the reduction potential of the free norepinephrine and the aluminium complex are very close, making difficult the quantitation of aluminium in real samples [31]. The main advantages of the use of DASA [24,25] as complexing agent for the voltammetric determination of aluminium is the low detection limit and the fast reaction kinetics, which obviate the need to heat the sample after addition of the reagent.

The present paper describes a sensitive and rapid adsorptive stripping procedure based on the reaction of the aluminium with pyrogallol red (3,4,5-trihydroxy-9-(2′-sulfophenyl)-6-isoxanthone, pyrogallolsulfophthalein, PR) in the presence of tetrabutylamonium tetrafluoroborate (TBATFB) to form an Al-PR-TBATFB complex, which is adsorbed, followed by reduction at −1.10 V versus Ag/AgCl. PR has four groups capable of dissociation with the abstraction of a proton: one sulfo group and three hydroxyl groups (Fig. 1). The dissociation constants were determined by spectrophotometric, computational and graphical methods and were calculated for different ionic strengths because cationic surfactants affect the dissociation of PR [33]. The pyrogallol structural group is found in many important natural and synthetic molecules, such as gallic acid, tannic acid and humic acid. Pyrogallol red has been used for the detection of aluminium and other metals via spectrophotometry and for other metal ions via adsorptive cathodic stripping voltammetry (copper [34], copper and molybdenum [35], antimony [36], germanium [37], and vanadium [38]), but this is the first report for the detection of aluminium via AdCSV in the presence of quaternary ammonium salt which it modifies acid–base properties of PR ligand and accelerating the complexation. The method was validated with synthetic sea water and sea water reference material CRM-SW, and it was also applied to the determina-

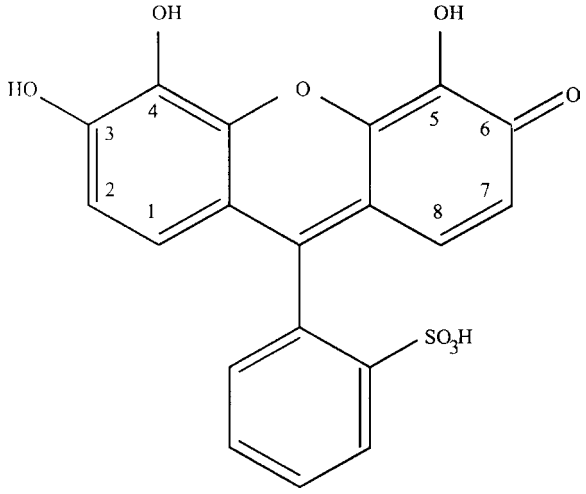

Fig. 1. Structural formula of pyrogallol red.

tion of aluminium in urine samples of a volunteer after oral administration of two tablets containing 400 mg of $Al(OH)_3$.

2. Experimental

2.1. Apparatus

Square wave adsorptive cathodic stripping voltammetry (SWAdCSV) was carried out with an MDE 150 polarographic stand (Radiometer Analytical, Lyon, France). The MDE 150 was controlled with TraceMaster 5 PC software. A 10-mL capacity measuring cell was equipped with a hanging mercury drop electrode (HMDE), a reference electrode (Ag/AgCl/KCl 3 mol L^{-1}), an auxiliary platinum electrode, a mechanical mini stirrer, and a capillary to supply an inert gas. All experiments were carried out in a nitrogen atmosphere. pH measurements were made with an Orion 430 pH meter. All potentials are given relative to the Ag/AgCl (KCl 3 mol L^{-1}) reference electrode.

2.2. Reagents and solutions

All solutions were prepared with Milli-Q water (18.2 MΩ). Standard stock solutions with 0.1, 0.4 and 1.0 μg mL^{-1} of aluminium were prepared from standard aluminium 1000 μg mL^{-1} solution (Merck, Darmstadt, Germany). The stock solutions of pyrogallol red (PR, Aldrich) and tetrabutylammonium tetrafluoroborate (TBATFB, Aldrich) in water were prepared freshly every day. NH_4Ac–NH_3 buffer 0.7 mol L^{-1}, pH 8.5 and NH_4Ac–$HClO_4$ buffer, pH 4.5 were prepared with Milli-Q water. Synthetic sea water (Aldrich) contaminated with a standard containing 22 metal ions (Merck) and sea water reference material CRM-SW (2% HNO_3, Al 0.5 mg kg^{-1}, High-Purity Standards) were used for validation measurements.

2.3. Urine samples

Urine samples were obtained after oral administration to a volunteer of two tablets containing 400 mg of $Al(OH)_3$. Samples of urine were collected 0; 0.3; 3.5; 9.0; 12.0 and 24.0 h after administration of the drug. The samples were introduced in polyethylene bottles previously washed with 1% HNO_3 solution and frozen at −20 °C until analysis. 50.0 mL of each sample were placed in a glass baker on a hot plate, and nitric acid and hydrogen peroxide was added until a colorless solution was obtained. Each analysis was carried out three times. The averages of all the measurements are reported.

2.4. Procedure

Ten millilter of water, 500 μL of buffer (pH 4.5 or 8.5), 100 μL of PR solution (2.5 mmol L^{-1}), 250 μL of TBATFB solution (3.0 mmol L^{-1}), and aliquots of aluminium standard solution (0.4 or 1.0 μg L^{-1}) or samples were pipetted into the electrochemical cell. The solution was purged with water-saturated nitrogen for 5 min in the first cycle and for 60 s in each successive cycle. Then, after eliminating 5 drops (size ≈0.75 mm^2), a new mercury drop was extruded to initiate the preconcentration for a given t_{ads} and E_{ads} at a stirring speed of 400 rpm. After a 10 s quiescent period, the potential was scanned between −0.60 and −1.40 V using square wave modulation with a step amplitude of 10 mV; a pulse amplitude of 25 mV, and a step duration of 0.1 s. The calibration curves were drawn and linear regression and detection limits were calculated.

2.5. Limit of detection (LOD)

The limit of detection was calculated using the approximation of Miller and Miller [39] for calibration curves. Minimum signal (y_{min}) = $a + 3s_{y/x}$, where a is intercept and $s_{y/x}$ is standard deviation of the calibration curve.

3. Results and discussion

The effect of buffer pH on the electrochemical reaction of the free PR and on the complexation reaction in the pH range from 2 to 10 using Britton Robinson, NH_4Ac–$HClO_4$ and NH_4Ac–NH_3 buffers, and HCl solution, was studied. The signal due to the Al-PR complex was never seen, probably because the complex needed time and/or temperature and was not formed, or the signal due to the electrochemical reaction of the complex was overlapped by signals due to reaction of the ligand. A solution containing 150 μmol L^{-1} PR ligand (NH_4Ac–NH_3 buffer, pH 8.5) and increasing amounts of aluminium was warmed up to 70–80 °C in a water bath for 10 min and then cooled and transferred to the electrochemical cell. The stripping voltammograms were recorded, and a very sensitive signal appeared at about −1.25 V versus Ag/AgCl when aliquots of aluminium were added (Fig. 2). However, control of the system was difficult, getting a constant current took several minutes, and the linearity of the curve was not good. Those conditions were therefore discarded.

The adsorption is dependent on the mercury electrode charge and the charge of the complex at the working potential. With the purpose of changing the charge of the complex or ligand and

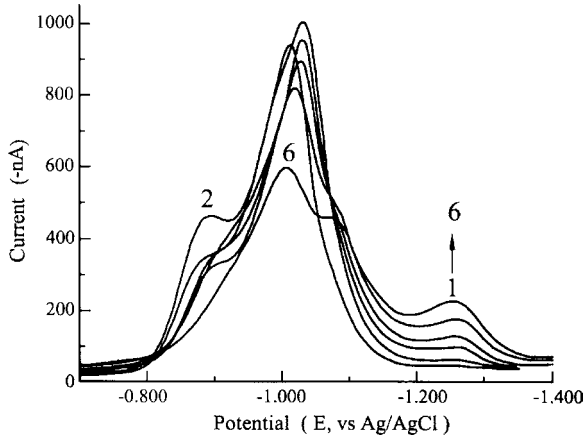

Fig. 2. Adsorptive stripping voltammograms of PR in the absence (curve 1) and presence of aluminium (curves 2–6) after heating the solution up to 70–80 °C. Aluminium concentration: 1.4; 2.7; 4.1; 5.4 and 6.7 μg L^{-1}. PR: 150 μmol L^{-1}; t_{ads} = 60 s; E_{ads} = −0.60 V at pH of 8.5. Step amplitude 5 mV, pulse amplitude 25 mV, step duration 0.04 s.

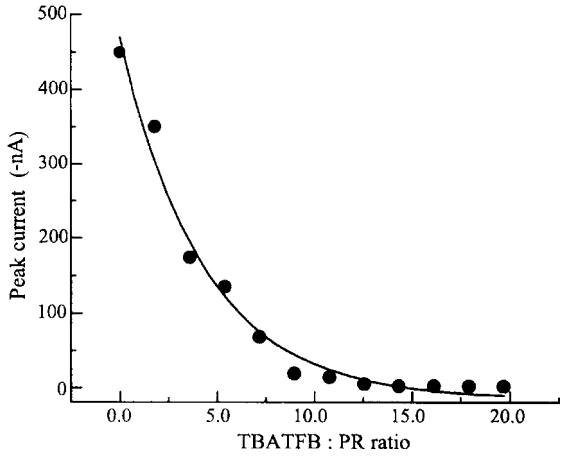

Fig. 3. Peak current as a function of TBATFB:PR ratio. PR 4.7 μmol L^{-1} and aliquots of TBATFB 3.13 mmol L^{-1} solution. pH 8.5; t_{ads} = 60 s; E_{ads} = −0.60 V. Step amplitude 10 mV, pulse amplitude 25 mV, step duration 0.1 s.

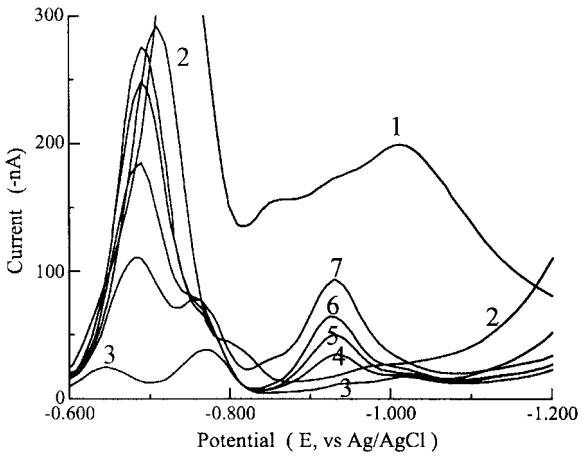

Fig. 4. Adsorptive stripping voltammograms of: PR 5 μmol L^{-1} (curve 1); PR 5 μmol L^{-1}, TBATFB 25 and 58 μmol L^{-1} (curves 2–3); PR 9 μmol L^{-1}, TBATFB 57 μmol L^{-1} and aluminium 6.3; 9.7; 13.0 and 19.5 μg L^{-1} (curves 4–7). t_{ads} = 60 s; E_{ads} = −0.60 V at pH of 4.5. Step amplitude 10 mV, pulse amplitude 25 mV, step duration 0.1 s.

producing the electrostatic interaction with the mercury electrode, a quaternary ammonium salt (TBATFB) was added to the electrochemical cell. When aliquots of TBATFB solution were added to a PR ligand, the reduction signal of the free ligand was slowly displaced to a positive potential and the peak current decreased almost completely. Fig. 3 shows a plot with the peak current of free ligand as a function of the TBATFB:PR ratio. The small peak current due reduction of pyrogallol red was almost constant when the ammonium salt-to-ligand ratio was ≈9:1. The effect of surfactants, organic solvents and quaternary ammonium salts on the acid–base properties of PR had been studied, and It has been proved that interactions of PR with quaternary ammonium salt is local and lead to changes in dihedral angles in the groups directly involved in the reaction. The existence of ion pairs formed by cationic surfactants, such as cetylpyridinium bromide chloride has been observed with reagents containing sulfo groups [33,40,41].

However, when aliquots of TBATFB solution were added to a solution containing aluminium and PR ligand, (1:3 ratio) the signal due to the aluminium complex was maximum for a TBATFB:PR ratio of 3:1. Fig. 4 shows the adsorptive voltammograms of the PR ligand solution without (curve 1) and with (curves 2 and 3) TBATFB, and in the presence of aluminium solution (curves 4–7) at pH 4.5 (NH_4Ac–$HClO_4$ buffer). The electrochemical reduction of free PR ligand occurred at −0.74 V and there was a wide signal at −1.01 V; in the presence of a quaternary ammonium salt the potential peak is displaced to more positive values (−0.68 V) and the wide signal disappears. When aluminium standard solution was added, a new signal appeared at −0.93 V that is linearly proportional to the concentration. Without quaternary ammonium salt this peak is not seen and the voltammogram is the same as that of the free ligand. Fig. 5 shows the adsorptive voltammograms at pH 8.5. The electrochemical reduction of PR at pH 8.5 occurred at −1.01 V. In the presence of the quaternary ammonium salt this signal decreases remarkably, allowing the signal of the complex to be measured with less interference. The new peak current at −1.12 V is proportional to the aluminium concentration.

Photometric titration (544 nm, 7.4×10^{-5} mol L^{-1} aluminium solution) were carried out with the purpose of determining the stoichiometry of the complex. PR solution is red-violet, and in the presence of aluminium the solution turns blue-violet. The curve intercept for an Al:PR ratio of 1:3 was obtained. The UV–vis spectra of these solutions with and without ammonium salt were almost the same. This indicates that the Al:PR complex is formed and the association with the ammonium salt is weak. However, this weak association is necessary for the complex to be adsorbed on the mercury electrode, and a signal depending on aluminium concentration can be seen. The signal was higher when complex and TBATFB ratio is 1:9. Dates reported in the literature are indicative of surfactants of different nature accelerate the complexation of metal ions with

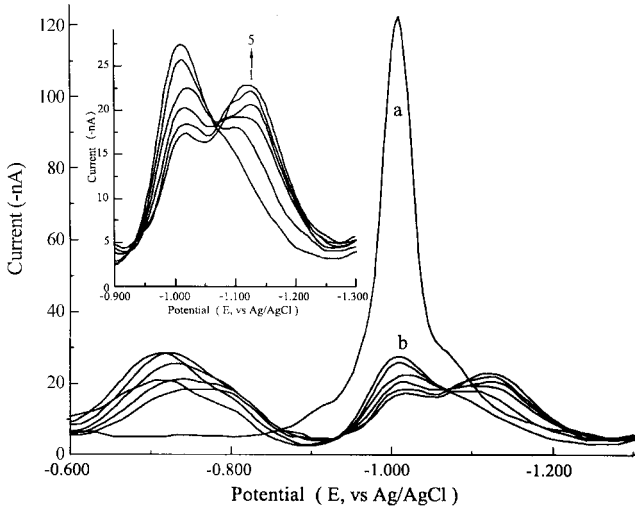

Fig. 5. Adsorptive stripping voltammograms of: PR 25 μmol L^{-1} (curve a); PR 25 μmol L^{-1}, TBATFB 0.3 mmol L^{-1} (curve b); PR 25 μmol L^{-1}, TBATFB 0.3 mmol L^{-1} and aluminium 3.7; 7.3; 10.9; 14.4 and 17.8 μg L^{-1} (curves 1–5). t_{ads} = 60 s; E_{ads} = −0.60 V at pH of 8.5. Step amplitude 5 mV, pulse amplitude 25 mV, step duration 0.4 s.

PR facilitating their extraction with organic solvent and increasing the molar absorptivities. Complexation of aluminum with PR in the presence of cetylpyridinium bromide and in the presence of cetylpyridinium bromide and EGTA were studied by photometric methods [42,43].

At both pH values complex formation is faster, but the peak current obtained at pH 4.5 is less than that at pH 8.5. However, the reduction of free ligand and of the aluminium complex occur at more different potential, giving better resolution at pH 4.5. Some authors have made studies of aluminium using Solochrome violet RS as the complexation agent in pH 4.5, and others have modified the method and changed the buffer to pH 8.5. Under the latter condition the complexation reaction was faster and better sensitivity was obtained. At pH 4.5 only inorganic monomeric aluminium species could be determined in real samples, while at pH 8.5 labile and non-labile (organically bound aluminium) could be determined. In the absence of complexing agent, when pH increases $Al(OH)_4^-$ becomes the main species.

Various experimental variables affecting the adsorptive stripping response were evaluated and optimized. The effect of the adsorption potential on the stripping peak current was studied over the 0.00 to −1.00 V range. The peak current increases up to −0.60 V, and then a slight decrease takes place. An adsorption potential of −0.60 V was used during this study.

The effect of PR concentration on the sensitivity of the proposed method was also studied. The results obtained (Fig. 6) show that the peak stripping current of the aluminium complex increased with increasing PR concentration up to 25 μmol L^{-1} (aluminium: 23.0 μg L^{-1}, TBATFB 0.3 mmol L^{-1}, t_{ads}: 60s).

Fig. 7 shows the voltammograms and the plot (inset) of the cathodic peak current of the aluminium complex as a function of adsorption time. At first, peak current increased almost linearly with accumulation time, and then it tended to a steady value. In this figure it is seen that the peak current of the ligand (−0.94 V) is almost constant because this compound is in solution; however the complex is adsorbed on the electrode.

The SW parameters studied were step amplitude, pulse amplitude, and frequency. Peak current increased as all the parameters increased. However, the complex peak current increased with increasing frequency and pulse amplitude (increasing scan rate), and at the same time the peak potential was shifted in the positive direction, and the separation of the free ligand peak with the electrochemical reaction was smaller, losing resolution. Another no less important parameter is stirring rate in the accumulation step: normally, if the complex is weakly adsorbed, a low scan rate is recommended. Fig. 8 shows the voltammograms and the plot (inset) of the cathodic peak current of the complex as a function of stirring rate.

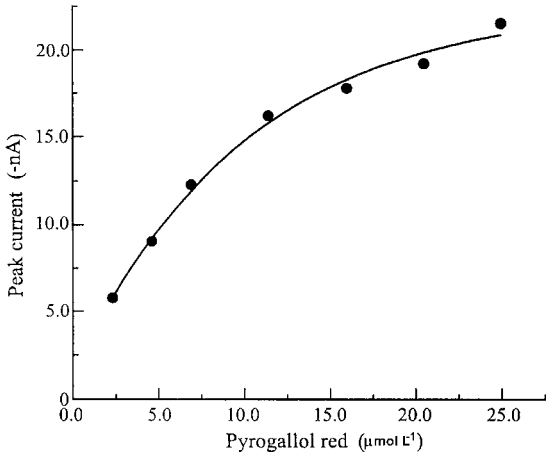

Fig. 6. Dependence of stripping peak current on PR concentration, 23 μg L^{-1} aluminium. TBATFB 0.3 mmol L^{-1}. t_{ads} = 60 s; E_{ads} = −0.60 V at pH of 8.5. Step amplitude 5 mV, pulse amplitude 25 mV, step duration 0.4 s.

The best analytical parameters were obtained by complexing aluminium with PR (25 μmol L^{-1}) in the presence of TBATFB with a concentration higher than (75 μmol L^{-1}) at pH 4.5 or 8.5; accumulation potential: −0.60 V; accumulation time: 60 s; stirring rate: 400 rpm; step amplitude 10 mV; pulse amplitude 25 mV, and frequency 10 Hz. Under these conditions the peak current was proportional to the concentration of aluminium over the 0.0–30.0 μg L^{-1} range, with a detection limit of 1.0 μg L^{-1}. Reproducibility of 9.0 μg L^{-1} Al(III) solution was 2.3% (n = 6). The detection limit can be further lowered by extending adsorption time.

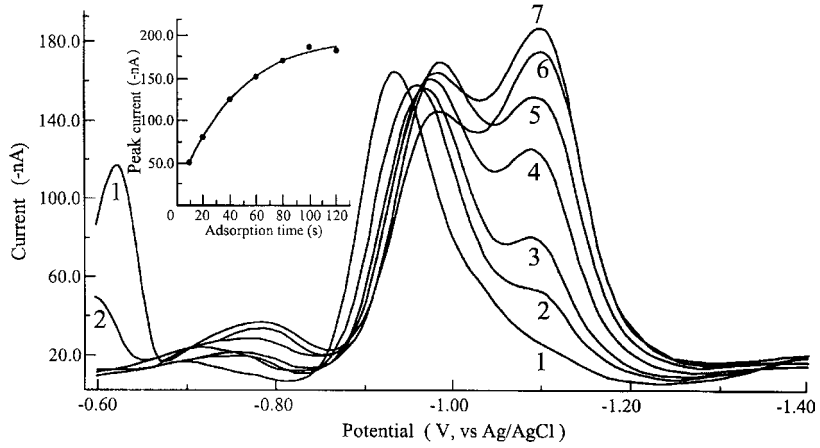

Fig. 7. Adsorptive voltammograms of $Al(PR)_3x9$TBATFB complex at different adsorption times (0–120 s). *Inset*: Dependence of peak current on t_{ads}. Aluminium 23 μg L^{-1}; PR 25 μmol L^{-1}; TBATFB 0.3 mmol L^{-1}. E_{ads} = −0.60 V at pH of 8.5. Step amplitude 5 mV, pulse amplitude 25 mV, step duration 0.1 s.

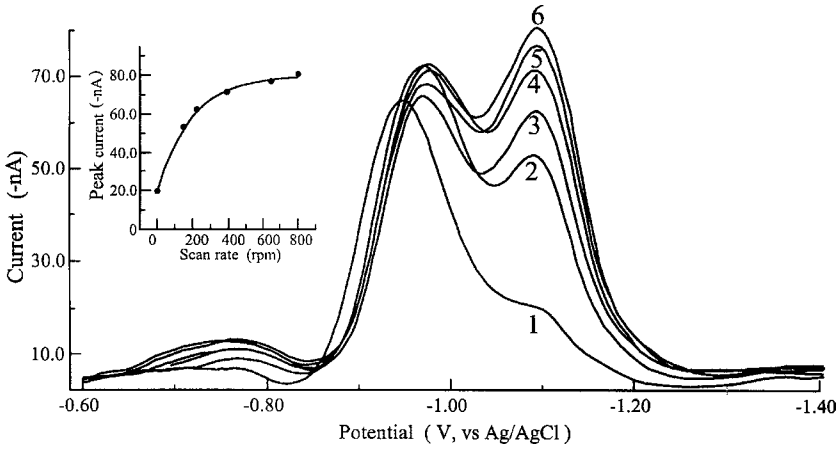

Fig. 8. Adsorptive voltammograms of Al(PR)$_3$*x*9TBATFB complex at different scan rates in the accumulation step (0–800 rpm). *Inset*: Dependence of peak current on scan rate. Aluminium 23.0 μg L^{-1}; PR 25 μmol L^{-1}; TBATFB 0.3 mmol L^{-1}; t_{ads}: 60 s; E_{ads} = −0.60 V at pH of 8.5. Step amplitude 5 mV; pulse amplitude: 10 mV; step duration 0.1 s.

Metal ions can interfere with the measurement by complexing with PR or by producing reduction peaks that overlap with, or even completely suppress, the Al(PR)$_3$*x*9TBATFB complex peak. Aluminium in real samples is analyzed by the standard addition method with excess ligand. Copper, cadmium, calcium, sodium and magnesium did not interfere with aluminium determination, but zinc does interfere because peak reduction of the Zn-PR complex occurs at the same potential as that of the Al(PR)$_3$*x*9TBATFB complex. This interference is avoided by addition of EDTA solution. The Zn-EDTA complex is not adsorbed on the mercury electrode, and the Al-EDTA complex is formed at an acid pH (2N HCl) to avoid hydroxyl complexes, and with heating because the kinetic rate is very slow. Fig. 9 shows adsorptive voltammograms of a 10.0-mL aliquot of water contaminated with a standard solution containing 22 metal ions: Ag, Al, B, Bi, Ca, Cd, Co, Cr, Cu, Fe, Ga, In, K, Li, Mg, Mn, Na, Ni, Pb, Sr, Tl and Zn in equal concentrations

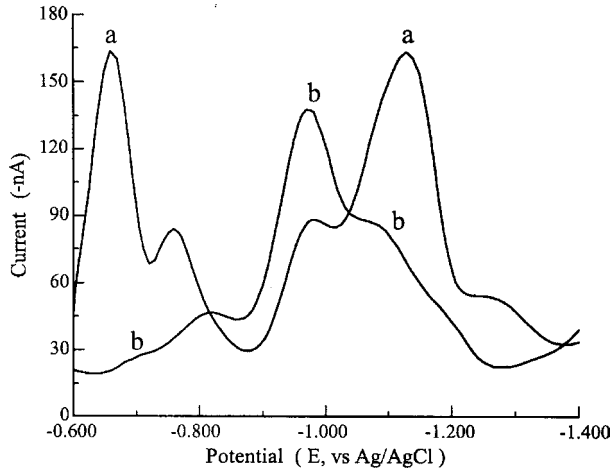

Fig. 9. Adsorptive voltammograms of a solution containing metal ions, such as: Al, Cd, Co, Cr, Cu, Ni, Pb, Zn, etc. 18.5 μg L^{-1}. PR 45 μmol L^{-1} and TBATFB 0.3 mmol L^{-1}; before and after adding 100 μL of EDTA 21.5 mmol L^{-1} solution (curves a and b, respectively). t_{ads} = 60 s; E_{ads} = −0.60 V at pH of 8.5. Step amplitude 10 mV; pulse amplitude: 25 mV; step duration 0.1 s.

Table 2
Analytical results of aluminium determination in synthetic sea water, in reference material CRM-SW and urine samples (n = 3)

Sample	Al found (μg L^{-1})
Synthetic sea water[a]	9.8 ± 0.3
CRM-SW[b]	503 ± 7
Urine 1 (0 h)	7.2 ± 0.2
Urine 2 (0.3 h)	180.7 ± 5.1
Urine 3 (3.5 h)	226.4 ± 4.3
Urine 4 (9.0 h)	338.1 ± 2.9
Urine 5 (12.0 h)	120.9 ± 3.3
Urine 6 (24.0 h)	11.6 ± 1.2

[a] Al added: 10.0 μg L^{-1}.
[b] Al certified: 500 μg L^{-1}.

(18.5 μg L^{-1} in solution) in the presence of PR 45 μmol L^{-1}, TBATFB 0.3 mmol L^{-1}, NH_4Ac–NH_3 pH 8.5 buffer before and after adding EDTA solution (curves a and b, respectively).

The method proposed was applied to the determination of aluminium in contaminated synthetic sea water, in a certified reference sea water material (CMR-SW), and in a study of the release of aluminium from urine after oral administration to a patient of 800 mg of $Al(OH)_3$. Urine samples were digested before the analysis. The results of aluminium determination by the proposed method are presented in Table 2. In order to eliminate the matrix effect and interference by other metal ions which form complexes with PR and consume ligand, the standard addition method was used.

4. Conclusions

In the present paper a novel aluminium determination was carried out forming an Al(PR)$_3$*x*9TBATFB complex which is adsorbed on a hanging mercury drop electrode. The presence of ammonium salt allowed the adsorption of the complex on the mercury electrode. The advantages of this new procedure are fast complexation kinetics which obviates the need to heat the solution after addition of ligand, high sensitivity, simplicity and speed. The method can be applied to both natural water and

biological samples where aluminium concentration is higher than 1 $\mu g\,L^{-1}$.

Acknowledgements

The authors acknowledge with thanks the financial support of FONDECYT under Project 1040630, and the Chemistry Faculty for a Ph.D. grant.

References

[1] J.M. Candy, A.E. Oakley, J. Klinowski, Lancet 1 (1986) 354.
[2] N. Xu, V. Majidi, W.R. Markesbery, W.D. Ehman, Neurotoxicology 13 (1992) 735.
[3] P.F. Good, D.P. Perl, L.M. Bierer, J. Schmeidler, Ann. Neurol. 31 (1992) 282.
[4] D.P. Perl, A.R. Brody, Science 208 (1980) 187.
[5] R.A. Yokel, Neurotoxicol 21 (2000) 813.
[6] J.P. Landsberg, B. McDonald, F. Watt, Nature 360 (1992) 65.
[7] M.A. Lovell, W.D. Ehmann, W.R. Markesbery, Ann. Neurol. 33 (1993) 36.
[8] A.H. Chafi, J.J. Hauw, J.P. Berry, C. Galle, Neurosci. Lett. 123 (1991) 61.
[9] C.N. Martyn, D.P.J. Barker, C. Osmond, Lancet 1 (1989) 59.
[10] T.P. Flaten, Environ. Geochem. Health 12 (1990) 152.
[11] W.F. Forbes, C.A. McAiney, L.M. Hayward, Can. J. Aging 13 (1994) 249.
[12] E. Gauthier, I. Fortier, F. Courchesne, Environ. Res. 84 (2000) 234.
[13] V. Rondeau, D. Commenges, H. Jacqmin-Gadda, Am. J. Epidemiol. 152 (2000) 59.
[14] D.P. Forster, A.J. Newens, D.W.K. Kay, J. Epidemiol. Commun. Health 49 (1995) 253.
[15] C.N. Martyn, D.N. Coggon, H. Inskip, Epidemiology 8 (1997) 281.
[16] A. Wettstein, J. Aeppli, K. Gautschi, Int. Arch. Occup. Environ. Health 63 (1991) 97.
[17] R.A. Yokel, S.S. Rhineheimer, R.D. Brauer, P. Sahrma, D. Elmore, P.J. McNamara, Toxicology 161 (2001) 93.
[18] J.L. Stauber, T.M. Florence, C.M. Davies, M.S. Adams, S.J. Buchanan, J. Am. Water Works Assoc. 91 (1999) 84.
[19] R. Street, O. Drábek, J. Száková, L. Mládková, Food Chem. in press.
[20] J. Wang, P.A.M. Farias, J.S. Mahmoud, Anal. Chim. Acta 172 (1985) 57.
[21] X. Wang, J. Lei, S. Bi, N. Gan, Z. Wei, Anal. Chim. Acta 449 (2001) 35.
[22] C. Locatelly, Electroanalysis 15 (2003) 1397.
[23] A.J. Downard, H. Kipton, J. Powell, S. Xu, Anal. Chim. Acta 262 (1992) 339.
[24] C.M.G. van den Berg, K. Murphy, J.P. Riley, Anal. Chim. Acta 188 (1986) 177.
[25] L.M. de Carvalho, P.C. do Nascimento, D. Bohrer, R. Stefanello, D. Bertagnoli, Anal. Chim. Acta 546 (2005) 79.
[26] J. Wang, J. Lu, R. Setiadji, Talanta 40 (1993) 351.
[27] J. Opydo, Talanta 44 (1997) 1081.
[28] N. Abo El-Maali, Y.M. Temerk, M. Sh-Abd El-Aziz, Anal. Chim. Acta 353 (1997).
[29] A. Komersova, M. Bartos, K. Kalcher, K. Vytras, Collect. Czech. Chem. Commun. 66 (1995) 693.
[30] M. Karpiuk, M. Politowicz, E. Stryjewska, S. Rubel, Fresenius' J. Anal. Chem. 351 (1995) 693.
[31] F. Zhang, M. Ji, Q. Xu, L. Yang, S. Bi, J. Inorg. Biochem. 99 (2005) 1756.
[32] G. Kefala, A. Economou, M. Sofoniou, Talanta 68 (2006) 1013.
[33] V.M. Ivanov, A.M. Mamedoc, J. Anal. Chem. 61 (2006) 1040.
[34] A. Safavi, E. Shams, Anal. Chim. Acta 385 (1999) 265.
[35] A.A. Ensafi, T. Khayamian, S.S. Khaloo, Anal. Chim. Acta 505 (2004) 201.
[36] M.J. Gómez, O. Domínguez, M.J. Arcos, Talanta 71 (2007) 691.
[37] C.Q. Sun, Q. Gao, L. Liu, Talanta 42 (1995) 881.
[38] S.B.O. Adeloju, F. Pablo, Anal. Chim. Acta 288 (1994) 157.
[39] J.C. Miller, J.N. Miller, Statistics for Analytical Chemistry, second ed., Ellis Horwood, London, 1988.
[40] D.I. Mustafin, L.A. Gribov, O.V. Sivanova, Zh. Strukt. Khim. 3 (1980) 62.
[41] S.B. Savvin, R.K. Chernova, S.N. Shtykov, Poverkhnostno-aktivnyev veshchestva (Surfactants), Nauka, Moscow, 1991.
[42] A.M. Mamedova, V.M. Ivanov, A.P. Korotych, S.A. Akhmedov, Vestn. Mosk. Univ., Ser. 2 Khim. 45 (2004) 316.
[43] X. Zheng, Y. Yan, Y. Li, Huaxue Fence 37 (1999) 315.

Available online at www.sciencedirect.com
ScienceDirect
Talanta 73 (2007) 514–522
Talanta
www.elsevier.com/locate/talanta

Determination of phosmet and its metabolites in olives by matrix solid-phase dispersion and gas chromatography–mass spectrometry

Sara C. Cunha *, José O. Fernandes, M. Beatriz, P.P. Oliveira

REQUIMTE/Serviço de Bromatologia, Faculdade de Farmácia, Universidade do Porto, Rua Aníbal Cunha 164, 4099-030 Porto, Portugal

Received 17 January 2007; received in revised form 28 March 2007; accepted 11 April 2007
Available online 24 April 2007

Abstract

An accurate method based on matrix solid-phase dispersion (MSPD), and gas chromatography–mass spectrometry (GC/MS) was developed for determination of phosmet residues and its metabolites (phosmet-oxon, phthalimide, *N*-hydroxymethylphthalimide, and phthalic acid) in olive fruits. After testing different sorbents and eluents for MSPD extraction, C_{18} and acetonitrile were found to be the most appropriate for clean-up of the samples, in terms of yields and efficient removal of interfering compounds. All analytes were determined in selective ion monitoring (SIM) mode following a derivatization step with *N*,*O*-bis-trimethylsilyltrifluoroacetamide (BSTFA) containing 1% of trimethylchlorosilane (TMCS), except for phosmet and phosmet-oxon which were analyzed directly. The method showed suitable linearity (correlation coefficients higher than 0.8919 for all the compounds) and suitable sensitivity (limit of detection lower than 0.06 mg/kg). It was successfully applied in the analysis of olive fruits collected during the preharvest interval and olive oil. Phosmet residues found in all samples were lower than the maximum residue limits established by legislation (2 mg/kg).

Keywords: Phosmet; Metabolites of phosmet; GC/MS; Olives; MSPD

1. Introduction

Phosmet [*N*-(mercaptomethyl)phthalimide-*S*-(*O*,*O*-dimethylphosphorodithioate)] is a nonsystemic organophosphate insecticide belonging to the phosphorodithioate subclass of organophosphates [1]. It is used in control of olive fruit fly (*Bactrocera oleae* Gml.) one of the pests that attack olive trees, reducing the production and the quality of the olive oil. Taking into account that the olive oil are products recognized by their high prices and excellent nutritional and biological properties, a strict control to protect consumers is necessary.

When sprayed on crops, phosmet is subject to photodegradation, microbial and chemical degradation reactions [2–5]. Although some degradation products of the pesticides can be less toxic and harmless, it is not uncommon for them to be more toxic than the parent pesticides. Indeed, the evaluation of the degradation products is important from the point of view of human health and environmental protection.

Toxic effects associated with exposure of phosmet are related to its irreversible inhibition of the acetylcholinesterase enzyme, which causes acute effects in humans [6]. To ensure consumer protection, the Codex Alimentarius Commission of Food and Agriculture Organization (FAO), the World Health Organization (WHO) and the European Union (EU) have established maximum residue limits (MRLs); in Portugal the MRL for phosmet in olives is 2 mg/kg [7].

In recent years a strong research effort has been done to identify the products arising from photodegradation of phosmet. Tanabe et al. [8] irradiated phosmet in diethyl ether and have identified *N*-methylphthalimide and *N*-methoxymethylphthalimide as its main degradation products. Weintraub et al. [9,10] described phosmet's photolysis on silica gel plates and on apples. More recently, Sinderhauf and Schwack [11–13] studied the photholysis mechanism of phosmet in model solvents (cyclohexane, cyclohexene and 2-propanol) and in fatty acid methyl esters (methyl stearate, methyl oleate, 12-hydroxymethyl stearate) simulating the structural characteristics found in wool wax. The obtained photoproducts generally include phthalimide, *N*-hydroxymethylphthalimide and *N*-methoxymethylphthalimide. Beside these, other com-

* Corresponding author. Tel.: +351 222078910; fax: +351 222003977.
E-mail address: sara.cunha@ff.up.pt (S.C. Cunha).

0039-9140/$ – see front matter © 2007 Elsevier B.V. All rights reserved.
doi:10.1016/j.talanta.2007.04.014

pounds such as *N*-hydroxyphthalimide, phthalic acid and phthalamic acid are also metabolites of phosmet in plants [14]. Unfortunately, there is a lack of methods for efficient determination of phosmet residues and its metabolites simultaneously.

Up to now, the scientific literature does not contain descriptions of methodologies employing GC/MS to quantify phosmet residues and its metabolites. Commonly, phosmet and its oxygen analogue are determined in food associated with other pesticide residues using several methods based on either gas-chromatography (GC) with nitrogen–phosphorus (NPD) [15,16], mass spectrometry (MS) [17,18] and MS/MS [19–21] detection or liquid chromatography (LC) with ultraviolet (UV) [22] and MS [10] detection. Most of the methods employed a previous extraction and/or purification step, which is essential when dealing with olives or olive oil, due to the presence of high molecular non-volatile components such as triglycerides. These components will condense in the injection port of the GC or in front of the capillary column, resulting in reduced chromatographic separation efficiency, and causing a sample matrix-induced enhancement effect [23,24].

Some authors have reported the use of liquid–liquid extraction (LLE) with acetonitrile [25] or hexane–acetonitrile partitioning [26] to remove the interferences in olives and olive oil. This type of extraction may provide adequate separation of the compounds from the matrix, but are often expensive in terms of time, labor, material used and organic solvent disposal cost. Therefore, solid-phase extraction (SPE) [12,27–30], matrix solid-phase dispersion (MSPD) [31] and gel permeation chromatography (GPC) [20,32–35] have been recently applied, offering alternative solutions to the LLE problems. All of these methods allow a rapid and efficient extraction of several pesticide residues from olives and olive oil although none of them were validated for phosmet metabolites. Recently, the methodology proposed by Diserens [28] (extraction of phosmet residues carried out in a SPE Extralut cartridge followed by secondary clean-up in a C_{18} cartridge) was used by Sinderhauf and Schwack [12] to quantify phosmet residues and its metabolites without any derivatization procedure in wool wax by LC/MS. However, the authors did not present any comments about the optimization or validation of the method.

The aim of this work was the development of a method to determine phosmet residues and its metabolites in olive fruits. The methodology entailed the use of a MSPD procedure for sample preparation followed by GC/MS determination of phosmet and its metabolites mostly as trimethylsilyl derivatives. The method was applied to measure the levels of phosmet residues and its metabolites in olive fruits and in olive oil.

2. Experimental

2.1. Chemicals

Phosmet, phosmet-oxon, phthalimide (Pi) (Dr. Ehrenstorfer, Augsburg, Germany), *N*-hydroxyphthalimide (PiOH), *N*-hydroxymethylphthalimide (PiMOH) (Fluka, Neu-Ulm, Germany), phthalic acid (Pa) and phthalamic acid (PaA) (Aldrich, St. Louis, MO, USA) were used as standards of analytical quality.

The internal standards were IS_1: *N*-hydroxyethylphthalimide (PiEOH), IS_2: tributylphosphate (TBP), IS_3: triphenylphosphate (TPP) and IS_4: *N*-hydroxypropylphthalimide (PiPOH), all from Aldrich.

The sorbents used for MSPD were C_{18} (55–105 μm, Waters, Milford, MA, USA), which was washed with methanol and water before use, silica gel (70–230 mesh pore size), alumina (60–325 mesh pore size), and aminopropyl silica gel–NH_2 (~9 nm pore size), from Sigma (St. Louis, MO, USA). Anhydrous $MgSO_4$ was analytical grade from Riedel-de Haën (Buchs, SG, Schweiz). To ensure efficient extraction of phthalates and residual water, $MgSO_4$ was kept for 5 h at 500 °C in a muffle furnace. SPE Extralut 3 was from Merck (Darmstadt, Germany).

The derivatization reagents *tert*-butyldimethylchlorosilane (TBDMCS), *N*-(*tert*-butyldimethylsilyl)-*N*-methyltrifluoroacetamide (MTBSTFA) with 1% of TBDMCS, *N*,*O*-bis-trimethylsilyltrifluoroacetamide (BSTFA) with 1% of trimethylchlorosilane (TMCS) and trimethyl orthoacetate (TMOA) were provided from Sigma. 2,3,4,5,6-Pentafluorobenzoyl chloride and pyridine were from Fluka. All other chemicals were analytical grade or for residue analysis from the same suppliers.

2.2. Standards

Individual standard stock solution of phosmet, Pi, PiOH, PiMOH, Pa, PaA, PiEOH, PiPOH, TBP and TPP (100 mg/l) were prepared in acetonitrile and stored at −20 °C. Phosmet-oxon (10 mg/l) was prepared in isooctane, flushed with nitrogen, and stored at −20 °C. Chromatographic standards were prepared by spiking blank samples with known amounts of pesticides.

2.3. Samples

The trial was carried out with olives of *Cv*. Cobrançosa from two pilot olive groves with 2.4 ha and 1.9 ha, in northeast of Portugal. One olive grove did not undergo any phytosanitary treatment and the other was treated with Fosdan 50, with a minimum of 50% of phosmet. The insecticide mixture was prepared as recommended by the manufacturer at the dose of 100 g a.i. ha^{-1} of Fosdan 50, being the application performed with an air blast sprayer. Sampling started 1 week after the treatment on 26 October 2004, and was repeated weekly until finished on 6 December 2004. Approximately 500 fruits were collected from 10 trees (50 per plant). They were then mixed together and stored at −20 °C until analysis. Before analysis the fruits were cut, pitted with a knife and homogenized in a chopper. Then, about 15 g of olive pulp was homogenized in an Ultra-turrax blender for 2 min at 8000 rpm.

Olive oil were obtained following the method described by Matos et al. [35]. Briefly, olive fruits from the same olive groves were handpicked and processed through a mill, a thermobeater and a pulp centrifuge, after which the oil was separated from the pulp by decantation, and kept in dark glass bottles at 4 °C in the absence of light.

2.4. Sample preparation

An aliquot (~0.5 g) of homogeneous sample was transferred into a mortar and blended gently with 2 g of C_{18} sorbent, 0.25 g of $MgSO_4$, 25 μl of IS_1 solution (PiEOH at 20 mg/l) and 25 μl IS_2 solution (TPP at 20 mg/l). The homogenous mixture was transferred into a glass cartridge covered with a filter paper (Whatman no. 2, Maidstone, UK). Another filter paper was placed on the top of the sample mixture. The analytes were eluted with 15 ml of acetonitrile, and finally the eluent was evaporated until dryness under a stream of nitrogen. The obtained extract was re-dissolved in 1 ml of acetonitrile. An aliquot of 250 μl added with 25 μl of IS_3 solution (TBP at 10 mg/l) was used for GC/MS analysis of phosmet and phosmet-oxon and other aliquot of 250 μl added with 25 μl of IS_4 solution (PiPOH at 10 mg/l) was derivatized in order to analyze the metabolites of phosmet by GC/MS.

2.4.1. Silylation procedure

After the extraction, 250 μl of the extract plus 25 μl of IS_4 were transferred into a silanized screw-cap vial (Supelco, Bellefonte, PA, USA) and evaporated under a gentle nitrogen stream. Then, 125 μl of BSTFA (with 1% TMCS) and 50 μl of pyridine were added to the dry residue, the mixture vortexed for about 10 s, and heated at 75 °C for 30 min on a "Reacti-therm" heating block (Pierce, Rockford, IL, USA). After cooling, 1 μl aliquots were directly injected into the gas chromatograph.

2.5. Gas chromatography/mass spectrometry analysis

GC/MS analyses were performed on an Agilent (Little Falls, DE, USA) gas chromatograph 6890 equipped with an electronically controlled split/splitless injection port and interfaced to a MSD-5973N mass selective detector. The chromatograph was equipped with a DB-5MS fused silica capillary column (30 m × 0.25 mm, 0.25 μm film thickness; J&W Scientific, Folsom, CA, USA) coupled directly to the mass detector.

Injection was performed at 250 °C in the pulsed splitless mode with a purge off time of 1 min. The glass liner was fitted with a carbofrit plug from Restek (Bellefonte, PA, USA). Helium was used as carrier gas, with a constant flow of 1 ml/min. The oven temperature was: 120 °C held for 1 min, ramp to 280 °C at 10 °C/min held for 20 min and finally ramp to 300 °C at 15 °C/min and held for 3 min. The MS detector was operated at ionization energy of 70 eV. The temperatures of the ion source, quadrupole, and transfer line were 150 °C, 230 °C, and 280 °C, respectively. The detector was switched off in the initial 4 min avoiding damage to the filament. Data acquisition was performed in the full-scan mode during the optimization of the method (mass range 50–600). The quantification was carried out in selective ion monitoring mode (SIM). Dwell time was 30 ms allowing at least 1.69 cycles/s. The overall system was controlled by Agilent MS Chemstation G2578A Software.

3. Results and discussion

3.1. Optimization of the extraction conditions

Based on the literatures [30,36,37], different polar sorbents (e.g. silica, alumina, florisil, and NH_2) were tested first as phases for matrix dispersion. All of them were unsuccessful in the simultaneous extraction of all the studied compounds (Table 1). Therefore, an apolar sorbent C_{18}, was tested, and the results were satisfactory as shown in Table 2. The importance of using lipophilic bonded-phases for the success of MSPD procedures was previously highlighted by Barker [38,39]. The author suggested that lipophilic phases lead to the formation of a new phase that resembles a cell membrane bi-layer assembly, giving unique dispersion characteristics. After the initial good results had been obtained, different amounts of C_{18} (from 1 g to 3 g) were further evaluated, as well as different quantities of anhydrous $MgSO_4$ (from none to 2 g). The addition of $MgSO_4$ was assayed due to its ability to bind large amounts of water, which promoted partitioning of pesticides into to the organic layer as showed by Anastassiades et al. [40]. The combination of 2 g of C_{18} with 0.25 g of $MgSO_4$ was found to be the best solution, providing good recoveries for all the compounds and a minimal presence of interferents.

To evaluate the influence of the solvent in MSPD extraction with C_{18} phase, *n*-hexane, acetone, ethyl acetate, acetonitrile, acetonitrile with 0.5% of acetic acid and acetonitrile with 2% of acetic acid were tested. MSPD elution as described, with *n*-

Table 1
Relative responses (100% = normalized peak area in C_{18}) of recoveries and relative standard deviation (R.S.D.) of phosmet, phosmet-oxon and other metabolites *tert*-butyldimethylsilyl derivatives (TBS) obtained in spiked olives at 2 mg/kg using MSPD with different sorbents 10 ml of acetonitrile ($n = 3$)

Compounds	Sorbents (1 g)							
	Silica		Alumina		Florisil		NH_2	
	Recovery (%)	R.S.D. (%)	Recovery (%)	R.S.D. (%)	Recovery (%)	R.S.D. (%)	Recovery (%)	R.S.D. (%)
Phthalimide	77	6	77	9	13	15	98	8
N-Hydroxyphthalimide	88	7	95	8	77	9	35	8
Phthalic acid	70	10	70	5	63	7	93	7
N-Hydroxymethylphthalimide	68	10	80	7	98	5	60	5
Phthalamic acid	125	11	49	10	61	8	84	15
Phosmet	65	15	64	9	68	10	88	12
Phosmet-oxon	78	11	82	13	73	10	98	10

Table 2
Comparison of the *tert*-butyldimethylsilyl derivatives (TBS), phosmet and phosmet-oxon recoveries using MSPD (2 g of C_{18} with 0.25 g of $MgSO_4$ and 15 ml of acetonitrile) and SPE extraction in spiked olives at 2 mg/kg, analyzed by GC/MS in SIM mode

Compounds	MSPD[a]		SPE[a]	
	Recovery (%)	R.S.D. (%)	Recovery (%)	R.S.D. (%)
Phthalimide (TBS)	77	6	78	6
N-Hydroxyphthalimide (TBS)	110	6	79	7
Phthalic acid (TBS)	109	8	81	9
N-Hydroxymethylphthalimide (TBS)	85	6	75	10
Phthalamic acid (TBS)	85	8	79	9
Phosmet	75	11	66	12
Phosmet-oxon	71	13	67	14

[a] Recoveries are expressed as (mean ± R.S.D.) % for $n = 3$.

hexane, acetone and ethyl acetate, showed many interferences, as visualized by the yellow color of the extracts after solvent evaporation and by the number and intensity of peaks reported by GC/MS analysis. Although acetonitrile with 0.5% and 2% of acetic acid allowed the extraction of phosmet and its metabolites with minor quantities of visible interferences, elution with acetonitrile alone gave the highest recoveries for all the compounds. Finally, the elution was carried out with different volumes (from 5 ml to 30 ml) to establish the best elution procedure. When elution volumes greater than 15 ml were applied, no increases in the peak areas for the compounds were observed. Decreasing the elution volumes to 10 ml or less had an adverse effect on the recovery. In view of these results, 15 ml was the elution volume chosen.

The extraction steps for olive oil was not thoroughly optimized, but the use of the same extraction conditions of olives showed good results. The optimized MSPD extraction procedure was considered enough to obtain a clean extract. However, in order to prevent eventual damage in chromatographic system by the lipidic interferences, a carbofrit plug was placed in the injector.

3.2. MSPD versus SPE procedure for olives

In order to evaluate the developed MSPD procedure, the SPE methodology proposed by Diserens [28] and applied by Sinderhauf and Schwack [12] in the determination of phosmet and its metabolites was used for olives. For this experiment 10 g of blank samples were spiked with a standard mixture at 2 mg/kg of all the studied compounds, same concentrations as those used in the MSPD and added with 5 ml of light petroleum (b.p. 40–60 °C) After homogenization, an aliquot (∼5 ml) of the solution was loaded to the Extralut column and eluted with 6× 5 ml of acetonitrile saturated with light petroleum. The collected eluate was loaded onto a C_{18} column and eluted with 6× 2 ml of acetonitrile. The eluate was then evaporated to dryness under a stream of nitrogen. The obtained extract was treated according to the procedures described for the samples subjected to MSPD extraction.

To evaluate recoveries, standard working mixtures underwent the MSPD and SPE procedures. In general, the recoveries of SPE were worse than those obtained with the MSPD extraction procedure, as shown in Table 2.

3.3. Optimization of the derivatization conditions

It was verified that the direct GC analysis of PiOH, PiMOH, PiEOH and PiPOH was not possible, resulting in a single peak with the same retention time for all the referred compounds, identified by its mass spectrum as phthalimide. In order to prevent the degradation reactions that probably occur inside the GC system, and to make possible the detection of all the compounds, a derivatization procedure was implemented.

Several metabolites of phosmet have polar functional carboxylic acid and/or amide groups which can be derivatized (Fig. 1). Therefore, different derivatization techniques, such as esterification/acetylation (trimethyl orthoacetate) [41], acylation (pentafluorobenzoyl chloride) [42] and silylation (BSTFA and MTBSTFA) [43] were tested (data not shown). Silylation, reported in literature as the most versatile technique currently available for enhancing GC analysis [43], was found to be the simplest and most sensitive for derivatization of these compounds.

Several silylating reagents, namely *N*,*O*-bis-trimethylsilylacetamide (BSA), *N*-methyl-*N*-trimethylsilylfluroacetamide (MSTFA), BSTFA (with 1% TMCS), and MTBSTFA (with 1% TBDMCS) were evaluated. They have been tested at different conditions (amount of silylating reagent, temperature and time of reaction). For all the experiments a mixture containing all the tested compounds in a concentration of 2 mg/kg each was used.

Generally, most of the *tert*-butyldimethysilyl derivatives showed greater peak areas and a more specific and favorable fragmentation pattern in MS than trimethysilyl derivatives. However, PiMOH remained underivatized for all combinations of MTBSTFA, solvent, temperature and time tested. We also found that the addition of 2%, 5% and 10% TBDMCS as a catalyst is not suitable to derivatize PiMOH (data not shown). The different results obtained with BSTFA (with 1% TMCS) and MTBSTFA (with 1% TBDMCS) in the derivatization of PiMOH cannot be easily explained. In fact, derivatization of PiMOH leads to Pi. A further investigation is required to understand the observed differences. Thus, the option for BSTFA (with 1% TMCS) as silylating reagent was used in the final method.

The use of BSTFA was optimized by testing several amounts of BSTFA (from 50 μl to 250 μl), several combinations of temperature (from room temperature to 120 °C) and time of reaction

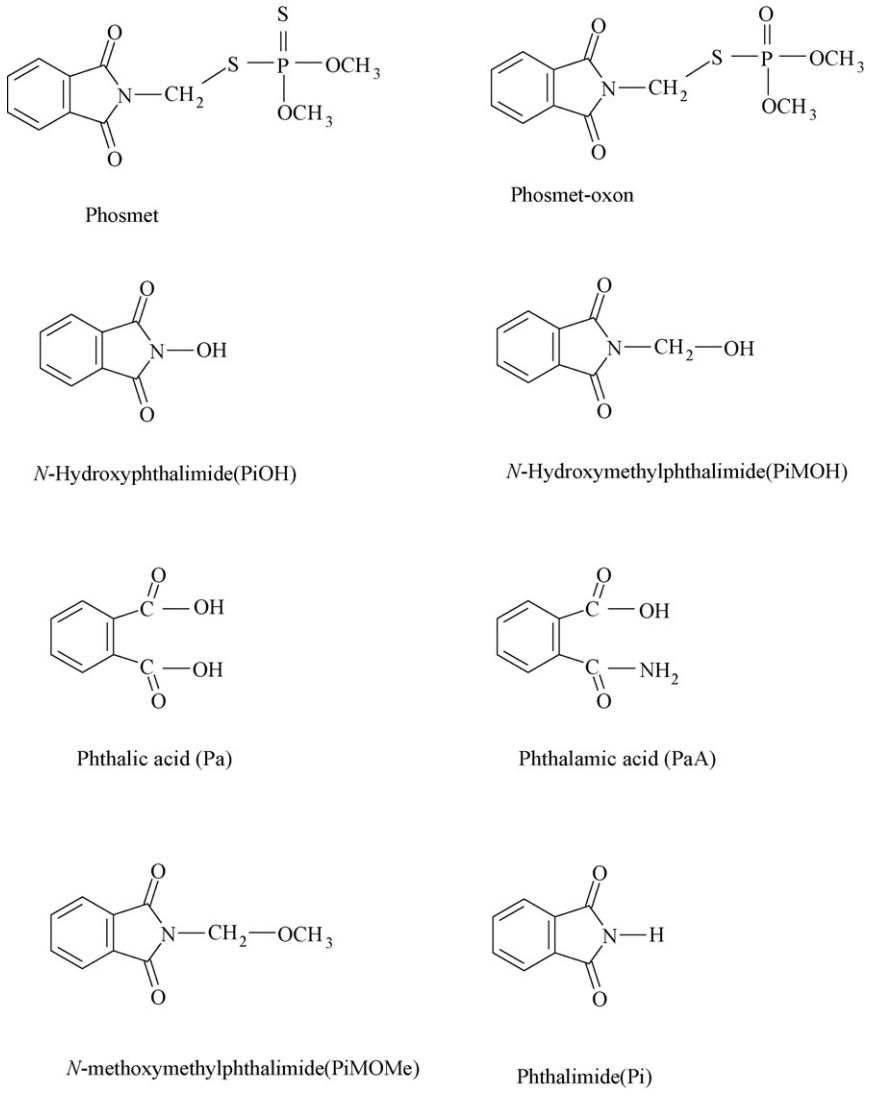

Fig. 1. Structures of phosmet and its metabolites.

(from 10 min to 30 min) and the use of pyridine as additional solvent.

The maximum derivative yield, was obtained using 125 μl of BSTFA with 50 μl of pyridine. It was verified that 75 °C for 30 min were necessary to achieve complete derivatization of all the metabolites of phosmet in the study.

The derivatives were kept at −18 °C and periodically injected over a 3-day period in order to monitor their stabilities. All compounds derivatized were stable at least 3 months.

For all the conditions studied, the derivatization always causes degradation of phosmet and phosmet-oxon thus these compounds should be analyzed directly after the MSPD extraction procedure.

3.4. Identification and quantification of phosmet and its metabolites in SIM mode

In order to identify the metabolites of phosmet present in real olive samples two aliquots of an extract obtained from a sample collected the day after treatment with Fosdan 50 were analyzed using full-scan MS (scan range from *m/z* 50–600) without derivatization and after derivatization with BSTFA (with 1% TMCS). Phosmet and Pi, PiMOH, *N*-methylthiomethylphthalimide and *N*-methoxymethylphthalimide derivatives were detected in the sample. Phosmet-oxon, PiOH, Pa and PaA were not detected in the sample analyzed, but was considered important and its inclusion in the validation study takes into consideration the reported literatures [10–12]. However, facing the commercial unavailability of some standards, the quantification performed in SIM mode was achieved only for phosmet, phosmet-oxon and Pi, PiOH, PiMOH, Pa and PaA derivatives. For each compound, at least, a target ion and three qualifying ions were chosen on the basis of their abundance and selectivity. The ions monitored in the SIM mode and the typical retention times are presented in Table 3.

In this study, two internal standards PiEOH and TPP were used for quantification of the phosmet metabolites derivatives, and phosmet and phosmet-oxon, respectively. TBP and PiPOH were internal standard used in monitoring the consistency of the chromatographic conditions.

Table 3
Ions monitored in SIM mode for quantification and confirmation of the compound

Analyses	Time group (min)	Compounds	Retention time (min)	*m/z* (Rel.Ab.%)	
				Ion quantification	Other ions
First injection	4.00	Phthalimide (TBS)	9.41	204 (100)	160 (23), 130 (26), 102 (18)
		N-Hydroxyphthalimide (TBS)	10.54	220 (100)	146 (30), 221 (16), 102 (7)
	9.65	Phthalic acid (TBS)	10.76	295 (20)	147 (100), 73 (28), 148 (15)
		N-Hydroxyethylphthalimide (TBS-IS_1)	11.08	248 (100)	73 (63), 204 (60), 130 (20)
		N-Hydroxymethylphthalimide (TBS)	11.32	234 (66)	204 (100), 160 (19), 130 (18)
	116	*N*-Hydroxyproplylphthalimide (TBS-IS_4)	12.15	262 (100)	130 (27), 160 (25), 263 (20)
		Phthalamic acid (TBS)	12.31	294 (36)	147 (100), 192 (72), 73 (44)
Second injection	4.00	Tributylphosphate (IS_2)	13.12	99 (100)	155 (27), 211 (19), 57 (11)
		Triphenylphosphate (IS_3)	15.28	326 (100)	325 (87), 77 (28), 215 (20)
		Phosmet-oxon	16.04	160 (100)	161 (10), 93 (5), 317 (5)
		Phosmet	16.16	160 (100)	161 (10), 104 (5), 301 (5)

Relative abundance in percentage (Rel.Ab.%).

The low-polarity DB5-MS analytical column offered high chemical and thermal stability which permitted raising the GC temperature high enough without significant column bleed. The loss of analytic response (namely, formation of double peaks) was noted when the initial temperature column was lower than 100 °C.

3.5. GC/MS method validation

Experiments were carried out in order to assess the possible matrix effect on the chromatographic response. Comparing the slopes of the calibration in standard solutions with those obtained in matrix-matched standards, the method showed only a slight suppression of response for all the compounds studied, not an enhancement. This effect, had been observed previously [34,44], could be attributed to the presence of fat traces in the final extract.

Therefore, the linearity in olives and olive oil was calculated using matrix-free calibration (standards added to blank samples) by analyzing in triplicate six concentrations levels, between 0.25 mg/kg and 2 mg/kg. The correlation coefficients obtained were satisfactory higher than 0.89 for the olives and higher than 0.90 for the olive oil (Table 4).

The precision in olives and olive oil was determined by analyzing spiked blank samples (2 mg/kg) using six replicates. The relative standard deviation (R.S.D.) are for most of the compounds less than 20%, as can be seen in Table 4.

The detection limits of the method were determined by successive analyses of chromatographic extracts of olive samples with decreasing amounts of the compounds until a signal-to-noise ratio 3:1 was reached [45]. The results were: 0.010 mg/kg for phosmet and for PiMOH, 0.05 mg/kg for phosmet-oxon, 0.005 mg/kg for Pi, 0.015 mg/kg for PiOH, 0.03 mg/kg for Pa and 0.06 mg/kg for PaA. The limit of quantifications were established as the lowest concentration assayed quantified with acceptable accuracy and precision [45]. The results were 0.10 mg/kg for phosmet, for phosmet-oxon and for PiMOH, 0.075 mg/kg for Pi, 0.15 mg/kg for PiOH and for PaA and 0.070 mg/kg for Pa, which gave levels well below the MRL set by legislation for phosmet.

Recoveries of the proposed method were determined in triplicate at three different concentration levels in spiked samples of olives, using a matrix-free calibration. The results, given in Table 5, provide evidence that the method achieves acceptable quantitative recoveries of all compounds, from 65% to 98%. The recovery studied in olive oil was performed by analyzing spiked

Table 4
Linearity and precision (R.S.D. %) of the method in olive fruits and olive oils analyzed by GC/MS in SIM mode

Compounds	Concentration range (mg/kg)	Linearity				R.S.D. (%)[a]	
		Olives		Olive oil		Olives	Olive oil
		Equation	*r* (R.S.D.[b])	Equation	*r* (R.S.D.[b])		
Phthalimide (TBS)	0.25–2	$y = 11.992x$ (4)	0.9563 (2)	$y = 10.11x$ (7)	0.9412 (1)	10	9
N-Hydroxyphthalimide (TBS)	0.25–2	$y = 1.8541x$ (10)	0.9290 (3)	$y = 2.2476x$ (13)	0.9847 (3)	12	10
Phthalic acid (TBS)	0.25–2	$y = 3.3274x$ (15)	0.8999 (6)	$y = 3.7526x$ (10)	0.9689 (3)	12	10
N-Hydroxymethylphthalimide (TBS)	0.25–2	$y = 1.0427x$ (11)	0.9462 (3)	$y = 1.5285x$ (12)	0.9654 (2)	9	9
Phthalamic acid (TBS)	0.25–2	$y = 2.5547x$ (10)	0.8919 (5)	$y = 2.7779x$ (10)	0.9080 (2)	10	11
Phosmet	0.25–2	$y = 4.2436x$ (11)	0.9212 (4)	$y = 4.8634x$ (12)	0.9390 (5)	8	10
Phosmet-oxon	0.25–2	$y = 1.2224x$ (9)	0.9261 (4)	$y = 1.5464x$ (12)	0.9290 (5)	14	16

[a] Spiked at 2 mg/kg ($n = 6$).
[b] $n = 3$.

Table 5
Mean recoveries and R.S.D. in olives ($n = 3$) at three concentrations levels obtained by GC/MS in SIM mode

Compounds	Amount Added (mg/kg)	Olives	
		Recovery (%)	R.S.D. (%)
Phthalimide (TBS)	0.15	89	10
	0.3	91	11
	0.6	68	8
N-Hydroxyphthalimide (TBS)	0.15	80	4
	0.3	89	6
	0.6	98	6
Phthalic acid (TBS)	0.15	68	12
	0.3	73	10
	0.6	97	8
N-Hydroxymethylphthalimide (TBS)	0.15	82	7
	0.3	84	8
	0.6	97	8
Phthalamic acid (TBS)	0.15	84	10
	0.3	76	8
	0.6	68	10
Phosmet	0.15	73	8
	0.3	85	8
	0.6	84	9
Phosmet-oxon	0.15	65	12
	0.3	72	11
	0.6	76	10

blank olive oil (2 mg/kg). The results were 74% for phosmet, 70% for phosmet-oxon, 82% for Pi, 79% for PiMOH, 84% for PiOH, 102% for Pa, 105% for PaA.

3.6. Analysis of phosmet and its metabolites in olives and olive oil

The developed method was applied to several samples of olive fruits colleted along the preharvest interval and in olive oil obtained from olive fruits colleted in the end of the pre-harvest interval after a treatment with phosmet. The results are presented in Table 6. Fig. 2 shows the typical chromatograms of the metabolites detected in olive fruits using the derivatization process.

The concentrations of phosmet residues found in all the samples were always lower than the limit established by legislation [7]. Pi, PiMOH, Pa and phosmet-oxon were the metabolites determined in olive fruits during the preharvest interval. The metabolites herein reported have some differences when compared with those previously reported for wool wax by Sinderhauf and Schwack [12] which detected Pi and *N*-methoxymethylphthalimide as photodegradation products. The qualitative differences verified can be explained by the matrix type and the determination technique employed.

As can be seen in Table 6 for the olives, the Pi concentrations ranged from 0.097 mg/kg to 0.113 mg/kg, PiMOH and from 0.320 mg/kg to 1.1691 mg/kg. Pa was detected 3 weeks after the treatment and it concentrations ranged from 0.072 mg/kg

Table 6
Quantification of phosmet and its metabolites in olive fruits and olive oil analyzed by GC/MS in SIM mode

Samples	Date of collection	Compound (mg/kg)						
		Derivatives						
		Phthalimide	Hydroxyphthalimide	Phthalic	Phthalic	Hydroxymethylphthalimide	Phosmet	Phosmet-oxon
Olives	26 October 2004	0.097	n.d.	n.d.	n.d.	0.320	0.21	n.d.
	2 November 2004	<LOQ	n.d.	n.d.	n.d.	0.245	<LOQ	0.20
	8 November 2004	<LOQ	n.d.	0.072	n.d.	0.355	<LOQ	n.d.
	16 November 2004	<LOQ	n.d.	0.242	n.d.	0.458	<LOQ	n.d.
	22 November 2004	<LOQ	n.d.	0.243	n.d.	0.518	<LOQ	n.d.
	29 November 04	0.100	n.d.	0.215	n.d.	1.691	<LOQ	<LOQ
	6 December 2004	0.113	n.d.	0.852	n.d.	1.445	<LOQ	<LOQ
Olive oil		0.184	n.d.	0.987	n.d.	1.887	<LOQ	<LOQ

n.d.: not detected; <LOQ: lower than limit of quantification.

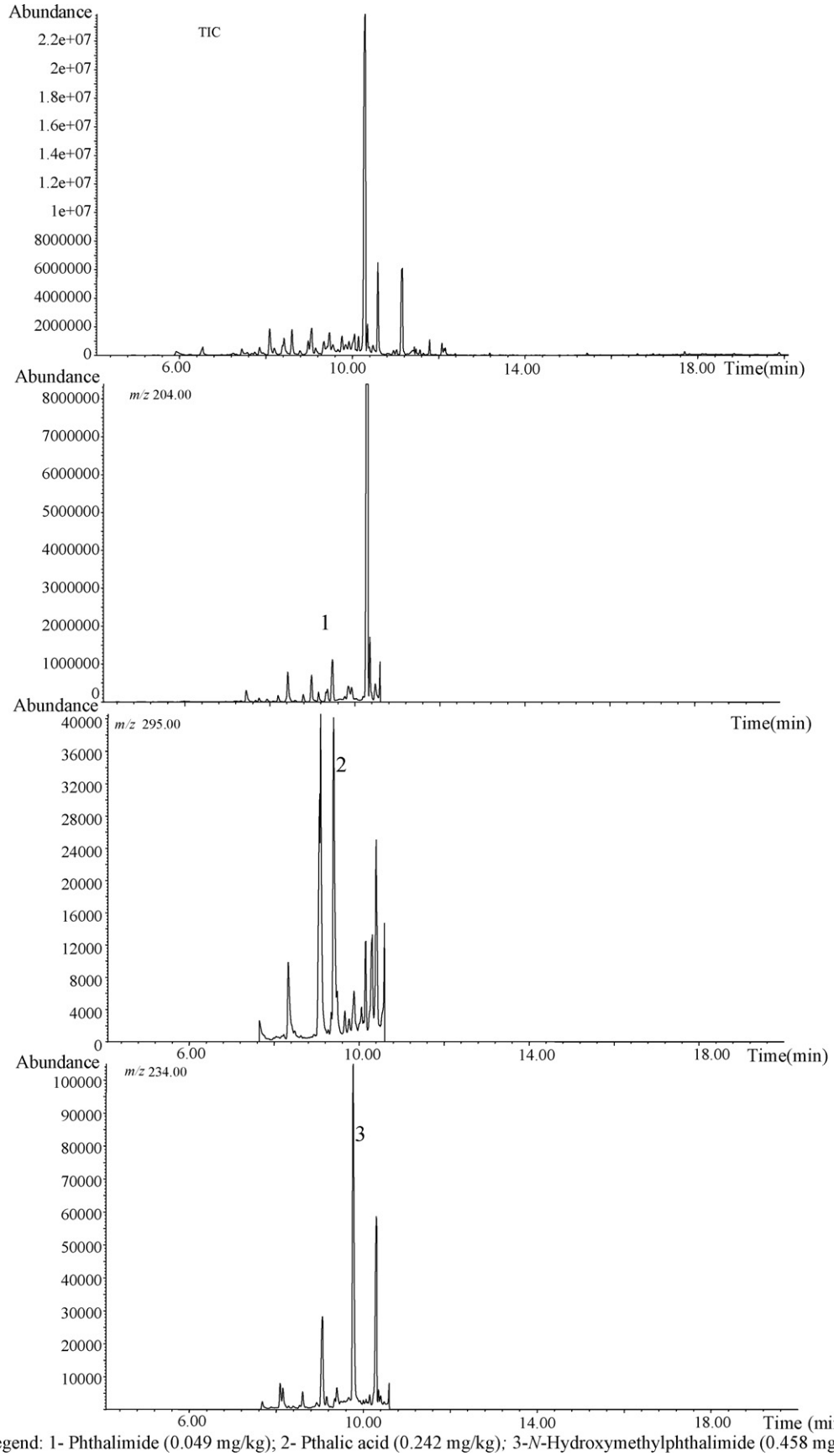

Fig. 2. Total ion compound (TIC) chromatogram of an olive fruit using the derivatization process, together with individual chromatograms in selective ion monitoring mode.

to 0.852 mg/kg. The highest concentration values for all compounds, exception made for PiMOH, was found in the last week of collection. With respect to phosmet-oxon, it was found in three alternate weeks of collection with concentrations ranging from lower than LOQ to 0.020 mg/kg.

In relation to olive oil, the levels of some compounds (Pi, PiMOH, and Pa) are higher than those reported in olives, which is understandable considering that to obtain 1 l of olive oil, 5 kg of olives were typically needed.

4. Conclusions

The presented study showed that phosmet and its metabolites can be efficiently extracted from olives and olive oil using a MSPD extraction procedure. C_{18} with $MgSO_4$ as matrix sorbents have advantageous effects on extraction yields compared with polar sorbents such as silica, alumina, florisil or aminopropyl. In general, the results from the described experiments indicate that MSPD extraction is a good option instead of SPE procedures.

The analysis of phosmet and its metabolites by GC/MS involved overcoming some drawbacks namely the fact of PiOH, PiMOH, PiEOH and PiPOH degraded into phthalimide when directly analyzed. The solution found was the derivatization with BSTFA (with 1% TMCS) and pyridine. It allows a good sensitivity and high precision.

The method was applied in evaluation of phosmet residues and its metabolites in olives during the preharvest interval and in olive oil. The results showed that phosmet concentrations were always lower than the maximum limits of residues established by Portuguese legislation. The metabolites phosmet-oxon, Pi, PiMOH and Pa were found in the samples and in general its concentrations increased along the preharvest interval.

Acknowledgments

S.C.C. is grateful to “Subprograma Ciência e Tecnologia do 3° Quadro Comunitário de Apoio (BD 8822/2002)” and to “Acção 8.1. PO AGRO no. 482” for financial support.

References

[1] C.D.S. Tomlin (Ed.), The Pesticide Manual, 13th ed., BCPC, Alton, UK, 2003, p. 772.
[2] M. Purdey, Med. Hypoth. 50 (1998) 91.
[3] W. Schwack, Rev. Environm. Contamin. Toxicol. 172 (2001) 129.
[4] H.D. Burrows, M.L. Cane, J.A. Santaballa, S. Steeken, J. Photochem. Photobiol. B 67 (2002) 71.
[5] J. Jauregui, B. Valderrama, A. Albores, R. Vasquez-Duhalt, Biodegradation 14 (2003) 397.
[6] C.N. Pope, J. Toxicol. Environ. Healthy B 2 (1999) 161.
[7] Portaria 649/96 de 12/11/96 reported in Diário da Republica I Série B No. 262, December 11, 1996, pp. 3965–4006.
[8] M. Tanabe, R.L. Dehn, R.R. Bramhall, J. Agric. Food Chem. 22 (1974) 54.
[9] F.P. Weintraub, G.F. Vylegzhanina, L.P. Dron, L.S. Keiser, I.P. Nesterova, F.I. Patrashku, Migr. Prevrashch. Pestits. Ok-ruzhayushchei Srede, Tr. Sov.-Am. Simp., 1976.
[10] F.P. Weintraub, G.F. Vylegzhanina, L.P. Dron, L.S. Keiser, I.P. Nesterova, F.I. Patrashku, Symposium on Environmental Transport and Transformation of Pesticides, EPA, Report EPA 600/9-78-003, US. Environmental Protection Agency, Washington, DC, 1978, pp. 140.
[11] K. Sinderhauf, W. Schwack, J. Agric. Food Chem. 51 (2003) 5990.
[12] K. Sinderhauf, W. Schwack, J. Agric. Food Chem. 52 (2004) 8046.
[13] K. Sinderhauf, W. Schwack, J. Agric. Food Chem. 53 (2005) 4873.
[14] Codex Alimentarius Commission, Codex Alimentarius Pesticide Residues in Food—Maximum Residues Limits, vol. 2B, 2nd ed., FAO/WHO, Rome, 1996.
[15] H. Sabik, R. Jeannot, J. Chromatogr. A 879 (2000) 73.
[16] C. Yagüe, S. Bayarri, P. Conchello, R. Lázaro, C. Pérez-Arquillueĭ, H.A. Ariño, J. Agric. Food Chem. 53 (2005) 5105.
[17] J. Hernandez, N.R. Robledo, L. Velasco, R. Quintero, M.A. Pickard, R. Vasquez-Duhalt, Pestic. Biochem. Physiol. 61 (1998) 87.
[18] T. Okumura, Y. Nishikawa, J. Chromatogr. A 709 (1995) 319.
[19] A.G. Sánchez, N.R. Martos, E. Ballesteros, Anal. Chim. Acta 558 (2006) 53.
[20] E. Ballesteros, A.G. Sánchez, N.R. Martos, J. Chromatogr. A 1111 (2006) 89.
[21] I.N. Tsakiris, T.G. Danis, I.A. Stratis, D. Nikitovic, I.A. Dialyna, A.K. Alegakis, A.M. Tsatsaki, Food Addit. Contam. 21 (2004) 670.
[22] K. Ďulák, F. Jonáš, J. Chromatogr. A 396 (1987) 433.
[23] J. Hajšlová, J. Zrostlíková, J. Chromatogr. A 1000 (2003) 181.
[24] F.J. Schenck, S.J. Lehotay, J. Chromatogr. A 868 (2000) 51.
[25] G. Dugo, G. Di Bella, L. La Torre, M. Saitta, Food Control 16 (2005) 435.
[26] P. Cabras, A. Angioni, M. Melis, E. Minelli, F.M. Pirisi, J. Chromatogr. A 761 (1997) 327.
[27] A.M. Gillespie, S.D. Daly, D.M. Gilvydis, F. Shneider, S.M. Walters, J. Assoc. Off. Anal. Chem. Int. 78 (1995) 431.
[28] H. Diserens, J. Assoc. Off. Anal. Chem. 72 (1989) 991.
[29] L. Rastrelli, K. Totaro, F.D. Simone, Food Chem. 79 (2002) 303.
[30] E. Amvrazi, T.A. Albanis, J. Agric. Food Chem. 54 (2006) 9642.
[31] C. Ferrer, M.J. Gómez, J.F. García-Reyes, I. Ferrer, E.M. Thurman, A.R. Fernández-Alba, J. Chromatogr. A 1069 (2005) 183.
[32] R. Sánchez, J.M. Cortés, J. Villén, A. Vázquez, J. Assoc. Off. Anal. Chem. Int. 88 (2005) 1255.
[33] J.J. Vreuls, R.J.J. Swen, V.P. Goudriaan, M.A.T. Kerkhoff, G.A. Jongenotter, U.A.Th. Brinkman, J. Chromatogr. A 750 (1996) 275.
[34] M. Guardia-Rubio, M.L.F. Córdova, M.J. Ayora-Cañada, A. Ruiz-Medina, J. Chromatogr. A 1108 (2006) 231.
[35] L.C. Matos, S.C. Cunha, J.S. Amaral, J.A. Pereira, M.R. Seabra, M.B.P.P. Oliveira, Food Chem. 102 (2007) 406.
[36] M. Ramil Criado, D. Hernanz Fernández, I. Rodríguez Pereiro, R. Cela Torrijos, J. Chromatogr. A 1056 (2004) 187.
[37] B. Albero, C. Sánchez-Brunete, J.L. Tadeo, J. Chromatogr. A 1007 (2000) 137.
[38] S.A. Barker, J. Chromatogr. A 885 (2000) 115.
[39] E.M. Kristenson, L. Ramos, U.A.T. Brinkman, Trends Anal. Chem. 25 (2006) 96.
[40] M. Anastassiades, S. Lehotay, D. Štajnbaher, F. Schenck, J. Assoc. Off. Anal. Chem. Int. 86 (2003) 412.
[41] C.D. Stalika, G.A. Pilidis, J. Chromatogr. A 872 (2000) 215.
[42] L.Y. Jayasinghe, P.J. Marriot, P.D. Carpenter, P.D. Nichols, J. Chromatogr. A 809 (1998) 109.
[43] K. Blau, Handbook of Derivatives for Chromatography, Wiley, Chichester, 1994, p. 31 (Chapter 3).
[44] S.C. Cunha, S.J. Lehotay, K. Mastovska, J.O. Fernandes, M.B.P.P. Oliveira, J. Sep. Sci. 30 (2007) 620.
[45] SANCO/10232/2006, Quality Control Procedures for Pesticide Residues Analysis. http://europa.eu.int/comm/food/plant/protection/resources/publications_en.htm.

Available online at www.sciencedirect.com
ScienceDirect
Talanta 73 (2007) 458–465
Talanta
www.elsevier.com/locate/talanta

Speciation analysis of antimony in marine biota by HPLC-(UV)-HG-AFS: Extraction procedures and stability of antimony species

Ida De Gregori [a,*], Waldo Quiroz [a], Hugo Pinochet [a], Florence Pannier [b], Martine Potin-Gautier [b]

[a] *Laboratorio de Química Analítica y Ambiental, Instituto de Química, Pontificia Universidad Católica de Valparaíso, Valparaíso, Chile*
[b] *Laboratoire de Chimie Analytique, Bioinorganique et Environnement LCABIE (UMR CNRS 3054), Université de Pau et des Pays de l'Adour, Pau, France*

Received 16 January 2007; received in revised form 9 April 2007; accepted 10 April 2007
Available online 24 April 2007

Abstract

Speciation analysis of antimony in marine biota is not well documented, and no specific extraction procedure of antimony species from algae and mollusk samples can be found in the literature. This work presents a suitable methodology for the speciation of antimony in marine biota (algae and mollusk samples). The extraction efficiency of total antimony and the stability of Sb(III), Sb(V) and trimethylantimony(V) in different extraction media (water at 25 and 90 °C, methanol, EDTA and citric acid) were evaluated by analyzing the algae *Macrosystis integrifolia* (0.55 ± 0.04 μg Sb g^{-1}) and the mollusk *Mytilus edulis* (0.23 ± 0.01 μg Sb g^{-1}). The speciation analysis was performed by anion exchange liquid chromatography (post-column photo-oxidation) and hydride generation atomic fluorescence spectrometry as detection system (HPLC-(UV)-HG-AFS). Results demonstrated that, based on the extraction yield and the stability, EDTA proved to be the best extracting solution for the speciation analysis of antimony in these matrices. The selected procedure was applied to antimony speciation in different algae samples collected from the Chilean coast. Only the inorganic Sb(V) and Sb(III) species were detected in the extracts. In all analyzed algae the sum of total antimony extracted (determined in the extracts after digestion) and the antimony present in the residue was in good agreement with the total antimony concentration determined by HG-AFS. However, in some extracts the sum of antimony species detected was lower than the total extracted, revealing the presence of unknown antimony species, possibly retained on the column or not detected by HPLC-(UV)-HG-AFS. Further work must be carried out to elucidate the identity of these unknown species of antimony.

Keywords: Speciation; Antimony; Extraction; HPLC-HG-AFS; Algae; Mollusk

1. Introduction

Antimony has the notoriety of being a toxic element, its compounds have no known biological role [1,2] and have been listed as priority pollutants by different international or government organizations [3,4]. It has been widely established that its toxicity is dependent on the chemical form in which it is found. Elemental antimony is more toxic than its salts and trivalent antimony compounds are generally more toxic than pentavalent forms.

Methodologies for determination of aqueous antimony speciation in environmental samples based on HPLC separation have been developed and are summarized in a number of recent critical review papers published since 1998 [2,5–8]. However, most of the analytical research related to speciation analysis of antimony in the environment is focused on liquid samples, such as water [9–14] drinking juices [14] and biological fluids [15–17].

The speciation of antimony in solid samples is a particularly challenging task, since direct determinations are generally not possible and the antimony species have to be extracted by suitable procedures, without conversion of species. No specific extraction procedure of antimony species from different solid matrices is reported in the literature. Some analytical methodologies for the chemical speciation of antimony in aqueous extracts of complex solid materials have been described, e.g. soils [9,18–21], airborne particulate matter [22,23], terrestrial plants [24,25], fly ash from coal fuel thermal power stations [26] and marine sediments [27]. Nevertheless, in spite of these advances, the total concentrations of antimony and its speciation analysis in marine biota matrices is scarcely documented

* Corresponding author. Tel.: +56 32 2273168; fax: +56 32 2273422.
E-mail address: idegrego@ucv.cl (I. De Gregori).

0039-9140/$ – see front matter © 2007 Elsevier B.V. All rights reserved.
doi:10.1016/j.talanta.2007.04.015

[28,29]. In a recent paper, Foster et al. [30] presented measurements of total antimony and its speciation in algae, plant and animal tissues. For speciation analysis, antimony was extracted from algae, plant and animal tissues by using water, diluted nitric acid, sodium hydroxide and enzymes. Highly variable amounts of antimony in these extracts were detected. Analyses of DOLT-2 and algae extracts indicated the presence of only inorganic antimony. Furthermore, as in most other previous works, extraction with water showed that Sb(III) was oxidized to Sb(V), which is one of the main difficulties encountered in the speciation of antimony [8,11,13,22,23,27,31–33].

In previous studies we described the optimization of analytical methodologies to carry out the speciation of antimony in sea water [13] and marine sediments [27]. Following our research on speciation of antimony in marine ecosystems, the objective of this work was to optimize the speciation of antimony in algae and mollusk samples by ion exchange HPLC-(UV)-HG-AFS. Attention was centered on the selection of the extracting solution and on the stability of Sb(III), Sb(V) and trimethylantimony(V) species during the extraction process. The efficiency of the extraction process under different conditions was evaluated by analyzing the sum of concentrations of antimony species extracted based on the total concentration determined by HG-AFS, after complete digestion. The selected procedure was applied to the speciation of antimony in Chilean marine biota samples with the highest total concentration of antimony. The mass-balance between the sum of the antimony extracted and the present in the digested extraction residue was established and compared to the total antimony concentration in the algae samples.

2. Experimental

2.1. Instruments

Algae and mollusk samples and reference material (CTA-VTL-2 Virginia Tobacco leaves, CTA Polish Academy of Sciences) were digested in a microwave oven operating system (Microdigest A 300, Prolabo) with an energy output of 0–200 W (0–100% potency, respectively). A continuous flow hydride generation atomic fluorescence spectrometer (Millenium Excalibur, PS Analytical, Orpington, Kent, England) coupled with an antimony boosted discharged lamp (Sb BDHCL Super lamp, Photon, Victoria, Australia) was used for antimony determination. The pre-fixed wavelength of 217 nm was used to monitor the fluorescence.

Speciation analysis of antimony was performed by anion HPLC-(UV)-HG-AFS coupling a Hewlett Packard HPLC (HP 1050) (post-column oxidation) to the continuous flow hydride generation atomic fluorescence spectrometer.

2.2. Chemicals and reagents

All chemicals and reagents used in this study were analytical-grade or higher purity. De-ionized water (18.2 M Ω cm^{-1}) was obtained from a Nanopure system (Barnstead, Dubuque, IA, USA). Glass and polyethylene wares were cleaned by soaking for 1 day in 10% (v/v) nitric acid (analytical grade) and were rinsed several times with de-ionized water before used. Chemicals used for digestion were: nitric acid (65%, w/v, suprapure grade), hydrogen peroxide H_2O_2 (30%, w/v), both purchased from Merck, Darmstadt, Germany, and concentrated tetrafluoroboric acid HBF_4, purchased from Sigma, USA.

Individual stock solutions of antimony species were prepared from potassium hexahydroxy-antimoniate $KSb(OH)_6$ (99.95%), potassium antimonyl tartrate $K(SbO)C_4H_4O_6H_2O$ (99.95%) and trimethylantimony dichloride $(CH_3)_3SbCl_2$ (96%) purchased from Sigma Aldrich (USA), and are termed as Sb(V), Sb(III) and TMSb(V), respectively. Stock solutions of Sb(V) (100 mg L^{-1}) and TMSb(V) (100 mg L^{-1}) were prepared by dissolving the appropriate amount of the respective compounds in de-ionized water and were stored in the dark at 4 °C until use. Standard solution of Sb(III) was prepared freshly before use by dissolving potassium antimonyl tartrate in de-ionized water. Working antimony standards of lower concentration (individual and/or mixed species) were prepared daily, as required, by an appropriate dilution of the stock solution with de-ionized water or with the mobile phase 20 mmol L^{-1} disodium dihydrogen ethylene diamine tetra-acetate salt dihydrate (EDTA) + 2 mmol L^{-1} potassium hydrogen phthalate (KHP), pH 4.5.

For determination of total antimony by HG-AFS, the conditions for the hydride generation system were: carrier solution 1.5 mol L^{-1} HCl prepared from hydrochloric acid (32% (w/w), analytical reagent grade, Merck); $NaBH_4$ 0.75% (w/v) solution prepared daily by dissolving appropriate amounts of powdered $NaBH_4$ (analytical reagent grade Merck) in 0.2% (w/v) NaOH (analytical reagent grade Merck). Sb(V) was reduced to Sb(III) with aqueous solutions of 1% (w/v) L-cysteine (Sigma, USA).

Marine biota samples were extracted by using de-ionized water, methanol (Merck, HPLC purity), 0.1 mol L^{-1} EDTA pH 4.5, or 0.1 mol L^{-1} citric acid, pH 2.0 (Merck).

The chromatographic mobile phases were prepared from analytical grade reagents purchased from Merck. The mixture 20 mmol L^{-1} EDTA + 2 mmol L^{-1} KHP, pH 4.5 was prepared by dissolving appropriate amounts of EDTA and KHP salts in water; diammonium hydrogen phosphate 50 mmol L^{-1}, pH 8.3 was prepared by dissolving the respective solid in water. The mobile phases were filtered on 0.45 μm membrane filters HA type (Millipore) and degassed by sonication before use. $K_2S_2O_8$, 1% (m/v) (99%, Merck), in 1% (m/v) NaOH (Merck) solution was used for photo-oxidation.

2.3. Determination of total antimony

Aliquots of reference material or freeze-dried samples (approximately 0.5 g weighed to 0.1 mg) were transferred into the PTFE digestion vessels. Nitric acid (10 mL) was added to the samples and shaken to mix the contents. Samples were digested in a microwave oven applying the heating program presented in Table 1. After reaching room temperature, the clear digested solutions were quantitatively transferred into 25 mL polyethylene flask and filled to the mark with de-ionized water. Blank

Table 1
Microwave program applied for the digestion of marine biota samples for determination of total antimony

	Step				
	1	2	3	4	5
Reagent	–	–	H_2O_2	HBF_4:H_2O = 4:1	–
Volume (mL)	–	–	4	1	–
Power (W)	20	70	100	140	100
Time (min)	2	3	3	2	3

solutions were prepared by application of the entire digestion procedure.

For the determination of total antimony, an aliquot of diluted digestion solution was transferred into a polyethylene flask. 0.5 mL of L-cysteine (5%, w/v) and 3 mL of concentrated HCl were added and the solution was filled up to 25 mL with de-ionized water. Solutions were allowed to stand 4 h at room temperature before measurements.

Total concentration of antimony in the digested Certified Reference Material and samples was determined by HG-AFS. The SbH_3 was generated in a continuous flow system using $NaBH_4$ 0.75% (w/v) in 0.2% (w/v) NaOH solution (4.5 mL min^{-1}), 1.5 mol L^{-1} HCl as carrier and the analyte solutions (both at 9 mL min^{-1}). Before detection, a supplementary hydrogen flow of 40 mL min^{-1} was injected to maintain the argon/hydrogen diffusion flame stable. The gas flow was dried through a hygroscopic membrane drying tube (Perma Pure product, dryer model MD-110-12 FP). A boosted discharge antimony hollow cathode lamp was used as radiation source of the atomic fluorescence detector. Total concentrations of antimony were determined from a six points calibration curve of Sb(V), by measuring the fluorescence intensity signal. All results were expressed as means ± standard deviation (dry weight).

2.4. Extraction of antimony from algae and mollusk samples

These experiments were performed with the algae sample *Macrocystis integrifolia* (total concentration of antimony 0.55 ± 0.04 μg g^{-1}) and the mollusk sample *Mytilus edulis* (total concentration of antimony 0.23 ± 0.01 μg g^{-1}). Algae and mollusk samples were extracted with de-ionized water (at room temperature and 90 °C), methanol, 0.1 mol L^{-1} EDTA, pH 4.5 and 0.1 mol L^{-1} citric acid pH 2, in a mechanical shaker (horizontal shaker, Junior orbit shaker, Labline instrument) for 2, 4 and 6 h. The mollusk sample was additionally extracted with citric acid at 75 °C.

Aliquots of 0.2 g of lyophilized samples (accurately weighed, in duplicate) were mixed with 10 mL of the extracting solution in polyethylene tubes, followed by centrifugation (30 min at 3000 rpm, Hettich Zentrifugen, model EBA 12) and decanting. The supernatants were filtered through a 0.45 μm membrane filter HA type and cleaned through C-18 cartridges (Millipore). When methanol was used, the solvent was evaporated and the extract water adjusted to 10 mL.

The stability of antimony species during the extraction process was investigated. Aliquots of samples spiked with 20 μg Sb L^{-1} of each antimony species separately (corresponding to 1 μg Sb g^{-1} dry mass) and samples without spiking were submitted simultaneously to the same extraction procedures.

2.5. Antimony speciation

The speciation of Sb(III), Sb(V) and TMSb(V) in the algae and mollusk extracts was carried out by anion exchange high performance liquid chromatography (HPLC-HG-AFS), except for citric acid extracts where a post-column photo-oxidation step was included (HPLC-UV-HG-AFS) [27]. The chromatographic separation was performed using a Hamilton PRP-X100 column (100 mm × 4.1 mm) with a gradient elution program between 20 mol L^{-1} EDTA + 2 mol L^{-1} KHP, pH 4.5 as the first mobile phase and a 50 mol L^{-1} phosphate solution, pH 8.3 as the second one. Aliquots of 100 μL were injected into the HPLC system. The determination of each antimony species was performed by the standard addition method, using peak area measurements. Detailed instrumental parameters and the optimization of the chromatographic separation and detection procedures for antimony species have been described elsewhere [13,27].

3. Results and discussion

3.1. Determination of total antimony

The total antimony concentration in CRM of Virginia Tobacco leaves, algae and mollusk samples was determined by HG-AFS after digestion with HNO_3, H_2O_2 and HBF_4. Samples were digested with oxidizing reagents together with HBF_4 because of the silica content of plants and algae samples [30]. When silicates are not specifically attacked, low recoveries or high standard deviations for antimony are found by HG techniques in samples containing high concentration of silicates. HBF_4 is preferable to HF because both acids have a nearly identical potential for dissolving silicates, and HBF_4 is less hazardous than HF [34,35].

For determination of antimony using HG techniques, antimony should be preferably in the most reactive state: Sb(III). As Sb(V) is the predominant species after digestion in oxidizing conditions, the quantitative pre-reduction of Sb(V) to Sb(III) must be performed. The most common pre-reduction reagents are KI/ascorbic acid, L-cysteine and thiourea. It has been reported that L-cysteine is the most appropriate reagent for this aim, as it enhances the stability of Sb(III) in solution and the efficiency of hydride generation at low acid concentration. Furthermore, compared to KI/ascorbic acid and thiourea, L-cysteine is a stronger chelating reagent which reacts with interfering ions, i.e. Fe(III), Ni(II), Co(II) and Cu(II) [34–36]. The concentration of antimony in aliquots of digested samples solutions pre-reduced by L-cysteine in HCl medium was determined by standard addition.

Table 2
Determination of total antimony concentrations in the CRM analyzed and % recoveries in spiked samples

CRM	Certified ($\mu g\,g^{-1}$)	Found ($\mu g\,g^{-1}$)	% Recovery
Analysis of CRM ($n=4$)			
Virginia tobacco leaves (CTA-VTL-2)	0.312 ± 0.025	0.33 ± 0.02	106 ± 6

Sample	Sb in the sample (ng)	Added (ng)	Found (ng)	% recovery
Recovery studies ($n=4$)				
Algae	20 ± 2	20	38 ± 2	96 ± 5
Mollusk	21 ± 3	20	44 ± 3	107 ± 7

3.1.1. Quality control

Due to the fact that no certified reference material for antimony in marine biota is currently available, the analytical methodology was evaluated by analyzing the CRM CTA-VTL 2 of tobacco leaves and realizing studies of spike and recovery on marine algae and mollusk samples. Results for antimony concentration in the CRM and the recovery spiking test are reported in Table 2. As can be clearly seen, the result for antimony concentration in the CRM agreed well with the reference value. Furthermore, very satisfactory results for the antimony recovery from the algae and mollusk samples were obtained (96 and 107%, respectively), even though the amount of antimony in the algae and mollusk samples was low.

3.1.2. Analytical figures of merit

The calibration curves were obtained from solutions with different concentrations of Sb(V) (50–500 $ng\,L^{-1}$) reduced by L-cysteine. Correlation coefficients for the calibration curves were always better than 0.999. The sensitivity was calculated from the slope of the calibration curve. The detection limit was calculated as the concentration corresponding to 3 times of the standard deviation (3s) of 10 blank solutions, and the quantification limit was based on 10 times the standard deviation (10s). The mean reproducibility expressed as % relative standard deviation (R.S.D.), obtained in 10 measurements performed per day, on 3 different days with fresh solutions of 50 ng Sb(V) L^{-1} was 3%. The method detection and quantification limits were calculated by multiplying the respective value by the dilution factor (sample mass of 500 mg filled up to 25 mL). Aliquots of digested samples were diluted in 1.5 M HCl to fit in the working range. The analytical figures of merit are summarized in Table 3.

Table 3
Analytical figures of merit

Working linear range ($ng\,L^{-1}$)	50–500
Sensitivity (I_{FS} ng^{-1} L)	1209
Correlation coefficient	0.9998
Detection limit ($ng\,L^{-1}$)	7
Quantification limit ($ng\,L^{-1}$)	24
Reproducibility 50 ng Sb(V) L^{-1} (% $n=5$)	3
Method detection limit ($\mu g\,kg^{-1}$)	0.9
Method quantification limit ($\mu g\,kg^{-1}$)	2.9

3.1.3. Determination of total antimony in marine biota samples

In the present study, total antimony concentrations were determined by HG-AFS in different algae (*Rodoficea iridaea laminarioides*, *Rodoficea sarcodiotheca*, *Feoficea colpomenia simosa*, *M. integrifolia*, *Nothogenia fastigiata*, *Ulva rigida*, *Halopteris hordeacea* and *Schimmelmannia plumose*) and mollusk samples (*Perumitilus purpuratus*, *Mytilus chilensis*, *Semele solida*, *Concholepas concholepas* and *Fissurella* spp).

Algae and mollusk samples analyzed by HG-AFS can be divided into two groups: the first set contains low antimony concentrations, ranging in algae samples from 5 to 40 $\mu g\,kg^{-1}$ and in mollusk samples from 7 to 60 $\mu g\,kg^{-1}$. The second set of mollusk and algae samples, collected from a harbor dock with a protection system based on anodes of antimony–lead alloy, clearly presented the highest antimony concentrations, ranging from 200 to 230 and 230 to 1030 μg Sb kg^{-1}, respectively. This second group represents predominantly the anthropogenic antimony contribution.

From all the analyzed marine biota samples, the algae *Macrosystis integrifolia* (total antimony concentration $0.55 \pm 0.04\ \mu g\,g^{-1}$) and the mollusk *M. edulis* (total antimony concentration $0.23 \pm 0.01\ \mu g\,g^{-1}$) were selected to carry out the extraction studies for antimony speciation analysis.

3.2. Extraction of antimony species from marine biota

Recently, Foster et al. carried out the antimony speciation in algae and animal tissue extracts. In accordance to other studies, it was shown that Sb(III) was oxidized to Sb(V) in this medium. In the present work, based on our experience in antimony speciation from other marine matrices [13,27] and taking into account that Sb(V) and Sb(III) form stable complexes with citric acid [14,17,23,37] and Sb(III) with EDTA [38], antimony was extracted from the selected algae and mollusk samples with 0.1 mol L^{-1} EDTA, pH 4.5 and 0.1 mol L^{-1} citric acid, pH 2.0. The use of extracting solutions with recognized complexing capacity can help to avoid some instability of the antimony species during extraction. Methanol has been used to extract antimony from plant materials [24] and arsenic species from algae and other biological tissues [39–41]. For comparative purposes, water was also included as extracting solution.

In a previous work about antimony speciation in marine sediment, we performed a detailed study on the compatibility of water, EDTA and citric acid extracting solutions with

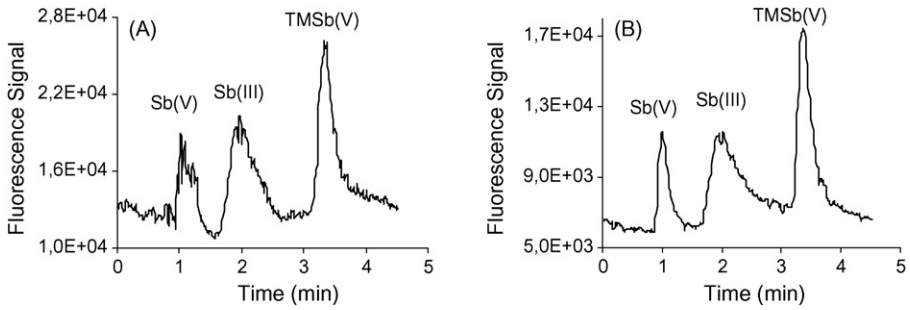

Fig. 1. Chromatograms of antimony species in (A) methanol, (B) methanol evaporated and replaced by water. Experimental conditions as described previously [27].

the HPLC separation procedure and HG-AFS detection system [27]. As in this study, methanol was also included as extracting reagent, the chromatographic and detection behavior of Sb(V), Sb(III) and TMSb(V) standard solutions prepared in this medium were evaluated. As shown in Fig. 1A, a high background signal was observed and the symmetry of Sb(V) peak was clearly affected when the antimony standards were prepared in methanol. Improved chromatographic behavior of Sb(V) and decreased background noise were obtained when the methanol was evaporated and replaced by water (see Fig. 1B).

In order to ascertain the optimum extraction conditions, the stability of antimony species during the extraction procedure was investigated. Recovery of antimony species from spiked algae and mollusk samples (20 $\mu g\,L^{-1}$ of Sb(V), Sb(III) and TMSb(V) solutions, separately, corresponding to 1 $\mu g\,Sb\,g^{-1}$ dry mass) under the extraction conditions assayed was determined. Extractions of samples without spiking were simultaneously carried out. The antimony species in the extract were determined by the optimized coupled technique HPLC-(UV)-HG-AFS by standard addition [13,27]. The results of duplicate experiments for the recovery of the individual species in algae extracts are shown in Fig. 2.

The antimony species in the extracting medium evaluated in this study exhibit notably different behavior. In all extracting media, Sb(V) and TMSb(V) presented a greater stability than the Sb(III). However, a significant decrease, especially for TMSb(V), was observed during the extraction, except for citric acid where approximately quantitative recoveries were obtained. TMSb(V) might be retained on the algae matrix probably due to the presence of methyl groups in its structure. In spite of the partial loss of Sb(V) and TMSb(V), additional peaks were not observed in the chromatograms.

As in marine sediments [27], the major problem encountered was the stability of Sb(III). Using water at ambient temperature, sorption of the Sb(III) specie was strongly retained and partially oxidized to Sb(V). Using water at 90 °C, a higher recovery was

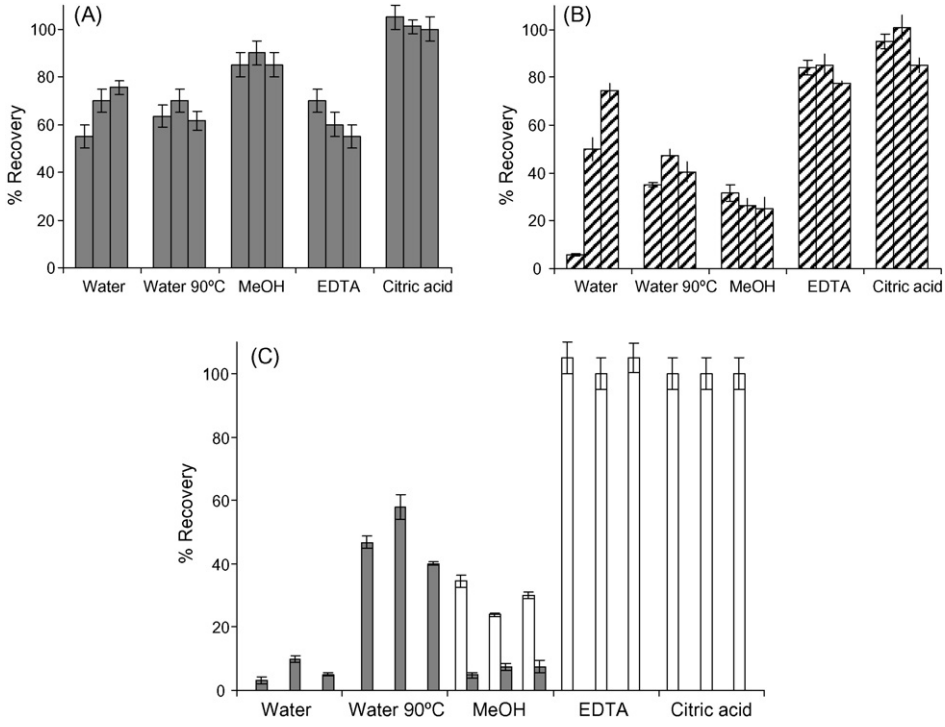

Fig. 2. Recovery of antimony species as a function of extraction time from *Macrosystis integrifolia* spiked with 20 $\mu g\,L^{-1}$ of (A) Sb(V); (B) TMSb(V); (C) Sb(III) extracted with water (25 and 90 °C), methanol, 0.1 mol L^{-1} EDTA and 0.1 mol L^{-1} citric acid. Detected species: Sb(V) (■), TMSb(V) (▨), Sb(III) (□) (first, second and third bar correspond to 2, 4, and 6 h, respectively).

Table 4
Naturally detected species in EDTA and citric acid extracts of algae *Macrosystis integrifolia* ($0.55 \pm 0.04\ \mu g\ Sb\ g^{-1}$)

Extracting solutions	Extraction time (h)	Detected species $\mu g\ g^{-1}$		% of total concentration
		Sb(V)	Sb(III)	
EDTA 0.100 mol L^{-1}	2	0.26 ± 0.01	0.27 ± 0.04	96 ± 7
	4	0.27 ± 0.02	0.27 ± 0.02	98 ± 5
	6	0.26 ± 0.03	0.23 ± 0.02	89 ± 7
Citric acid 0.100 mol L^{-1}	2	0.20 ± 0.04	0.15 ± 0.01	64 ± 7
	4	0.12 ± 0.04	0.15 ± 0.01	49 ± 7
	6	0.10 ± 0.02	0.16 ± 0.03	47 ± 7

obtained, but Sb(III) was completely oxidized to Sb(V). With methanol as extraction medium, the recovery of Sb(III) was low, a strong sorption and oxidation of Sb(III) to Sb(V) also occurred, and these phenomena increased with the extraction times.

The best extracting reagents for algae were found to be citric acid and EDTA, for which recoveries of Sb(III) were almost quantitative, without oxidation, even after 6 h of extraction. This behavior is likely to be the result of complexation reactions of Sb(III) in the presence of high concentrations of complex-forming EDTA and citric acid ligands. These results confirm that both reagents avoid the oxidation of Sb(III) during the whole extraction process.

The natural concentrations of antimony species in EDTA and citric acid extract from *M. integrifolia* determined by HPLC-(UV)-HG-AFS are listed in Table 4. The TMSb(V) specie was not detected.

Results show that the antimony species were quantitatively extracted by EDTA after only 2 h. Furthermore, in this medium the concentrations of both species were independent of the extraction times, indicating that no sorption of the released antimony species occurred during extraction.

With citric acid the extraction yields were always lower than with EDTA. In this medium, Sb(V) was the predominant specie, and its concentration decreased on the function of the extraction times, possibly due to re-adsorption process. On the contrary, the amount of Sb(III) extracted was practically constant.

Based on these results, EDTA represents the best compromise for speciation of antimony, as it was the most efficient extracting agent for antimony present in algae, and was furthermore capable of preserving the oxidation states of Sb(III) and Sb(V) species.

A chromatogram of antimony species detected by HPLC-HG-AFS in an EDTA extracts is shown in Fig. 3. An acceptable chromatographic separation of Sb(V) and Sb(III) in EDTA algae extract was achieved, without major interferences of the matrix. The quantification limits achieved by this analytical methodology are 0.1, 0.05 and 0.09 $\mu g\ L^{-1}$ for Sb(V), Sb(III) and TMSb(V) species, respectively.

Results of similar stability studies realized with the mollusk sample *M. edulis* are presented in Fig. 4. It is important to remark that the concentrations of all antimony species naturally present in the sample were lower than the quantification limits. As can be seen in Fig. 4, Sb(V) and TMSb(V) were stable in all extracting media. However, for Sb(V) and TMSb(V), sorption phenomena were observed during the extraction with methanol, water at 90 °C, and EDTA. Apparently, the solid matrix contains binding

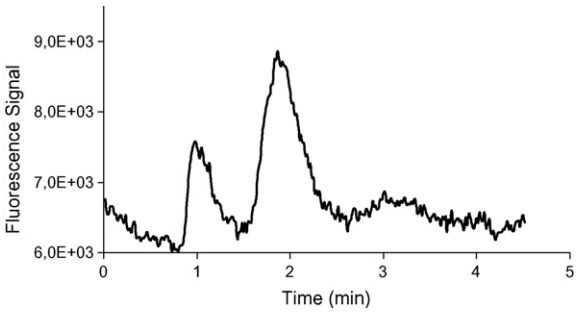

Fig. 3. Chromatogram of the 0.1 mol L^{-1} EDTA extract of *Macrosystis integrifolia*, after 2 h of extraction.

or reactive sites that are responsible for the low recovery rates of the aforementioned species. Citric acid was the only extracting medium where both species were quantitatively recovered.

As for algae, EDTA and citric acid were the best options to stabilize Sb(III), since no oxidation of Sb(III) to Sb(V) was observed, obtaining recoveries of about 70–90%. Extraction times and temperature had no significant effects on the recovery yields.

3.3. Application

The developed methodology (extraction with 0.1 mol L^{-1} EDTA, pH 4.5 and mechanical agitation during 2 h, subsequent analysis by HPLC-HG-AFS) was applied to the aqueous speciation analysis of antimony in different marine algae. The total antimony concentrations present in samples, extracts and residues were determined by HG-AFS. Then, the mass-balance between the sum of the antimony extracted and the present in the residue was established and compared to the total antimony concentration in the algae samples.

Results of the speciation analysis of antimony in different algae samples are listed in Table 5. TMSb(V) was not detected in any sample. Quantitative extraction yields of total antimony were obtained for three of the analyzed algae, except for those with the highest concentration, where only 62% of antimony was extracted.

It is important to note that the sum of total antimony extracted (determined in the extracts after digestion) and the antimony present in the residue agreed well with the total antimony concentration in all algae analyzed. Furthermore, in all algae samples, with exception of *M. integrifolia*, the sum of the detected species was lower than 60% of the total antimony

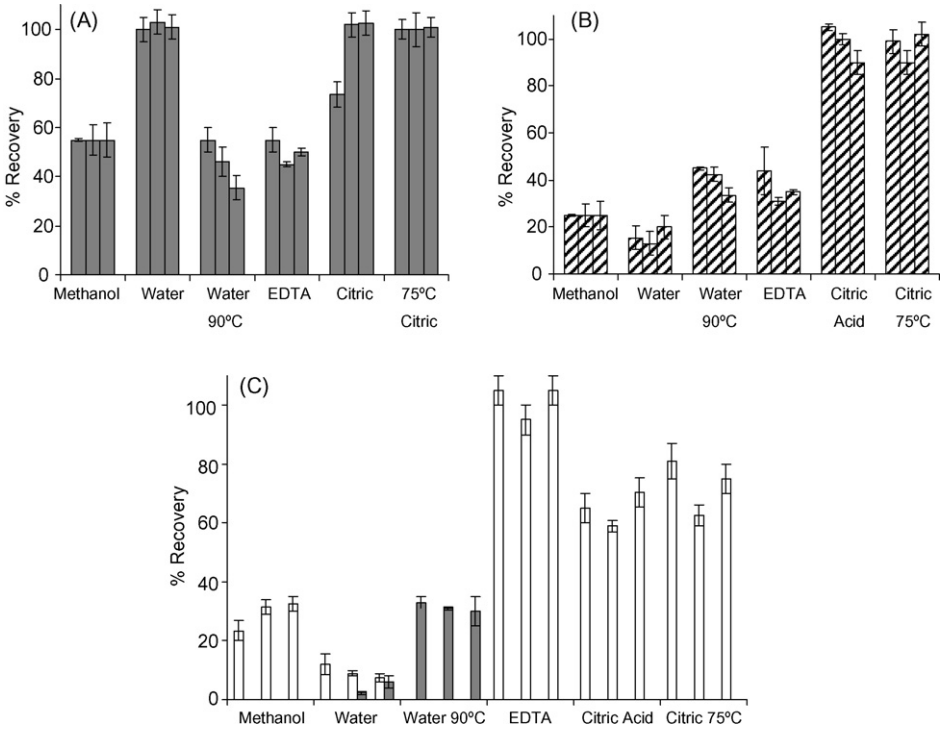

Fig. 4. Recovery of antimony species as a function of extraction time from *Mytilus edulis* spiked with 20 μg L^{-1} of (A) Sb(V); (B) TMSb(V); (C) Sb(III) extracted with water (25 and 90 °C), methanol, 0.1 mol L^{-1} EDTA and 0.1 mol L^{-1} citric acid. Detected species: Sb(V) (■), TMSb(V) (▨), Sb(III) (□) (first, second and third bar correspond to 2, 4, and 6 h, respectively).

Table 5
Speciation analysis of antimony in different marine algae

Algae	Antimony species (μg g^{-1})		Total antimony concentration (μg g^{-1})		
	Sb(V)	Sb(III)	Extracted	Residue	Sample
Macrosystis integrifolia	0.26 ± 0.01	0.27 ± 0.04	0.57 ± 0.04	N.D.	0.55 ± 0.04
Schimmelmannia plumosa	0.17 ± 0.03	N.D.	0.40 ± 0.05	N.D.	0.41 ± 0.03
Fotogenia fastigiata	0.14 ± 0.02	N.D.	0.24 ± 0.04	N.D.	0.25 ± 0.04
Halopteris hordacea	0.12 ± 0.03	N.D.	0.64 ± 0.04	0.48 ± 0.04	1.03 ± 0.03

N.D.: not detected.

extracted. This indicates the presence of unidentified species that either did not elute from the column or were not detected by HG-AFS.

4. Conclusions

The present study confirms that in aqueous speciation analysis of antimony in solid matrices one of the most critical step is the extraction process. Many problems can occur during this step, such as low extraction efficiency and/or instability of species, particularly oxidation of Sb(III) to Sb(V). To choose an adequate extraction solution, both the stability of species and extraction efficiency must be considered. For the speciation of antimony in marine biota samples, water, methanol, citric acid and EDTA were assayed as extracting reagents, of which EDTA showed to be the best choice. High extraction efficiency of antimony from algae samples are obtained and Sb(III) is stable in this medium.

Only the inorganic species Sb(V) and Sb(III) were detected in extracts of marine algae. This is in contrast to arsenic, which is mainly present in organic form, for example, arsenosugars. The mass balances revealed the presence of unknown antimony species in one of the EDTA algae extracts, which were not detected by anion exchange HPLC-HG-AFS. Further work must be carried to elucidate the identity of these unknown species of antimony.

The speciation method developed in this work has a very good potential to become a routine procedure for antimony speciation in marine biota samples.

Acknowledgements

The authors gratefully acknowledge the financial support of FONDECYT (project 1030897), Pontificia Universidad Católica de Valparaíso (project 125.755) and the Program ECOS-CONICYT (Scientific Cooperation between France and

Chile), through the Action C01E010. W. Quiroz also thanks CONICYT and the Government of France for the fellowships granted.

References

[1] R. Iffland, Handbooks on Toxicity of Inorganic Compounds, Marcel Dekker, New York, 1988, p. 67 (Chapter 7).
[2] M. Filella, N. Belzile, Y.W. Chen, Earth Sci. Rev. 57 (2002) 125.
[3] USEPA, Water Related Fate of the 129 Priority Pollutants, vol. 1, United States Environmental Protection Agency USEPA, Washington, DC, 1979 (EP-440/4-79-029A).
[4] Council of European Union. Council Directive 98/83/EC of 3 November 1998, Quality of Water Intended for Human Consumption. Official J. L 330, 05/12/1998, pp. 32–54.
[5] P. Smichowski, Y. Madrid, C. Cámara, Fresenius J. Anal. Chem. 360 (1998) 623.
[6] M. Krachler, H. Emons, Trends Anal. Chem. 20 (2001) 79.
[7] M.J. Nash, J.E. Maskall, S. Hill, J. Environ. Monit. 2 (2002) 97.
[8] M. Filella, N. Belzile, Y.W. Chen, Earth Sci. Rev. 59 (2002) 265.
[9] J. Lintschinger, I. Koch, S. Serves, J. Feldmann, W.R. Cullen, Fresenius J. Anal. Chem. 359 (1997) 484.
[10] A. Sayago, R. Beltran, M.A.F. Recamales, J.L. Gómez-Ariza, J. Anal. At. Spectrom. 17 (2002) 1400.
[11] R. Miravet, J.F. López-Sánchez, R. Rubio, J. Chromatogr. A 1052 (2004) 121.
[12] W. Shotyk, M. Krachler, B. Chen, J. Environ. Monit. 8 (2006) 288.
[13] I. De Gregori, W. Quiroz, H. Pinochet, F. Pannier, M. Potin-Gautier, J. Chromatogr. A 1091 (2005) 94.
[14] H.R. Hansen, S.A. Pergantis, J. Anal. At. Spectrom. 21 (2006) 731.
[15] M. Krachler, H. Emons, J. Anal. At. Spectrom. 16 (2001) 20.
[16] N. Miekeley, S.R. Mortari, A.O. Schubach, Anal. Bioanal. Chem. 372 (2002) 495.
[17] H.R. Hansen, S.A. Pergantis, J. Anal. At. Spectrom. 21 (2006) 1240.
[18] J. Lintschinger, B. Michlake, S. Schulte-Hostede, P. Schramel, Int. J. Environ. Anal. Chem. 72 (1998) 11.
[19] N. Ulrich, Anal. Chim. Acta 359 (1998) 245.
[20] T. Lindemann, A. Prange, W. Dannecker, B. Neidhart, Fresenius J. Anal. Chem. 368 (2000) 214.
[21] S. Amereih, T. Meisel, R. Scholger, W. Wegscheider, J. Environ. Monit. 7 (2005) 1200.
[22] J. Zheng, M. Ohata, N. Furuta, Analyst 125 (2000) 1025.
[23] J. Zheng, A. Lijima, N. Furuta, J. Anal. At. Spectrom. 16 (2001) 812.
[24] R. Miravet, E. Bonilla, J.F. López-Sánchez, R. Rubio, J. Environ. Monit. 7 (2005) 1207.
[25] R. Miravet, E. Bonilla, J.F. López-Sánchez, R. Rubio, Appl. Organomet. Chem. 20 (2006) 12.
[26] T. Narukawa, A. Takatsu, K. Chiba, K.W. Riley, D.H. French, J. Environ. Monit. 7 (2005) 1342.
[27] M. Potin-Gautier, F. Pannier, W. Quiroz, H. Pinochet, I. De Gregori, Anal. Chim. Acta 553 (2005) 214.
[28] N. Essen, S. Topcuoğlu, E. Eğilli, D. Kurt, J. Radioanal. Nucl. Chem. 240 (1999) 673.
[29] X. Hou, J. Radioanal. Nucl. Chem. 242 (1999) 49.
[30] S. Foster, W. Maher, F. Krikowa, K. Telford, M. Ellwood, J. Environ. Monit. 7 (2005) 1214.
[31] M. Krachler, H. Emons, Anal. Chim. Acta 429 (2001) 125.
[32] J.L. Gómez-Ariza, E. Morales, D. Sánchez-Rodas, I. Giraldes, Trends Anal. Chem. 19 (2000) 200.
[33] J. Zheng, M. Ohata, N. Furuta, Anal. Sci. 16 (2000) 75.
[34] B. Chen, M. Krachler, W. Shotyk, J. Anal. At. Spectrom. 18 (2003) 1256.
[35] W. Shotyk, M. Krachler, B. Chen, Anthropogenic impact on the biogeochemistry and cycling of antimony, in: A. Siegel, H. Siegel, R.K.O. Siegel (Eds.), Biogeochemistry, Availability, and Transport of Metals in the Environment, Metal Ions in Biological Systems, vol.44, M. Dekker, New York, 2005, pp. 177–203.
[36] R. Miravet, J.F. López-Sánchez, R. Rubio, Anal. Chim. Acta 511 (2004) 295.
[37] A. Guy, P. Jones, S.J. Hill, Analyst 123 (1998) 1513.
[38] Stability Constants of Metal-ion Complexes. Part B. Organic Ligand, IUPAC Chemical Data Series N° 22, Compiled by D.D. Perrin, Pergamon Press, 1979, pp. 770.
[39] W. Goessler, J. Lintschinger, J. Szakova, P. Mader, J. Kopecky, J. Doucha, Appl. Organomet. Chem. 11 (1997) 57.
[40] S. McSheehy, J. Szpunar, J. Anal. At. Spectrom. 15 (2000) 79.
[41] S. McSheehy, J. Szpunar, R. Morabito, P. Quevauviller, Trends Anal. Chem. 22 (2003) 191.

Available online at www.sciencedirect.com
ScienceDirect
Talanta 73 (2007) 561–566
Talanta
www.elsevier.com/locate/talanta

A sensitive flow analysis system for the fluorimetric determination of low levels of formaldehyde in alcoholic beverages

Fabio Santos de Oliveira, Eliane Teixeira Sousa, Jailson B. de Andrade *

Instituto de Química, Universidade Federal da Bahia, Campus Universitário de Ondina, 40170-290 Salvador, BA, Brazil

Received 22 January 2007; received in revised form 16 April 2007; accepted 17 April 2007
Available online 4 May 2007

Abstract

A sensitive FIA method was developed for the selective determination of formaldehyde in alcoholic beverages. This method is based on the reaction of Fluoral-P (4-amine-3-pentene-2-one) with formaldehyde, leading to the formation of 3,5-diacetyl-1,4-dihydrolutidine (DDL), which fluoresces at $\lambda_{ex} = 410$ nm and $\lambda_{em} = 510$ nm. The analytical parameters were optimized by the response surface method using the Box–Behnken design. The proposed flow injection system allowed for the determination of up to 3.33×10^{-5} mol L^{-1} of formaldehyde with R.S.D. < 2.5% and a detection limit of 3.1 ng mL^{-1}. The method was successfully applied to determine formaldehyde in alcoholic beverages, without requiring any sample pretreatment, and the results agreed with the reference at a 95% confidence level by paired *t*-test. In the optimized condition, the FIA system proved able to analyze up to 60 samples/h.

Keywords: Formaldehyde determination; Alcoholic beverages; Fluoral-P; Box–Behnken design

1. Introduction

In recent years, efforts have focused increasingly on quantifying carbonyl compound levels in alcoholic beverages [1–11]. The importance of such analyses is understandable in view of the known toxicity of several aldehydes, including formaldehyde, acetaldehyde, acrolein and benzaldehyde [12–14]. In this context, information regarding aldehyde profiles may be a valuable tool in assessing the authenticity and/or aging conditions of different alcoholic beverages [15] since aldehydes are extracted from wood into alcoholic beverages during the aging process, thereby contributing to their final flavor [5].

The formaldehyde level is important to evaluate the quality of alcoholic beverages, for it presents toxic activity at levels above 16.65×10^{-5} mol L^{-1} [16]. Formaldehyde can be formed during the alcoholic fermentation process, or it can occur due to aldehyde contamination when plastic bottles are employed.

The development of automatic methods for formaldehyde determination in spirits is important in view of the growing interest of Brazilian government agencies to establish chemical profiles and markers that differentiate Brazilian *cachaça* (sugar-cane brandy) from other types of beverages such as rum.

Several methods have been developed for aldehyde determination, including color reaction with chromotropic acid [17,18], pararosaniline-bisulfite (Schiff reagent) [19,20], malachite green-bisulfite [21,22], brilliant green-bisulfite [23], enzymatic methods [8–10], liquid chromatography by derivatization with 2,4-dinitrophenylhydrazine [24–28], reaction with 3-methyl-2-benzothiazolone hydrazone (MBTH) [29–33] and reaction with Fluoral-P [1,11,34–43].

The chromotropic acid method employs concentrated sulfuric acid (>85%), which increases the viscosity of reaction media, making its application in flow systems difficult. Spectrophotometric methods based on the reaction with pararosaniline, malachite green or brilliant green associated with HSO_3^- are subject to interference from low levels of ethanol [21–23], making them unsuitable for determining formaldehyde in alcoholic beverages.

The standard method for determining carbonyl compounds in atmospheric air samples is HPLC, using 2,4-dinitrophenilhydrazine (2,4-DNPH) as the chromogenic reagent and spectrophotometric detection at 365 nm, which offers excellent sensitivity and selectivity [24–28]. Nonetheless, the development of automatic flow systems using 2,4-DNPH without the

* Corresponding author. Tel.: +55 7132375524; fax: +55 7132375524.
E-mail address: jailsong@ufba.br (J.B. de Andrade).

0039-9140/$ – see front matter © 2007 Elsevier B.V. All rights reserved.
doi:10.1016/j.talanta.2007.04.027

chromatographic separation step is considered unfeasible, since the reagent and reaction products have absorption maxima in the same wavelength range. The MBTH method has been employed for the determination of total aliphatic aldehydes in several samples [29–33]. On the other hand, the MBTH method is not selective for formaldehyde determination and several other aliphatic aldehydes can interfere in this determination.

The Fluoral-P method [34-43] is based on the reaction of this compound (4-amino-3-penten-2-one) with formaldehyde, producing 3,5-diacetyl-1,4-dihydrolutidine (DDL). When excited at 410 nm, DDL fluoresces at 510 nm. Although Fluoral-P presents reactions similar to those of other aliphatic aldehydes, the reaction product with formaldehyde is the only one that produces a high fluorescent emission. Thus, the Fluoral-P method is specific for formaldehyde [1,11,34–43], allowing for the determination of this analyte even in the presence of acetaldehyde concentrations 1000 times higher than formaldehyde [1].

In this work, a flow injection system was developed for the selective determination of formaldehyde in different alcoholic beverages. The proposed flow system was based on the reaction of formaldehyde with Fluoral-P with the selective production of a fluorescent compound (λ_{ex} = 410 nm and λ_{em} = 510 nm).

Because many parameters related to the flow system can affect the fluorescent response, a multivariate optimization approach was adopted. This optimization strategy presents several advantages such as: (a) valuable information is obtained with fewer experiments than when using traditional one-factor-at-a-time optimization; (b) a mathematical model that describes the dependency of the experimental response and evaluated parameters is obtained; (c) it provides information regarding the interactions between the factors under study; (d) even if optimal conditions are not located in the evaluated domain, the mathematical model can indicate the optimal direction and steepest ascent method that can be used.

2. Experimental

2.1. Reagents and solutions

All the solutions were prepared from analytical grade reagents using distilled and deionised water with a resistivity greater than 18 MΩ cm^{-1}.

The Fluoral-P solution was prepared by reacting 0.2 mL of acetylacetone with 15.4 g of ammonium acetate in the presence of 0.3 mL of acetic acid. The volume was adjusted to 100 mL with distilled water.

A 0.033 mol L^{-1} formaldehyde stock solution was prepared by diluting 2.5 mL of 37% formaldehyde solution with distilled water and standardized by 2,4-DNPH/HPLC method [25].

Samples of alcoholic beverages were purchased in the local market and analyzed by the proposed flow system without any further pretreatment.

2.2. Apparatus

A Rheodyne, USA, model 5020 six-port rotary injection valve was employed for sampling aliquots in the flow path and a Minipuls 3 (Gilson, France) peristaltic pump was utilized for fluid propulsion. Polyethylene and PTFE tubes (0.8 mm i.d.) were used in the flow systems as peristaltic and connection tubes, respectively. A Spectra-Physics FS-970D-A1 fluorimeter whose excitation wavelength was adjusted at 410 nm was used with a high-pass filter (which transmits at wavelengths above 440 nm, transmittance at 440 nm being 0.8) to collect maximum DDL fluorescent emission at 510 nm. Bathwise fluorescence determinations were carried out with a spectrofluorimeter (Jasco, model FP-777) equipped with a 1.0 cm quartz cell. An Intralab 4290 integrator was used to record transient signals produced by the FIA system.

Statistica 6.0 (Statsoft, USA) was employed for calculations related to multivariate response surface optimization.

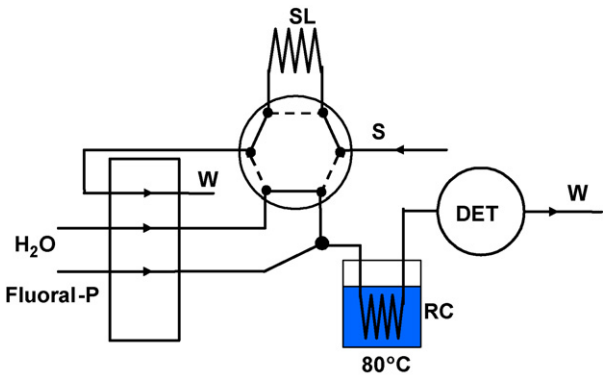

Fig. 1. Flow manifold for the fluorimetric determination of formaldehyde in alcoholic beverage samples. S = sample, SL = sampling loop, RC = reaction coil, DET = fluorimetric detector (λ_{ex} = 410 nm and λ_{em} = 510 nm), W = waste. Flow rate = 0.95 mL min^{-1} and sample volume = 414 μL.

2.3. Flow system

Fig. 1 shows a schematic diagram of the flow manifold. In the FIA manifold an aliquot of 414 μL of alcoholic beverage sample solution was inserted into the flow system and the Fluoral-P reagent was continuously added by confluence. The mixture was then directed to a reaction coil heated in a thermostatic bath at 80 °C in order to improve the sample/reagent mixture and reaction rate, then to the fluorimetric detector (λ_{ex} = 410 nm and λ_{em} = 510 nm) where the signal was acquired and recorded by an integrator.

3. Results and discussion

3.1. Effect of reaction coil temperature

Previous work showed that, in the batch condition, the highest and most stable fluorescent responses were obtained several hours after the addition of reagent at room temperature (25 °C) or after 20 min of sonication [1]. To reduce the long time interval required to complete the reaction of formaldehyde with Fluoral-P, a reaction coil was inserted into a thermostatic water bath to heat the Fluoral-P—sample segment and thus accelerate DDL formation.

The effect of heating time on fluorescent emission was evaluated and the heating temperature of 80 °C was selected, since higher temperatures did not significantly increase the analytical signals and led to the formation of air bubbles.

Because temperature affects the fluorescence emission of several compounds, the addition of a cooling coil before the fluorescence detector was evaluated. The use of the cooling coil led to a 6% increase in the analytical signal, and this cooling step was not employed in further experiments due to the low gain in sensitivity and the longer analysis time interval.

3.2. Optimization by response surface method

In this work, we employed the response surface method and Box–Behnken [44,45] design to optimize the sensitivity of the proposed flow system. The Box–Behnken [44,45] design can be considered a highly fractionalized three-level factorial design where the treatment combinations are the midpoints of edges of factor levels and the center point. These designs are rotatable (or nearly rotatable) and require three levels of each factor under study. Like other designs such as central composite [45] and Doehlert [46], Box–Behnken designs can fit full quadratic response surface models and offer advantages over other designs.

The advantages of the Box–Behnken design over other response surface designs are: (a) it needs fewer experiments than central composite design and similar ones used for Doehlert designs; (b) in contrast to central composite and Doehlert designs, it has only three levels; (c) it is easier to arrange and interpret than other designs; (d) it can be expanded, contracted or even translated; and (e) it avoids combined factor extremes since midpoints of edges of factors are always used.

To optimize the sensitivity of the proposed flow system, a multivariate optimization design was adopted to evaluate the influence of the flow rate ($flow_R$), reaction coil length (l_{RC}), and sampling loop length (l_{SL}) on the analytical signal. The univariate evaluation of these flow parameters can be difficult for, although the sampling loop and reaction coil length ratios are closely related to the mixture condition and sample zone dispersion, the flow rate determines the residence time of the sample zone in the heating bath, so interactions among these parameters can occur.

A Box–Behnken design was employed for multivariate optimization, and the levels of the evaluated variables are presented in Table 1. The response surface obtained by Box–Behnken design (Fig. 2) was described by the equation $S = 16.5 + 2.5l_{RC} - 1.7l_{RC}^2 + 1.6l_{SL} - 1.8l_{SL}^2 - 2.7\,flow_R - 1.4\,flow_R^2$, with the variables at coded levels, revealing a parabolic response surface whose maximum was located within the evaluated domain. The equation obtained by the response surface method revealed that linear and quadratic terms were significant while interaction terms were not.

Table 1
Experimental levels employed for Box–Behnken optimization design

Variable	Coded variable		
	(−1)	(0)	(+1)
Sampling loop (cm)	20	55	90
Reaction coil (cm)	55	125.5	200
Flow rate (mL min^{-1})	0.90	1.75	2.60

The optimized values of flow variables obtained by the Box–Behnken method were calculated by Statistica 6.0 using derivative techniques [44,46]. Flow system optimal conditions were attained using a sampling loop with 82.4 cm, reaction coil with 158.0 cm and flow rate at 0.95 mL min^{-1}. The optimization methodology allowed for maximization of the analytical sensitivity with only 15 experiments.

3.3. Interference study

3.3.1. Evaluation of ethanol level

The ethanol level in alcoholic beverages can be related to the type of beverage (cachaça, rum, wine, vodka and others), to the producer, and to variations in production processes. Thus, the proposed method must be insensitive to ethanol variations within the range expected for this kind of sample.

The effect of the ethanol level in samples was evaluated, since variations in solvent composition could lead to fluctuating fluorescence signals. Additionally, flow systems with poor mixing conditions can lead to strong solvent concentration gradients when an alcoholic sample is inserted into an aqueous carrier stream, resulting in the occurrence of a liquid lens in the ethanolic/aqueous medium interface [47] due to differences in the refraction indexes. This phenomenon, known as the Schlieren effect [47], is well described in light absorption measurements, but there is little information about its extension to fluorescence and how it affects signal repeatability.

The results obtained by these experiments showed that the ethanol level had a non-significant effect on the fluorescent signal magnitude and repeatability up to 50% (v/v) of ethanol. The observation of non-significant Schlieren effect may be ascribed to the fact that the excitation beam diffracted by a liquid lens was blocked by a high-pass filter positioned in front of the photomultiplier. Additionally, the geometry of the fluorimeter and flow cell produces an incident/excitation beam angle of 45° in relation to the collected fluorescent emission beam, and diffraction of the excitation beam by Schlieren's effect at such a high angle is not expected to occur.

Hence, the results indicated that the proposed system is insensitive to ethanol levels within the evaluated range, and is suitable for determining formaldehyde in the alcoholic media of beverages without requiring analyte/ethanol separations.

3.3.2. Effect of acetaldehyde level

Aliphatic aldehydes are expected to react with Fluoral-P, producing colored species [38]. On other hand, the literature [1,11,34–43] has shown that the fluorimetric determination of formaldehyde using Fluoral-P as reagent is almost specific, since the product of the reaction of Fluoral-P with other aldehydes does not present a significant fluorescent signal. Despite the selectivity of the Fluoral-P fluorimetric method for formalde-

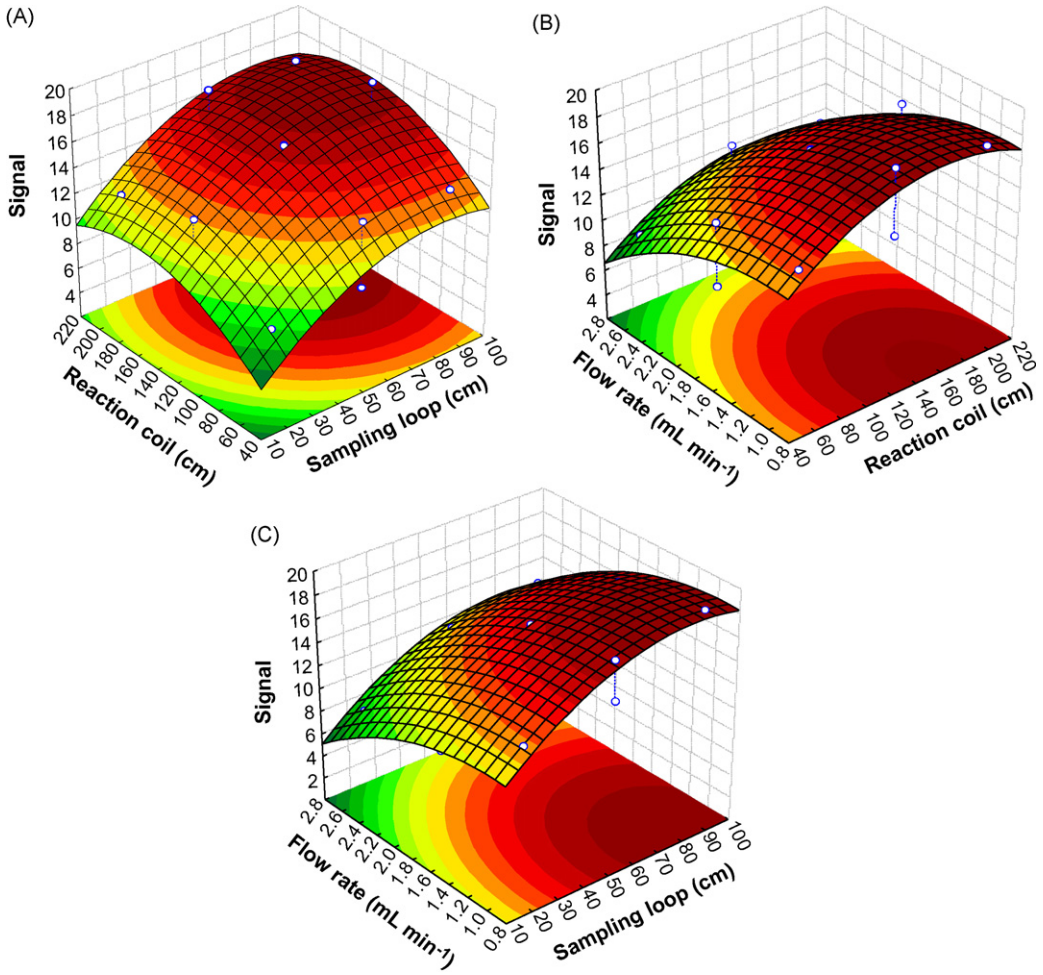

Fig. 2. Response surfaces obtained by the Box–Behnken design for optimization of the flow parameters: (A) sampling loop and reaction coil, (B) reaction coil and flow-rate, and (C) flow-rate and sampling loop.

hyde determination, high levels of other aliphatic aldehydes could lead to interferences due to Fluoral-P consumption and absorption of analyte fluorescent radiation by reaction products of these interferents.

Acetaldehyde is the prevalent carbonyl compound in alcoholic beverages, so interference studies were conducted to evaluate the maximum tolerable level of this compound that would still allow for formaldehyde to be determined accurately.

The results of these experiments indicated that the proposed method is selective for formaldehyde in the presence up to 0.0033 mol L^{-1} of acetaldehyde.

3.3.3. *Effect of bisulfite level*

Bisulfite and S(IV) oxides form a strong oxidation-resistant adduct with formaldehyde, hydroxymethanesulfonate (HMSA) [36]. The kinetics of the decomposition of HMSA is slow at the optimum pH for the formation of DDL, and problems in determining bisulfite-bound formaldehyde are expected to occur. Moreover, the presence of bisulfite is expected in some alcoholic beverages such as wines and beer, since it is employed as antioxidant. Thus, the interference of S(IV) in the determination of formaldehyde by the Fluoral-P method was evaluated.

The results obtained by the proposed flow system revealed that bisulfite levels above 1.0 mg L^{-1} resulted in recoveries of less than 95%. Therefore, the elimination of bisulfite interference through the addition of H_2O_2, followed by alkalinization with NaOH solution [35], must be carefully evaluated to determine total formaldehyde in alcoholic beverages preserved with bisulfite.

3.4. *Figures of merit*

The proposed procedure presented good precision with a relative standard deviation of less than 2.5% for all determinations and an analytical throughput of 60 samples/h. The formaldehyde detection limit was 3.1 ng mL^{-1} and was calculated as three times the standard deviation of the blank signal from 10 replicates divided by the slope of the analytical curve [48]. The linear range for formaldehyde determination was obtained up to 3.33×10^{-5} mol L^{-1} ($S = (40.6 \pm 0.3)$ C (mg L^{-1}) $+ 0.7 \pm 0.1$, $R = 0.9998$).

Table 2 compares the proposed method against other Fluoral-P based fluorimetric methods for determining formaldehyde in alcoholic and other liquid phase samples. The proposed method presents a higher analytical throughput, lower sample/reagent

Table 2
Comparison of the performance of the proposed flow system and other Fluoral-P based methods for determining formaldehyde

	Bathwise method [1]	Previous flow based method [42]	Present work
Reagent volume per determination (mL)	9	2–3	1–2
Sample volume per determination (μL)	1000	25	414
Analytical throughput (sample h^{-1})	2	12	60
Average R.S.D.%	1.7	0.2	2.02
Limit of detection (ng mL^{-1})	2.0	15	3.1

Table 3
Results obtained by the FIA procedure and the batchwise method to determine formaldehyde in samples of alcoholic beverages ($n = 3$)

Sample	Formaldehyde (μg mL^{-1})	
	FIA	Batch
Cachaça 1	0.150 ± 0.001	0.152 ± 0.006
Cachaça 2	0.073 ± 0.002	0.076 ± 0.001
Cachaça 3	0.095 ± 0.002	0.093 ± 0.003
Cachaça 4	0.073 ± 0.002	0.076 ± 0.003
Cachaça 5	0.095 ± 0.001	0.097 ± 0.001
Cachaça 6	0.093 ± 0.003	0.088 ± 0.003
Cachaça 7	0.256 ± 0.004	0.255 ± 0.002
Cachaça 8	0.159 ± 0.003	0.163 ± 0.007
Rum 1	0.125 ± 0.001	0.122 ± 0.001
Rum 2	0.042 ± 0.001	0.044 ± 0.001
Rum 3	0.47 ± 0.01	0.462 ± 0.002
Vodka 1	ND[a]	ND[a]
Vodka 2	0.034 ± 0.001	0.032 ± 0.001

[a] ND = not detected.

consumption and similar detection limits compared with the bathwise method [1]. In comparison with other flow injection systems described in the literature [42], the proposed method was able to determine formaldehyde without any interference removal step, allowing for higher analytical throughput and lower reagent consumption. Moreover, when compared with results described in the literature [42], the proposed flow system allowed for the determination of lower levels of formaldehyde with a low average relative standard deviation (R.S.D.).

3.5. Formaldehyde determination in alcoholic beverages

The proposed method was applied to determine formaldehyde in alcoholic beverage samples with no further pretreatment, which were injected directly into the proposed flow system. All the alcoholic beverages evaluated here except the vodka sample contained formaldehyde in the range of 1.4×10^{-6} to 8.6×10^{-6} mol L^{-1}, reinforcing the need for evaluating the levels of this carbonyl compound in this type of sample. The results obtained by the proposed method were compared with the Fluoral-P bath procedure (Table 3) [1] as reference, and a paired *t*-test [48] confirmed their congruence at a 95% confidence level.

4. Conclusions

The proposed system was successfully applied to determine formaldehyde in alcoholic beverage samples, providing good repeatability and accuracy. The flow analysis system displayed high sensitivity, a low detection limit and a wide linear range. This system proved suitable for routine analyses, as indicated by its high sample throughput, low reagent consumption, minor waste generation, and the fact that it requires no sample pretreatment.

References

[1] J.B. de Andrade, M.S. Bispos, M.V. Rebouças, M.L.S.M. Carvalho, H.L.C. Pinheiro, American Lab. 28 (1996) 56.
[2] D.M. Rodríguez, K. Wrobel, K. Wrobe, Eur. Food Res. Technol. 221 (2005) 798.
[3] R. Rodriguez Madrera, D. Blanco Gomis, J.J. Mangas Alonso, J. Agric. Food Chem. 51 (2003) 7969.
[4] C.G. Barroso, M.C. Rodrıguez, D.A. Guillen, J.A. Perez-Bustamante, J. Chromatogr. A 724 (1996) 125.
[5] S. Canas, A.P. Belchior, M.I. Spranger, R. Bruno-de-Sousa, J. Sep. Sci. 26 (2003) 496.
[6] R.F. Nascimento, J.C. Marques, B.S. Lima Neto, D. De Keukeleire, D.W. Franco, J Chromatogr. A 782 (1997) 13.
[7] J. Quesada-Granados, M. Villalon-Mir, H. Lopez-Garcia-Serrana, M.C. Lopez-Martinez, Food Chem. 52 (1995) 203.
[8] F. Lázaro, M.D.L. de Castro, M. Valcárcel, Anal. Chim. Acta 185 (1986) 57.
[9] A.M. Almuaibed, A. Townshend, Anal. Chim. Acta 198 (1987) 37.
[10] N. Kiba, L. Sun, S. Yokose, M.T. Kazue, T.T. Suzuki, Anal. Chim. Acta 378 (1999) 169.
[11] H. Tsuchiya, S. Ohtani, K. Yamada, M. Akagiri, N. Takagi, Analyst 119 (1994) 1413.
[12] Formaldehyde and other aldehydes. National Research Council Committee on Aldehydes, National Academy of Science Press, Washington, 1981, p. 14.
[13] B.M. Golldschmidt, J. Environ. Sci. Health 2 (1984) 231.
[14] M.V.A.S. Andrade, H.L.C. Pinheiro, P.A.P. Pereira, J.B. de Andrade, Quim. Nova 25 (2002) 1117.
[15] C. Bauer-Chriostoph, N. Christoph, B.O. Aguilar-Cisneros, M.G. Lopez, E. Richling, A. Rosmmann, P. Schreider, Eur. Food Res. Technol. 217 (2003) 438.
[16] J.K. Faweel, S. Hunt, Environmental Toxicology of Organic Pollutants, Ellis Horwood, Chichester, 1988, p. 332.
[17] E. Fagnani, C.B. Melios, L. Pezza, H.R. Pezza, Talanta 60 (2003) 171.
[18] A. Pretto, M.R. Milani, A.A. Cardoso, J. Environ. Monit. 2 (2000) 566.
[19] J.M. Bosque-Sendra, S. Pescarolo, L. Cuadros-Rodríguez, A.M. García-Campaña, E.M. Almansa-López, Fresenius J. Anal. Chem. 369 (2001) 715.
[20] G.L. Kok, S.N. Gitlin, B.W. Gandrud, A.L. Lazrus, Anal. Chem. 56 (1984) 1993.
[21] A. Afkhami, M. Rezaei, Microchem. J. 63 (1999) 243.
[22] A. Afkhami, H. Parham, M. Rezaei, Anal. Lett. 33 (2000) 527.
[23] A. Safavi, A.A. Ensafi, Anal. Chim. Acta 252 (1991) 167.
[24] J.B. de Andrade, A.H. Miguel, Quím. Nova 356 (1985) 1985.
[25] J.B. de Andrade, M.V. Andrade, H.L.C. Pinheiro, R.A. Martins, E.L. Borges, American Lab. 31 (1999) 22.
[26] A.E. Oliveira, J.B. de Andrade, Quim. Nova 17 (1994) 13.
[27] J.B. de Andrade, J.O.N. Reis, M.V. Rebouças, H.L.C. Pinheiro, Quim. Anal. 15 (1996) 144.

[28] K. Takami, K. Kuwata, A. Sugimae, M. Nakamoto, Anal. Chem. 57 (1985) 243.
[29] E. Sawicki, T.W. Stanley, T.R. Hauser, W. Elbert, J.L. Noe, Anal. Chem. 33 (1961) 722.
[30] G. Zurek, U. Karst, Anal. Chim. Acta 351 (1997) 247.
[31] E.A. Pereira, A.A. Cardoso, Quim. Nova 24 (2001) 443.
[32] F.S. Oliveira, B.C.O. Leite, M.V.A.S. Andrade, M. Korn, J. Braz, Chem. Soc. 16 (2005) 87.
[33] J. Ledauphin, D. Barillier, M. Beljean-Leymarie, J. Chromatogr. A 1115 (2006) 225.
[34] H.L.C. Pinheiro, M.V. Andrade, P.A.P. Pereira, J.B. de Andrade, Microchem. J. 78 (2004) 15.
[35] S. Dong, P.K. Dasgupta, Environ. Sci. Technol. 21 (1987) 581.
[36] K. Motyka, P. Mikuska, Anal. Chim. Acta 518 (2004) 51.
[37] S. Belman, Anal. Chim. Acta 29 (1963) 120.
[38] B.J. Compton, W.C. Purdy, Anal. Chim. Acta 119 (1980) 349.
[39] A.L. Lazrus, K.L. Fong, J.A. Lind, Anal. Chem. 60 (1988) 1074.
[40] J. Li, P.K. Dasgupta, W. Luke, Anal. Chim. Acta 531 (2005) 51.
[41] L.S.G. Teixeira, E.S. Leão, A.F. Dantas, H.L.C. Pinheiro, A.C.S. Costa, J.B. de Andrade, Talanta 64 (2004) 711.
[42] H. Tsuchiya, S. Ohtani, K. Yamada, M. Akagiri, N. Takagi, M. Sato, Analyst 119 (1994) 1413.
[43] L. Lagace, J. Dumont, G. Brazeau, A. Soucy, J. Hache, V. Marquis, J. AOAC Int. 85 (2002) 1144.
[44] J.M. Bosque-Sendra, S. Pescarolo, L. Cuadros-Rodriguez, A.M. Garcia-Campaña, E.M. Almansa-López, Fresenius J. Anal. Chem. 369 (2001) 715.
[45] K.H. Esbensen, Multivariate Data Analysis in Practice: An Introduction to Multivariate Data Analysis and Experimental Design, 5th ed., CAMO, New Jersey, 2002, p. 400.
[46] S.L.C. Ferreira, W.N.L. dos Santos, C.M. Quintella, B.B. Neto, J.M. Bosque-Sendra, Talanta 63 (2004) 1061.
[47] A.C. Dias, E.P. Borges, E.A.G. Zagatto, P.J. Worsfold, Talanta 68 (2006) 1076.
[48] J.C. Miller, J.N. Miller, Statistics for Analytical Chemistry, 2nd ed., Ellis Horwood, 1984, p. 100.

Available online at www.sciencedirect.com
ScienceDirect
Talanta 73 (2007) 451–457
Talanta
www.elsevier.com/locate/talanta

Exploiting *in situ* hydride trapping in tungsten coil atomizer for Se and As determination in biological and water samples

Samuel Simião de Souza [a], Dário Santos Jr. [a], Francisco J. Krug [a], Fernando Barbosa Jr. [b,*]

[a] *Centro de Energia Nuclear na Agricultura, Laboratório Henrique Bergamin Filho, Ave. Centenário 303, São Dimas, 13400-970 Piracicaba, SP, Brazil*
[b] *Faculdade de Ciências Farmacêuticas de Ribeirão Preto, Departamento de Análises Clínicas, Toxicológicas e Bromatológicas, Universidade de São Paulo, Ave. do Café s/n, 14040-903 Ribeirão Preto, SP, Brazil*

Received 5 January 2007; received in revised form 8 April 2007; accepted 9 April 2007
Available online 4 May 2007

Abstract

A flow injection hydride manifold was coupled to a 150 W tungsten coil electrothermal atomizer for *in situ* hydride collection followed by selenium and arsenic determination by ET AAS. Rhodium (200 μg), thermally reduced over the double layer tungsten atomizer, was very efficient at collecting selenium or arsenic hydrides. Prior to analysis, biological samples were digested in closed-vessels microwave digestion system. Prior to the hydride formation, both selenium and arsenic were reduced to valence state (IV) and (III), respectively. The detection limit was 35 ng L^{-1} for selenium and 110 ng L^{-1} for arsenic. Sample throughput was 70 h^{-1} using 30 s of hydride trapping time. Method accuracy was evaluated by analyzing biological-certified reference materials from the National Institute of Standard and Technology (SRM-1577a and SRM-1577b "bovine liver" and RM-8414 "bovine muscle powder") and from the International Agency for Energy Atomic (A-13 "animal blood") and one water-certified reference material from the National Institute of Standard and Technology (SRM-1640 trace elements in natural water). By applying a *t*-test, there was no significant difference at the 95% probability level between the results obtained with the proposed method and those certified values.

Keywords: Flow injection; Hydride generation; *In situ* trapping; Selenium hydride; Arsenic hydride; Tungsten coil atomizer; Rhodium permanent modifier

1. Introduction

Hydride generation is a useful preconcentration technique that improves sensitivity and selectivity in atomic absorption spectrometry for elements able to form volatile hydrides. Traditionally, a heated quartz cell is used as atomizer to both decompose the volatile hydrides and atomize the element before determination by atomic absorption spectrometry. However, the use of *in situ* trapping techniques, with atomizers acting as both a hydride collector medium and atomization cell, are much more attractive, providing easily automation, improving the detection limits and eliminating interferences in vapor phase. Over the last years, graphite furnaces have been extensible used for this approach [1–13]. The atomizer surface can be either an uncoated tube or a tube treated with a chemical modifier (mainly a noble metal and/or a carbide-forming element). These chemical modifiers are usually able to interact with selenium, arsenic and other hydride-forming elements, stabilizing them to much higher temperatures [10,11,14–19].

Nowadays, with the interest to development of low cost, compact and portable instrumentation mainly for clinical and environmental analysis, the use of a filament or coil atomizers appear to be a good alternative to traditional graphite furnaces in electrothermal atomic absorption spectrometry. More than that, these atomizers should be considered to be a complementary atomizer. Tungsten coils are inexpensive and chemically inert. Moreover, a fast heating rate (>10 K ms^{-1}) is attained with a low power supply, which is also associated with the low coil mass (100 mg), and the low specific heat of tungsten (0.133 J g^{-1} K^{-1}). Then, as the coil cool very fast there is no need for an external cooling system. Unfortunately, in spite of its simplicity and promising analytical capabilities, open atomizers, such as tungsten coils, provide far from isothermal conditions. Then, determinations can be severely affected by interference effects [20–22], limiting the applications of this atomizer. As a good alternative, the use of a preliminary preconcentration step may overcome its limitations [20,23,24]. However, to stimulate the use in routine analysis,

* Corresponding author. Tel.: +55 1636024701.
E-mail address: fbarbosa@fcfrp.usp.br (F. Barbosa Jr.).

0039-9140/$ – see front matter © 2007 Elsevier B.V. All rights reserved.
doi:10.1016/j.talanta.2007.04.031

the selected preconcentration method needs to be simple and fast.

Barbosa et al. [25] demonstrated the feasibility of the use of a 150 W tungsten coil atomizer with the surface modified with rhodium acting as *in situ* hydride collector and electrothermal atomizer for selenium determination in water samples at ppt levels. After that, Cankur et al. [26] illustrated the use of a W-coil for on-line trapping of Bi hydride and determination by atomic absorption spectrometry. In that work, the hydride was previously trapped on a W-coil and then vaporized (at 1200 °C) and transported to a externally heated silica tube atomizer placed in the optical path for bismuth determination by AAS.

In the present work, we investigated the feasibility of the use of a 150 W tungsten coil atomizer as both atomizer and concentration medium for *in situ* trapping of selenium and arsenic hydrides and determination by electrothermal atomic absorption spectrometry in biological and water samples.

2. Material and methods

2.1. Instruments and apparatus

A Varian SpectrAA-40 atomic absorption spectrometer was coupled to a Varian DS-15 data station. Selenium and arsenic hollow cathode lamp from the same manufacturer were used for measurements of atomic signals at 196.0 and 197.3 nm, respectively. Measurements were based on peak height absorbance recorded with a time constant of 50 ms.

The tungsten coil (OSRAM 150 W) atomizer was fixed in two copper electrodes supported by a PTFE fitting, which was inserted into a 10 cm flow through cell mounted in a perspex base. The whole assembly replaced the Varian GTA-96 graphite furnace as previously described [27]. The tungsten coil was heated by a programmable power supply with a voltage feedback circuit (Anacom Equipment and Systems, São Bernardo do Campo, SP, Brazil). The power supply was interfaced with the DS-15 Data Station, thereby enabling the tungsten coil furnace operation to be started by pushing the START GTA command [27]. A mixture of 90% argon + 10% hydrogen was used as protective gas, and argon was used as a carrier gas for hydrides.

Coil temperatures used during this work and showed in Celsius degrees were attained by the use of two-band optical pyrometer and the use of some substances melting points and were measured with a dried filament [28].

2.2. Reagents

All reagents used were of analytical-reagent grade, except HCl and HNO_3 which were previously purified in a quartz sub-boiling stills (Kürner) before use. A clean laboratory and laminar-flow hood capable of producing class 100 were used for preparing solutions. High purity de-ionized water (resistivity 18.2 mΩ cm) obtained using a Milli-Q water purification system (Millipore, Bedford, MA, USA) was used throughout. All solutions were stored in high-density polyethylene bottles. Plastic bottles, autosampler cups and glassware materials were cleaned by soaking in 10% (v/v) HNO_3 for 24 h, rinsing five times with Milli-Q water and dried in a class 100 laminar flow hood before use. All operations were performed in a clean bench.

Stock solutions of selenium(IV) 1000 mg L^{-1} were obtained from Na_2SeO_4 (Aldrich) and of arsenic(III) 1000 mg L^{-1} from As_2O_3 (Aldrich). Analytical calibration standards were prepared daily over the range of 0–10 μg L^{-1} for Se and As by suitable serial dilutions of Se(IV) stock solution in 10% (v/v) HCl and As(III) stock solution in 10% (v/v) HCl, respectively.

Rhodium stock solution, 1000 mg L^{-1}, was prepared by dissolving 51 mg of $RhCl_3$ (Sigma, USA) in 25 mL of 2% (v/v) HNO_3.

Sodium tetrahydroborate solutions were prepared daily by dissolving of the powder (Merck, USA) in 1 L of 0.05% (m/v) sodium hydroxide (Merck) solution. L-Cysteine (Sigma) was used for As(V) reduction. A solution of 40% (m/v) urea was obtained by dissolving 40 g urea (ACS reagent, Aldrich, USA) in 100 mL of Milli-Q water.

For comparative purposes and to check the system daily, arsenic and selenium analytical calibration curves was built with solutions containing 0.0–250 μg L^{-1} Se in 0.2% (v/v) HNO_3 and with solutions containing 0.0–250 μg L^{-1} As in 0.2% (v/v) HNO_3 which were directly delivered on the tungsten coil surface previously coated with 200 μg Rh.

Signal stability in the pyrolysis step for both conditions (direct injection or trapped) up to 1400 and 1500 °C was attained for selenium and arsenic, respectively.

For all experiments, signals were obtained by peak high absorbance, and the background absorption measurement was unnecessary.

The heating program showed in Table 1 was used for selenium and arsenic determination by tungsten coil atomic absorption spectrometry using *in situ* hydride collection and direct injection of the standard Se and As solutions.

2.3. Samples

The following reference materials were used for checking the accuracy of the proposed method: animal blood (A-13), from International Atomic Energy Agency (IAEA, Viena, Austria); bovine liver (SRM-1577a and SRM-1577b), bovine muscle powder (SRM-8414), trace elements in natural water (SRM-1640) from National Institute of Standards and Technology (NIST, Gaithersburg, USA).

Table 1
Tungsten coil furnace heating programs

Step	Temperature (°C)		Time (s)	Gas flow rate (L min^{-1})
	Direct injection	*In situ* trapping		
1	120	(400[a]–520[b])	10.0 (30.0)	0.8
2	1400[c]–1500[d]	–	10.0	0.8
3	2200	2200	1.0	0.8

[a] *In situ* trapping of selenium hydride.
[b] *In situ* trapping of arsine.
[c] Pyrolysis temperature for selenium.
[d] Pyrolysis temperature for arsenic.

Table 2
Microwave oven heating program for the decomposition of biological materials

Step	Temperature (°C)	Power (W)	Time (min)
1	160	550	3.0
2	160	0	0.5
3	180	700	5.0
4	230	1000	15.0

2.4. Wet digestion

2.4.1. Selenium determination in biological samples

Samples were digested in closed-vessels by using microwave wet decomposition system (Milestone ETHOS 1600) according to the following procedure.

Samples (0.10–0.25 g) were accurately weight in a PFA digestion vessel, and then 4 ml of 20% (v/v) nitric acid + 2 mL of 30% (v/v) H_2O_2 was added. The bomb was placed inside the microwave oven, and the decomposition was carried out according to the program shown in Table 2. After cooling, the bomb caps were withdrawn of the microwave oven, and 2 mL of concentrate HCl was added to each one. Then, only the third step of the MW oven program shown in Table 2 was applied for Se(VI) reduction to Se(IV). Finally, 200 μL of 40% (m/v) urea solution was added to the digestate (with shaking carefully) before the determination of selenium for NO_x fumes elimination that might be present after sample digestion.

2.4.2. Arsenic determination in water samples

For As(V) reduction to As(III), L-cysteine (0.1 g per 100.0 mL of solution) was added to water samples and left to stand for 30 min at room temperature before analysis.

2.5. Coating of the tungsten coil atomizer

The permanent coating was made by delivering 10 aliquots of 20 μL (1000 mg L^{-1} Rh) over the tungsten coil surface (mass overall = 200 μg Rh). Each aliquot was run through a heating cycle (drying 300 °C, 40 s; pyrolysis 1200 °C, 10 s; atomization 2000 °C, 3 s).

2.6. Flow injection hydride generation

The flow system was similar to that already described [20], and consisted of an Ismatec IP12N peristaltic pump and NResearch 161T031 three-way solenoid valves controlled by a PC 486 microcomputer. The solenoid valves and the tungsten coil power supply were simultaneously controlled by a software written in Visual Basic [20,27].

PTFE conduit tubes (0.80 mm i.d.) were used throughout. To automatically set up the quartz capillary over the tungsten coil during the collection of hydrides, we have first modified the autosampler of the AAS by replacing the end section of the PTFE sample delivery tube by a quartz capillary tube of 50 mm long × 1.5 mm o.d. × 1.1 mm i.d. as previously described [25]. The distance between the atomizer and quartz tube was optimized in 1 mm. The gas–liquid separator was a stripping-type cylinder made of acrylic (10 mm internal diameter, 60 mm height) with 50% of its volume filled with glass beads. The outlet of the gas liquid separator was passed through a PTFE membrane to remove moisture.

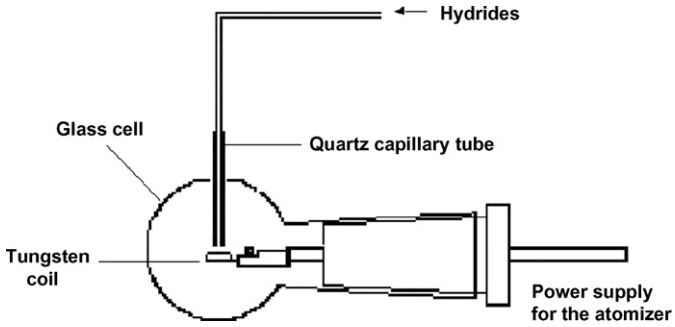

Fig. 1. Design for selenium and arsenic hydride *in situ* trapping over the tungsten coil atomizer.

In situ collection took place when the hydride came from the quartz tube and touched the tungsten rhodium-coated surface. Fig. 1 shows the design of the coupled system used in this work.

2.7. Procedure

In the first step, the autosampler arm containing the quartz tube is moved to the coil furnace keeping a distance of 1 mm from the coil atomizer, by pushing the button "align sampler" in the DS-15 Data Station. In the next step, valves V_1 and V_2 are switched on for 30 s for selenium or arsenic hydride trapping over the tungsten coil. After this, valves are switched-off, and the align sampler button was pressed. During this step, the reagent re-circulates, and sample is replaced by another one. The complete procedure is described in Table 3.

Then, one pushes the start GTA button for simultaneously starting the heating programs of the tungsten coil (Table 1) and furnace, so that the transient signals could be visualized in the data station during the atomization. The synchronism was possible by using a two-step heating program running at 40 °C for the furnace, the second step time duration being adjusted accordingly for recording the transient signals. This furnace can be operated outside the spectrometer optical path. Thus, the SpectrAA-40 original software was used throughout with the tungsten coil furnace in its path.

Table 3
Operating parameters and sequence for *in situ* trapping over the tungsten coil

Step	Function	V_1	V_2	W-coil Temperature (°C)	Duration (s)
1	Move autosampler arm to the tungsten coil atomizer	Off	Off	Room temperature	10
2	Hydride collection (Fig. 1)	On	On	400[a]/520[b]	30
3	Move autosampler arm back to the resting position, atomize and read	Off	Off	2200	10

[a] Selenium.
[b] Arsenic.

Table 4
Optimized conditions for generation of selenium and arsenic hydrides and determination by TC AAS

Parameter	Se	As
Spectrometer conditions		
Resonance wavelength (nm)	196.0	193.7
Band pass (nm)	1.0	0.5
Hydride generation conditions		
$NaBH_4$ concentration (%, m/v)	0.7	1.0
$NaBH_4$ flow rate (mL min^{-1})	2.2	2.2
Sample flow rate (mL min^{-1})	3.0	3.0
Ar flow rate (mL min^{-1})	77.0	25.0
Trapping time (s)	30	30
Trapping temperature (°C)	400	520
Sample throughput (h^{-1})	70	70

The procedure was repeated for each analysis and a sample throughput of 70 samples h^{-1} was attained. The analytical curve was then obtained by pumping (0.0–10.0 μg L^{-1} Se in 10% (v/v) HCl) or (0.0–10.0 μg L^{-1} As in 10% (v/v) HCl) reference solutions at a flow rate of 3.0 mL min^{-1} during 30 s. The optimized conditions showed in Table 4 were used.

3. Results and discussion

3.1. Preliminary studies

In the preliminary experiments, pyrolysis temperature curves were obtained for the direct injection of arsenic and selenium aqueous solutions in W-coils previously treated with rhodium. For this experiment, 10 μL of a solution containing 300 μg L^{-1} Se(IV) or 10 μL of a solution containing 200 μg L^{-1} As(III) was delivered into the tungsten coil-coated with 100 μg Rh. The atomization temperature was kept at 2200 °C. In these conditions, selenium and arsenic was thermally stable up to 1400 and 1500 °C, respectively (Fig. 2A and B). On the other hand, for untreated W-coils, selenium absorbance dropped for temperatures higher than 250 °C. Conversely, a thermal stability up to 1400 °C was observed for arsenic in untreated tungsten coils. Bruhn et al. [29] also observed a thermal stability for arsenic in untreated tungsten coil surface. This may occur through interactions of As with W metal or W species formed in the coil surface generating the formation of W compounds with As [30]. However, the use of the permanent rhodium modifier improved arsenic sensitivity by a factor of two when compared to untreated coils (Fig. 2B). We found the same thermal stability for both direct injection of selenium and arsenic aqueous solutions and trapped hydrides over the rhodium-coated W-coil. It means that in both forms, trapped as hydrides or as aqueous solutions, selenium and arsenic are able to form a stable compound with the permanent coating. Several authors have previously observed the same findings [6,11,19,29,30].

3.2. W-coil coating

In order to determine the most suitable amount of rhodium modifier for *in situ* trapping of the selenium and arsenic hydrides on the tungsten coil, 2.0 μg L^{-1} Se(IV) in 10% (v/v) HCl and 2.0 μg L^{-1} As(III) in 10% (v/v) HCl were used throughout as reference solutions. Different masses of modifier were investigated within the range 10–250 μg Rh. For both elements, similar sensitivities were attained for thermally reduced rhodium masses from 10 up to 250 μg (Fig. 3). However, in order to increase the coating lifetime, 200 μg of the modifier were chosen, assuming that the lifetime has a close relationship with the modifier mass.

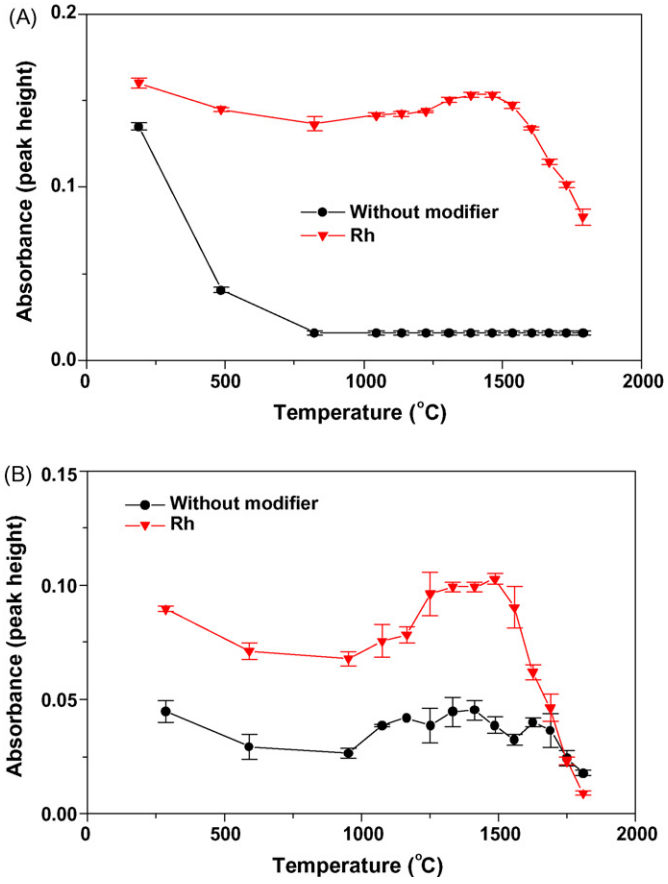

Fig. 2. Pyrolysis curves for direct injection of selenium and arsenic on the W-coil atomizer with and without Rh permanent modifier (100 μg Rh). (A) Direct injection of selenium and (B) direct injection of arsenic. See text for details.

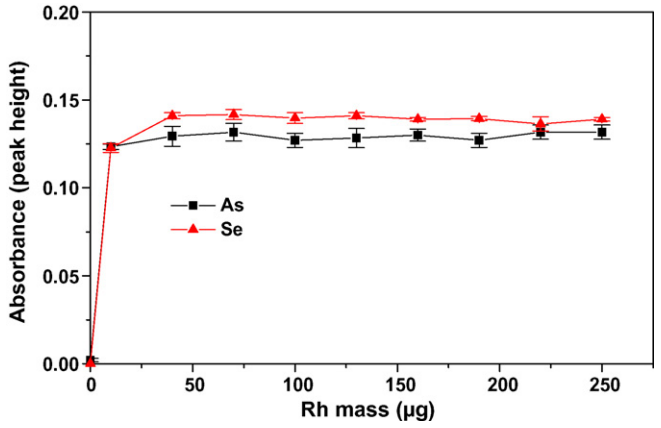

Fig. 3. Influence of the rhodium mass on selenium and arsenic hydride trapping.

3.3. Evaluation of microwave sample decomposition and pre-reduction conditions for selenium and arsenic hydride generation

Nitric acid with hydrogen peroxide has demonstrated to be an efficient mixture to decompose organic materials in open-vessel heating or close-vessel systems. When closed systems combined to microwave heating are used, sample matrix can be destroyed with the use of dilute acid solutions and reduced volumes of concentrated hydrogen peroxide [31,32]. In our study, a mixture of 4.0 mL of 20% (v/v) HNO_3 + 2.0 mL of 30% (v/v) H_2O_2 was sufficient to decompose the biological materials. However, to generate the hydrides, the analyte pre-reduction is required after sample decomposition. For selenium, it is usually performed in HCl medium. Then, after digestion, the rotor with the vessels was transferred into a water bath and cooled down to room temperature. From 1.0 to 5.0 mL of concentrate HCl was evaluated as a reduction medium. The covered vessels were heated in the microwave oven for 5 min at 700 W (Table 3, step 3). In this study, as low as 2.0 mL of concentrate HCl was efficient in total selenium reduction (selenium recovery in CRMs >90%). In the case of arsenic, L-cysteine has been widely used as a pre-reductor for the determination of this element by Hydride Generation AAS. Tsalev et al. [33] described some advantages for its use: rapid and efficient reduction compared to other pre-reductor systems, such as KI mineral acid and KI–ascorbic acid; stability of the reducing solution, which may be stored for a long time; higher tolerance to interfering species. Bortoleto and Cadore [34] have demonstrated that L-cysteine in acidic medium was able to reduce up to 5 μg L^{-1} of As(V) in 30 min at room temperature. In our study, we evaluated different concentrations of L-cysteine for arsenic reduction, and 0.1 g of reagent per 100.0 mL of solution was sufficient for the total reduction of arsenic to arsenic(III) (samples were left 30 min at room temperature prior analysis). Similar results were also observed by Bortoleto and Cadore [34].

Decomposition procedures with the use of HNO_3 result in NO_x fumes absorbed in the digestate that can lead to erroneously high results for determinations of hydride elements by HG-AAS. The removal of these fumes usually requires open-vessel heating with concentrated sulfuric acid in a microwave oven, which was both potentially dangerous and labor intensive. In our study, 200 μL of 40% (m/v) urea solution was added to the digestate (with shaking carefully) before the determination of elements [35]. The amount of urea selected was found useful in ridding the sample of interfering NO_x fumes that might be present after digestion [35].

3.4. Optimization of borohydride concentration

The $NaBH_4$ concentration was evaluated in order to obtain the maximum sensitivity for selenium and arsenic determination (Fig. 4). For this study, sodium tetrahydroborate flow rate was fixed at 2.5 mL min^{-1} and the concentration varied from 0.1 to 1.5% (m/v). These concentrations were selected based on previous papers with *in situ* trapping of arsenic and selenium hydrides over the graphite surfaces [4,5,36–41]. It was observed

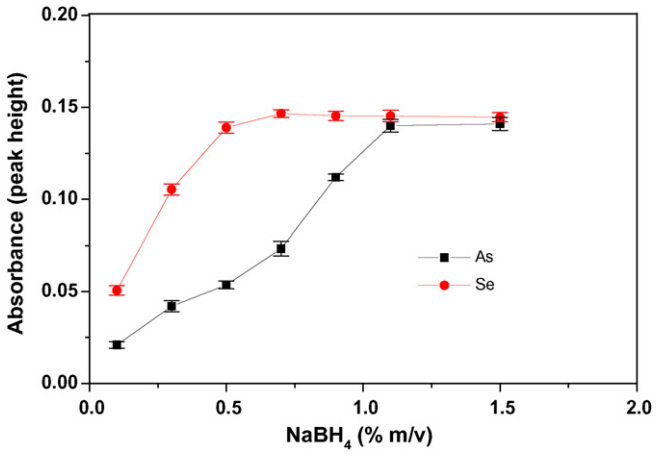

Fig. 4. Effect of $NaBH_4$ concentration. Atomizer was modified with 200 μg Rh. For other parameters, see Table 4.

that the best sensitivity was achieved when the $NaBH_4$ concentration ranged between 0.50 and 0.70% (m/v) for selenium and between 1.0 and 1.5% (m/v) for arsenic (Fig. 4). Same results were observed by Liao and Haug [42] for selenium and by An et al. [3] for arsenic in graphite atomizers coated with Pd. However, with the use of $NaBH_4$ concentrations higher than 1.0% (m/v), a reduction on selectivity during arsine formation has been observed [3]. Therefore, as a compromise between selectivity and sensitivity in the further experiments 0.70% and 1.0% (m/v) $NaBH_4$ was used for selenium and arsenic *in situ* hydride collection, respectively.

3.5. Optimizaton of collecting temperature

The optimum collecting temperature for selenium and arsenic hydrides on the tungsten coil was evaluated. For this study, we used W-coils previously coated with 200 μg of Rh. First experiments were performed without heating the tungsten coil. In these conditions, only selenium hydride trapped over the coated W-coil. For the subsequent experiments, the temperature of the tungsten coil was varied from 50 to 1000 °C. The best temperature for selenium and arsenic hydride collection was 400 and 520 °C, respectively.

3.6. Effect of carrier gas flow rate

The effect of argon carrier gas flow rate on Se and As sensitivity was investigated as a function of peak height absorbance. For this study, gas flow rates were varied from 0 to 340 mL min^{-1}. The protective gas flow rate (90% Ar + 10% H_2) was maintained at 0.8 L min^{-1} during the collection step. When a protective gas was not flowing during collection, a reduced hydride trapping efficiency was observed for both analytes, but the effect is more evident for selenium. The optimal carrier gas flow rates for the proposed *in situ* hydride trapping method was 77 and 25 mL min^{-1} for selenium and arsenic, respectively. For this study, a 2.0 μg L^{-1} Se(IV) and a 2.0 μg L^{-1} As(III) reference solutions in 10% (v/v) HCl, flowing at 2.5 mL min^{-1} during 30 s, was used.

Table 5
Determination of Se and As in standard reference materials

Sample	Certified value	Found value
Selenium		
A-13 "animal blood" ($\mu g\,g^{-1}$)[a]	0.24	0.22 ± 0.04
SRM-1577a "bovine liver" ($\mu g\,g^{-1}$)[b]	0.71 ± 0.07	0.68 ± 0.10
SRM-1577b "bovine liver" ($\mu g\,g^{-1}$)[b]	0.73 ± 0.06	0.70 ± 0.10
RM-8414 "bovine muscle powder" ($\mu g\,g^{-1}$)[b]	0.076 ± 0.010	0.071 ± 0.012
Arsenic		
Trace elements in natural water(1640)[b] ($\mu g\,L^{-1}$)	26.67 ± 0.41	25.90 ± 0.51

[a] International Atomic Energy Agency (IAEA).
[b] National Institute of Standard and Technology (NIST).

3.7. Sample analysis

Accuracy of the proposed method was assessed with the analysis of four biological reference materials for selenium determination, and one water reference material for arsenic determination. In all the cases, the calibration was run against aqueous reference solutions.

The obtained analyte contents were in agreement with the certified values (Table 5). After applying a *t*-test between each pair of data (certified and found), no differences were found among each pair of results at the 5% probability level, which is good indication of the accuracy of the proposed method.

3.8. Analytical figures of merit

With the proposed system, the detection limit was 35 ng L^{-1} for selenium and 110 ng L^{-1} for arsenic (3 S.D., $n = 20$). Sample throughput was 70 h^{-1} using 30 s of hydride trapping time. Under the optimized conditions shown in Table 4, the achieved enrichment factor for selenium and arsenic was 150 and 95, respectively. Higher enrichment factors can be achieved by increasing the trapping time. The analytical calibration curve was linear within the 0.035–10.00 and 0.11–10.00 $\mu g\,L^{-1}$ for selenium and arsenic, respectively.

Each coating (200 μg of Rh), remained stable for at least 250 firings. Repeatability was <6% for Se ($n = 50$, SRM-1577a "bovine liver", target value = 0.71 $\mu g\,g^{-1}$ Se) and <4% for As ($n = 50$, SRM-1640 "trace elements in natural water", target value = 26.67 $\mu g\,L^{-1}$). Reproducibility (between days) was <10% for Se ($n = 20$, SRM-1577a "bovine liver", target value = 0.71 $\mu g\,g^{-1}$ Se) and <9% for As ($n = 20$, SRM-1640 "trace elements in natural water", target value = 26.67 $\mu g\,L^{-1}$). It was observed that there was no need for re-calibration during the coating lifetime (approximately 1 day of routine analysis), as the slope of analytical calibration curve did not show variations higher than 5%. The final optimized conditions for selenium and arsenic hydride trapping using the proposed system are described in Table 4.

4. Conclusion

This paper describes an easy and a very sensitivite method for selenium and arsenic determination in biological and water samples by using hydride generation W-coil (*in situ* trapping) atomic absorption spectrometry. The detection limit (DL) achieved in 'ng L^{-1}' is comparable to those methods using *in situ* trapping in graphite furnaces. Moreover, considerable improvement on the enrichment factors can be achived by increasing the hydride collection time.

Our group is now evaluating the feasibility of the use of a 150 W tungsten coil for simultaneous *in situ* trapping of hydrides and determination by eletrothermal vaporization-ICP-MS.

Acknowledgements

The authors are grateful to Fundação de Amparo à Pesquisa do Estado de São Paulo (FAPESP) and Conselho Nacional de Desenvolvimento Científico e Tecnológico (CNPq).

References

[1] J.Y. Cabon, W. Erler, Analyst 123 (1998) 1565.
[2] Z. Ajtony, N. Szoboszlai, Z. Bella, S. Bolla, P. Szakal, L. Bencs, Mikrochim. Acta 150 (2005) 1.
[3] Y. An, S.N. Willie, R.E. Sturgeon, Spectrochim. Acta B 47 (1992) 1403.
[4] J.L. Burguera, M. Burguera, C. Rivas, P. Carrero, Talanta 45 (1998) 531.
[5] J.L. Burguera, P. Carrero, M. Burguera, C. Rondon, M.R. Brunetto, M. Gallignani, Spectrochim. Acta B 51 (1996) 1837.
[6] C.D. Freschi, G.P.G. Freschi, J.A.G. Neto, At. Spectrosc. 25 (2004) 133.
[7] C.D. Freschi, G.P.G. Freschi, J.A.G. Neto, J.A. Nobrega, P.V. Oliveira, Spectrochim. Acta B 60 (2005) 759.
[8] H.O. Haug, Y.P. Liao, J. Anal. At. Spectrom. 10 (1995) 1069.
[9] F. Laborda, J. Medrano, J.I. Cortes, J.M. Mir, J.R. Castillo, Spectrochim. Acta B 54 (1999) 343.
[10] J. Murphy, P. Jones, G. Schlemmer, I.L. Shuttler, S.J. Hill, Anal. Commun. 34 (1997) 359.
[11] J. Murphy, G. Schlemmer, I.L. Shuttler, P. Jones, S.J. Hill, J. Anal. At. Spectrom. 14 (1999) 1593.
[12] J.F. Tyson, R.I. Ellis, G. Carnrick, F. Fernandez, Talanta 52 (2000) 403.
[13] S. Garbos, M. Walcerz, E. Bulska, A. Hulanicki, Spectrochim. Acta B 50 (1995) 1669.
[14] F. Barbosa, E.C. Lima, R.A. Zanao, F.J. Krug, J. Anal. At. Spectrom. 16 (2001) 842.
[15] E.C. Lima, F. Barbosa, F.J. Krug, J. Anal. At. Spectrom. 14 (1999) 1913.
[16] E.C. Lima, F. Barbosa, F.J. Krug, M.M. Silva, M.G.R. Vale, J. Anal. At. Spectrom. 15 (2000) 995.
[17] E.C. Lima, F. Barbosa, F.J. Krug, Anal. Chim. Acta 409 (2000) 267.
[18] Y. Zhou, R.A. Zanao, F. Barbosa, P.J. Parsons, F.J. Krug, Spectrochim. Acta B 57 (2002) 1291.
[19] R.A. Zanao, F. Barbosa, S.S. Souza, F.J. Krug, A.L. Abdalla, Spectrochim. Acta B 57 (2002) 291.
[20] F. Barbosa, F.J. Krug, E.C. Lima, Spectrochim. Acta B 54 (1999) 1155.
[21] C.G. Bruhn, J.Y. Neira, M.I. Guzman, M.M. Darder, J.A. Nobrega, Fresenius J. Anal. Chem. 364 (1999) 273.
[22] X.D. Hou, Z. Yang, B.T. Jones, Spectrochim. Acta B 56 (2001) 203.
[23] A.S. Ribeiro, M.A.Z. Arruda, S. Cadore, Spectrochim. Acta B 57 (2002) 2113.
[24] A.S. Ribeiro, M.A.Z. Arruda, S. Cadore, J. Anal. At. Spectrom. 17 (2002) 1516.
[25] F. Barbosa, S.S. de Souza, F.J. Krug, J. Anal. At. Spectrom. 17 (2002) 382.
[26] O. Cankur, N. Ertas, O.Y. Ataman, J. Anal. At. Spectrom. 17 (2002) 603.
[27] M.M. Silva, F.J. Krug, P.V. Oliveira, J.A. Nobrega, B.F. Reis, D.A.G. Penteado, Spectrochim. Acta B 51 (1996) 1925.
[28] Z.F. Queiroz, P.V. Oliveira, J.A. Nobrega, C.S. Silva, I.A. Rufini, S.S. de Souza, F.J. Krug, Spectrochim. Acta B 57 (2002) 1789.
[29] C.G. Bruhn, V.N. Huerta, J.Y. Neira, Anal. Bioanal. Chem. 378 (2004) 447.
[30] F. Barbosa, F.J. Krug, E.C. Lima, Analyst 125 (2000) 2079.

[31] G.C.L. Araujo, M.H. Gonzalez, A.G. Ferreira, A.R.A. Nogueira, J.A. Nobrega, Spectrochim. Acta B 57 (2002) 2121.
[32] P.Y.T. Chow, T.H. Chua, K.F. Tang, B.Y. Ow, Analyst 120 (1995) 1221.
[33] D.L. Tsalev, M. Sperling, B. Welz, Talanta 51 (2000) 1059.
[34] G.G. Bortoleto, S. Cadore, Talanta 67 (2005) 169.
[35] F.S. Li, W. Goessler, K.J. Irgolic, Anal. Commun. 35 (1998) 361.
[36] J.F. Tyson, N.G. Sundin, C.P. Hanna, S.A. McIntosh, Spectrochim. Acta B 52 (1997) 1773.
[37] H. Matusiewicz, M. Kopras, J. Anal. At. Spectrom. 18 (2003) 1415.
[38] H. Matusiewicz, M. Krawczyk, Anal. Sci. 22 (2006) 249.
[39] M. Burguera, J.L. Burguera, M.R. Brunetto, M. Delaguardia, A. Salvador, Anal. Chim. Acta 261 (1992) 105.
[40] P. Carrero, A. Malave, J.L. Burguera, M. Burguera, C. Rondon, Anal. Chim. Acta 438 (2001) 195.
[41] P.E. Carrero, J.F. Tyson, Analyst 122 (1997) 915.
[42] Y.P. Liao, H.O. Haug, Microchem. J. 56 (1997) 247.

Available online at www.sciencedirect.com
ScienceDirect
Talanta 73 (2007) 589–593
Talanta
www.elsevier.com/locate/talanta

Short communication

A simple approach for fabrication of dual-disk electrodes with a nanometer-radius electrode and a micrometer-radius electrode

Ning Gao, Xiaohong Lin, Wenzhi Jia, Xiaoli Zhang *, Wenrui Jin *

School of Chemistry and Chemical Engineering, Shandong University, Jinan 250100, China

Received 22 December 2006; received in revised form 6 April 2007; accepted 6 April 2007
Available online 24 April 2007

Abstract

We developed a new simple approach to fabricate dual-disk electrodes with a nanometer-radius electrode and a micrometer-radius electrode. First, nanometer-sized electrodes and micrometer-sized electrodes were constructed using 10-μm-radius metal wires, respectively. To fabricate the nanometer-sized electrode, after the apex of the 10-μm-radius metal wire was electrochemically etched to an ultrafine point with a nanometer-radius, the metal wire was electrochemically coated with a phenol–allyphenol copolymer film. The micrometer-sized electrode was fabricated by directly electrochemical coating the metal wire with an extremely thin phenol–allyphenol copolymer film. Then, the nanometer-radius electrode (the first electrode) and the 10-μm-radius electrode (the second electrode) were inserted into two sides of a thick-septum borosilicate theta (θ) tubing, respectively. The second electrode protruded from the top of the θ tubing. The top of the θ tubing was sealed with insulating ethyl α-cyanoacrylate. The top of the θ tubing with both electrodes was ground flat and polished successively with fine sandpaper and aluminum oxide powder until the tip of the first electrode was exposed. Since the second electrode protruded from the top of the θ tubing, its 10-μm-radius tip was naturally formed during polishing. The dual-disk electrodes were characterized by scanning electron microscopy and cyclic voltammetry. The success rate for fabrication of the dual-disk electrodes is ∼80% due to double insurance from two coating layers of different polymers.

Keywords: Electrode; Electrochemical detection; Voltammetry

1. Introduction

During the last two decades, nanometer-to-micrometer-radius electrodes have received considerable attention for characterization of electrode/electrolyte processes [1,2], imaging of single biological macromolecules [1,3], investigation of heterogeneous electron-transfer kinetics and mass-transport mechanisms [1,4–10] due to small capacitances, high mass transport rate, low ohmic potential drop (*iR* drop) and low double-layer charging current, enabling electrochemical measurements with small cell time constants in micro-environmental and biological specimens [11–15]. Micrometer-sized electrodes have been successfully used as tips in scanning electrochemical microscopy (SECM) for investigation of homogeneous and heterogeneous electrochemical and chemical processes, imaging of surface topography or reactivity, and fabrication of microstructures on surfaces [16–18]. Recently, there has been increasing interest in using of nanometer-sized electrodes to detect single molecules, to obtain high-resolution electrochemical images and to measure fast heterogeneous electron-transfer kinetics [19–33]. Disk-shaped nanometer-sized electrodes are often used because they are relatively simple and can attain true steady-state current. Two approaches have been used to fabricate nanometer-sized electrodes. One is the glass-sealed approach. A metal wire is sealed into a glass pipette. Then the metal wire covered with glass is pulled into a nanometer-sized tip with the help of a laser pipette puller. Finally, the tip covered with glass is exposed either by etching away or by micropolishing a small portion of glass insulator. An important advantage of the nanometer tips covered with glass is its rigidity. Another is the insulator-coated approach. Usually, the apex of a micrometer-radius metal wire is electrochemically etched to a nanometer size. Then, the etched metal wire is coated with an insulator. Finally, the nanometer-sized apex is exposed. This approach is simple and no laser pipette puller is needed. This type of nanometer-sized electrodes has been fabricated in our laboratory [34]. However, the

* Corresponding authors. Fax: +86 531 8856 5167.
E-mail address: jwr@sdu.edu.cn (W. Jin).

0039-9140/$ – see front matter © 2007 Elsevier B.V. All rights reserved.
doi:10.1016/j.talanta.2007.04.012

success rate is low due to cracking of the films coaled on the electrodes. Moreover, the electrodes coated with polymer are elastic. Therefore, simple approaches for fabrication of rigid nanometer-sized electrodes should be developed. The technique for detection of dual species and collection of dual information in a sample has been developed. Simultaneous amperometric measurement of ascorbate and catecholamine secreted from a single cell using two individual micrometer-sized electrodes has been reported [35]. Dual-disk electrodes with two micrometer-sized electrodes are very convenient for detection of two electroactive species [36] and for acquirement of dual information in single cells [37]. Micrometer-sized dual-disk electrodes have been used for distance control and detection of nitric oxide release from cells [38,39]. There is no report on dual electrodes with a nanometer-sized electrode.

In this work, we developed a simple approach with a high success rate to fabricate dual-disk electrodes consisting of a nanometer-radius electrode and a micrometer-radius electrode. First, a nanometer-radius electrode was constructed by using electrochemical etching the tip of a 10-μm-radius metal wire and electrochemical coating an extremely thin phenol–allyphenol copolymer film on the etched tip. Then, the nanometer-radius electrode (the first electrode) and a micrometer-radius electrode (the second electrode), which was fabricated by electrochemical coating an extremely thin phenol–allyphenol copolymer film on the surface of a 10-μm-radius metal wire, were inserted into two sides of a thick-septum borosilicate θ tubing pulled by a laser micropipette puller, respectively. The first electrode was embedded in the tip of the θ tubing and the second electrode was slightly protruded from the top of the θ tubing. The θ tubing was sealed with insulating ethyl α-cyanoacrylate. Finally, the top of the θ tubing with both electrodes was successively ground with fine sandpaper, and then polished with finer aluminum oxide powder until the nanometer-radius tip of the first electrode was exposed. Since the second electrode was protruded from the top of the θ tubing, its 10-μm-radius tip was naturally formed during polishing. Gold as the electrode material was chosen in this work. Using this approach, the success rate for fabrication of the dual-disk electrodes is very high due to double insurance from two coating layers of different polymers.

2. Experimental

2.1. Reagents

Reagents and solution preparation were the same as in our previous work [34].

2.2. Apparatus

A CHI 900 scanning electrochemical microscope (CH Instruments, Austin, TX, USA) was used to perform electrode characterization. Electrochemical experiments were carried out with a three- or a four-electrode system that consisted of one or two electrodes of a dual-disk electrode, an Ag/AgCl electrode (1 mol/L KCl) as the reference electrode, and a Pt wire as the auxiliary electrode. The detection cell with the three- or four-electrode system was housed in a Faraday cage in order to minimize the interference from noise from external sources. A P-2000 laser micropipette puller (Sutter Instrument Co., Novato, CA, USA) was used to make a dual pipette by pulling borosilicate θ tubing (1.5-mm o.d., BT-150-10, Sutter Instrument Co.).

2.3. Fabrication of dual-disk electrodes with a nanometer-radius disk electrode and a micrometer-radius electrode

First, nanometer-sized Au disk electrodes and micrometer-sized Au electrodes were constructed, respectively. To fabricate a nanometer-sized Au electrode, a 10-μm-radius Au wire with a copper lead was electrochemically etched and then electrochemically coated with an extremely thin phenol–allyphenol copolymer film according to our previous work [34]. For fabrication of a micrometer-sized Au electrode, a 10-μm-radius Au wire with a copper lead was directly electrochemically coated with the phenol–allyphenol copolymer film. In this case, the nanometer-sized and micrometer-sized tips of all Au wires were thoroughly insulated. To make sure the insulativity of the Au wires, the tip of the Au wire was inserted in a solution consisting of 0.500 mol/L KCl and 1.0×10^{-2} mol/L $K_3Fe(CN)_6$, and scanned in the potential range of 0.45 to −0.05 V. When there was no current response, the insulated Au wire was used to make the dual-disk electrode. The dual-electrode with a nanometer-radius Au disk electrode and a micrometer-radius Au electrode was constructed using a borosilicate θ tubing, named for its resemblance to the Greek letter theta (θ). The borosilicate θ tubing was pulled using a P-2000 laser micropipette puller to make a dual pipette with two orifices. Then, a nanometer-sized electrode and a 10-μm-radius electrode were inserted with care into two sides of the thick-septum borosilicate θ tubing from their two large openings, respectively. The 10-μm-radius electrode was slightly protruded from the top of the θ tubing. The copper leads of both electrodes were secured in the θ tubing with epoxy resin. The pulled fine top of the θ tubing was sealed with ethyl α-cyanoacrylate by inserting the top of the θ tubing to the low-viscosity adhesive that could permeate into the θ tubing by capillary force. The top of the θ tubing with both sealed electrodes was ground flat with emery paper. The top of the θ tubing was periodically monitored under an optical inverted microscope. When the distance between the surface and the tip of the nanometer-sized electrode was less than 1 μm, the insulated layer was polished on a wetted felt pad with successively finer aluminum oxide powder (1 and 0.05 μm diameter). During polishing, the insulated layer was rinsed with water each 5 min. To know whether the tip of the nanometer-sized electrode was exposed, the electrochemical response of the nanometer-sized electrode was periodically determined by using voltammetry in a solution containing 0.500 mol/L KCl and 1.0×10^{-2} mol/L $K_3Fe(CN)_6$. At this stage, the polishing rate should be very slow. When the voltammetric response could be obtained, polishing the dual electrode was stopped. In this case, the radius of the micrometer-sized electrode was 10-μm. Thus, the dual-

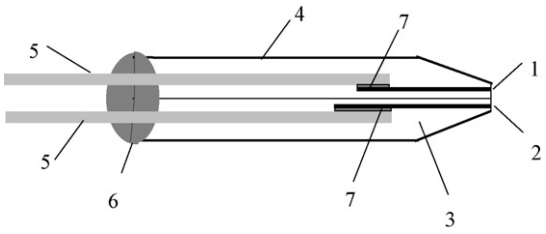

Fig. 1. Schematic representation of the dual-disk electrode with a nanometer-radius Au electrode and a 10-μm-radius Au electrode. 1, 10-μm-radius Au wire with a nanometer-sized tip coated with phenol–allyphenol copolymer; 2, 10-μm-radius Au wire coated with phenol–allyphenol copolymer; 3, ethyl α-cyanoacrylate; 4, borosilicate θ tubing; 5, copper lead; 6, epoxy resin; 7, silver epoxy.

disk electrodes with a nanometer-radius disk electrode and a micrometer-radius electrode was constructed. The schematic representation of the dual-disk electrode with a nanometer-radius Au electrode and a 10-μm-radius Au electrode was shown in Fig. 1.

3. Results and discussion

Cyclic voltammetry can be used to test the electrochemical characteristics of nanometer-radius disk electrodes and to obtain their effective radius from the diffusion-limiting steady-state current based on Eq. (1) [40]:

$$I_{T,\infty} = 4nFDcr \quad (1)$$

where D and c are the diffusion coefficient and the bulk concentration of the mediator species, respectively, r the effective radius of the electrode, n the number of electrons transferred and F is the Faraday constant. Fig. 2 shows the cyclic voltammograms of nanometer-radius electrodes in dual-disk electrodes in 0.500 mol/L KCl and 1.0×10^{-2} mol/L $K_3Fe(CN)_6$. Six to eight voltammograms for each electrode were recorded. The steady-state currents on all voltammograms of each electrode are almost the same, implying the no cracks between the Au tip and the insulation layer as well as good stability of the dual-disk electrodes. All voltammograms remain sigmoidal and are very well shaped

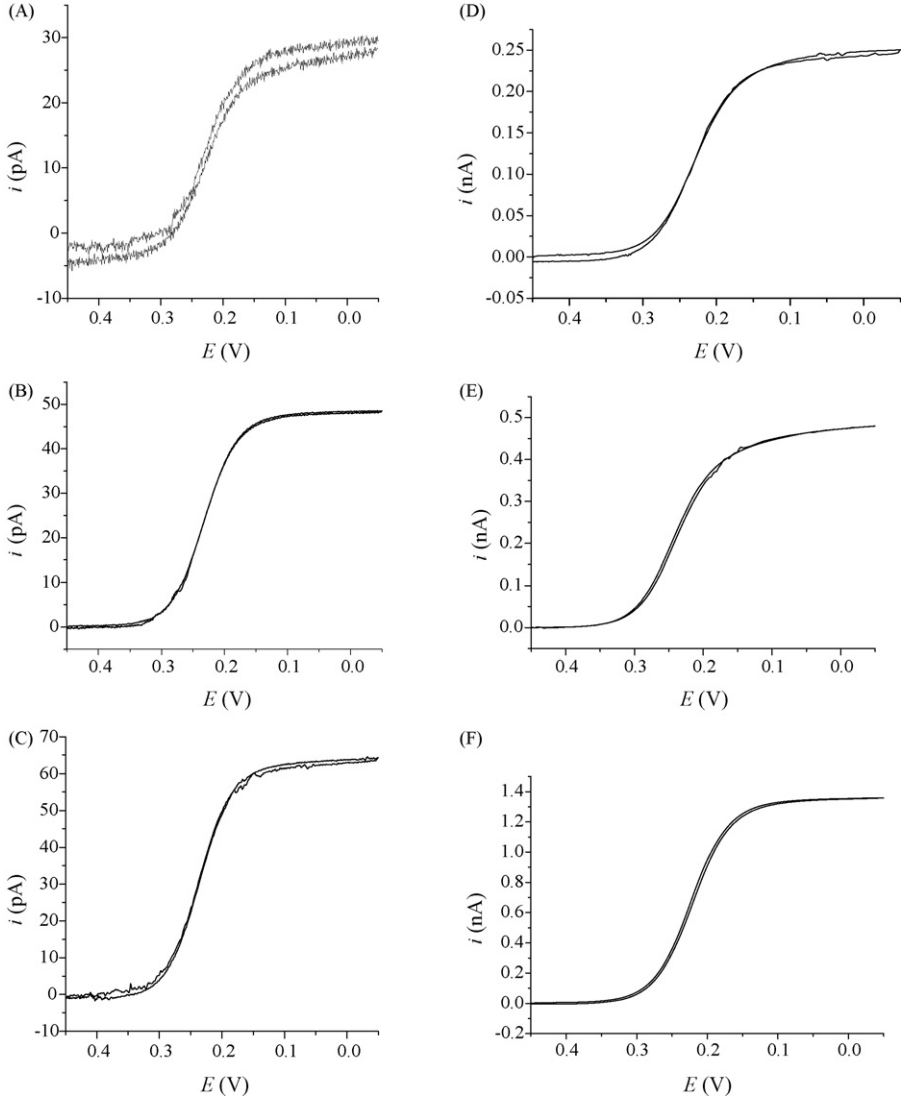

Fig. 2. Cyclic voltammograms of nanometer-sized Au electrodes with different radii in dual-disk electrodes in 1.0×10^{-2} mol/L $K_3Fe(CN)_6$ and 0.500 mol/L KCl. Calculated effective radius (nm): (A) 10 nm, (B) 17 nm, (C) 22 nm, (D) 90 nm, (E) 158 nm and (F) 504 nm. Scan rate, 10 mV/s.

with a flat plateau for scan rates of 10–50 mV/s. Moreover, relatively low charging current can be observed in the voltammograms, indicating that these electrodes in the dual-disk electrodes are disk-shaped, not "lagooned" [1,24]. It can be noted from these voltammograms that the background currents are very low. This also demonstrates that there is no apparent solution leakage through the insulator. When $D = 7.2 \times 10^{-6}$ cm^2/s [41], $c = 1.0 \times 10^{-2}$ mol/L and $n = 1$ are used, the radii of the electrodes for the voltammograms shown in Fig. 2 are calculated to be 10, 17, 22, 90, 158 and 504 nm, respectively. The success rate for fabrication of the dual-disk electrodes is ~80% due to double insurance from two coating layers of different polymers.

Fig. 3 shows the scanning electron microscopy (SEM) micrograph of a dual-disk electrode with a 10-nm-radius Au electrode and a 10-μm-radius Au electrode shown in Fig. 2A. It is clear that the surface of both electrodes in the dual-disk electrode is smooth and flat without cracks between the Au tip and the α-cyanoacrylate adhesive. The α-cyanoacrylate adhesive surrounding both Au tips slightly protrudes the wall of the θ tubing. This does not affect voltammetric behavior of both tips, because the α-cyanoacrylate adhesive is flat relative to both Au tips.

For two neighboring working electrodes, the cross-talking influence, i.e., one electrode collects the electrogenerated species from another electrode due to the overlapping of the steady-state diffusion layers at both electrodes, should be investigated. Matsue and co-worker [37] measured the collection efficiency (the ratio of the reduction current at one disk electrode to that at another disk electrode) for micrometer-sized dual-disk electrodes. They indicated that when the gap between two disks was ~16 μm for a dual-disk electrode with a radius of ~2.7 μm for each, the collection efficiency is 6%. To estimate the collection efficiency of the dual-disk electrodes reported here, we simultaneously recorded the voltammograms of a electrode and the currents of another electrode for the dual-disk electrode consisting of two 10-μm-radius Au electrodes with a gap of ~83 μm. In the experiment, the potential of one disk electrode (electrode A) is scanned with a scan rate of 20 mV/s and another disk electrode (electrode B) is held at different potentials from 0 to 0.500 V. Fig. 4 shows the cyclic voltammograms of electrode A in 1.0×10^{-2} mol/L $K_3Fe(CN)_6$. The currents at electrode B at different potentials are different. When the potentials of 0–0.3 V are applied at electrode B, $K_3Fe(CN)_6$ is reduced to $K_4Fe(CN)_6$, which can be judged from the voltammograms of electrode A. The more positive the potential is, the less the current is. The cyclic voltammograms and the steady-state currents of electrode A do not change with potential of electrode B, implying that the product $K_4Fe(CN)_6$ of electrochemical reaction generated by electrode B is not detected by electrode A. When the potential applied at electrode A is scanned from 0.5 to −0.1 V, the currents of electrode B held at different potentials are almost the same. The phenomena indicate that $K_4Fe(CN)_6$ generated by electrode A in the range of 0.3 to −0.1 V is not detected by electrode B. The zero collection efficiency between both electrodes in the dual-disk electrode means that the electrochemical interference from the neighboring disk

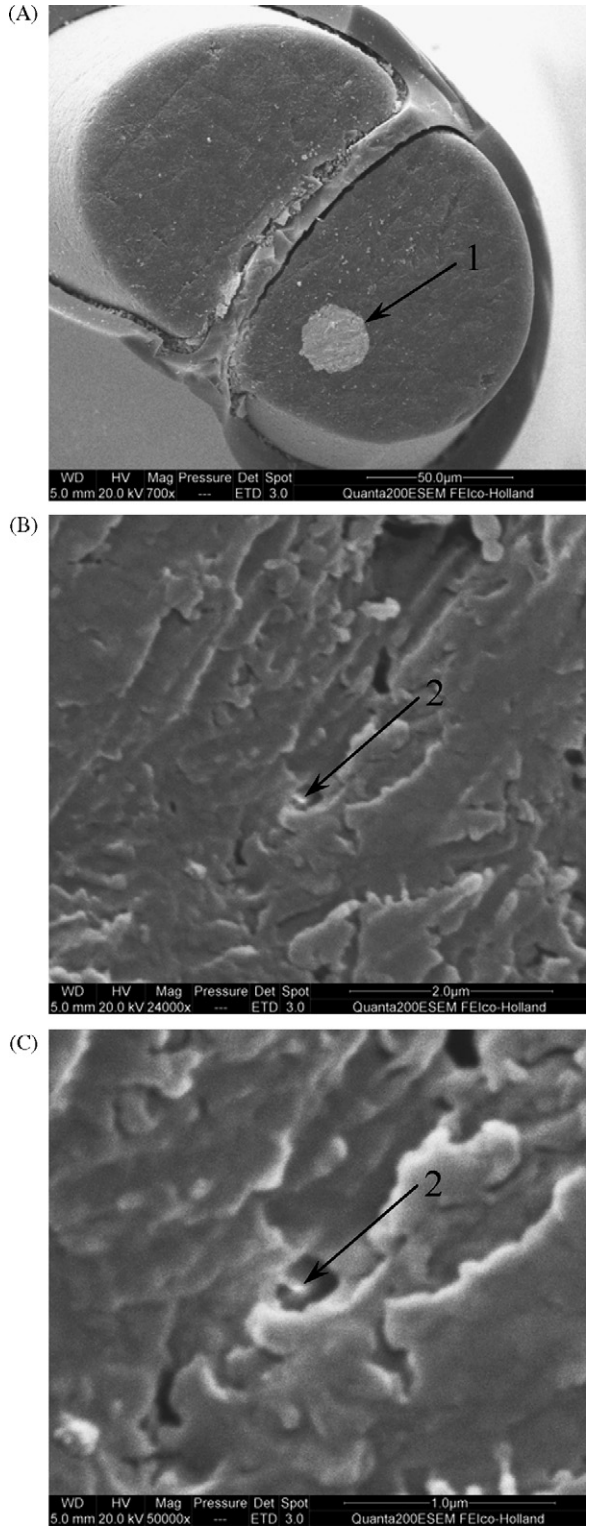

Fig. 3. Scanning electron microscope (SEM) micrograph of (A) a dual-disk electrode with a 10-nm-radius Au electrode and a 10-μm-radius Au electrode shown in Fig. 2A with an amplification factor of 700 and SEM micrographs of the 10-nm-radius Au electrode in the dual-disk electrode with an amplification factor of (B) 24,000 and (C) 50,000. 1, 10-μm-radius Au electrode and 2, 10-nm-radius Au electrode.

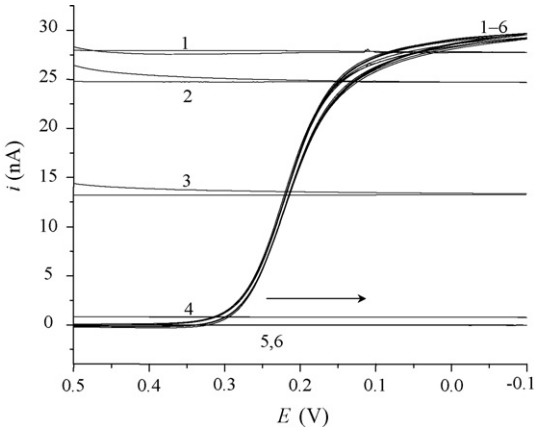

Fig. 4. Cyclic voltammograms of electrode A in a dual-disk electrode with a radius of 10 μm for each in 1.0×10^{-2} mol/L $K_3Fe(CN)_6$ and 0.500 mol/L KCl, as well as relationship between current of electrode B held at different potentials and scan potential on electrode A. Potential scan rate of electrode A, 20 mV/s; potential of electrode B: 1, 0 V; 2, 0.1 V; 3, 0.2 V; 4, 0.3 V; 5, 0.4 V; 6, 0.5 V.

electrode is negligible. Based on the experimental results, the collection efficiency for the dual-disk electrodes with a nanometer-radius disk electrode and a 10-μm-radius disk electrode should be also zero due to larger gap than ∼83 μm. It is not surprise, because the collection efficiency reduces with increasing the gap. This conclusion is agreement in Matsue's work, because the gap of the dual-disk electrodes described here is much larger than that reported by Matsue et al. (∼16 μm).

4. Conclusions

It has been demonstrated that the dual-disk electrodes with a nanometer-radius electrode and a micrometer-radius electrode described herein have following advantages: (1) The fabrication approach is simple and the success rate is high; (2) The risk for the leakage of the insulating sheath is reduced due to double insurance from two coating layers of different polymers; (3) The dual-disk electrodes can be made of different materials; (4) There is no electrochemical cross-talking influence between both electrodes in the dual-disk electrodes; (5) The approach can also be used to fabricate single electrodes with nanometer-radius tips; (6) The electrodes fabricated by using the approach are hard, not easy to be broken and often can be reused.

Acknowledgments

This project was supported by the National Natural Science Foundation of China (Nos. 20235010, 20475033, 20675047), the Natural Science Foundation of Shandong Province in China (Y2003B04) and the State Key Laboratory of Electroanalytical Chemistry, Changchun, Institute of Applied Chemistry, Chinese Academy of Science. We are grateful to Professor Yuanhua Shao of Peking University for fabricating the dual pipets from θ tubing.

References

[1] R.B. Morris, D.J. Franta, H.S. White, J. Phys. Chem. 91 (1987) 3559.
[2] A.J. Bard, H.D. Abruna, C.E. Chidsey, L.R. Faulkner, S.W. Feldberg, K. Itaya, M. Majda, O.R.W. Melroy, J. Phys. Chem. 97 (1993) 7147.
[3] F.R. Fan, A.J. Bard, Proc. Natl. Acad. Sci. U.S.A. 96 (1999) 14222.
[4] J.D. Norton, H.S. White, S.W. Feldberg, J. Phys. Chem. 94 (1990) 6772.
[5] R.M. Penner, M.J. Heben, T.L. Longin, N.S. Lewis, Science 250 (1990) 1118.
[6] C.P. Smith, H.S. White, Anal. Chem. 65 (1993) 3343.
[7] J.L. Conyers Jr., H.S. White, Anal Chem. 72 (2000) 4441.
[8] S. Chen, A. Kucernak, J. Phys. Chem. B 106 (2002) 9396.
[9] S. Chen, A. Kucernak, Electrochem. Commun. 4 (2002) 80.
[10] J.J. Watkins, J. Chen, H.S. White, H.D. Abruna, E. Maisonhaute, C. Amatore, Anal. Chem. 75 (2003) 3962.
[11] J.B. Chien, R.A. Wallingford, A.G. Ewing, J. Neurochem. 54 (1990) 633.
[12] Y.Y. Lau, J.B. Chien, D.K.Y. Wong, A.G. Ewing, Electroanalysis 3 (1991) 87.
[13] K. Pihel, T.J. Schroeder, R.M. Wightman, Anal. Chem. 66 (1994) 4532.
[14] P.S. Cahill, Q.D. Walker, J.M. Finnegan, G.E. Mickelson, E.R. Travis, R.M. Wightman, Anal. Chem. 68 (1996) 3180.
[15] B. Giros, M. Jaber, S.R. Jones, R.M. Wightman, M.G. Caron, Nature 379 (1996) 606.
[16] A.J. Bard, F.F. Fan, M.V. Mirkin, Electroanalytical Chemistry, Marcel Dekker, New York, 1994.
[17] M.V. Mirkin, B.R. Horrocks, Anal. Chim. Acta 406 (2000) 119.
[18] A.J. Bard, M.V. Mirkin, Scanning Electrochemical Microscopy, Marcel Dekker, New York, 2001.
[19] F.R.F. Fan, J. Kwak, A.J. Bard, J. Am. Chem. Soc. 118 (1996) 9669.
[20] B.D. Pendley, H.D. Abruna, Anal. Chem. 62 (1990) 782.
[21] M.V. Mirkin, F.F. Fan, A.J. Bard, J. Electroanal. Chem. 328 (1992) 47.
[22] F.F. Fan, A.J. Bard, Science 267 (1995) 871.
[23] D.K.Y. Wong, L.Y.F. Xu, Anal. Chem. 67 (1995) 4086.
[24] Y. Shao, M.V. Mirkin, G. Fish, S. Kokotov, D. Palanker, A. Lewis, Anal. Chem. 69 (1997) 1627.
[25] C.J. Slevin, N.J. Gray, J.V. Macpherson, M.A. Webb, P.R. Unwin, Electrochem. Commun. 1 (1999) 282.
[26] J.V. Macpherson, P.R. Unwin, Anal. Chem. 72 (2000) 276.
[27] N.J. Gray, P.R. Unwin, Analyst 125 (2000) 889.
[28] P. Sun, Z. Zhang, J. Guo, Y. Shao, Anal. Chem. 73 (2001) 5346.
[29] C. Kranz, G. Friedbacher, B. Mizaikoff, A. Lugstein, J. Smoliner, E. Bertagnolli, Anal. Chem. 73 (2001) 2491.
[30] Y. Zu, Z. Ding, J. Zhou, Y. Lee, A.J. Bard, Anal. Chem. 73 (2001) 2153.
[31] J. Abbou, C. Demaille, M. Druet, J. Moiroux, Anal. Chem. 74 (2002) 6355.
[32] B.B. Katemann, W. Schuhmann, Electroanalysis 14 (2002) 22.
[33] A. Lugstein, E. Bertagnolli, C. Kranz, B. Mizaikoff, Surf. Interface Anal. 33 (2002) 146.
[34] N. Gao, M. Zhao, X. Zhang, W. Jin, Anal. Chem. 78 (2006) 231.
[35] P.S. Cahill, R.M. Wightman, Anal. Chem. 67 (1995) 2599.
[36] F.M. Matysik, Electrochim. Acta 42 (1997) 3113.
[37] T. Yasukawa, T. Kaya, T. Matsue, Anal. Chem. 71 (1999) 4637.
[38] S. Borgmann, I. Radtke, T. Erichsen, A. Blochl, R. Heumann, W. Schuhmann, Chem. Biol. Chem. 7 (2006) 662.
[39] S. Isik, M. Etienne, J. Oni, A. Blochl, S. Reiter, W. Schuhmann, Anal. Chem. 76 (2004) 6389.
[40] A.M. Bond, K.B. Oldham, C.G. Zoski, J. Electroanal. Chem. 245 (1988) 71.
[41] K.T. Kawagoe, J.A. Jankowski, R.M. Wightman, Anal. Chem. 63 (1991) 1589.

Available online at www.sciencedirect.com
ScienceDirect
Talanta 73 (2007) 553–560
Talanta
www.elsevier.com/locate/talanta

Highly selective and sensitive copper membrane electrode based on a new synthesized Schiff base

M.B. Gholivand [a,*], M. Rahimi-Nasrabadi [a], M.R. Ganjali [b], M. Salavati-Niasari [c]

[a] *Department of Chemistry, Razi University, Kermanshah, Iran*
[b] *Department of Chemistry, Tehran University, Tehran, Iran*
[c] *Department of Chemistry, Kashan University, Kashan, Iran*

Received 13 December 2006; received in revised form 16 April 2007; accepted 16 April 2007
Available online 22 April 2007

Abstract

Bis(2-hydroxyacetophenone)butane-2,3-dihydrazone (BHAB) was used as new N-N Schiffs base which plays the role of an excellent ion carrier in the construction of a Cu(II) membrane sensor. The best performance was obtained with a membrane composition of 30% poly(vinyl chloride), 55% *o*-nitrophenyloctyl ether (NPOE), 7% BHAB and 8% oleic acid (OA). This sensor shows very good selectivity and sensitivity towards copper ion over a wide variety of cations, including alkali, alkaline earth, transition and heavy metal ions. The effect of membrane composition and pH and influence of additive anionic on the response properties of electrode were investigated. The electrode exhibits a Nernstian behavior (with slope of 29.6 mV per decade) over a very wide concentration range (5.0×10^{-8} to 1.0×10^{-2} mol L^{-1}) with a detection limit of 3.0×10^{-8} mol L^{-1} (2.56 ng mL^{-1}). It shows relatively fast response time, in whole concentration range (<15 s), and can be used for at least 12 weeks in the pH range of 2.8–5.8. The proposed sensor was successfully used to determination of copper in different water samples and as indicator electrode in potentiometric titration of copper ion with EDTA.

Keywords: Copper ion-selective electrode; Potentiometry; Bis(2-hydroxyacetophenone)butane-2,3-dihydrazone (BHAB)

1. Introduction

Determination of copper assumes importance in view of its widespread occurrence in environmental samples. As such large concentrations of copper can be tolerated by human beings, however, excessive dosage and long term exposure may cause irritation of the nose, mouth and eyes and it causes headache, stomach ache, dizziness, vomiting and diarrhea. Copper deficiency results in anemia while its accumulation resulting in Wilson disease [1]. A number of instrumental methods such as inductively coupled plasma/mass spectrometry [2,3], stripping potentiometry with matrix-exchange techniques [4], voltammetry [5], atomic absorption spectrometry [6–8] and UV–vis spectrometry [9,10] are employed for the determination of copper at low concentration levels. Most of these methods are either time consuming, involving multiple sample manipulations, or too expensive for most analytical laboratories. Potentiometric method with using an ion sensor as an indicator electrode is an alternative method for determination of copper. The development and application of ion-selective electrodes continue to be an interesting area of analytical research as they provide accurate, rapid, non-destructive and low cost methods of analysis. Besides this, online monitoring is possible by these devices but efforts made so far for developing good copper-selective electrodes [11–20] have not been very successful. Most of them suffer from poor selectivity, narrow concentration range, non-Nernstian response, long response time, and poor reproducibility. Efforts are, therefore, still continued to develop selective and sensitive sensor systems.

The Schiff bases (SB) are known to form stable complexes with transition metal ions, and they act as ion carriers in the polymeric membrane. Almost all of metals form 1:1 metal complexes with SBs. The feature of SBs give geometric and cavity control of host–guest complexation and modulation of its lipophilicity, and produce remarkable selectivity, sensitivity and stability for a specific ion. The resulting SB complexes have attracted

* Corresponding author.
E-mail address: mbgholivand@yahoo.com (M.B. Gholivand).

0039-9140/$ – see front matter © 2007 Elsevier B.V. All rights reserved.
doi:10.1016/j.talanta.2007.04.010

increasing attention in the area of ionic binding due to their unique properties and reactivity. Schiff bases with N and O as donor atoms are well known to form strong complexes with transition metal ions and recently were used as ionophore in ion-selective electrodes for determining cations such as Ni(II) [15], Pb(II) [21], La(III) [22], Co(II) [23] and Al(III) [24]. Schiff base upon deprotonation form complexes with Cu^{2+}, which act as charge carriers in the membrane matrix. In the present work a Schiff base, bis(2-hydroxyacetophenone)butane-2,3-dihydrazone (BHAB) as a ionophore with N and O donor atoms was used for construction of Cu(II) ion-selective sensor. It shows a good Nernstian response with low detection limit and long linear range in comparison with other reports [17,18,25–29].

2. Experimental

2.1. Reagents

Reagent grade, *o*-nitrophenyloctyl ether, benzyl acetate (BA), sodium tetraphenylborate (NaTPB), oleic acid (OA), tetrahydrofuran (THF) and high relative molecular weight PVC (all from Merck) were used as received. The nitrate and chloride salts of all cations used (all from Merck) were of the highest purity available and were used without any further purification except for vacuum drying over P_2O_5. Triply distilled deionized water was used throughout.

2.2. Synthesis of BHAB

The Schiff's base bis(2-hydroxyacetophenone)butane-2,3-dihydrazone (BHAB) (Fig. 1) was synthesized as follows:

Step one, the synthesis of butane-2,3-dihydrazone: To a boiling solution of 11.63 g of aqueous hydrazine (0.24 M) in 100 mL of methanol, were added 75 mL of biacetyl (0.12 mol, 10.33 g), over a period of 120 min. Refluxing was continued for an additional 60 min. Then 200 mL of water were added and the methanol was removed by distillation. After cooling the resulting aqueous solution in an ice-bath, white crystals of the product were formed. These were filtered, washed with a little water, recrystallized from 100 mL of hot methanol, and dried in vacuum, m.p. 158–159 °C (reported 158 °C); Yield ~54%. Anal. Calcd. for $C_4H_{10}N_4$: C, 42.09; H, 8.83; N, 49.08. Found: C, 42.16; H, 8.71; N, 49.74. IR (KBr, cm^{-1}): 3330, 3180 (νN–H); 1580 (νC=N); 1615 (νNH_2).

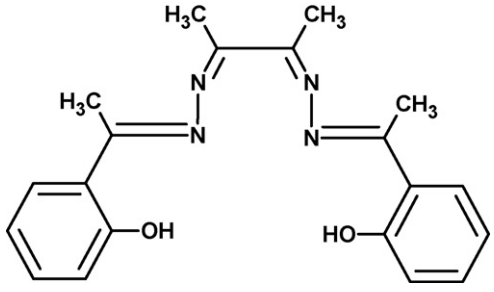

Fig. 1. Structure of the ionophore bis(2-hydroxyacetophenone)butane-2,3-dihydrazone (BHAB).

Step two, the Schiff-base ligand was prepared according to literature through the well known, as follows: 2,3-butanedihydrazone (1.14 g, 0.01 mol) was dissolved in 50 mL ethanol and then transferred into a 250 mL three-necked flask. Under reflux 2.72 g (0.02 mol) of 2-hydroxyacetophenone in 80 mL of ethanol was added drop wise to the flask. The stirred mixture was kept reacting for 3 h under reflux, and then cooled to room temperature. The solid product was filtered, and the product was recrystallized from chloroform. Yield ~68%. Anal. Calcd. for $C_{20}H_{22}N_4O_2$: C, 68.55; H, 6.33; N, 15.99. Found: C, 68.41; H, 6.26; N, 9.24%. IR (KBr, cm^{-1}): 3443 (ν_{O-H}); 1608, 1575 ($\nu_{C=N}$).

2.3. Apparatus

Conductivity measurements were carried out with a Metrohm 660 conductometer. A dip-type conductivity cell made of platinum black, with a cell constant of 0.8210 cm^{-1} was used. In all measurements, the cell was thermostated at the desired temperature 25 ± 0.05 °C using a Phywe immersion thermostat.

2.4. Preparation of the electrode

The general procedure to prepare the PVC membrane was to mix thoroughly 30 mg PVC, 55 mg of NPOE, 8 mg of OA and 7 mg of ionophore BHAB in a glass dish of 2 cm diameter. The mixture was completely dissolved in 3 mL of THF. The resulting clear mixture was evaporated slowly until an oily concentrated mixture was obtained. A Pyrex tube (3–5 mm i.d.) was dipped into the mixture for about 5 s so that a nontransparent membrane of about 0.3 mm thickness is formed [25–34]. The tube was then pulled out from the mixture and kept at room temperature for about 12 h. The tube was then filled with internal filling solution (1.0×10^{-3} mol L^{-1} of $Cu(NO_3)_2$). The electrode was finally conditioned for 24 h by soaking in a 1.0×10^{-2} mol L^{-1} copper nitrate. A silver/silver chloride electrode was used as an internal reference electrode.

2.5. The emf measurements

The emf measurement with the polymeric membrane electrode was carried out with the following cell assembly: Ag–AgCl|internal solution, 1.0×10^{-3} mol L^{-1} $Cu(NO_3)_2$|PVC membrane|test solution|Hg–Hg_2Cl_2, KCl (satd.).

3. Results and discussion

Due to sufficient insolubility of BHAB in water and the presence of oxygen and nitrogen-donating atoms in its structure, this ligand was expected to act as a suitable ion carrier in the PVC membrane based sensors. Thus, in the preliminary experiments, the interaction of this ligand with some metal ions was investigated using conductometric method. Thus, some primary tests, including theoretical calculations and conductance study of complexation of this Schiff base with some metal ions were carried out.

Table 1
Interaction energy between metal ions-ionophore

Compounds	Interaction energy (kcal mol^{-1})
Cu^{2+}-ligand	−48254.394
Pb^{2+}-ligand	−24123.087
Zn^{2+}-ligand	−19870.283
Sr^{+}-ligand	−15241.713
Li^{+}-ligand	−9097.923
Cs^{+}-ligand	−14560.556
Ag^{+}-ligand	−12158.694

3.1. Theoretical calculations

In order to obtain a clue about the tendency of ionophore to copper and some other metal ions, some ab initio quantum-mechanical calculations were carried out. From the difference between the energy of the complex $E(A-B)$ and the energies of isolated partners, the pair wise interaction energy $\Delta E(A-B)$ between two molecules A and B is estimated:

$$\Delta E(A-B) = E(A-B) - E(A) - E(B) \quad (1)$$

The second-order Møller–Plesset (MP2) perturbation theory [35,36] was used for calculations, which includes the electron correlation energy in addition to the Hartree–Fock (HF) energy. The use of such level of calculation is fully justified by the fact that the description of base stacking requires calculations with explicit inclusion of the electron correlation [37]. The interaction energy at a given order of the Møller–Plesset (MP) perturbation expansion is calculated as

$$\Delta E_{\mathrm{MP}n} = \Delta E_{\mathrm{HF}} + \sum_{i=2}^{n} \Delta E_{\mathrm{Corr}}\,(\mathrm{MP}i) \quad (2)$$

where ΔE_{HF} is the HF energy and ΔE_{Corr} (MPi) is the ith order perturbative correction to the correlation energy. Only the valence electrons were explicitly correlated in our computations, which correspond to the usual frozen core approximation. We have also limited the perturbation expansion (2) to the second order, which is expected to take into account the major contributions to the Van der Waals energies (electrostatic, polarization, dispersion, electron transfer and exchange contributions) [38].

The lanl2mb basis set for all atoms used for optimizing molecules. All the calculations were performed using the Gaussian 98 package [39].

Interaction energies for ionophore and some metal ions were calculated from Eq. (1) and are listed in Table 1. From the data given in Table 1 it is obvious that the interaction energy calculated decreases in the order: $Cu^{2+} \gg Pb^{2+} > Zn^{2+} > Sr^{2+} > Cs^{+} > Ag^{+} > Li^{+}$. Thus, based on the above ab initio calculation results, ionophore could possibly be used as a suitable ionophore in preparation of a copper ion-selective membrane electrode.

3.2. Study of the complexation

To the best of our knowledge, there is no report on the stability of BHAB complexes with different cations. In order to determine the stoichiometry and stability of the resulting metal–BHAB complexes, the interactions between ion carrier (BHAB) and different cation in an acetonitrile solution were tested conductometrically. In typical experiments 15 cm^3 of cation nitrate solution (1.0×10^{-4} mol L^{-1}) was placed in water jacketed cell equipped with magnetic stirrer and connected to the thermostat circuling water at the desired temperature. In order to keep the electrolyte concentration constant during the titration, both the starting solution and titrant had the same cation concentration. Then, a known amount of the BHAB (1.0×10^{-2} mol L^{-1}) solution was added in a stepwise manner using a calibrated micropipette. The conductance of the solution was measured after each addition. Addition of the BHAB was continued until the desired BHAB-to-cation mole ratio was achieved. The resulting molar conductance versus ligand/cation mole ratio (Fig. 2) showed the formation of 1:1 complex between BHAB and copper. The 1:1 binding of the cations with BHAB can be expressed by the following equilibrium:

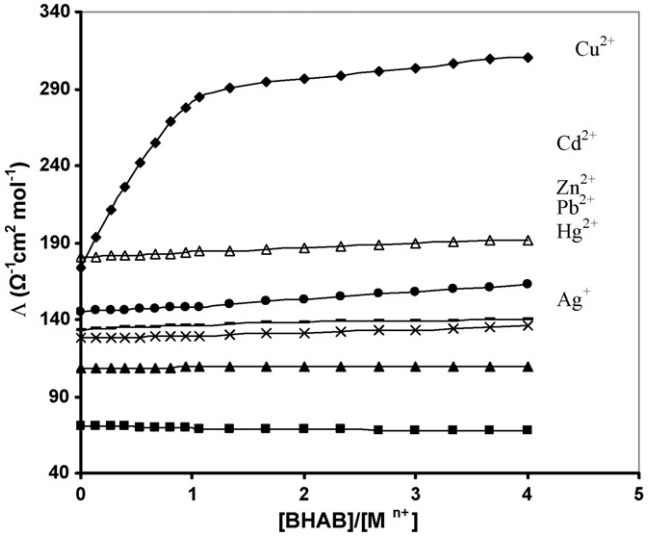

Fig. 2. Molar conductance vs. [BHAB]/[M^{n+}] curves for different metal ions in acetonitrile in 25 °C.

$$\mathrm{M}^{n+} + \mathrm{L} = \mathrm{ML}^{n+} \quad (3)$$

The corresponding equilibrium constant, K_{f}, is given by

$$K_{\mathrm{f}} = \frac{[\mathrm{ML}^{n+}]}{[\mathrm{M}^{n+}][\mathrm{L}]} \frac{f(\mathrm{ML}^{n+})}{f(\mathrm{M}^{n+})f(\mathrm{L})} \quad (4)$$

where [ML^{n+}], [M^{n+}], [L] and f represent the equilibrium molar concentration of complexes, free cation, free BHAB and the activity coefficient of the species indicated, respectively. Under the dilute condition we used, the activity coefficient of the uncharged ligand, f(L) can be reasonably assumed as unity [40]. The use of Debye–Hückel limiting law of 1:1 electrolytes [41] lead to the conclusion that $f(\mathrm{M}^{n+}) \sim f(\mathrm{ML}^{n+})$, so the activity coefficient in Eq. (4) is canceled out. Thus the complex formation constant in term of the molar conductance can be expressed

as [42]:

$$K_f = \frac{[ML^{n+}]}{[M^{n+}][L]} = \frac{\Lambda_M - \Lambda_{obs}}{(\Lambda_{obs} - \Lambda_{ML})[L]} \quad (5)$$

where

$$[L] = C_L - \frac{C_M(\Lambda_M - \Lambda_{obs})}{\Lambda_M - \Lambda_{ML}} \quad (6)$$

Here Λ_M is the molar conductance of the cation before addition of BHAB, Λ_{ML} the molar conductance of the complexed, Λ_{obs} the molar conductance of the solution during titration, C_L the analytical concentration of the BHAB added, and C_M is the analytical concentration of the cation salt. The complex formation constant, K_f and the molar conductance of complex, Λ_{ML}, were obtained by computer fitting of Eqs. (5) and (6) to the molar conductance-mole ratio data using a nonlinear least-squares program KINFIT [43]. The results showed that the stability constant of the Cu^{2+}–BHAB complex ($\log K_f = 6$) was at least 1.0×10^4-fold greater than those obtained with other cations tested such as Zn^{2+}, Ni^{2+}, Cd^{2+}, Hg^{2+}, Co^{2+}, Ag^{+}, Li^{+}, Rb^{+}, Mg^{2+}, Ba^{2+}, Sr^{2+}, Tl^{+}, Ce^{3+}. Thus, BHAB may be used as a suitable selective ionophore in construction of a Cu^{2+} ion-selective membrane electrode.

Thus, in the next experiments BHAB was used as a neutral carrier in construction of PVC-membrane electrodes for a number of metal ions, including alkali, alkaline earth, transition, and heavy metal ions, the potential responses of them are shown in Fig. 3.

As it is seen, except for the Cu^{2+} ion-selective electrode, for all other cations, the slope of the corresponding potential pM plots is much lower than the expected Nernstian slopes of 59, 29.5 and 20 mV per decade for the univalent, bivalent and trivalent cations, respectively.

3.3. Investigation of membrane composition

The proposed membrane sensor generates stable potential response in aqueous solutions containing copper ions after conditioning for 24 h in a 0.01 mol L^{-1} copper solution.

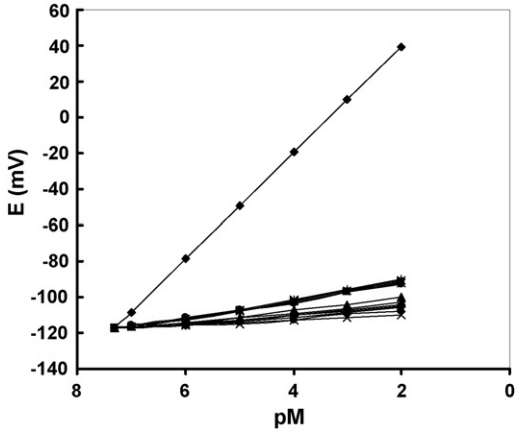

Fig. 3. Potential responses of different ion-selective electrodes based on BHAB : (♦) Cu^{2+}, Mg^{2+}; (■) Zn^{2+}; (▲) Cd^{2+}; (×) Ni^{2+}, Li^{+}; (*) Ag^{+}; (●) Co^{2+}, Sr^{2+}; (+) Pb^{2+}, Na^{+}; (-) Gd^{3+}, (–) Ce^{3+}.

It is well known that some important features of the PVC-based membranes, such as the nature and amount of ionophore, the properties of the plasticizer, the plasticizer/PVC ratio and, especially, the nature of additives used, significantly influence the sensitivity and selectivity of the ion-selective electrodes [44–46]. Thus, different aspects of membrane preparation based on BHAB were optimized and the results are given in Table 2. Solvent polymeric membrane ion-selective electrodes are usually based on a matrix of the solvent mediator/PVC ratio about 2. Polymeric films with such a plasticizer/PVC ratio will result in optimum physical properties and high enough mobility of their constituents. In this study, a plasticizer/PVC ratio of nearly 2 was found to be the most suitable ratio. It is well known the selectivity and working concentration range of the membrane sensors are affected by the nature and amount of plasticizer used. This is due to the influence of plasticizer on the dielectric constant of the membrane phase, the mobility of the ionophore molecules and the state of ligands. As it is seen from Table 2, among four different plasticizers used, NPOE (no. 7) with the higher polarity than DBP, AP and BA is a more effective solvent mediator in preparing the copper ion-selective electrode. It should be noted that the nature of the plasticizer influences both the dielectric

Table 2
Optimization of membrane ingredients

Number of membrane	Composition (%)				Slope (mV per decade)
	PVC (%, w/w)	Plasticizer (%, w/w)	BHAB (%, w/w)	Additive	
1	33	67, NPOE	–	–	~3 mV
2	30	67, NPOE	3	–	11.5 ± 0.3
3	30	65, NPOE	5	–	15.3 ± 0.2
4	30	63, NPOE	7	–	19.7 ± 0.2
5	30	61, NPOE	9	–	18.5 ± 0.3
5	30	60, NPOE	5	5, OA	17.8 ± 0.4
6	30	57, NPOE	5	8, OA	21.2 ± 0.3
7	30	55, NPOE	7	8, OA	29.6 ± 0.2
8	30	60, NPOE	6	4, NaTPB	22.8 ± 0.2
9	30	55, BA	7	8, OA	17.8 ± 0.3
10	30	55, DBP	7	8, OA	15.3 ± 0.4
11	30	55, AP	7	8, OA	18.1 ± 0.1

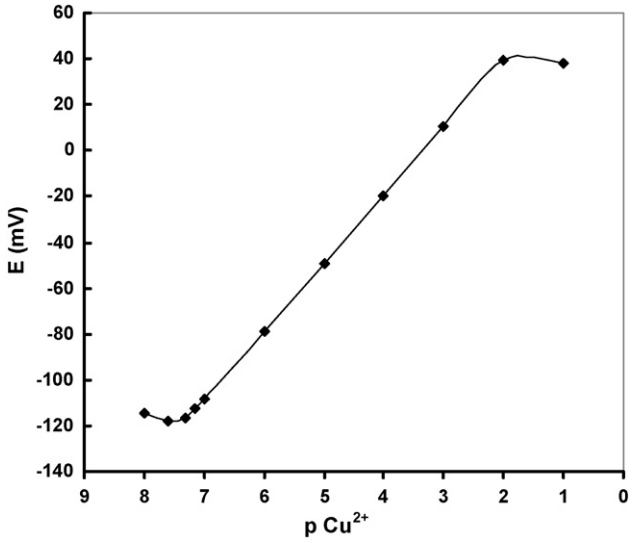

Fig. 4. Calibration curves of copper electrode based on BHAB (membrane no. 7).

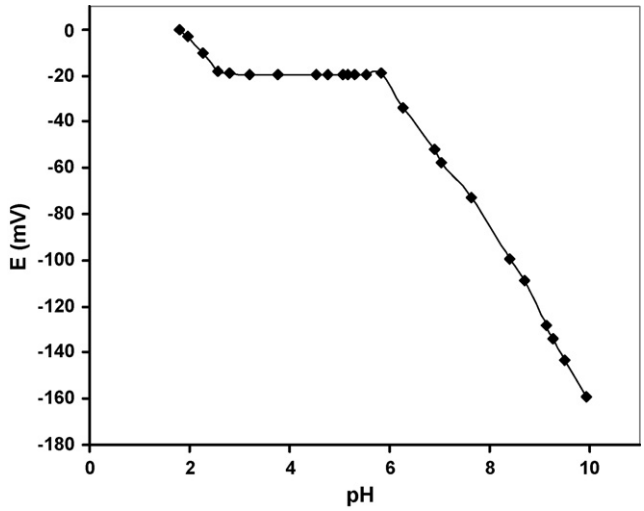

Fig. 5. The effect of the pH of the test solution (1.0×10^{-4} mol L^{-1} Cu^{2+}) on the potential response of the copper sensor based on BHAB (membrane no. 7).

constant of the membrane and the mobility of the ionophore and its complex. The quantity of the BHAB was also found to affect the sensitivity of the membrane electrode (nos. 1–4). The sensitivity of the electrode response increases with increasing ionophore content until a value of 7% is reached.

The optimization of perm-selectivity of membrane sensors is known to be highly dependent on the incorporation of additional membrane compounds [43–45]. It is well understood that, the presence of lipophilic negatively charged additives, improves the potentiometric behavior of certain cation-selective electrodes, not only by reducing the ohmic resistance and improving the response behavior and selectivity, but also in cases, where the extraction capability of the ionophore is poor, by enhancing the sensitivity of the membrane electrode [45,46].

The data given in Table 2 revealed that in the absence of a proper additive, the sensitivity of the PVC membrane based on BHAB is low (nos. 2–4 with slopes 11.5, 15.3 and 19.7 mV per decade, respectively). However, the presence of 8% OA as a suitable additive will improve the sensitivity of the Cu^{2+} sensor considerably (no. 7 with slope 29.6 mV per decade).

The optimum response of the electrode was tested after conditioning for different periods of time in 0.01 mol L^{-1} copper ions. The slope obtained using 24 h of conditioning was closer to the theoretical slope expected on the basis of the Nernstian equation. Longer conditioning times produced no further improvements in the response.

3.4. Calibration curve and statistical data

The potential response of the electrode at varying concentration of Cu(II) ions displays a linear response to the concentration of Cu^{2+} ions in the range of 5.0 ($\pm$0.6) $\times 10^{-8}$ to 1.0 ($\pm$0.5) $\times 10^{-2}$ mol L^{-1} (Fig. 4). The slope of calibration graph was 29.6 ± 0.2 mV per decade of the activity of Cu^{2+} ions. The detection limit of the sensor, as determined from the intersection of the two extrapolated segments of the calibration graph was 3.0 ($\pm$0.4) $\times 10^{-8}$ mol L^{-1} (2.56 ng mL^{-1}). The standard deviation of 10 replicate measurements is $\pm$ 0.2 mV.

3.5. Effect of pH

The influence of the pH of the test solution on the potential response of the membrane sensor for a solution containing 1.0×10^{-4} mol L^{-1} Cu(II), was considered in the pH range of 1.8–10.0 (pH was adjusted by concentrated $HONO_2$ or NaOH) and the results are shown in Fig. 5. As can be seen, the potential remains constant over a pH range of 2.8–5.8. At alkali media, the potential sharply decreased, due to the formation of some hydroxy complexes of Cu(II) ions in solution. On the other hand, at pH < 2.8, the electrode response increased rather irregularly with increasing analyte acidity.

At such high acidic solutions, the observed increase in potential indicates that the protonated ionophore possesses a poor response to the Cu(II) ions and strong response to H_3O^+ ions in solution.

3.6. Response time

For any ion-selective, response time is one of the most important factors. In this study, the practical response time of the sensor was recorded by changing the Cu^{2+} concentration in solution, over a concentration range of 1.0×10^{-2} to 1.0×10^{-7} mol L^{-1}. The potentials versus time traces are shown in Fig. 6. As can be seen, over the entire concentration range the plasticized membrane electrode reaches its equilibrium responses in a very short time (~15 s). This is most probably, due to the fast exchange kinetics of complexation–decomplexation of Cu^{2+} ion with the ionophore at the test solution–membrane interface. To evaluate the reversibility of the electrode, a similar procedure in the opposite direction was adopted. The measurements were performed in the sequence of high-to-low sample concentrations and the results showed that the potentiometric response of the sensor is

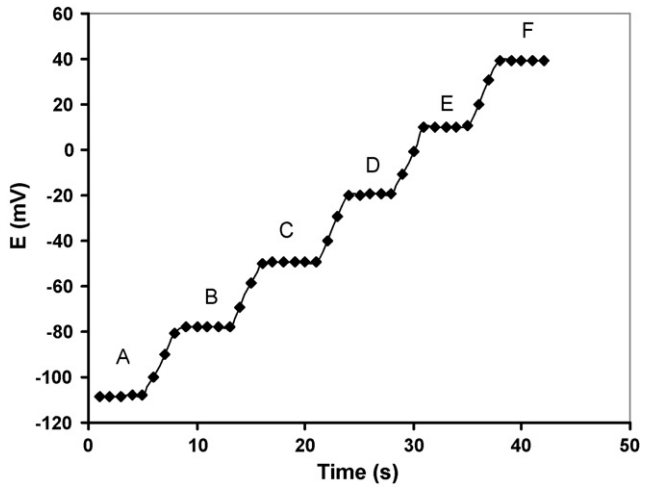

Fig. 6. Dynamic response time of the copper electrode based on BHAB (membrane no. 7) for step changes in concentration of Cu^{2+}: (A) 1.0×10^{-7} mol L^{-1}, (B) 1.0×10^{-6} mol L^{-1}, (C) 1.0×10^{-5} mol L^{-1}, (D) 1.0×10^{-4} mol L^{-1}, (E) 1.0×10^{-3} M and (F) 1.0×10^{-2} mol L^{-1}.

reversible, although the time needed to reach the equilibrium values were longer than that for the low-to-high sample concentration procedure (55 s). It is well documented that, in the case of high-to-low concentrations, the time needed to attain a stable potential is some 100 times larger than that required for the case of low-to-high concentrations (for a 10 times change in the cation concentration) [47].

The lifetime of the proposed electrode was carried out by performing periodic calibration (twice in a week) with standard solutions and calculating the response and slope over the range 5.0×10^{-8} to 1.0×10^{-2} mol L^{-1} Cu^{2+} solution and it was found that electrode worked well over the period of more than 3 months without showing any significant divergence in concentration range, slope and response time. During non-usage, the electrodes were stored in air and before use; they were re-equilibrated by dipping in 1.0×10^{-3} mol L^{-1} Cu^{2+} solution for 5 h.

3.7. Potentiometric selectivity

The influence of interfering ions on the response behavior of ion-selective membrane electrodes is usually described in terms of selectivity coefficients, $K^{\mathrm{Pot}}_{\mathrm{A,B}}$. In this work, matched potential method (MPM) was used for calculation of the selectivity coefficient [48]. According to the MPM, the selectivity coefficient is defined as the activity ratio of the primary ion (A) and the interfering ion (B) that gives the same potential change in a reference solution [49]. The selectivity coefficient, K^{MPM}, is determined as

$$K^{\mathrm{MPM}} = \frac{\Delta A}{a_{\mathrm{B}}}, \quad \Delta A = a'_{\mathrm{A}} - a_{\mathrm{A}}$$

Table 4
Comparison of selectivity coefficient of various Cu^{2+} selective electrodes

DL (M)	Slop (mV per decade)	Linear range (M)	$(-\log K^{\mathrm{Pot}}_{\mathrm{Cu,B}})$	Ref.
4.0×10^{-8}	29.5	5.0×10^{-8} to 1.0×10^{-2}	Co^{2+} (1.1), Pb^{2+} (1.5), Zn^{2+} (2.4), Ni^{2+} (2.9), Cd^{2+} (2.2), Hg^{2+} (0.8), Ag^{+} (0.5), Li^{+} (4.7), Mg^{2+} (4.5), Sr^{2+} (3.9), Ce^{3+} (4.7), Ca^{2+} (3.5), Ba^{2+} (4.2), Na^{+} (2.9), K^{+} (4.9)	[17]
7.5×10^{-7}	30.3	1.0×10^{-6} to 1.0×10^{-2}	Co^{2+} (2.71), Pb^{2+} (0.52), Zn^{2+} (1.7), Ni^{2+} (2.52), Cd^{2+} (2.39), Hg^{2+} (2.52), Ag^{+} (3.09), K^{+} (5.10), Li^{+} (5.10), Na^{+} (5.15), Mg^{2+} (3.22), Sr^{2+} (2.82), Ca^{2+} (3.40), Ba^{2+} (3.00), Cs^{+} (4.30), Al^{3+} (4.06), Fe^{3+} (3.20)	[18]
3.2×10^{-7}	28.0 ± 1	6.3×10^{-7} to 2.5×10^{-1}	Co^{2+} (3.35), Pb^{2+} (2.37), Zn^{2+} (3.38), Ni^{2+} (5.00), Cd^{2+} (2.66), Hg^{2+} (2.92), Ag^{+} (1.64), Na^{+} (2.21), K^{+} (2.25), Tl^{+} (3.92), Mg^{2+} (3.46), Ca^{2+} (3.37), Cr^{3+} (2.92), Fe^{3+} (3.49)	[19]
7.8×10^{-6}	30.0	1.0×10^{-5} to 1.0×10^{-1}	Co^{2+} (1.72), Pb^{2+} (1.70), Zn^{2+} (1.48), Ni^{2+} (1.74), Cd^{2+} (1.00), Hg^{2+} (1.49), Ag^{+} (1.64), Na^{+} (1.70), Li^{+} (1.64), K^{+} (1.46), Ca^{2+} (1.52), NH_4^{+} (1.60), Fe^{3+} (1.52), Al^{3+} (1.55)	[20]
3.0×10^{-8}	29.1 ± 0.1	6.0×10^{-8} to 1.0×10^{-1}	Co^{2+} (3.48), Pb^{2+} (3.48), Zn^{2+} (3.77), Ni^{2+} (3.64), Cd^{2+} (3.96), Hg^{2+} (5.46), Ag^{+} (4.24), Ca^{2+} (4.12), Sr^{2+} (4.10), Na^{+} (4.01), K^{+} (4.00)	[25]
–	28.5	1.0×10^{-5} to 1.0×10^{-1}	Fe^{3+} (3.48), Pb^{2+} (2.30), Zn^{2+} (2.77), Ni^{2+} (2.00), Cd^{2+} (2.00), Hg^{2+} (1.70), Ag^{+} (0.00), Ca^{2+} (1.82), Sr^{2+} (2.40), K^{+} (1.50), Cs^{+} (2.4), NH_4^{+} (1.60), Ba^{2+} (1.80), Mg^{2+} (1.90), Cr^{3+} (2.60),	[26]
–	30.3 ± 0.3	2.5×10^{-5} to 1.0×10^{-1}	Co^{2+} (0.89), Pb^{2+} (0.85), Zn^{2+} (0.68), Ni^{2+} (0.17), Cd^{2+} (1.00), Al^{3+} (0.74), Ce^{3+} (0.96), Ag^{+} (0.85), Ca^{2+} (0.77), Li^{+} (0.85), K^{+} (0.51), Mg^{2+} (0.68), Sr^{2+} (0.85), Ba^{2+} (0.85), Fe^{3+} (0.77), NH_4^{+} (0.68), Na^{+} (0.15), Bi^{3+} (0.85), Cr^{3+} (0.89), Tl^{+} (0.74), Cs^{+} (0.89)	[27]
1.56×10^{-6}	29.3	2.0×10^{-6} to 1.0×10^{-1}	Co^{2+} (1.20), Pb^{2+} (1.19), Zn^{2+} (1.49), Ni^{2+} (1.17), Cd^{2+} (1.62), Hg^{2+} (1.42), Ag^{+} (1.55), Ca^{2+} (2.06), Li^{+} (1.92), K^{+} (1.54), Mg^{2+} (1.92), Sr^{2+} (2.03), Ba^{2+} (2.04), Mn^{2+} (1.92), Na^{+} (1.60)	[28]
4.37×10^{-6}	29.3	4.4×10^{-6} to 1.0×10^{-1}	Co^{2+} (1.36), Pb^{2+} (1.4), Zn^{2+} (1.72), Ni^{2+} (0.46), Cd^{2+} (1.2), Hg^{2+} (1.82), Ag^{+} (1.36), Ca^{2+} (1.49), Li^{+} (2.05), K^{+} (1.2), Sr^{2+} (1.2), NH_4^{+} (1.51), Tl^{+} (1.77), Na^{+} (3.82), Cs^{+} (1.55)	[29]
4.0×10^{-8}	29.6 ± 0.2	5.0×10^{-8} to 1.0×10^{-2}	Co^{2+} (4.45), Pb^{2+} (4.64), Zn^{2+} (4.54), Ni^{2+} (4.55), Cd^{2+} (5.04), Hg^{2+} (4.96), Ag^{+} (5.14), Rb^{+} (5.39), Li^{+} (5.74), Tl^{+} (5.04), Mg^{2+} (5.51), Sr^{2+} (5.57), Ce^{3+} (4.96), Gd^{3+} (4.68)	This work

Table 3
Selectivity coefficients of various interfering cations

M^{n+}	$K^{MPM}_{Cu^{2+},B}$
Co^{2+}	3.5×10^{-5}
Pb^{2+}	2.3×10^{-5}
Zn^{2+}	2.9×10^{-5}
Ni^{2+}	2.8×10^{-5}
Cd^{2+}	9.1×10^{-6}
Hg^{2+}	1.1×10^{-5}
Ag^{+}	7.3×10^{-6}
Rb^{+}	4.1×10^{-6}
Li^{+}	1.8×10^{-6}
Tl^{+}	9.1×10^{-6}
Mg^{2+}	3.1×10^{-6}
Sr^{2+}	2.7×10^{-6}
Ce^{3+}	1.1×10^{-5}
Gd^{3+}	2.1×10^{-5}

where a'_A is the initial primary ion activity and a_A is the activity of A in the presence of interfering ion, a_B. The concentration of Cu^{2+} used as primary ion in this study was 1.0×10^{-8} mol L^{-1}.

The resulting values are shown in Table 3. As it is seen, for all alkali and alkaline earth metal ions used, the selectivity coefficients are smaller than 4.1×10^{-6}. In the case of monovalent and divalent transition metal ions, the selectivity coefficients are in the order of 3.5×10^{-5} or smaller, indicating they would not significantly disturb the functioning of the copper ion-selective electrode.

3.8. Comparison with the previous works

Table 4 compared the performance characteristics of the proposed sensor with those of the best previously reported copper sensors. It is immediately obvious its selectivity coefficients are superior to those reported for the copper ion-selective membrane electrodes. Only in one case (Ref. [25]) the selectivity coefficient of mercury is smaller than that obtained by proposed sensor.

3.9. Analytical applications

The proposed Cu^{2+} ion-selective membrane electrode was used as an indicator electrode in titration of copper with EDTA at pH of 5.5 (acetate buffer). From the resulted curve the amount of Cu^{2+} can be obtained correctly. The electrode was also successfully applied to the determination of copper in different environmental (drinking and river water) samples. The copper content was measured using PVC ion-selective electrode (33.05 ± 0.47 and 237.65 ± 0.79 μmol L^{-1} for drinking and river samples, respectively) and also by atomic absorption spectrometry (34.62 ± 0.16 and 240.79 ± 0.63 μmol L^{-1} for drinking and river samples, respectively), with standard addition method. Each sample was analyzed in triplicate and the analysis by sensors was repeated under identical conditions, a number of times (four), to assess the reliability of the results. Potentials were measured after adjusting their pH. As it is seen the results obtained by proposed sensor are in agreement with those obtained by AAS.

4. Conclusions

The proposed copper(II) selective membrane electrode, based on BHAB, revealed a Nernstian response over a wide copper concentration range, very fast response time and selectivity over a large number of metal ions. A comparison between the response characteristics of the proposed potentiometric sensor and those that reported previously [17–20,25–29] indicated that the presented sensor is invariably superior in terms of the detection limits and, especially, the selectivity over other metal ions. It can be used to determination of copper(II) in different environmental (drinking and river water) samples.

References

[1] H. Scheinberg, A.G. Morell, Inorganic Biochemistry, Elsevier, Amsterdam, 1973.
[2] A.O. Jacintho, E.A.G. Zagatto, H. Bergamin, F.F.J. Krug, B.F. Reis, R.E. Bruns, B.R. Kowalski, Anal. Chim. Acta 130 (1981) 243.
[3] E.A.G. Zagatto, A.O. Jacintho, F.F.J. Kurg, B.F. Reis, Anal. Chim. Acta 145 (1983) 169.
[4] A. Hu, R.E. Dessy, A. Graneli, Anal. Chem. 55 (1983) 320.
[5] J. Janata, J. Ruzicka, Anal. Chim. Acta 139 (1982) 105.
[6] W.R. Wolf, K.K. Stewart, Anal. Chem. 51 (1979) 1201.
[7] S.S.M. Hassan, Organic Analysis Using Atomic Absorption Spectrometry, Ellis Horwood, Chichester, England, 1984.
[8] Z. Fang, S. Xu, S. Zhang, Anal. Chim. Acta 164 (1984) 41.
[9] K. Minoura, K. Fukushima, Chikyu Kagaku 22 (1988) 47.
[10] A. Asan, M. Andac, I. Isildak, Anal. Sci. 17 (2001) 1125.
[11] R. De Marco, D.J. Mackey, A. Zirino, Electroanalysis 9 (1997) 330.
[12] J. Kouljenovic, V. Martinac, N. Radic, Anal. Chim. Acta 231 (1990) 137.
[13] S. Yoshimoto, H. Mukai, T. Kitano, Y. Sohrin, Anal. Chim. Acta 494 (2003) 207.
[14] V.K. Gupta, R. Prasad, A. Kumar, Talanta 60 (2003) 149.
[15] M.H. Mashhadizadeh, I. Sheikhshoaie, S. Saeid-Nia, Sens. Actuators B 94 (2003) 241.
[16] A.R. Fakhari, T.A. Raji, H. Naeimi, Sens. Actuators B 104 (2005) 318.
[17] A.K. Singh, S. Mehtab, A.K. Jain, Anal. Chim. Acta 575 (2006) 25.
[18] S.S.M. Hassan, E.M. Elnemma, A.H.K. Mohamed, Talanta 66 (2005) 1034.
[19] A.K. Jain, V.K. Gupta, B.B. Sahoo, L.P. Singh, Anal. Proc. (RSC) 32 (1995) 99.
[20] V.K. Gupta, R. Prasad, A. Kumar, J. Appl. Electrochem. 33 (2003) 381.
[21] T. Jeong, H.K. Lee, D. Jeong, S. Jeon, Talanta 65 (2005) 543.
[22] M.R. Ganjali, M. Qomi, A. Daftari, P. Norouzi, M. Salavati-Niasari, M. Rabbani, Sens. Actuators B 98 (2004) 92.
[23] M.H. Mashhadizadeh, I. Sheikhshoaie, Anal. Bioanal. Chem. 375 (2003) 708.
[24] M.B. Gholivand, F. Ahmadi, E. Rafiee, Electroanalysis 18 (2006) 1620.
[25] M.R. Ganjali, T. Poursaberi, L. Haji-Agha Babaei, S. Rouhani, M. Yousefi, M. Kargar-Razi, A. Moghimi, H. Aghabozorg, M. Shamsipur, Anal. Chim. Acta 440 (2001) 81.
[26] A.K. Jain, V.K. Gupta, L.P. Singh, J.R. Raisoni, Talanta 66 (2005) 1355.
[27] M.H. Mashhadizadeh, A. Mostafavi, R. Razavi, M. Shamsipur, Sens. Actuators B 86 (2002) 222.
[28] V.K. Gupta, R.N. Goyal, N. Bachheti, L.P. Singh, S. Agarwal, Talanta 68 (2005) 193.
[29] V.K. Gupta, A.K. Jain, G. Maheshwari, H. Lang, Z. Ishtaiwi, Sens. Actuators B 117 (2006) 99.
[30] M.R. Ganjali, M. Rahimi, B. Maddah, A. Moghimi, S. Borhany, Anal. Sci. 20 (2004) 1427.

[31] M.R. Ganjali, M. Rahimi, B. Maddah, A. Moghimi, M. Faal-Rastegar, S. Borhany, Talanta 63 (2004) 899.
[32] M.R. Ganjali, M.B. Gholivand, M. Rahimi-Nasrabadi, B. Maddah, M. Salavati-Niasari, F. Ahmadi, Sens. Lett. 4 (2006) 1.
[33] M.R. Ganjali, M. Tahami, M. Shamsipur, T. Poursaberi, S. Haghgoo, M. Hosseini, Electroanalysis 15 (2003) 1038.
[34] M.R. Ganjali, P. Norouzi, A. Tamaddon, M. Adib, Sens. Actuators B 114 (2006) 855.
[35] C. Møller, M.S. Plesset, Phys. Rev. 46 (1934) 618.
[36] M. Head-Gordon, J.A. Pople, M. Frisch, J. Chem. Phys. Lett. 153 (1988) 503.
[37] J. Sponer, I. Berger, N. Spackova, J. Leszczynski, P. Hobza, J. Biomol. Struct. Dyn. 11 (2000) 383.
[38] G. Chalasinski, M.M. Szczesniak, Chem. Rev. 94 (1994) 1723.
[39] M.J. Frisch, G.W. Trucks, H.B. Schlegel, G.E. Scuseria, M.A. Robb, J.R. Cheeseman, V.G. Zakrzewski, J.A.J. Montgomery, R.E. Stratmann, J.C. Burant, S. Dapprich, J.M. Millam, A.D. Daniels, K.N. Kudin, M.C. Strain, O. Farkas, J. Tomasi, V. Barone, M. Cossi, R. Cammi, B. Mennucci, C. Pomelli, C. Adamo, S. Clifford, J. Ochterski, G.A. Petersson, P.Y. Ayala, Q. Cui, K. Morokuma, D.K. Malick, A.D. Rabuck, K. Raghavachari, J.B. Foresman, J. Cioslowski, J.V. Ortiz, A.G. Baboul, B.B. Stefanov, G. Liu, A. Liashenko, P. Piskorz, I. Komaromi, R. Gomperts, R.L. Martin, D.J. Fox, T. Keith, M.A. Al-Laham, C.Y. Peng, A. Nanayakkara, C. Gonzalez, M. Challacombe, P.M.W. Gill, B. Johnson, W. Chen, M.W. Wong, J.L. Andres, C. Gonzalez, M. Head-Gordon, E.S. Replogle, J.A. Pople, Gaussian Inc., Pittsburgh, PA, 1997.
[40] K.M. Tawarah, S.A. Mizyed, J. Solut. Chem. 18 (1989) 387.
[41] P. Debye, H. Huckel, Phys. Z 24 (1928) 305.
[42] Y. Takeda, Bull. Chem. Soc. Jpn. 56 (1983) 3600.
[43] V.A. Nicely, J.I. Dye, J. Chem. Educ. 48 (1971) 443.
[44] E. Ammann, P. Pretsch, W. Simon, E. Lindner, A. Bezegh, E. Pungor, Anal. Chim. Acta 171 (1991) 1380.
[45] R. Eugster, P.M. Gehring, W.E. Morf, U. Spichiger, W. Simon, Anal. Chem. 63 (1990) 2285.
[46] T. Rosatzin, E. Bakker, K. Suzuki, W. Simon, Anal. Chim. Acta 280 (1993) 197.
[47] E. Bakker, P. Buhlmann, E. Pretsch, Chem. Rev. 97 (1997) 3083.
[48] K. Srinivasan, G.A. Rechnitz, Anal. Chem. 41 (1969) 1203.
[49] V.P. Gadzepko, G.D. Christian, Anal. Chim. Acta 164 (1984) 279.

Available online at www.sciencedirect.com
ScienceDirect
Talanta 73 (2007) 577–582
Talanta
www.elsevier.com/locate/talanta

Glass particles produced by laser ablation for ICP-MS measurements

Jhanis J. Gonzalez, Chunyi Liu, Sy-Bor Wen, Xianglei Mao, Richard E. Russo *

Lawrence Berkeley National Laboratory, Berkeley, CA 94720, USA

Received 29 January 2007; received in revised form 13 April 2007; accepted 17 April 2007
Available online 4 May 2007

Abstract

Pulsed laser ablation (266 nm) was used to generate glass particles from two sets of standard reference materials using femtosecond (150 fs) and nanosecond (4 ns) laser pulses with identical fluences of 50 J cm^{-2}. Scanning electron microscopy (SEM) images of the collected particles revealed that there are more and larger agglomerations of particles produced by nanosecond laser ablation.

In contrast to the earlier findings for metal alloy samples, no correlation between the concentration of major elements and the median particle size was found. When the current data on glass were compared with the metal alloy data, there were clear differences in terms of particle size, crater depth, heat affected zone, and ICP-MS response. For example, glass particles were larger than metal alloy particles, the craters in glass were less deep than craters in metal alloys, and damage to the sample was less pronounced in glass compared to metal alloy samples. The femtosecond laser generated more intense ICP-MS signals compared to nanosecond laser ablation for both types of samples, although glass sample behavior was more similar between ns- and fs-laser ablation than for metal alloys.
Published by Elsevier B.V.

Keywords: Laser ablation; Glass; Particles; ICP-MS

1. Introduction

Laser ablation processes depend on many parameters which can be grouped by the source. For example, parameters associated to the laser (wavelength, energy, pulse length, spot size, etc.), the environment surrounding the sample (cell design, gas composition, pressure, etc.), and the material properties (absorptivity, thermal diffusivity, etc.) are also relevant [1,2]. The total number of parameters that can affect the overall ablation process is too large to be evaluated all at once. Therefore, maintaining some of these parameters fixed is the more efficient way to study their influence on the overall process. For this study, we used the same conditions (Table 1) as a previous study on metal particles produced by nanosecond and femtosecond laser ablation, in which the only varied condition was the pulse length.

The present study is focused on glass particles produced from ablation of two series of glass standard reference materials and their characterization by measuring particle size distributions, crater volumes, crater profiles, and establishing correlations with ICP-MS performance. The study of these glass samples is of interest due to their relevance in fields like geochemistry, forensic science, etc.; fields in which samples with similar properties (optical absorptivity, thermal diffusivity, etc.) are found.

In general, the first step of the ablation process involves the absorption of the laser energy by the sample, followed by the diffusion of the absorbed energy into the sample. After a portion of the laser energy is absorbed, the time to transfer that energy to the sample lattice and to start the removal of the material is approximately 10 ps [3,4]. When this energy is delivered on the nanosecond time scale, the transfer time is sufficient to thermally dissipate that energy into the lattice (glass or metals), as opposed to femtosecond laser pulses. For laser pulses with nanosecond duration, the thermal diffusion of the energy will cause a larger heat affected zone compared to femtosecond laser pulses [5]. This effect will be more pronounced in metals than in glasses due to their higher thermal diffusivity. However, glass samples possess lower absorptivity (higher penetration depth) compared to metal samples. Therefore, the energy density experienced by the glass sample during the interaction is smaller than the energy density experienced by metals. The combination of the appropriate conditions (i.e. pulse length and wavelength) which influence these two processes (light absorption and thermal diffusion) can be optimized to improve ablation efficiency.

* Corresponding author. Tel.: +1 510 486 4258; fax: +1 510 483 7303.
E-mail address: rerusso@lbl.gov (R.E. Russo).

0039-9140/$ – see front matter. Published by Elsevier B.V.
doi:10.1016/j.talanta.2007.04.028

Table 1
Experimental conditions

Conditions
Argon flow = 1.25 L/min
Laser energy = ∼0.25 mJ
Spot size ∼ 25 μm
Fluence = ∼50 J/cm^2
Scan speed = 10 μm/s
Frequency = 10 Hz
τ_{fs} = 150 fs
τ_{ns} = 4 ns

2. Experimental

The experimental system was described in detail elsewhere [6]; in short it included a hybrid femtosecond laser system (150 fs), and a Nd:YAG nanosecond (4 ns) laser. An ICP-MS was used to chemically analyze the ablated mass and a differential mobility analyzer (DMA) was used for particle size measurements. The glass samples used in this study were a series of standard reference materials from the National Institute of Standard and Technologies (NIST) and X-ray fluorescence (XRF) monitor samples from Glen Spectra. Table 2 shows the matrix composition for these standards.

3. Results and discussion

3.1. Particle size measurements

As in a previous report [6] for metal particles, the number density, particle diameter and span were used to describe the particle size distributions functions.

Throughout these experiments, each sample was ablated at six different surface locations, which resulted in six particle size distribution measurements. The average of these six particle size measurements was calculated and is presented in Fig. 1 (NIST standards), and Fig. 2 (XRF standards). The error bars represent the standard deviation of this average.

3.2. Number density

Significant differences in normalized number concentration ($dN/d\log D_p$) of particles (Figs. 1a and 2a) was measured in the 10–400 nm range when using femtosecond compared to nanosecond laser ablation. The larger number concentration particles from nanosecond laser ablation originate from a higher ablation rate (more mass per pulse) Fig. 3. Figs. 1b and 2b show the particle size distributions normalized to the maximum value. In these two figures, it can be observe that: the closeness of the distributions within a standard series, and the smaller standard deviation between the six repetitions (more reproducible), when using femtosecond laser pulsed ablation compared to nanosecond laser pulsed ablation.

Table 3
fs-to-ns volume and response ratios

Sample	NIST 610
Volume net ratio (fs/ns)	0.50
Total concentration (μm^3/cm^3) ratio (fs/ns)	0.50
Integrated signal intensity ratio (fs/ns)	4

To evaluate if the larger number density of particles observed for nanosecond laser ablation were due to higher ablation rate, three different approaches to determine the volume was used. The first approach consisted of direct measurement of the volume with the white light intereferometric microscope (Zygo, New View 200). Fig. 3 shows the crater profiles produced by ns- and fs-laser pulses on NIST 610. These profiles showed that the nanosecond crater is deeper than the femtosecond crater and there was no mass deposited around the craters (no rim formed) as opposed to the case of metals. The net volume ratio (fs/ns) of these craters sections shows that fs-laser ablation produces 0.50 times less ablated volume compared to nanosecond pulsed ablation (Table 3). These data support the premise that the larger number density of particles measured using the DMA system for nanosecond laser ablation is associated with the larger amount of mass ablated from the sample.

The second approach used to determine the volume of mass ablated per second involved the calculation using a prism volume equation (as in previous paper [6]). The data obtained from this approach are presented in Table 4. These data reveals that 875 μm^3/s and 1625 μm^3/s were ablated by the femtosecond laser and nanosecond laser, respectively. Thus, the fs/ns ratio of calculated volume per second was 0.5 as it was from the volume net ratio.

The last approach used to verify fs/ns volume ratios was the use of the number concentration of particles normalized by vol-

Table 2
Compositions of the reference standard series NIST 610–616 and XRFs

SRM	Note	SiO_2	CaO	Al_2O_3	Na_2O	MgO	MnO	B_2O_3	K_2O	Fe_2O_3
N610	Si base glass	72	12	2	14					
N612	Si base glass	72	12	2	14					
N614	Si base glass	72	12	2	14					
N616	Si base glass	72	12	2	14					
BRA3	XRF monitor samples	37.4	0.83	14	0.13	3.2	20.8	4.2	2.16	1.16
BRB2	XRF monitor samples	41.8	21	8.6	0.09	0.23	0.89		0.04	12.3
BRC3	XRF monitor samples	9.9	0.03	27.1	7.9		0.47	19.1	6.9	5.4
BRD2	XRF monitor samples	5.3	14.2	20.6	9.6	7.4		21.9	0.09	0.58
BRE2	XRF monitor samples	48.9	0.6	8.5	15.3		6.5	4	0.95	0.03
BRF2	XRF monitor samples	58.2	2.84	3	1.2	0.82		2	18.4	0.07

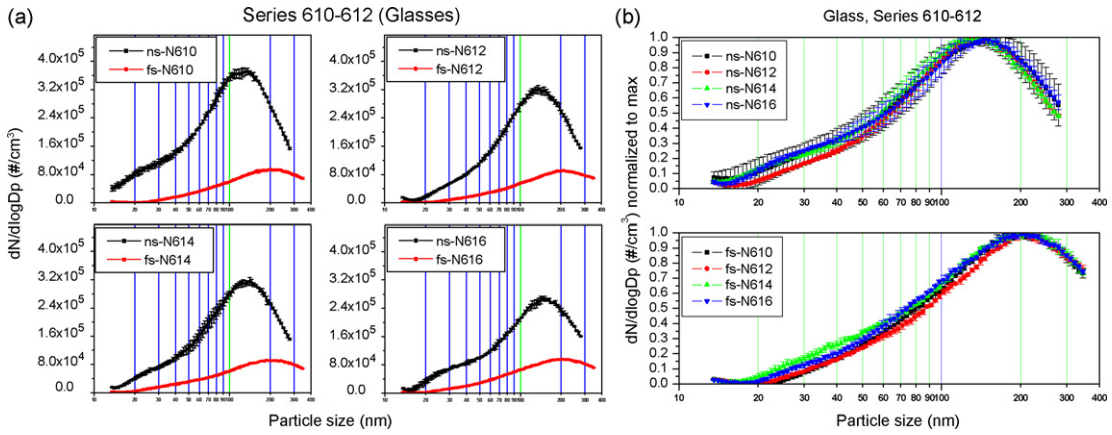

Fig. 1. (a) NIST 610–616 particle size distribution (DMA) and (b) normalized particle size distributions.

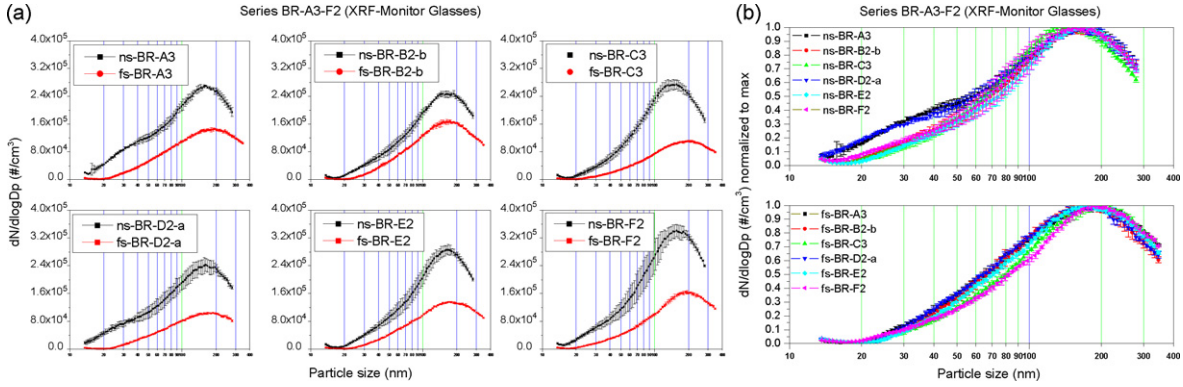

Fig. 2. (a) XRF monitor samples particle size distribution (DMA) and (b) normalized particle size distributions.

ume obtained from the DMA. In this case, the DMA number concentration of particles per second reveals that 1598 μm^3/s and 3197 μm^3/s were ablated by the femtosecond laser and nanosecond laser, respectively. This approach also leads to the fs/ns ratio of 0.5, Table 3.

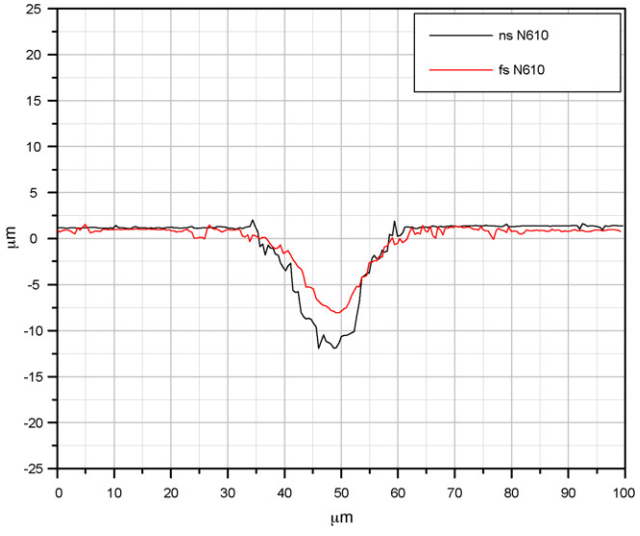

Fig. 3. White light interferometer microscope measurements of the NIST 610 crater profile.

The breadth of the distributions in term of particle size (Span) was not calculated due to break in the distribution after 380 nm for both lasers, due to measurements limitations of the DMA system.

3.3. Particle diameter

The mode of the particle diameter for the NIST glasses (610–616) was ~150 nm and ~200 nm for ns- and fs-pulses, respectively, and 160 nm and 180 nm for XRF monitor samples. These data show that nanosecond laser ablation produced slightly smaller particles than femtosecond laser ablation, as was the case of metals (previous paper [6]). The next step was the characterization of particles by means of scanning electron microscopy (SEM). The characterization was carried out to investigate if the difference obtained with the DMA data, showing that the nanosecond pulsed laser produces smaller particles than the femtosecond pulsed laser in the measured range, is due to primary particle size or due to differences in the agglomeration of particles. For SEM measurements, NIST 610 was ablated using the same conditions as above; the ablated mass was collected on clean silicon substrates, Fig. 4. Particles were collected at the exit of the ablation chamber after a distance of one meter of tubing (normal input to the ICP-MS). The particle collection time for both nanosecond and femtosecond ablation was the same (480 s).

Table 4
Volumes calculated from crater geometric shape and from DMA measurements

	From crater								From DMA				
	Scan speed (μm/s)	Time (s)	Distance (μm)	Base (μm)	High (μm)	Area (μm^2)	Volume (μm^3)	Volume/time (μm^3/s)	nm^3/cm^3	$\mu m^3/cm^3$	Flow rate (cm^3/s)	Volume/time (μm^3/s)	Volume (fs/ns)
N610													
ns	10	170	1700	25	13	162.5	276250	1625	6.40E+11	639.5	5	3197.5	0.50
fs	10	170	1700	25	7	87.5	148750	875	3.20E+11	319.7	5	1598.3	

Fig. 4a–d (ns) and e–h (fs) shows the SEM images of the mass collected from nanosecond and femtosecond laser ablation. Considering that experimental conditions were the same for both lasers and the mass was collected in the same fashion, there is evidence that there are more and larger agglomerates of particles produced by the nanosecond laser compared to the femtosecond laser. However, the primary size of particles does not appear to be significantly different between these two cases, Fig. 4d (ns) and h (fs). In this figure, it is also observed almost exclusively spherical primary particles fro both lasers.

From the ICP point of view, transport efficiency of the large agglomerates could influence the ICP-MS performance in term of precision and accuracy. Considering the case in which the transport of large agglomerates is inefficient due to settling in the chamber or transport tubing, nanosecond laser ablation could generate a lower response compared to femtosecond laser ablation, even though more mass is being ablated. On the other hand, if we consider the case in which these large agglomerations of particles reaches the ICP, there is a strong probability that they will not be completely digested by the plasma; even if they are composed of small primary particles, affecting accuracy due to fractionation and generating spikes in the signal affecting the precision. The ICP-MS response for the matrix element ^{29}Si supports these two premises (Fig. 5); the femtosecond pulsed laser ablation produces a signal which intensity is four times greater than the nanosecond pulsed laser ablation case, with fewer spikes in the transient signal (TRSD of 7% and 3.5% for nanosecond and femtosecond pulses, respectively).

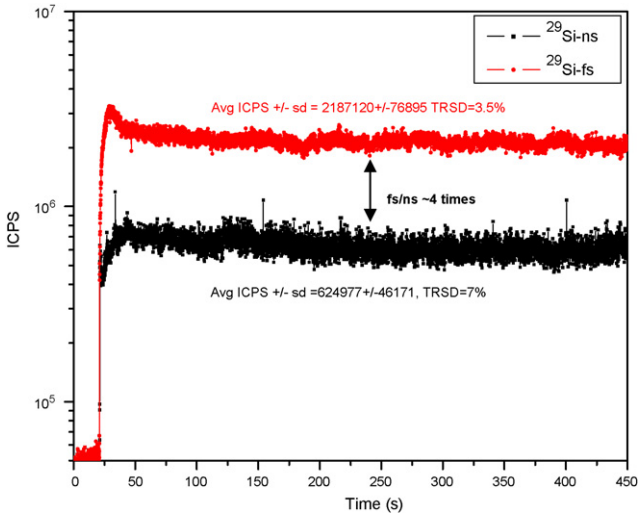

Fig. 5. ^{29}Si transient signals generated by 10 μm/s ablation (nanosecond and femtosecond).

The mechanisms of soft-agglomerates of different sizes for ns- and fs-laser ablation are not understood. Nevertheless, similarities between the primary particle size and morphology from these two lasers suggest that it is unlikely that the observed behavior is due to the laser–material interaction, but rather a post-ablation effect. The nature of these soft-agglomerates, which are assemblies of primary particles held together by weak van der Waals forces [7,8], indicated that they are produced from collision between the solid particles after they are formed.

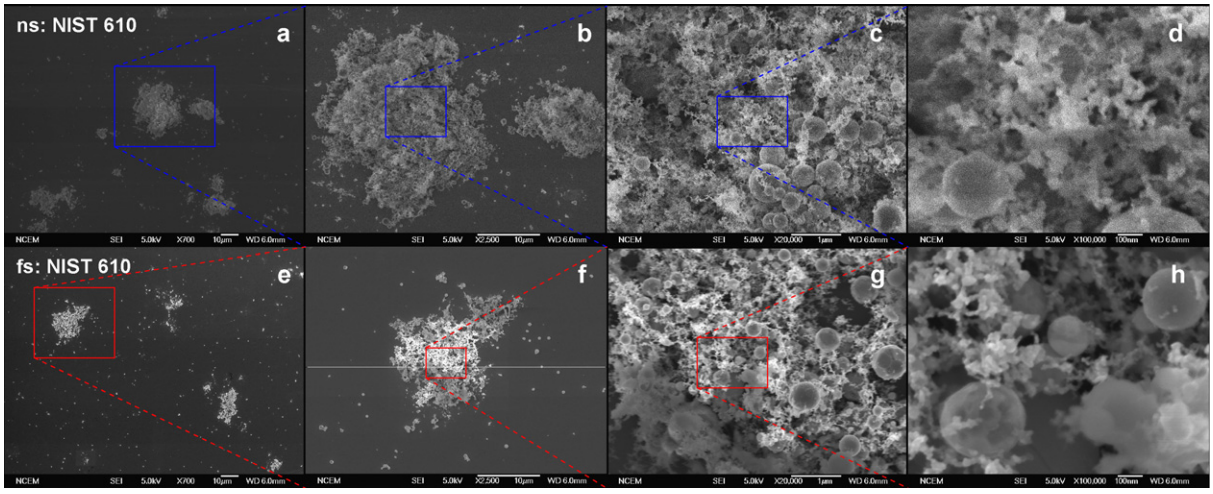

Fig. 4. SEM images of NIST 610 particles: (a–d) nanosecond and (e–h) femtosecond laser ablation.

Table 5
Diffusion length calculated using $L = \sqrt{a\tau}$

Element	Density at 25 °C (g/cm^3)	Specific heat capacity (J/g K)	Thermal conductivity at 27 °C (W/cm K)	Thermal diffusivity (m^2/s)	Diffusion length, L	
					Nanosecond (nm)	Femtosecond (nm)
SiO_2	2.19	0.834	1.15E−02	6.29E−09	8	0.03
Al	2.7	0.897	2.37	8.89E−05	596	3.6
Zn	7.14	0.388	1.16	4.18E−05	408	2.6

Values for Ak and Zn are included since they were the main components of the alloys studied in Ref. [6]

The rate of the collision between primary particles could be affected by increasing the number of particles (more mass as in the nanosecond case), by increasing the collision time (longer plasma cooling time), or by changes in the dynamic expansion patterns of these particles [9].

It has been reported that for particle formation using flame aerosol reactors, the formation of soft-agglomerates starts when particles reach a zone of lower temperature and sintering of primary particles effectively stops [10]. Collision between these primary particles in the region of low temperature leads to the formation of soft-agglomerates. Therefore, increasing or decreasing the time that these primary particles spend in this region (by changing flow rate, flame size, etc.) will affect the final size of the soft-agglomerates [8,10–12]. As parallelism to laser ablation is possible to speculate that the larger size of soft-agglomerates when comparing nanosecond laser ablation to femtosecond laser ablation, could be due to the larger amount of mass ablated by the nanosecond laser, and/or by changes in the dynamic expansion patterns of these particles [9].

The ablation behavior, in terms of particle size, crater depth, heat affected zone, and ICP-MS response, of these glasses was completely different from the ablation behavior of metals when comparing nanosecond versus femtosecond lasers. However, it is notable that the ratio of the integrated signal intensity to volume net (Table 3) as a measure of the overall improved efficiency is eight times more efficient for femtosecond compared to nanosecond laser ablation as was the case for the metal samples in which it was shown that there is an improvement of 10, 2.5, and 1.7 times for pure Zn, NIST 627, and NIST 1711, respectively.

Among the differences in the ablation behavior between glass and metal samples are that: glass particles are larger than metal particles, the craters in glass are less deep than craters in metal, and damage (rim formation, debris surrounding the ablated area, etc.) to the sample is less pronounced in glass samples. However, when comparing ns- to fs-laser ablation the differences of: particle size, ablated volume, and heat affected zone are much greater for metals than for glasses. For glasses it is notable, in particular, that the rim surrounding the crater is absent, even for nanosecond laser ablation. In general, metal samples could dissipate the energy deeper into the lattice due to their higher thermal diffusivity (a) compared to SiO_2, which is the main component of the glass samples used in this study. Table 5 shows a rough estimation of the diffusion length using $L = \sqrt{a\tau}$, where L is the diffusion length, a the thermal diffusivity, and τ is the pulse length. As can be seem, metals possess higher diffusion length compared to SiO_2. Therefore, a larger volume of the metal is thermally affected compared to glass samples when ablated with nanosecond laser pulses.

4. Summary

The particles produced from nanosecond and femtosecond laser ablation of glass samples showed similar primary sizes and morphology. However, SEM images showed that soft-agglomerates of particles after nanosecond laser ablation are more numerous and larger compared with those from femtosecond laser ablation. This observation could be the result of a larger amount of mass (higher number of particles/cm^3) being ablated with nanosecond laser ablation which will increase the number of collision between primary particles, and/or by changes in the dynamic expansion patterns of these particles, as shown in Ref. [9].

Moreover, even though the nanosecond laser ablated a larger amount of mass the femtosecond laser still produced a higher transient ICP-MS signal (approximately four times) and fewer spikes (TRSD of 7% and 3.5% for nanosecond and femtosecond pulses, respectively), most likely due to settling of the larger agglomerates during transport and/or the inefficient digestion of the larger agglomerates (ns-laser) by the ICP.

Acknowledgements

We would like to thank Sotiris E. Pratsinis, for his helpful advice on aerosol particle formation; and Paul Berdahl for productive discussions and for editing the manuscript. This work was supported by the Office of Science, Office of Basic Energy Sciences, Chemical Sciences, Geosciences, and Biosciences Division, and the Deputy Administrator for Defense Nuclear Nonproliferation, Research and Development of the U.S. Department of Energy under Contract No. DE-AC02-05CH11231.

References

[1] D. Gunther, B. Hattendorf, Trends Anal. Chem. 24 (2005) 255–265.
[2] R.E. Russo, X.L. Mao, C.Y. Liu, J. Gonzalez, J. Anal. At. Spectrom. 19 (2004) 1084–1089.
[3] K. Sokolowski-Tinten, J. Bialkowski, A. Cavalleri, D. vonderLinde, A. Oparin, J. MeyerterVehn, S.I. Anisimov, Phys. Rev. Lett. 81 (1998) 224–227.
[4] J. Gonzalez, X.L. Mao, S. Mao, R.E. Russo, J. Anal. At. Spectrom. 17 (2002) 1072–1075.

[5] C. Liu, X.L. Mao, S.S. Mao, X. Zeng, R. Greif, R.E. Russo, Anal. Chem. 76 (2004) 379–383.
[6] J. Gonzalez, C. Liu, S. Wen, X. Mao, R.E. Russo, Talanta 73 (2007) 567–576.
[7] R. Bandyopadhyaya, A.A. Lall, S.K. Friedlander, Powder Technol. 139 (2004) 193–199.
[8] S. Tsantilis, S.E. Pratsinis, Langmuir 20 (2004) 5933–5939.
[9] J. Koch, S. Schlamp, T. Rosgen, D. Fliegel, D. Gunther, Spectrochim. Acta Part B: At. Spectrosc. 62 (2007) 20–29.
[10] S.E. Pratsinis, Prog. Energy Combust. Sci. 24 (1998) 197–219.
[11] T. Tani, K. Takatori, S.E. Pratsinis, J. Am. Ceram. Soc. 87 (2004) 365–370.
[12] S.E. Pratsinis, S. Vemury, Powder Technol. 88 (1996) 267–273.

Available online at www.sciencedirect.com
ScienceDirect
Talanta 73 (2007) 567–576
Talanta
www.elsevier.com/locate/talanta

Metal particles produced by laser ablation for ICP–MS measurements

Jhanis J. Gonzalez, Chunyi Liu, Sy-Bor Wen, Xianglei Mao, Richard E. Russo *

Lawrence Berkeley National Laboratory, Berkeley, CA 94720, USA

Received 29 January 2007; received in revised form 13 April 2007; accepted 17 April 2007
Available online 4 May 2007

Abstract

Pulsed laser ablation (266 nm) was used to generate metal particles of Zn and Al alloys using femtosecond (150 fs) and nanosecond (4 ns) laser pulses with identical fluences of 50 J cm^{-2}. Characterization of particles and correlation with inductively coupled plasma mass spectrometer (ICP–MS) performance was investigated. Particles produced by nanosecond laser ablation were mainly primary particles with irregular shape and hard agglomerates (without internal voids). Particles produced by femtosecond laser ablation consisted of spherical primary particles and soft agglomerates formed from numerous small particles. Examination of the craters by white light interferometric microscopy showed that there is a rim of material surrounding the craters formed after nanosecond laser ablation. The determination of the crater volume by white light interferometric microscopy, considering the rim of material surrounding ablation craters, revealed that the volume ratio (fs/ns) of the craters on the selected samples was approximately 9 (Zn), 7 (NIST627 alloy) and 5 (NIST1711 alloy) times more ablated mass with femtosecond pulsed ablation compared to nanosecond pulsed ablation. In addition, an increase of Al concentration from 0 to 5% in Zn base alloys caused a large increase in the diameter of the particles, up to 65% while using nanosecond laser pulses. When the ablated particles were carried in argon into an ICP–MS, the Zn and Al signals intensities were greater by factors of ∼50 and ∼12 for fs versus ns ablation. Femtosecond pulsed ablation also reduced temporal fluctuations in the ^{66}Zn transient signal by a factor of 10 compared to nanosecond laser pulses.
Published by Elsevier B.V.

Keywords: Laser ablation; Particles; Metal; ICP–MS

1. Introduction

The aerosol size and size distributions are central topics in current laser ablation ICP–MS research. The particle size is a primary parameter that determines the entrainment, transport efficiency, composition, and decomposition of laser-ablated particles in the ICP [1–5]. To optimize particle size and the size distribution for laser ablation chemical analysis, it is necessary to identify and study particle growth mechanisms [6,7]. A schematic representation of particle formation from vapor is presented in Fig. 1. At high temperatures (but below the material boiling temperature), primary particles are formed by nucleation followed by condensation. Afterwards, collision of primary liquid particles leads to coalescence and an increase in the primary size (collision–coalesce process). As the temperature decreases, coalescence ceases and colliding particles tend to form hard and soft agglomerates which can continue to grow by a cluster–cluster collision process [8–11]. Experimental conditions in which any of these processes is favored will establish the final particle size and shape.

The characteristics of particles generated by laser ablation, namely, number density, composition, shape and size distribution are dependent on parameters such as those that influence the amount of ablated mass: laser power density, beam diameter and profile, wavelength, etc. Parameters that influence the plasma properties and evolution (gas environment, pressure, etc.), and sample chemical and physical properties are important as well [2,4,5,12–14].

It has been demonstrated that experimental conditions in laser ablation studies could be established in order to customize particle size and size distribution [15–17]. However one question that immediately emerges is; are ideal laser ablation conditions suitable for providing appropriately sized particles for ICP–MS analysis? Experimental conditions in which a particular size is generated could lead to conditions less than ideal for ICP–MS chemical analysis. For example, changes in the sample environment such as decreasing pressure inside the ablation chamber or even the use of vacuum has been shown to decrease the particle

* Corresponding author. Tel.: +1 510 486 4258; fax: +1 510 483 7303.
E-mail address: rerusso@lbl.gov (R.E. Russo).

0039-9140/$ – see front matter. Published by Elsevier B.V.
doi:10.1016/j.talanta.2007.04.029

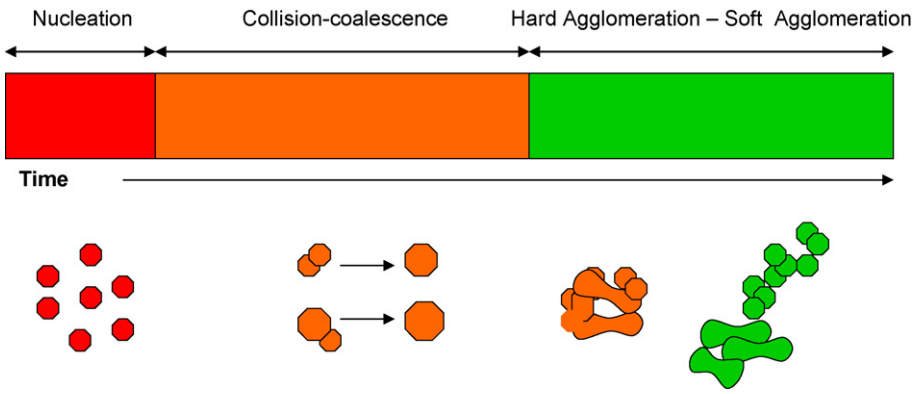

Fig. 1. Schematic representation of particle generation mechanisms.

size [17]. But these environments prevent the transport of the ablated mass out of the ablation chamber and into the ICP–MS. Therefore compromise conditions (laser, environment and detection) that allow control of the particle size, efficient transport and subsequent analysis are necessary.

The ablation "behavior" of a sample can be described by three parameters, namely ablation rate, particle size distribution, and particle chemistry. These parameters govern the ICP–MS signal in terms of accuracy, precision and sensitivity. The importance of controlling these parameters is observed for example, when using calibration curves for quantitative analysis. In many cases a calibration curve (ICP–MS signal versus concentration) would not be an accurate representation of the analyte behavior between samples unless the ICP–MS signal was normalized to the mass, the volume of mass ablated or an internal standard of known concentration. Even if the amount of mass or volume ablated was the same for different samples, there is no guarantee that the particle size, size distribution and overall "behavior" would be the same.

There have been many studies about particle size distributions reported using nanosecond and femtosecond laser ablation [1,3,12,18–23]. However, an ideal particle size for LA–ICP–MS has not been established mainly due to inherent differences between instruments, experimental conditions, and samples. In many cases, as in this study, it is necessary to determine particle size and size distribution, and then examine how these particles affect the ICP–MS chemical analysis.

In the case of nanosecond laser ablation, it has been well documented [1–5] that the particle size and size distribution will strongly depend on the experimental conditions and sample properties. The primary thermal nature of nanosecond laser ablation can lead to formation of a molten layer, preferential

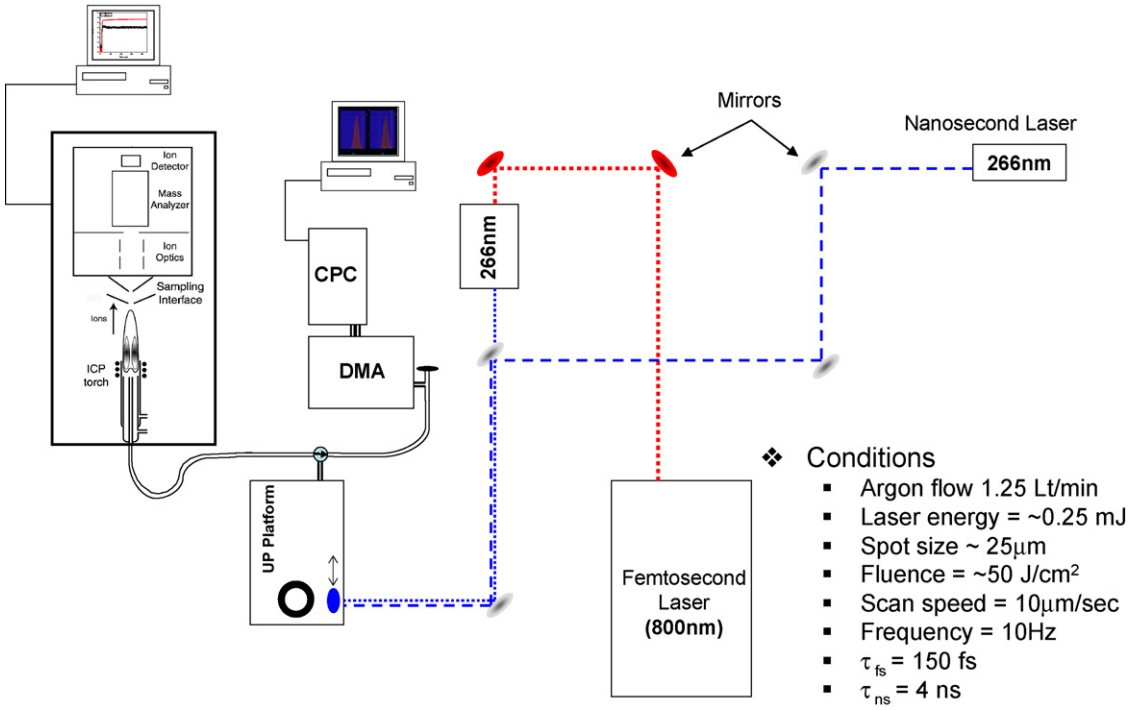

Fig. 2. Experimental setup and conditions.

Table 1
Elemental composition (mass fraction, in %) ($Zn_{95}Al_5$)

SRM	SRM	Cu	Al	Mq	Fe	Pb	Cd	Sn	Cr	Mn	Ni	Si	~Zn
625	Zinc-base	0.034	3.06	0.07	0.036	0.0014	7E-04	0.0006	0.0128	0.01	0.0184	0.017	96.7181
626	Zinc-base	0.056	3.56	0.002	0.103	0.002	0.0012	0.002	0.0395	0.048	0.047	0.042	96.0795
627	Zinc-base	0.132	3.88	0.03	0.023	0.021	0.005	0.0042	0.0038	0.014	0.0029	0.021	95.8758
628	Zinc-base	0.611	4.59	0.0094	0.066	0.0045	0.004	0.0017	0.0087	0.0091	0.03	0.008	94.6576
629	Zinc-base	1.5	5.15	0.094	0.017	0.0135	0.016	0.012	0.0008	0.017	0.0075	0.078	93.1100
630	Zinc-base	0.976	4.3	0.03	0.023	0.0083	0.005	0.004	0.0031	0.0106	0.0027	0.022	94.6155

Compositions of the reference standard series NIST 625–630. http://srmors.nist.gov/.

vaporization of elements, and ejection of melted particles, in addition to particles formed from condensation. The ejection of molten mass leads to the formation of large particles (>200 nm) [4,24]. Large particles (>200 nm) that are successfully transported to the ICP may not be completely vaporized, which may result in elemental fractionation in the ICP [5,12]. The formation of these particles is primarily determined by the laser (energy, spot size, focusing conditions, etc.); as well as surface tension and fluid stability. Femtosecond laser ablation, on the other hand, can be predominantly non-thermal; the phonon relaxation time (heating) in a solid is of the order of ~100 fs to a few ps. With femtosecond-pulsed ablation, the irradiated volume can explode (Coulomb explosion) before the photon energy is dissipated as heat in the lattice; melting is reduced (reducing or eliminating melt ejection) and the ablation process could produce a more uniform aerosol compared to nanosecond laser ablation [25]. Improved chemical analysis precision and accuracy by reducing systematic errors related to the particle size distribution and resultant spikes in the transient signal as well as a relaxation of matrix dependence has been shown for the analysis of glass and metal alloy samples when using femtosecond laser pulses [26–30].

The goal of this work was to characterize particles produced by UV-nanosecond and UV-femtosecond laser ablation for three series of alloy standard reference materials and pure Zn, by measuring particle size distributions, crater volumes, crater profiles, and establishing correlations with ICP–MS performance.

A set of useful definitions for this paper is based on the morphological properties of the particles: *Primary particles* are defined as the smallest identifiable individual particles. *Hard agglomerates* are assemblies of primary particles held together by strong bonds, probably ionic/covalent in nature. *Soft agglomerates* are assemblies of primary particles or hard agglomerates held together by weak bonds which may be due to van der Waals forces or ionic/covalent bonds operating over very small contact areas [9,31], cf (Fig. 1).

2. Experimental

The experimental system and conditions are shown in Fig. 2. The experimental setup included a femtosecond laser system consisting of a Spectra Physics Mai Tai Ti:sapphire seed laser and Spitfire regenerative amplifier. The 150 fs pulses at 800 nm were frequency tripled to obtain the 266-nm wavelength. The fourth harmonic of the Nd:YAG laser was used for the nanosecond (4 ns) ablation studies. An ICP–MS (VG PQ3 from VG Elemental) was used to chemically analyze the ablated mass and a DMA (Differential Mobility Analyzer) was used for the particle size measurement.

Laser ablation occurred in an argon environment under atmospheric pressure; the flow rate of the argon in the chamber was 1.25 L/min. The same laser energy and spot size was used (same fluence) for both laser systems. For the particle size distribution measurements, a flow switch was installed before the inlet to the DMA to ensure the working flow rate of 0.3 L/min; the rest of the flow was discarded through a filter. The differential mobility analyzer (DMA) with air under atmospheric pressure can measure particle diameter from 10 to 850 nm. However in argon, arc discharging occurred at voltages lower than the design value in air and reduced the maximum measured particle size from 850 to ~400 nm. In addition, the measurement process requires a scanning time of at least 1 minute for each data acquisition. However, the size of laser-ablated particles may change with time as a crater is developed. Therefore, to get a uniform particle generation during the measurement, the samples were translated at a constant speed during ablation (10 μm/s) to eliminate the effects of changing crater shape on particle size; this was confirmed by preliminary ICP–MS measurements that showed steady signal under these conditions. A white light interferometer microscope (Zygo-New View 200) was used for the craters profiles and volumes measurements, this instrument posses a vertical resolution of <0.1 nm and a lateral resolution of 0.37–9.5 μm objective dependent.

The samples (series of standard reference materials) used in this study were high purity zinc (99.99%, Goodfellow), zinc alloy from the National Institute of Standard and Technology (NIST) series 625–630 ("$Zn_{95}Al_5$"), zinc-aluminum alloy NIST 1736–1742 ("$Zn_{99.5}Al_{0.5}$"), and aluminum alloy NIST 1710–1712 ("Al"). Tables 1–3 show the trace element concentration and matrix composition for these standards. (http://srmors.nist.gov/).

Table 2
Elemental composition (mass fraction, in %) (Al)

SRM	SRM	Cd	Pb	~Al
1710	Aluminum base	0.0008	0.00177	99.9974
1711	Aluminum base	0.0021	0.00639	99.9915
1712	Aluminum base	0.0052	0.01559	99.9792

Compositions of the reference standard series NIST 1710–1712. http://srmors.nist.gov/.

Table 3
Elemental composition (mass fraction, in %) ($Zn_{99}Al_{0.5}$)

SRM	SRM	Al	Pb	~Zn
1736	Zinc-base	0.3076	0.0029	99.6895
1737	Zinc-base	0.6302	0.0029	99.3669
1738	Zinc-base	0.1014	0.0101	99.8885
1739	Zinc-base	0.2049	0.0302	99.7649
1740	Zinc-base	0.4177	0.0691	99.5132
1741	Zinc-base	0.5242	0.1571	99.3187
1742	Zinc-base	0.7917	0.0081	99.2002

Compositions of the reference standard series NIST 1736–1742. http://srmors.nist.gov/.

3. Results and discussion

3.1. Particle size measurements

Most particle size distribution functions can be described using the following parameters: *number density*, *particle diameter and span*.

Number density: when using the differential mobility analyzer (DMA) system the primary measurement is the differential number concentration (dN) of the aerosol per unit volume of gas sampled, which is the concentration of particles in a given channel. The DMA system is sensitive to the number of particles in the aerosol sample as opposed to particle mass, color, shape composition or other characteristics. The normalized number concentration, dN/dlogDp, is calculated by dividing dN by the geometric width of the size channel. This normalized concentration format allows particle size distributions to be compared regardless of the channel resolution. *Span*: The span illustrates the breadth of the distribution in terms of particle size. Span is calculated from:

$$Span = (D_{90} - D_{10})/D_{50}$$

Here D_{10}, D_{50}, and D_{90} refer, respectively, to the particle diameters below which 10, 50, and 90% of the cumulative aerosol are found. *Particle diameter*: the electrical mobility diameter (D_m) is the diameter of a sphere with the same migration velocity in a constant electric field as the particle of interest (physical diameter, D_p). For spherical particles $D_m = D_p$ [32].

During these experiments, each sample was ablated at 6 different surface locations, which resulted in six particle size distribution measurements. The average of these six particle size measurements was calculated and is presented in Fig. 3. The error bars represent the standard deviation of this average.

Number density: In Fig. 3a–d, significant differences in the number density of particles was measured in the 10–400 nm range by using femtosecond compared to nanosecond laser ablation. The larger number density of particles from femtosecond laser ablation originates from a higher ablation rate (more ablated mass hence more particles). Fig. 4 shows the crater profiles (samples Zn (a), NIST 627 (b), and NIST 1711 (c)) measured with a white light interferometer microscope (Zygo-New

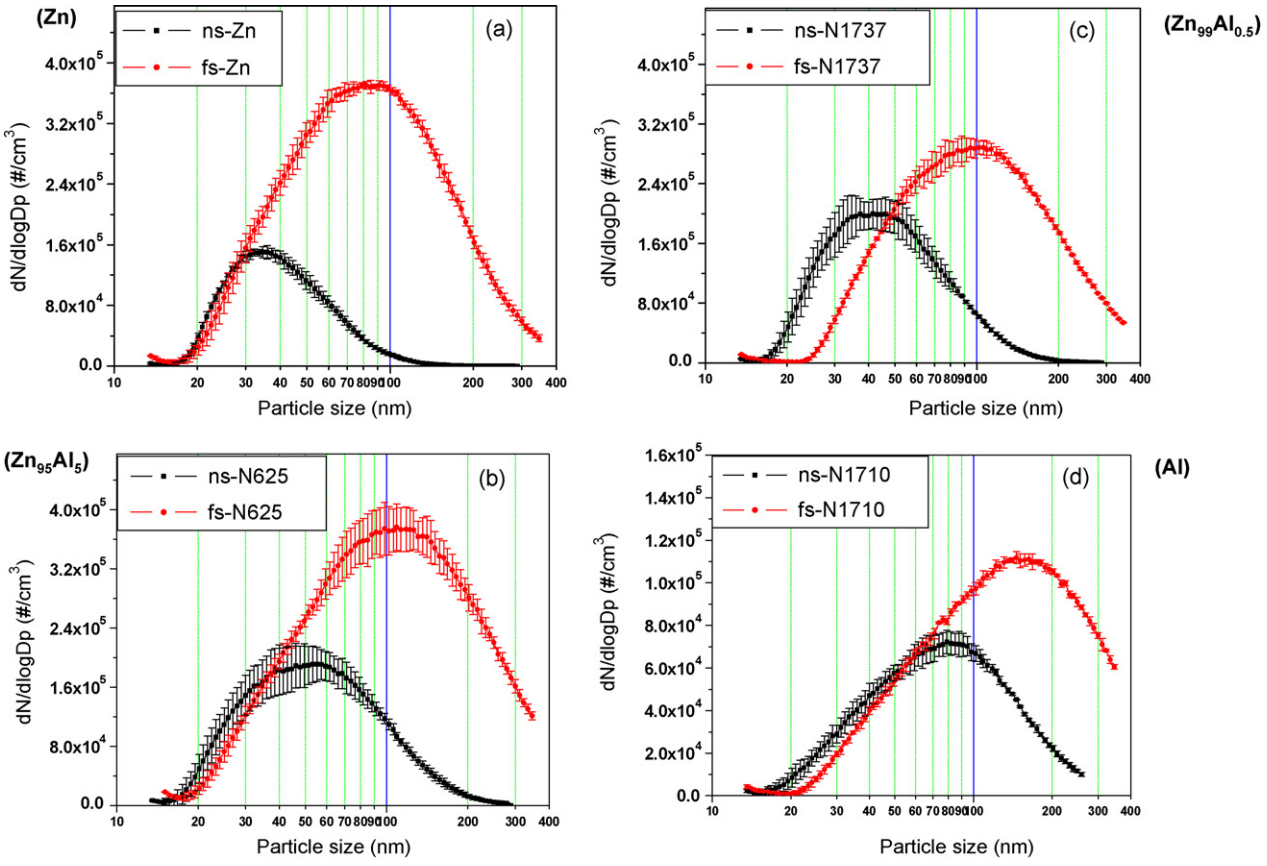

Fig. 3. Particle size distribution (DMA) for samples (a) Zn; (b) NIST 625, (c) NIST 1737, (d) NIST 1710.

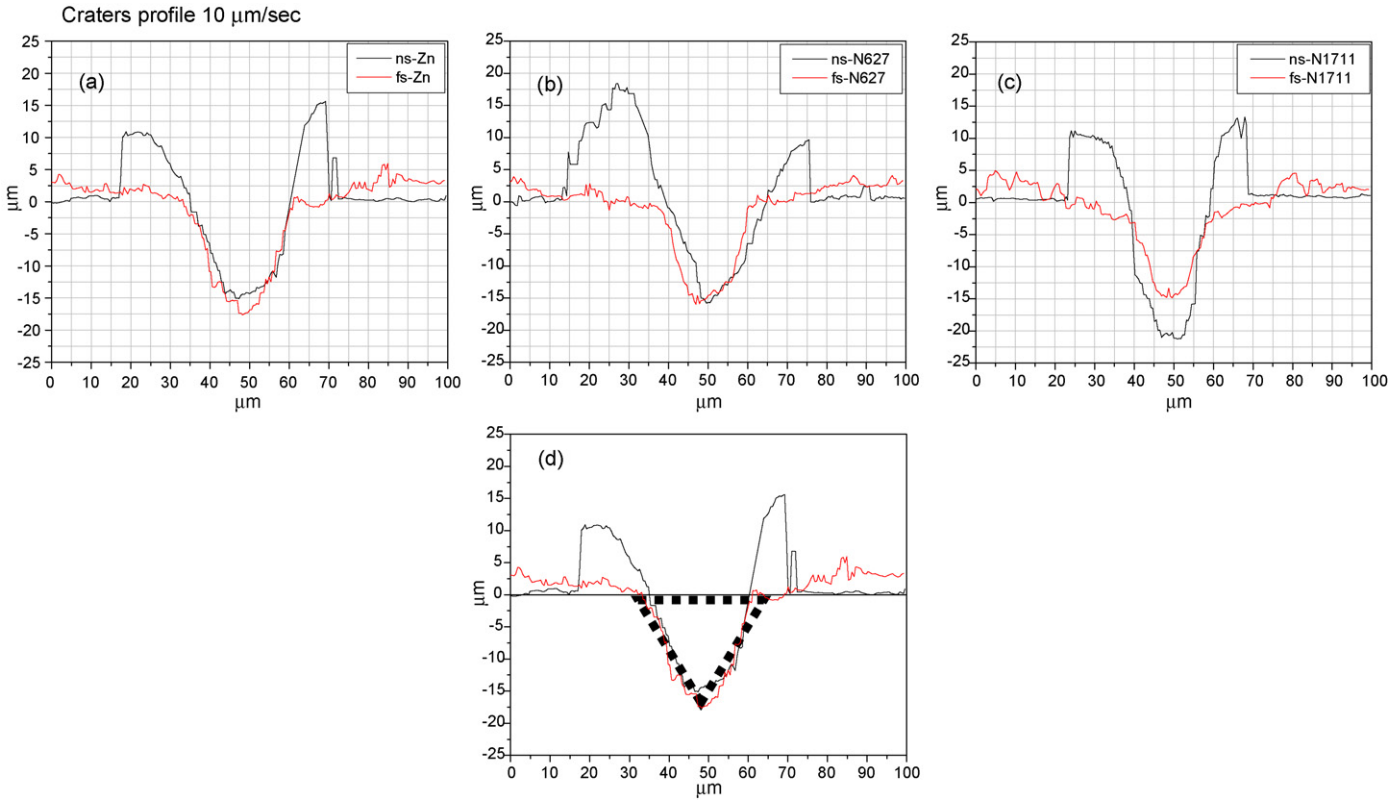

Fig. 4. White light interferometer microscope measurements of the crater profile (a) Zn, (b) NIST627, and (c) NIST1711. (d) Triangle shape used for volume calculations.

View 200). These profiles showed similar crater depths. However, mass deposit was not observed around the craters (rim) produced by femtosecond pulsed laser ablation. Therefore, the net volume, measured with white light interferometric microscope, which is the difference between the volume below and above the sample surface (represented by 0 in the *y-scale*), was higher for femtosecond laser ablation. Net volume ratio (fs/ns) for the selected samples shows that fs–laser ablation produce approximately 9 (Zn), 7 (NIST627) and 5 (NIST1711) times more ablated mass compared to nanosecond pulsed ablation (Table 4). These data support that the larger number density of particles produced by femtosecond laser ablation is associated with the larger amount of mass ablated from the sample. But how much mass was removed from the sample per second and how much of the ablated mass reached the DMA in an appropriate form to be measured?.

To answer these questions comparison based on the volume of ablated material per second, calculated from the sample craters, to the number concentration of particles per second from the DMA, was made. The volume of ablated material per second from the sample craters was calculated using a prism volume equation. The prism volume equation $V = A_{\text{triangle}}h$ was used due to the triangular shape of the crater profile (Fig. 4d). Here h is the length of the trench (ablation time 170 s × scan speed 10 µm/s) and A is the triangle area. For these calculations only the volume of the trench removed (volume below surface, 0 in the *y-scale*) was considered. The results of these calculations as well as the data of number concentration of particles per second obtained from the DMA are presented in Table 5. From these calculations the percentage of ablated mass per second that reaches the DMA was: pure zinc 91% (fs)–1.5% (ns), NIST627 125% (fs)–12% (ns) and NIST1711 96% (fs)–15% (ns). These results indicate that for fs–laser ablation, essentially all ablated mass was in suitable form to be transported to and measured by the DMA. Similar levels of transport efficiency were recently reported for NIR-fs laser ablation of brass in helium [33]. In this paper, the lower limit of transport efficiency (independent of the cell used) was reported to be about 77%. This efficiency was calculated after: weighing the sample before and after ablation with a microbalance, collecting the particles by low-pressure impaction, and evaluation of the impacted masses by X-ray fluoresce spectroscopy (XRF).

To account for the missing volume, especially for nanosecond laser ablation, is not an easy task. However, it can be assumed that some of the missing volume went to the material deposited around the crater (rim or volume above the surface), and some went to large particles that were not transported to or were not measured by the DMA (>400 nm).

Table 4
Volumes calculated from crater geometric shape and from DMA measurements

Sample	Zn	NIST 627	NIST 1711
Volume net ratio (fs/ns)	5	9	7
Total concentration ($\mu m^3/cm^3$) ratio (fs/ns}	62	10	5
Integrated signal intensity ratio (fs/ns)	50	23	12

Table 5
Femtosecond to nanosecond ratios; volume net (μm^3), total concentration (#/cm^3) and ICP–MS integrated signal intensities

	From crater								From DMA				
	Scan speed (μm/s)	Time (s)	Distance (μm)	Base (μm)	High (μm)	Area (μm^2)	Volume (μm^3)	Volume/s (μm^3/s)	nm^3/cm^3	$\mu m^3/cm^3$	Flowrate (cm^3/s)	Volume/s (μm^3/s)	Volume (fs/ns)
Zn													
ns	10	170	170	20	20	200	340000	2000	5.86E+09	5.86	5	29.3	62
fs	10	170	170	20	20	200	340000	2000	3.64E+11	364	5	1820	
N627													
ns	10	170	170	20	20	200	340000	2000	4.91E+10	49.1	5	245.5	10
fs	10	170	170	20	20	200	340000	2000	5.02E+11	502	5	2510	
N1711													
ns	10	170	1700	13	25	162.5	276250	1625	5.87E+10	58.7	5	293.5	5
fs	10	170	170	13	22	143	243100	1430	2.77E+11	277	5	1385	

The breadth of the distributions in terms of particle size (*Span*) shows no significant difference between nanosecond and femtosecond laser ablation. The calculated spans for all the samples particle size distribution functions yield an average of 1.6 for nanosecond laser ablation and 1.7 for femtosecond laser ablation.

Particle diameter: Comparison of the median particle size (median particle size represents the value in which the distribution function is split in half, 50% of the particles are above and below this value) shows that nanosecond laser ablation produced smaller particles than femtosecond laser ablation (cf. Fig. 3). This observation is consistent for all the samples within and between the different series of alloy standards and pure zinc. An apparent contradiction to the general assumption that femtosecond laser ablation generates smaller particles compared to nanosecond laser ablation is notable [28]. One explanation could be provided by evidence that nanosecond laser ablation produces a bimodal distribution in which there is a maximum at particle size range of 10–200 nm and another at larger particle sizes (>600 nm) [15]. Since particles size measurements, in this study, are only been carry out for particles between the range of 10–400 nm (due to DMA limitations), it is plausible to assume that the majority of mass ablated by nanosecond laser pulses were particles >600 nm. From this point of view, femtosecond laser ablation is producing a larger number of particles in the range of 10–400 nm, which are better suited for ICP–MS.

Another uncertainty derives from the fact that the method used for measuring the particle size distribution assumes spherical shape of the particles [32]. However, this is not always the case and deviation of the spherical shape leads to discrepancies in the size determined (over- or underestimation). For DMA measurements, the electrical mobility Z_p is related to the size of the aerosol particles. The definition of Z_p is $Z_p = (neC_c(D_m)/3\pi\eta_m)$ where, n is the number of elementary charges on a particle, e is the elementary charge (1.6×10^{-19} Coulomb), C_c is the Cunningham slip correction, η is the gas viscosity, and D_m is the electrical mobility diameter. When particles deviate from spherical, in particular for the case of soft or hard agglomerates of particles, the drag force experienced is larger but the electrical force is the same, so it is "sized" as a mobility-equivalent sphere that is larger than its sphere physical diameter. For compact hard agglomeration of particles with and

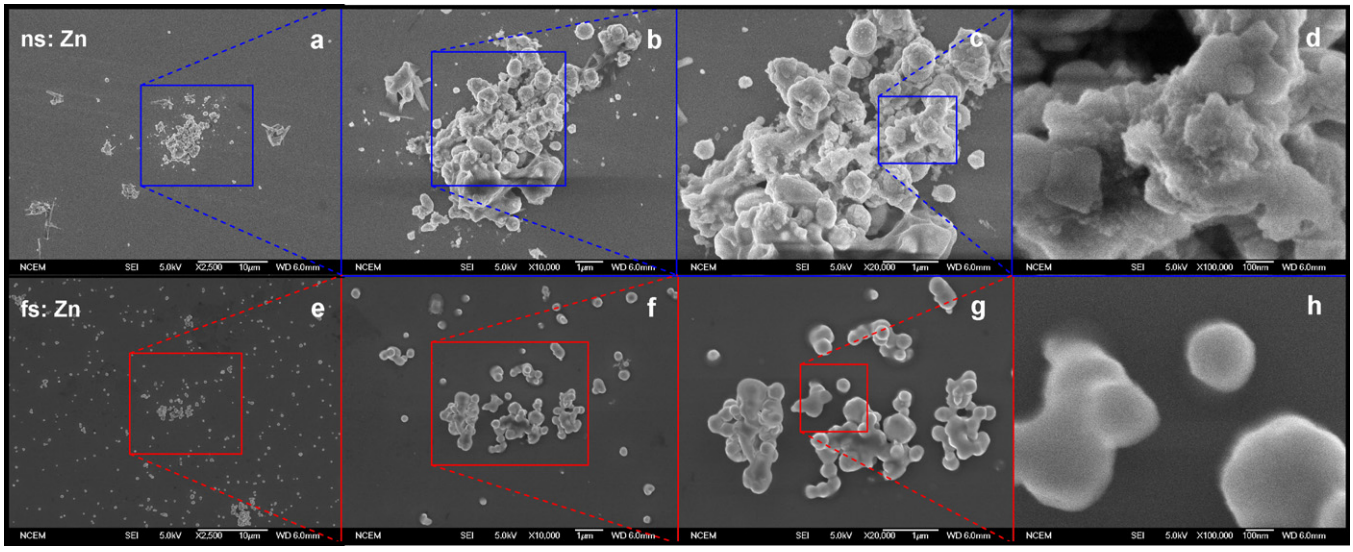

Fig. 5. SEM images of Zn particles; (a–d) nanosecond e–h) femtosecond laser ablation.

without internal voids, $D_m \approx D_p$, and for soft agglomeration of particles with or without internal voids $D_m > D_p$, where D_p is the physical diameter [32]. To investigate which of the possibilities presented above is responsible for the DMA data showing that the nanosecond pulsed laser produces smaller particles than the femtosecond pulsed laser, characterization of particles by means of scanning electron microscopy (SEM) was performed.

For SEM measurements, NIST 1711 and Zn were ablated using the same conditions as above; the ablated mass was collected on small clean silicon substrates. Particles were collected at the exit of the ablation chamber after a distance of 1 meter of tubing (normal input to the ICP–MS). The particle collection time for both nanosecond and femtosecond ablation was the same (480 s).

SEM images show that the particle shapes and sizes were different for nanosecond and femtosecond laser ablation, Figs. 5 and 6. Individual particles and clusters were observed with both lasers. From nanosecond laser ablation, individual particles and clusters have irregular shapes. Clusters of particles appearing to be melted together are referred to here as hard agglomeration of particles [with irregular shape as is the case of nanosecond Zn (Fig. 5b and c) and NIST 1711 (Fig. 6b and c) or with compact shape as for femtosecond Zn (Fig. 5f and g)]. From femtosecond ablation, however, most of the individual particles have spherical shape and the clusters of particles are gathering of primary particles to form soft agglomerations (except for zinc sample, where some hard-agglomerates are also visible). The differences between soft and hard agglomeration of particles reside in the type of interaction between the primary particles. A soft agglomeration of particles can be separated into its primary constituents without losing their shape and properties, while this is not possible from a hard agglomeration of particles. Soft agglomeration of particles can be broken into primary particles and/or hard agglomerates. From these images, it is reasonable to speculate that DMA measurements are more reliable for particles generated by the femtosecond laser due to their spherical shape. Moreover, femtosecond laser ablation particles in the SEM images are in concordance with the DMA particle size distributions. However, even though for femtosecond laser ablation most of the produced particles were transported and measured by the DMA, an overestimation of the size cannot be completely ruled out, due to the appearance of soft agglomerates in these images.

Studies of particle formation by flame aerosol reactors [8–11] show that the particle size strongly depends on: the precursor concentration [affects number of collisions (atoms and clusters) at early times, which will affect the size of the primary particles]. A high maximum flame temperature accelerates reaction kinetics and prolongs particle coalescence, promoting the formation of larger primary particles. High cooling rate prevents coalescence, resulting in smaller primary particle sizes. Long residence times prolong particle coalescence, thereby increasing the primary particle size. By controlling these parameters, researchers can customize the particle size in a flame. Experimental conditions in a flame aerosol reactor may be "easier" to control than in a laser ablation experiment. Nonetheless, parameters such as the amount of ablated mass and cooling rate are expected to play similar roles in laser ablation experiments. In laser ablation, as in flame aerosol reactors, a larger amount of precursor (amount of ablated mass) will increase vapor density and number of atomic collisions at early times, thus increasing the primary particle size. However, even though the effect of cooling rate in the particle formation and growth is not completely understood for laser ablation, it is safe to assume that a faster plasma cooling rate will influence the volume of material melted and the production of particles from the molten layer. Femtosecond laser induced plasma temperature and electron number density decrease faster in the first 250 ns after the laser pulse interacts with the sample compared to nanosecond induced plasmas [34]. Even though femtosecond laser ablation generated a larger amount of ablated mass compared to nanosecond laser ablation under the conditions in this study, the contribution of particles from the melted layer by nanosecond laser ablation appears to be significant for all analyzed samples. In addition to the mentioned parameters

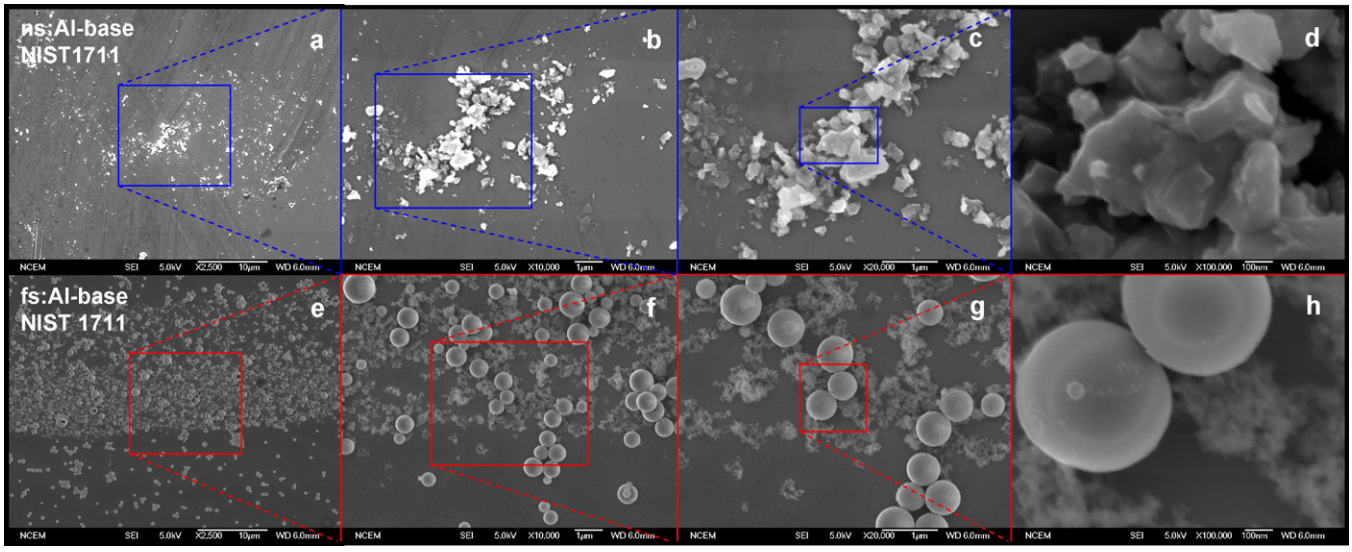

Fig. 6. SEM images of NIST 1711 particles; (a–d) nanosecond (e–h) femtosecond laser ablation.

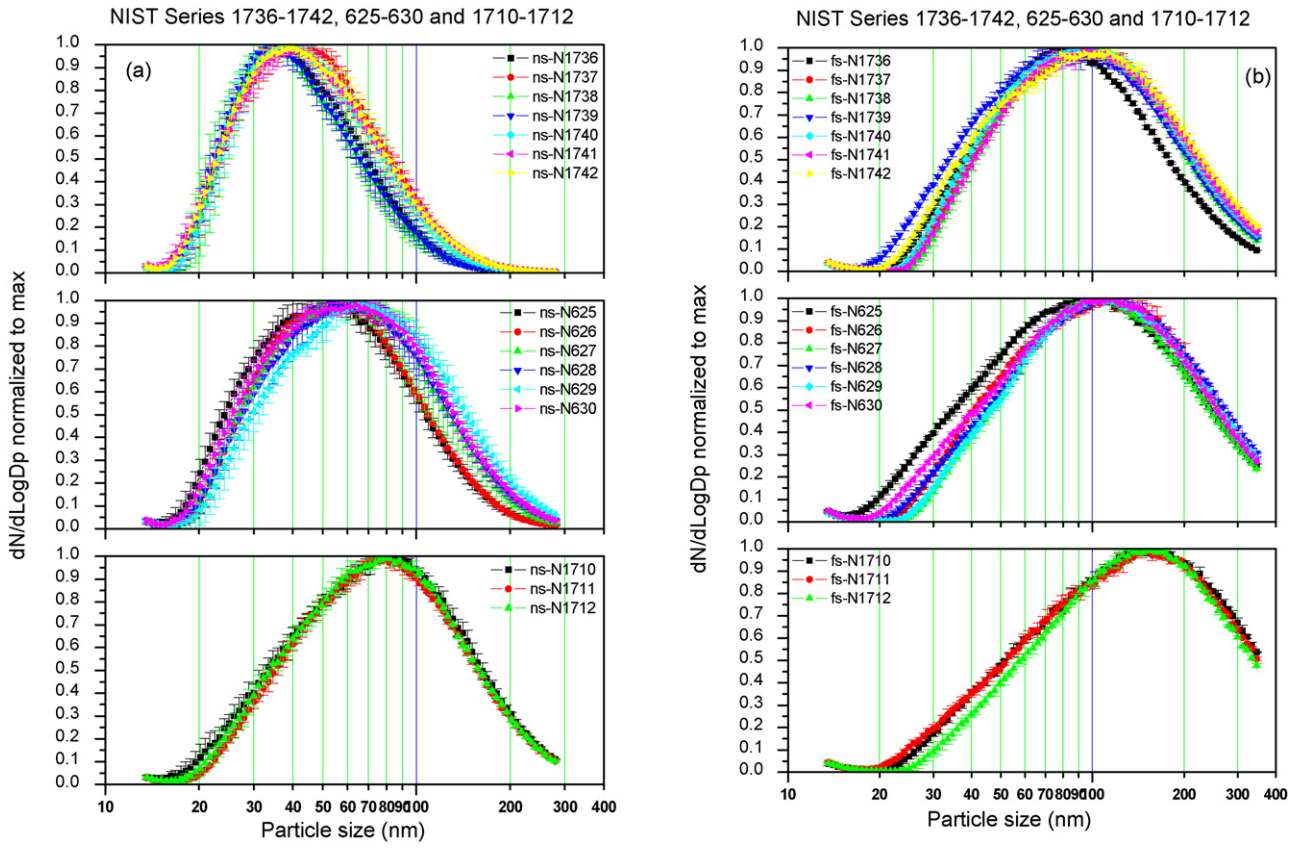

Fig. 7. Normalized particle size distribution (DMA) for the series NIST 1736-1742, NIST 625-630 and NIST 1710–1712. (a) Nanosecond laser ablation and (b) femtosecond laser ablation.

that have an effect on the mechanisms of particle formation, it was recently reported by Koch et al. [35] that when using NIR-ns-LA, predominantly larger particles were formed in the present of argon compared to helium. They attributed these observations to the increased collisions frequency between particles product of the dynamic expansion patterns. In contrast for NIR-fs-LA, these dynamic expansion patterns were chaotic and consisted in multiple branches independent of the background gas, producing smaller particles and agglomerates compared to NIR-ns-LA. A close observation of the particles in Figs. 5 and 6 shows that in addition to large agglomeration of particles some individual particles were as large as micrometers in size, suggesting that they have been ejected from the melted surface instead of being condensed from the ablated plasma vapor.

The sizes of particles (primary and hard agglomerates) from nanosecond ablation ranged widely from several tens to thousands of nanometers. The large particles (primary and soft agglomerates) from femtosecond ablation have a different structure. They were neck-shaped (Zn) or perfectly spherical particles (NIST 1711) and soft agglomerates formed from several small particles. These small particles seem ranged from 10 to 50 nm (unresolved particles on the SEM Images 6 g and h), which are positioned next to each other reaching dimensions of several micrometers. There were fewer single large droplets compared to those observed with nanosecond ablation, suggesting that melting and ejection of molten mass was less prominent. This data confirmed that nanosecond pulsed ablation produces larger particles compared to femtosecond pulsed laser ablation as was also showed by Koch et al. [35] for NIR-ns and NIR-fs-LA.

The different particle shapes and sizes between the studied samples cannot directly be explained by chemical composition, due to the complexity of some of the samples. However, a trend was observed when plotting the number concentration, dN/dlogDp (normalized to the maximum value) for: (a)

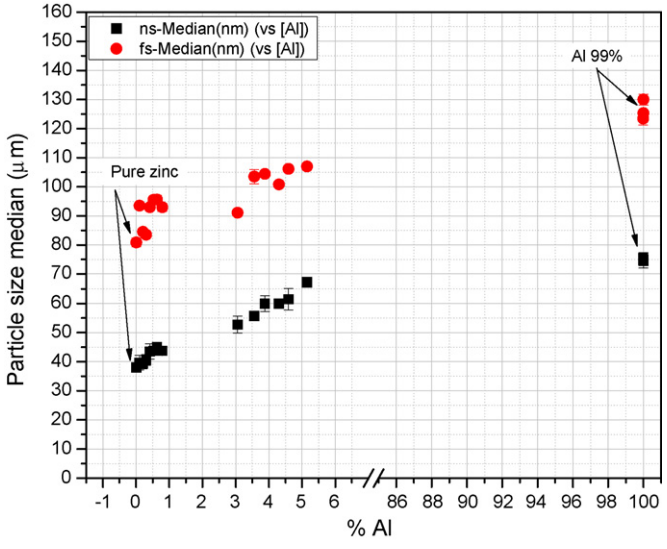

Fig. 8. Median particle size vs. aluminum concentration (%).

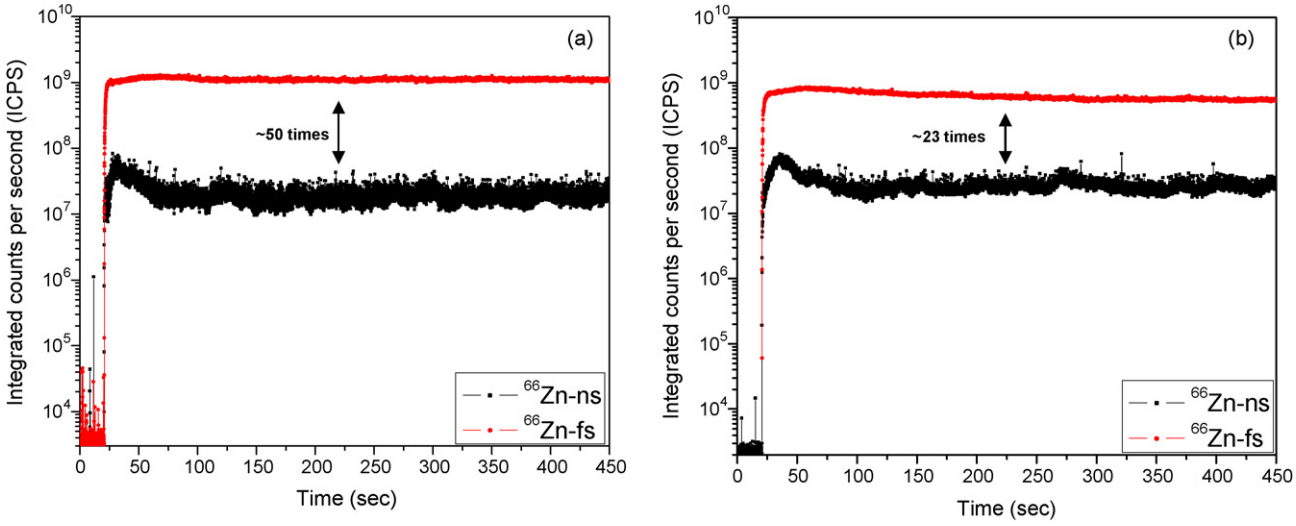

Fig. 9. ^{66}Zn transient signals produced by 10 μm/s ablation (nanosecond and femtosecond) (a) pure Zn and (b) NIST 627.

nanosecond and (b) femtosecond (Fig. 7) and the median particle size versus the aluminum concentration (Fig. 8). For nanosecond laser ablation (Fig. 7a) the particle size distribution modes (which represent the maxima of the distribution functions) are shifted with respect to each other when compared between the standard series. It is also noticeable that the error bars (representing standard deviation between particle size distributions) in each distribution for nanosecond laser ablation are larger than those from femtosecond laser ablation. The modes shift from 40 nm for NIST 1736–1742 to 65 nm for NIST 625–630 and 80 nm for NIST 1710–1712. In contrast, for femtosecond laser ablation the mode is 90 nm for NIST 1736–1742, 110 nm for NIST 625–630, and 140 nm for NIST 1710–1711. The total size variation measured with the nanosecond laser is a range of about 2:1, whereas the same ratio for femtosecond laser ablation is about 1.5:1.

An increase in the median particle size was observed with increased aluminum concentration (Fig. 8). Based only on the Zn and Al properties, it is possible to speculate that, as the plasma and surroundings cool down [assuming the same starting plasma and surrounding temperatures, above the sample boiling point] the ablated mass with higher boiling point will condense and resolidify sooner than the ablated mass with lower boiling point. The ablated mass that condenses first will have a higher probability to coalesce, due to the longer time in the liquid phase. The boiling and melting temperatures of zinc (1180 and 693 K, respectively) are lower than aluminum (2792 and 993 K); coalescence could be more important in aluminum ablation. From this analysis it is expected that samples with higher aluminum concentration would present the largest particles, which seems to be the case from the SEM images and DMA measurements. A concentration of 5% Al in the Zn alloy increases the particle size by about 65% for nanosecond laser ablation. A similar but less dramatic effect (∼30%) was observed with femtosecond pulses. We speculate that small concentrations of Al in Zn may accelerate nucleation of liquid droplets in the supercooled vapor phase.

The effects of these particles on the ICP–MS performance also were studied. The ICP–MS transient signals were consistently greater for femtosecond compared to nanosecond laser ablation (Fig. 9). The ratio of the integrated signals (fs/ns) and temporal relative standard deviation (%TRSD, as a measurement of the signal stability) were used as a basis of comparison between femtosecond and nanosecond laser ablation. For ^{66}Zn in pure zinc the ratio of the integrated signals (fs/ns) was 50, with TRSD of 17% ns and 2% fs, for ^{66}Zn in NIST 627 the ratio of the integrated signals was 23 with TRSD of 20% ns and 2% fs, and 12 times for ^{27}Al in NIST 1711 with TRSD of 23% ns and 3% fs. As showed earlier, the total size variation measured with the nanosecond laser is a range of about 2:1, whereas the same ratio for femtosecond laser ablation is about 1.5:1. And even though, these ratios do not appear to be that remarkably different, when introducing these aerosols into the ICP–MS these small differences become significant when comparing ns to fs–LA.

A clear trend indicating advantages of femtosecond over nanosecond laser ablation for the ablation of metallic samples was observed for all measurements performed in this study; the *net ablated volume* from the crater profile measurements indicates that more mass was removed from the sample with femtosecond laser pulses with less thermal damage (heat affected zone and rim formation). The total concentration of particles normalized by volume demonstrates that a greater number of particles with suitable sizes to be transported and measured by the DMA was produced by femtosecond laser ablation (Table 5), and the ratio of the ICP–MS integrated signal demonstrated that more mass from femtosecond laser ablation reached and was digested by the ICP compared to nanosecond laser ablation (Table 4). The ratio of the integrated signal to volume net (Table 4) could be used as a measure of the overall improved efficiency by femtosecond compared to nanosecond laser ablation; for these samples it was shown that there is an improvement of 10, 2.5, and 1.7 times for Zn, NIST 627, and NIST 1711, respectively.

The discussion in this study is focused specifically on metallic samples and the results cannot be generalized to other materials even using the same laser conditions. In general, significant differences in material properties such as the absorption coefficient, thermal diffusivity, etc. could generate completely different ablation behavior. A study of glass samples under the same condition used in this paper is presented in a follow-up paper.

4. Summary

Metal particles produced by nanosecond and femtosecond laser ablation at a fluence of 50 J cm^{-2} in argon were different in size and morphology. Particles produced by nanosecond laser ablation mainly consisted of primary particles with irregular shape and hard agglomerates (without internal voids). Particles produced by femtosecond laser ablation consisted of spherical primary particles and soft agglomerates formed from numerous small particles. There were fewer single large droplets formed by femtosecond laser ablation compared with those observed with nanosecond ablation. Melting and ejection of molten mass was less prominent with femtosecond ablation.

Crater net volume showed that a larger amount of mass from the metallic samples was ablated using femtosecond laser compared to nanosecond laser ablation. Furthermore, comparison between the calculated volume from the crater and total particle concentration normalized by volume from the DMA demonstrated that most of the ablated mass using femtosecond laser ablation reached the DMA while there was a large amount of mass unaccounted for from the nanosecond craters.

The larger amount of mass ablated from the samples with the femtosecond laser pulses from these metallic samples, as in a flame aerosol reactor (with high precursor concentration), could increase the number of atomic collisions at early times, promoting the increase of the primary particle size. However, the contribution of large particles from melted layer ejection becomes an important factor in the overall aerosol quality when using nanosecond laser ablation (as observed in the SEM images) causing more mass to deposit around the craters, reduction in transport efficiency, reduction in ICP–MS signal, and increasing signal fluctuations (%TRSD).

Acknowledgements

We would like to thank Sotiris E. Pratsinis, for his helpful advice on aerosol particle formation and Paul Berdahl for productive discussions and for editing the manuscript. This work was supported by the Office of Science, Office of Basic Energy Sciences, Chemical Sciences, Geosciences, and Biosciences Division, and the Deputy Administrator for Defense Nuclear Nonproliferation, Research and Development of the U.S. Department of Energy under Contract No. DE-AC02-05CH11231.

References

[1] J. Kosler, M. Wiedenbeck, R. Wirth, J. Hovorka, P. Sylvester, J. Mikova, J. Anal. Atom. Spectrom. 20 (2005) 402–409.
[2] H.-R. Kuhn, D. Gunther, Analytical and bionalytical chemistry on line paper (2005).
[3] J. Koch, A. von Bohlen, R. Hergenroder, K. Niemax, J. Anal. Atom. Spectrom. 19 (2004) 267–272.
[4] R.E. Russo, X.L. Mao, C. Liu, Y.J. Gonzalez, J. Anal. Atom. Spectrom. 19 (2004) 1084–1089.
[5] D.B. Aeschliman, S.J. Bajic, D.P. Baldwin, R.S. Houk, J. Anal. Atom. Spectrom. 18 (2003) 1008–1014.
[6] R. Hergenroder, Spectrochim. Acta Part B 61 (2006) 284–300.
[7] A. Bogaerts, Z.Y. Chen, R. Gijbels, A. Vertes, Spectrochim. Acta Part B-Atom. Spectrosc. 58 (2003) 1867–1893.
[8] T. Tani, K. Takatori, S.E. Pratsinis, J. Am. Ceram. Soc. 87 (2004) 365–370.
[9] S. Tsantilis, S.E. Pratsinis, Langmuir 20 (2004) 5933–5939.
[10] S.E. Pratsinis, S. Vemury, Powder Technol. 88 (1996) 267–273.
[11] S.E. Pratsinis, Prog. Energ. Combust. Sci. 24 (1998) 197–219.
[12] H.R. Kuhn, M. Guillong, D. Gunther, Anal. Bioanal. Chem. 378 (2004) 1069–1074.
[13] R. Jaworski, E. Hoffmann, H. Stephanowitz, Int. J. Mass Spectrom. 219 (2002) 373–379.
[14] C. Liu, A study of particle generation during laser ablation with applications, Ref Type: Thesis/Dissertation, 2005.
[15] H.-R. Kuhn, J. Koch, R. Hergenroder, K. Niemax, M. Kalberer, D. Gunther, J. Anal. Atom. Spectrom. 20 (2005) 894–900.
[16] M. Ullmann, S.K. Friedlander, A. Schmidt-Ott, J. Nanoparticle Res. 4 (2002) 499–509.
[17] Z. Pászti, Z.E. Horváth, G. Peto, A. Karacs, L. Guczi, Appl. Surf. Sci. 109/110 (1997) 67–73.
[18] J. Heitz, J.T. Dickinson, Appl. Phys. A 68 (1999) 515–523.
[19] H.R. Kuhn, D. Gunther, J. Anal. Atom. Spectrom. 19 (2004) 1158–1164.
[20] C. Liu, X.L. Mao, J. Gonzalez, R.E. Russo, J. Anal. Atom. Spectrom. 20 (2005) 200–203.
[21] J. Koch, H. Lindner, A. von Bohlen, R. Hergenroder, K. Niemax, J. Anal. Atom. Spectrom. 20 (2005) 901–906.
[22] P. Weis, H.P. Beck, D. Gunther, Anal. Bional. Chem. 381 (2005) 212–224.
[23] J. Koch, M. Walle, J. Pisonero, D. Gunther, J. Anal. Atom. Spectrom. 21 (2007) 932–940.
[24] J.H. Yoo, S.H. Jeong, X.L. Mao, R. Greif, R.E. Russo, Appl. Phys. Lett. 76 (2000) 783–785.
[25] J. Gonzalez, X.L. Mao, S. Mao, R.E. Russo, J. Anal. Atom. Spectrom. 17 (2002) 1072–1075.
[26] J. Gonzalez, S.H. Dundas, C. Liu, X.L. Mao, R.E. Russo, J. Anal. Atom. Spectrom. 21 (2005) 778–784.
[27] J. Gonzalez, C.Y. Liu, X.L. Mao, R.E. Russo, J. Anal. Atom. Spectrom. 19 (2004) 1165–1168.
[28] C. Liu, X.L. Mao, S.S. Mao, X. Zeng, R. Greif, R.E. Russo, Anal. Chem. 76 (2004) 379–383.
[29] Q.Z. Bian, J. Koch, H. Lindner, H. Berndt, R. Hergenroder, K. Niemax, J. Anal. Atom. Spectrom. 20 (2005) 736–740.
[30] Q.Z. Bian, C.C. Garcia, J. Koch, K. Niemax, J. Anal. Atom. Spectrom. 21 (2006) 187–191.
[31] R. Bandyopadhyaya, A.A. Lall, S.K. Friedlander, Powder Technol. 139 (2004) 193–199.
[32] P.F. De Carlo, J.G. Slowik, D.R. Worsnop, P. Davidovits, J.L. Jimenez, Aerosol Sci. Technol. 38 (2004) 1185–1205.
[33] C.C. Garcia, H. Lindner, K. Niemax, Spectrochim. Acta Part B-Atom. Spectrosc. 62 (2007) 13–19.
[34] X. Zeng, X.L. Mao, R. Greif, R.E. Russo, Appl. Phys. A: Mater. Sci. Process. 80 (2004) 237–241.
[35] J. Koch, S. Schlamp, T. Rosgen, D. Fliegel, D. Gunther, Spectrochim. Acta Part B-Atom. Spectrosc. 62 (2007) 20–29.

Available online at www.sciencedirect.com
ScienceDirect
Talanta 73 (2007) 483–489
Talanta
www.elsevier.com/locate/talanta

Development and validation of HPLC method for determination of clotrimazole and its two degradation products in spray formulation

Renata Hájková, Hana Sklenářová, Ludmila Matysová, Petra Švecová, Petr Solich *

Department of Analytical Chemistry, Faculty of Pharmacy, Charles University, Heyrovského 1203, 500 05 Hradec Králové, Czech Republic

Received 11 December 2006; received in revised form 31 March 2007; accepted 11 April 2007
Available online 25 April 2007

Abstract

A novel simple isocratic HPLC method with UV detection for the determination of three compounds in spray solution (active component clotrimazole and two degradation products imidazole and (2-chlorophenyl)diphenylmethanol) using ibuprofen as an internal standard was developed and validated. The complications with different acido-basic properties of the analysed compounds in HPLC separation – while clotrimazole has pK_a 4.7, imidazole has pK_a 6.9 compared to relatively more acidic (2-chlorophenyl)diphenylmethanol – were finally overcome using a 3.5 μm Zorbax® SB-Phenyl column (75 mm × 4.6 mm i.d., Agilent Technologies).

The optimal mobile phase for separation of clotrimazole, degradation products imidazole and (2-chlorophenyl)diphenylmethanol and ibuprofen as internal standard consists of a mixture of acetonitrile and water (65:35, v/v) with pH* conditioned by phosphoric acid to 3.5. At a flow rate of 0.5 ml min^{-1} and detection at 210 nm, the total time of analysis was less than 6 min.

The method was applied for routine analysis (batch analysis and stability tests) in commercial spray solution.

Keywords: Clotrimazole; HPLC; Pharmaceuticals; Degradation products; Stability studies; Simultaneous determination

1. Introduction

Clotrimazole (CLO, Fig. 1), 1-[(2-chlorophenyl)diphenylmethyl]-1*H*-imidazole, is relatively non-toxic synthetic imidazole derivative with broad-spectrum of antimicrobial activity, first described in 1969. It is a well-established drug used in dermatology and gynaecology, available in the form of tablet, cream and solution formulations. Ointments containing CLO are widely used for the treatment of various systemic mycoses including candidiasis; the compound is highly effective, but can cause liver enzyme changes [1–6].

Pharmaceutical formulations are usually complex mixtures of compounds comprising the effective substance, auxiliary substances, and, in some cases, preservatives. There is a need to determine not only the active substance to confirm its quality in the preparation, but also very small amounts of its degradation products to obtain information about the stability of the active substance.

Some methods have been described for identification and quantification of active substance CLO, such as densitometry [7], spectrophotometry [8,9], voltammetry [10], polarographic determination [11], capillary electrophoresis separation [12,13], micellar electrokinetic chromatography [14], thin-layer chromatography [15] and HPLC [16–19], but no method has been found for the simultaneous determination of all three important components—CLO and its two degradation products: (*o*-chlorophenyl)diphenylmethanol (CDM, Fig. 1) and imidazole (IM, Fig. 1). Moreover, the current United States Pharmacopoeia USP 29 specifies an HPLC method for the determination of CLO and only one of its degradation products – CDM in the topical creams, but not simultaneously in the presence of the second degradation product, which usually occurs – IM [20]. Two methods [21] were recently developed for HPLC determination of five components in pharmaceutical product – Clotrimazole cream 1% – for internal purposes in our workplace in 2002. The first method deals with the simultaneous determination of CLO and two preservatives (methylparaben and propylparaben), the second separate method describes the determination of degradation products of CLO (CDM, IM) after long-term stability tests. No method has been developed for the

* Corresponding author. Tel.: +420 49 5067294; fax: +420 49 5067164.
E-mail address: petr.solich@faf.cuni.cz (P. Solich).

0039-9140/$ – see front matter © 2007 Elsevier B.V. All rights reserved.
doi:10.1016/j.talanta.2007.04.023

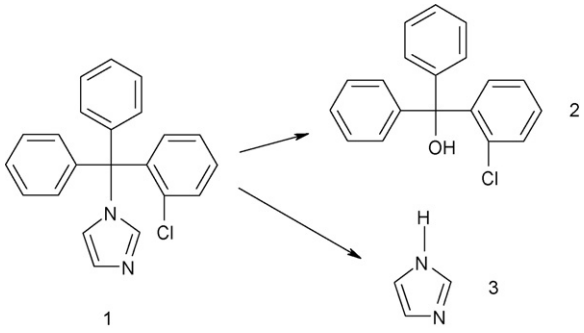

Fig. 1. Chemical structures—major component clotrimazole (1) and its degradation products (*o*-chlorophenyl)diphenylmethanol (2) and imidazole (3).

determination of all three compounds of interest in one step with respect to their different chemical properties and the different acido-basic behaviours in HPLC system.

The purpose of this study was to develop a new simple and quick isocratic HPLC method with UV detection for simultaneous determination of the active substance CLO and its two degradation products CDM and IM (presented usually in a very low quantity) in one step, in a clotrimazole formulation—Clotrimazole spray 1% solution. Due to the different acido-basic characteristics (pK_a) of all three compounds (clotrimazole and imidazole are basic compounds) and thus problematic separation on RP-HPLC, their simultaneous determination has not been described in literature yet.

2. Experimental

2.1. Chemicals and reagents

Stock solutions of clotrimazole, imidazole, (2-chlorophenyl) diphenylmethanol and ibuprofen, flurbiprofen, ketoprofen, hexachlorophene and terbinafin (tested as internal standards), were used for the purpose of this study. Clotrimazole as well as both degradation products imidazole and (2-chlorophenyl)diphenylmethanol were provided by Amoli Organics Ltd. (Mumbai, India). Ibuprofen and flurbiprofen were obtained from Sigma–Aldrich (Schelldorf, Germany), ketoprofen, hexachlorophene and terbinafin from Herbacos-Bofarma Ltd. (Pardubice, Czech Republic). All of these compounds were checked by comparison with European Pharmacopoeia CRS standards (Strasbourg, France).

Phosphoric acid 85% p.a. was obtained from Merck (Darmstadt, Germany), acetonitrile Chromasolv for HPLC from Sigma–Aldrich (Schelldorf, Germany). HPLC grade water was prepared by Milli-Q reverse osmosis by Millipore (Bedford, USA) and meets European Pharmacopoeia requirements.

2.2. Chromatographic system

Shimadzu LC-2010C system (Kyoto, Japan) was used to perform all experiments. The instrument was equipped with column oven temperature control and built-in autosampler. Chromatographic software Class VP 6.12 was used for data collection and processing.

Various chromatographic columns were tested: Supelco Discovery R Cyano (100 mm × 4 mm, 5 μm, Sigma–Aldrich), Supelco Discovery ZR-PBD (150 mm × 4.6 mm, 5 μm, Sigma–Aldrich), Zorbax SB-phenyl (75 mm × 4.6 mm, 3.5 μm, Agilent Technologies), Zorbax TMS (250 mm × 4.6 mm, 5 μm, Agilent Technologies), Purospher LiChroCART RP-18 endcapped (125 mm × 4 mm, 5 μm, Merck).

UV spectra measurements were carried out by Hewlett Packard 8453 spectrophotometer equipped with Chemstation software. Acetonitrile solutions of individual compounds were prepared and tested by comparison with acetonitrile blank solution.

2.3. Standard preparation

Stock solutions of individual chemicals (active ingredient, degradation products and internal standard) were prepared dissolving appropriate amount in acetonitrile. The reference standard solutions were prepared diluting the respective stock solutions to the final concentrations of CLO (500 mg l^{-1}), ibuprofen (100 mg l^{-1}), IM (5 mg l^{-1}) and CDM (5 mg l^{-1}) in 100 ml volumetric flask in acetonitrile. The stock solution of internal standard (ibuprofen) was prepared dissolving 500 mg in 100 ml of acetonitrile and used for standard and sample preparation as well.

All solutions were stored in the refrigerator (4 °C) because of the stability reasons.

2.4. Sample preparation

1.0 g of Clotrimazole spray solution (1%) – this amount corresponds to 10 mg of CLO – was accurately weighed into the 20 ml volumetric flask; 400 μl of the stock solution of internal standard was added and filled up with acetonitrile and directly injected to the chromatographic system.

2.5. Method optimization and validation

Chromatographic separation was optimized with the respect of the stationary and mobile phase compositions, flow rate, sample volume, detection wavelength and internal standard.

The objective of method validation was to demonstrate suitability for routine application of the developed methodology under stated requirements of ICH guidelines Q2A and Q2B [22]. Recommended validation characteristics depend on the type of analytical procedure. An important part is system suitability test which covers in detail number of theoretical plates, peak asymmetry, resolution of individual components and repeatability of injection which is evaluated by retention time and peak area values.

The method accuracy (% of recovery and % of individual measurements as R.S.D.) and method precision were tested using six samples in three replicates. Linearity (correlation coefficient) was tested in the range 50–150% of the expected amount of CLO (250–750 mg l^{-1}). Degradation products were tested in the range of 0.1–1.0% of active substance content (0.5–5.0 mg l^{-1}). Six concentration levels were used.

Method selectivity was verified by comparison of sample of pharmaceutical formulation, reference standard solution and placebo chromatograms. Limits of detection and quantification were provided for both degradation products and calculation was made by mean of signal-to-noise ratio method. Standard solution short-term stability (2 days) was tested at ambient temperature (25 °C) and at 4 °C. Method robustness with respect to the mobile phase composition was studied as well and validated by retention time and peak area values.

3. Results and discussion

3.1. Method optimization

All the separated compounds are organic substances with different structures and different retention on various stationary phases.

HPLC with UV detection was chosen as a simple, fast and effective separation method for determination of CLO and its two degradation products. All tested compounds had a low detector response at wavelengths in the range of 230–350 nm. The optimal absorption wavelength for detection of the compounds was chosen especially with regard to absorption spectra of degradation products; both give higher detector response at 210 nm, therefore the final absorption wavelength for detection was chosen at 210 nm.

Several analytical columns were chosen and tested during the development of this method. Agilent Zorbax reversed-phase bonded phases based on ultra-pure silica – StableBond (SB) – provide the best peak shape and sample resolution, as well as long column lifetimes. Zorbax SB columns are designed for high stability at low pH (pH range 1–6). Zorbax StableBond packaging of Zorbax SB-Phenyl column (75 mm × 4.6 mm, 3.5 μm) is made by chemically bonding dimethylphenethylsilane to Zorbax Sil particles, it is not endcapped in order to provide exceptional stability and reproducibility under acidic mobile phase conditions. The packing of Zorbax TMS column (250 mm × 4.6 mm, 5 μm) is produced by chemically bonding trimethylsilane groups to Zorbax silica particles [23]. The base material for Purospher high-purity HPLC columns is made of tetraalkoxysilane. Due to the absence of heavy metals in the silica matrix and in combination with a complete coverage of the silica surface, this stationary phase enables tailing-free chromatography. LiChroCART Purospher RP-18 endcapped column (125 mm × 4.0 mm, 5 μm) is designed for both the separation of basic compounds with simple neutral eluents and for the elution of strongly acidic compounds [24]. The packing of Supelco Discovery CN column (100 mm × 4.0 mm, 5 μm) has low hydrophobicity for rapid elution of hydrophobic analytes and excellent peak shape and retention of strongly basic analytes. The Supelco column containing Discovery Zr zirconia particles are not susceptible to acidic or basic hydrolysis and, therefore, do not have the pH limitation of silica. Discovery Zr particles also have ion-exchange character via the adsorbed Lewis base buffer ions. The packing of the Supelco Discovery ZR-PBD column (150 mm × 4.6 mm, 5 μm) has selectivity similar to C18-silica for nonionic compounds [25].

Different mobile phases consisting of acetonitrile and water were tested; pH* of mobile phase was adjusted with 85% phosphoric acid to 2.7 according to the previous experiments [21]. Finally the best results were obtained using a mobile phase consisting of acetonitrile and water in the ratio 65:35 (v/v), pH* 2.7. The analysis times with analytical columns Zorbax TMS and Supelco Discovery Zr-PBD were too long—60 min and 45 min, respectively; on Supelco Discovery CN column all tested compounds were not completely separated. The best results were

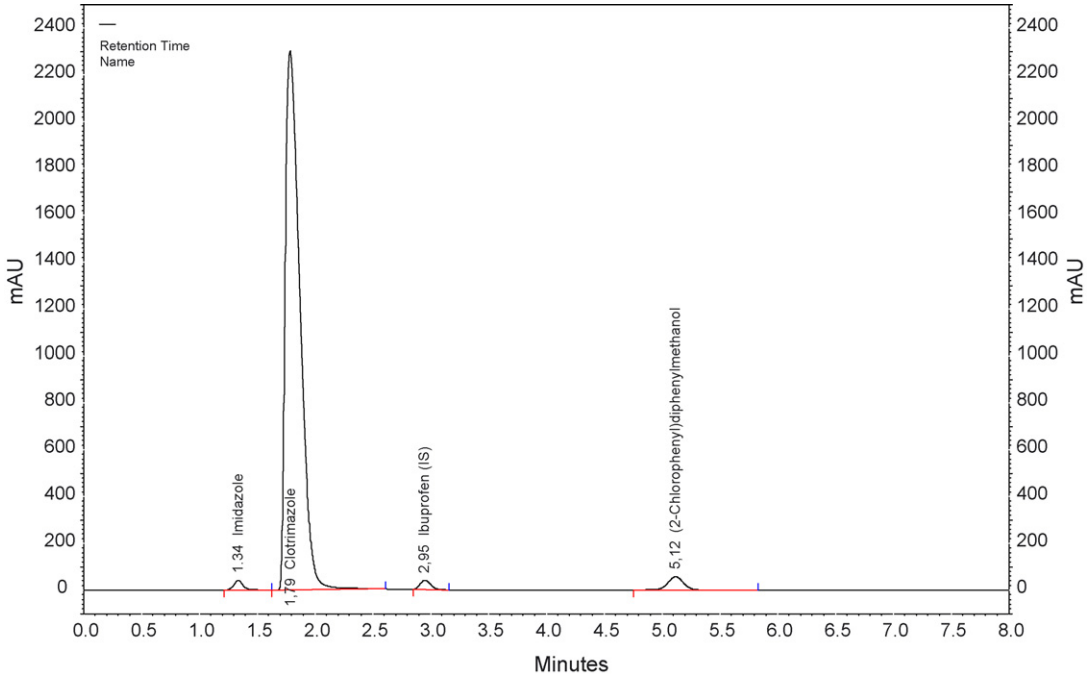

Fig. 2. LC–UV chromatogram (210 nm) obtained from the analysis of standard solutions using the mobile phase acetonitrile and water (65:35, v/v), pH* 2.7.

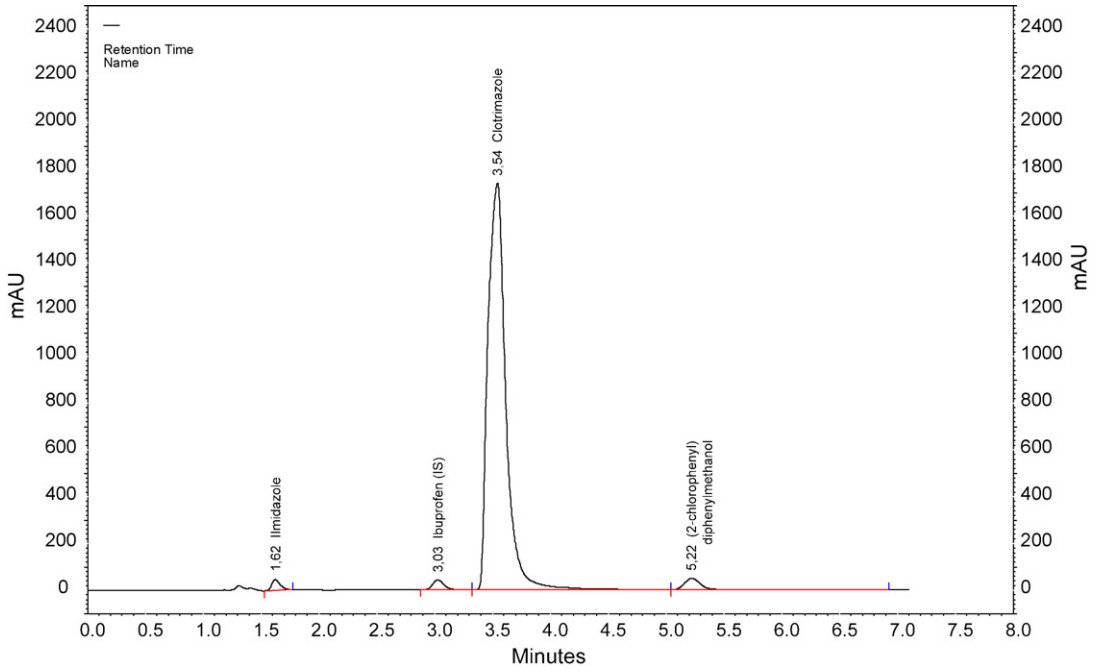

Fig. 3. LC–UV chromatogram (210 nm) obtained from the analysis of standard solutions using the mobile phase acetonitrile and water (65:35, v/v), pH* 3.5.

obtained using Purospher LichroCARD RP-18e column (the analysis time was about 14 min) and Zorbax SB-Phenyl column (about 6 min), the later was finally chosen for validation because all tested compounds were sufficiently separated in short analysis time (Fig. 2).

Another problem erased with placebo interference because the retention time of IM was very short. The pH* of mobile phase used was therefore adjusted to pH* 3.5 when ibuprofen was better ionized and CLO and IM were worse ionized; therefore the peaks of CLO and IM changed their positions on chromatogram and the retention times of peaks of IM and CDM were enlarged (Fig. 3). With increasing the pH* to 3.8 CLO was eluted lately, CDM and CLO were not completely separated and moreover peak shapes were not acceptable. Therefore, the pH* of mobile phase 3.5 was finally chosen.

3.2. Internal standard

The method using internal standard was used for the purposes of this study. Ibuprofen, flurbiprofen, ketoprofen, terbinafin and hexachlorofen were tested. The retention time of hexachlorofen was about 19 min, thereby the analysis was too long; the peaks of flurbiprofen, ketoprofen and terbinafin were not completely separated from the peak of CLO. Ibuprofen was successfully separated from other compounds in solution, having the retention time about 2.9 min in between IM and CLO; therefore, ibuprofen (IBU, Fig. 4) has been used as internal standard.

3.3. Final conditions

Zorbax SB-Phenyl column (75 mm × 4.6 mm, 3.5 μm), mobile phase composed of acetonitrile and water in ratio 65:35 (v/v) and pH* 3.5 (adjusted with 85% phosphoric acid) at flow rate 0.5 ml min^{-1} were finally used for the analysis. IBU was used as the internal standard, the sample volume was 5 μl, the final wavelength for detection was chosen at 210 nm at ambient temperature. The resolution for IM and the internal standard IBU was 6.09, for CLO and CDM 3.68, respectively (shown in Table 3 validation results). The analysis time at those conditions was 6 min.

3.4. Method validation

Recommended validation characteristics including method precision (%R.S.D.), method accuracy (% of recovery, %R.S.D.) linear range (correlation coefficient) and method selectivity using placebo of pharmaceutical formulation were measured. LOD and LOQ were provided for degradation products CDM and IM by means of signal-to-noise ratio method.

The short-term stability of the compounds of interest was tested. Standard solutions were kept at ambient temperature

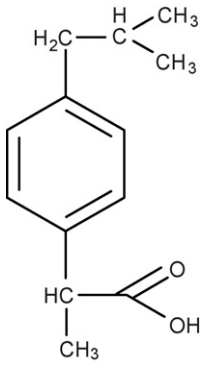

Fig. 4. Internal standard ibuprofen.

Table 1
Short-term stability study of tested compounds

Time of storage (h)	Concentration changes during storage (%)					
	Clotrimazole		(2-Chlorophenyl)diphenylmethanol		Imidazole	
	25 °C	4 °C	25 °C	4 °C	25 °C	4 °C
0	100.00	100.00	100.00	100.00	100.00	100.00
24	+0.55	+0.53	+1.54	+1.36	+0.33	+0.60
48	+0.40	+0.83	−0.07	+0.84	+0.36	+0.65
72	+0.55	+0.68	−0.18	−0.29	+0.33	+0.69

Table 2
The influence of changes in mobile-phase composition (method robustness)

Mobile-phase composition (pH* 3.5)	Clotrimazole		(2-Chlorophenyl)diphenylmethanol		Imidazole	
	t_R	A	t_R	A	t_R	A
ACN:H_2O (75:25, v/v)	4.22	106.27	3.24	100.29	1.98	144.48
ACN:H_2O (70:30, v/v)	–	–	–	–	1.86	107.87
ACN:H_2O (65:35, v/v)	3.45	100.00	4.95	100.00	1.72	100.00
ACN:H_2O (60:40, v/v)	4.04	100.93	6.30	104.32	1.72	102.59
ACN:H_2O (55:45, v/v)	–	–	9.35	96.95	1.59	100.25

ACN: acetonitrile; t_R: retention time; A: peak area (%).

(25 °C) and in refrigerator (4 °C). Changes in content of CDM, higher than 1%, were observed during the storage at ambient and at lowered temperatures even after 24 h (Table 1). The same changes were not observed during storage of all other compounds showing peak area changes up to 1%. This indicates that stock and standard solutions of CDM should be prepared freshly and solutions of CLO and IM could be stored at 4 °C or at 25 °C for 72 h.

Influences of changes in mobile-phase composition (±10%) were studied to determine robustness of the method. Peak area and retention time changes were observed. Results are clearly seen in Table 2. Relative peak area related to the peak area for optimal mobile phase composition ranged from 100.93% to 106.27% for CLO, from 100.29% to 104.32% for CDM and from 100.25% to 144.48% for IM. Mobile phase with the acetonitrile–water ratio 75:25 (v/v) was unsuitable because of high value of peak area for IM. Mobile phase prepared in the ratio 70:30 (v/v) did not allow complete separation of the peaks of CDM and CLO, in the ratio 55:45 (v/v) peaks of CLO and the internal standard IBU were not completely separated. In other experiments complete separation of CLO and degradation products was achieved but the composition of the mobile phase affected the total time of analysis. With the ration of MF ACN: H_2O (75:25, v/v) the change of sequence of CLO and

Table 3
Method validation results of individual compounds

Parameter	Clotrimazole	(2-Chlorophenyl)diphenylmethanol	Imidazole	Limits
SST				
Theoretical plates[a]	1046	5641	1535	$N > 900$
Asymmetry[a]	1.14	1.05	1.03	$T < 2$
Resolution[a]	2.34	3.68	2.14	$R_{ij} > 1.5$
Repeatability-t_r[b]	0.04	0.33	0.47	R.S.D. < 1%
Repeatability-A[b]	0.05	0.29	0.20	R.S.D. < 1%
Validation				
Precision[c] (%R.S.D.)	0.59	0.28	0.47	R.S.D. < 5%
Linearity (correlation coefficient)	0.999991[d]	0.99968[e]	0.999945[e]	$R > 0.9990$
Accuracy[c] (%R.S.D.)	1.13	0.28	0.48	R.S.D. < 5%
Accuracy[c] (%recovery)	99.12	100.61	103.85	$X = 100 \pm 5\%$
Selectivity	No interference	No interference	No interference	–
LOD (mg ml^{-1})	–	8.60×10^{-4}	1.19×10^{-3}	–
LOQ (mg ml^{-1})	–	2.86×10^{-3}	3.97×10^{-3}	–

[a] Made in three replicates.
[b] Made in six replicates.
[c] Six samples injected three times each.
[d] At 50, 75, 100, 125, 150% levels, three replicates.
[e] At 0.1–1.0% range of active substance concentration.

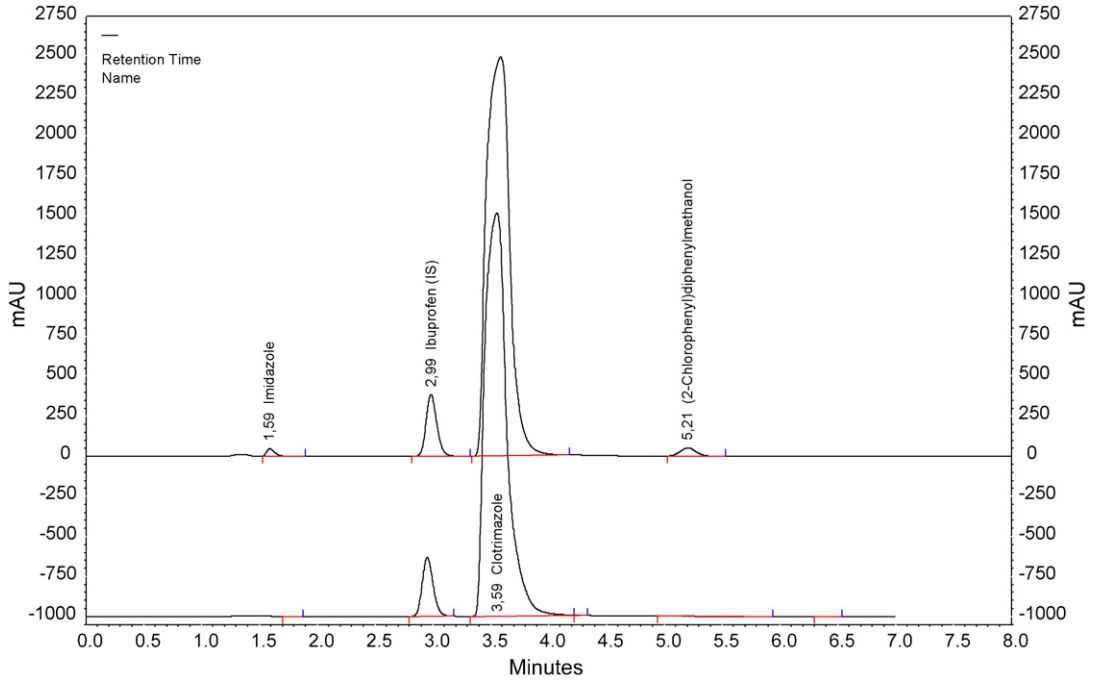

Fig. 5. LC–UV chromatogram (210 nm) obtained from the analysis of compounds in pharmaceutical formulation Clotrimazole spray 1% after 3 months stability test; upper chromatogram: analysis of compounds in standard solution.

CDM peaks happened and thus alteration of retention time values of both peaks were found. Small reduction of retention time of Imidazole with reduction of ACN volume in MF was not so strong with respect to its acido-basic features and very low retention time values (near to dead volume). In view of these findings application of mobile phase of pH 3.5* with the composition acetonitrile–water 65:35 (v/v) was recommended and strong affect of pH value of the mobile phase on positions and shapes of peaks was proved. The method is robust only for change of MF composition ±3%, where significant changes of peak areas and retention times of individual peaks were not found.

All validation results are summarized in Table 3, showing that they are in agreement with the expected values. Limits were mentioned in the Czech Pharmacopoeia (CL 2005 – Resolution) and some of them were cited from Guidelines of ICH [22].

3.5. Pharmaceutical application

The chromatogram in Fig. 5 was obtained using the developed HPLC method for analysis of a real sample (Clotrimazole spray 1%) after a long-term stability test (stored for 3 months in original packaging at 25 ± 2 °C and relative humidity 60 ± 5%). Although the absence of IM and CDM in the sample was expected and proved, both degradation products would be clearly separated from other compounds present in the sample. The average determined amount of CLO in Clotrimazole spray 1% was 101.2 ± 0.6% of the declared amount.

4. Conclusion

A novel simple and quick isocratic HPLC method for determination of clotrimazole and its two degradation products on a 3.5 μm Zorbax® SB-Phenyl column (75 mm × 4.6 mm i.d.) using ibuprofen as an internal standard was described. The time of analysis was less than 6 min. The method has been completely validated, the results obtained were precise and accurate and limits of detection of degradation products were sufficiently low.

The Zorbax® SB-Phenyl column was found to be ideal for a quick separation of compounds with different acido-basic properties, which usually cause problems and complications in HPLC separation.

The method can be used for routine analysis of the tested compounds (active component clotrimazole and two degradation products imidazole and (2-chlorophenyl)diphenylmethanol using ibuprofen as an internal standard) after long-term stability tests in spray formulation Clotrimazole spray 1% containing active compound clotrimazole and degradation products in the quality control laboratory.

Acknowledgement

The authors gratefully acknowledge financial support by the Ministry of Education of the Czech Republic—MSM 0021620822.

References

[1] Micro Version AISLP, v. 2006.3.
[2] Czech Pharmacopoeia, Grada Publishing, Prague, Czech Republic, 2005, p. 1331.
[3] C. Valenta, A. Lecer, P. Spiegl, Pharmazie 47 (1992) 641.
[4] J.C. Hoogerheide, S.H. Strusiak, C.R. Taddei, E.R. Townley, B.E. Wyka, J. Assoc. Off. Anal. Chem. 64 (1981) 864.
[5] D.J. Zegarelli, Otolaryngol. Clin. North Am. 26 (1993) 1069.

[6] OSPAR Commission, OSPAR background dokument on clotrimazole, 2005, www.ospar.org.
[7] G. Indrayanto, L. Aditama, W. Tanudjaja, S. Widjaja, J. Planar Chromatogr. Mod. TLC 11 (1998) 201.
[8] P.Y. Khashaba, S.R. El-Shabouri, K.M. Emara, A.M. Mohamed, J. Pharm. Biomed. Anal. 22 (2000) 363.
[9] H.K. Li, G.Z. Zhao, Y.Q. Zhao, Z. Li, Chin. J. Anal. Chem. 30 (2002) 334.
[10] F.C. Pereira, N.R. Stradiotto, M.V.B. Zanoni, J. Braz. Chem. Soc. 12 (2001) 202.
[11] F.C. Pereira, M.V.B. Zanoni, C.C.I. Guaratini, A.G. Fogg, J. Pharm. Biomed. Anal. 27 (2002) 201.
[12] F. Wienen, S. Laug, K. Baumann, A. Schwab, S. Just, U. Holzgrabe, J. Pharm. Biomed. Anal. 30 (2003) 1879.
[13] A. Arranz, C. Echerarria, J.M. Moreda, A. Cid, J.F. Arranz, J. Chromatogr. A 871 (2000) 399.
[14] R. Hamoudová, M. Pospíšilová, A. Kavalírová, P. Solich, J. Šícha, J. Pharm. Biomed. Anal. 40 (2006) 215.
[15] B. del-Fabro, N. Kacic, M. Prosek, J. Planar Chromatogr. Mod. TLC 10 (1997) 178.
[16] E.M. Abdel-Moety, F.I. Khattab, K.M. Kelani, A.M. AbouAl-Alamein, Farmaco 57 (2002) 931.
[17] J. Zhu, C. Coscolluella, J. Chromatogr. B: Biomed. Appl. 741 (2000) 55.
[18] M. Lin, N. Wu, J. Pharm. Biomed. Anal. 19 (1999) 945.
[19] N. Rifai, M. Sakamoto, T. Law, O. Platt, M. Mikati, C.C. Armsby, C. Brugnara, Clin. Chem. 41 (3) (1995) 387.
[20] United States Pharmacopoeia, vol. 29, The United States Pharmacopoeial Convention Inc., Rockville, MD, 2006.
[21] P. Solich, R. Hájková, M. Pospíšilová, J. Šícha, Chromatogr. Suppl. 56 (2002) 181.
[22] International Conference on Harmonization (ICH), Q2(R1): validation of analytical procedures: text and methodology, http://www.ich.org/LOB/media/MEDIA41-10/2006.
[23] Agilent Zorbax Column Selection Guide for HPLC, Agilent Technologies, 2004.
[24] ChromBook 06/07, Chromatography at Merck—experience drives innovation, 2006.
[25] Chromatography—Product for Analysis and Purification, Supelco, Sigma–Aldrich, 2005.

Available online at www.sciencedirect.com
ScienceDirect
Talanta 73 (2007) 583–588
Talanta
www.elsevier.com/locate/talanta

Short communication

Carbon response characteristics of a micro-flame ionization detector

Taylor C. Hayward, Kevin B. Thurbide *

Department of Chemistry, University of Calgary, 2500 University Drive, NW, Calgary, Alberta T2N 1N4, Canada

Received 7 March 2007; received in revised form 4 April 2007; accepted 4 April 2007
Available online 8 April 2007

Abstract

The carbon response characteristics of a recently noted micro-flame ionization detector (μFID) mode are examined in detail. The μFID supports an extremely small (30 nL) "upside-down" flame that is generated from a low counter-current flow of oxygen immersed in hydrogen. Ionization measurements made in the μFID are directly compared to those obtained from a conventional FID. In terms of reproducibility of response and relative sensitivity towards different types of hydrocarbons, the μFID and a conventional FID produce no major differences with respect to either of these characteristics for a variety of compounds examined. Of note, for replicate measurements made in each detector, the average %R.S.D. of response typically differs by less than 2% between the two devices, while the average normalized sensitivity differs by less than 4%. In contrast to this, regarding absolute sensitivity, the analyte signal from the conventional air-rich FID is found to be three times larger than that of the hydrogen-rich μFID mode explored here. This discrepancy is ascribed directly to the difference in flame stoichiometry between the two detectors.

Keywords: Micro-flame detection; Carbon response; Flame ionization detector; Counter-current flame

1. Introduction

An area of increasing interest in gas chromatography (GC) is instrument miniaturization, leading to portable field GC units and separations performed on a micro-analytical chip [1–5]. Subsequently, the development of sensitive detectors compatible with these devices is also of importance. To date, several such detectors have been reported based on a variety of principles [6–14]. These include diverse methods of surface acoustic wave transmission [5,6], plasma based optical emission [7–11], thermal conductivity [12], and ion mobility [13,14]. However, even though conventional GC applications very often employ informative flame-based sensors such as the flame ionization detector (FID) or the flame photometric detector (FPD), their adaptation into a micro-analytical GC format has been relatively limited [15–20].

Earlier, we reported a novel micro-FPD (μFPD) that operates an extremely minute flame using relatively small gas flows [21]. As part of that broad investigation, we briefly noted that a useful micro-FID (μFID) response can also be simultaneously derived from the same flame. The device is based upon a very small (30 nL) and very stable flame that is supported by modest opposing flows of hydrogen and oxygen [21]. In the detector design, hydrogen and column effluent are directed upward against a downward counter flow of oxygen delivered from a stainless steel capillary, on the end of which the tiny flame is situated. Ionization response is then obtained by placing a potential difference across the stainless steel capillary and a nearby metal sleeve surrounding the column outlet. The few results obtained from the preliminary work indicated that the μFID produces a very reasonable response linearity and detection limit toward carbon that appears to be within about a factor of 10 to that reported for a conventional FID. However, the primary focus of that study was exploring photometric response in the micro-counter-current flame. Therefore, the μFID response was only very marginally probed and a more comprehensive investigation of carbon response characteristics in the detector was not undertaken. Such an investigation is important since it would be very interesting to know how carbon response in the μFID and a conventional FID directly compare.

For example, the conventional FID is operated air-rich and derives carbon response from a relatively large diffusion flame that is often supported by several hundred milliliters per minute of air. In contrast, the favorable μFID response reported earlier was obtained from a very tiny flame, supported by comparatively smaller gas flows. Further, the μFID flame is unconventional

* Corresponding author. Tel.: +1 403 220 5370; fax: +1 403 289 9488.
E-mail address: thurbide@ucalgary.ca (K.B. Thurbide).

0039-9140/$ – see front matter © 2007 Elsevier B.V. All rights reserved.
doi:10.1016/j.talanta.2007.04.005

not only in its size but also in its counter-current structure of opposing fuel and oxidant flows. As well, in order to facilitate the orthogonal photometric signal production, it operates hydrogen-rich. Therefore, since only two simple test analytes were briefly surveyed earlier, it would be very beneficial to explore a much wider range of hydrocarbon solutes in the μFID and directly compare the response characteristics observed to those obtained from a conventional FID. Such information would be useful in ascertaining to what extent the hydrogen-rich stoichiometry of the micro-counter-current flame is capable of providing a response that is similar in quantity and quality to a conventional FID flame. These efforts would expand the knowledge of the micro-counter-current flame device and assist in its development as a potentially useful analytical tool.

This paper explores carbon response in the μFID and compares it to that of a conventional FID. Specifically, the reproducibility of response was measured in both devices for a wide range of standard compounds varying in structure and functional group composition. Related data was also acquired regarding the relative sensitivity of each detector toward the different hydrocarbons examined. Finally, measurements of absolute sensitivity toward carbon were also made in each detector. Results of these comparisons between the μFID and a conventional FID are presented and discussed.

2. Experimental

Fig. 1 presents a schematic illustration of the μFID arrangement, which is the same as that described earlier [21]. Briefly, the detector consists of a 1.5 cm length of stainless steel tubing (1.5875 mm o.d.) that is centered upon and welded to a tube stub (6.35 mm o.d.), which is secured to the gas port of the FID detector base on a Shimadzu model GC-8A instrument (Shimadzu, Kyoto, Japan). A Vespel ferrule is used for this connection in order to keep the tube stub electrically insulated from the GC (*Note*: to ensure that thermal expansion/contraction of the Vespel material did not promote any gas leaks in this connection, gas flows through this ferrule were monitored in repeated heating/cooling cycles of the detector block and no leakage was observed). The capillary separation column is inserted up to approximately 1 mm before the end of this stainless steel "sleeve", which also carries hydrogen through it. Opposing the hydrogen and column effluent flow streaming from the metal sleeve is a counter flow of oxygen delivered by a stainless steel capillary (0.4572 mm o.d. × 0.254 mm i.d.; Small Parts, Inc., Miami Lakes, FL, USA), which supports the "upside-down" flame. The existing electrical leads from the original FID are connected such that the metal sleeve is the collector and the stainless steel capillary burner carrying the flame is polarized. Typically, the burner and the metal sleeve surrounding the column are separated by approximately 1–2 mm. This flame arrangement is enclosed in a quartz sleeve (6 mm o.d. × 2 mm i.d.) extending upward from the tube stub. The gas flow rates used for the μFID configuration (i.e. 7 mL/min of oxygen and 40 mL/min of hydrogen) are the same as those used in the earlier study [21].

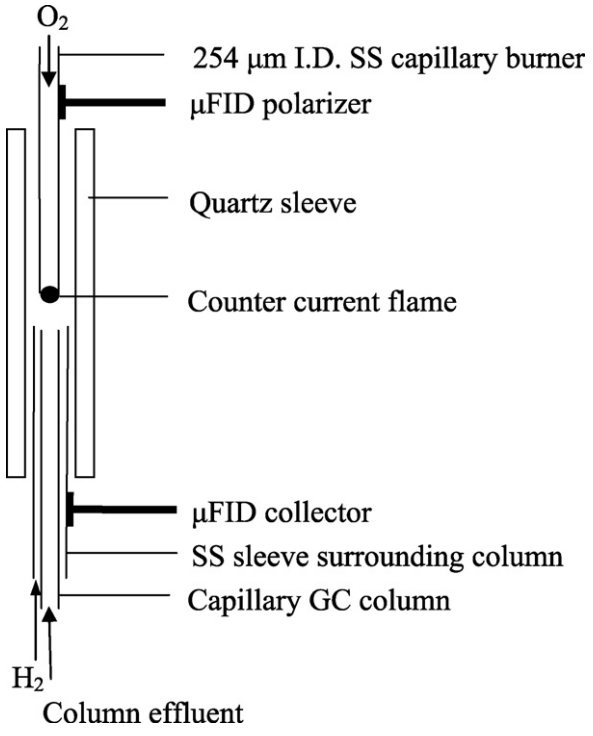

Fig. 1. Schematic illustration of the μFID counter-current flame arrangement.

Separations are performed with an EC-5 [(5%-phenyl)–95% methylpolysiloxane] megabore column (30 m × 0.53 mm i.d.; 1.00 μm thick; Alltech, Deerfield, IL, USA) using high purity helium (Praxair, Calgary, Canada) at approximately 5 mL/min as the carrier gas. Medical-grade oxygen (Praxair) and high purity hydrogen (Praxair) are used to support the μFID. The original Shimadzu GC-FID system is used in direct comparison experiments and employs breathing-grade air (Praxair) and high purity hydrogen as the flame gases at optimized flow rates of 300 and 35 mL/min, respectively.

Various test samples (each introduced as 1 μL injections) are used in comparative experiments between the two detectors. The first is a qualitative *n*-alkane (C_6–C_{24}) mixture that was prepared by Dow Chemical (Fort Saskatchewan, Canada) and analyzed as received. The components of this sample are listed in Table 1. The GC temperature program used to separate the mixture is 80 °C initially for 1 min, then up to 280 °C at 20 °C/min. Since information regarding the mass of the individual solutes in this sample was not available, it could not be used for quantitative studies and the other samples were utilized instead for this purpose. The next is a sample mixture of hydrocarbons (shown in Table 2), chosen to contribute various organic structures and functional groups for testing, that was prepared in the lab. This is referred to in the text as the "organic compound mixture" and it contains 401 ng/μL of decane (99%; BDH Lab Supplies, Toronto, Canada), 317 ng/μL of heptanol (98%; Aldrich, Oakville, Canada), 338 ng/μL of phenol (lab grade; Anachemia, Vancouver, Canada), 492 ng/μL of octanol (99.5%; Aldrich), 346 ng/μL of 4-methylbenzylamine (97%; Aldrich), 311 ng/μL of naphthalene (Fisher Scientific Company, Fair Lawn, NJ, USA), and 317 ng/μL of ethyl caprate (99%, Aldrich), which are dissolved in hexane (analytical reagent;

Table 1
Figures of merit for an *n*-alkane mixture[a] measured in a conventional FID and the μFID

Solute	FID		μFID	
	Average peak area	R.S.D.[b] (%)	Average peak area	R.S.D.[b] (%)
C_6	930.5190	7.1	309.7770	7.0
C_8	203.1847	2.0	64.3484	8.3
C_{10}	363.7404	2.7	115.3707	5.5
C_{12}	406.4498	2.4	131.6146	6.1
C_{14}	699.5386	3.3	188.4946	6.0
C_{16}	672.4399	3.0	192.4956	6.8
C_{18}	704.6691	2.6	195.3614	5.9
C_{20}	671.2977	3.4	194.5237	4.0
C_{22}	533.1240	4.8	171.9945	5.6
C_{24}	246.1164	6.0	107.3913	5.7

[a] Note, this is only a qualitative sample and quantitative information about its contents was unavailable. For quantitative data regarding detector sensitivity see Tables 2 and 3.
[b] $n = 10$.

Table 2
Figures of merit for an organic compound mixture measured in a conventional FID and the μFID

Solute	Injected amount (ng)	FID				μFID			
		Average peak area	R.S.D.[a] (%)	Sensitivity (area/gC)	Normalized sensitivity	Average peak area	R.S.D.[a] (%)	Sensitivity (area/gC)	Normalized sensitivity
Decane	401	73.6412	1.7	217,564,950	0.74	25.627	2.2	75,712,196	0.72
Heptanol	317	67.1207	4.8	292,666,155	1.00	24.0653	2.3	104,931,906	1.00
Phenol	338	124.618	1.6	481,525,024	1.65	39.9685	3.9	154,438,504	1.47
Octanol	492	121.530	1.7	334,808,272	1.14	41.3534	4.7	113,925,995	1.09
4-Methyl-benzylamine	346	56.7182	7.7	206,752,257	0.71	21.8384	5.0	79,606,477	0.76
Naphthalene	311	110.534	4.0	379,306,004	1.30	30.8406	3.5	105,831,914	1.01
Ethyl caprate	317	68.3057	9.2	299,501,010	1.02	19.4538	8.7	85,299,426	0.81

[a] $n = 10$.

BDH Lab Supplies). The GC temperature program used to separate the mixture is 80 °C initially for 6 min, then up to 240 °C at 20 °C/min. The last is a BTEX sample (shown in Table 3) that was prepared by Dow Chemical (Fort Saskatchewan, Canada) and analyzed as received. It is composed of benzene (185 ng/μL), toluene (186 ng/μL), ethyl benzene (196 ng/μL), and xylenes (396 ng/μL *meta*/*para* combined, and 200 ng/μL of *ortho*). This sample is separated isothermally at 50 °C. Further data pertaining to these standards can be found in Tables 1–3. Any other variations and details are described in the text.

3. Results and discussion

Initial experiments were focused on directly comparing the carbon response of the μFID to that of a conventional FID for a wide range of compounds. This was achieved by analyzing each of three different test mixtures 10 times in both detectors and recording the resulting peak areas from each trial. Data was then tabulated for each analyte from separations using both the μFID and the conventional FID, and it is presented in Tables 1–3 for discussion. It should be noted that for the BTEX data given in Table 3, *meta*- and *para*-xylene coeluted under the conditions

Table 3
Figures of merit for a BTEX mixture measured in a conventional FID and the μFID

Solute	Injected amount (ng)	FID				μFID			
		Average peak area	R.S.D.[a] (%)	Sensitivity (area/gC)	Normalized sensitivity	Average peak Area	R.S.D.[a] (%)	Sensitivity (area/gC)	Normalized sensitivity
Benzene	185	61.2137	1.1	358,680,554	0.99	21.9435	2.1	128,577,641	1.03
Toluene	186	63.3554	1.3	372,916,604	1.03	25.8529	2.7	152,172,737	1.22
Ethyl benzene	196	62.1651	1.6	349,575,215	0.97	21.3463	1.2	120,037,407	0.96
meta/*para*-Xylene[b]	396	129.4860	1.3	361,587,423	1.00	44.8344	1.4	125,199,233	1.00
ortho-Xylene	200	70.4255	2.8	388,125,443	1.07	24.3059	1.6	133,953,168	1.07

[a] $n = 10$.
[b] Compounds coeluted; therefore injected amounts were summed.

employed and therefore their injected amounts were summed for use in subsequent calculations.

3.1. Reproducibility

The first aspect investigated was reproducibility of response. As can be seen overall in Tables 1–3, no major differences appear between the two detectors in this regard. For instance, the %R.S.D. values for response across all three mixtures range from 1.1 to 9.2% in the conventional FID and from 1.2 to 8.7% in the μFID. Further, in many of these instances, a larger %R.S.D. value noted for one detector is usually reflected by a similar change in the other. For example, in Table 2 both detectors produce relatively larger %R.S.D. values near 9% for ethyl caprate. Overall, the average %R.S.D. of response for all of the compounds measured was 3.5% in the conventional FID and 4.5% in the μFID. Therefore, while some variability in %R.S.D. does exist from compound to compound, there are no apparent general response trends that greatly differentiate one detector from the other on this basis. One minor exception to this, however, appears for some of the solutes in the *n*-alkane sample of Table 1.

For instance, the averages of the %R.S.D. values obtained for the conventional FID and the μFID differ by less than 0.06% for the compounds listed in Table 2 and less than 0.2% for those listed in Table 3. In contrast to this, the averages of the %R.S.D. values given in Table 1 differ by just over 2% between the two detectors in this trial. Numerically, this stems from the %R.S.D. values being consistently lower by a factor of about 2.5 in the conventional FID for *n*-alkanes between C_8 and C_{18}. The actual reason for this discrepancy, though, is currently unclear and it is not certain if it perhaps resulted from some artifact of the μFID experimental setup or if it is indeed related to the μFID carbon response toward these specific compounds. However, the latter is difficult to rationalize given that the alkane compounds analyzed in Table 1 have the same core chemical structure and should therefore provide similar response characteristics in the μFID flame. This is additionally supported by the fact that the %R.S.D. of response values for the lowest (i.e. C_6) and the higher (i.e. C_{20}–C_{24}) members of this series agree very well between the two detectors.

3.2. Relative and absolute sensitivity

Another aspect of detector response worthy of investigation was the relative detector sensitivity toward various different organic compounds. This was explored using the BTEX and organic compound mixtures since the *n*-alkane blend was only a qualitative sample and complete quantitative information on the composition of its individual components was not available. Nonetheless, to ensure that *n*-alkanes were still represented in this regard, decane was included in the organic compound mixture (Table 2) for this purpose. Using the data in Tables 2 and 3, the sensitivity was calculated as follows. The average peak area response (based on 10 replicate injections of the same analyte mass) per gram of carbon was calculated for each of the compounds analyzed in the conventional FID and the μFID. This sensitivity, reported as response per gram of carbon, was then normalized using the median value as unity, as shown in Tables 2 and 3. As seen, the μFID data is very similar to that obtained in the conventional FID. Closer inspection of the data reveals that the average normalized sensitivity value, calculated for each detector from all of the compounds measured, differs by less than 4% between the devices. Alternatively, on a compound by compound basis, the individual differences in this parameter had an average value of 0.08. Therefore, despite the dissimilarity in flame structure between the μFID and the conventional FID, their response toward carbon compounds in the above respects is very similar. Fig. 2 demonstrates this with a sample chromatogram of the BTEX separations. As seen, the chromatographic profiles obtained for this sample in the conventional FID (upper plot) and in the μFID (lower plot) are quite comparable. Similar findings were also obtained for the other samples investigated. This is important since the FID is well known and very widely used for its uniform equimolar sensitivity toward carbon compounds of varying composition [22,23].

With regard to absolute detector sensitivity, it should be noted that a good quality commercial FID typically yields a signal of about 15 mC/gC for saturated, non-functionalized hydrocarbons [22]. Earlier preliminary results in the μFID suggested that it produced a value near 5 mC/gC [21]. In the current study, these indications were confirmed when the absolute sensitivity of each detector was measured. For example, under fully optimized conditions, the conventional FID used in these experiments produced a signal of 13 mC/gC, whereas the μFID generated 4.4 mC/gC. Therefore, there appears an approximate three-fold difference in absolute response between the two. This general trend is further supported by the data collected from the broad range of compounds listed in Tables 1–3. Of note, the average difference in peak area measured between the detectors for all of the compounds listed amounts to a factor of 3.06.

3.3. Analytical calibrations

It should be noted that calibrations with the μFID have established that the carbon mass flow minimum detectable limit (MDL) of the device is about 2×10^{-10} gC/s ($S/N_{p-p} = 2$), which is within about an order of magnitude larger than that reported in the literature for a conventional FID [21,22]. In fact, the conventional FID used in these experiments was actually observed to yield a detection limit of about 6×10^{-11} gC/s. In terms of *n*-decane as a test analyte, this translates into a MDL of about 0.37 ng, and a limit of quantitation (LOQ; $S/N_{p-p} = 20$) of about 3.7 ng for the conventional FID. By comparison, the MDL and LOQ for *n*-decane in the μFID were found to be about 1 and 10 ng, respectively. With regard to linear range, the μFID produced a linear response over five orders of magnitude, while the conventional FID response was linear over the entire six orders of magnitude investigated up to milligram quantities of injected analyte.

It is interesting to point out that, also true to the above sensitivity measurements, the detection limit for the conventional FID is found to be about three times lower than that noted for the μFID. However, when measuring baseline characteristics in both the conventional FID and the μFID used in this study, each

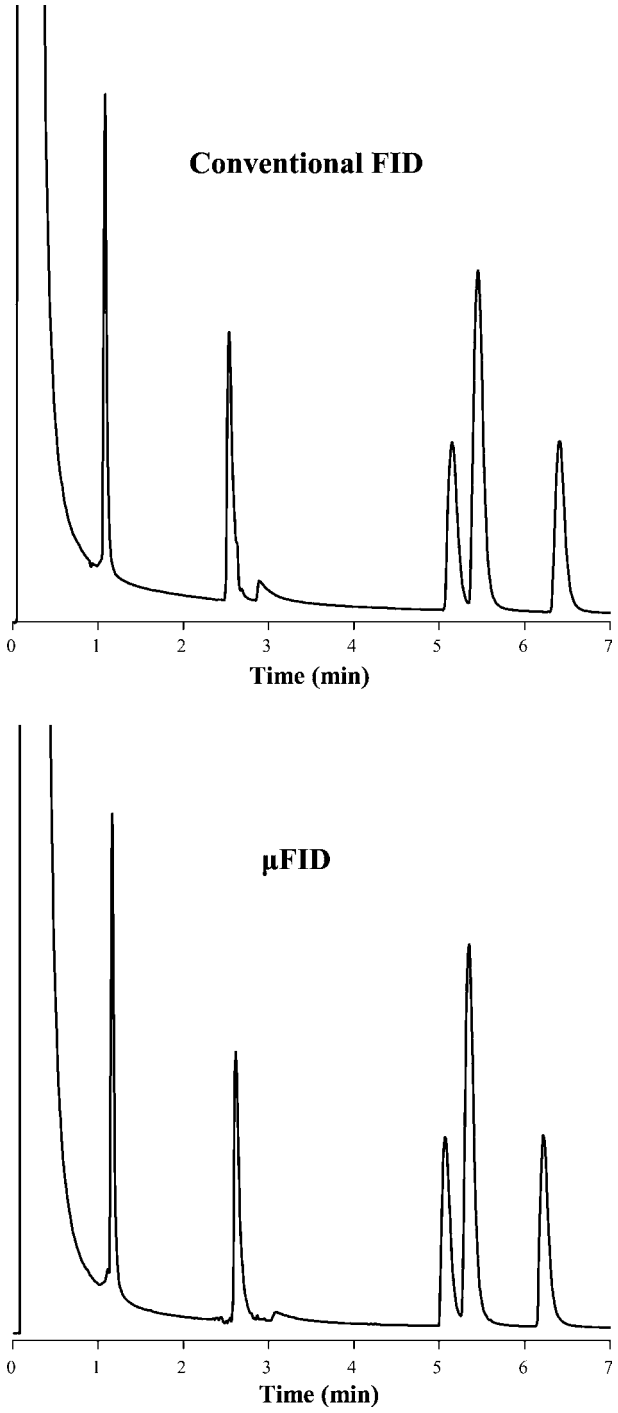

Fig. 2. Sample chromatogram of a 1 μL injection of the BTEX mixture as analyzed in the conventional FID (top) and also the μFID (bottom). Conditions for the separation are outlined in the text. The analyte elution order is benzene, toluene, ethyl benzene, *meta*- and *para*-xylene, and *ortho*-xylene.

was observed to yield similar background currents and peak to peak noise levels in the low picoampere range. Therefore, rather than a sizeable difference in their noise characteristics, it appears that the difference in detection limit between the two devices can indeed be primarily ascribed to the consistent three-fold difference in absolute sensitivity toward carbon that they each, respectively, produce. This being the case, the variation in quantitative signal observed between these detectors very likely stems from the considerable difference in their respective flame stoichiometry.

For instance, under optimized conditions, the conventional FID used here was supported with reagent gas flows that maintained an oxygen:hydrogen ratio of 1.7, which is substantially oxygen-rich with respect to a stoichiometric flame (i.e. a ratio of 0.5). In contrast to this, however, the μFID explored in this study was operated using an oxygen:hydrogen ratio of 0.175, which is quite hydrogen-rich by comparison. As mentioned above, this ratio was established previously to sustain chemiluminescence and good photometric response in the orthogonal μFPD channel [21]. Still, it is quite interesting that the tiny μFID counter-current flame is 10 times less abundant in oxygen, but still maintains respectable sensitivity relative to the larger diffusion flame of a conventional FID.

While it would be interesting to explore oxygen-rich response modes in the micro-counter-current flame, and the potential that they may offer for operating a dedicated μFID with the same sensitivity as a conventional FID, the burner design used in the μFPD has been noted to cause flame instability under such conditions [21]. Thus, more development of this area is required in order to investigate this further. Still, however, in its current form the μFID predominantly serves a very useful secondary function of providing a sensitive simultaneous universal detection mode for the fully optimized selective μFPD sensor. Overall, therefore, the many similar response characteristics observed to date between the μFPD/μFID device modes and their conventional GC analogues indicates that this detector may be useful for incorporation into portable micro-analytical units.

Acknowledgements

The authors are grateful to the Natural Sciences and Engineering Research Council of Canada for a Discovery Grant in support of this work. Special thanks are also extended to Jim Luong and Ronda Gras at Dow Chemical (Fort Saskatchewan, Canada) for generously supplying the *n*-alkane and BTEX mixtures.

References

[1] R.R. Reston, D. Iossifidis, P.-A. Auroux, A. Manz, Anal. Chem. 74 (2002) 2623.
[2] E.B. Overton, K.R. Carney, N. Rouques, H.P. Dharmasena, Field Anal. Chem. Technol. 5 (2001) 97.
[3] J.A. Dziuban, J. Mroz, M. Szczyglielska, M. Malachowski, A. Gorecka-Drzazga, R. Walczak, W. Bula, D. Zalewski, L. Nieradko, J. Lysko, J. Koszur, P. Kowalski, Sens. Actuators A 115 (2004) 318.
[4] G. Lambertus, A. Elstro, K. Sesenig, J. Potkay, M. Agah, S. Schearing, K. Wise, F. Dorman, R. Sacks, Anal. Chem. 76 (2004) 2629.
[5] J.J. Whitting, C.-J. Lu, E.T. Zellers, R.D. Sacks, Anal. Chem. 73 (2001) 4668.
[6] M. Rapp, J. Reibel, A. Voigt, M. Balzer, O. Bulow, Sens. Actuators B 65 (2000) 169.
[7] J.C.T. Eijkel, H. Stoeri, A. Manz, Anal. Chem. 71 (1999) 2600.
[8] J.C.T. Eijkel, H. Stoeri, A. Manz, Anal. Chem. 72 (2000) 2547.
[9] R. Guchardi, P.C. Hauser, J. Anal. Atom. Spectrom. 18 (2003) 1056.
[10] O.B. Minayeva, J.A. Hopwood, J. Anal. Atom. Spectrom. 18 (2003) 856.

[11] S. Pedersen-Bjergaard, T. Greibrokk, J. Microcol. Sep. 6 (1994) 11.
[12] G.C. Frye-Mason, R.J. Kottenstette, E.J. Heller, C.M. Matzke, S.A. Casalnuovo, P.R. Lewis, R.P. Manginell, W.K. Schubert, V.M. Hietala, R.J. Shul, in: D.J. Harrison, A. van den Berg (Eds.), Micro Total Analysis Systems'98, Kluwer, Dordrecht, 1998, p. 477.
[13] A.L. Makas, M.L. Troshkov, J. Chromatogr. B 800 (2004) 55.
[14] G.A. Eiceman, E.G. Nazarov, R.A. Miller, E. Krylov, A. Zapata, Analyst 127 (2002) 466.
[15] S. Zimmerman, B. Riepenhusen, J. Muller, in: D.J. Harrison, A. van den Berg (Eds.), Micro Total Analysis Systems'98, Kluwer, Dordrecht, 1998, p. 473.
[16] S. Zimmerman, S. Wischhusen, J. Muller, Sens. Actuators B 63 (2000) 159.
[17] S. Zimmerman, J. Muller, Microsyst. Technol. 6 (2000) 241.
[18] S. Zimmerman, P. Krippner, A. Vogel, J. Muller, Sens. Actuators B 83 (2002) 285.
[19] C. Deng, X. Yang, N. Li, Y. Huang, X. Zhang, J. Chromatogr. Sci. 43 (2005) 355.
[20] G. Frishman, A. Amirav, Field Anal. Chem. Technol. 4 (2000) 170.
[21] K.B. Thurbide, T.C. Hayward, Anal. Chim. Acta 519 (2004) 121.
[22] H.H. Hill, D.G. McMinn (Eds.), Detectors for Capillary Chromatography, Wiley, New York, 1992, p. 7.
[23] T. Holm, J. Chromatogr. A 782 (1997) 81.

Available online at www.sciencedirect.com
ScienceDirect
Talanta 73 (2007) 415–419
Talanta
www.elsevier.com/locate/talanta

Capillary and microchip gel electrophoresis for simultaneous detection of *Salmonella pullorum* and *Salmonella gallinarum* by *rfb*S allele-specific PCR

Seonsook Jeon [a], Seong Kug Eo [b], Yongseong Kim [c], Dong Jin Yoo [d], Seong Ho Kang [a,*]

[a] *Department of Chemistry and Research Institute of Physics and Chemistry (RINPAC), Chonbuk National University, Jeonju 561-756, South Korea*
[b] *College of Veterinary Medicine, Chonbuk National University, Jeonju 561-756, South Korea*
[c] *Division of Natural Science, Kyungnam University, Masan 631-701, South Korea*
[d] *Department of Chemistry, Seonam University, Namwon 590-711, South Korea*

Received 3 February 2007; received in revised form 31 March 2007; accepted 1 April 2007
Available online 8 April 2007

Abstract

We report the use of capillary gel electrophoresis (CGE) based on a *rfb*S allele-specific polymerase chain reaction (PCR) for the analysis and simultaneous detection of *Salmonella pullorum* and *Salmonella gallinarum*, which are the major bacterial pathogens in poultry. *rfb*S allele-specific PCR was used to concurrently amplify two specific 147- and 187-bp DNA fragments for the simultaneous detection of *S. pullorum* and *S. gallinarum* at an annealing temperature of $54 \pm 1\,^{\circ}C$ and an $MgCl_2$ concentration of 2.8–5.6 mM. Under an electric field of 333.3 V/cm and a sieving matrix of 1.0% poly(ethyleneoxide) (M_r 600 000), the amplified PCR products were analyzed within 6 min by CGE separation. This CGE assay could be translated to microchip format using programmed field strength gradients (PFSG). In the microchip gel electrophoresis with PFSG, both of the *Salmonella* analyses were completed within 30 s, without decreasing the resolution efficiency. *rfb*S allele-specific PCR-microchip gel electrophoresis with the PFSG technique might be a new tool for the simultaneous detection of both *S. pullorum* and *S. gallinarum*, due to its ultra-speed and high efficiency.

Keywords: *Salmonella gallinarum*; *Salmonella pullorum*; Allele-specific PCR; Capillary electrophoresis; Microchip electrophoresis

1. Introduction

Salmonella spp. are the major bacterial pathogens in poultry and are responsible for significant economic losses to the poultry industry in many parts of the world. They are also human pathogens and the most common agents found in cases of food poisoning [1–5]. Among these *Salmonella* spp., *Salmonella pullorum* and *Salmonella gallinarum* are the most common causative agents of chicken salmonellosis resulting in high morbidity and mortality [3]. Both *S. gallinarum* and *S. pullorum* are similar from the viewpoint of their antigenic structure, even though they cause distinctly different diseases in chickens [5]. *S. gallinarum*, causes fowl typhoid, which is an acute intestinal disease in young chickens, and *S. pullorum* causes white diarrhea, which is a severe intestinal infection of chicks. The development of a rapid and reliable method for the simultaneous detection of both *Salmonella* species with a simple sample preparation is essential.

Conventionally, culture-based methods have been used to identify *Salmonella*, but they are labor-intensive and time-consuming, requiring 3–6 days to yield results [6–8]. The polymerase chain reaction (PCR) can be a particularly useful tool for the rapid and definitive detection of avian *Salmonella* serotypes. The PCR-restriction fragment length polymorphism (PCR-RFLP) assay has mainly been used to make a differential diagnosis of *S. pullorum* and *S. gallinarum* [3,9,10]. The allele-specific PCR method based on the amplification of the *rfb*S gene for specific detection of serotypes belonging to *Salmonella*

* Corresponding author. Tel.: +82 63 270 3421; fax: +82 63 270 3408.
E-mail address: shkang@chonbuk.ac.kr (S.H. Kang).

0039-9140/$ – see front matter © 2007 Elsevier B.V. All rights reserved.
doi:10.1016/j.talanta.2007.04.002

serogroup D was also developed [11,12]. Among the PCR methods, the allele-specific amplification assay was found to be precise, reproducible and less time consuming than the standard bacteriological methods used to detect *S. gallinarum*. This method could be an effective molecular tool for the rapid definitive diagnosis of fowl typhoid in endemic areas where fowl typhoid infection exists [12]. Amplified PCR products have been traditionally detected by electrophoresis on agarose gels followed by the ethidium bromide staining of DNA. While the traditional agarose gel-based methods for the analysis of both *Salmonella* are simple, they are low-sensitivity, resolution-weak and time-consuming. Capillary electrophoresis (CE), which is an alternative method for biomedical and clinical applications, offers several unique advantages over the traditional slab gel electrophoresis, such as high efficiency, speed, resolution and small reagent/sample consumption [13–15]. Although several methods of CE based on PCR analyses to detect *Salmonella* have been developed [2,16–19], these methods are not suitable for differentiating between *S. pullorum* and *S. gallinarum*. Currently, microchip electrophoresis (ME) is establishing itself as an alternative method for performing CE, because the main techniques of microchip electrophoresis originated from CE [20–22].

This report describes the optimization of *rfb*S allele-specific PCR condition to coamplify two specific DNA fragments (147-bp of *S. pullorum* and 187-bp DNA of *S. gallinarum*) under the same PCR condition and the simultaneous detection of both *Salmonella* using the capillary gel electrophoresis (CGE) method in a sieving gel matrix. The potential provided by translating this CGE method to microchip format using programmed field strength gradients (PFSG) was also demonstrated. Microchip electrophoresis with PFSG is ideally suited to the ultra-fast simultaneous analysis of both *S. pullorum* and *S. gallinarum* within several seconds in clinical or research-based genetics laboratories.

2. Experimental

2.1. Materials and reagents

Ten times Mg free buffer, 1.4 mM $MgCl_2$ and 2.5 U Taq DNA polymerase were purchased from Promega (Madison, WI, USA). The 1× TE buffer solution (pH 8.0 with Trisma-base) was made with 50 mM Tris–HCl and EDTA (Sigma, USA) in deionized water. The dynamic coating matrix of the microchip was prepared by dissolving 1.0% (w/v) of polyvinylpyrrolidone (PVP, M_r 1 000 000) (Polyscience, Warrington, England) in the 1× TE buffer containing 0.5 μg/mL EtBr (Sigma, St. Louis, MO, USA). The mixture was shaken for 2 min and left to stand for 2 h to remove any bubbles. The sieving matrix was prepared by dissolving 1.0% (w/v) of poly(ethyleneoxide) (PEO, M_r 600 000) (Sigma, St. Louis, MO, USA) in the 1× TE buffer together with 0.5 μg/mL EtBr. The solution was stirred slowly overnight. A 100-bp DNA ladder (72 ng/μL) (Genepia, Korea) was used in the slab gel electrophoresis, and a 100-bp ladder premix personalizer (Seegene, Korea) was used in the CE and microchip electrophoresis after mixing the 100-, 200- and 300-bp DNA fragments obtained from PCR amplification.

Table 1
Comparisons of the peak areas (PA)[a] of SG and SP in CGE as a function of annealing temperature at the *rfb*S allele-specific PCR conditions ($n = 5$)

Temperature (°C)	SG	SP
52	28.65 (±8.51)	117.87 (±6.63)
53	25.67 (±12.27)	164.22 (±12.58)
54	33.41 (±16.45)	138.23 (±18.44)
55	28.32 (±4.81)	129.91 (±8.41)
56	28.52 (±7.07)	131.05 (±10.67)
58	28.41 (±8.51)	127.92 (±12.12)
60	15.18 (±12.27)	99.43 (±12.06)
62	0.36 (±0.62)	79.05 (±8.10)
64	–	59.29 (±8.58)

[a] PA values show the mean (±S.D.) with a relative intensity.

2.2. Allele-specific PCR with clinical samples

The *Salmonella* clinical samples were acquired from the Biosafety Research Institute at Chonbuk National University [12]. The liver, spleen, heart, lung and kidney specimens from representative chickens suspected to have died due to fowl typhoid were collected from four different outbreaks of fowl typhoid in Chungnam and Chonbuk province in Korea. The tissue samples were processed for the isolation of *S. gallinarum* according to the method described elsewhere [12]. Briefly, the tissues were triturated in a sterile mortar and pestle followed by direct plating on to maconkey's agar (MCA, Difco) and brilliant green agar (BGA, Difco). These one-step protocols involved direct plating on to MCA and BGA plates, incubation overnight at 37 °C and the performance of colony PCR on the presumptive *Salmonella* colonies. Subsequently, the presumptive *Salmonella* colonies were used as a template for allele-specific colony PCR. The identification of the clinical isolates of *Salmonella* was also made using previously described biochemical tests [8]. The forward primer (5′-GTA TGG TTA TTA GAC GTT GTT-3′) and reverse primer (5′-TAT TCA CGA ATT GAT ATA TCC-3′) (Genotech, Korea) were used to amplify the 147-bp DNA fragment from *S. pullorum*. The forward primer (5′-GTA TGG TTA TTA GAC GTT GTT-3′) and reverse primer (5′-TAT TCA CGA ATT GAT ATA CTC-3′) (Genotech, Korea) were also used to amplify the 187-bp DNA fragments from *S. gallinarum*. The PCR used for the coamplification of both specific target DNA molecules under the same PCR conditions were performed in a thermal cycler (MJ Research PTC-200, USA) using the following temperature protocol: 5 min incubation at 94 °C; 30 cycles of denaturing at 94 °C for 1 min, annealing at 48–64 °C for 1 min (Table 1), extension at 72 °C for 1 min and then 1 cycle of final extension at 72 °C for 5 min. Each reaction mixture of *S. gallinarum* and *S. pullorum* contained 2 μL template DNA (22.4 ng *S. gallinarum*, 32.1 ng *S. pullorum*) and 23 μL solution as follows: 2.5 mM dNTPs (iNtRon Biotechnology, Korea), 10× Mg free buffer, 0–7.0 mM $MgCl_2$ (Table 2), 2.5 U Taq polymerase, 11.2 pmol forward primer and 12.2 pmol reverse primer for *S. pullorum* (or 19.4 pmol of the forward primer and 19.0 pmol of reverse primer for *S. gallinarum*). The amplification products were analyzed by slab gel electrophoresis, capillary gel electrophoresis and microchip gel electrophoresis.

Table 2
Comparisons of the peak areas (PA)[a] of SG and SP in the CGE as a function of the $MgCl_2$ concentration at the *rfb*S allele-specific PCR conditions ($n = 5$)

$MgCl_2$ (mM)	SG	SP
1.4	–	0.37 (±0.64)
2.8	27.83 (±9.09)	167.85 (±22.83)
4.2	62.82 (±11.18)	272.51 (±38.85)
5.6	51.47 (±4.46)	168.48 (±13.36)
7.0	62.75 (±10.31)	139.39 (±23.19)

[a] PA values show the mean (±S.D.) with a relative intensity.

2.3. Capillary gel electrophoresis

The experimental CGE setup was similar to that described elsewhere [13]. A He–Ne laser ($\lambda_{ex} = 543.5$ nm; Melles Griot 05-LGR-193, USA) was used as the light source in a home-built CE system, which was coupled to a laser-induced fluorescence (LIF) detector. A Spellman 1000R high-voltage power supply (Spellman High Voltage Inc., New York, USA) was used to drive the electrophoresis. A 60-cm total length (30-cm effective length) and 50-μm i.d. bare fused-silica capillary (Polymicro Technologies, Inc., Phoenix, AZ, USA) was used as the separation capillary. The running buffer consisted of 1× TE buffer with 0.5 μg/mL EtBr. The capillary coating matrix and the sieving matrix were made by dissolving 1.0% (w/v) of 1 000 000 M_r PVP and 1.0% (w/v) of 600 000 M_r PEO (Sigma, USA) in the running buffer, respectively. Both the coating material and sieving matrix were hydrodynamically injected at one end of the capillary through a syringe. After the sample was injected electrokinetically at 50 V/cm for 30 s, sample separation was performed in an electric field of 333.3 V/cm. After each run, the capillary was reconditioned before the next analysis by rinsing it successively in water, 0.1 M NaOH, water and the running buffer. The data was recorded as a function of time during CGE, and saved on an IBM-compatible computer (1.70-GHz Pentium IV) at 10 Hz. Data treatment and analysis were performed using an Autochro data system (Young Lin Instrument Co., Anyang, Korea).

2.4. Microchip gel electrophoresis

Microchip gel electrophoresis (MGE) was performed on a DBCE-100 Microchip CE system (Digital Bio Technology Co., Korea) equipped with a diode-pumped solid-state laser (exciting at 532 nm and collecting fluorescence at 605 nm; Power Technology, Inc., Little Rock, AZ, USA) and a high-voltage device (DBHV-100, Digital Bio Technology Co., Korea). The injection design of the glass microchip was a double-T channel with a 100-μm offset. The chip channel was 50-μm wide and 50-μm deep. The reservoirs were 2.0 mm in diameter and 1-mm deep. The injection channel length was 8.0 mm. The separation channel was 66.5-mm long and detection was performed at 30 mm away from the injection reservoir. The MGE running buffer was a 1× TE buffer containing 0.5 μg/mL of EtBr. The coating matrix and sieving matrix were made by dissolving 1.0% PVP (M_r 1 000 000) and 1.0% PEO (M_r 600 000) in the running buffer, respectively. The microchip channel was hydrodynamically coated with the coating matrix through the microchannel by applying a vacuum of 8.67×10^4 Pa (EYELA A-3S vacuum aspirator, Tokyo Rikakikai Co., Japan) before the filling with the sieving matrix. The sieving matrix was also hydrodynamically filled by applying a vacuum of 8.67×10^4 Pa to the reservoir for 5 min. The sample was pipetted into the sample inlet reservoir of the microchip. The DNA sample was injected by conventional electrokinetic injection in the injection-T region by applying a potential of 480 V at the sample outlet reservoir followed by grounding the sample inlet reservoir for 60 s. The separation constant electric field strength was in the range of 100–600 V/cm at the buffer inlet and sample outlet. In the MGE-PFSG experiment, which was performed according to the procedure described elsewhere [23,24], the PFSG separation was optimized as follows: an attempt was made to determine the optimum constant electric field strength in the range of 100–600 V/cm for the separation of the 100-, 200- and 300-bp DNA fragments. After separation, we decided whether PFSG or a constant strength would be preferable. If PFSG was chosen, the portions of the gradient before the first DNA peak (100-bp DNA) and after the last DNA peak (300-bp DNA) were eliminated or decreased. Finally, if separation in the second step was acceptable, the gradient time was reduced in an attempt to reduce the run time. The PFSG was programmed to give the best separation of all the target DNA fragments (147- and 187-bp DNA) with a resolution (R) >1.5. After each run, the microchip channel was rinsed successively with water and the running buffer for 5 min each.

3. Results and discussion

3.1. CGE for the simultaneous detection

The optimum allele-specific PCR conditions for the amplification of the specific DNA fragments of *S. pullorum* and *S. gallinarum* were carried out using CGE-based analysis (Tables 1 and 2). In order to evaluate the possibility of performing the PCR coamplification of both *S. pullorum* and *S. gallinarum* in same PCR conditions, the allele-specific PCR conditions, which could generate two specific DNA fragments with lengths of 147- and 187-bp as the expected PCR products, were determined after several rounds of amplifications using different annealing temperatures and $MgCl_2$ concentrations. Using two pairs of the designed primers and the annealing temperature range of 48–64 °C, we examined the possibility of coamplifying both the 147- and 187-bp DNA fragments of the *S. pullorum* and *S. gallinarum* genes in the DNA of the *Salmonella* within the serotype D group. In the range of 54–62 °C, the amplification of the 187-bp DNA fragment was decreased with increasing temperature (Table 1). Above 64 °C, none of the amplified-DNA fragments were detected by 1.0% PEO capillary gel electrophoresis. In the case of *S. pullorum*, below the annealing temperature of 53 °C, the amplification of the 147-bp DNA fragment was decreased with increasing annealing temperature. An annealing temperature of 54 °C showed the best amplification of both DNA fragments according to the data obtained using CGE, even though this annealing temperature value differed from those reported elsewhere [1,3,12].

Table 3
Comparisons of resolution (R)[a] between 100- and 200-bp DNA ladder in the CGE as a function of the applied electric field at 0.5–1.5% PEO sieving matrix

Applied electric field (V/cm)	R		
	0.5% PEO	1.0% PEO	1.5% PEO
83.3	6.25 (±2.86)	17.91 (±3.93)	24.52 (±1.06)
166.7	7.19 (±2.38)	12.28 (±0.39)	18.13 (±0.75)
250.0	4.85 (±0.17)	5.01 (±1.17)	12.44 (±0.33)
333.3	3.75 (±0.30)	4.44 (±1.01)	9.06 (±3.15)
416.7	2.05 (±0.31)	4.12 (±1.07)	4.00 (±0.35)

[a] R(mean ± S.D.) = $2(t_2 - t_1)/(w_{ave})$, where t_1 and t_2 are migration times of 100- and 200-bp DNA ladder peaks; w_{ave} is the average peak width of baseline ($n = 5$).

Table 4
Comparisons of the resolution (R)[a] between SG and SP in the CGE according to the applied voltages

Applied electric field (V/cm)	R		
	0.5% PEO	1.0% PEO	1.5% PEO
83.3	3.01 (±0.78)	9.35 (±3.84)	9.33 (±1.91)
166.7	2.39 (±0.54)	5.76 (±1.48)	6.77 (±0.81)
250.0	2.01 (±0.07)	3.28 (±0.91)	4.28 (±0.37)
333.3	1.27 (±0.03)	2.46 (±0.23)	2.79 (±0.04)
416.7	–	2.15 (±0.10)	0.96 (±1.67)

[a] R(mean ± S.D.) = $2(t_2 - t_1)/(w_{ave})$, where t_1 and t_2 are migration times of 187-bp (SG) and 147-bp DNA (SP) fragments peaks; w_{ave} is the average peak width of baseline ($n = 5$).

Since $MgCl_2$ is essential for activating Taq polymerase [25], various $MgCl_2$ concentrations ranging from 0 to 7.0 mM were examined in an attempt to simultaneously coamplify both DNA fragments under the *rfb*S allele-specific PCR condition (Table 2). The results show that the specific DNA fragments (147- and 187-bp DNA fragments of *S. pullorum* and *S. gallinarum*, respectively) were coamplified under the same PCR conditions in a single PCR tube when the $MgCl_2$ concentrations was in the range of 2.8–7.0 mM. Below 1.4 mM, no amplification of SG was observed. At concentrations ranging from 2.8 to 5.6 mM, amplifications of both SG and SP DNA fragments were detected. Therefore, considering the amplification efficiency and chemical matrix effects, a $MgCl_2$ concentration between 2.8 and 5.6 mM was selected as the optimum concentration.

The effects of the sieving matrix and applied electric field on the baseline separation of the 100-bp DNA ladder and both *Salmonella* fragments (147- and 187-bp) in quantitative CGE based on *rfb*S allele-specific PCR analysis were also investigated (Tables 3 and 4). In general, higher electric field strength yields shorter analysis times but decreases the resolving power of DNA fragments >800-bp in CE [26]. However, the resolving power of the DNA fragments decreased with increasing electric field even though the size of the specific target DNA molecules ranged from 100 to 300 bp (Tables 3 and 4). Above an applied electric field of 416.7 V/cm, the baseline of the electropherograms was not stable. This is because of joule heating, and the resolution between *S. pullorum* and *S. gallinarum* was <1.0. Therefore, a value of 333.3 V/cm was selected as the optimum applied electric field in

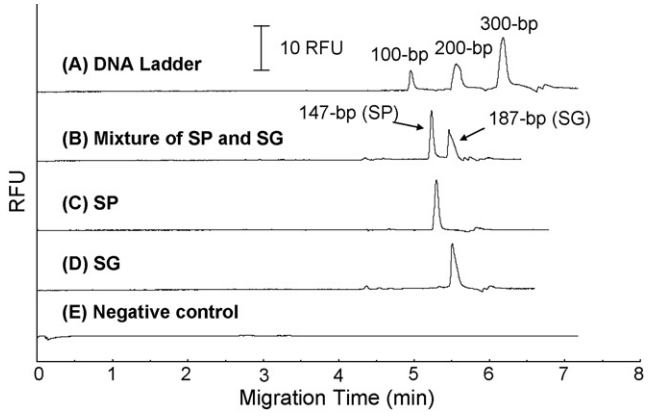

Fig. 1. Representative CGE electropherograms of (A) 100-, 200- and 300-bp DNA ladder fragments (B) a mixture of *Salmonella pullorum* and *Salmonella gallinarum*, (C) *S. pullorum*, (D) *S. gallinarum* and (E) negative control under the optimum CGE conditions. CGE separation condition: the running buffer, 1× TE buffer (pH 8.0) with 0.5 (g/mL EtBr; coating matrix, 1.0% PVP (M_r 1 000 000); sieving matrix, 1.0% PEO (M_r 600 000); sample injection, electrokinetic injection of 50 V/cm for 30 s; sample separation electric field, 333.3 V/cm. RFU: relative fluorescence unit.

CGE separation in order to obtain rapid simultaneous detection. The 100- and 200-bp DNA fragments were distinguished with a resolution of 4.44(±1.01) ($n = 5$) within 6 min under CGE conditions (Table 3 and Fig. 1A). Using the optimum CGE condition, the migration times of the specific 147-bp (*S. pullorum*) and 187-bp (*S. gallinarum*) DNA fragments were 5.18(±0.10) and 5.41(±0.11) min, respectively, with a resolution of 2.46 (Table 4 and Fig. 1B). The specific DNA peaks of the 147- and 187-bp fragments showed percentage relative uncertainties of 1.93% and 2.03% for these migration times ($n = 5$), respectively.

3.2. MGE-PFSG for the simultaneous detection

Fig. 2 shows the potential for the translation of these CGE conditions used for ultra-fast electrophoretic analysis to the

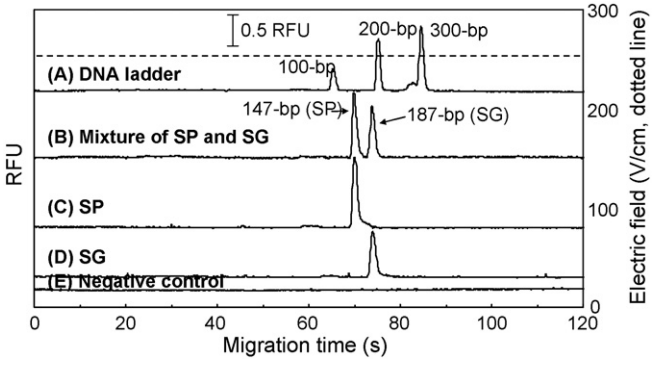

Fig. 2. Representative MGE electropherograms of the following using a constantly applied electric field: (A) 100-, 200- and 300-bp DNA ladder fragments (B) the mixture of *S. pullorum* and *S. gallinarum*, (C) *S. pullorum*, (D) *S. gallinarum* and (E) negative control under the optimum MGE conditions. MGE separation condition: the running buffer, 1× TE buffer (pH 8.0) with 0.5 (g/mL EtBr; coating matrix, 1.0% PVP (M_r 1 000 000); sieving matrix, 1.0% PEO (M_r 600 000); sample injection, electrokinetic injection of 480 V/cm for 60 s; sample separation electric field, 266.7 V/cm. RFU: relative fluorescence unit. The dotted line represents the applied electric field.

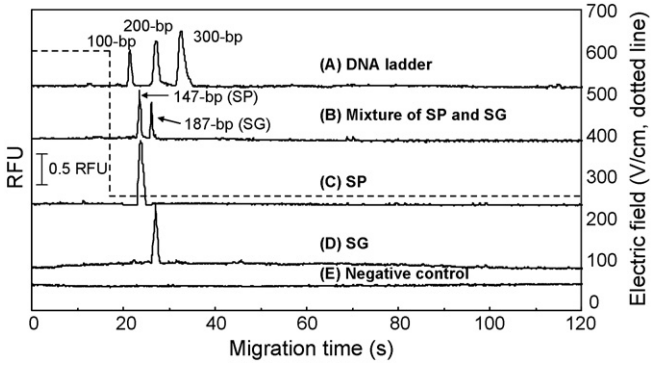

Fig. 3. Representative MGE electropherograms of the following using PFSG (A) 100-, 200- and 300-bp DNA ladder fragments (B) the mixture of *S. pullorum* and *S. gallinarum*, (C) *S. pullorum*, (D) *S. gallinarum* and (E) negative control under the optimum microchip gel electrophoresis conditions. MGE-PFSG separation condition: applied separation electric field, 600 V/cm for 0–20 s and 266.7 V/cm for 20–150 s. The dotted line represents the applied electric field. The other MGE-PFSG conditions are the same as those in Fig. 2.

microchip format. Under the optimum MGE condition, the separation of the 147- and 187-bp DNA fragments on a glass microchip was accomplished in <80 s, which is 4.5 times faster than that achieved by the CGE–based *rfb*S allele-specific PCR analysis shown in Fig. 1, and approximately 50 times faster than that expected by conventional slab gel electrophoresis. With a separation PFSG of 600 V/cm for 0–20 s and 266.7 V/cm for 20–150 s, the 147- and 187-bp DNA fragments were coanalyzed within 30 s without decreasing the resolution efficiency (Fig. 3). The analysis time was also decreased 2.7 times compared with that of the MGE using a constantly applied electric field. Under the optimum MGE-PFSG conditions, the specific DNA peaks of the 147-bp (*S. pullorum*) and 187-bp (*S. gallinarum*) fragments showed migration times of 23.813(±0.094) and 27.031(±0.087) s at the 95% confidence interval ($n = 5$), respectively. Both *Salmonella* were analyzed with a resolution of 2.51(±0.02) ($n = 5$) within 30 s under the MGE-PFSG conditions (Fig. 3B). These results show that *rfb*S allele-specific PCR-MGE using the PFSG method can be employed to simultaneously detect both *S. pullorum* and *S. gallinarum* with reasonable precision, speed and high efficiency.

4. Conclusions

An allele-specific PCR method was developed based on the *rfb*S sequence for the concurrent amplification of *S. pullorum* and *S. gallinarum* at the same PCR conditions. The amplification of the two specific 147- and 187-bp DNA fragments for the simultaneous detection of both *Salmonella* showed the best efficiency at a $MgCl_2$ concentration between 2.8 and 5.6 mM and an annealing temperature of 54 ± 1 °C. Under an electric field of 333.3 V/cm and with a sieving matrix of 1.0% PEO (M_r 600 000), the amplified PCR products were coanalyzed within 6 min by CGE separation. The CGE assay could be translated to microchip format, where *rfb*S allele-specific PCR analysis was completed within 80 s. The enhanced and more rapid separation of the PCR products could be achieved by applying MGE-PFSG. In the MGE-PFSG experiment, the analyses of both *Salmonella* strains were completed within only 30 s, without decreasing the resolution efficiency, and provided a 135-fold faster analysis time than that obtained by traditional slab gel electrophoresis. These results show that the *rfb*S allele-specific PCR-MGE with the PFSG method can be applied to making a differential diagnosis between *S. pullorum* and *S. gallinarum*, due to its ultra-speed and high efficiency.

Acknowledgments

The authors wish to thank Dr. Joon-Seok Chae and Dr. Mi-Jin Lee for their technical assistance and for supplying the *Salmonella* samples. This work was supported by a grant from the Basic Research Program of the Korea Science & Engineering Foundation (R01-2004-000-10056-0).

References

[1] A.R. Desai, D.H. Shah, S. Shringi, M.J. Lee, Y.-H. Li, M.R. Cho, J.-H. Park, S.J. Eo, J.H. Lee, J.S. Chae, Avian Dis. 49 (2005) 558.
[2] B. Alarcon, V. Garcia-Canas, A. Cifuentes, R. Gonzalez, R. Aznar, J. Agric. Food Chem. 52 (2004) 7180.
[3] M.K. Park, K.S. Choi, M.C. Kim, J.S. Chae, J. Vet. Sci. 2 (2001) 213.
[4] H.J. Kwon, K.Y. Park, H.S. Yoo, J.Y. Park, Y.H. Park, S.J. Kim, J. Microbiol. Methods 40 (2000) 33.
[5] H.L. Shivaprasad, Rev. Sci. Tech. 19 (2000) 405.
[6] R.W. Harvey, T.H. Price, J. Appl. Bacteriol. 46 (1979) 27.
[7] I. Perales, A. Audicana, Appl. Environ. Microbiol. 55 (1989) 3032.
[8] D.H. Shah, A. Roy, J.H. Purohit, Indian J. Comp. Microbiol. Immunol. Infect. Dis. 22 (2001) 131.
[9] J.M. Luk, U. Kongmuang, P.R. Reeves, A.A. Lindberg, J. Clin. Microbiol. 31 (1993) 2118.
[10] J.M. Luk, U. Kongmuang, R.S. Tsang, A.A. Lindberg, J. Clin. Microbiol. 35 (1997) 714.
[11] J.F. Timoney, J.H. Gillespie, F.W. Scott, J.E. Barlough, Hagan and Bruner's Microbiology and Infectious Diseases of Domestic Animals, 8th ed., Cornell University Press, New York, 1992, p. 74.
[12] D.H. Shah, J.H. Park, M.R. Cho, M.C. Kim, J.S. Chae, J. Microbiol. Methods 60 (2005) 169.
[13] S.H. Kang, S. Jang, H.K. Yi, J. Korean Chem. Soc. 49 (2005) 537.
[14] P.E. Williams, M.A. Marino, S.A. Del Rio, L.A. Turni, J.M. Devaney, J. Chromatogr. A 680 (1994) 525.
[15] L. Chen, J. Ren, Comb. Chem. High Throughput Screen 7 (2004) 29.
[16] T. Shintani, K. Yamada, M. Torimura, FEMS Microbiol. Lett. 210 (2002) 245.
[17] K.T. Carli, C.B. Unal, V. Caner, A. Eyigor, J. Clin. Microbiol. 39 (2001) 1871.
[18] B.A. Lindstedt, E. Heir, T. Vardund, G. Kapperud, J. Clin. Microbiol. 38 (2000) 1623.
[19] C. Zhao, G. Xu, P. Gao, J. Yang, X. Shi, J. Tian, J. Sep. Sci. 28 (2005) 513.
[20] D.K. Kim, S.H. Kang, J. Chromatogr. A 1064 (2005) 121.
[21] M. Park, H. Lee, S.H. Kang, J. Korean Chem. Soc. 49 (2005) 255.
[22] C.G. Koh, W. Tan, M.Q. Zhao, A.J. Ricco, Z.H. Fan, Anal. Chem. 75 (2003) 4591.
[23] Y.J. Kim, J.S. Chae, J.K. Chang, S.H. Kang, J. Chromatogr. A 1083 (2005) 179.
[24] S.H. Kang, M. Park, K. Cho, Electrophoresis 26 (2005) 3179.
[25] M.L. Seoh, S.M. Wong, L. Zhang, J. Virol. Methods 72 (1998) 197.
[26] A. Guttman, B. Wanders, N. Cooke, Anal. Chem. 64 (1992) 2344.

Available online at www.sciencedirect.com
ScienceDirect
Talanta 73 (2007) 498–504
Talanta
www.elsevier.com/locate/talanta

Automatic screening method for the preconcentration and determination of *N*-nitrosamines in water

Beatriz Jurado-Sánchez [a], Evaristo Ballesteros [b,*], Mercedes Gallego [a]

[a] *Department of Analytical Chemistry, Campus de Rabanales, University of Córdoba, E-14071 Córdoba, Spain*
[b] *Department of Physical and Analytical Chemistry, E.P.S. of Linares, University of Jaén, Alfonso X, El Sabio, 28, E-23700 Linares, Jaén, Spain*

Received 13 December 2006; received in revised form 30 March 2007; accepted 11 April 2007
Available online 21 April 2007

Abstract

A screening method was developed to discriminate among water samples contaminated or uncontaminated with *N*-nitrosamines in order to reduce the use of expensive instruments such as chromatographs. The system is based on the preconcentration of the analytes onto a sorbent column, elution and derivatization to form nitrite, then formation of a coloured product (Griess reaction) and photometric detection. The limit of detection achieved for 100 ml of sample volume was 0.2 μg/l and the sample frequency $3\,h^{-1}$. The reliability of the proposed method of the *N*-nitrosamines was established at five concentrations (between 0.5 and 3 times the limit of detection). For a level concentration of 0.6 μg/l (three times the limit of detection), the percentage of false negatives is 0%. The method was applied to the screening of several water samples (river, pond, well, tap and waste) with a positive response only for waste water samples.

Keywords: Screening system; Photometry; Solid-phase extraction; *N*-Nitrosamines; Waters

1. Introduction

N-Nitroso compounds and specially *N*-nitrosamines (NAms) exhibit mutagenic, carcinogenic, and teratogenic activities. It is demonstrated that nitrosamines developed a carcinogenic effect in a wide range of animal species like fishes, reptiles, birds, and mammals, including five species of primates. These substances are discharged into the environment by human activities or are formed by a nitrosation reaction between secondary amines and nitrosating agents such as nitrite and nitrate [1,2]. All NAms have in common the N–N=O functional group and their chemical and physical properties depend on the substituents of this group. NAms are found in drinking waters, where are formed by reaction of precursors with disinfection products [3] and in contaminated ground and waste waters, where they can be formed by the chemical reaction between a nitrogen-containing organic compound such as an amine or amide and a nitrosating agent, such as chemicals derived from nitrites or nitrogen oxides [4,5]. Humans are also exposed to NAms from endogenous synthesis within the body as well as from diet. Microorganism could take part in formation of NAms by nitrates reduction to nitrites and degradation of proteins to amines and amino acids. In addition, NAms are formed after cooking of meat in a complex process that is influence by a large variety of substances [6]. In fish, the main precursors of NAms are believed to be formed by reaction of nitrogen oxides (that are generated from nitrites and are also present in wood smoke) with, mainly, secondary amines present in the fish [7].

The US Environmental Protection Agency (US EPA) established control levels of NAms in drinking water at ng/l levels [8] and for this reason, a sensitive and selective method for the determination of these compounds at trace levels is required. Almost all of the analytical methods include extraction, preconcentration and clean-up steps prior to the analysis. Liquid–liquid extraction [9] requires the use of a large volume of toxic solvents and is very intensive labour so, as an alternative procedure, solid-phase extraction (SPE) has lower cost, shorter processing time and is easily automatizable. Most common sorbents used in SPE for the analysis of NAms are Ambersorb 572 [10], RP-C_{18} [11], active charcoal [12] or the combination of SPE materials like LiChrolut® EN and Ambersorb 572 [5] or Extrelut and Florisil [13]. Other preconcentration techniques employed for

* Corresponding author. Tel.: +34 953648560; fax: +34 953648560.
E-mail address: eballes@ujaen.es (E. Ballesteros).

0039-9140/$ – see front matter © 2007 Elsevier B.V. All rights reserved.
doi:10.1016/j.talanta.2007.04.007

this purpose are supercritical fluid extraction [14] and solid-phase microextraction [15].

Samples with simple matrix have been determined directly using polarographic or spectrophotometric methods which possess interferences and limited applications for trace analysis; for these reasons, analytical methods for NAms usually include separation techniques as capillary electrophoresis [16], thin-layer chromatography [17] or gas chromatography [10,15]. Liquid chromatography (LC) with diode array or UV detection is a powerful technique that allows the determination of complex mixtures, non-volatile analytes and thermally labelled analytes; however, NAms do not show absorption in the UV region, so to increase sensitivity and selectivity many methods employ derivatization agents with pre-column [18,19] or post-column separations [20,21]. More sensitive methods are based in the denitrosation of NAms and the detection of the secondary amines or the nitrite liberated.

Flow injection (FI) methods have been also used for the determination of NAms that are based on the continuous photochemical degradation of NAms [21–23] or continuous denitrosation with a hydrobromic acid–acetic acid–acetic anhydride mixture [24]. The nitrites generated were determined after derivatization with Griess reagent by photometry with limits of detection 0.8–15 μg/l [22] or 5.0×10^{-8} M [24], respectively. In another method amines generated in the denitrosation process of *N*-nitrosodimethylamine can be determined by chemiluminescence with a detection limit of 0.3 μg/l [23]. Some authors include sorbent columns in the flow system for the elimination of the interference of nitrite in the sample [22] or nitrite formed in the denitrosation reaction [23] previous the determination of *N*-nitrosamines derivatized or dimethylamine derivatized, respectively. Also, sorbent columns [20] or cartridges [21] were included in a continuous system for the SPE extraction of NAms, increasing the sensitivity and detection limits 0.1–3.0 ng/l [21], in the determination of these compounds in alcoholic beverages or water samples, respectively.

Screening methods are intended to classify samples into two groups (positive or negative) in relation to a specific property of the sample. Sample screening systems can be classified from a practical point of view according to the sample treatment required. Thus, there are direct screening systems, which involve no sample treatment (undoubtedly the best option), others are applied after a simple or full sample treatment; the last is only justified if the equipment involved in the conventional analytical system is expensive to maintain. If a negative response is obtained, no further sample processing is needed. Positive samples are then subjected to a conventional analytical process to confirm the response [25–28].

In this paper we developed a sample screening system for the determination of the total concentration of NAms in water. The fully automated method developed uses on-line solid-phase extraction of the NAms from water, followed by their derivatization to a purple dye which is monitored at 545 nm. Various sorbents and eluents were assayed in order to adopt the best possible analytical conditions for the determination of NAms at the lowest levels possible.

2. Experimental

2.1. Materials

All reagents were of analytical grade or better. Seven NAms were analysed: *N*-nitrosodiphenylamine (NDPA), *N*-nitrosodiethylamine (NDEA), *N*-nitrosopiperidine (NPIP), *N*-nitrosomorpholine (NMOR), *N*-nitrosopyrrolidine (NPIR), *N*-nitrosodimethylamine (NDMA) and *N*-nitrosodibutylamine (NDBA) (Sigma–Aldrich, Madrid, Spain). All solvents (acetonitrile, ethyl acetate, methanol, dichloromethane, ethanol, 2-propanol and diethyl ether) were supplied by Merck (Darmstadt, Germany). All products were handling with care, using efficient fume hoods and wearing protective gloves. LiChrolut® EN (40–120 μm) was purchased from Merck. Others sorbents (Amberlites, RP-C_{18} and Ambersorb 572) were supplied by Supelco (Madrid, Spain). Inert material of poly(tetrafluoroethylente) white beads was supplied by Fluka (Madrid, Spain). High-purity deionised water purified with a Milli-Q analytical-reagent grade water purification system (Milli-Q A10 Academic Gradient system) was used for preparation of reagents and standards.

Standard stock solutions containing 10 g/l of each NAm were prepared in methanol and stored in glass-stopped bottles at −4 °C in the dark. Standard working solutions were daily prepared by dilution of the stock in Milli-Q water and adjusted at pH 7.4 with dilute $NaHCO_3$. Denitrosation reagent (2.5%) was prepared by mixing 13 ml of 48% hydrobromic acid (Fluka), 39.4 ml of acetic anhydride (Fluka) and diluted to 250 ml with acetic acid (Fluka). Griess reagent solution was freshly prepared before use by dissolving 1.5 g of sulfanilamide (Fluka), 0.22 g of *N*-(1-naphthyl) ethylenediamine dihydrochloride (Fluka) and 5.2 ml of concentrated hydrochloric acid (Merck) in 100 ml of Milli-Q water.

2.2. Apparatus

Analysis was performance with a Perkin-Elmer Lambda 20 UV/VIS spectrophotometer (Perkin Elmer, Überlingen, Germany) equipped with a Hellma (Jamaica, NY, USA) QS.1000 flow cell (18 μl inner volume, pathlength 10 mm). The absorbance at 545 nm was continuously monitored by a Radiometer REC-80 Servograph recorder (Copenhagen, Denmark). The flow system consisted on a Gilson Minipuls-3 peristaltic pump (Villiers-Bel, France) fitted with poly(vinylchloride) pumping tubes, and two Rheodyne 5041 injection valves (Cotati, CA, USA). PTFE tubing of 0.5 mm i.d. and commercially available connectors and a PTFE tubing (8 cm × 3 mm i.d.) laboratory-made sorption column containing 75 mg of LiChrolut® EN were also employed. Because of its small particle size, the LiChrolut® EN sorbent is very prone to compaction when soaked in the flow system. In order to avoid abrupt changes in column compactness that might stop the solution flow and dislodge the system connections, each LiChrolut® EN segments (1.0 cm long) was separated by one segment of an inert material (e.g. PTFE beads, segments of ∼0.5 cm long). The sorbent column was conditioned by passing 450 μl of ace-

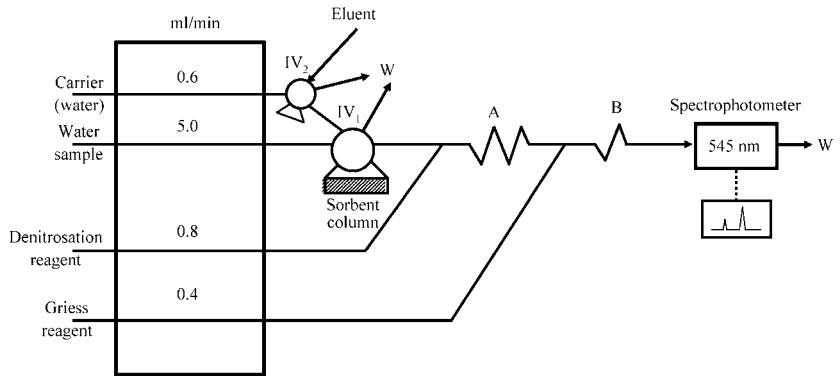

Fig. 1. Schematic diagram of the proposed continuous system for the preconcentration and determination of *N*-nitrosamines in water. IV, injection valve; W, waste; A and B, denitrosation and Griess reactors, respectively.

tonitrile and 5 ml of Milli-Q water. Under these conditions, the sorbent column remained active for 3 months.

2.3. Sample preparation procedure

Water samples were collected in amber-glass bottles with PTFE lids. Sample bottles were rinsed with a small volume of sample and the rinsate discharged. After that, bottles were filled without headspace and 20 mg/l of ascorbic acid were added. Samples were then stored at 4 °C and analysed within 2 weeks of collection. Prior the analysis, samples (e.g. waste water) were filtered through a 0.45 μm membrane filter (mixed cellulose esters, Millipore, Ibérica, Spain) and the pH was adjusted to 7.4.

2.4. Screening procedure

The continuous flow system is depicted in Fig. 1. First, 100 ml of sample or standard solution at pH 7.4 (adjusted with $NaHCO_3$) was passed through the sorbent column (located in the loop of injection valve IV_1) at 5 ml/min, retention of NAms was immediate and the sample matrix was sent to waste. NAms were then eluted (in the opposite direction to flow of the sample) with 150 μl of ethyl acetate–acetonitrile (9:1) mixture (eluent) by switching IV_1 and IV_2 at 0.6 ml/min (Milli-Q water as carrier). The extract and the denitrosation reagent were mixed in a 150 cm × 0.5 mm i.d. reaction coil. The nitrite generated was then mixed with the Griess reagent in an 80 cm × 0.5 mm reaction coil. The absorbance of the azo-dye generated was measured at 545 nm. A volume of 150 μl of eluent was used as blank, giving negligible absorbance (ca. 0.003 units). Peak height was used as the analytical signal.

3. Results and discussion

3.1. Optimization of the sorption/elution process

In order to select the most suitable sorbent and eluent for the intended purpose, a manifold similar to that depicted in Fig. 1 was employed. In all experiments, 100 ml of an aqueous standard solution containing 25 μg/l of different NAms were passed through the sorbent column at 5 ml/min.

Several typical sorbent materials (Amberlites XAD-2, XAD-4, XAD-7, and XAD-16, RP-C_{18}, Ambersorb 572 and LiChrolut® EN) were tested for the preconcentration of NAms. Sorption test was done by using a column packed with 100 mg of the sorbent assayed in each case. Fractions of 1 ml of sample were collected before and after the sorbent column in glass vials. Both fractions were mixed with 1.4 ml of the denitrosation reagent and 300 μl of the Griess reagent. The sorption efficiency of the sorbent materials was assessed by comparing the absorbance of both fractions. As can be seen from Table 1, the best results were obtained with LiChrolut® EN and Ambersorb 572, where all NAms were quantitatively retained with sorption efficiency of ca. 100%, whereas for other sorbents, retention ranged from 50 (Amberlite XAD-7) to 90% (Amberlite XAD-4). Although LiChrolut® EN and Amberlites are styrene-divinylbenzene copolymers, the differences found in their sorption efficiency can be explained by the different particle size, mesh size and polarity of sorbents. Different organic

Table 1
Sorption efficiency (%) of various materials for *N*-nitrosamines

N-Nitrosamine	LiChrolut® EN	XAD-2	XAD-4	XAD-7	XAD-16	RP-C_{18}	Ambersorb 572
N-Nitrosodimethylamine	99.9	55.6	100.0	100.0	100.0	100.0	99.9
N-Nitrosodiethylamine	100.0	60.3	68.8	48.1	100.0	52.8	99.5
N-Nitrosopyrrolidine	99.0	62.2	100.0	10.3	57.7	12.5	99.4
N-Nitrosopiperidine	99.6	62.6	67.3	8.1	31.0	25.5	100.0
N-Nitrosomorpholine	100.0	62.2	100.0	14.6	57.0	13.9	99.6
N-Nitrosodibutylamine	99.5	94.3	99.9	86.1	100.0	100.0	100.0
N-Nitrosodiphenylamine	99.9	91.7	99.7	83.3	80.0	100.0	90.9

solvents were assayed as eluent, namely: ethyl acetate, acetonitrile, acetone, methanol, ethanol, diethyl ether, dichloromethane and 2-propanol. None organic solvents (150 μl) provided quantitative elution (lower than ca. 50%) when using Ambersorb 572, therefore it was discarded as sorbent. By using LiChrolut® EN quantitative elution ca. 100% was only obtained with acetonitrile; since the presence of ethyl acetate (90% elution efficiency) improves the Griess reaction, a mixture of both solvents ethyl acetate–acetonitrile (9:1) was finally selected as eluent.

The optimum amount of LiChrolut® EN sorbent was studied by using various columns containing between 25 (2.5 cm × 3 mm i.d.) and 150 mg (15 cm × 3 mm i.d.) of the sorbent. A series of calibration graphs were run for each NAm and column, by passing 100 ml of aqueous standard solutions containing between 1 and 40 μg/l of NAms and eluting with 150 μl of ethyl acetate–acetonitrile (9:1). The analytical signal increased as increasing the amount of sorbent up to 75 mg and decreased above 90 mg of LiChrolut® EN, because higher volume of eluent for complete elution of NAms is required. Finally, a working column packed with 75 mg of LiChrolut® EN (8 cm × 3 mm i.d.) was selected. The retention of NAms depends on the sample pH, and this effect was studied over a wide range (1.0–12.0); in all instances, the desired values were adjusted with dilute HCl or NaOH. The signal remained almost constant from pH 6.0–8.5, with a sharply decrease above this value. Samples were adjusted to pH 7.4 with dilute $NaHCO_3$. The ionic strength of the water samples, adjusted with potassium nitrate, had no effect on the signal up to 2 M.

The flow rate of the sample through the column during the preconcentration step had no effect on the sorption efficiency over the studied range (0.4–5.5 ml/min); therefore, a sample flow rate of 5.0 ml/min was selected. The effect of the elution process was studied by changing the carrier flow rate (water) between 0.4 and 2.8 ml/min. The maximum signal with no carry-over was obtained with a flow rate of 0.6 ml/min. The effect of the eluent volume was studied between 50 and 400 μl by using loops of variable length in the injection valve (IV_2 in Fig. 1). As the eluent volume was increased, desorption was more efficient, but analytes were also diluted. The signal increased with increasing volume up to 150 μl, above which it started to decrease as the likely result of the analytes were diluted. An injection volume of 150 μl of ethyl acetate–acetonitrile was selected. A second injection with the same eluent volume revealed the absence of carry-over. The breakthrough volume depends on the packing efficiency of the sorbent bed and on the strength with which the analytes are retained. The effect of this variable was examined by using standard solutions containing 25 μg of each NAm in variable volumes (from 10 to 400 ml), for insertion into the SPE system. Sorption efficiency of ca. 100% was obtained with volumes up to 300 ml of the aqueous solution.

3.2. Selection and optimization of the derivatization reaction

It is well known that NAms easily undergo cleavage at the N–NO bond that can be carried out by UV irradiation [22,23] or by denitrosation with a hydrobromic acid–acetic acid–acetic anhydride mixture [24]. The amine liberated can be detected by reaction with dansyl chloride by fluorescence [18] or with tris(2,2′-bipyridyl) ruthenium (III) by chemiluminescence [23], or the nitrites generated in the reaction can be also monitored by reaction with the Griess reagent by photometry [20,22,24]. In the present work, we selected a hydrobromic acid–acetic acid–acetic anhydride mixture for the denitrosation of NAms and the nitrites generated are derivatized with the Griess reagent, being monitored the final products at 545 nm. This derivatization procedure was selected because its simplicity and rapidity, and allows the use of conventional instrumentation. Preliminary experiments were focused on the selection of the optimum conditions for the derivatization, using an aqueous solution containing 25 μg/l of each NAm. After preconcentration and elution, the extract was mixed with the denitrosation reagent using the continuous system depicted in Fig. 1.

The HBr concentration in the denitrosation reagent were optimized between 1 and 5% and, as can be seen in Fig. 2, the maximum signal was obtained at an HBr concentration of 2.5% in the mixture (13 ml of 48% hydrobromic acid, 39.4 ml of acetic anhydride and diluted to 250 ml with acetic acid). The flow rate of the denitrosation reagent was varied between 0.6 and 1.2 ml/min, and the maximum absorbance was obtained at a flow rate of 0.8 ml/min. Finally, the length of the coil, where the reaction between the analytes and the denitrosation reagent took place, was also studied. Reaction within the plug was virtually complete for a long of 150 cm.

The nitrites liberated in the previous reaction were derivatized by the Griess reagent. A solution containing a mixture of reagents (sulfanilamide, *N*-(1-naphthyl) ethylenediamine dihydrochloride and concentrated hydrochloric acid) were tested. For this purpose, individual solutions of these three reagents were evaluated by insertion of each reagent in a different stream of the FI system, but the best results in terms of sensitivity were obtained with a mixture of them. The concentration of sulfanilamide in the mixture over the range 0.1–3.0% was also studied. The signal increased with increasing sulfanilamide concentration up to 1–3%, reaching a steady state above this value. So, a concentration of the Griess reagent of 1.5% in sulfanilamide was taken as optimal. The concentration of *N*-(1-naphthyl) ethylenediamine dihydrochloride was varied from 0.06 to 0.60%; the maximum peak, as can be seen in Fig. 3, was obtained with a concentration of this Griess reagent of 0.2%, which was selected. Various acids at 5% (v/v) in the Griess reagent (phosphoric acid, acetic acid and hydrochloric acid) where tested and the maximum signal was obtained with HCl.

On the other hand, the flow rate of the Griess reagent was optimized between 0.1 and 0.8 ml/min and the maximum signal were found at 0.4 ml/min. Finally, we also studied the length of the mixing coil where the reaction between the nitrites generated and the Griess reagent took place, over the range 30–200 cm and the maximum signal without dilution was obtained for a coil of 80 cm long.

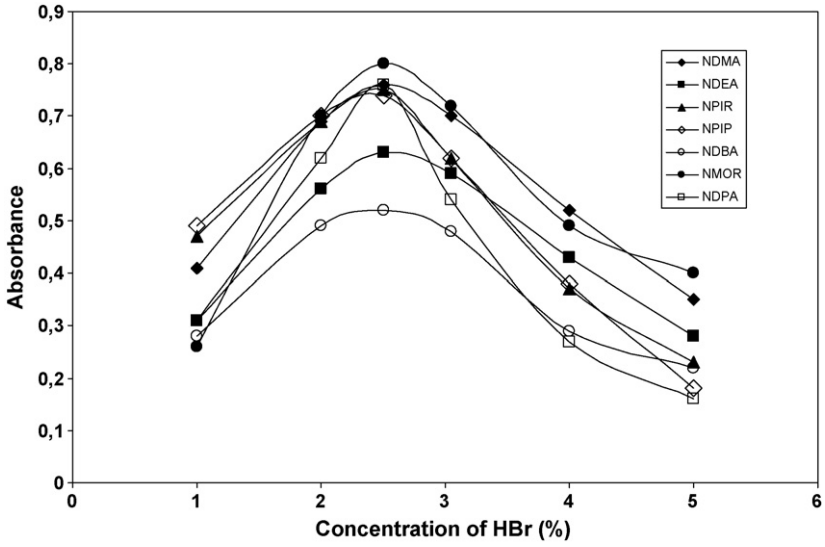

Fig. 2. Optimization of the HBr concentration in the denitrosation reagent. NDMA: *N*-nitrosodimethylamine; NDEA: *N*-nitrosodiethylamine; NPIR: *N*-nitrosopyrrolidine; NPIP: *N*-nitrosopiperidine; NMOR: *N*-nitrosomorpholine; NDBA: *N*-nitrosodibutylamine; NDPA: *N*-nitrosodiphenylamine.

3.3. Sensitivity and selectivity of the method

Analytical curves for aqueous samples were constructed by introducing 100 ml of aqueous solutions containing variable concentrations of NAms between 0.7 and 45 μg/l. The sensitivity (slope of the calibration graph) and the linear ranges are listed in Table 2. The limits of detection (LOD) and quantification (LOQ) were calculated as the blank signal plus 3 times (LOD) or 10 times (LOQ) its standard deviation, respectively [29]. Preconcentration factors increased with increasing sample volume and are limited by solvent quantity and analysis time. The preconcentration factor was calculated as the ratio between the slopes of the calibration graphs obtained by using the flow system depicted in Fig. 1 and the slopes obtained by analysis of aqueous standards solutions containing between 0.5 and 5 mg/l of NAms at pH 7.4 by the flow system depicted in Fig. 1, using the same flow system without the sorbent column. The mean values (for the seven NAms studied) of these factors were 60, 310 and 620 for samples volumes of 10, 50 and 100 ml, respectively. When using 300 ml of sample the sensitivity increases but in detriment of the sampling frequency (sample flow rate of 5 ml/min implies 1 h per analysis). The precision of the method (as repeatability), expressed as relative standard deviation, was checked on 11 individual samples containing 1 μg/l of each analyte and ranged between 2.7 and 4.5%.

A systematic study of interferences was carried out, including the following compounds: nitrite and nitrate, typical anions present in water. Cations [Fe, Cu, Ca, Mg, Na, K, and others], ascorbic acid (added to water samples as preservative), citric acid, sorbate, phosphates and lactic acid were also studied. All the compounds studied at concentrations of 200 mg/l (sample volume, 100 ml) caused no interference in the determination of 1 μg/l of each NAm. This effect can be ascribed to these compounds are not retained on the sorbent column, being eliminated in the waste.

3.4. Reliability of the proposed screening method

The confidence level of the proposed screening method was established on the basis of the level of false positives and negatives through a simple chemometric study. The cut-off concentration was set at a concentration corresponding to two times the limit of detection (2LOD). A false negative arises when a water sample spiked with a concentration of analyte higher than

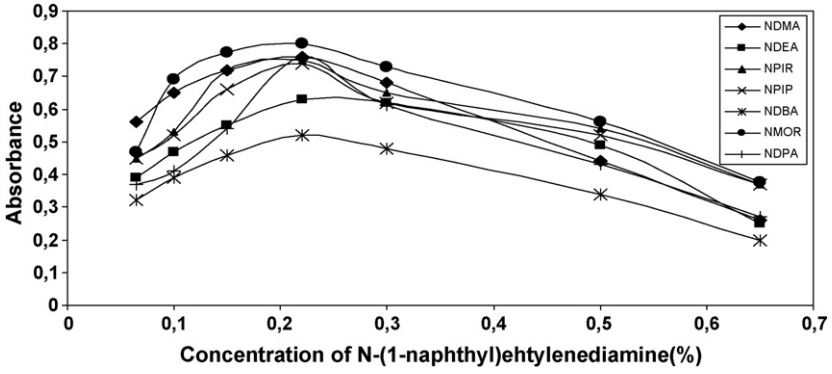

Fig. 3. Optimization of *N*-(1-naphthyl) ethylenediamine concentration (see Fig. 2).

Table 2
Analytical figures of merit of the proposed method

N-Nitrosamine	Sensitivity (absorbance/(μg l))	Linear range (μg/l)	*R*[a]	Limit of detection (μg/l)	Limit of quantification (μg/l)	R.S.D.[b] (%)	Preconcentration factor (100 ml sample)
N-Nitrosodimethylamine	0.0353	0.7–35	0.997	0.2	0.5	4.5	621
N-Nitrosodiethylamine	0.0303	0.7–40	0.995	0.2	0.6	3.7	622
N-Nitrosopyrrolidine	0.0334	0.7–35	0.992	0.2	0.6	2.7	615
N-Nitrosopiperidine	0.0338	0.7–35	0.992	0.2	0.5	3.7	619
N-Nitrosomorpholine	0.0257	0.9–45	0.993	0.3	0.7	3.3	622
N-Nitrosodibutylamine	0.0345	0.7–35	0.991	0.2	0.5	4.4	619
N-Nitrosodiphenylamine	0.0340	0.7–35	0.994	0.2	0.5	3.6	620

[a] *R*: regression coefficient.
[b] R.S.D.: relative standard deviation ($n = 11$) for 1 μg/l.

2LOD gives an absorbance measurement lower than the cut-off signal. A false positive is produced when a water sample spiked with a concentration of analyte lower than 2LOD gives an absorbance measurement higher than the cut-off signal. *N*-Nitrosodimethylamine (LOD = 0.2 μg/l) was the *N*-nitrosamine selected for this study because it is one of the most common and toxic NAm present in water. A systematic study at five concentrations levels (0.5LOD, 1LOD, 1.5LOD, 2.5LOD and 3LOD) was carried out by using 25 samples at each concentration. The results obtained are shown in Fig. 4, where at each concentration level, the reliability at a confidence level of 95% is given. As can be observed, the percentage of false negatives decreases as the concentration of *N*-nitrosodimethylamine increases, being zero at 3LOD. The percentage of false positives turned out to be 13% at a 1.5LOD; as expected, no false positives were obtained at concentrations lower than LOD.

As no certified reference materials with this type of NAms in water were available, a recovery study was carried out on real water samples (tap, well, river, pond and waste) to test the accuracy of the proposed method. For this purpose, the *N*-nitrosamines studied were added to aliquots of the blank sample at three different concentrations (1, 2 and 5 μg/l) and the samples were processed according to the proposed procedure. The samples were all run in triplicate ($n = 3$) and the relative standard deviation was calculated for each one. Average recoveries varied between 90 and 103% with an average relative standard deviation of ca. 4%.

Table 3
Determination of *N*-nitrosamines in water samples

Water sample	Screening response[a]	Concentration found (μg/l)[b]
River (Guarrizas)	Negative	–
River (Guadalquivir)	Negative	–
Pond (La Fernandina)	Negative	–
Pond 2 (Puente Nuevo)	Negative	–
Well (Linares)	Negative	–
Well (La Carolina)	Negative	–
Tap (Linares)	Negative	–
Tap (La Carolina)	Negative	–
Waste (La Carolina)	Positive	2.1
Waste (Mengibar)	Positive	1.0

[a] Response of the screening photometric method for a cut-off of 2LOD for *N*-nitrosodimethylamine.
[b] Concentration expressed as *N*-nitrosodimethylamine.

3.5. Application to water samples

The proposed method was applied to the determination of *N*-nitrosamines in various types of Spanish waters, namely: tap, well, river, pond and waste.

If any sample (e.g. waste water) requires filtering, this should be done at the time of sampling and then adjusted at pH 7.4; a volume of 100 ml of each water sample was analysed using the proposed screening method. The results are listed in Table 3. Only two waste waters were classified as positive. By using the

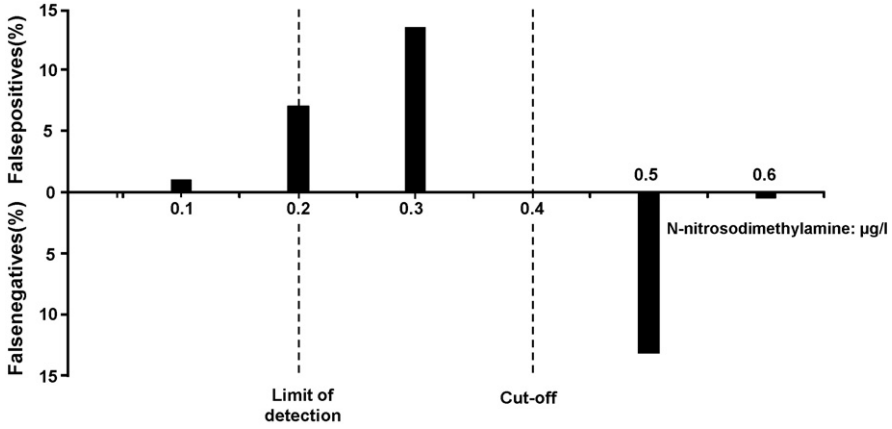

Fig. 4. Graphical summary of the reliability of the proposed screening system as applied to water samples with *N*-nitrosodimethylamine at concentrations near the detection limit of the method.

calibration graph of *N*-nitrosodimethylamine the concentration of NAms ($n = 5$) was calculated in both waste waters. All the same, quantitative determination of each NAm is only possible if only one is present and its identity is known. For this reason, every positive result must be confirmed by using procedures of higher analytical rank – for example, gas chromatography coupled ideally with mass spectrometer – that are able to separate and identify the NAms.

4. Conclusions

The proposed method is focused on the development of an automatic system that allows the solid-phase extraction of *N*-nitrosamines for the preconcentration and clean-up of the sample, and derivatization for their photometric detection. This method is straightforward (it requires minimum sample preparation), expeditious (the throughput is 3 samples/h) and reliable (it provides no false negatives for a cut-off of 0.6 μg/l). The method uses few microlitres of the eluent (150 μl) whereas other authors use several millilitres of solvents by using a sorbent column [20] or a cartridge [21], being necessary a manual evaporation step to increase the sensitivity, which can cause losses of volatile NAms. Thus, this step could explain the low recoveries obtained for volatile NAms (*N*-nitrosodimethylamine, *N*-nitrosodiethylamine and *N*-nitrosomorpholine) [21]. The detection limits of the proposed method (ca. 0.2 μg/l) are lower than others using FI system and photometric detection (0.8 or 5.4 μg/l) for the determination of NAms in water samples [22,24]. The sensitivity of the proposed methodology is lower than that obtained by Pérez Ruiz et al., which use a flow system and LC with chemiluminescent detection. Detection limits within the range 0.1–3.0 ng/l were achieved by using 250 ml of water, being the eluate manually evaporated and the residue dissolved with 0.5 ml of water [21]. In the present work the detection limits can be also decreased by using sample volumes of 300 ml.

Acknowledgements

The authors would like to thank the DGI of the Spanish Ministry of Science and Technology for financial support awarded in the form of Grant CTQ 2004-02798. Beatriz Jurado-Sánchez would like to thank DGI for the award of a predoctoral grant.

References

[1] IARC Monographs on the Evaluation of the Carcinogenic Risk of Chemicals to Humans, Some *N*-Nitroso Compounds, International Agency for Research on Cancer, vol. 17, Lyon, 1978.
[2] A.M. Afonso Perera, in: L.M.L. Nollet (Ed.), Chromatographic Analysis of the Environment, CRC Press–Taylor & Francis, Boca Raton, 2006, pp. 419–452.
[3] W.A. Mitch, D.L. Sedlak, Environ. Sci. Technol. 38 (2004) 1445.
[4] B.A. Tomkins, W.H. Griest, C.E. Higgins, Anal. Chem. 67 (1995) 4387.
[5] J.W.A. Charrois, M.W. Arend, K.L. Froese, S.E. Hrudey, Environ. Sci. Technol. 38 (2004) 4835.
[6] S. Yurchenko, U. Mölder, Food Chem. 96 (2006) 325.
[7] S. Yurchenko, U. Mölder, Food Chem. 100 (2007) 1713.
[8] Iris Substance List, U.S. Environmental Protection Agency, http://www.epa.gov/iris/subst/index.html.
[9] A. Raksit, S. Johri, J. AOAC Int. 84 (2001) 1413.
[10] V.Y. Taguchi, S.W.D. Jenkins, D.T. Wang, J.P.F.P. Palmentier, E.J. Reiner, Can. J. Appl. Spectrosc. 39 (1994) 87.
[11] B.A. Tomkins, W.H. Griest, Anal. Chem. 68 (1996) 2533.
[12] P.J. Sanches Filho, A. Rios, M. Valcárcel, K.D. Zanin, E. Bastos Caramao, J. Chromatogr. A 985 (2003) 503.
[13] S. Raoul, E. Gremaud, H. Biaudet, R.J. Turesky, J. Agric. Food Chem. 45 (1997) 4706.
[14] F. Reche, M.C. Garrigós, M.L. Marín, A. Cantó, A. Jiménez, J. Chromatogr. A 963 (2002) 419.
[15] S. Ventanas, J. Ruiz, Talanta 70 (2006) 1017.
[16] P.J. Sanches Filho, A. Rios, M. Valcárcel, E. Bastos Caramao, Water Res. 37 (2003) 3837.
[17] C.K. Cross, K.R. Bharucha, J. Agric. Food Chem. 27 (1979) 1358.
[18] J. You, X. Fan, W. Lao, Q. Ou, Q. Zhu, Talanta 48 (1999) 437.
[19] L. Cárdenes, J.H. Ayala, V. González, A.M. Afonso, J. Chromatogr. A 946 (2002) 133.
[20] G. Bellec, J.M. Cauvin, M.C. Salaun, K. Le Calvé, Y. Dréano, H. Gouérou, J.F. Ménez, F. Berthou, J. Chromatogr. A 727 (1996) 83.
[21] T. Pérez Ruiz, C. Martínez Lozano, V. Tomás, J. Martín, J. Chromatogr. A 1077 (2005) 49.
[22] E. Luque-Pérez, A. Ríos, M. Valcárcel, Fresenius J. Anal. Chem. 371 (2001) 891.
[23] T. Pérez Ruiz, C. Martínez Lozano, V. Tomás, J. Martín, Anal. Chim. Acta 541 (2005) 69.
[24] T. Ohta, N. Goto, S. Takitani, Analyst 113 (1988) 1333.
[25] M. Valcárcel, S. Cárdenas, M. Gallego, Trends Anal. Chem. 18 (1999) 685.
[26] B.M. Simonet, A. Ríos, M. Valcárcel, Anal. Chim. Acta 516 (2004) 67.
[27] R. Kellner, J.M. Mermet, M. Otto, M. Valcárcel, H.M. Widmer (Eds.), Analytical Chemistry, 2nd ed., Wiley–VCH Verlag GmbH & Co., Weinheim, 2004, p. 1110.
[28] M. Valcárcel, S. Cárdenas, Trends Anal. Chem. 24 (2005) 67.
[29] L.C. Currie, Anal. Chim. Acta 391 (1999) 105.

Available online at www.sciencedirect.com
ScienceDirect
Talanta 73 (2007) 425–430
Talanta
www.elsevier.com/locate/talanta

A new method for simultaneous determination of Co(II), Ni(II) and Pd(II) as morpholine-4-carbodithioate complex by SPME–HPLC–UV system

Varinder Kaur, Ashok Kumar Malik *

Department of Chemistry, Punjabi University, Patiala 147002, Punjab, India

Received 20 February 2007; received in revised form 3 April 2007; accepted 3 April 2007
Available online 8 April 2007

Abstract

A new approach for the analysis of Co(II), Ni(II) and Pd(II) as morpholine-4-carbodithioate (MDTC) complexes in aqueous medium by using solid phase microextraction (SPME)–high performance liquid chromatography (HPLC)–UV has been developed. The method involves sorption of metal complexes on PDMS fiber from aqueous solution followed by desorption in the desorption chamber of SPME–HPLC interface using acetonitrile:water (60:40) as mobile phase. A good separation of metal complexes is achieved on C_{18} column. The detection limits of Co(II), Ni(II) and Pd(II) are 0.17, 0.11 and 0.06 ng ml^{-1}, respectively. These can be determined by the proposed method without interference from other common metal ions such as Mo(VI), V(V), Ag(I), Sn(IV), Cd(II), Pb(II), Zn(II), Ag(I), Sn(II), Cr(III) and Cr(VI). The method was applied to the determination of these metals in different alloy samples and drinking water sample.

Keywords: Solid phase microextraction; High performance liquid chromatography; Morpholine-4-carbodithioate; Cobalt; Nickel; Palladium

1. Introduction

Some of the metal ions are the most dangerous pollutants due to their acute toxicity and carcinogenecity. These metal ions are cumulative poisons capable of being assimilated in the tissues of organisms causing noticeable adverse physiological effects [1]. Effects on the lungs, including asthma, pneumonia, and wheezing, have been found due to toxicity of these metal ions. The respiratory system is the primary target of nickel toxicity following inhalation. Exposure to high concentrations of these metal ions causes lung, nasal and throat cancers. Therefore, interest and demand is increasing for metal determination in biological and environmental samples [2].

Different separation and detection techniques have been applied in the determination of metal species. HPLC is a technique, which meets most of the analytical requirements of metal determination as it provides separation and quantitation of different species down to trace levels in one procedure. Current methods used for extracting metal ions are liquid–liquid extraction (LLE) [3], salting out liquid–liquid extraction (SOE) [4] and solid phase extraction (SPE) [5] using bonded silica sorbents. LLE and SOE are time consuming, require large volumes of solvents and can lead to different extraction efficiencies depending on the analyte investigated. SPE offers the advantage of lower consumption of organic solvent but it involves a multistep procedure such as conditioning, retention, rinse and elution, which makes it very lengthy and time consuming.

Solid phase microextraction (SPME) developed by Pawliszyn [6–8] is a rapid, simple, solvent free and sensitive method for the extraction of metal ions. It is solvent free and eliminates the need for extraction of analytes in very expensive organic solvents. It requires less time for extraction and easy to use. It prevents the loss of analytes and allows field sampling with portable field sampler. It is highly sensitive and able to detect analytes up to ppb and sometimes, ppt levels. Few methods using SPME–GC for the analysis of metal-ions are reported in the literature [9]. These methods are very sensitive, but they are limited only to volatile metal complexes. Reviews are available on the application of SPME to different metal species, which report the limited use of SPME–HPLC for the analysis of Hg(II), organotins and organomercury species [10,11]. The present paper describes an analytical method that integrates the sorption of metal complexes on SPME fiber for very sensitive and direct determination of metal ions in aqueous solution. It extends application of SPME

* Corresponding author. Tel.: +91 175 2359557; fax: +91 175 2283073.
E-mail address: malik_chem2002@yahoo.co.uk (A.K. Malik).

0039-9140/$ – see front matter © 2007 Elsevier B.V. All rights reserved.
doi:10.1016/j.talanta.2007.04.003

to the analysis of toxic metal ions and direct application to real samples. Special attention is given to the optimization of instrumental parameters of SPME–HPLC and UV system for proper extraction, separation and detection of Co(II), Ni(II) and Pd(II) metal ions. Analytical figures of merit including analysis time, precision and limit of detection are discussed.

2. Experimental

2.1. Reagents

All the solvents used were of HPLC grade purchased from J.T. Baker Chemicals, USA and filtered by using Nylon 6,6-membrane filters (Rankem, India) in filtration assembly (from Perfit, India). Co(II) (cobaltous chloride), Ni(II) (nickel nitrate), Pd(II) (palladium chloride), sodium acetate, acetic acid and sodium hydroxide were obtained from Merck, India. All HPLC solvents were degassed with an ultrasonic bath prior to use. Morpholine-4-carbodithioate (MDTC) reagent was prepared in the lab by using method reported by Macrotrigiano et al. [12]. It was purified by recrystallization with 2-propanol. The purity was checked by recording melting point and IR spectra on Perkin-Elmer FTIR. Sodium acetate (0.02 M)/acetic acid buffer of pH 6.0 was prepared by adjusting the pH on digital pH meter using NaOH and acetic acid. Sodium chloride used for optimization of extraction conditions was purchased from Sisco Chemicals, India.

2.2. Synthesis of morpholine-4-carbodithioate and complex formation

MDTC has been used as complexing agent. It was prepared by the method reported by Macrotrigiano et al. [12].

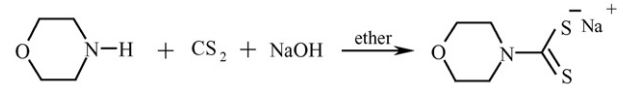

Morpholine Carbon disulphide Morpholine-4-carbodithioate

Morpholine in dry ether was taken in 250 ml Erlenmeyer flask and to this solution; stoichiometric amount of CS_2 was added dropwise with constant stirring. Reaction mixture was cooled in an ice salt mixture thoroughly and stoichiometric amount of NaOH (dissolved in minimum quantity of water) was added dropwise with constant stirring. Addition was complete in about 3–4 h. The crude product was filtered over suction and washed several times with solvent ether. Residue was recrystallized twice from isopropyl alcohol. Obtained product was in the form of white needle shaped crystals with melting point 175 °C and was highly soluble in water. FTIR studies showed characteristic bands for C=S str at 1083 cm^{-1} and two bands at 1437 and 1164 cm^{-1} due to υ(C–N) and υ(C–O), respectively.

2.3. Apparatus

The Dionex HPLC unit consisted of the following components; a P 680 solvent delivery pump, an UVD 170 detector capable of detecting at four wavelengths, interfaced to a computer loaded with Chromeleon software, in conjunction with HP laser 1010 printer. A Dionex C_{18} stainless steel reversed phase column of 250 mm × 4.6 mm (i.d.) filled with C_{18} material (5 μm) (Acclaim 120) was used for separation. HPLC was hyphenated to SPME by using a specially designed interface with an injection loop of 50 μl (Supelco Corp., Bellenfonte, PA). For extraction of analytes, nonbonded PDMS fiber having 100 μm film thickness and stable in pH 2–10 with water-miscible organic solvents, was purchased from Supelco, Bellenfonte, PA.

2.4. Procedure

It involves the selective extraction of Co(II), Ni(II) and Pd(II) ions as MDTC complexes from aqueous solution on PDMS fiber. The complex formed was then, desorbed from the fiber onto HPLC column through a specially designed interface. The complex formed by MDTC with these metals was well separated from the free ligand. The extracted amount of metal ions was quantitatively determined by UV detection at 310 nm.

2.5. Preparation of metal complexes

A 1–2 ml solution containing Co(II), Ni(II) and Pd(II) between 1 and 100 ng was taken in a 5 ml measuring flask. To this, 1.0 ml of 0.02% MDTC reagent and 1 ml of sodium acetate buffer of pH 6.0 was added. The final volume was adjusted to 5 ml with triply distilled water.

2.6. Extraction, desorption and separation of complexes

Metal complexes can be sorbed from aqueous solution by using PDMS fiber. The fiber was conditioned in the mobile phase before use. During the process of sorption, the fiber was lowered into the sample vial sealed with a septum type cap. The fiber was extended into the metal solution through needle. A 1.5 g of NaCl salt was added to it. The solution was stirred continuously with magnetic stirrer at a rate of 1200 rpm for about 30 min. Sorption was conducted at room temperature. The fiber was retraced within its holder after extraction of metal complexes. The analytes were desorbed from the fiber by soaking it in mobile phase for 15 min in the desorption chamber of SPME–HPLC interface at 'load' position. Then, the injector was turned to 'inject' mode, which delivered the metal complexes to C_{18} column for separation. The elution of analytes was done by using acetonitrile:water (60:40) as mobile phase at a flow rate of 0.8 ml/min The analytes were detected at a 310 nm (conditions are summarized in Table 1).

3. Results and discussion

3.1. Spectrophotometric conditions

Co(II), Ni(II) and Pd(II) metal ions react very rapidly with MDTC to form corresponding metal dithiocarbamates. Co(II) and Ni(II) form stable and colored complexes with MDTC in

Table 1
Analysis of calibration curves by SPME–HPLC–UV

Parameters	Co(II)	Ni(II)	Pd(II)
Regression equation	$0.0219x + 0.0046$	$0.0297x + 0.059$	$0.0603x + 0.033$
Correlation coefficient (r^2)	0.9999	0.9992	0.9995
R.S.D. (%)	5.0	2.3	3.4
LOD, S/N = 3 (ng ml^{-1})	0.17	0.11	0.06
Retention time (min)	9.22	10.23	10.92
Variation time (R.S.D.)	0.3	0.5	0.5

pH range of 5–7 and Pd(II) can form complex up to 6.0 pH. Therefore pH was adjusted to 6.0 by using sodium acetate buffer. It was found that 1.0 ml of 0.02% MDTC was sufficient to chelate 500 ppb of Co(II), Ni(II) and Pd(II) ions. The composition of metal chelates was investigated by changing the metal:ligand mole ratio spectrophotometrically, which was found 1:2 for these metal ions. It is in accordance with literature [13]. The absorption spectra for metal complexes are shown in Fig. 1.

3.2. Effect of NaCl concentration on sorption

The salt was added to the sample during extraction to reduce the solubility of metal complexes in solution. Addition of salt favors the extraction of analyte in some cases. Increase in amount of salt increased the separation and sorption of metal complexes on SPME fiber. The effect was studied by varying the amount of salt from 10 to 40%. The concentration of NaCl was optimized to 30% as maximum sorption was obtained at this concentration (Fig. 2A).

3.3. Effect of sorption time

Sorption efficiency depends upon the distribution constant between the fiber and the solution, thickness of fiber, and diffusion coefficient of analyte. The extraction time was optimized for metal ion complexes by changing the exposure time of fiber to solution of metal complexes. With the increase in extraction time, sorption of metal complexes increased up to 30 min. Therefore, 30 min sorption provides optimum time for maximum efficiency (Fig. 2B).

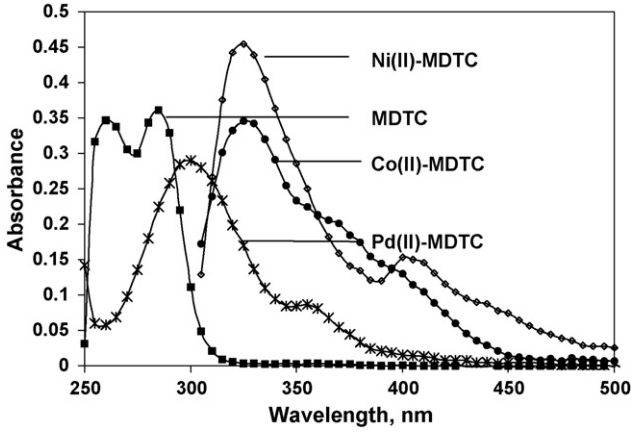

Fig. 1. Absorption spectra of (a) MDTC, (b) Co(II)–MDTC complex, (c) Ni(II)–MDTC complex, and (d) Pd(II)–MDTC complexes. [Co(II) = ,0.1 μg ml^{-1}, Ni(II) = 0.1 μg ml^{-1}, Pd = 0.1 μg ml^{-1}, MDTC = 1 ml of 0.1 %, pH 6.0].

3.4. Effect of stirring

Effect of stirring was studied by using magnetic stirrer. The solution was stirred at constant rate of 1200 rpm during sorption on fiber. It was observed that extracting efficiency is very low in the absence of rapid stirring. Without stirring poor repro-

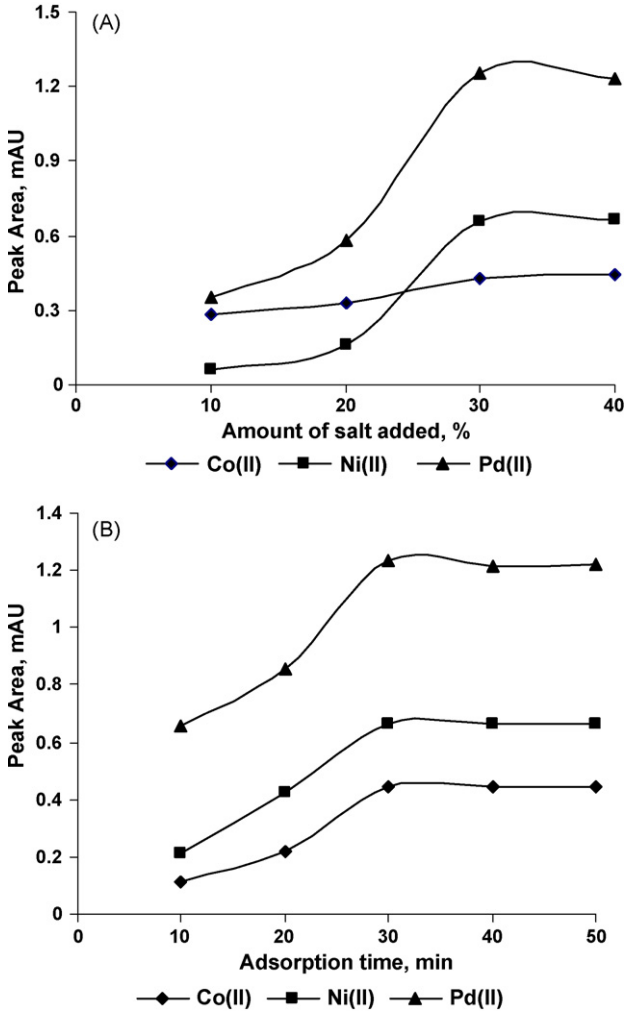

Fig. 2. (A) Effect of salt concentration on the sorption of metal complexes at 10, 20, 30 and 40% NaCl. (B) Sorption time profiles at 10, 50, 100, 250 and 500 min [Co(II), Ni(II) and Pd(II); 20 ng ml^{-1}, 1 ml of 0.02% MDTC, 30 min sorption on PDMS fiber, 15 min desorption, acetonitrile:water (60:40) at a flow rate of 0.8 ml/min, detection at 310 nm].

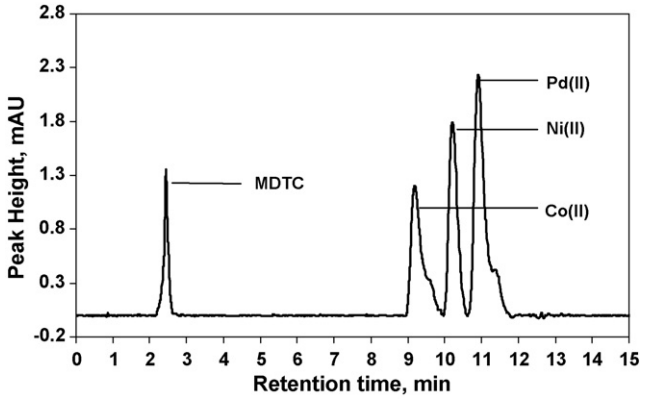

Fig. 3. SPME–HPLC chromatogram for mixture of metal complexes containing Co(II), Ni(II) and Pd(II), each at 20 ng ml^{-1}, 0.5 ml of 0.02% MDTC, 30% NaCl, 30 min sorption on PDMS fiber, 15 min desorption, acetonitrile:water (60:40) at flow rate of 0.8 ml/min and detection at 310 nm.

ducibility was observed. Therefore, constant and rapid stirring of solution was done for sorption of metal complexes.

3.5. Chromatographic conditions

The separation of Co(II)–MDTC, Ni(II)–MDTC and Pd(II)–MDTC complexes was performed by using C_{18} column. The composition of acetonitrile was varied from 95 to 60% (v/v) with water to optimize the separation of metal complexes. The use of 60% acetonitrile composition provided a fast separation with sufficient resolution. The flow rate was selected by studying the effect of variation of flow from 0.8 to 1.0 ml/min. A sufficient separation was observed at a flow rate of 1.0 ml/min but column pressure was high. To reduce the column pressure, flow rate was decreased to 0.8 ml/min by using a mobile phase with acetonitrile:water (60:40) composition. A chromatogram showing the separation of Co(II), Ni(II) and Pd(II) complexes with MDTC is shown in Fig. 3.

4. Method performances

4.1. Preparation of SPME calibration curves

The optimized conditions established above were then used to prepare calibration curves for these three analytes spiked at 10, 50, 100, 250 and 500 ng ml^{-1} using PDMS fiber. The calibration curves were linear over this range. The characteristics of calibration curves are given in Table 1. The detection limit for different metal ions was calculated by using S/N ratio equal to 3.

4.2. Accuracy, repeatability and detection limits

The method detection limits were calculated for the metal complexes according to published guidelines, as three times the standard deviation. Similarly, the method quantification limits can be estimated as 10 times the standard deviation. The accuracy (% recovery) and precision (%R.S.D.) of SPME–HPLC–UV method was evaluated for each analyte by analyzing a standard of known concentration (50 ng ml^{-1}) five times, and quantifying it using calibration curves established above. The results for detection limit and relative standard deviation are given in Table 1. The relative standard deviation in retention time found up to 0.5. The method gave satisfactory results when used to quantify metal ions in alloys.

4.3. Interference

The interference from various metal ions such as Mo(VI), V(V), Ag(I), Sn(IV), Cd(II), Zn(II), Cr(III), Pb(II) and Cu(II) was studied. The Zn(II), Ag(I) and Sn(II) did not interfere as no complex was observed for these metal complexes. It is due to unstability of metal complexes and is in agreement with the literature [14,15]. Cr(III) forms complex on heating at a temperature of 60 °C with dithiocarbamate [16]. Cu(II) forms a complex which can be separated from these metal complexes at a different retention time. It was observed that Mo(VI) and V(V) form complex at very low pH. Small amounts of Fe(II) showed disturbances in the baseline. The complexes of Cd(II) and Pb(II) show poor peak shapes and form unstable complexes with dithiocarbamates which decompose during separation [17–19].

5. Application to alloys and drinking water

This method was applied to drinking water (Fig. 4) and a number of alloys such as Borcher alloy, palladium–cobalt alloy, Oakay alloy and Eligloy (Fig. 5). About 0.1 g of each of alloy was taken and dissolved in aqua regia. Solution was heated to near dryness and nitrate was expelled from residue by conc. HCl acid. Residue was dissolved in triple distilled water and volume was made up to 500 ml. An appropriate aliquot of solution was studied for Co(II), Ni(II) and Pd(II) determination by same procedure given above. Results are shown in Table 2. Amounts of metals were calculated from the regression equation obtained from calibration curve. On

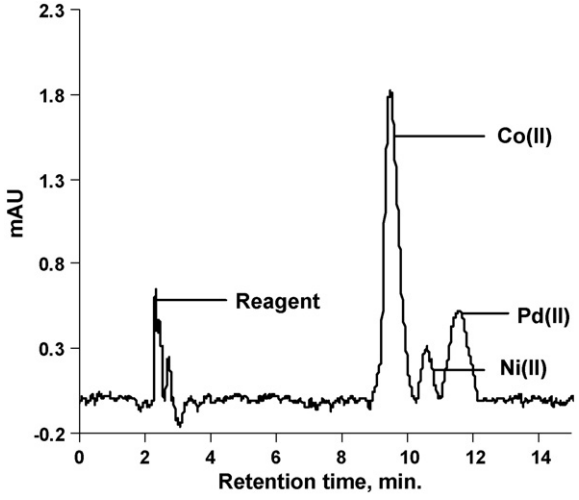

Fig. 4. SPME–HPLC chromatogram for water sample containing Co(II), Ni(II) and Pd(II), each at 30, 5 and 5 ng ml^{-1}, respectively, at same conditions as given in Fig. 3.

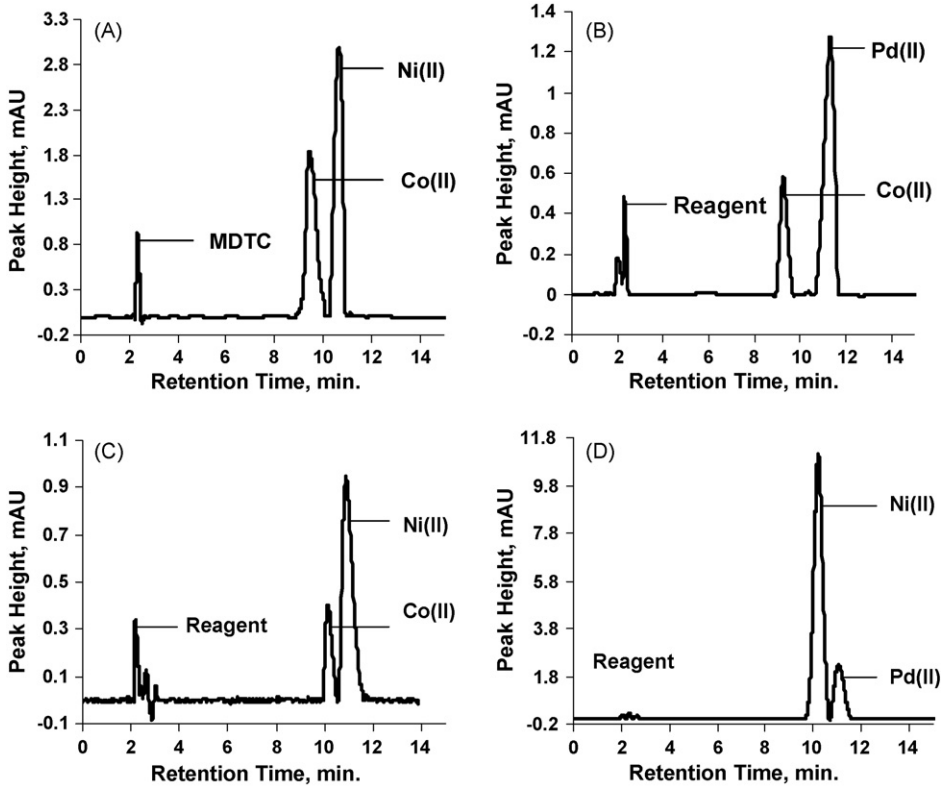

Fig. 5. SPME–HPLC chromatogram for alloy samples, (A) Borcher alloy, (B) palladium–cobalt alloy, (C) Eligloy and (D) Oakay alloy.

Table 2
Determination of Co(II), Ni(II) and Pd(II) in different alloys and water sample

Alloy and composition	Co(II) (ng ml^{-1})		Ni(II) (ng ml^{-1})		Pd(II) (ng ml^{-1})		Recovery (%)		
	Present	Found	Present	Found	Present	Found	Co(II)	Ni(II)	Pd(II)
Borcher alloy: Cr = 30%, Ni = 35%, Co = 35%	35	30.65	35	33.49	–	–	87.57	95.68	
Palladium–cobalt alloy: Pd = 50%, Co = 50%	10	9.74			10	9.39	97.40		93.9
Oakay alloy: Pd = 10%, Ni = 60%, Pt = 20%, V = 9.5%	–	–	120.0	120.4	20.0	19.66		100.3	98.3
Eligloy: Mo = 7%, Cr = 20%, Ni = 40%, Co = 15%, Fe = 15%, Mn = 2%, Be = 0.05%, C = 0.015%	4.0	4.14	10.0	10.50	-	-	103.5	105.0	
Drinking water sample: [a]Co(II) = 30 ppb, [a]Pd(II) = 5 ppb, [a]Ni(II) = 5 ppb	30	29.5	5.00	3.95	5	4.48	98.33	79.0	89.6

the basis of calculated value and actual value of metals in alloys, recoveries were calculated. These were found more than 80%. The drinking water was spiked with 30 ng ml^{-1} of Co(II) and 5 ng ml^{-1} of Ni(II) and Pd(II) metals. Similar procedure was applied and amounts of metal ions were calculated.

6. Conclusion

SPME is demonstrated to be a simple, rapid convenient and an efficient tool for the determination of metal ions after complex formation for the first time. The separation of Co(II), Ni(II) and Pd(II) as MDTC complex by using SPME as preconcentration technique is simple, fast and reproducible. The detection limits for the method are found to be in the range of ppb levels for the metal ions, which are approximately 10 times better than HPLC methods using LLE as sampling technique. The sensitivity, precision and accuracy of SPME are proved to be satisfactory. Because of the need to detect trace levels of metal ions in drinking water, the present method can be used for such purposes. SPME–HPLC–UV system represents an integrated approach capable of precon-

centration and sensitive direct determination of metal ions in alloys.

Acknowledgements

We are thankful to UGC, New Delhi for providing financial support and S. Swaran Singh Boparai, Honorable Vice-chancellor, Punjabi University, Patiala for providing the partial grant for the purchase of HPLC–UV system.

References

[1] M.R. Spivey Fox, R.M. Jacobs, Metal ions in biological systems—concepts of metal ion toxicity, vol. 20, Helmut Sigel, CRC Press.
[2] P. WardenbachSustainable, Metals Management, Toxic Effects of Metals and Metal Compounds, 19, Springer, Netherlands, 2006, pp. 393–402.
[3] A. Beni, R. Karosi, J. Posta, Microchem. J. 85 (2007) 103–108.
[4] N.H. Chung, M. Tabata, Hydrometallurgy 73 (2004) 81–89.
[5] V. Camel, Spectrochim. Acta, Part B 58 (2003) 1177–1233.
[6] C.L. Arthur, J. Pawliszyn, Anal. Chem. 62 (1990) 2145–2148.
[7] J. Pawliszyn, Solid Phase Microextraction-A Practical Guide, CRC Press, 1999.
[8] Z. Zhang, M.J. Yang, J. Pawliszyn, Anal. Chem. 66 (1994) 844–851.
[9] S. Mishra, R.M. Tripathi, S. Bhalke, V.K. Shukla, V.D. Puranik, Anal. Chim. Acta 551 (2005) 192–198.
[10] A.K. Malik, V. Kaur, N. Verma, Talanta 68 (2006) 842–849.
[11] V. Kaur, A.K. Malik, N. Verma, J. Sep. Sci. 29 (2006) 333–345.
[12] G. Macrotrigiano, G.C. Pellacani, C. Preti, G. Tosi, Bull. Chem. Soc., Jpn. 48 (1975) 1018–1020.
[13] S.R. Hutichns, P.R. Hadded, S. Dilli, J. Chromatogr. A 252 (1982) 185–192.
[14] M. Sarwar, S. Ahmad, S. Ahmad, S. Ali, S.A. Awan, Transition metal chemistry 32 (2007) 199–203.
[15] S. Dilli, P. Tong, Anal. Chim. Acta. 395 (1999) 101.
[16] J.S. Wang, K. Chiu, Anal. Sci. 20 (2004) 841–846.
[17] A.M. Bond, G.G. Wallace, Anal. Chem. 56 (1984) 2085–2090.
[18] S. Ichinoki, M. Yamazaki, Anal. Chem. 57 (1985) 2219–2222.
[19] R.M. Smith, A.M. Butt, A. Thakur, Analyst 110 (1985) 35–37.

Available online at www.sciencedirect.com
ScienceDirect
Talanta 73 (2007) 466–470
Talanta
www.elsevier.com/locate/talanta

A rapid method for detection of cell adhesion molecules (CAMs) on human umbilical vein endothelial cells (HUVECs)

Saroj Kumar [a], Laboni Ghosh [b], Sarvesh Kumar [a], Balaram Ghosh [a], Pradip Nahar [a,*]

[a] *Institute of Genomics and Integrative Biology (CSIR), Mall Road, Delhi 110007, India*
[b] *University of Iowa, Iowa City, IA, USA*

Received 18 January 2007; received in revised form 10 April 2007; accepted 10 April 2007
Available online 24 April 2007

Abstract

Detection of cell surface proteins is widely used as molecular markers for initiation, progression and severity of many diseases. In particular, detection of cell adhesion molecules (CAMs) on endothelial cells is important as it indicates the extent of inflammation associated with several diseases including arthritis, asthma, tumor metastasis, etc. Here, we report, a rapid method for detection of CAMs on endothelial cells by covalently immobilizing TNF-α induced cells on a photoactivated polystyrene microtiter plate at 50 °C in 45 min followed by performing enzyme-linked immunosorbent assay (ELISA) technique at elevated temperature. Our method reduced the time of cell-ELISA to 3 h with results akin to conventional cell-ELISA carried out in 38 h. The method thus described herein could be potentially useful in clinical and research laboratories for rapid detection of cell surface proteins including CAMs on intact cell samples.

Keywords: Activated surface; Cell immobilization; Heat-mediated cell-ELISA; Cell-HELISA; Cell adhesion molecules

1. Introduction

The detection of cell surface proteins is widely used as molecular markers for initiation, progression and severity of many diseases [1,2]. For example, the expression of cell adhesion molecules (CAMs), such as intercellular cell adhesion molecule-1 (ICAM-1), vascular cell adhesion molecule-1 (VCAM-1) and E-selectin, on endothelial cells is used as markers for severity in several inflammatory diseases, such as arthritis, asthma, multiple sclerosis, tumor metastasis [3–7]. VCAM-1 expression on the surface of activated endothelial cells is used as a marker for atherosclerosis progression and severity in humans [8]. Activated leukocyte cell adhesion molecule (ALCAM) (CD166) expression is associated with melanoma progression [9]. For the detection of cell surface CAMs, most of the laboratories use cell-ELISA, flowcytometry, immunohistochemistry or In situ hybridization [10,11]. Most of these techniques are time consuming and require sophisticated instruments. As cell-ELISA does not require sophisticated instruments, it is the method of choice in most of the laboratories for the detection of CAMs.

Cell adhesion molecules are expressed in soluble as well as in intact form on the cell surface. Depending on their expression pattern, different types of methods are used to measure these molecules. The assays for measuring soluble cell adhesion molecules were well documented by Meager et al. [12]. However, the CAMs which are expressed on the surface of cells are usually measured by cell-ELISA, which is usually carried out by adhering cells on a gelatinized microtiter plate for around 16 h followed by induction with TNF-α for 16 h. Cells were then crosslinked through glutaraldehyde before proceeding for conventional cell-ELISA [13,14]. Thus, conventional cell-ELISA needs anywhere from 38 to 48 h. Therefore, there is a need to develop a rapid cell-ELISA for the detection of cell surface protein present on the intact cells.

Earlier, we developed a rapid method of detecting soluble proteins covalently bound in a well of an activated microtiter plate [15]. In this communication, we report a rapid method of

Abbreviations: ICAM-1, intercellular adhesion molecule-1; VCAM-1, vascular cell adhesion molecule-1; BSA, bovine serum albumin; FNAB, 1-fluoro-2-nitro-4-azidobenzene; HUVECs, human umbilical vein endothelial cells; HELISA, heat-mediated enzyme-linked immunosorbent assay; cell-HELISA, heat-mediated cell-ELISA; EC, endothelial cell; OPD, *o*-phenylenediamine dihydrochloride

* Corresponding author. Tel.: +91 11 27667439; fax: +91 11 27667471.
E-mail address: pnahar@igib.res.in (P. Nahar).

0039-9140/$ – see front matter © 2007 Elsevier B.V. All rights reserved.
doi:10.1016/j.talanta.2007.04.016

cell-ELISA by covalently immobilizing the endothelial cells in a microtiter plate at 50 °C. The covalently immobilized cell is then used for cell-ELISA at elevated temperature (cell-HELISA). The procedure takes less than 3 h in comparison to 38 h by conventional cell-ELISA procedure. This rapid cell-HELISA procedure may find a broad range of applications for detecting cell surface proteins in different areas of research including diagnostics.

2. Materials and methods

2.1. Materials

Bovine serum albumin (BSA), human anti-ICAM-1, human anti-VCAM-1, human anti-E-selectin, anti-mouse IgG-HRP conjugate, L-glutamine, antibiotic and antimycotic solution, endothelial cell growth factor, trypsin, pucks saline, HEPES and *o*-phenylenediamine dihydrochloride (OPD) were purchased from Sigma (USA). Fetal calf serum was purchased from Biological Industries, Israel. All other chemicals used were of analytical grade. Nunc maxisorp microtiter plates were purchased from Nunc, USA.

1-Fluoro-2-nitro-4-azidobenzene (FNAB) is a heterobifunctional photolinker. It was prepared from 4-fluoro-3-nitro aniline by a simple diazotization reaction [16]. Polystyrene microtiter plates were activated by reacting the polystyrene surface with FNAB, as described by Nahar et al. [17]. In all cell-ELISA experiments at elevated temperature, these activated polystyrene microtiter plates were used.

2.2. Cells and cell culture

Endothelial cells were isolated from umbilical cord using mild trypsinization [14]. The endothelial cells were grown in M-199 medium supplemented with 20% heat inactivated fetal calf serum, 2 mM L-glutamine, 100 units/ml penicillin, 100 μg/ml streptomycin, 0.25 μg/ml amphotericin, endothelial cell growth factor (10 μg/ml) in 5% CO_2 and 95% humidified water jacketed incubator. The purity of the cells was checked by E-selectin expression upon TNF-α induction [18].

A549 cells were grown in DMEM with glutamine and 1 g/l glucose supplemented with 10% heat inactivated FCS and 3.7 g/l $NaHCO_3$.

2.3. Induction of cells for conventional and heat-mediated cell-ELISA (cell-HELISA)

For conventional cell-ELISA, human umbilical cord vein endothelial cells (HUVECs) were plated onto gelatinized 96-well plates (2×10^4 cells/well) and allowed to adhere for 16 h. Cells were then induced with TNF-α (10 ng/ml) for 16 h for the expression of ICAM-1.

For cell-HELISA, endothelial cells were induced with TNF-α in the culture flask itself overnight and the cells were collected in PBS after mild trypsinization. These induced cells were used for cell-HELISA in the successive experiments. Control experiments in both the cases were carried out with uninduced cells.

2.4. Effect of temperature and time for covalent and non-covalent binding of cells on cell-ELISA

TNF-α induced cells (30,000 cells/well) were loaded into the treated and untreated wells of polystyrene microtiter plates and incubated for 45 min at 30, 40, 50, 60 and 70 °C, respectively, in a routine laboratory incubator. For optimization of time, cells were incubated for 35, 40, 45, 50 and 60 min, respectively, at 50 °C. After incubation, wells of a microtiter plate were thoroughly washed and kept for blocking the non-specific binding in 2% BSA at 40 °C for 40 min. Cells were incubated with anti-human ICAM-1 mAb (1:4000 dilution in blocking buffer) for 45 min at 50 °C. After washing, cells were incubated with HRP-conjugated goat anti-mouse secondary antibody (1:1000) at 50 °C for 40 min. The cells were exposed with substrate-dye buffer (*o*-phenylenediamine dihydrochloride 40 mg/100 ml in citrate phosphate buffer, pH 5, H_2O_2 0.03%). After 5 min, 20 μl of stop solution (2N H_2SO_4) was added to each well and absorbance was recorded at 490 nm in an automated microplate reader (Spectramax 190, Molecular Devices, USA). Control experiment was carried out similarly with uninduced cells.

2.5. Optimization of number of cells required for their covalent binding onto the treated and untreated well of a Nunc maxisorp plate

Different number of TNF-α induced cells (10,000, 20,000, 30,000, 40,000 and 50,000 cells/well) were loaded into wells of the treated and untreated polystyrene microtiter plates and incubated for 45 min at 50 °C. Control experiment was carried out simultaneously with uninduced endothelial cells. The efficacy of binding was checked by carrying out subsequent ELISA steps as described in Section 2.4.

2.6. Estimation of expression of ICAM-I, VCAM-I and E-selectin by heat-mediated cell-ELISA

TNF-α induced cells were loaded (30,000 cells/well) into the treated wells of polystyrene microtiter plates and incubated at 50 °C for 45 min. After, washing nonspecific binding was blocked with 2% BSA (200 μl/well) by incubating at 40 °C for 40 min followed by washing with PBS. Plates were incubated at 50 °C for 45 min, with anti-human ICAM-1 mAb, VCAM-1 mAb or E-selectin mAb (1:4000, 1:500 and 1:1000 diluted in blocking buffer), respectively, and washed seven times with PBS. The cells were further incubated with peroxidase-conjugated goat anti-mouse secondary antibody (1:1000 dilution in blocking buffer) for 45 min at 50 °C. After washing peroxidase substrate was added and absorbance was recorded as in Section 2.4. Control experiment was carried out similarly with uninduced cells.

2.7. Comparative studies on heat-mediated cell-ELISA (HELISA) and conventional cell-ELISA (38 and 25 h)

Expression of ICAM-I was determined by heat-mediated cell-ELISA as described in Section 2.6. The conventional cell-

ELISA was performed as described earlier [14]. Briefly, cells were adherered to the untreated nunc maxisorp plate for 16 h as described in Section 2.3 and crosslinked with 1.0% glutaraldehyde at 4 °C for 20 min. Non-specific binding of antibody was blocked by 2% BSA at 37 °C for 3 h. Binding of anti ICAM-1 (1:4000) were carried out at 4 °C for 16 h followed by peroxidase-conjugated antibody binding at 37 °C for 3 h. The cells were again washed with PBS and peroxidase was assayed as in Section 2.4. Twenty-five hour conventional cell-ELISA was performed similarly as conventional procedure (38 h) except that antibody binding was carried out at 37 °C for 3 h instead of 16 h as in conventional cell-ELISA.

2.8. Sensitivity of cell-HELISA in presence of an inhibitor

Curcumin was used as a known cell adhesion molecules inhibitor for studying the sensitivity of cell-HELISA [18]. The expression of ICAM-I was determined by cell-HELISA in curcumin treated epithelial cells (A549). In brief, cells were pretreated with different concentrations of curcumin for 2 h, then induced with TNF-α (10 ng/ml) for 16 h. Expression of ICAM-1 was estimated as mentioned in Section 2.6 and results were compared with conventional cell-ELISA.

2.9. Statistical analysis

All the statistical analysis was performed using software Microcal Origin (ver 3.0; Microcal Software Inc., Northampton, MA). Results are given as mean ± S.D. from three independent experiments. Differences were considered statistically significant for $P < 0.05$ by using independent two-tailed Student's *t*-test. All the experiments were carried out in triplicates.

3. Results and discussion

In conventional cell-ELISA, the cells were not attached to the surface either directly or indirectly through a covalent linkage. In this study, we are binding the cells by a covalent linkage onto an activated microtiter plate which are either commercially available or can be prepared by different methods. Cells were covalently bound onto the treated microtiter plate after the expression of ICAM-1 to avoid undesirable reaction of the activated group of the treated surface by the amino group of the proteins present in the media.

Nunc maxisorp microtiter plates were activated by a photochemical reaction using a heterobifunctional photolinker, FNAB [17]. Photolinker coated plate when exposed to UV light at 365 nm for 10 min, generates highly reactive nitrene which binds to the polystyrene plate through insertion reaction leaving active fluoro group intact. It is likely that the cell is immobilized by the displacement of the fluoro group of the treated plate by the incoming amino group of the expressed protein.

Immobilization of cells was carried out at different temperature and time to find out the optimum conditions at which best immobilization occurred. Fig. 1 showed that the absorbance value was increased upto 50 °C beyond which it started decreasing. Decrease in absorbance value at higher temperature is likely due to thermal injury on the biomolecule. Untreated surface where immobilization occurred through adsorption showed two-fold less binding than the treated surface. This was expected as adsorption is a slow process and needs more time to bind. Control experiment with uninduced cells showed negligible binding, indicating the absence of non-specific binding.

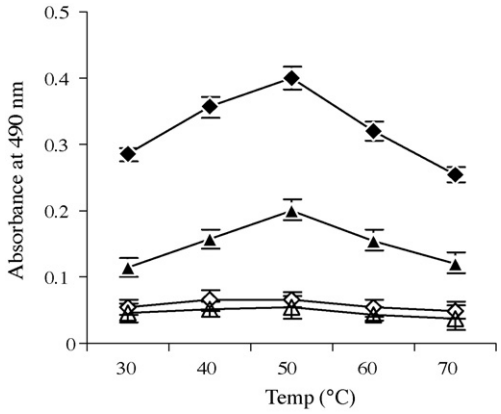

Fig. 1. Effect of temperature on immobilization of cells. Uninduced (hollow symbol) and TNF-α induced (dark symbols) cells were immobilized onto the treated (♦, ◊) and untreated (▲, △) microtiter plates by incubating for 45 min at 30, 40, 50, 60 and 70 °C, respectively. Expression of ICAM-1 was detected as described in Section 2.4.

The optimum time for immobilization of cells at 50 °C was shown in Fig. 2. Here, the absorbance value increased till 45 min onto the treated surface, after which it decreased, indicating the optimum time for immobilization. Thus, the best cell immobilization on a treated surface occurs at 50 °C in 45 min. Induced cells showed around seven times greater absorbance compared to the uninduced cells (control experiment).

In cell-HELISA it was necessary to find out whether more number of cells is required for rapid binding onto the activated microtiter plate. When the experiment was carried out by varying the amount of cells, it was found that 30,000 cells per well was optimum for binding to the wells beyond which no appreciable binding was observed. Requirement of cells to immobilize

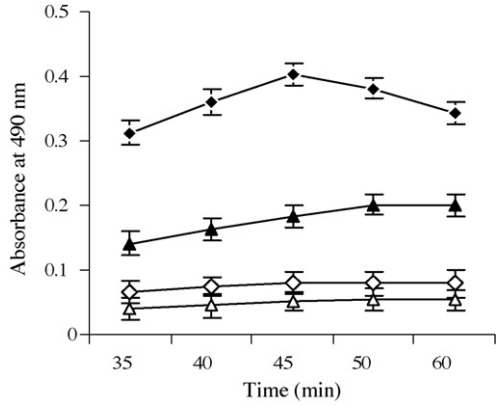

Fig. 2. Optimization of time for covalent attachment of cells. Uninduced (hollow symbol) and TNF-α induced (dark symbols) cells were immobilized onto the treated (♦, ◊) and untreated (▲, △) microtiter plates by incubating at 50 °C for 35, 40, 45, 50 and 60 min, respectively. Expression of ICAM-1 was detected as described in Section 2.4.

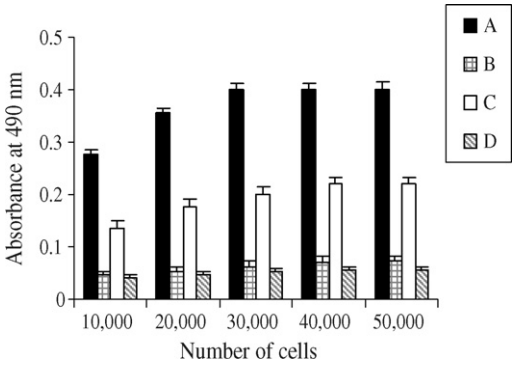

Fig. 3. Number of cells required for optimum immobilization. Different number (10,000, 20,000, 30,000, 40,000 and 50,000) of TNF-α induced cells were immobilized onto the treated (A) and untreated (C) microtiter plates at 50 °C for 45 min. Expression of ICAM-1 was detected by carrying out ELISA as described in Section 2.5. Control ELISA was carried out without induction onto the treated (B) and untreated (D) microtiter plates.

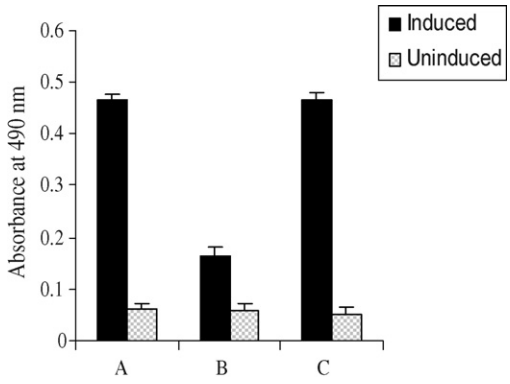

Fig. 5. Comparative studies of conventional cell-ELISA, conventional cell-ELISA in reduced time and cell-HELISA. Cell attachment, blocking, primary antibody binding and conjugate binding were carried out by conventional cell-ELISA in 38 h (A), conventional cell-ELISA in 25 h (B) and cell-HELISA in 3 h (C) in different conditions: (A) 16 h/4 °C, 3 h/37 °C, 16 h/4 °C and 3 h/37 °C, respectively. (B) 16 h/37 °C, 3 h/37 °C, 3 h/37 °C and 3 h/37 °C, respectively. (C) 45 min/50 °C, 40 min/40 °C, 45 min/50 °C and 45 min/50 °C, respectively.

in the experiment is similar to conventional cell-ELISA. Rapidity of binding in this case does not require higher no of cells (Fig. 3).

Further steps of cell-HELISA such as blocking, antibody (ICAM-1) binding and HRP-conjugated secondary antibody binding were also carried out by optimizing time and temperature for each step (experiments and results were not shown). The optimized conditions were found as 45 min/50 °C for antigen binding, 40 min/40 °C for blocking, 45 min/50 °C for antibody binding, and 45 min/50 °C for conjugate binding, respectively. Thus, cell surface protein such as ICAM-1, VCAM-1 and E-selectin were detected by immobilizing the cells onto the treated microtiter plates followed by carrying out the ELISA steps rapidly in the optimized conditions. The induced cells showed more than six- to seven-fold higher absorbance than uninduced cells (Fig. 4).

Further, cells attached to untreated microtiter plate through gelatin followed by gluteraldehyde cross-linking as in conventional procedure could not be used for cell-ELISA at elevated temperature as it failed to give substantial ELISA value (results not shown). This most probably happened due to leaching of gelatin along with cells at higher temperature (50 °C) as the cells were not covalently bound to the plate either directly or indirectly (through gelatin) in conventional cell-ELISA.

Finally, we have compared heat-mediated cell-ELISA with that of conventional cell-ELISA. Cell-ELISA carried out in 3 h showed ELISA value akin to that of the convention cell-ELISA carried out in 38 h. We have also tried to reduce the time for conventional cell-ELISA. Reduction in time either for attachment of cells to gelatinized microtiter plate or for antibody binding steps failed to give similar absorbance value as that of 38 h conventional cell-ELISA. In fact, reduction in time to 25 h in conventional cell-ELISA gave around 2.5-fold decrease in ELISA reading (Fig. 5).

Sensitivity of cell-HELISA was also checked in the presence of a known cell adhesion molecules inhibitor, curcumin [18]. Fig. 6 showed that cell-HELISA can effectively differentiates the levels of ICAM-1 expression in presence of curcumin. The results were akin to that of conventional cell-ELISA. The experiment was carried out using A549, lung epithelial cells to show the versatility of the present method. The results further support that cell-HELISA is not limited to endothelial cells but can also

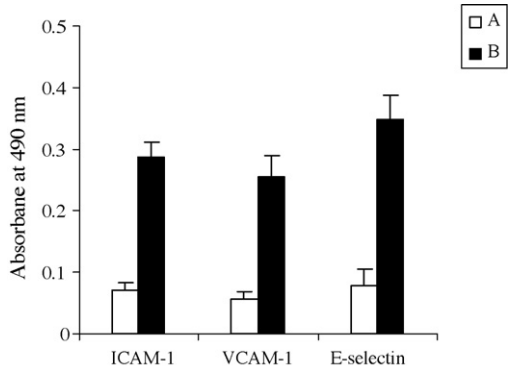

Fig. 4. Detection of ICAM-1, VCAM-1 and E-selectin on TNF-α induced HUVECs. CAMs were detected before (A) and after (B) TNF-α induction by cell-HELISA as described in Section 2.6.

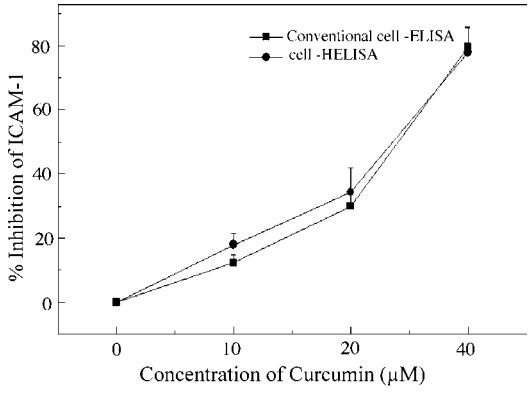

Fig. 6. Sensitivity of cell-HELISA in presence of an inhibitor. Different concentrations of curcumin were used before the TNF-α induction and ICAM-1 expression was determined by conventional and heat-mediated cell-ELISA.

be used to detect the expression of cell adhesion molecules on other cell type like epithelial cells.

4. Conclusion

Covalently immobilized cells enhance cell-ELISA onto a photoactivated polystyrene microtiter plate at elevated temperature. Thus, cell adhesion molecules, ICAM-1, VCAM-1 and E-selectin were detected by cell-HELISA in less time 3 h compare to that of conventional cell-ELISA carried out in 38 h. The procedure has potential applications in many studies involving detection of cell surface protein in various clinical as well as research laboratories.

Acknowledgements

The authors thank Professor S.K. Brahmachari, Director IGIB, for his constant support during the work. L.G. thanks Director IGIB for allowing her to carry out the work in IGIB. This work is a part of OLP 0009 (CSIR) and SMM0006 (CSIR) programs.

References

[1] Y. Ohene-Abuakwa, M. Pignatell, Int. J. Surg. Path. 8 (2000) 191–200.
[2] D.A. Blann, M.P. Ridker, H.Y.G. Lip, J. Am. Heart Assoc. 33 (2002) 2141–2143.
[3] T. Nubel, W. Dippold, B. Kaina, G. Fritz, Carcinogen 25 (2004) 1335–1344.
[4] M. Sasaki, D. Ostanin, J.W. Elrod, T. Oshima, P. Jordan, M. Itoh, T. Joh, A. Minagar, J.S. Alexander, Am. J. Physiol. Cell Physiol. 284 (2003) 422–428.
[5] T.A. Springer, Cell 76 (1994) 301–314.
[6] A. Mantovani, F. Bussolino, M. Introna, Immunol. Today 18 (1997) 231–240.
[7] A. Meager, Cytokine Growth Factor Rev. 10 (1999) 27–39.
[8] K. Ley, Y. Huo, J. Clin. Invest. 107 (2001) 1209–1210.
[9] J.A. King, S.F. Ofori-Acquah, T. Stevens, A.B. Al-Mehdi, O. Fodstad, W.G. Jiang, Breast Cancer Res. 6 (2004) 478–487.
[10] A.M. Khorshid, N.A.E. Wahab, H. Gaballa, N.M. Kholoussi, S.A.M. Farrag, O.K.E. Gebally, Egypt. Med. J. N. R. C. 5 (2004) 213–236.
[11] J.W. Rice, J.E. Davis, R.M. Crowl, P.A. Johnston, Anal. Biochem. 241 (1996) 254–259.
[12] A. Meager, C. Bird, A. Mire-Sluis, J. Immunol. Methods 191 (1996) 97–112.
[13] K.E. Foreman, A.A. Vaproyan, B.K. Bonish, M.L. Jones, K.J. Johnson, M.M. Glovsky, S.M. Eddy, P.A. Ward, J. Clin. Invest. 95 (1994) 1147–1155.
[14] S. Kumar, P. Arya, B.K. Singh, N. Singh, V.S. Parmar, A.K. Prasad, B. Ghosh, Biochemistry 44 (2005) 15944–15952.
[15] U. Bora, K. Kannan, P. Nahar, J. Immunol. Methods 293 (2004) 43–50.
[16] A. Naqvi, P. Nahar, Anal. Biochem. 327 (2004) 68–73.
[17] P. Nahar, N.M. Wali, R.P. Gandhi, Anal. Biochem. 294 (2001) 148–153.
[18] B. Gupta, B. Ghosh, Int. J. Immunopharmacol. 21 (1999) 745–757.

Available online at www.sciencedirect.com
ScienceDirect
Talanta 73 (2007) 444–450
Talanta
www.elsevier.com/locate/talanta

Studies on the interaction between antibiotics and DNA

Xiaoquan Lu *, Lan Wang, Hongde Liu, Rui Wang, Jing Chen

College of Chemistry and Chemical Engineering, Northwest Normal University, Lanzhou 730070, China

Received 17 December 2006; received in revised form 9 April 2007; accepted 9 April 2007
Available online 21 April 2007

Abstract

In this paper, 24 parameters (descriptors) that can influence the interaction of selected antibiotic compound (antibiotics) and DNA have been investigated. Principal components analysis (PCA) and hierarchical cluster analysis (HCA) were employed in order to reduce dimensionality and investigate which subset of variables could be more effective for classifying the antibiotics according to their binding mode with DNA. Results of the PCA and HCA study showed that there are 12 descriptors closely related to the interaction. Based on these descriptors, multiple linear regression (MLR) and artificial neutral network (ANN) allowed us to propose three models which can predict binding constant and binding mode. For the prediction of binding constant, the minimal relative error is only 0.17% (MLR) and 0.72% (ANN); for the prediction of binding mode (ANN), five test molecules are all consistent with experimental results.

Keywords: Drug–DNA interactions; MLR; PCA; HCA; ANN

1. Introduction

DNA plays a major role in the life process because it carries heritage information and instructs the biological synthesis of proteins and enzyme through the process of replication and transcription of genetic information. Recognition and exploration of duplex DNA through molecules is a promising approach to developing novel reagents which can recognize sites and probe the structure and function of nucleic acid. Moreover, an understanding of how molecules bind to DNA would be potentially useful in the design of new drugs, therapy and genetic diseases, etc. [1,2].

Many anticancer, antibiotic, and antiviral drugs exert their primary biological effects by reversibly interacting with nucleic acids. Therefore, these biomolecules represent a major target in drug development strategies designed to produce next generation therapeutics for diseases such as cancer [3]. Researchers have made a great progress in exploring the interaction between these series drugs and DNA [4–6]. Up to now, a variety of analytic techniques such as fluorescence spectroscopy [7,8], ultraviolet-visible spectroscopy [9,10], capillary electrophoresis [11] and electrochemical techniques [12] have been developed for the identification and characterization of interactions between them. It was found that there are two principal modes by which drugs can bind noncovalently to DNA: intercalation and groove binding. Typically intercalating drugs possess flat, heteroaromatic ring systems that can insert between two adjacent base pairs in a helix. The complex is stabilized by π–π stacking interactions between the drug molecule and the DNA bases that surround it. For the minor groove binder, these drugs are typically composed of several aromatic rings such as pyrrole, furan, or benzene that are connected by bonds possessing torsional freedom [13]. Minor groove drugs generally adopt a characteristic curved shape that is isohelical with the target groove. The resulting DNA–drug complex is stabilized by a number of noncovalent interactions such as Van der Waals interactions, hydrophobic forces, and hydrogen bonds. However there are still some problems in this field. First, it is difficult to find the influencing factors from the structure of molecules. Second, for batches of unknown molecules, it is difficult to predict the interaction from the experimental results.

In this paper, based on molecular structure data and experimental results, multivariate analysis and artificial neural network were applied to study the following problems: (1) what factors can influence the interaction between DNA and antibiotics? (2)

* Corresponding author. Tel.: +86 931 7971276; fax: +86 931 7971276.
E-mail address: luxq@nwnu.edu.cn (X. Lu).

0039-9140/$ – see front matter © 2007 Elsevier B.V. All rights reserved.
doi:10.1016/j.talanta.2007.04.006

Table 1
The reported and predicted binding constant and mode

Number	Antibiotics	Reported and predicted binding constant	Reported binding mode	ANN mode training values	References
A1	NOM	5.6469	(3)	1.5000	[14]
A2	DAM	5.3711	(1)	0.5000	[14]
A3	ADM	5.2529	(1)	0.5001	[14]
A4	DADM	4.9370	(1)	0.5010	[14]
A5	2,7-DAM	4.5955	(3)	1.5000	[15]
A6	Ethidum bromide	5.0414	(1)	0.4996	[16]
A7	Netropsin	6.3874	(2)	1.0000	[17]
A8	Distamycin	8.6628	(2)	**1.0830**	[17]
A9	Hoechst 33258	8.3424	(2)	**1.0450**	[13]
A10	DNR	8.4000	(1)	**0.5015**	[18]
A11	WP776	6.6000	(1)	**0.4969**	[18]
A12	WP756	5.9000	(1)	**0.5150**	[18]
A13	WP758	7.2000	(1)	0.4995	[18]
A14	Mitoxantrone	9.9494	(1)	0.4999	[19]
A15	APTQ	6.2788	(1)	0.4996	[20]
A16	MDPTQ	6.3711	(1)	0.5000	[20]
A17	NMHE	7.1139	(1)	0.4998	[20]
A18	MHE	6.3617	(1)	0.4998	[20]
A19	DB226	6.0792	(2)	0.9999	[21]
A20	DB244	7.3424	(2)	1.0001	[21]
A21	AMAC	4.8921	(1)	0.4998	[22]
A22	CGP 40215A	7.8451	(2)	1.0000	[23]
A23	MMQ1	5.9345, ^{M}**6.1870** (**4.2**%)	(1)	0.5000	[24]
A24	Proflavine	5.4314, ^{M}**5.6272** (**3.6**%)	(1)	0.5008	[15]
A25	Propidium	4.7160, ^{M}**4.7575** (**0.88**%)	(1)	0.5000	[15]
A26	DB293	7.0414, ^{M}**7.8410** (**11.4**%), ^{A}**7.2690** (**3.2**%)	(2)	1.0000	[13]
A27	DB351	6.8751, ^{M}**7.4103** (**7.8**%), ^{A}**6.9246** (**0.72**%)	(2)	1.0001	[13]
A28	DB818	8.4472, ^{M}**8.1827** (3.1%), ^{A}**7.3714** (12.7%)	(2)	1.0000	[25]
A29	DB75	7.1461, ^{M}**7.1582** (**0.17**%), ^{A}**6.9246** (**3.1**%)	(2)	1.0000	[25]
A30	Berenil	6.0000, ^{M}**6.4617** (**7.7**%), ^{A}**6.0682** (**1.1**%)	(4)	1.5000	[13]

Annotate: "M" is the regressed binding constant by MLR. "A" is the predicted binding constant by ANN. The relative error is in parenthesis. Bold in AAN mode training values is the predicted binding mode. (1) Intercalation, (2) minor groove, (3) intercalation, electrostatic, (4) minor groove, intercalation.

Table 2
The characters of molecular structure

Characters	Characters
Number of N atom	Lone-pair electrons
Number of O atom	Connolly solvent-excluded volume
Length of N–N bond	Molar refractivity
Length of N–O bond	Molecular Topological Index
Length of O–O bond	Principal Moment of Inertia-*X*
Sum of atom	Principal Moment of Inertia-*Y*
Double bond	Principal Moment of Inertia-*Z*
Sum of rings (the atom C > 5)	Radius
Partition coefficient (octanol/water)	Connolly accessible area
Balaban Index	Electronicenergy
Wiener Index	HOMOEnergy
Connolly Molecular Area	LUMOEnergy

How can we predict binding mode and constant of unknown antibiotics?

2. Methodology

2.1. Data

The molecules of the 30 antibiotics [13–25] studied are shown in Table 1. Twenty-four descriptors, which are shown in Table 2, of each molecule were calculated by Chem3D (Cambridge Soft). The calculated descriptors were chosen because they could represent different classes of molecular properties according to different sources of chemical information in terms of electronic, hydrophobic and steric features of the compounds.

For the spatial conformational structure descriptors, Wiener (Eq. (1)) and Balaban (Eq. (2)) Index can be calculated by the following two equations respectively:

$$W(G) = \frac{1}{2}\sum_{i}\sum_{j} d_{ij} \tag{1}$$

where d_{ij} is the number of bond between i and j atom.

$$J = n_{\mathrm{e}}\sum_{ij}(S_i S_j)^{-1/2} \tag{2}$$

where n_{e} is the number of border of the tree graph, S_i and S_i is sum of the row i and j in distance matrix of the tree graph.

The molecule area, accessible area and solvent-excluded volume were calculated with the Chem3D by using the routine developed by Connolly [26]. Principal Moment of Inertia-(*X*, *Y*,

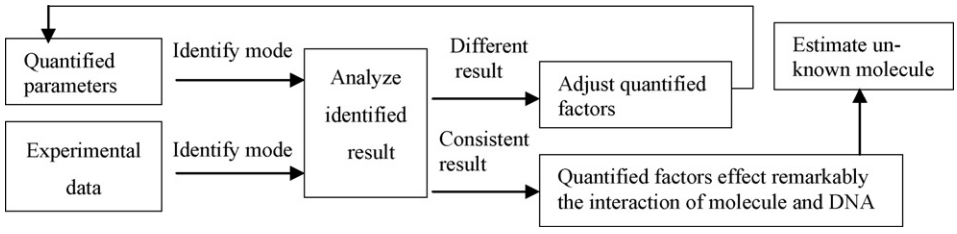

Fig. 1. The study path of the interaction of molecule and DNA.

Z) were derived by the following equation:

$$I_A = \sum_i m_i r_{ix}^2, \qquad I_B = \sum_i m_i r_{iy}^2, \qquad I_C = \sum_i m_i r_{iz}^2 \quad (3)$$

where m_i is the relative atomic weight of i atom, r_{ix}, r_{iy} and r_{iz} are the distance of i atom to the principal moment of x, y and z.

Here two parts of data were computed. One is 24 descriptors of 30 antibiotics; the other is the binding constants and binding modes of 30 antibiotics obtained from literature (Table 1). The binding modes were quantified as 0.5, 1.0 and 1.5, corresponding to intercalation, groove binding and two modes (intercalation and electrostatic, intercalation and groove binding or electrostatic and groove binding), respectively.

2.2. Selection of descriptors

Different combinations of 24 descriptors generated by "enumerative algorithm" were evaluated according to the procedure shown in Fig. 1. The sum of descriptors involved in combinations varied from 8 to 24. For a combination, its cluster of principal component analysis (PCA) was compared with the experimental cluster obtained from interactive binding mode and constant in reference. The combination having the same cluster inclination as the experimental cluster can be regarded as an influencing factor of interaction, i.e., those descriptors have important effects on the interaction of DNA and antibiotics. Then HCA was used to verify the results obtained by PCA.

3. Results and discussion

3.1. Descriptors influencing the interaction of DNA and antibiotics

3.1.1. Principal component analysis (PCA)

PCA is a linear analysis technique that can find the most efficient representation of a data set in several dimensions. It is often employed in data representation and data compression tasks, where representing a large data set in a smaller number of dimensions might be desirable. This method generates a new set of variables named principal component (PCs) as linear combination of the initial variables. The largest variance in the data set is described by PC1, while PC2, orthogonal to PC1, has the second maximum variance and so on. The elements of the eigenvectors in the PCA method are called weights; the eigenvalues represent the amount of original variance in each eigenvectors.

In order to compare the variables on a same scale, each of them was auto-scaled before applying the PCA methodology. After several attempts to achieve a good classification of the antibiotics, the best separation was obtained with a small set of 12 variables which we found to be the most important.

The PCA results in Table 3 show that the first three principal components (PC1, PC2 and PC3) describe 81.56% of the overall variables as follows: PC1 = 54.97%, PC2 = 15.14 and PC3 = 11.45%, i.e., the first three PCs can present information of original data completely [27,28]. Since almost all variables can be explained by the first three PCs, their score plot is a reliable representation of the spatial distribution of the points for the data

Table 3
Loadings corresponding to the first three principal components for PCA and contribution of each to the variable of the original data set

	Parameter	PC1	PC2	PC3
P1	Number of N atom	−0.0144	−0.5982	0.5901
P2	Length of N–O bond	−0.0271	−0.2416	0.4644
P3	Double bond	0.0152	0.4034	0.1688
P4	Sum of rings (the atom C > 5)	−0.2234	−0.0637	0.0004
P5	Lone-pair electrons	0.0210	0.2565	0.1647
P6	Balaban Index	−0.2159	−0.1185	−0.0535
P7	Connolly Molecular Area	−0.0705	−0.0112	0.0587
P8	Molecular Topological Index	0.4425	−0.2826	−0.2914
P9	Principal Moment of Inertia-*X*	−0.5620	−0.0949	−0.1221
P10	Principal Moment of Inertia-*Y*	0.6097	0.0419	0.1503
P11	Principal Moment of Inertia-*Z*	0.1016	-0.3816	-0.3987
P12	Electronic Energy	0.0555	0.3176	0.3047
Eigenvalue		6.5964	1.8166	1.3744
Contribution to total variance		54.97%	15.14%	11.45%

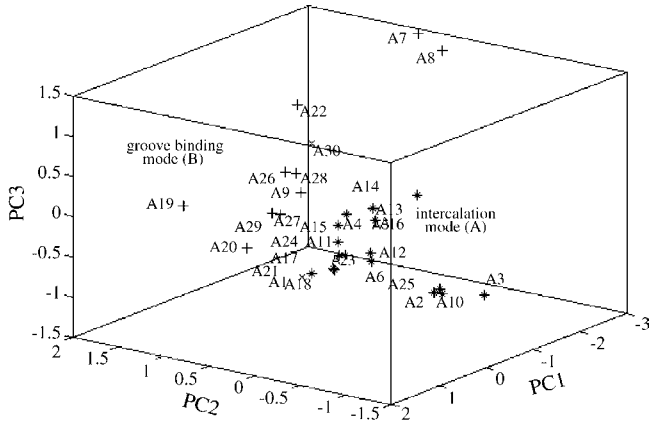

Fig. 2. Cluster of the scores of the first three PCs vs. binding mode (*: intercalation mode, +: groove binding mode, ×: two modes).

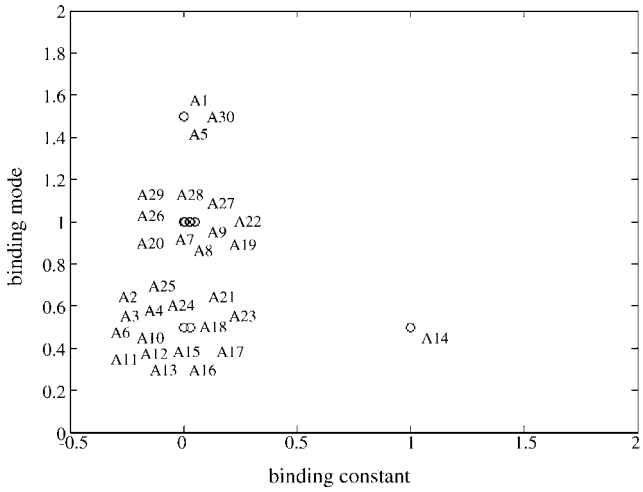

Fig. 3. Plot of the binding constant and mode. The binding constants were normalized. The binding modes were expressed by numbers, i.e., 0.5 refers to intercalation mode, 1.0 refers to groove binding mode, 1.5 refers to two modes.

set studied. Fig. 2 displays the cluster of the scores of the first three PCs of 30 antibiotics versus binding mode. From which we can see that the 30 antibiotics under study are separated according to their binding modes. Fig. 3 is the cluster of experimental data, which was obtained by plotting the logarithm of binding constants and binding modes. Upon comparison of Figs. 2 and 3, it is clear that the cluster of experimental results are very similar to the cluster based on descriptors data, which imply that the 12 selected descriptors are very important for the interaction, and they can be considered as the factors that influence interaction. The 12 selected descriptors include: P1 (the number of N atoms), P2 (the length of N–O bond), P3 (the double bond), P4 (the sum of rings (the atom C > 5)), P5 (the lone-pair electrons), P6 (Balaban Index), P7 (Connolly Molecular Area), P8 (Molecular Topological Index), P9 (Principal Moment of Inertia-*X*), P10 (Principal Moment of Inertia-*Y*), P11 (Principal Moment of Inertia-*Z*) and P12 (Electronic Energy).

3.1.2. Hierarchical cluster analysis (HCA)

The HCA method is an excellent tool for preliminary data analysis and it is very useful for examining data sets for expected or unexpected clusters. This technique examines the distances between the samples in a data set and represents this information as a two-dimensional plot called dendrogram which can be used to provide information on chemical behavior and verify the results obtained by PCA.

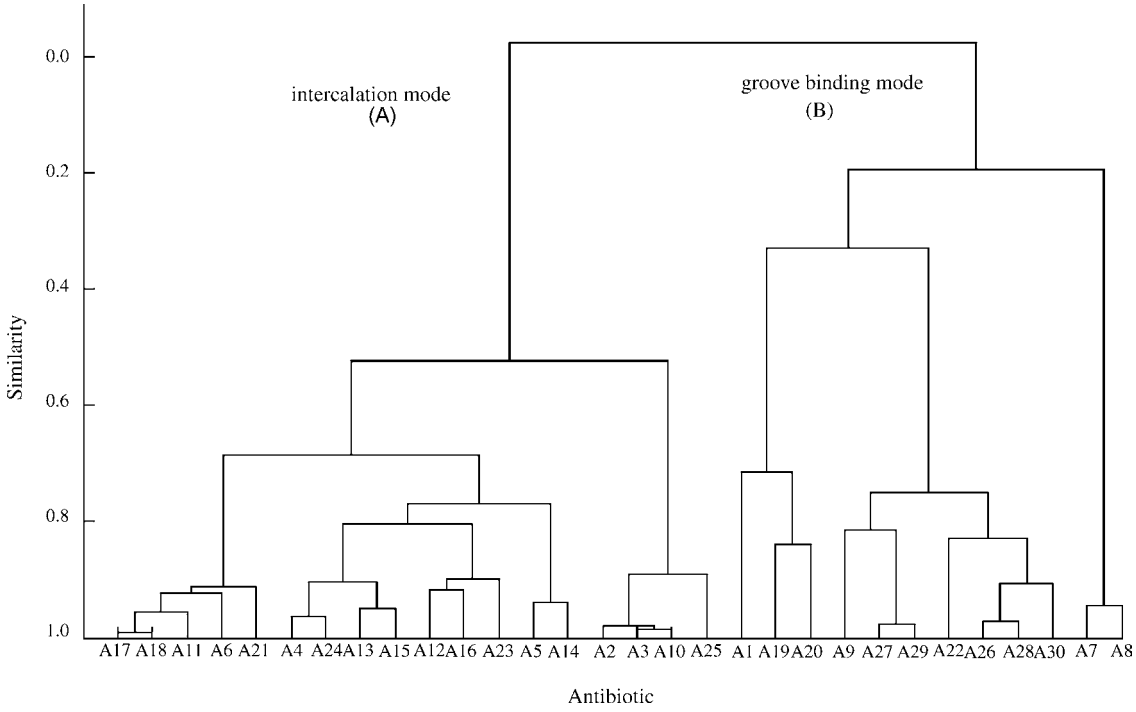

Fig. 4. Dendrogram obtained with the HCA for the 30 antibiotics. The HCA classifies the antibiotics into two groups: intercalation mode antibiotics (group A) and groove binding mode antibiotics (group B).

The results obtained with the HCA analysis are similar to those obtained with PCA and are displayed in the dendrogram as shown in Fig. 4. The vertical lines represent the antibiotics and the horizontal lines represent the similarity values. We can see from Fig. 4 that group A and group B have similarity values equal to zero and they correspond to groups in Fig. 2 (PCA analysis). Both PCA and HCA methods classified the 30 antibiotics studied into two groups in the same manner. Based on the classification obtained with the PCA and HCA we can say that 12 descriptors are responsible for the interaction between DNA and antibiotics.

3.2. Analysis of the influence factors

The PCA loadings values of the first two components and the corresponding scores of 30 antibiotics are displayed in the same plot (Fig. 5). According to Fig. 5, we can see that: (1) the loadings of descriptors P1, P2, P3, P5, P11 and P12 are among the antibiotics that have intercalation and the ones that have groove binding mode, and they have larger weights in PC2, which indicate that P1, P2, P3, P5, P11 and P12 are all closely related to intercalation and groove binding; (2) the loading of P4, P6 and P9 is close to the antibiotics which have intercalation mode, P4 and P6 have larger weights in PC2, and P9 has larger weight in PC1, which indicate that they are all correlative with intercalation mode. For the groove binding, P1–P3, P5 and P11–P12 have larger weights in PC2, P10 has larger weight in PC1, i.e., P1-P3, P5, P11–P12 and P10 remarkably influence groove binding mode; and (3) for two modes, P4, P6 and P8 have larger weights in PC1, from which we can infer that the topological index is also a crucial factor apart from the sum of rings (the atom C > 5) and the lone-pair electrons of molecules.

From the above analysis about the interactions between antibiotics and DNA, we can say that the compounds should present different characteristics in different interactive mode. For the intercalation mode, the compounds need high sum of rings (the atom C > 5), Balaban Index and Principal Moment of Inertia-*X* values, while for the groove binding mode, the compounds need high Molecular Topological Index and Principal Moment of Inertia-*Y* values. Suitable values of number of N atom, number of O atom, double bond, lone-pair electrons, Connolly Molecular Area and Electronic Energy are all responsible for the intercalation and groove binding mode. In fact, these characteristics of antibiotic compounds observed and studied in this work can be useful in future studies of new antibiotic molecules with effective anticancer, antitumor activity.

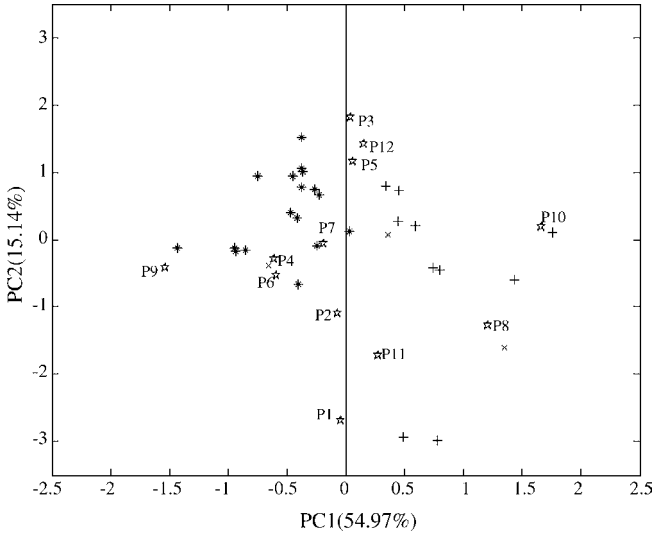

Fig. 5. Biplot the scores of the first two PCs and the load of the first two PCs (*: intercalation mode, +: groove binding mode, ×: two modes, ☆: the loading of descriptions).

Some of the above results are approximately in agreement with experimental results. For example, for the intercalation mode, experimental studies show that the spatial conformation of molecules should match with DNA [29,30], as a part of a planar structure in molecules inserted between adjacent base-pairs of DNA. For the grooving binding mode, there must have been atoms which could form hydrogen bond, such as the atom N and O can form hydrogen bond with the atom H of base-pairs [31,32].

3.3. MLR and ANN models

3.3.1. Prediction with MLR

The binding constant characterizes the binding intensity of DNA and molecules. It is mainly obtained from the experimental techniques which are complicated and time-consuming. Moreover, it is more difficult for large number of molecules to obtain their binding constants with experimental techniques. In this work, based on the selected descriptors and MLR, a model was made to predict the binding constant. The detailed procedure of MLR is as follows: let $M_{n\times p}$ represents the original data, n is the number of the samples (antibiotics) and p is number of variables (descriptors). $K_{n\times 1}$ represents the binding constant of each antibiotic. Supposed that M has linear relationship with K, β can be calculated from the equation:

$$\beta = (M^{\mathrm{T}}M)^{-1}M^{\mathrm{T}}K \tag{4}$$

where β is the coefficient matrix, so the binding constant ($\hat{K}$) of unknown molecules can be computed from the following equation:

$$\hat{K} = M\beta \tag{5}$$

Descriptor data of 30 antibiotics were randomly classified into two classes, a training set consisting of 22 antibiotics and a test set including 8 antibiotics. For training data set, the logarithms of binding constants were used as dependent variable (Y), and the 12 descriptors data (auto-scaled) were used as independent variable (X). Supposed that Y and X have linear relationship, a MLR model was established by commutation of Eqs. (4) and (5) This model is expressed as the following equation:

$$\begin{aligned} Y = {} & 6.6066 + 7.2058\times 10^{-2}x_1 + 1.7576x_2 + 0.96213x_3 \\ & + 0.50888x_4 + 0.32419x_5 + 2.744x_6 + 1.5909x_7 \\ & + (-4.6799)x_8 + (-1.5241)x_9 + 6.6235x_{10} \\ & + (-6.6675)x_{11} + (-0.56329)x_{12} \end{aligned} \tag{6}$$

Table 4
Scores of the first three principal components corresponding to the sample

Number of molecules	PC1	PC2	PC3	Number of molecules	PC1	PC2	PC3
A1	1.3494	−1.6066	−1.4109	A16	−0.24406	−0.084666	0.023554
A2	−0.9476	−0.12085	−0.68561	A17	−0.3715	1.0092	−0.32086
A3	−0.85619	−0.16353	−0.7564	A18	−0.37523	1.0627	−0.2903
A4	−0.23041	0.67298	0.11679	A19	1.7602	0.099075	−0.23726
A5	−0.66027	−0.39202	0.11968	A20	1.4351	−0.60775	−0.84377
A5	−0.74685	0.94927	−0.13832	A21	−0.37974	1.5228	−0.2447
A7	0.77777	−2.9803	1.4371	A22	0.79661	−0.44966	1.1224
A8	**0.49225**	**−2.9366**	**1.3062**	A23	0.037158	0.12508	−0.43544
A9	**0.74503**	**−0.42467**	**0.044917**	A24	−0.27049	0.74916	−0.052928
A10	**−0.93978**	**−0.17799**	**−0.75182**	A25	−1.4333	−0.11631	−0.64021
A11	**−0.45402**	**0.93988**	**−0.13587**	***A26***	***0.44225***	***0.26902***	***0.51398***
A12	**−0.41543**	**0.32724**	**−0.26169**	***A27***	***0.45376***	***0.73914***	***0.12263***
A13	−0.46927	0.40034	0.33375	***A28***	***0.59197***	***0.19865***	***0.48024***
A14	−0.40521	−0.66336	0.24518	***A29***	***0.33779***	***0.80231***	***0.15379***
A15	−0.38215	0.77583	0.31357	***A30***	***0.36221***	***0.081602***	***0.87227***

Annotate: bold values are the test matrix of predicting mode by ANN. Italic values are the test matrix of predicting constant by ANN.

where x_i ($i = 1, 2, \ldots, 12$) are the element of X, i.e., x_i ($i = 1, 2, \ldots, 12$) are the 12 selected descriptors.

In order to check the efficiency of the model, the constants of the test data set (eight antibiotics) were predicted and the results were listed in Table 1. Compared with the reported binding constants of literatures, the predicted maximal relative error is 11.4% (for A26, DB293), and the minimal relative error is only 0.17% (for A29, DB75), indicating that our model is precise.

3.3.2. Prediction with ANN

ANN is a multivariate calibration method used mainly for modeling non-linear data. The neural network behavior is determined by their topologies. In this work, back-propagation ANN [33,34] was used as topology and the neural network architecture was composed of three layers: the first layer corresponding to data input, one hidden layer with an appropriate number of neurons and an output layer. In order to reduce the net structure and speed up the running time, the ANN was generated using the first three PCs scores (Table 4) as input data [35], and the logarithm of binding constant as target output. A 3-3-1 ANN with a sigmoidal transfer function was developed, and the training method is "trainlm". A set of five antibiotics (A26–A30) out of 30 antibiotics were chosen randomly as a prediction set, and a network was developed using the remaining antibiotics and then the binding constants of these five antibiotics were predicted using the ANN model. The predicted constants of these antibiotics are listed in Table 1. Based on the data given in Table 1, a comparison between the results obtained by the ANN and MLR methods indicates the superiority of the ANN over that of the MLR model.

The net used to predict binding mode was constructed with the similar method of predicting binding constant. The differences are such that the target output is quantified binding mode and the training method is "trainbfg". Five antibiotics (A8–A12) were chosen randomly, their binding modes were predicted with the ANN model, and the results are shown in Table 1. It is found that all binding modes can be predicted accurately.

4. Conclusions

In this work, the factors that influence the interaction between DNA and antibiotics were investigated. Three models of predicting binding constant and mode were established with MLR and ANN. The results show that there are 12 descriptors playing important roles in interaction of DNA and antibiotics, and the established models are accurate to predict binding constant and binding mode of DNA and antibiotics. The investigations in this work provide a way to understand the interaction of DNA and antibiotics without experimental work; moreover, it is easy and effective to predict the interaction of batches of unknown molecules and DNA.

Acknowledgements

We thank the Natural Science Foundation of China (No. 20335030), the Teaching and Research Award Program for Outstanding Young Teachers in Higher Education Institutions of MOE P.R.C. and Key Laboratory Gansu polymer materials.

References

[1] Z.Q. Frank Qiu, M. Lu, Appl. Soft Comput. 3 (2003) 177–189.
[2] P.U. Maheswari, M. Palaniandavar, Inorg. Chim. Acta 357 (2004) 901–912.
[3] J.S. Lee, L.J.P. Latimer, K.J. Hampel, Biochemistry 32 (1993) 5591–5597.
[4] D.S. Pilch, M.T. Martin, C.H. Nguyen, J.S. Sun, E. Bisagni, J. Am. Chem. Soc. 115 (1993) 9942–9951.
[5] J.B. Chaires, N. Dattagupta, D.M. Crothers, Biochemistry 21 (1982) 3933–3940.
[6] L.L. Shen, L.A. Mitscher, P.N. Sharma, T.J. O'Donnell, D.W.T. Chu, C.S. Cooper, T. Rosen, A.G. Pernet, Biochemistry 28 (1989) 3886–3894.
[7] E. Feinstein, E. Canaani, L.M. Weiner, Biochemistry 32 (1993) 13156–13161.
[8] L. Guo, W.J. Dong, X.F. Tong, C. Dong, S.M. Shuang, Talanta 70 (2006) 630–636.
[9] D.P. Arya, R.L. Coffee Jr., B. Willis, A.I. Abramovitch, J. Am. Chem. Soc. 23 (2001) 5385–5395.
[10] D.P. Arya, R.L. Coffee Jr., I. Charles, J. Am. Chem. Soc. 123 (2001) 11093–11094.
[11] G.B. Onoa, V. Moreno, Int. J. Pharm. 245 (2002) 55–65.

[12] M. Rodriguez, A.J. Bard, Anal. Chem. 62 (1990) 2658–2662.
[13] K.X. Wan, T. Shibue, M.L. Gross, J. Am. Chem. Soc. 122 (2000) 300–307.
[14] M.S. Ibrahim, Anal. Chim. Acta 443 (2001) 63–72.
[15] G.S. Kumar, Q.Y. He, D. Behr-Ventrua, M. Tomasz, Biochemistry 34 (1995) 2662–2671.
[16] X.G. Qu, J.B. Chaires, J. Am. Chem. Soc. 123 (2001) 1–7.
[17] I. Haq, Arch. Biochem. Biophys. 403 (2002) 1–15.
[18] H.T.-B. Haj, M. Salemo, W. Priebe, H. Kozlowski, A. Garnier-Suillerot, Chem. Biol. Interact. 145 (2003) 349–358.
[19] S.F. Wang, T.Z. Peng, C.F. Yang, J. Biochem. Biophys. Methods 55 (2003) 191–204.
[20] M. Gopal, S. Shenoy, L.S. Doddamani, J. Photochem. Photobiol. B 72 (2003) 69–78.
[21] S. Mazur, F.A. Tanious, D.Y. Ding, A.K.D.W. Boykin, L.J. Simpson, S. Neidle, W.D. Wilson, J. Mol. Biol. 300 (2000) 321–337.
[22] C.V. Kumar, E.H. Asuncion, J. Am. Chem. Soc. 115 (1993) 8547–8553.
[23] B. Nguyen, M.P.H. Lee, D. Hamelberg, A. Joubert, C. Bailly, R. Brun, S. Neidle, W.D. Wilson, J. Am. Chem. Soc. 124 (2002) 13680–13681.
[24] M.-P. Teulade-Fichou, C. Carrasco, L. Guittat, C. Bailly, P. Alberti, J.-L. Mergny, A. David, J.-M. Lehn, W.D. Wilson, J. Am. Chem. Soc. 125 (2003) 4732–4740.
[25] S. Mallena, M.P.H. Lee, C. Bailly, S. Neidle, A. Kumar, D.W. Boykin, W.D. Wilson, J. Am. Chem. Soc. 126 (2004) 13659–13669.
[26] M.L. Connolly, J. Appl. Crystallogr. 16 (1983) 548–558.
[27] Q.L. Ma, A.X. Yan, Z.D. Hu, Z.X. Li, B.T. Fan, Anal. Chim. Acta 406 (2000) 247–256.
[28] G.W. Zhang, Y.N. Ni, J. Churchill, S. Kokot, Talanta 70 (2006) 293–300.
[29] M.T. Carter, M. Rodriguez, A.J. Bard, J. Am. Chem. Soc. 111 (1989) 8901–8911.
[30] Z. Hossain, F. Huq, J. Inorg. Chem. Biochem. 91 (2002) 398–404.
[31] C.C. Wetzel, S.J. Berberich, BBA 1517 (2001) 392–397.
[32] Y. Cao, X.W. He, Spectrochim. Acta A 54 (1998) 883–892.
[33] E.D. Dorn, G.D. McDonald, M.C. Storrie-Lombardi, Icarus 166 (2003) 403–409.
[34] W. Wu, D.L. Massart, Chemometr. Intell. Lab. 35 (1996) 127–135.
[35] Z. Ramadan, P.K. Hopke, M.J. Johnson, K.M. Scow, Chemometr. Intell. Lab. 75 (2005) 23–30.

Available online at www.sciencedirect.com
ScienceDirect
Talanta 73 (2007) 420–424
Talanta
www.elsevier.com/locate/talanta

Copper-enhanced gold nanoparticle tags for electrochemical stripping detection of human IgG

Xun Mao, Jianhui Jiang *, Yan Luo, Guoli Shen, Ruqin Yu *

State Key Laboratory of Chem/Biosensing and Chemometrics, Chemistry and Chemical Engineering College, Hunan University, Changsha 410082, China

Received 3 February 2007; received in revised form 31 March 2007; accepted 3 April 2007
Available online 8 April 2007

Abstract

We demonstrate herein a novel electrochemical protocol for quantification of human IgG based on the precipitation of copper on gold nanoparticle tags and a subsequent electrochemical stripping detection of the dissolved copper. The immunoassay was conducted by following the typical procedure for sandwich-type immunoreaction. Goat anti-human IgG was immobilized on the wells of microtiter plates. The human IgG analyte was first captured by the primary antibody and then sandwiched by secondary antibody labeled with gold nanoparticles. The copper enhancer solution was then added to deposite copper on the gold nanoparticle tags. After dissolved with HNO_3, the released copper ions were then quantified by ASV. The detection limit is 0.5 ng/mL by 3σ-rule. In order to investigate the feasibility of the newly developed technique to be applied for clinical analysis, several standard human IgG serum specimens were also examined by the method. To our knowledge, the copper enhancing procedure is the first time to be developed for immunoassay. The new strategy of using copper-enhanced gold nanoparticle tags for electrochemical stripping detection holds great promise for immunoassay and DNA detection.

Keywords: Gold nanoparticle; Copper enhancer solution; Adsorptive stripping voltammetry; Immunoassay

1. Introduction

Recent years have seen increasing interest in developing new, simple, sensitive, and specific immunoassays for the quantification of analytes of clinical and biological importance. Non-radioactive labels for bioassay have been extensively developed including enzymes [1,2], fluorescent molecules [3,4], and metal nanoparticles [5–13]. When metal nanoparticles are employed as labels for immunoassay, many analytical methods are available for their quantification such as absorption spectrometry [5–7], photothermal deflection spectroscopy [8], surface plasmon resonance spectroscopy [9], Raman spectroscopy [10,11], and electrochemical techniques [12,13]. The electrochemical detection holds great promise for immunoassay owning to its unique advantages such as low sample volume, excellent sensitivity and inexpensive instrumentation.

Metal nanoparticles provide three important functions for electroanalysis. These include the conductivity properties of nanoparticles at nanoscale dimensions that allow the electrical contact of redox-centers in proteins with electrode surfaces, the roughening of the conductive sensing interface and the catalytic properties of the nanoparticles permitting their enlargement with metals. Metal and semiconductor nanoparticles also provide versatile labels for amplified electroanalysis. Dissolution of the nanoparticle labels and the electrochemical collection of the dissolved ions on the electrode followed by the stripping-off of the deposited metals represents a general electroanalytical procedure.

Biomaterial-metallic nanoparticle hybrid systems are extensively used in different bioanalytical applications [14,15]. Gold nanoparticles, coupled to biomolecules such as antigens (or antibodies) were employed as active units in different immunoassay systems. Biosensing of immunoassay was accomplished by using gold nanoparticle as electrochemical markers or as catalytic labels for the enlargement of the nanoparticle and the generation of conductive paths across electrodes. For enhancing the sensitivity of bioassay, silver or gold enhancing protocols combined with electrochemical quantification have been applied [16–18]. Willner also reported a copper enhancing protocol for detection of 1,4-dihydro-*b*-nicotinamide

* Corresponding authors. Tel.: +86 731 8822577; fax: +86 731 8822577.
E-mail addresses: jianhuijiang@hnu.cn (J. Jiang), rqyu@hnu.cn (R. Yu).

0039-9140/$ – see front matter © 2007 Elsevier B.V. All rights reserved.
doi:10.1016/j.talanta.2007.04.004

adenine dinucleotide (NADH) and quantification of ethanol by the NAD+-dependent alcohol dehydrogenase [19]. The silver enhancer solutions always have some drawbacks such as light and temperature-sensitive. The gold enhancing procedure has a limitation associated with the unavoidable use of poisonous reagent Br_2. The copper enhancing protocol developed in present study could solve these problems. The copper enhancer solution containing ascorbic acid and copper sulphate is easy to prepare and preserve. The quantification of copper by ASV is also relatively simple and sensitive. To explore the feasibility of this protocol, the immunoassay was performed by following the typical procedure for sandwich-type immunoreaction in microtiter plates. The human IgG is first captured by the primary antibody passively adsorbed on the walls of the microwell and consecutively sandwiched by the secondary antibody labeled with gold nanoparticles (Au–Ab). The copper enhancer solution was added to deposite copper on the gold nanoparticle tags. After the copper was dissolved by HNO_3, quantification of the released Cu(II) ions would be realized by ASV.

2. Experimental section

2.1. Apparatus

Voltammograms were recorded at a CHI660 electrochemical workstation (Shanghai Chenhua Instruments, Shanghai) with a three-electrode system consisting of a carbon paste working electrode (CPE) of a diameter of 5 mm, a saturated calomel electrode (SCE) reference electrode and a platinum wire auxiliary electrode in a 25 mL beaker.

2.2. Materials

Goat anti-human IgG antibody, human IgG antigen and albumin bovine serum (BSA) were products of Dingguo Biological Products (Beijing). Standard human serum specimens were obtained from Weifang Biological Products (Weifang, Shandong). $HAuCl_4{\cdot}4H_2O$, $CuSO_4{\cdot}5H_2O$, ascorbic acid, HNO_3, citrate sodium, H_2O_2 and other reagents were all of analytical reagent grade.

The copper enhancer solution was prepared by 1:1 mixing of 0.1 M ascorbic acid and 0.18 M $CuSO_4{\cdot}5H_2O$ solution before use.

The buffers used include 0.05 M $NaHCO_3$–Na_2CO_3 as coating buffer of pH 9.6 and 0.01 M sodium phosphate-buffered saline (PBS) as incubating and washing buffer of pH 7.4. Ultrapure water of specific resistance 18 MΩ was used throughout all experiments.

2.3. Preparation of carbon paste electrode

Carbon paste was prepared by thoroughly mixing 1 g of paraffin with 1 g of spectrally pure graphite powder. The carbon paste was packed into a polytetrafluoroethylene tube to form the working electrode with the surface polished on an ultrafine paper. For repeated use, the surface was renewed by turning the tube nut to extrude a 1 mm thick outer paste layer with subsequent polishing.

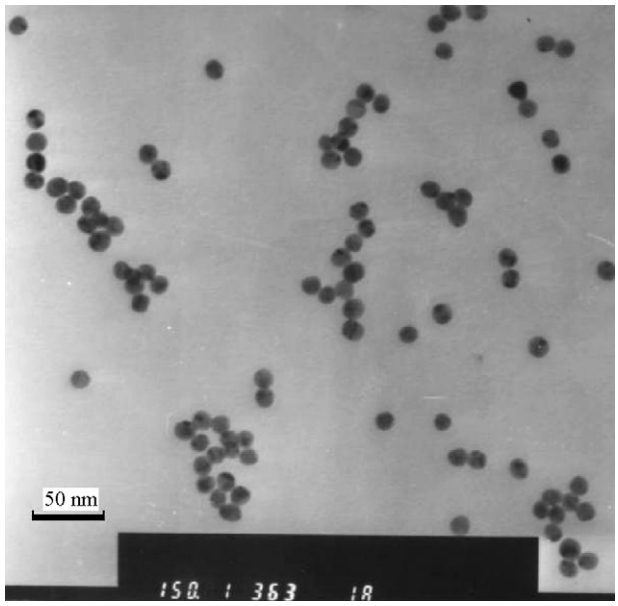

Fig. 1. TEM image of the gold nanoparticles.

2.4. Preparation of gold nanoparticles and Au–Ab conjugate

Gold nanoparticles were prepared according to the method reported in reference [20] with some minor modifications. In a 250 mL round-bottom flask, 1 mL of 1% $HAuCl_4$ solution was mixed with 100 mL of H_2O. The yellow solution was then brought to boil under stirring. Rapid addition of 2.5 mL of 1% sodium citrate to the vortex of the solution resulted in a color change from blue to burgundy. Boiling was continued for 10 min, followed by continued stirring until the solution reached room temperature. TEM micrograph shows the diameter of the resulted gold nanoparticles was about 13 nm (Fig. 1). Au–Ab conjugates were prepared according to the method in reference [21] with some modification. The goat anti-human IgG antibody (600 μL of 1 mg/mL) was added to 10 mL of pH-adjusted (0.1 M K_2CO_3 and HCl were used to adjust pH) colloidal Au suspension followed by incubation at room temperature for 1 h. Then 1 mL 10% BSA solution was added under stirring followed by incubation at room temperature for 0.5 h. The conjugate was centrifuged at 18,500 rpm for 20–30 min, and the soft sediment was washed and resuspended in PBS solution. Addition of NaN_3 to a final concentration of 0.05% allows storage of the Au–Ab conjugate at −20 °C for several months. The color of the Au–Ab solution is similar to that of gold nanoparticle solution. UV–vis spectra of the gold nanoparticle solution and Au–Ab solution were present as Fig. 2.

2.5. Immunoassay protocol

The immunoassay was conducted by following a typical procedure of sandwich immunoreaction (Fig. 3). To each microtiter

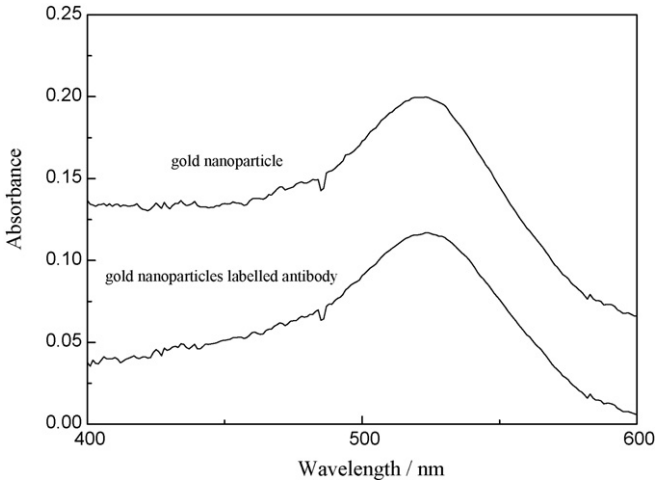

Fig. 2. UV–vis spectra of the gold nanoparticle solution and Au–Ab solution.

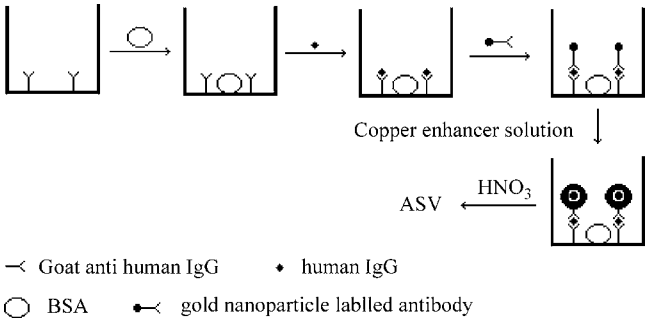

Fig. 3. The immunoassay procedure.

well, 100 μL of 0.5 mg/mL goat anti-human IgG solution in 0.05 M $NaHCO_3$–Na_2CO_3 buffer were added followed by incubation at 4 °C overnight. After removing the solution, the well was rinsed with 0.01 M PBS (pH 7.4) several times followed by addition of 150 μL of 1% BSA solution to block active sites of the wells. Then 100 μL of human IgG antigen analyte were added and incubated for 1 h at 37 °C. Next, 100 μL of Au–Ab in PBS were added to incubate for another 1 h at 37 °C. For the deposition of copper on gold nanoparticles, 100 μL of copper enhancer solution were added to incubate at 4 °C for 15 min. After the well was washed with H_2O, 100 μL of concentrated HNO_3 were pipetted in to dissolve copper. The HNO_3 solution containing released copper ions was then transferred into a 25 mL beaker. After diluted to 5 mL with H_2O, the released Cu(II) ions were then quantified by ASV.

3. Results and discussion

3.1. Determination of copper(II) at carbon paste electrode

To quantify the copper deposited on gold nanoparticle tags by ASV in the final procedure of the immunoassay, the copper metal must be dissolved to free ionic Cu(II) form by HNO_3. Quantification of copper was carried out in diluted HNO_3 solution.

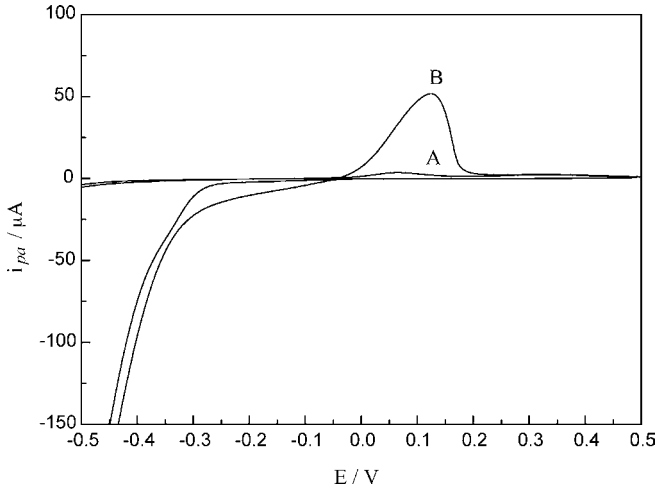

Fig. 4. Anodic stripping voltammograms of copper. In the absence (A) and presence (B) of 100 ng/mL human IgG. The reacting time of the copper enhancer solution was 15 min. Scan rate: 100 mV/s.

Several experimental parameters were studied in order to establish optimal conditions for quantification of Cu(II). An electro-deposition time of 420 s and deposition potential of −0.5 V versus SCE were selected for further studies.

Fig. 4 shows the anodic stripping voltammograms of copper in the presence and absence of 100 ng/mL human IgG when the incubation time of Au–Ab was 120 min, the reacting time of copper enhancer solution was 15 min. When carrying out an anodic scan from −0.5 to 0.5 V at 100 mV/s, an anodic peak at about 0.125 V would be observed in the presence of certain quantity of human IgG.

3.2. Optimization of immunoassay conditions

Several experimental parameters were optimized when we performed experiments using 50 ng/mL human IgG as the analyte. First, we performed the copper enhancing experiments with several reducing agent such as H_2O_2, ascorbic acid and hydroxylamine hydrochloride. Finally, ascorbic acid was selected as

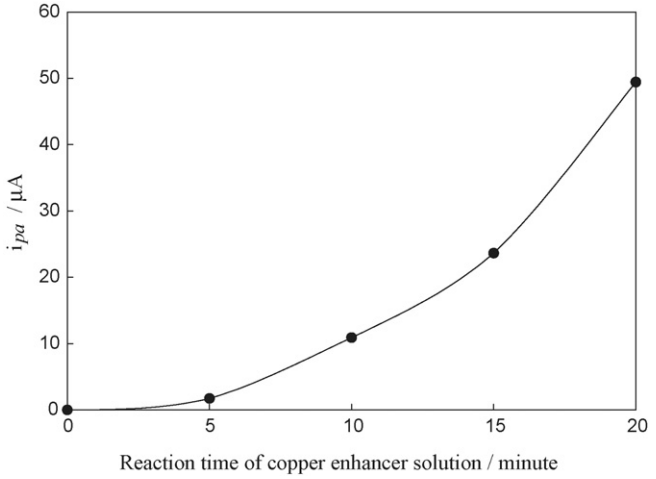

Fig. 5. Effect of the reacting time of copper enhancer solution, 50 ng/mL human IgG were used.

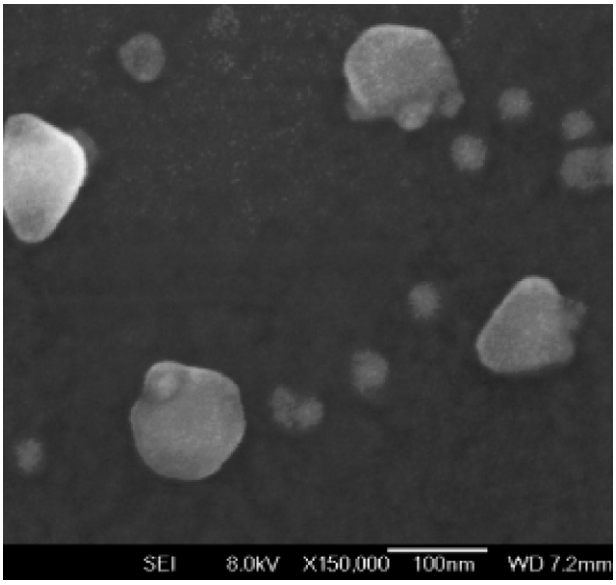

Fig. 6. SEM image of microtiter well, which have been conducted with copper enhancing protocol.

the reducing agent for copper enhancing reaction. No precipitation appear when copper(II) solution and ascorbic acid were mixed together in the absence of gold nanoparticles. However, dark precipitation would appear gradually in the presence of gold nanoparticles. The phenomenon indicated the gold nanoparticles serve as a catalyzer absolutely necessarily in copper enhancing experiments. Then we studied the influence of the reacting time of copper enhancer solution on i_{pa} (Fig. 5). Experiments showed that when the reacting time is shorter than 5 min, the response would not be evident if lower concentration of human IgG was applied. i_{pa} would increase when the reacting time of copper enhancer solution was increased from 5 to 20 min. But the background was also increased gradually. The relatively high stripping currents and low background currents were observed when the experiments were conducted with 15 min reacting time of the copper enhancer solution. Fig. 6 was the SEM image

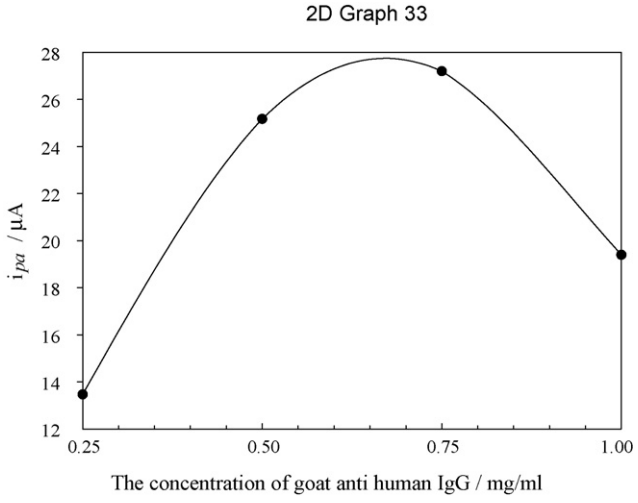

Fig. 7. Effect of the concentration of goat anti-human IgG. The reacting time of copper enhancer solution was 15 min, 50 ng/mL human IgG were used.

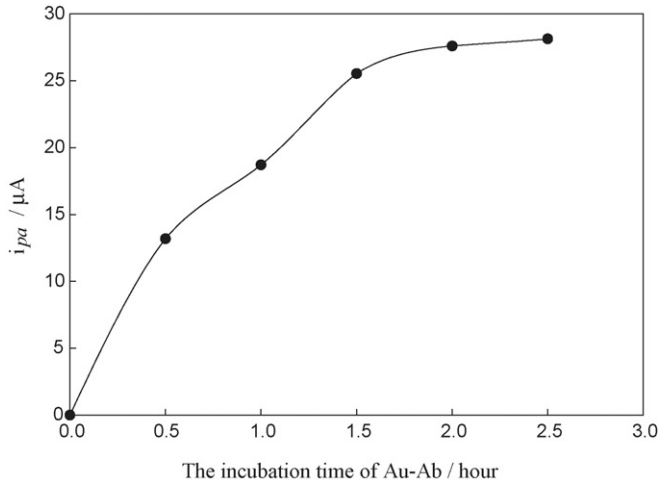

Fig. 8. Effect of the incubation time of Au–Ab. The incubation time of copper enhancer solution was 15 min, 50 ng/mL human IgG were used.

of microtiplate well, which had been conducted with copper enhancing protocol. The SEM image indicated the growth of copper on gold nanoparticles was evidently. However, the deposition of copper on gold nanoparticles was not very uniform.

Fig. 7 shows the effect of concentration of goat anti-human IgG on i_{pa}. One can see that i_{pa} increases gradually with the increasing concentration in the range of 0.25–0.75 mg/mL. i_{pa} would decrease when the concentration of goat anti-human IgG reached 1 mg/mL. A goat anti-human IgG concentration of 0.5 mg/mL was applied throughout all experiments.

Fig. 8 shows that the effect of incubation time of Au–Ab solution on i_{pa}. When the incubation time of Au–Ab solution is in the range of 0.5–2 h, i_{pa} would increase gradually with the increasing incubation time. When the incubation time of Au–Ab solution is higher than 2 h, i_{pa} tends to stabilize. Two hours of incubation time was selected in our experiments.

3.3. Calibration curve for determination of human IgG

Fig. 9 shows the anodic peak current of copper is proportional to the concentration of human IgG in the range of 2–250 ng/mL. The linear regression equation was $\log i_{pa} = 0.0292 \log C + 0.8829$, with a correlation coefficient of 0.9990. The detection limit as defined by 3σ-rule is 0.5 ng/mL. The RSD of the method is 9.91% for eight times determination of 50 ng/mL human IgG under the same conditions. In order to investigate the feasibility of the newly developed technique to be applied for clinical analysis, several standard human IgG serum specimens were examined by the method. The compari-

Table 1
Analysis results of hIgG for human serum specimens

Samples	IgG concentration (g/L)	IgG concentration by the method (g/L)
1	2.24	2.06 ± 0.21
2	4.47	4.23 ± 0.43
3	19.41	20.01 ± 1.91

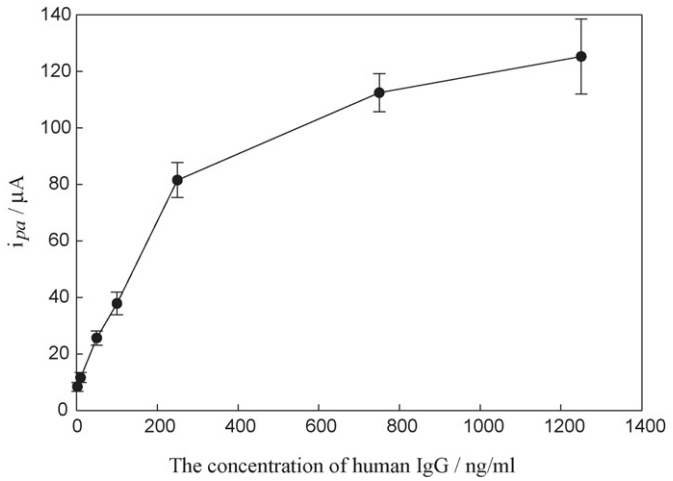

Fig. 9. Calibration curve for the determination of human IgG. The reacting time of copper enhancer solution was 15 min.

son of results is shown in Table 1. The analytical results show the feasibility of applying the developed method for real samples.

4. Conclusion

A new protocol was reported for determination of human IgG based on the copper precipitation on gold nanoparticle tags and a subsequent ASV quantification of the dissolved copper. For depositing copper on the respective biosensing interface, gold nanoparticles labeled with antibody were first captured through the typical sandwich immunoreaction. Taking advantage of the catalytic properties of the gold nanoparticles, the subsequent treatment with copper enhancer solution would realize the enlargement of gold tags with copper. Compared with protocols of silver enhancement and gold enhancement, the copper enhancing procedure have some unique advantages such as easy to prepare and preserve the copper enhancer solution and use of relatively lower poisonous reagents. To our knowledge, the copper enhancing procedure is the first time to be developed for immunoassay. The new copper-enhanced colloidal gold stripping detection strategy holds great promise for immunoassay and DNA detection.

Acknowledgements

This work was supported by the National Natural Science Foundation of China (Grants No. 20435010, 20205005, 20375012) and the Foundation of Science Commission of Hunan Province.

References

[1] C.H. Liu, K.T. Liao, H.J. Huang, Anal. Chem. 72 (2000) 2925–2929.
[2] T.C. Tang, A.P. Deng, H.J. Huang, Anal. Chem. 74 (2002) 2617–2621.
[3] C. Nistor, A. Oubina, M.P. Marco, D. Barcelo, D.J. Emnesu, Anal. Chim. Acta 426 (2001) 185–195.
[4] F. Loescher, S. Boehme, J. Martin, S. Seeger, Anal. Chem. 70 (1998) 3202–3205.
[5] T.A. Taton, C.A. Mirkin, R.T. Letsinger, Science 289 (2000) 1757–1760.
[6] I. Alexandre, S. Hamels, S. Dufour, J. Collet, N. Zammatteo, F.D. Longueville, J.L. Gala, J. Remacle, Anal. Biochem. 295 (2001) 1–8.
[7] R. Elghanian, J.J. Storhoff, R.C. Muclc, R.L. Letsinger, C.A. Mirkin, Science 277 (1997) 1078–1081.
[8] C.Y. Tu, T. Kitamori, T. Sawada, Anal. Chem. 65 (1993) 3631–3635.
[9] L.A. Lyon, M.D. Musick, M.J. Natan, Anal. Chem. 70 (1998) 5177–5183.
[10] Y.C. Cao, R. Jin, C.A. Mirkin, Science 297 (2002) 1536–1540.
[11] J. Ni, R.J. Lipert, G.B. Dawson, M.D. Porter, Anal. Chem. 71 (1999) 4903–4908.
[12] J. Wang, D. Xu, R. Polsky, J. Am. Chem. Soc. 124 (2002) 4208–4209.
[13] M. Dequaire, C. Degrand, B. Limoges, Anal. Chem. 72 (2000) 5521–5528.
[14] C.M. Niemeyer, Angew. Chem. Int. Ed. 40 (2001) 4128–4158.
[15] E. Katz, I. Willner, J. Wang, Electroanalysis 16 (2004) 19–44.
[16] X. Chu, X. Fu, K. Chen, G.L. Shen, R.Q. Yu, Biosens. Bioelectron. 20 (2005) 1805–1812.
[17] J. Wang, R. Polsky, D. Xu, Langmuir 17 (2001) 5739–5741.
[18] K.T. Liao, H.J. Huang, Anal. Chim. Acta 538 (2005) 159–164.
[19] B. Shlyahovsky, E. Katz, Y. Xiao, V. Pavlov, I. Willner, Small 1 (2005) 213–216.
[20] K.C. Grabar, R.G. Freeman, M.B. Hommer, M.J. Natan, Anal. Chem. 67 (1995) 735–743.
[21] C. Zhang, Z.Y. Zhang, B.B. Yu, J.J. Shi, X.R. Zhang, Anal. Chem. 74 (2002) 96–99.

Available online at www.sciencedirect.com
ScienceDirect
Talanta 73 (2007) 594–597
Talanta
www.elsevier.com/locate/talanta

Short communication

Cattle breeding: A fast screening procedure to control the bovine fodder contamination

S. Materazzi *, S. De Angelis Curtis, S. Aquili, D. Finotti, A. Gentili

Department of Chemistry, University of Roma "La Sapienza", p.le A. Moro 5, 00185 Roma, Italy

Received 28 December 2006; received in revised form 31 March 2007; accepted 11 April 2007
Available online 4 May 2007

Abstract

The European Commission has adopted a large number of emergency measures to prevent the spread of the Bovine spongiform encephalopathy (BSE) in the Member States, and among them, a European Regulation prohibits the feeding to ruminants of animal protein and animal feed containing such protein. Aim of this work has been to propose the thermal analysis as a new rapid and sensitive screening tool for a preliminary determination of possible contamination in products destined to bovine growth, since the possibility to screen the samples by a rapid and sensitive tool could reduce the time of analysis required by the actual methodology and could allow the systematic surveillance of bovine feeding, with the official EU methods applied only to positive samples.

Keywords: TGA; DTG; Bovine feeding; Fodder; Cattle breeding

1. Introduction

Bovine spongiform encephalopathy (BSE) is a transmissible, neurodegenerative and fatal disease of the family of transmissible spongiform encephalopathies (TSEs) which affects the brains of cattle. Various hypotheses have been advanced and many studies are in progress to explain and stop the emergence of the pathogenic agent, such as its spontaneous presence in cattle whose carcasses are subsequently introduced into the food chain or its entry into this chain via the intermediary of sheep carcasses affected by a similar disease, scrapie [1–5].

Diagnosed for the first time in the United Kingdom in 1986, the "mad cow disease" took on epidemic proportions and finally posed a genuine public health problem following the discovery of a possible link between BSE and its human variant, Creutzfeldt-Jakob Disease, first diagnosed in 1996. By 1 December 2003 a total of 151 confirmed or suspected cases were registered in the European Union, mainly among young people. Most of the cases occurred in the United Kingdom (143), some in France (6), Ireland (1) and Italy (1).

Since 1997 the European Commission has thus committed itself to completely overhauling food safety legislation. In particular, the Directorate-General "Health and Consumer Protection" has been responsible since September 1997 for measures designed to protect public health and to guarantee food safety.

Very soon after the emergence of BSE, British scientists suspected that the consumption by bovine animals of meat and bone meal was responsible for the spread of the epizootic. Since July 1998, the United Kingdom has banned the use of mammalian proteins in the feeding of ruminant animals. This prohibition entered into force in the European Union in June 1994, the date of adoption of the first Community decision in this connection [6]. The Regulation prohibits the feeding to ruminants of animal protein and animal feed containing such protein. As regards the feeding of farmed animals with the exception of carnivorous fur-producing animals, it is forbidden to use processed animal protein, gelatin of ruminant origin, blood products, hydrolyzed protein, dicalcium and tricalcium phosphate of animal origin. To ensure the uniformity of scientific analysis and reliable results, national and Community reference laboratories have been designated. The analysis and sampling methods used comply with the Manual of Standards established by the International Office of Epizootic Diseases.

The European Commission has adopted a large number of emergency measures to prevent the spread of this disease in

* Corresponding author.
E-mail address: stefano.materazzi@uniroma1.it (S. Materazzi).

0039-9140/$ – see front matter © 2007 Elsevier B.V. All rights reserved.
doi:10.1016/j.talanta.2007.04.030

the other Member States. Since January 2001 the ban on using "animal meal" in animal feeding has been in force throughout the territory of the European Union.

In the framework of Community law, all the emergency measures adopted are now being replaced by basic legislation which reinforces the rules governing the prevention, control and eradication of all transmissible spongiform encephalopathies (TSEs). This is the role of Regulations (EC) No 999/2001 and 1326/2001 [7,8].

Aim of this work has been to propose the thermal analysis (thermogravimetry and its first derivative curve) as a new rapid and sensitive screening tool for a preliminary determination of possible contamination in products destined to bovine growth.

As a consequence, the possibility to screen the samples by a rapid but also sensitive tool could reduce the time of analysis and could allow the systematic surveillance of bovine feeding, with the official EU methods applied only to positive samples.

2. Experimental

2.1. Materials

All the analyzed fodder samples were collected from commercially available products: among them, several certified "for bovine growth", while fodder for general pet-use were used as examples of contaminated samples since animal products and by-products are allowed in pet nutrition.

To verify the reproducibility of the results, at least 100 g of each product were transferred in a mortar and reduced to the smallest homogeneous powder. The sample collection was performed from different lots and each lot was achieved from a different store.

In addition, laboratory-made mixtures of the analyzed "animal-free" certified fodder samples and bones were realized, with the bone addition percent increased from 10 to 30% (w/w).

2.2. Thermal analysis

The thermogravimetric curves were obtained using a Perkin Elmer TGA7 thermobalance (range 20–1000 °C); the atmosphere was air, at a flow rate of 100 ml min^{-1}, to evaluate the behavior in oxidizing conditions; the heating rate was varied between 5 and 40 °C min^{-1}, with the best resolution achieved at a scanning rate of 10 °C min^{-1}.

3. Results and discussion

The official methods to determine the presence of animal contamination in bovine feeding are stated by European Regulations. Two different data have to be compared: (i) the evidence by microscopy of typical characteristics (presence of muscular fibers, bone fragments, blood, etc.); (ii) the microscopy analysis of precipitates obtained by solvent extraction and specific reactions. The time required, the accuracy and the reproducibility are the main problems of this methodology.

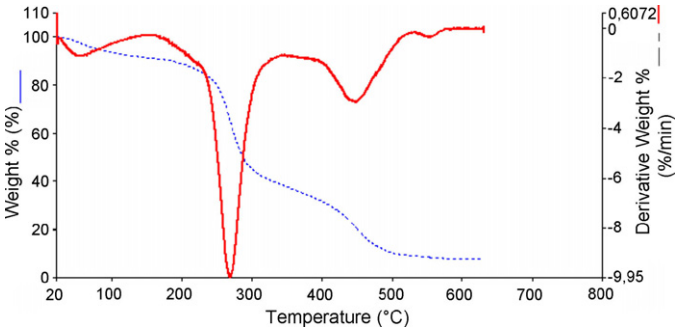

Fig. 1. TG and DTG profiles of a commercially available, "animal-free" certified fodder samples. Scanning rate: 10 °C min^{-1}; air flow at 100 ml min^{-1} rate.

To propose the thermal analysis as a new preliminary screening tool, several commercially available, "animal-protein-free" certified fodder samples specific for the bovine growth and nutrition were investigated by thermogravimetry without any kind of pretreatment.

The typical TG and DTG curves are shown in Fig. 1. Four main processes can be noted: the first of them is due to the release of water, while the second one, very sharp and characterized by a symmetric DTG peak, can be assigned to the cellular matrix disruption of the vegetal components. The third and fourth peaks, related to the loss of more stable components, complete the decomposition profile. Because of the presence of many possible combinations of different vegetal components, it not simple to assign the decomposition process to specific substances: it is obvious the presence of cellulose and consequently of lignin, but many other contributions have to be taken into account, since the fodders for the bovine growth can include hay, straw, silage, vitamins and proteins added to enrich the diet, etc.

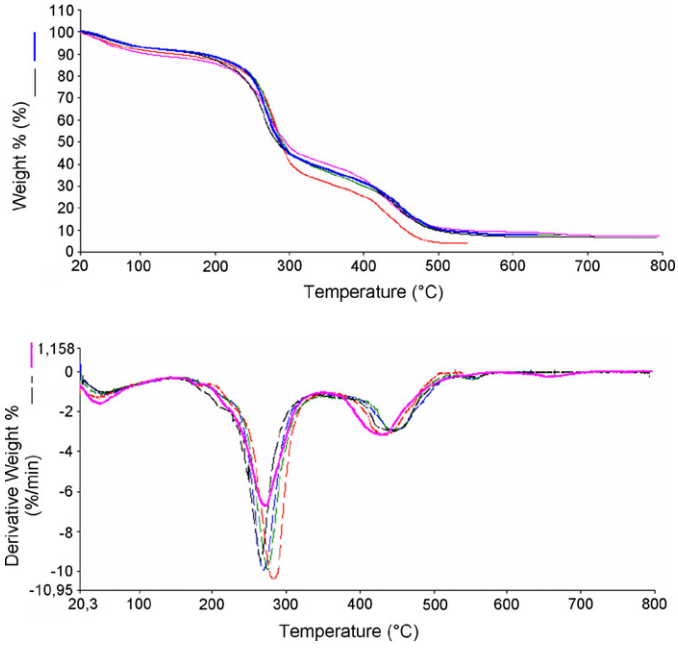

Fig. 2. TG and DTG profiles of several different, commercially available, "animal-free" certified fodder samples. Scanning rate: 10 °C min^{-1}; air flow at 100 ml min^{-1} rate.

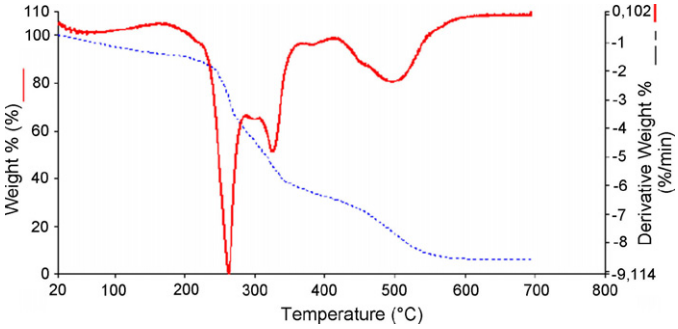

Fig. 3. TG and DTG profiles of a commercially available pet fodder sample. Scanning rate: 10 °C min^{-1}; air flow at 100 ml min^{-1} rate.

In Fig. 2 it can be noted that, while the percent mass loss can not be assumed as a discriminant parameter, the DTG profile of the second releasing process for all the certified samples is always characterized by one, very sharp, symmetric peak.

Instead of only one DTG peak, the thermal profiles (TG and DTG) of a pet fodder, reported in Fig. 3, show the above mentioned second DTG peak overlapped by many other different processes in the same temperature range (200–400 °C). The overlapping is confirmed in all the DTG curves of the analyzed pet-fodders (Fig. 4), due to the loss of other added compounds like milk and milk-derivative, eggs, animal by-product, fish by-products, etc. that are allowed in pet foods. Again, the experimental evidence shows that it is not the percent weight loss, but the DTG profile the driving parameter to determine the contamination. Unfortunately, the exact composition is never reported on the labels of the fodder package, so it is very hard to

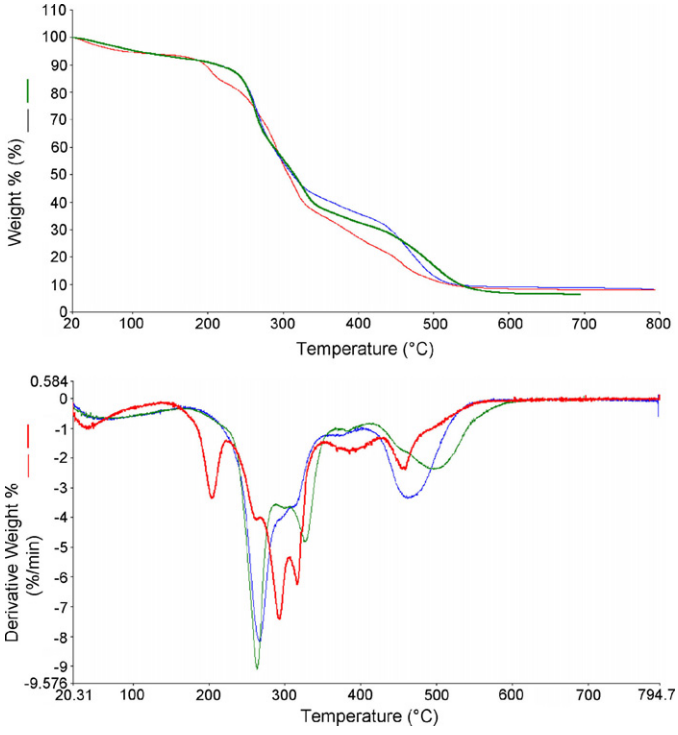

Fig. 4. TG and DTG profiles of several different commercially available pet fodder sample. Scanning rate: 10 °C min^{-1}; air flow at 100 ml min^{-1} rate.

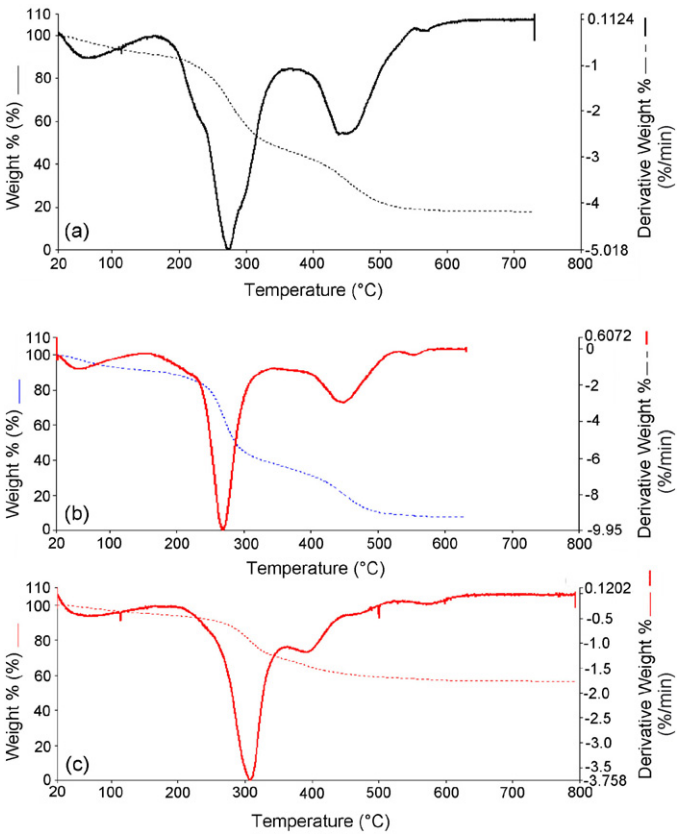

Fig. 5. TG and DTG profiles of a laboratory-made mixture (a) obtained by mixing the analyzed "animal-free" certified fodder sample (b) and powdered bones (c) (bone addition percent is 30% (w/w)). Scanning rate: 10 °C min^{-1} Air flow at 100 ml min^{-1} rate.

certify the presence of specific additives. However, the composition is not really relevant for the applications of this proposed instrumental method, because the European rules prohibit any kind of addition.

To confirm the assumption that the DTG profile can be modified by the presence of non-vegetal components contamination, laboratory-made mixtures of the analyzed "animal-free" certified fodder samples and bones were realized, with the bone addition percent increased from 10 to 30% (w/w). The addition percent range was suggested by the authority that is the surveillance public reference.

Fig. 5 shows the thermogravimetric profile of the mixture obtained by the addition of 30% powdered bone. Looking at the DTG curve, it can be clearly seen the overlapping of the two decomposition processes in the 200–400 °C temperature range, with a different shape with respect to the DTG curves of each single starting component.

The possible explanation to the experimental evidence is that, since the vegetal cellular matrix is characterized by a minor compartmentalization, under these thermoanalytical conditions the break down of the cells happens in one major step. On the other hand, when present, any other animal components decompose in multiple overlapped steps.

To verify the detection limit of this approach, several different w/w ratios were realized among the laboratory-made mixtures.

The results showed that, when the contamination is around 10% (w/w) or below, the reproducibility is low and the DTG profile is sometime not significantly modified.

However, the evidence of a contamination always appeared in all the five analysis of the same sample, and even the less influenced DTG curve always showed a small overlapped process that changed the DTG shape that is typical of non-contaminated samples, suggesting a deeper investigation.

These results allow to propose the thermogravimetry as a useful tool of cattle fodder preliminary screening, with the DTG peak shape in the temperature range 200–400 °C acting as the discriminant factor.

The main advantages are the absence of sample pretreatment, the short time required for the analysis, the low cost of each characterization.

Moreover, the operating procedure is easy enough to allow the application as a routine analysis performed by non-specialized operators.

References

[1] T. Onodera, A. Sakudo, G. Wu, K. Saeki, Microbiol. Immunol. 50 (2006) 565.
[2] J. Poerschmann, U. Trommler, W. Biedermann, U. Truyen, E. Luecker, J. Chromatogr. A 1127 (2006) 26.
[3] S. Siso, L. Gonzalez, F. Houston, N. Hunter, S. Martin, M. Jeffrey, Blood 108 (2006) 745.
[4] A.A. Bencsik, A.W. Coleman, S.O.S. Debeer, H. Perron, A. Moussa, J. Histochem. Cytochem. 54 (2006) 849.
[5] S.A. Priola, I. Vorberg, Mol. Biotechnol. 33 (2006) 71.
[6] REGULATION (EC) No 381/1994 of 27 June 1994 concerning certain protection measures with regard to bovine spongiform encephalopathy and the feeding of mammalian derived protein (Text with EEA relevance).
[7] REGULATION (EC) No 999/2001 of the European Parliament and of the Council of 22 May 2001 laying down rules for the prevention, control and eradication of certain transmissible spongiform encephalopathies.
[8] REGULATION (EC) No 1326/2001 of 29 June 2001 laying down transitional measures to permit the changeover to the Regulation of the European Parliament and of the Council (EC) No 999/2001 laying down rules for the prevention, control and eradication of certain transmissible spongiform encephalopathies.

Available online at www.sciencedirect.com
ScienceDirect
Talanta 73 (2007) 407–414
Talanta
www.elsevier.com/locate/talanta

Development and validation of a reversed phase liquid chromatographic method for separation and determination of related-substances of modafinil in bulk drugs☆

R. Nageswara Rao*, Dhananjay D. Shinde, M.V.N. Kumar Talluri

HPLC Group, Discovery laboratory, Analytical Chemistry Division, Indian Institute of Chemical Technology, Tarnaka, Hyderabad-500 007, India

Received 2 February 2007; received in revised form 23 March 2007; accepted 23 March 2007
Available online 6 April 2007

Abstract

A reversed-phase high-performance liquid chromatographic (RP-HPLC) method for determination and evaluation of purity of modafinil in bulk drugs using Kromasil C_{18} column with acetonitrile: 0.02 M ammonium acetate as a mobile phase in gradient elution mode at 30 °C and detection at 225 nm using photodiode array detector has been developed. The effects of pH, temperature and the percent of organic modifier on resolution were studied. Related substances, viz, sulphide, sulphoxide, sulphones of the modafinil, acid and ester derivatives, were separated and quantified. The method was found to be simple, rapid, selective and capable of detecting all process related impurities at trace levels in the finished products of modafinil with detection limits of 0.6–2.4 × 10^{-8} g. The method was validated with respect to accuracy, precision, linearity, ruggedness, and limits of detection and quantification. It was found to be suitable not only for monitoring the reactions during the process development but also quality assurance of modafinil.

Keywords: Psycho stimulants; Narcolepsy; Modafinil; Related substances; Reversed-phase HPLC

1. Introduction

Narcolepsy is a disabling, neurological sleeping disorder characterized by chronic steepness and marked disorganization of sleep/awake behavior. A person with narcolepsy nods off while talking, driving, eating and working. It is particularly distressing and potentially dangerous disorder that impairs the quality of life. Patients with obstructive sleep apnea/hypopnea syndrome (OSA/HS), narcolepsy and shift work sleep disorder (SWSD) suffer from excessive sleepness. Armodafinil, the R-enantiomer of modafinil, [2-(1,1-diphenyl methyl sulfinyl) acetamide] is a unique psycho-stimulant α_1- adrenoreceptor agonist that has been recently approved by the food and drug administration (FDA), USA for treatment of narcolepsy. It has shown to be quite effective in improving the wakefulness in such patients. It is currently used to treat patients with daytime sleepness associated with narcolepsy. It may also find usefulness in treatment of attention deficit hyperactivity disorders. Armodafinil at present is undergoing a regulatory review at the FDA for use in improving wakefulness in patients with excessive sleepness associated with narcolepsy, shift work sleep disorder and obstructive sleep apnea/hypopnea syndrome [1–4].

A thorough literature search has revealed that only a few analytical methods are available for determination of modafinil in bulk drugs and pharmaceuticals. Its pharmacokinetic profiles in healthy subjects [5,6] had been well characterized. Detection of modafinil and its major metabolites in equine urine, in human plasma, had been reported [7–10]. Tseng et al. [11] had analysed modafinil by gas chromatography-mass spectrometry. Cass et al. [12], had developed a method for enantioselective assay for (±)-modafinil in human plasma using amylose tris [(*S*)-1-phenylethylcarbamate] chiral stationary phase and elution with acetonitrile: water (25:75 v/v) as a mobile phase. Becue [13] had evaluated the chemical structure of by-products during the synthesis of modafinil by liquid chromatography-mass spectrometry. Drouin and Broquaire [14] had optimized the mobile phase composition for liquid chromatographic separation of optical isomers of modafinil on a chiral-AGP column.

☆ IICT communication no.: 070123.

* Corresponding author. Tel.: +91 40 27193193; fax: +91 40 27173387.
E-mail addresses: rnrao@ins.iictnet.com, rnrao55@yahoo.com (R. Nageswara Rao).

0039-9140/$ – see front matter © 2007 Published by Elsevier B.V.
doi:10.1016/j.talanta.2007.03.057

However, none of these methods address to the problem of separation and determination of all process related impurities, which are most likely to be present in the finished products of modafinil. Further, to best of our knowledge, modafinil is not yet official in any of the pharmacopoeia and no method for determination of its impurities has been reported either in bulk drugs or pharmaceuticals. According to ICH-guidelines [15,16], the limits of related substances and impurities in active ingredient should be ≤0.1%. For finished products, the impurities in daily drug dose ≤2 g/day should be with reporting threshold ≤0.05%, identification threshold ≤0.10%, and qualification threshold ≤0.15%. For daily drug dose ≥2 g/day these should be 0.03, 0.05 and 0.05%, respectively. Thus, there is a great need for analytical methods, which will be helpful to monitor the levels of impurities in the finished products of modafinil during process development. In the present study, separation and determination of sulfide, sulfoxide and sulfone of modafinil, its acid and ester was examined by reversed-phase high-performance liquid chromatography (RP-HPLC) using a C_{18} column connected to photo diode array (PDA) detector at 30 °C temperature.

2. Experimental

2.1. Materials and reagents

All reagents were of analytical-grade unless stated otherwise. Glass-distilled and de-ionized water (Nanopure, Barnsted, USA), HPLC-gradient grade acetonitrile (Qualigens Fine-chem. Mumbai, India) and ammonium acetate (S.D. Fine-chem. Mumbai, India) were used. Process intermediates, viz, sulfide, sulfoxide, sulfone of modafinil, its acid and ethyl ester were synthesized in our laboratory following known procedures [17,18].

2.2. Apparatus

The HPLC system consisting of two LC-20AT pumps, an SPD-M20A diode array detector, a SIL-20AC auto sampler, a DGU-20A_3 degasser and CBM-20A communications bus module (all from Shimadzu, Kyoto, Japan) was used. A reversed-phase Kromasil C_{18} (Hichrome) column (25 cm × 4.6 mm i.d.; particle size 5 μm) was used for separation. The chromatographic and the integrated data were recorded using HP-Vectra (Hewlett Packard, Waldron, Germany) computer system using LC-Solution data acquiring software (Shimadzu, Kyoto, Japan).

2.3. Chromatographic conditions

The mobile phase was 0.02 M ammonium acetate-acetonitrile. The analysis was carried out in a gradient elution mode with 30% acetonitrile at 0 min gradually increased to 60% at 8 min, then increased to 80% at 13 min, from 13 min to 20 min 90% using a flow rate of 1.0 ml/min. at 30 °C. Before delivering into the system the solvent was filtered through 0.45 μm, PTFE filter and degassed under vacuum. The chromatograms were recorded at 225 nm.

Table 1
Gradient program

Time (min)	Solvent A (%)	Solvent B (%)
0.01	70	30
8	40	60
13	20	80
20	10	90
22	70	30
30	70	30

A = 0.02 M ammonium acetate, B = acetonitrile.

2.4. Analytical procedure

Solutions of sulfide, sulfoxide, sulfone of modafinil, its acid and ethyl ester were prepared by dissolving known amounts of the components in the mobile phase. These solutions were adequately diluted to study the accuracy, precision, linearity and limits of detection and quantification (Table 1).

2.5. System suitability

The system suitability was conducted by using 0.1% of all process intermediates spiked to the modafinil and evaluated by making five replicate injections. The system was deemed to be suitable for use as the tailing factor for modafinil was ≤1.2; the resolution was greater than 3.9 or higher. Synthetic mixtures and process samples were analyzed under identical conditions. The quantities of intermediates and assay of modafinil were determined from their respective peak areas (Table 2).

3. Results and discussion

3.1. Synthesis of modafinil and its related substances

Fig. 1 describes the chemical reactions involved in synthesis of modafinil and its related substances. Modafinil acid sulfoxide (I), modafinil acid sulfide (III), modafinil (sulfoxide) (IV), modafinil sulfide (VI), modafinil ester sulfoxide (VII) and modafinil ester sulfide (IX) were synthesized according to the procedure reported by Prisinzano et al. [17]. Initially a mixture of benzhydrol (X) and thioglycolic acid in trifluoroacetic acid (TFA) was stirred at room temperature for 3 h to prepare modafinil acid sulfide (III) as shown in Fig. 1. Substances I, II, VI and IX were synthesized from modafinil acid sulfide (III) following the reactions as shown in Fig. 1. Substances I, IV and VII were synthesized by oxidation of III, VI and IX by H_2O_2 in acetic acid at 40 °C, respectively. A solution of thionyl chloride ($SOCl_2$) in benzene was added dropwise to III in benzene and the resulting mixture was refluxed for 1.5 h at 80 °C. The solvent was removed under reduced pressure to afford a crude orange oil. It was dissolved in dichloromethane (DCM) and added cautiously to a vigorously stirred solution of NH_4OH to form IV. Substance IX was synthesized by refluxing overnight a mixture of substance III in ethanol in presence of H_2SO_4. Sulfones of acid (II), amide (V) and ester (VIII) were synthesized by the over-oxidation of (±)-acid (I), amide (IV) and (±)-ester (VII) respectively at −40 °C with *meta*-chloroperbenzoic

Table 2
System suitability data

No. of determination t_R (min)						Average				
Sample	1	2	3	4	5	t_R (±S.D.) [a](min)	RRT	R_s	As	N
I	4.29	4.30	4.32	4.28	4.38	4.31 ± 0.037	0.50	–	1.08	36428
II	6.32	6.36	6.33	6.40	6.34	6.35 ± 0.031	0.74	8.62	1.03	47419
III	7.89	7.85	7.82	7.80	7.90	7.85 ± 0.044	0.91	6.02	1.14	20449
IV	8.57	8.62	8.71	8.67	8.63	8.64 ± 0.048	1.00	3.95	1.20	22315
V	11.30	11.29	11.31	11.26	11.21	11.27 ± 0.041	1.30	12.23	1.05	32427
VI	12.91	12.90	12.88	12.89	12.91	12.90 ± 0.018	1.49	7.67	1.09	37714
VII	14.61	14.43	14.48	14.50	14.52	14.50 ± 0.066	1.68	6.96	1.21	52289
VIII	16.29	16.36	16.31	16.33	16.36	16.34 ± 0.036	1.89	9.58	1.30	55409
IX	19.65	19.76	19.80	19.76	19.70	19.74 ± 0.055	2.28	16.91	1.18	66135

t_R: retention time; RRT: relative retention time; R_s: resolution; As: tailing factor; S.D.: relative standard deviation; *a*: average of five determinations; *N*: theoretical plate number.

acid ($ClC_6H_4CO_3H$) in dry DCM [12]. These sulfones were also obtained as by-products during the synthesis of sulfoxide [18]. All these substances were characterized by ^{1}H NMR and Mass spectrometry. Modafinil acid sulfide (III) (yield: 99%), ^{1}H NMR (DMSO-d_6): δ 7.1–7.6 (m, 10H), 5.3 (s, 1H), 3.0 (s, 2H), M^+ = 259 Da, melting point 125 °C [19,20]. Modafinil acid sulfoxide (I) (yield: 85%), ^{1}H NMR (DMSO-d_6): δ 13.2 (bs, 1H), 7.2–7.5 (m, 10H), 5.4 (s, 1H), 3.6 (d, J = 14.3 Hz, 1H), 3.3 (d, J = 14.2Hz, 1H), M^+ = 275 Da, melting point 149 °C. Modafinil acid sulfone (II) (yield: 85%): ^{1}H NMR ($CDCl_3$): δ 7.5–7.8 (m, 10H), 5.7 (s, 1H), 3.8 (s, 2H), M^+ = 291 Da. Modafinil (sulfide) (VI) (yield: 95%), ^{1}H NMR ($CDCl_3$): δ 7.2–7.4 (m, 10H), 6.5 (bs, 1H), 5.5 (bs, 1H), 5.2 (s, 1H), 3.0 (s, 2H), M^+ = 238 Da, melting point 109 °C (literature value 110 °C). Modafinil (sulfoxide) (IV) (yield: 65%), ^{1}H NMR (DMSO-d_6): δ 7.3–7.6 (m, 10H), 6.1 (s, 1H), 5.3 (s, 1H), 3.7 (s, 1H), 3.2 (d, J = 13.6 Hz, 1H), 3.1 (d, J = 13.6 Hz, 1H), M^+ = 274 Da, melting point 164 °C [21]. Modafinil sulfone (V) (yield: 85%), ^{1}H NMR (DMSO-d_6): δ 7.75–7.4 (m, 10H), 6.0 (s, 1H), 3.74 (s, 2H), M^+ = 290 Da. Modafinil ester sulfide (IX) (yield: 98%), ^{1}H NMR ($CDCl_3$): δ 7.2–7.5 (m, 10H), 5.4 (s, 1H), 4.2 (q, J = 7.1 Hz, 2H), 3.1 (m, 2H), 1.2 (t, J = 7.1 Hz, 3H), M^+ = 287 Da. Modafinil ester sulfoxide (VII) (yield: 85%), ^{1}H NMR (DMSO): δ 7.2–7.5 (m, 10H), 5.4 (s, 1H), 3.6 (d, J = 14.3 Hz, 1H), 3.3 (d, J = 14.2 Hz, 1H), 4.2 (q, J = 7.1 Hz, 2H), 1.3 (t, J = 7.1 Hz, 3H). Modafinil ester sulfone (VIII) (yield: 83%), ^{1}H NMR (DMSO-d_6): δ 7.70–7.33 (m, 10H), 5.80 (s, 1H), 3.73 (s, 2H), 4.3 (q, J = 14.2 Hz, 2H), 1.4 (t, J = 14.2 Hz, 3H), M^+ = 319 Da.

3.2. Optimization of chromatographic conditions

Chemical structures of sulfide, sulfoxide, sulfone of modafinil (VI, IV, V), its acid (III, I, II) and ethyl ester (IX, VII, VIII) respectively are shown in Fig. 1. It could be seen from Fig. 1 that there are eight compounds and intermediates that could be present as potential impurities in the finished products of modafinil. The present study is aimed at developing a chromatographic system capable of eluting and resolving modafinil and its related substances originated from the synthesis. All the impurities and derivatives of modafinil such as sulfide, sulfoxide, sulfone of modafinil, its acid and ethyl ester were subjected to separation by reverse-phase HPLC on a Kromasil C_{18} column with 0.02 M ammonium acetate: acetonitrile with gradient elution (Table 1) at 30 °C. The compounds were analyzed on several linear gradient programs, but failed to get the good resolution as the compounds III (sulfide of acid) and IV (sulfoxide of amide) have shown close resolution. In linear gradient starting from 25% ACN to 90% at 15 min compounds III and IV are merged in each other. When extended the gradient program linear from 25 to 90% at 30 min, both the compounds were shown the resolution of 0.67 and also analysis time increased to more than 45 min. Several isocratic systems have been tested for separation and resolution of the compounds. But due to the high difference in polarity of the sulfide, sulfoxide, sulfone compounds, the efforts did not yield satisfactory results. Isocratic systems with methanol: water; methanol: buffers (of different pH adjustment); acetonitrile: water; acetonitrile: buffers also had been studied. As sulfide compounds (III, VI, IX) are less polar as compared to sulfoxides (I, IV, VII) and sulfones (II, V, VIII) at isocratic conditions with ACN: (0.02 M) ammonium acetate, 50:50 (v/v) compounds I, II, III, IV, V eluted within 15 min where as compounds VI, VII, VIII, IX had retention time more than 70 min. The developed method has shown best resolution >3.9 for all compounds within 20 min. A typical chromatogram of modafinil along with all related substances in nearly equal concentration is shown in Fig. 2. The chromatogram of modafinil spiked with 0.1% of each related substances is shown in Fig. 3. As the polarity was different, all compounds shown different behavior of retention. Elution order of all nine compounds in specified condition was acid > amide > ester and also sulfoxide > sulfone > sulfide. It was found that the starting material benzhydrol (X) eluted along with ester sulfoxide (VII) and difficult to resolve (Fig. 4). However, it could be detected by comparing UV/MS spectra of both the compounds. As both benzhydrol and sulfoxide ester have different UV/MS spectra, benzhydrol could be easily identified (for compound X, absorption wavelengths are 210, 254 nm, M^+ = 185 Da, fragmentation; 167, 142, 116, 77, 43 Da, similarly for compound VII, absorption wavelengths are 210, 225 nm, M^+ = 303 Da, fragmentation; 256, 167, 152 Da). Modafinil and its related substances were subjected to UV-absorption analysis and the spectra recorded in the range of 190–400 nm are shown in Fig. 5. It could be

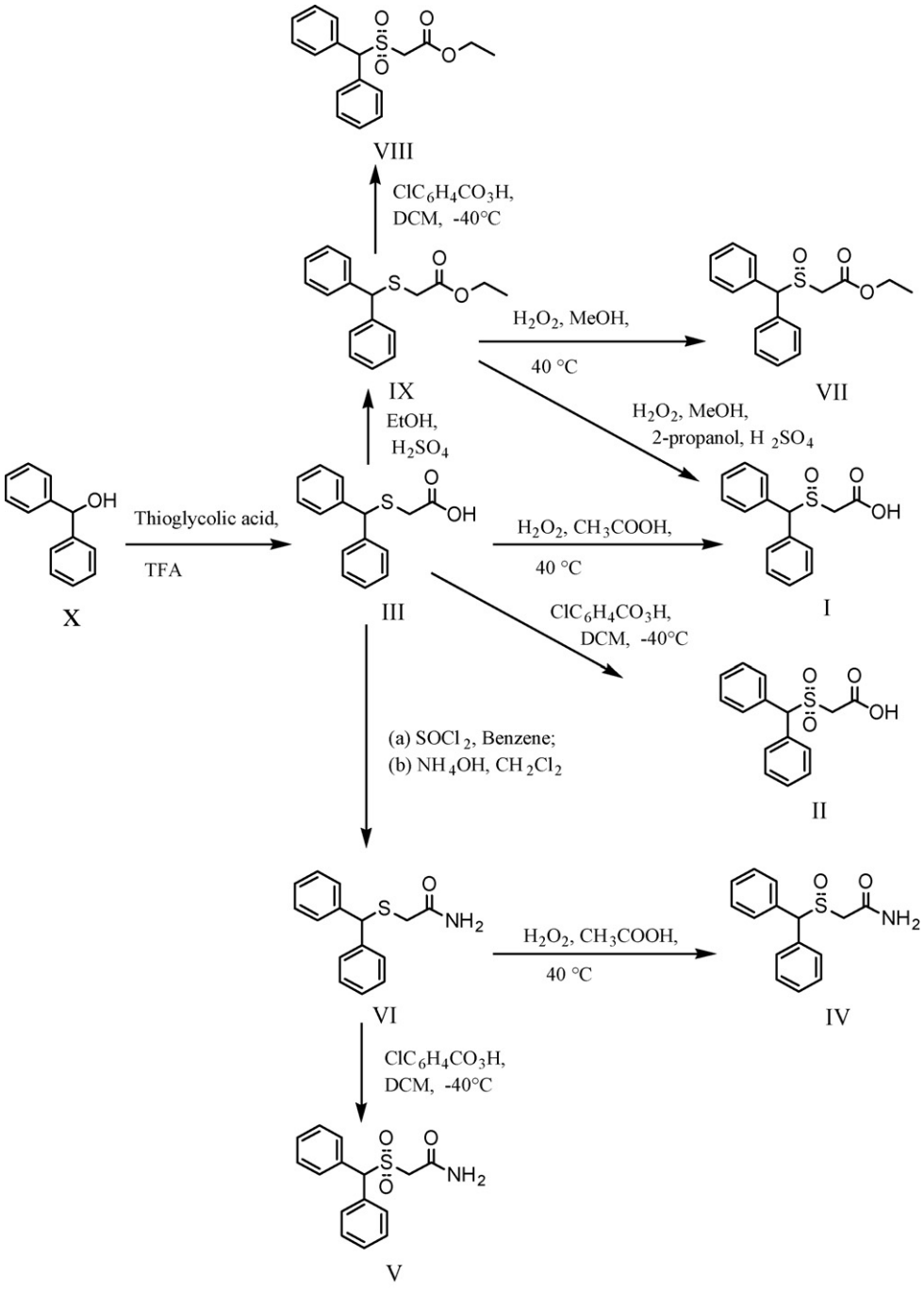

Fig. 1. Chemical reactions involved in synthesis of modafinil and its related substances. I: modafinil acid sulfoxide; II: modafinil acid sulfone; III: modafinil acid sulfide ; IV: modafinil (sulfoxide); V: modafinil sulfone; VI: modafinil sulfide; VII: modafinil ester sulfoxide; VIII: modafinil ester sulfone; IX: modafinil ester sulfide ; X: benzhydrol.

seen that modafinil has shown highest absorption at 225 nm. All the related substances have shown absorption in the range of 210–235 nm. The effects of temperature and pH on the retention behavior of all the compounds were studied.

3.3. Effect of temperature

Temperature did not show any change in the elution order but did a small effect on retention time, resolution and on tailing factor (Figs. 6 and 7). Its effect at seven different temperatures, i.e., 15, 20, 25, 30, 35, 40, 45 °C was studied. Temperature effect had shown least resolution of 3.69 for modafinil (IV) at 15 °C and highest resolution of 4.0 at 30 °C. So, 30 °C temperature was selected for analysis as all compounds have shown good resolution and tailing factors in acceptable range.

3.4. Effect of pH

Studies were carried out on the effect of buffer pH on resolution and retention. The pH had no effect on retention of

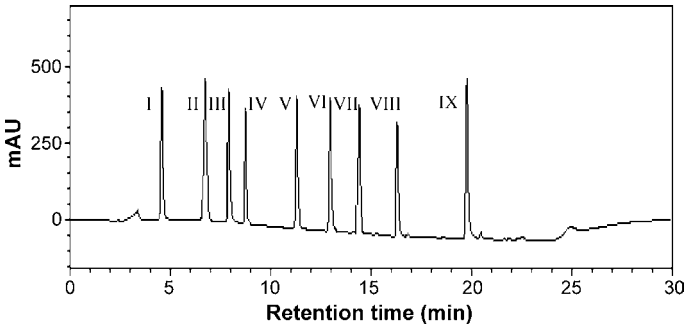

Fig. 2. Typical chromatogram of a synthetic mixture of modafinil (IV) and its related compounds. For identification of peaks please see text.

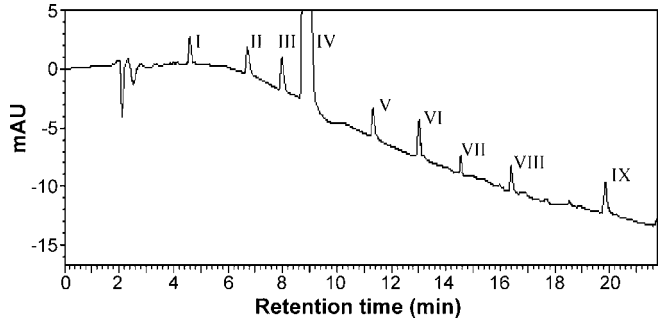

Fig. 3. Typical chromatogram of modafinil (IV) spiked with 0.1% of related substances.

compounds IV, V, VI, VII, VIII and IX. While compounds I, II and III showed increased retention as the pH of the buffer decreased from 6.5 to 3.0 and at pH 5.0. substance IV eluted first when compared III. At pH 4.5 compound III was eluted at 11.58 min after compounds I, II, IV, and V. At pH 4 compound III showed the resolution less than 1.2 and retention at 13.15 min. At pH 3.5, compounds II and IV were merged with each other where as compounds VII and III showed resolution less than 1.0. With decrease in pH, tailing was also increased and capacity factor decreased (Table 3; Fig. 8) for all the compounds. It could be seen from the Fig. 2 that at pH

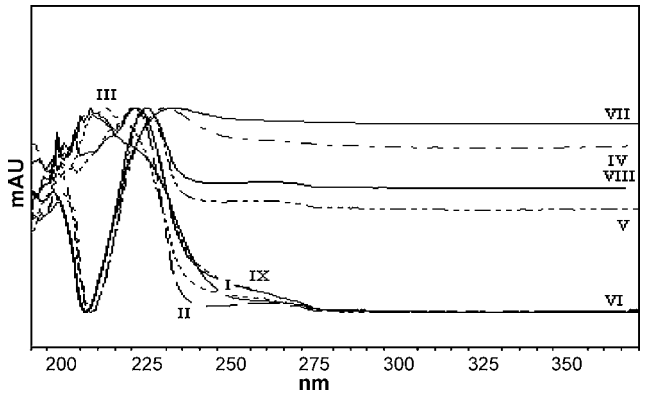

Fig. 5. UV-absorption spectra of modafinil (IV) and its related substances.

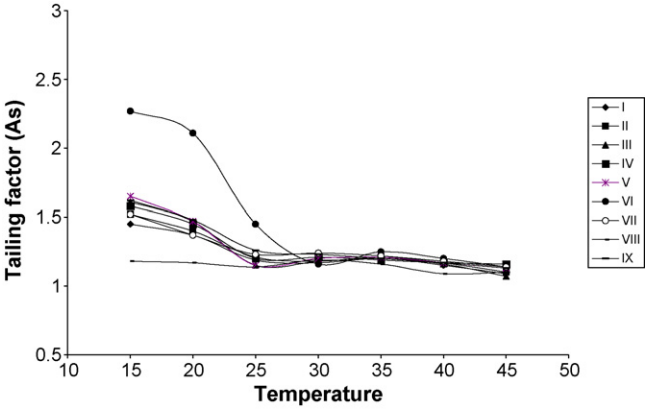

Fig. 6. Effect of temperature on peak tailing.

6.5, all the peaks with symmetrical and good resolution were obtained.

3.5. Assay

The assay of modafinil was estimated using a working standard and the method was validated by the following parameters.

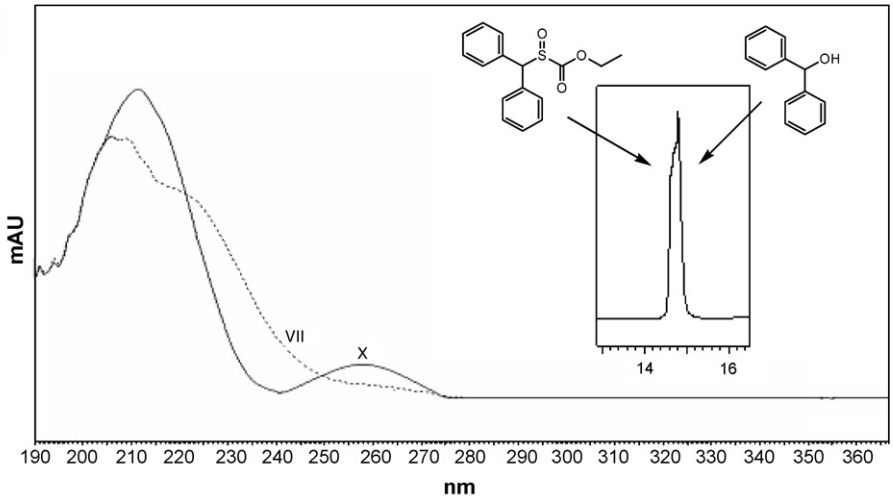

Fig. 4. On-line UV-differentiation of benzhydrol (X) and ester sulfoxide (VII).

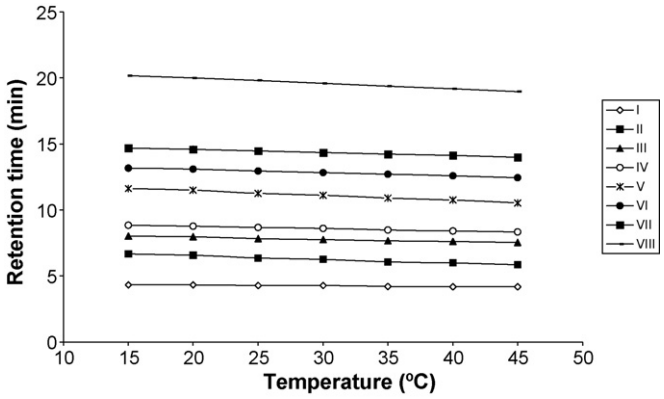

Fig. 7. Effect of temperature on retention.

Table 3
Effect of pH on tailing of peaks

	Tailing factor (As)								
pH	I	II	III	IV	V	VI	VII	VIII	IX
6.5	1.08	1.05	1.14	1.20	1.05	1.11	1.21	1.29	1.20
6.0	1.21	1.25	1.30	1.33	1.28	1.25	1.29	1.37	1.34
5.5	1.42	1.34	1.42	1.50	1.24	1.33	1.45	1.42	1.37
5.0	1.47	1.37	1.47	1.53	1.33	1.40	1.49	1.51	1.46
4.5	1.51	1.46	1.41	1.54	1.46	1.49	1.54	1.53	1.60
4.0	1.74	1.53	1.55	1.61	1.63	1.54	1.57	1.64	1.71
3.5	1.55	1.59	1.57	1.83	2.12	1.95	1.71	1.71	1.98

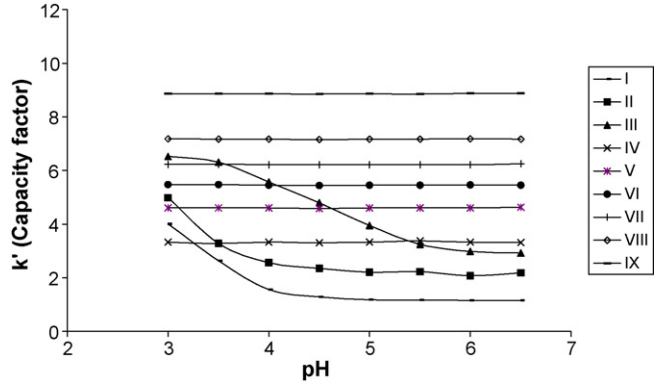

Fig. 8. Effect of pH on capacity factors of modafinil (IV) and its related substances.

Table 4
Specificity data

S. no.	Assay (%)	
	Unspiked sample	Sample spiked with impurities
1	100.01	99.88
2	99.84	99.95
3	99.88	99.92
Mean	99.91	99.91
S.D.	0.06	0.14
R.S.D. (%)	0.05	0.14

3.5.1. Specificity

Specificity is the ability of the method to measure the analyte response in presence of all potential impurities. The results are recorded in Table 4. PDA was used to evaluate the homogeneity of the peaks in the chromatogram. Chromatographic peak purity was determined using wavelength comparison at 210, 225, 233 and 254 nm. The plot with flattop showed that modafinil exhibited a homogeneous peak with no detectable impurities embedded in it.

3.5.2. Accuracy

The recoveries of I, II, III, V, VI, VII, VIII and IX were determined by spiking impurity at six different levels ranging from 25 to 150% with respect to the concentration of modafinil (IV) at a specified level. The recovery range and R.S.D. for all impurities were found to be 97.77–99.61% and 0.55–3.71, respectively (Table 5). Similarly the accuracy in determination of the assay of modafinil was checked at six concentration levels, i.e., 125, 250, 375, 500, 625, 750 μg/ml each in triplicate for 3 days and the percentage recoveries are recorded in Table 6. The R.S.D. values were found to be <0.6%.

3.5.3. Precision

The precision of the method was tested by six ($n = 6$) injections of modafinil spiked with 0.1% (w/w) of each intermediate and the R.S.D. of retention time (t_R), peak area were determined. The R.S.D. ranges from 0.14 to 0.85% for retention time and 0.59–2.80% for peak area (Table 7). The precision in determina-

Table 5
Recovery data

	Nominal 0.1% of impurity spiked to modafinil					
	25	50	75	100	125	150
Amount added (μg/ml)	1.25	2.50	3.75	5.0	6.25	7.5
% Recovery (±R.S.D %)						
(a) I	98.70 ± 0.55	98.97 ± 1.30	98.71 ± 1.90	98.95 ± 2.13	97.89 ± 2.06	98.75 ± 1.91
(b) II	98.80 ± 1.20	98.63 ± 1.57	97.95 ± 3.10	98.27 ± 3.71	98.99 ± 1.76	97.98 ± 2.01
(c) III	98.20 ± 1.80	97.98 ± 2.05	99.10 ± 0.67	98.39 ± 0.91	97.92 ± 2.22	99.01 ± 2.02
(d) V	98.97 ± 1.30	99.41 ± 2.10	98.85 ± 2.00	98.75 ± 2.13	98.46 ± 3.05	98.40 ± 1.85
(e) VI	98.89 ± 2.70	98.78 ± 3.05	99.11 ± 1.89	97.97 ± 1.89	99.61 ± 2.27	98.26 ± 1.32
(f) VII	97.85 ± 3.10	98.95 ± 2.95	97.77 ± 3.15	98.35 ± 2.05	98.81 ± 1.98	98.46 ± 2.81
(g) VIII	99.31 ± 3.00	99.12 ± 1.73	99.05 ± 1.77	98.43 ± 1.98	98.21 ± 2.30	97.85 ± 2.04
(h) IX	98.75 ± 2.60	99.07 ± 2.03	98.85 ± 1.23	98.56 ± 2.03	98.54 ± 3.10	98.12 ± 2.18

Table 6
Accuracy data for modafinil

S. no.	Concentration of modafinil (mg/ml)			
	Taken	Found ($n=3$)	% Recovery	R.S.D. (%)
1	0.125	0.1248	99.84	0.12
2	0.250	0.2479	99.16	0.40
3	0.370	0.3703	100.08	0.56
4	0.500	0.4970	99.40	0.20
5	0.625	0.6248	99.97	0.03
6	0.750	0.7489	99.85	0.13

$n=3$: average of three determinations; R.S.D.: relative standard deviation.

Table 7
Precision data

Compound	Retention time (t_R)		Peak area	
	Average[a]	R.S.D. (%)	Average[a]	R.S.D. (%)
I	4.31	0.85	106682	1.76
II	6.35	0.49	99677	1.47
III	7.75	0.56	106838	2.80
IV	8.60	0.56	25637001	1.16
V	11.10	0.36	82014	0.93
VI	12.83	0.14	76254	0.59
VII	14.35	0.45	74052	1.33
VIII	16.28	0.22	75245	1.83
IX	19.59	0.28	69754	1.61

[a] Average of six determinations.

tion of assay was studied by repeatability, intermediate precision and reproducibility (ruggedness). Repeatability is the intra-day variation in assay obtained at different concentration levels of armodifinil and expressed in terms of R.S.D. calculated each day. The R.S.D. values were found to be <0.9%, indicating a good repeatability (Table 8). The intermediate precision is the inter-day variation at the same concentration level determined on successive days. Inter-day variations calculated for each concentration level from the data of 3 days are expressed in terms of R.S.D. values. At each concentration level, the R.S.D. values were below 1% indicating a good intermediate precision. The ruggedness of the method is defined as the degree of reproducibility obtained by the analysis of the same sample under a variety of conditions at different labs, different analysts, different instruments, and different lots of reagents. The same samples of three concentrations were analyzed in triplicate on 2 days by another instrument (LC-10AVP Module HPLC gradient system containing two pumps and SPD-10AVP PDA detector) by a different analyst with different lots of reagents and columns. The data obtained were within 2% R.S.D.

Table 8
Intra and inter-day assay variation of modafinil

Intra-day			
Day 0			
Mean of concentration (mg/ml; $n=3$)	1.250	2.51	3.748
S.D.	0.0025	0.02	0.0035
R.S.D. (%)	0.20	0.80	0.09
Day 1			
Mean of concentration (mg/ml; $n=3$)	1.2493	2.512	3.751
S.D.	0.0015	0.0189	0.001
R.S.D. (%)	0.12	0.75	0.03
Day 2			
Mean of concentration (mg/ml; $n=3$)	1.2517	2.5133	3.751
S.D.	0.0015	0.0091	0.0036
R.S.D. (%)	0.12	0.36	0.10
Inter-day			
Mean of concentration (mg/ml; $n=3$)	1.25	2.51	3.75
S.D.	0.0016	0.0225	0.0173
R.S.D. (%)	0.09	0.89	0.46

Table 9
Linearity data

Compound	Range (μg/ml)	Regression equation	r^2
I	0.250–2.00	$Y=52804x+553.75$	0.9994
II	0.250–2.00	$Y=50728x+628.71$	0.9984
III	0.250–2.00	$Y=53674x+642.93$	0.9996
IV	125–1000	$Y=25287x+74593$	0.9996
V	0.250–2.00	$Y=41086x-226.39$	0.9999
VI	0.250–2.00	$Y=38874x-248.43$	0.9963
VII	0.250–2.00	$Y=36520x-226.39$	0.9997
VIII	0.250–2.00	$Y=36796x+422.61$	0.9973
IX	0.250–2.00	$Y=34735x-391.11$	0.9984

3.5.4. Linearity

The linearity of detector response to different concentrations of impurities were studied by analyzing modafinil spiked with each impurity at eight levels ranging from 25 to 200% (0.25–2.0 μg/ml) (Table 9). Similarly, linearity of modafinil was also studied by preparing standard solutions at eight different levels ranging from 125–1000 μg/ml. The data were subjected to the statistical analysis using a linear-regression model, the standard deviation of slope and intercept are calculated. The results have indicated good linearity (Fig. 9).

3.5.5. Limits of detection and quantitation

Limits of detection (LOD) and quantitation (LOQ) represent the concentration of the analyte that would yield signal-to-noise ratio of 3 for LOD and 10 for LOQ were determined by measuring the magnitude of analytical background by injecting blank samples and calculating the signal-to-noise ratio for each compound by injecting a series of solutions until the S/N ratio 3 for LOD and 10 for LOQ. The results are recorded in Table 10.

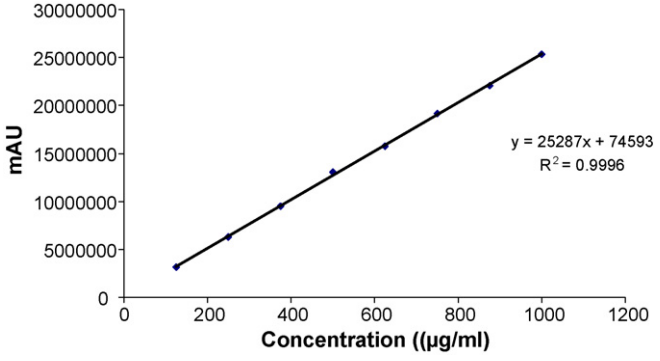

Fig. 9. Linearity graph of modafinil.

Table 10
Limits of detection and quantification

S. no.	Compound	LOD ($\times 10^{-8}$ g)	LOQ ($\times 10^{-8}$ g)
1	I	0.70	2.16
2	II	1.50	4.60
3	III	0.60	2.02
4	IV	0.65	2.05
5	V	1.60	5.02
6	VI	2.00	6.15
7	VII	2.10	6.11
8	VIII	2.40	6.92
9	IX	1.78	5.85

4. Conclusions

A gradient elution RP-LC method has been developed and validated for evaluation of purity and determination of modafinil in bulk drug. The developed method has been found to be selective, sensitive, precise. The method is applicable for detecting intermediates and other process-related impurities, which may be present at trace level in bulk drug as well as finished products.

Acknowledgements

The authors thanks to Dr. J.S. Yadav, Director, Indian Institute of Chemical Technology and Dr. M. Vairamani, Head, Analytical Chemstry Division, Indian Institute of Chemical Technology for encouragement and permission to communicate the results for publication. Mr. Dhananjay D. Shinde thanks Council of Scientific and Industrial Research (CSIR), New Delhi, India for grant of a junior research fellowship.

References

[1] B. Boyd, J. Castaner, Drugs Fut. 31 (2006) 17–21.
[2] T. Roth, C.A. Czeisler, J.K. Walsh, K.A. Wesnes, M. Williams, G.E. Niebler, S. Arora, Neuropsychopharmacology 30 (2005) S140.
[3] Robertson, Philmore Jr., Hellriegel, T. Edward, Clin. Pharmacokinet. 42 (2003) 123–137.
[4] J. Castaner, Drugs Fut. 15 (1990) 130–132.
[5] S.H. Gorman, J. Chromatogr. B 767 (2002) 269–276.
[6] H.A. Schwertner, S.B. Kong, J. Pharm. Biomed. Anal. 37 (2005) 475–479.
[7] A.R. Makinney, C.J. Suann, A.M. Stenhouse, Rapid Commun. Mass Spectrom. 19 (2005) 1217–1220.
[8] P. Bernat, F. Robles, Bernord Do, J. Chromatogr. B 706 (1998) 295–304.
[9] G. Moachon, D. Matinier, J. Chromatogr. B 654 (1994) 91–96.
[10] S.H. Gorman, J. Chromatogr. B 730 (1999) 1–7.
[11] Y. Tseng, V. Uralets, C.-T. Lin, F.-H. Kuo, J. Pharm. Biomed. Anal. 39 (2005) 1042–1045.
[12] Q.B. Cass, C.K. Kohn, S.A. Calafatti, H.Y. Abdul-Enein, J. Pharm. Biomed. Anal. 26 (2001) 123–130.
[13] Th. Becue, J Chromatogr. 557 (1991) 489–494.
[14] J.E. Drouin, M. Broquaire, J Chromatogr. 605 (1992) 19–31.
[15] ICH International conference on harmonization of technical requirements for registration of Pharmaceuticals for Human use, Impurities in New Drug Products, Geneva, Switzerland, 2002, Q3A (R1).
[16] ICH International conference on harmonization of technical requirements for registration of Pharmaceuticals for Human use, Impurities in New Drug Products, Geneva, Switzerland, 2003, Q3B (R1).
[17] T. Prisinzano, J. Podobinski, K. Tidgewell, M. Luo, D. Swenson, Tetrahedron-Asymmetr. 15 (2004) 1053–1058.
[18] N. Chetterjie, J.P. Stables, H. Wang, G.J. Alexander, Neurochem. Res. 29 (2004) 1481–1486.
[19] E. Carceller, M. Merlos, M. Giral, C. Almansa, J. Batroli, J. Garcia-Rafanell, J. Forn, J. Med. Chem. 36 (1993) 2984–2997.
[20] L.H. Brannigan, R.J. Brinker, R.J. Kaufman, S. Metz, U.S. Patent 4,964,893 (1990).
[21] L. Lafon, U.S. Patent 4,066,686 (1978).

Available online at www.sciencedirect.com
ScienceDirect
Talanta 73 (2007) 505–513
Talanta
www.elsevier.com/locate/talanta

Determination of the alkyl- and methoxy-phenolic content in wood extractives by micellar solid-phase microextraction and gas chromatography–mass spectrometry

Verónica Pino, Juan H. Ayala, Venerando González, Ana M. Afonso *

Department of Analytical Chemistry, Nutrition and Food Science, University of La Laguna. Campus de Anchieta, Astrofísico Francisco Sánchez s/n, E-38205 La Laguna, Spain

Received 16 January 2007; received in revised form 30 March 2007; accepted 11 April 2007
Available online 24 April 2007

Abstract

This work combines the utilization of the micellar media during the extraction step and the focused microwave-assisted extraction followed by the solid-phase microextraction–gas chromatography/mass spectrometry (SPME–GC/MS) to determine the alkyl- and methoxy-phenolic content in wood extractives. The proposed environmental-friendly method is mainly characterized by short analysis times (5 min for the microwaves extraction step) and for avoiding the use of organic solvents. Different surfactants were tried for the extraction process: the cationic surfactant CTAB and the non-ionic surfactants Triton X-100 and POLE, with similar extraction efficiencies (85.5–99.7%). The overall method presents limits of detection in the ng g^{-1} region for the alkylphenols (from 7 to 150 ng g^{-1}) and in the μg g^{-1} region for the methoxyphenols (from 0.80 to 22.9 μg g^{-1}). The vanillin was the compound most abundant in the wood extractives studied, with concentrations up to 116.2 mg kg^{-1}.

Keywords: Micellar media; Focused microwave-assisted extraction; Solid-phase microextraction; Alkylphenols; Methoxyphenols; Wood extractives; Gas chromatography–mass spectrometry

1. Introduction

Most phenols in environmental samples come from industrial waste sources; some, however, originate from degradation of natural sources (e.g. lignin and humic acids) [1]. The lignin is a complex biopolymer that constitutes 20–30% (w/w) of the vegetal biomass. It decomposes in phenolic compounds, aldehydes, ketones, carboxylic acids and alcohols when heated at temperatures between 270 and 400 °C. Among these compounds, phenols and methoxyphenols are components of great importance for the smoke flavour, preservation of foods and antioxidant effects when the vegetal biomass is used as the source for food smoking [2–4]. In this sense, it may be interesting to know a priori the phenolic content in the vegetal biomass, and so to differentiate it from the compounds originated in the smoking process with the purpose of selecting *a priori* certain flavours.

Wood extractives are defined as compounds that can be extracted from wood by means of both polar and non-polar solvents [5]. They include a large variety of compounds including phenols [6]. Creosote-treated woods, which are allowed in Japan even for decorative furniture, contain numerous chemical as polycyclic aromatic hydrocarbons and water extractable phenols, with subsequent health risks [7]. Some polyphenols (tannins) that are present in hardwoods (e.g. oak and ash-tree) are associated to risk of nasal cancer in workers of the wood industry [8,9]. In addition, some compounds emitted by woods during its hot-pressing may be attributed to volatile and semi-volatile extractive compounds, degradation products of the wood and chemical reaction products of the wood extractives [10]. Thus, rapid procedures for the identification and quantification of problematic wood extractive components are highly desirable.

The wood extractives are not always problematic. Some volatile compounds extracted from the wood (especially oak) during barrel-ageing are very important, because they are related to some flavour properties of alcoholic beverages. The accumulation of volatile oak compounds in the alcoholic drinks during the maturation period depends on many factors, particularly the

* Corresponding author. Fax: +34 922318090.
E-mail address: aafonso@ull.es (A.M. Afonso).

0039-9140/$ – see front matter © 2007 Elsevier B.V. All rights reserved.
doi:10.1016/j.talanta.2007.04.013

quantity of volatile compounds available and their precursors presented in the wood's matrix [11,12]. Although all these precedents, the phenol content of most wood species has not yet been determined [13–15].

Soxhlet and ultrasound-assisted extraction [16], liquid–liquid extraction (LLE) [17] and solid-phase extraction (SPE) [18,19] are the most commonly used techniques for the isolation and/or the enrichment of phenols prior to the chromatographic analysis. Derivatization of wood extractives for GC analysis is usually carried out to improve compound resolution, and can be achieved by methylation, acetylation or silylation [16,20,21]. However, these procedures are tedious and introduce a degree of error in quantitative analysis because there is an increase in the number of experimental steps for the overall method. These methods are also hazardous to human health as they use organic solvents. Great concern over the disposal of such toxic organic solvents has led to move towards cleaner extraction methods such as solid-phase microextraction (SPME) [22,23]. However, when analyzing complex solid samples, it is necessary to use more specific extraction procedures combined with SPME in order to get the analyte out of the solid matrix [24,25].

The micellar extraction is a friendly-environmental method that has been applied to a wide range of analytes and solid samples, especially when combined with microwaves [26,27]. The coupling of the micellar extraction with the solid-phase microextraction gives place to the micellar-solid-phase microextraction (MSPME) method, which combines the advantages of both analytical resources. This technique has been successfully applied to the determination of polycyclic aromatic hydrocarbons (PAHs) in certified reference sediment [28]. The SPME with micellar media has also been applied to the determination of analyte-micelle partition coefficients for PAHs and phenols [29–31] or to study interactions between phenols and different micellar media [32]. More recently, it has also been applied to the determination of chlorophenols in sawdust samples [33].

This work tries to take advantage of the focused microwave-assisted micellar extraction, mainly in terms of speed and to avoid using organic solvents when extracting phenols from woods, altogether with the advantages of the SPME in combination with a GC–MS, like the automation and especially avoiding the clean-up or any other preconcentration step because it is not necessary to remove the surfactant prior to GC injection. In this sense, the main aim of this work is to offer an environment-friendly method to determine a group of alkyl- and methoxy-phenols in complex matrixes like woods, which are not well studied. Among the studied compounds, 2,4-dimethylphenol, 4-methylphenol, 4-chloro-3-methylphenol, and 2,4,6-trimethylphenol, have been included by the US Environmental Protection Agency (EPA) [34] as well as by the European Union [35] in their lists of priority pollutants.

2. Experimental

2.1. Reagents

The standard solution of 4-chloro-3-methylphenol (4-C-3-MP) at a concentration of 10 ng μL^{-1} in acetonitrile was supplied by Dr. Ehrenstorfer, Reference Materials (Augsburg, Germany). This standard solution was used to prepare a stock standard solution of 1 ng μL^{-1} in acetonitrile. The standard solution of 4-C-3-MP for spiking purposes was prepared at a concentration of 160 ng mL^{-1}. The standard mixture solution of 14 phenols (Phenol-Mix-1) with a concentration of 50 ng μL^{-1} (in methanol) was supplied by Dr. Ehrenstorfer. These 14 phenols were phenol (P), 2-methylphenol (2-MP), 3-methylphenol (3-MP), 4-methylphenol (4-MP), 2,6-dimethylphenol (2,6-DMP), 2,4-dimethylphenol (2,4-DMP), 2,5-dimethylphenol (2,5-DMP), 2,3-dimethylphenol (2,3-DMP), 3,5-dimethylphenol (3,5-DMP), 3,4-dimethylphenol (3,4-DMP), 2,4,6-trimethylphenol (2,4,6-TMP), 2,3,6-trimethylphenol (2,3,6-TMP), 2,3,5-trimethylphenol (2,3,5-TMP), and 3,4,5-trimethylphenol (3,4,5-TMP). The standards of 2-ethylphenol (2-EP) and 3-ethylphenol (3-EP) were supplied by Dr. Ehrenstorfer with purity higher than 99% (w/w). These ethylated phenols standards were used for the preparation of a stock standard solution of 2000 ng μL^{-1}. The standards of 3-methoxyphenol (3-MeP), 2,6-dimethoxyphenol (2,6-DMeP), vanillin (V), and eugenol (Eu) were supplied by Fluka (Buchs, Switzerland) with a purity higher than 98% (w/w). These standards were used for the preparation of stock standard solutions of 2000 ng μL^{-1} each one. These five standard solutions of 2000 ng μL^{-1} and the Phenol-Mix-1 were employed in the preparation of a stock standard solution of 2.5 ng μL^{-1} for the 14 phenols, Eu, 2-EP and 3-EP, 100 ng μL^{-1} for the 3-MeP, and 250 ng μL^{-1} for the 2,6-DMeP and V. This stock standard solution was used in the preparation of the final working standard solutions. Acetonitrile of HPLC grade (Merck, Darmstadt, Germany) was used for such dilutions.

Polyoxyethylene-10-lauryl ether (POLE) and *t*-octylphenoxypolyethoxyethanol (Triton X-100) were supplied by Sigma (St. Louis, MO, USA). Cetyltrimethylammonium bromide (CTAB) was supplied by Aldrich (Beerse, Belgium). Deionized water was obtained from a Milli-Q water purification system (Millipore, Bedford, MA, USA).

The wood samples were collected from a local carpentry. The four selected samples belong to the common ones used in regular carpentry works. Wood samples 1 and 3 correspond to the so-called wooden conglomerates (with a high content of resins and glue), whereas wood samples 2 and 4 are natural woods. The four samples present similar organic matter content: between 929 and 985 mg g^{-1}. The determination of the organic matter content was based on the standard method ASTM D2974.

2.2. Instrumentation

Focused microwave-assisted extractions were performed at atmospheric pressure using a CEM Focused Microwave™ Synthesis System apparatus, model Discover (CEM Corporation, Matthews, NC, USA) equipped with an infrared temperature control system, stirring and cooling options. The cooling is carried out by means of a flow of air. The ChemDriver™ software (CEM) was used for data acquisition.

For SPME analysis, an autosampler fiber holder (model 57331) from Supelco (Bellefonte, PA, USA) was used. In this system, it is necessary to use a 12-vial carousel, prepared for 10-mL vials (2-7389 from Supelco). The vials are always completely filled to leave no headspace. This SPME system incorporates an agitation mechanism consisting of a small motor and a cam to vibrate the needle. The fiber in this design works as a stirrer. This automatic autosampler for SPME is very useful because it avoids the use of stir bars, which are related to problems of analytes' adsorption [36]. The amber vials were capped with PTFE-coated septa. The SPME fiber used was a 85 μm polyacrylate (PA) (Supelco). The extraction time for the fiber was 180 min. The fiber was conditioned in the hot injector port of the GC according to the instructions given by the manufacturer: 2 h at 300 °C. Blanks were run periodically during the analysis to confirm the absence of contaminants.

The identification and quantification of phenols were achieved using SPME and gas chromatography/mass spectrometry (GC/MS). GC/MS was performed on a Varian (Varian Inc., Palo Alto, CA, USA) model 3800 Varian Saturn 2000 GC/MS system, equipped with a 30 m × 0.25 mm i.d. VF-5ms column (Varian) and equipped with a Varian autosampler (model 8200 CX). The Saturn GC/MS workstation 5.52 software was used for data acquisition. The GC column was employed under the following temperature program: 60 °C, 4 min isothermal, 8 °C min^{-1} to 120 °C, 2 °C min^{-1} to 135 °C, and 8 °C min^{-1} to 280 °C. The carrier gas was helium, with a flow of 1 mL min^{-1}.

The temperature of the injector was maintained at 300 °C. The desorption time for the fiber in the GC injector was always 5 min. The use of higher times does not improve the peak-area of the extracted analytes. The temperature of the transfer line was maintained at 290 °C. The ionization was performed with a kinetic energy of the impacting electrons of 70 eV. The temperature of the ion trap was 200 °C. The MS analysis was carried out in scan mode with a mass range between 65 and 300 *m/z* (u). The quantitative determination was carried out using the mass values corresponding to the molecular ions of the different phenols (SIM mode).

The glassware used in this study was first washed with detergent and deionized water and then rinsed with deionized water, methanol (Merck), and a mixture of acetone/ethanol (1:1), both from Merck. Finally, the non-graduated glassware and, especially, the sample vials were dried in an oven at 550 °C and wrapped with aluminum foil before use.

2.3. Procedures

Sawdust samples were produced from the selected wood samples using specific carpentry instruments. Afterwards, sawdust samples were sieved, and fractions under 500 μm were selected for the analysis. Twenty gram of the sieved sawdust sample was placed in a glass vessel, and mixed with 25 mL of the 4-C-3-MP spiking solution (in acetonitrile). This solution was slowly added to form a dough which was mechanically stirred for several minutes. Once the sawdust sample was spiked, it was stored in the dark for 24 h. This spiked procedure tries to ensure the complete elimination of the acetonitrile from the wood sample before the analysis, also avoiding any kind of photodecomposition. The spiked level was 200 ng g^{-1}. It is assumed that any analyte–matrix interaction occurs to a similar extent to those in real samples.

Twelve milliliters of the aqueous micellar solution were added to 0.6 g of the sawdust sample (spiked or non-spiked) with a surfactant concentration dependent on the particular surfactant that was being used, and placed in a Pyrex® tube of 40 mL. The selected surfactant concentrations were 0.5% (w/v) for POLE and Triton X-100, and 0.04% (w/v) for CTAB. After ensuring that an agitation bar is placed in the solution, the extraction tube was introduced into the microwave cavity. Extraction was performed at a fixed maximum temperature of the vessels of 65 °C and at a fixed level of microwave oven power (150 W). When the maximum temperature was reached, it was kept constant during a fixed time of 1.5 min. Afterwards, the tube was allowed to cool at room temperature. The supernatant was then quantitatively transferred and filtered through 0.80 μm Millex®-AA Sryinge Driven Filter Unit (Millipore). Ten milliliters of the filtrate were placed in SPME vials and subjected to the SPME–GC–MS analysis.

3. Results and discussion

3.1. Chromatographic separation

Fig. 1 shows a representative SPME–GC–MS chromatogram under the optimized conditions. The chromatogram was obtained using SPME and a solution with nominal concentration of 15 μg L^{-1} for the alkylphenols, Eu and 4-C-3-MP, 0.6 ng μL^{-1} for 3-MeP, and 1.5 ng μL^{-1} for 2,6-DMeP and V, all dissolved in POLE (0.5% w/v). It was not possible to achieve a satisfactory chromatographic resolution between 3-MP and 4-MP. In addition, these compounds generate the same ions in the detection system. Therefore, the peak is expressed as 3-MP + 4-MP. The same problems took place with the pairs 2,4-DMP + 2,5-DMP, and 3-EP + 3,5-DMP. The chromatographic resolution was not good between 3-MeP and 2,3,6-TMP. However, these compounds have different ionizations by electronic impact and therefore their identification was possible. On the other hand, the phenol (P) did not have enough sensitivity to be accurately detected under these experimental conditions. The obtained peak-shape for methylated and especially methoxylated phenols is due to the fact that the determination is carried out without derivatization. Any derivatization step was discarded in order to decrease the experimental time of the extraction process. Table 1 summarizes the retention time window (RTW) determined for each compound. The RTW is defined for each analyte as the average of the retention times, obtained for 30 different replicas during 2 months and using three different PA fiber coatings, plus or minus three times the standard deviation, using different surfactants and also phenolic solutions at different concentrations. This table also includes the ions used for the analytes' quantification.

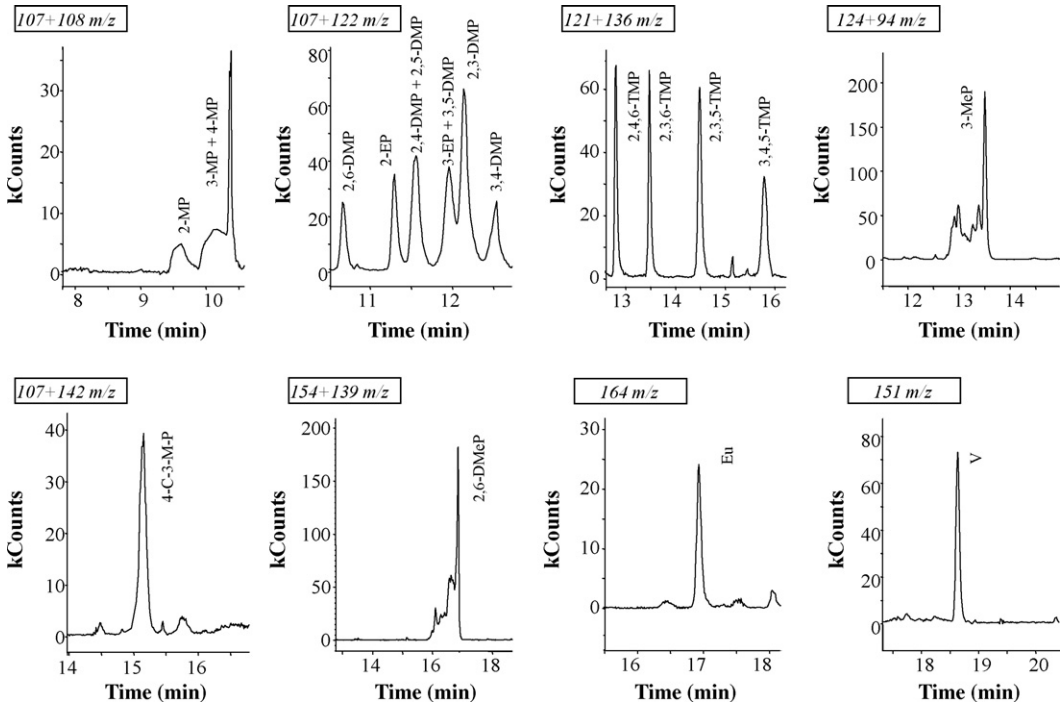

Fig. 1. SPME–GC–MS chromatogram (SIM) of the studied phenols obtained with the PA SPME fiber coating in a micellar solution of POLE 0.5% (w/v). The rest of experimental conditions are as described in the text.

3.2. Characteristics of the MSPME method for alkyl- and methoxy-phenols

The sensitivity of a SPME method using micellar media is dictated by the amount of free analyte in the aqueous phase. It is assumed that the analyte retained onto the SPME fiber coating comes from the aqueous phase, whereas the analyte bound to the micelle remains in solution [28–30]. In this sense, the importance of the surfactant concentration is decisive in the extraction efficiency: high surfactant concentrations imply low extraction efficiencies by MSPME. Hence, low surfactant concentrations are apparently the key to achieve better results. However, this efficiency in MSPME cannot be considered isolated. The surfactant concentration is also related to the extraction efficiency of analytes from solid matrixes when using microwave-assisted micellar extraction. A compromise solution must therefore be achieved between an adequate surfactant concentration to extract analytes from solid samples when using microwaves (high concentration are generally adequate), and at the same time, such surfactant concentration should not be so high that avoids the subsequent quantification of the analytes by MSPME–GC–MS.

Table 1
Retention time window and quantifying ions for the studied phenols

Compound name (abbreviation in parenthesis)	RTW (min)	Ion (*m*/*z*)
2-Methylphenol (2-MP)	9.60 ± 0.26	107 + 108
3-Methylphenol + 4-methylphenol (3-MP + 4-MP)	10.15 ± 0.22	107 + 108
2,6-Dimethylphenol (2,6-DMP)	10.68 ± 0.06	107 + 122
2-Ethylphenol (2-EP)	11.31 ± 0.16	107 + 122
2,4-Dimethylphenol + 2,5-dimethylphenol (2,4-DMP + 2,5-DMP)	11.58 ± 0.15	107 + 122
3-Ethylphenol + 3,5-dimethylphenol (3-EP + 3,5-DMP)	11.99 ± 0.09	107 + 122
2,3-Dimethylphenol (2,3-DMP)	12.16 ± 0.26	107 + 122
3,4-Dimethylphenol (3,4-DMP)	12.54 ± 0.04	107 + 122
2,4,6-Trimethylphenol (2,4,6-TMP)	12.81 ± 0.09	121 + 136
3-Methoxyphenol (3-MeP)	13.47 ± 0.23	124 + 94
2,3,6-Trimethylphenol (2,3,6-TMP)	13.49 ± 0.09	121 + 136
2,3,5-Trimethylphenol (2,3,5-TMP)	14.50 ± 0.13	121 + 136
4-Chloro-3-methylphenol (4-C-3-MP)	15.11 ± 0.05	107 + 142
3,4,5-Trimethylphenol (3,4,5-TMP)	15.81 ± 0.18	121 + 136
2,6-Dimethoxyphenol (2,6-DMeP)	16.78 ± 0.24	154 + 139
Eugenol (Eu)	16.94 ± 0.06	164
Vanillin (V)	18.66 ± 0.14	151

Chromatographic conditions as described in the experimental part.

Attending to the results obtained in a previous work [30], where we studied the interactions between phenols and micellar media, we might conclude some general remarks. The cationic surfactant CTAB gives low extraction efficiency by MSPME and at the same time high partition coefficients for alkylphenols, that is, it would be a good extractant of alkylphenols from solid matrixes because of the affinity between alkylphenols and CTAB. In other words, CTAB could be considered a good extractant for micellar microwave-assisted extraction, but not as good for MSPME. On the other hand, the non-ionic surfactant Triton X-100 gives high extraction efficiencies by MSPME and low partition coefficient values. That is, Triton X-100 would not be a very good extractant for micellar microwave-assisted extraction of alkylphenols, but good to achieve adequate efficiencies by MSPME. The non-ionic surfactant POLE gives fairly good extraction efficiencies by MSPME and also moderate partition coefficient values for the alkylphenols. However, it should be noted that the differences between the partition coefficients for alkylphenols in all surfactants (obtained by MSPME) are not so accused as the differences obtained between chlorophenols in all surfactants, as can be observed from Table 2. For chlorophenols, the POLE surfactant gave better extraction efficiencies for the overall method [33]. On the contrary, it is expected similar behaviours for the overall microwave extraction-MSPME when using these three surfactants for the alkyl- and methoxy-phenols, despite the slight differences aforementioned.

The methoxyphenols presented very low partition coefficients in micellar media [30]. Thus, these compounds are going to be hardly extracted from solid samples by micellar microwave-assisted extraction.

The selected concentrations for POLE and Triton X-100 were 0.5% (w/v) in order to have intermediate conditions, and to compare between them. The selected concentration for CTAB was 0.04% (w/v) in order to improve its MSPME extraction efficiency. The polyacrylate (PA) fiber coating was selected by its polar nature. Its efficiency to extract phenols has been demonstrated in other works [37].

Table 2
Partition coefficient values ($K_{M,m}$) obtained for a group of phenols with different surfactants by MSPME

Compound	$K_{M,m}$ [30]		
	CTAB	Triton X-100	POLE
2-Chlorophenol	356.2	32.4	143.6
4-C-3-MP	1351.3	162.8	878.3
3,5-Dichlorophenol	4752.1	319.7	2996.1
3,4-Dichlorophenol	1820	362.3	2030.8
3,4-DMP	689.9	109.1	150.8
2-EP	549.3	34.5	113.1
2,4,6-TMP	845.2	67.7	235.2
2,3,6-TMP	709	43.3	265.7
2,3,5-TMP	1155	73.1	379
3,4,5-TMP	1037.9	55.2	246.3
3-MeP	234.4	11.9	37.8
2,6-DMeP	231.1	–	20.8

The figures of merit were studied to evaluate the performance of the MSPME–GC–MS procedure with the selected surfactant concentrations and without considering the microwaves extraction step. Table 3 illustrates the slopes and the linear regression coefficients of the calibration plots for the studied phenols, as well as the detection limits (DL) calculated according to Cuadros et al. [38]. All phenols showed linearities with correlation coefficients (R) greater than 0.990 within the linearity ranges: 2–20 ng mL^{-1} for 4-C-3-MP; 10–125 ng mL^{-1} for the methylphenols, ethylphenols, and eugenol; 0.1–5 ng μL^{-1} for 3-MeP; and 1–12 ng μL^{-1} for 2,6-DMeP and V. The slope of the calibration plot can be used as a qualitative way to measure the sensitivity. As it has been pointed out in a previous work [30], it can be observed that Triton X-100 generates higher sensitivities than POLE for all the studied phenols in MSPME, except

Table 3
Figures of merit of the MSPME–GC–MS method for the studied phenols using without considering the microwave-assisted micellar extraction step

Compound	POLE, 0.5% (w/v)			Triton X-100, 0.5% (w/v)			CTAB, 0.04% (w/v)		
	Slope ± S.D.[a]	R	DL (ng mL^{-1})	Slope ± S.D.[a]	R	DL (ng mL^{-1})	Slope ± S.D.[a]	R	DL (ng mL^{-1})
2-MP	17,749 ± 367	0.999	5.86	33,185 ± 2,212	0.996	2.07	51,710 ± 1,509	0.999	1.29
3-MP + 4-MP	25,829 ± 694	0.999	7.55	65,606 ± 2,751	0.998	1.30	132,497 ± 14,508	0.994	4.83
2,6-DMP	31,447 ± 326	0.999	3.14	73,161 ± 1,521	0.999	0.98	157,304 ± 5,431	0.999	1.52
2-EP	42,150 ± 322	0.999	2.37	132,872 ± 2,980	0.999	1.10	159,355 ± 16,323	0.995	4.52
2,4-DMP + 2,5-DMP	139,623 ± 5595	0.994	6.20	214,666 ± 4,909	0.999	0.59	224,924 ± 19,102	0.996	1.87
3-EP + 3,5-DMP	132,023 ± 828	0.999	1.90	253,518 ± 4,644	0.999	0.77	578,376 ± 8,582	0.999	0.66
2,3-DMP	40,743 ± 5093	0.998	5.32	100,682 ± 14,383	0.997	1.60	16,598 ± 2,371	0.996	4.02
3,4-DMP	45,402 ± 923	0.999	6.16	129,273 ± 4,132	0.998	1.38	18,792 ± 1,766	0.996	4.15
2,4,6-TMP	69,591 ± 771	0.999	3.36	237,988 ± 5,921	0.998	1.29	264,179 ± 23,705	0.996	3.96
3-MeP	12,533 ± 166	0.999	0.16 ng μL^{-1}	23,061 ± 425	0.999	0.04 ng μL^{-1}	21,260 ± 1,347	0.998	0.11 ng μL^{-1}
2,3,6-TMP	60,284 ± 434	0.999	2.18	184,061 ± 5,619	0.998	1.58	247,335 ± 16,328	0.998	2.91
2,3,5-TMP	81,021 ± 572	0.999	2.18	322,724 ± 2,205	0.999	0.35	415,887 ± 26,890	0.998	2.85
4-C-3-MP	65,913 ± 1797	0.999	1.15	384,536 ± 12,114	0.998	1.61	470,590 ± 39,216	0.997	2.42
3,4,5-TMP	61,600 ± 556	0.999	2.74	243,529 ± 8,679	0.997	1.68	321,954 ± 18,790	0.998	2.58
2,6-DMeP	4,433 ± 128	0.997	0.90 ng μL^{-1}	11,557 ± 414	0.997	0.18 ng μL^{-1}	12,821 ± 1,745	0.991	0.60 ng μL^{-1}
Eu	40,260 ± 419	0.999	3.22	200,873 ± 9,078	0.995	2.34	142,419 ± 16,968	0.993	5.26
V	7,933 ± 111	0.999	0.01 ng μL^{-1}	5,230 ± 161	0.999	0.12 ng μL^{-1}	10,486 ± 2,542	0.99	1.15 ng μL^{-1}

[a] Slope of the calibration plot and error for $n = 8$.

for V. The comparison of POLE and Triton X-100 with CTAB must be carried out taking into account the concentrations used in this study. The CTAB concentration employed was 0.04%, much lower than POLE and Triton X-100 (0.5%).

The detection limits of the calibration curves support the considerations made about the sensitivities. Comparing POLE and Triton X-100 (both at the same concentration), the lowest detection limits mainly correspond to Triton X-100. The detection limits of the calibration plots for the alkylphenols ranged from 0.35 ng mL^{-1} for 2,3,5-TMP in Triton X-100 to 7.55 ng mL^{-1} for 3-MP + 4-MP in POLE. Higher values were obtained for the methoxyphenols, from 0.04 ng μL^{-1} in Triton X-100 to 0.90 ng μL^{-1} in POLE. The vanillin was an important exception, as can be observed from data in Table 3. This compound is much better detected using POLE, than using Triton X-100 or CTAB. One important factor that must be kept in mind is that these results are related only to the MSPME–GC–MS method. The different affinities phenols-micelles during the microwave extraction step from woods will be crucial in the extraction efficiencies and sensitivity of the overall method.

3.3. Focused microwave-assisted micellar extraction in combination with MSPME

The focused microwave system (using micellar solutions as the extracting media) was selected for this study due to its advantages over the conventional microwaves: the safety due to operation at atmospheric pressure or the possibility of using programmable addition of reagents at any time during the extraction.

The optimization of the focused microwave system was carried out taking into account the subsequent utilization of the MSPME method. As it has been mentioned early about the MSPME characteristics, the adequate surfactant concentrations to develop the extraction procedures are 0.5% (w/v) for POLE and Triton X-100, and 0.04% (w/v) for CTAB. The extraction volume was also another important parameter for the extraction process. Ten milliliters was the selected value to fill completely the SPME vials according to our SPME device, and so to have the maximum efficiency by SPME. Considering possible losses during the filtration step, 12 mL of surfactant solution are first added during the microwave extraction process, and only 10 mL are placed into the SPME vials after filtration. Given these precedents, where some variables are already fixed by the MSPME method, it is just necessary to optimize two parameters related with the focused microwave system: the microwave power and the maximum temperature to be reached in the extraction vessel. In addition, our skills using the focused microwave system dictated us to fix the time where the temperature in the microwave vessels is kept constant, because it is not a significant variable. In this sense, it was kept constant to a value of 1.5 min.

The optimization of the extraction method was carried out with the target analyte 4-C-3-MP spiked to wood sample 1 as described in the experimental section. This compound is known by its toxicity. Its presence in wood samples can be due to the fact that higher chlorophenols are commonly used in the pressure treatment in the wood preservation industry (they are added to the glue), and other contamination sources. The rest of alkyl- and methoxy-phenols were not used as target analytes to evaluate the extraction efficiency of the method because many of these compounds are probably already present (natural components of the woods), and over-recoveries problems would arise.

Table 4
Extraction parameters and factor levels used in the central design (2^2 + star with 2 central points), with a total number of 10 runs

Variable	Fixed	Low	High	Center	Optimum
Extracting volume (mL)	12				12
Amount of sawdust sample (g)	0.6				0.6
Temperature (°C)		30	65	47.5	65
Time maintaining the fixed temperature (min)	1.5				1.5
Microwave power (W)		40	150	95	150
% POLE concentration (w/v)	0.5				0.5
% Triton X-100 concentration (w/v)	0.5				0.5
% CTAB concentration (w/v)	0.04				0.04

The method was optimized using a simple experimental design with the following levels: 40 and 150 W for the microwave power, and 30 and 65 °C for the maximum temperature, as it can be observed from Table 4. The optimum levels dictated by the central composite design 2^2 + star with two central points and face centered were 65 °C for the maximum temperature to be reached inside the vessels, and a microwave power of 150 W. In these optimized conditions, the focused microwave system only requires 2–3 min to reach the optimal conditions and hence, only 5 min are required for the microwave extraction process. It should be highlighted the short analysis times required for the microwave extraction method. The automatic MSPME method requires 180 min for each sample, and up to 12 samples can be left in the autosampler to be analyzed without the necessity of any extra-attention on the chemist's side.

The proposed method therefore needs 5 min (manual manipulation by microwaves) and 180 min (automatic SPME), using 12 mL of micellar media, directly followed by GC–MS. Buhr et al. [16] determine pentachlorophenol in wood and wood-base products using a combination of ultrasonication (45 min) and shaking (15 h) in the solvent mixture toluene-sulphuric acid, followed by derivatization with acetic anhydride and determination by GC–ECD. Diserens [21] determines 19 chlorophenols in wood samples by GC–MS. The method starts by an acetyla-

Table 5
Extraction efficiencies, intermediate precision and detection limits obtained in the optimized focused microwave-assisted micellar extraction method and MSPME–GC–MS for 4-C-3-MP using spiked wood samples

	Extraction efficiency (%)[a]	R.S.D. (%)[b]	DL (ng g^{-1})[c]
POLE	99.7	9.7	35
CTAB	89.3	10.2	43
Triton X-100	85.5	8.3	39

[a] $n = 6$ Analysis.
[b] Intermediate precision expressed as relative standard deviation (%).
[c] Calculated as described in the text.

tion step with sodium carbonate in acetic anhydride, followed by liquid–liquid extraction in hexane with 30 min of shaking.

The evaluation of the extraction efficiency for the focused microwave-assisted micellar extraction and MSPME–GC–MS in the already optimized conditions was carried out with six portions of wood sample 1 spiked with 4-C-3-MP. Table 5 shows the recoveries, intermediate precision and detection limits of the optimized method for 4-C-3-MP. The obtained extraction efficiencies oscillated between 85.5 and 99.7%, whereas Diserens [21] obtained average recovery from wood of approximately 50% for chlorophenols, which appeared to be sufficient when the poor homogeneity of the chlorophenols content in board was considered. In the proposed method, it can be observed that the best efficiencies are achieved with POLE for the total micellar microwave-MSPME method due to its intermediate qualities in both the microwave extraction and in MSPME, but with slight improvements with respect to Triton X-100 and CTAB. The CTAB showed slightly higher extraction efficiencies than Triton X-100 for the overall method, due to its high strength to remove phenols from a solid matrix by microwaves, and for using low CTAB concentration to increase its MSPME sensitivity. Nonetheless, extraction efficiencies around 100% are obtained, showing up the efficiency of the overall method with all the surfactants studied.

Intermediate precision was evaluated by doing two consecutive extractions of spiked wood samples during three different days under the optimized conditions. The obtained relative standard deviation (R.S.D.) ranged between 8.3 and 10.2%, showing the repeatability of the proposed method.

The detection limits of the overall method were calculated as three times the standard deviation of the signal corresponding to a spiked wood sample with a 4-C-3-MP concentration close to the lowest value of its linear range (60 ng g^{-1}), and analyzed under the optimized procedure. This way of calculating DLs usually generates higher values but they are more realistic. It is because these DLs include all the analytical procedure, and not just the chromatographic separation. They ranged between 35 and 43 ng g^{-1}.

The detection limits for the methoxy-phenols and the rest of alkyl-phenols were calculated assuming 100% extraction efficiency for the overall method. DLs ranging from 7 ng g^{-1} for 2,3,5-TMP in Triton X-100 to 151 ng g^{-1} for 3-MP + 4-MP in POLE are obtained. For methoxyphenols, the DLs would range from 0.80 mg kg^{-1} for 3-MeP in Triton X-100 to 17.9 mg kg^{-1} for 2,6-DMeP in POLE. V would have DLs of 0.20, 22.9, and 2.40 mg kg^{-1} in POLE, CTAB, and Triton X-100, respectively. There are not reported values of DLs for alkylphenols or methoxyphenols in woods. The DL for pentachlorophenol in woods reported by Buhr et al. [16] using a conventional extraction method with organic solvents and derivatization was 140 ng g^{-1}. Diserens [21] reports DLs around 20 ng g^{-1} for chlorophenols in wood samples.

The influence of the nature of the matrix in the extraction efficiency of the optimized method was assessed. Three wood samples (2, 3 and 4) were analyzed in the same conditions as wood sample 1. Fig. 2 shows the extraction efficiencies obtained with the spiked wood samples when using POLE as the extracting surfactant in the overall optimized method. The spiked level for 4-C-3-MP was 200 ng g^{-1}. All wood samples were analyzed by quadruplicate. The obtained extraction efficiencies for the studied wood samples show the robustness of the method.

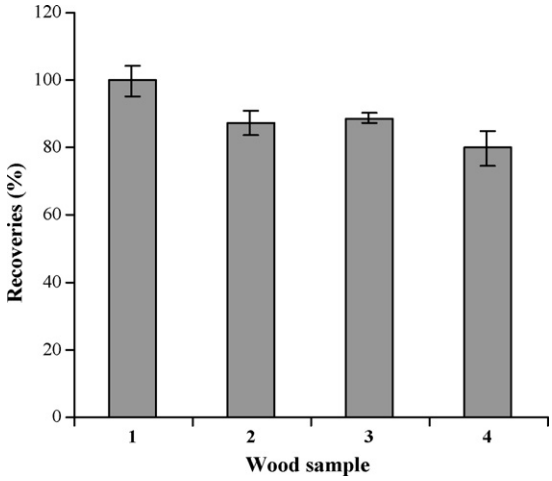

Fig. 2. Extraction efficiencies for 4-C-3-MP in different spiked wood samples using POLE as the extracting surfactant using the optimized procedure.

3.4. Alkyl- and methoxy-phenolic content in wood extractives

The optimized procedure using several surfactants was applied to evaluate the phenolic content of several non-spiked woods. Table 6 shows the observed amounts of alkyl- and methoxy-phenols found in non-spiked wood sample 1 using POLE, CTAB and Triton X-100 as the extractive systems. It can be observed that V was the main compound found, with a high concentration (roughly around 30 mg kg^{-1}). This compound is usually related to flavour effects when the woods are used as smoking material for foods [4]. The second compound in importance in this wood extractive is the 2,6-DMeP, which is also an important component related to flavours in smoked foods. The rest of alkyl-phenols found in this wood extractive have concen-

Table 6
Alkyl- and methoxy-phenolic content in non-spiked wood sample 1 (mg kg^{-1}) evaluated with different surfactants as extracting systems, and following the whole optimized extracting procedure

Compound	POLE	Triton X-100	CTAB
V	29.8 ± 1.7[a]	41.3 ± 2.9[a]	24.3 ± 0.3[a]
2,6-DMeP	19.1 ± 0.2[a]	18.9 ± 0.03[a]	17.6 ± 1.7[a]
3,4-DMP	0.34 ± 0.04[a]	0.20 ± 0.08[a]	0.28 ± 0.06[a]
2,6-DMP	DL (0.06)[b]	0.10 ± 0.01[a]	0.10 ± 0.01[a]
2-EP	0.09 ± 0.01[a]	0.06 ± 0.01[a]	0.07 ± 0.03[a]
2-MP	0.19 ± 0.04[a]	0.16 ± 0.01[a]	0.15 ± 0.01[a]
3-MP + 4-MP	0.18 ± 0.01[a]	0.15 ± 0.02[a]	0.14 ± 0.01[a]
3-EP + 3,5-DMP	0.05 ± 0.01[a]	0.06 ± 0.01[a]	0.07 ± 0.01[a]
Eu	0.07 ± 0.01[a]	0.05 ± 0.01[a]	DL (0.09)[b]
2,4-DMP + 2,5-DMP	DL (0.12)[b]	0.04 ± 0.02[a]	DL (0.04)[b]
2,3,5-TMP	0.06 ± 0.01[a]	0.09 ± 0.02[a]	DL (0.06)[b]

[a] Standard deviation for $n = 3$.
[b] Detection limit (mg kg^{-1}) in parenthesis.

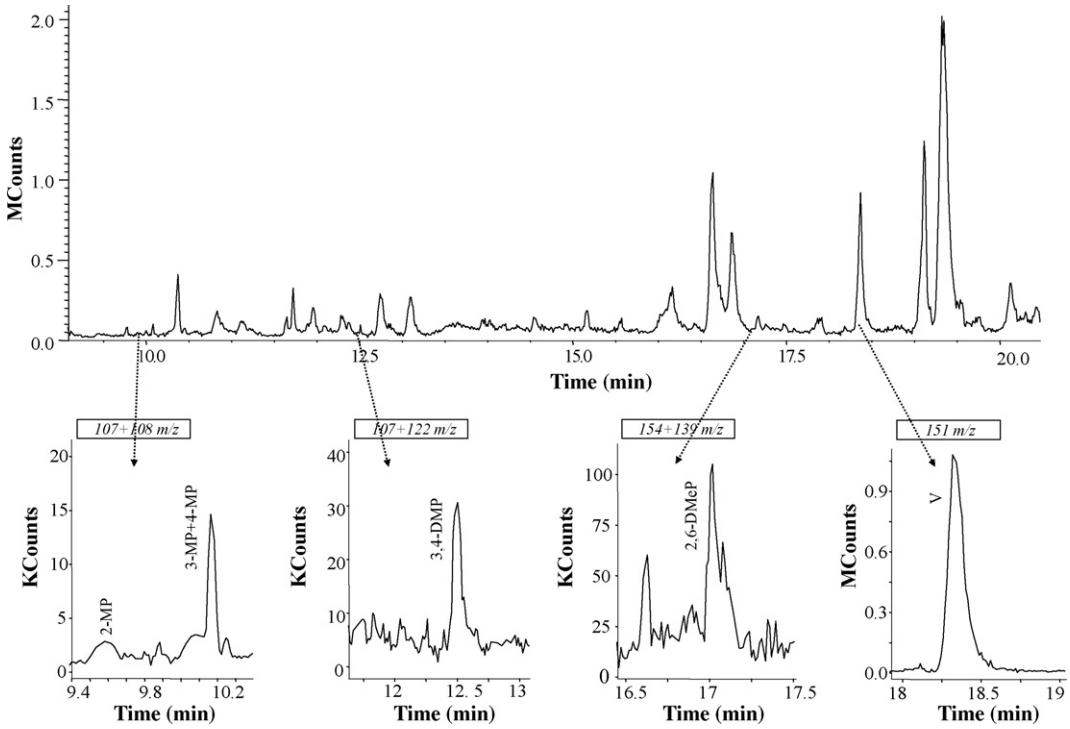

Fig. 3. Chromatogram of the non-spiked wood sample 1 extracted with POLE following the whole optimized extraction procedure: resulting ion chromatogram (up), and single ion monitoring (bottom) for several significant compounds quantified.

trations between 0.04 and 0.34 mg kg^{-1}. It should be highlighted that the concentrations found for the alkyl- and methoxy-phenols are independent on the surfactant used during the extraction process. Hence, all these surfactants are good alternatives to organic solvents for the extraction of these compounds. The exception corresponds to V when using Triton X-100 as the extracting system, showing a high extractability for V when using Triton X-100.

Fig. 3 shows a representative chromatogram for the non-spiked wood sample 1 extracted with POLE following the optimized method. It can be observed the high intensity of the peak corresponding to V, even in the presence of many interferences from the matrix, as well as some other compounds also quantified like 2-MP, 3-MP + 4-MP, 3,4-DMP, and 2,6-DMeP.

Different non-spiked wood samples were subjected to the extraction process to evaluate the robustness of the proposed method with woods of different nature (natural wood samples and also wooden conglomerates). Table 7 shows the obtained results with the non-ionic surfactant POLE as the extracting system. It can be observed that V was also the main compound found in all the studied non-spiked wood extractives, with concentration up to 116.2 mg kg^{-1} for wood sample 2. However, 2,6-DMeP, which was quantified as a majority compound for non-spiked wood sample 1, could not be quantified in the rest of non-spiked wood samples studied. The rest of phenols found in woods presented concentration ranging from 0.06 to 0.22 mg kg^{-1}. It is hard to find relationships between natural and wooden conglomerate samples attending to the amount and/or number of phenols found, and this is basically due to the low number of samples studied. For example, the highest amount of V corresponds to wood sample 2 (natural wood) and wood sample 3 (wooden conglomerate). Compounds such as 3-MP + 4-MP and 3-EP + 3,5-DMP are found in all the studied samples, and with similar contents. There are no specific compounds found in natural woods but not in wooden conglomerates, and *vice versa*. Nevertheless, the purpose of the study was to propose an alternative method to conventional methods to characterize the alkyl- and methoxy-phenolic content in woods rather than to characterize exhaustively the phenolic content of the studied samples.

Table 7
Alkyl- and methoxy-phenolic content in different non-spiked woods when using POLE as the extracting system, and following the whole optimized extraction procedure

Compound	Wood sample 2	Wood sample 3	Wood sample 4
V	116.2 ± 13.2[a]	111.6 ± 1.7[a]	30.0 ± 3.4[a]
2,6-DMeP	DL[b]	DL[b]	DL[b]
3,4-DMP	DL[b]	0.14 ± 0.01[a]	0.22 ± 0.02[a]
2,6-DMP	DL[b]	DL[b]	0.08 ± 0.01[a]
2-EP	DL[b]	DL[b]	0.20 ± 0.01[a]
2-MP	DL[b]	DL[b]	DL[b]
3-MP + 4-MP	0.16 ± 0.02[a]	0.22 ± 0.06[a]	0.22 ± 0.01[a]
3-EP + 3,5-DMP	0.08 ± 0.01[a]	0.14 ± 0.02[a]	0.19 ± 0.04[a]
Eu	0.11 ± 0.01[a]	0.07 ± 0.01[a]	DL[b]
2,4-DMP + 2,5-DMP	0.13 ± 0.02[a]	0.13 ± 0.01[a]	0.18 ± 0.05[a]
2,3,5-TMP	0.07 ± 0.01[a]	DL[b]	0.08 ± 0.01[a]
2,4,6-TMP	0.10 ± 0.01[a]	DL[b]	DL[b]
3,4,5-TMP	0.06 ± 0.01[a]	DL[b]	DL[b]

[a] Standard deviation for $n = 3$.
[b] Detected but not quantified.

4. Conclusions

The determination of alkyl- and methoxy-phenols in woods has been carried out by a friendly environmental method based on the focused microwave-assisted micellar extraction in combination with solid-phase microextraction/gas chromatography–mass spectrometry. The overall method is characterized by being faster than other conventional extraction methods (5 min for the microwave-assisted extraction) and by avoiding the use of potentially hazardous organic solvents during the extraction process. The overall method presents limits of detection ranging from 7 to 150 ng g^{-1} for the alkylphenols, and from 0.80 to 22.99 μg g^{-1} for the methoxyphenols. In this sense, this method can be used as a screening method to evaluate the alkyl- and methoxy-phenolic content in wood extractives, with the purpose to evaluate the suitability of different woods for smoking processes.

Acknowledgment

Verónica Pino would like to acknowledge the Ministerio de Educación y Ciencia (Spain) for the Juan de la Cierva contract with the University of La Laguna.

References

[1] M.A. Crespín, M. Gallego, M. Valcárcel, J. Chromatogr. A 897 (2000) 279–293.
[2] T. Sérot, R. Baron, C. Knockaert, J.L. Vallet, Food Chem. 85 (2004) 111–120.
[3] M.D. Guillén, M.J. Manzanos, M.L. Ibargoitia, J. Agric. Food Chem. 49 (2001) 2395–2403.
[4] F.J. Conde, A.M. Afonso, V. González, J.H. Ayala, Anal. Bioanal. Chem. 385 (2006) 1162–1171.
[5] D. Fengel, G. Wegener, Wood Chemistry, Ultrastructure, Reactions, Walter de Gruyter, Berlin, 1983, p. 132.
[6] M.P. Fernandez, P.A. Watson, C. Breuil, J. Chromatogr. A 922 (2001) 225–233.
[7] Y. Ikarashi, M.-A. Kaniwa, T. Tsuchiya, Chemosphere 60 (2005) 1279–1287.
[8] A. Leclerc, M. Martínez Cortes, M. Gérin, D. Luce, J. Brugère, Am. J. Epidemiol. 140 (1994) 340–349.
[9] EU Directive N° L138/66, 1999.
[10] W. Wang, D.J. Gardner, M.G.D. Baumann, Forest Prod. J. 53 (2003) 65–72.
[11] I. Caldeira, M.C. Clímaco, R. Bruno-de-Sousa, A.P. Belchior, J. Food Eng. 76 (2006) 202–211.
[12] L.J. Perez-Prieto, M.L. Hera-Orts, J.M. López-Roca, J.I. Fernández-Fernández, E. Gómez-Plaza, J. Sci. Food Agric. 83 (2003) 1445–1450.
[13] P. Mämmelä, Analyst 126 (2001) 1535–1538.
[14] S.P. Pohjamo, J.E. Hemming, S.M. Willför, M.H.T. Reunanen, B.R. Holmbom, Phytochemistry (2003) 165–169.
[15] M. Balaban, Phytochem. Anal. 15 (2004) 385–388.
[16] A. Buhr, C. Genning, T. Salthammer, Fresenius' J. Anal. Chem. 367 (2000) 73–78.
[17] EPA Method 8041. Phenols by Gas Chromatography: Capillary Column Technique, Environmental Protection Agency, Washington, DC, 1995, p. 1.
[18] I. Rodríguez, M.P. Llompart, R. Cela, J. Chromatogr. A 885 (2000) 291–304.
[19] H. Bagheri, A. Mohammadi, A. Salemi, Anal. Chim. Acta 513 (2004) 445–449.
[20] J. Peng, R. Leone, A.N. Serreqi, B. Breuil, Tappi J. 82 (1999) 204–211.
[21] J.M. Diserens, J. AOAC Int. 84 (2001) 853–860.
[22] M.N. Sarrión, F.J. Santos, M.T. Galcerán, J. Chromatogr. A 947 (2002) 155–165.
[23] C. Domeño, G. Munizza, C. Nerín, J. Chromatogr. A 1095 (2005) 8–15.
[24] M.C. Wei, J.F. Jen, J. Chromatogr. A 1012 (2003) 111–118.
[25] S. Bieri, Y. Ilias, C. Bicchi, J.L. Veuthey, P. Christen, J. Chromatogr. A 1112 (2006) 127–132.
[26] C. Padrón-Sanz, R. Halko, Z. Sosa-Ferrera, J.J. Santana-Rodríguez, J. Chromatogr. A 1078 (2005) 13–21.
[27] V. Pino, J.H. Ayala, A.M. Afonso, V. González, J. Chromatogr. A 869 (2000) 515–522.
[28] V. Pino, J.H. Ayala, A.M. Afonso, V. González, Anal. Chim. Acta 477 (2003) 81–91.
[29] V. Pino, J.H. Ayala, V. González, A.M. Afonso, Anal. Chem. 76 (2004) 4572–4578.
[30] V. Pino, F.J. Conde, J.H. Ayala, A.M. Afonso, V. González, J. Chromatogr. A 1099 (2005) 64–74.
[31] V. Pino, A.M. Afonso, J.H. Ayala, V. González, Anal. Bioanal. Chem. 387 (2007) 2271–2281.
[32] V. Pino, F.J. Conde, J.H. Ayala, V. González, A.M. Afonso, Chromatographia 63 (2006) 167–174.
[33] V. Pino, J.H. Ayala, V. González, A.M. Afonso, Anal. Chim. Acta 582 (2007) 10–18.
[34] US Environmental Protection Agency [EPA], Ground water and drinking water: list of drinking water contaminants and MCLs, Available online at: http://www.epa.gov/safewater/mcl.html (accessed January 2007).
[35] The list of priority substances in the field of water policy and amending directive, Council directive 2455/2001/ECC, Official Journal L331, November 20, 2001, pp. 1–5.
[36] E. Baltussen, P. Sandra, F. David, H.G. Janssen, C. Cramers, Anal. Chem. 71 (1999) 5213–5216.
[37] V. Pino, J.H. Ayala, V. González, A.M. Afonso, Int. J. Environ. Anal. Chem. 87 (2007) 159–175.
[38] L. Cuadros-Rodríguez, A.M. García-Campaña, C. Jiménez-Linares, M. Román-Ceba, Anal. Lett. 26 (1993) 1243–1258.

Available online at www.sciencedirect.com
ScienceDirect
Talanta 73 (2007) 476–482
Talanta
www.elsevier.com/locate/talanta

Rapid measurements of concentrations of natural uranium in process stream samples via gamma spectrometry at an extraction facility

Uma Sundar, Vasantha Ramamurthy, Vinay Buche, D. Narasinga Rao, P.C. Sivadasan, R.B. Yadav *

Control Laboratory, Nuclear Fuel Complex, Hyderabad 500 062, India

Received 19 January 2007; received in revised form 10 April 2007; accepted 10 April 2007
Available online 24 April 2007

Abstract

A new application of gamma spectrometry in the efficient measurement of natural uranium in the process stream at an extraction plant is described here. The inherent nuclear properties of uranium viz. emanation of characteristic gamma rays (185.7 keV) has been exploited for the determination of concentrations ranging from 5 to 450 g l^{-1} by passive photon counting of 185.7 keV gamma rays from ^{235}U isotope for a maximum of 3–10 min per sample. This technique is totally matrix independent unlike other instrumental analytical techniques like wavelength dispersive X-ray fluorescence spectrometry and UV–vis spectrophotometry. Solution samples of aqueous and organic phase can be directly counted without the requirement of sample preparation. A MINIM-based gamma spectrometer consisting of a multichannel pulse height analyzer and a 3 in. × 3 in. well-type NaI(Tl) scintillation detector with an approximately 2 in. thick lead shield has been employed for the measurements. The results are compared with those obtained by potentiometry and wavelength dispersive X-ray fluorescence spectrometry (WD-XRF). Relative standard deviation of 1–5% has been obtained depending upon the concentration of uranium, which is more than adequate for routine process control samples. This paper also discusses in detail the problems associated with the determination of high concentrations of uranium in using 63 and 93 keV gamma rays emanating from ^{234}Th ($t_{1/2}$ 24 days) the immediate daughter of ^{238}U isotope in samples that have attained secular equilibrium and the limitations of these energies in the routine analysis of freshly extracted uranium.

Keywords: Uranium; Gamma spectrometry; Process streams; Well-type NaI(Tl) scintillation detector

1. Introduction

Natural uranium dioxide pellets are the most widely used nuclear fuels in the pressurized heavy water nuclear power reactors (PHWR). The manufacturing process of uranium dioxide pellets involves various steps that include leaching of uranium from the ore using sulphuric acid [1], purification using anion exchange [2], precipitation as magnesium diuranate (MDU), purification through solvent extraction [3], precipitation of uranium as ammonium diuranate (ADU) [4], drying, calcination and reduction to uranium dioxide. In our uranium extraction plants, MDU is digested with nitric acid and uranium is extracted using TBP–kerosene mixture followed by precipitation using ammonia. The process flow sheet is given in Fig. 1.

Concentrations of uranium in the process stream samples provide essential information required for process monitoring, such as material input in UNF/UNS, extraction efficiency in UNE, effective stripping in UNPS/UNPE and over all material balance in LS and raffinate. Destructive techniques, such as gravimetry [5], volumetry [6], polarography [7], coulometry [8], X-ray fluorescence spectrometry [9] and spectrophotometry [10,11], etc. are available for the determination of uranium. Yet, each technique possesses some merits and demerits and cannot be applied without difficulty to all samples of process streams. Gravimetric methods, though highly precise, are time consuming. Volumetric methods consist of several steps and require varieties of chemicals. As a result these methods generate larger volumes of analytical effluents. While electroanalytical techniques are familiar alternative analytical methods, they are not preferred for routine analysis again owing to the multifunctional execution of procedural requirements and associated indispensable chemical consumption and effluent generation problems,

* Corresponding author.
E-mail address: rby@nfc.gov.in (R.B. Yadav).

0039-9140/$ – see front matter © 2007 Published by Elsevier B.V.
doi:10.1016/j.talanta.2007.04.018

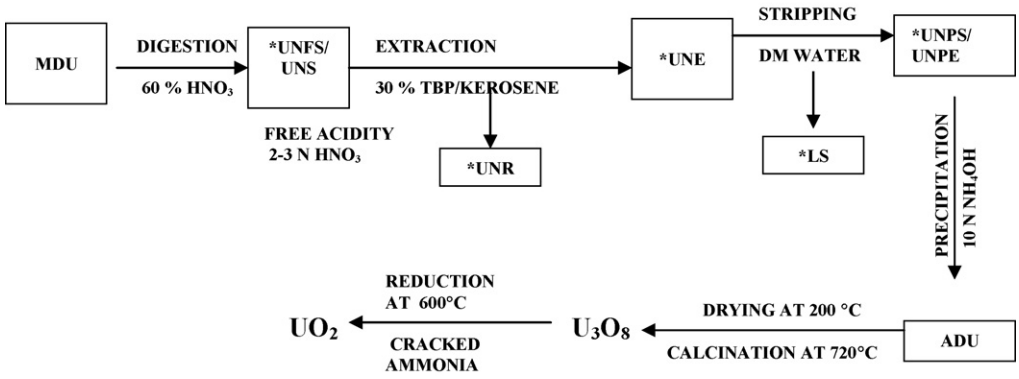

Fig. 1. Process flow sheet of extraction of natural uranium: MDU–Magnesium diuranate; UNFS–Uranyl nitrate feed solution/slurry; UNE–Uranyl nitrate extract; UNPS/UNPE–Pure/evaporated pure solution; LS- Lean solvent; UNR–Uranyl nitrate raffinate; ADU–Ammonium diuranate.

which are not desirable again. X-ray fluorescence techniques involve very high capital and operational maintenance cost on sophisticated instrumentation besides the disadvantage of strong matrix dependency. In these techniques linearity of counts with respect to concentration is observed only in the lower concentrations of uranium. As a result these techniques are limited to a very narrow dynamic range leading to several-fold dilution of samples to working range prior to analysis. In addition, if uranium is present in organic matrix as in the case of UNE and LS samples, the calibration standards also must be prepared in the identical matrix in order to obtain accurate results.

Earlier, in our laboratory a method based on the measurement of absorption of uranyl ions in visible region using UV–vis spectrophotometry was developed and communicated [12]. However, the technique requires sample dilution to the working range where high quantities of uranium are present. In samples containing very small quantities of uranium complexation of uranium using Arsenazo III in a strictly maintained acidity conditions is required. A lot of precaution had to be taken to avoid interference from the accompanying impurities in significant quantities causing bias in the results. In the case of organic samples, uranium had to be quantitatively stripped into aqueous medium prior to analysis. Thus this technique is a time consuming one besides being a destructive and effluent generating method. These limiting factors of the conventional techniques stressed the need for a routine nondestructive analytical method that is simple, rapid, sensitive, accurate and cost-effective.

We find that passive gamma spectrometry overcomes the impediments discussed in the foregone paragraphs and is quite desirable for the routine measurements of uranium in the process streams. Thus this technique stands as an excellent nondestructive analytical tool for this specific application. Reports on the gamma spectrometric measurements found in literature provide information regarding the application mainly for the determination of ^{235}U isotope content in the fuel pellets during production [13–19] and in spent fuel for the disposal of nuclear waste [20], both online and offline. Only the feasibility of the determination of the concentration of uranium by gamma spectrometry using high purity germanium (HPGe) detector [21,22] by monitoring the 1001 keV peak is available in literature. However, routine exploration for continuous monitoring of the process streams in natural uranium extraction plants exploiting 185.7 keV photon counting using well-type NaI(Tl) detector has scarcely been reported.

Gamma photons with energies 63, 93, 143, 185.7, 776 and 1001 keV are significant in the spectrum of natural uranium decay series. The 185.7 keV gamma photons exhibit the maximum yield of 57% [23,24]. Although natural uranium consists of only 0.71% of ^{235}U content, owing to the very high yield of the 185.7 keV gamma photons considerable counts can be obtained in 3–5 min for uranium samples in the range of 5–450 g l^{-1} using a multichannel gamma spectrometer equipped with a 3 in. × 3 in. well-type NaI(Tl) detector. The area under the peak of the 185.7 keV gamma rays are correlated to the concentration of uranium present in the sample and the content of uranium in the sample is determined from the calibration curves obtained with the standard solutions of uranium. The valuable advantage of this technique is found in that there is no matrix effect. Hence the calibration curves made using aqueous standards itself can be used conveniently for the determination of concentration of uranium in organic samples viz. UNE and LS. The nondestructive nature of the method offers the advantage of no effluent generation and thus eliminates the expenditure and labour involved in the recovery of uranium values from the analytical waste that accumulate in large quantities in the existing conventional methods of analysis.

The detailed account of the experimentation and the results are discussed in the foregoing pages of this paper. In order to ascertain the validity and establish the superiority of this technique, the results are compared with volumetry, WD-XRF, spectrophotometry and differential pulse voltametry. A systematic study has also been undertaken to study the feasibility of determination of concentrations of uranium using 63 and 93 keV gamma rays from ^{234}Th, the immediate daughter of ^{238}U and the results are discussed in detail.

2. Experimental

2.1. Reagents

A standard stock solution of 450 g l^{-1} of uranium was prepared as follows: pure U_3O_8 powder from Uranium Oxide Plant was calcined at 850 °C in a muffle furnace for 4–5 h. After cool-

ing, 530.7537 g of the U_3O_8 was dissolved in about 500 ml of 1:1 nitric acid by heating over a hot plate and made up to 1000 ml using demineralised water. Working standard solutions of concentrations ranging from 5 to 400 g l^{-1} were prepared by suitable dilutions of the above standard stock solution.

2.2. Instrumentation

Analysis was performed using MINIM-based Gamma Spectrometer GRS 11M supplied by M/s Nucleonics Systems Private Limited, Hyderabad, India, which is equipped with 3 in. × 3 in. well-type NaI(Tl) detector with approximately 2 in. thick lead shield and 8 K multichannel pulse height analyser. The gamma ray spectrum displays 63, 93 and 185.7 keV peaks and the corresponding area under the respective peaks is evaluated by the emulation software associated with the system after subtracting the background and is displayed. Sample holder is specially designed using Teflon to resemble a Buchner funnel closed at the bottom that fits into the well of the detector. This geometry allows the analysis solution well exposed to the detector so that maximum possible gamma photons could be counted.

2.3. Procedures

2.3.1. Gamma spectrometric measurements

Five millilitres of standard or sample solution is pipetted out into the sample holder and counted for 500 s where uranium concentration lies between 5 and 20 g l^{-1} and 200 s for 30 g l^{-1} and above. This procedure is applicable to UNF, UNS, UNPS, UNPE and LS samples.

UNR samples usually contain very low level of uranium ranging between 0.1 and 1 g l^{-1}. Two procedures were followed in this case. In the first method, 10 ml aliquots of standards and samples were counted for 1800 s. In the second method, a calculated quantity of uranium standard was added into the sample and 10 ml of the sample was counted for 1800 s.

2.3.2. Potentiometric method

U(VI) in the sample is reduced to U(IV) by excess Fe(II) in phosphoric acid medium. After destroying the excess Fe(II) using nitric acid in the presence of Mo(VI) catalyst, U(IV) is oxidized back to U(VI) in sulphuric acid medium and the liberated Fe(II) which is quantitatively equal to uranium content is titrated using standard dichromate solution on weight basis. A digital voltmeter coupled with a platinum working electrode and a saturated calomel reference electrode was used for the potentiometric end point determination. V(IV) was used to obtain sharp end point.

2.3.3. X-ray fluorescence method

Measurements were performed using Philips PW 1404 wavelength dispersive X-ray spectrometer. In this method, suitably diluted standard/sample solution placed in a liquid sample cell covered with a mylar film is subjected to the interaction of primary X-rays generated by a rhodium target. The secondary fluorescence X-rays characteristic to uranium that emerges out are diffracted by LiF220 crystal and measured at a 2θ angle of 37.235°. Content of uranium present in the sample is deduced from the calibration curves of concentrations versus count rates. For UNE and LS samples, calibration standards were prepared in TBP–kerosene matrix of composition exactly matching that of samples.

2.3.4. Differential pulse voltametric method for the determination of uranium in UNR samples

U(VI) present in the sample was determined in 1 M sulphuric acid medium by measuring the peak current at 200 ± 20 mV with a Metrohm 646 VA processor using a hanging mercury drop working electrode, a platinum auxiliary electrode and a Ag/AgCl reference electrode following standard addition method.

2.3.5. UV–vis spectrophotometric determination of uranium in UNR samples

Sample aliquot was treated with sulphamic acid, 4 M HCl and 0.1% Arsenazo III reagent and the absorbance was measured at 655 nm. Concentration of uranium was determined from a calibration curve.

3. Results and discussion

Typical gamma spectrum of natural uranium recorded in the present investigation is presented in Fig. 2. Three prominent peaks due to 63, 93 and 185.7 keV gamma photons are present in this spectrum. The peaks at 63 and 93 keV are from ^{234}Th, the first generation daughter product of ^{238}U. The 185.7 keV peak is from ^{235}U. The peak height is dependent upon the combined influence of percentage yield of the gamma rays, isotopic composition and the concentration of the isotope present in the solution besides the nature and geometry of the detector. Since the percentage yield for a particular energy of gamma ray and the isotopic composition of natural uranium are fixed, the peak height and the area under the peak depends upon the concentration of uranium and counting time when measured using a particular type of detector with a defined geometry. This fact has been exploited for the convenient determination of concentrations of uranium in the process stream samples on routine basis. Since the efficiency of a well-type NaI(Tl) detector is superior to HPGe, Ge(Li) detectors and is cheaper, a 3 in. × 3 in. NaI(Tl) well-type detector was chosen for the present investigation.

It can be seen from Fig. 2 that the 185.7 keV peak is sufficiently isolated from other peaks whereas the 63 and 93 peaks remain partially resolved. This is due to the poor resolving power

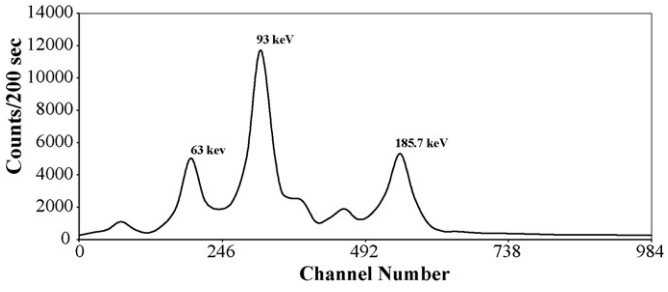

Fig. 2. Gamma spectrum of natural uranium decay series.

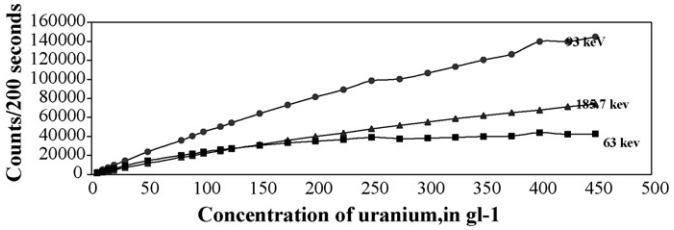

Fig. 3. Concentration of uranium vs. counts.

of the NaI(Tl) scintillation detector. However, the excellent counting efficiency of the detector enabled to obtain high counts even in a short period of counting time as low as 200–500 s. Consequently, high sample throughput is achieved which is very much desirable for routine analysis.

Twenty-four standard solutions of natural uranyl nitrate of concentrations between 5 and 450 g l^{-1} were counted by four analysts on 40 different days, 10 days by each analyst, in a span of 4–5 months. The purpose of this exercise was to study the day-to-day variations in the count rates for the same concentrations due to drift in the instrument and influence from other probable sources. However, the high precision obtained for the counts of all energies are in support of absence of such effects. The relative standard deviation (R.S.D.) values of the counts for various concentrations obtained are between ±0.5 and 1.8%. The excellent precisions of counts obtained for the standards indicate that the U_3O_8 used for the preparation of standards is sufficiently old, i.e., the time required for the attainment of secular equilibrium between ^{238}U and its immediate daughter ^{234}Th. The cumulative counts obtained for 63, 93 and 185.7 keV phtons were plotted against the concentrations and is presented in Fig. 3. These counts represent the total photo peak areas obtained after correction for Compton background [22]. The correction factor is programmed in the instrument software itself and is automatically incorporated during the counting. However, the natural background is made insignificant with the use of a thick lead shield enclosing the detector.

It is clear from Fig. 3 that the linearity of the curve with respect to concentration of uranium is improved from lower to higher energy of gamma photons. The curves follow a linear path at low concentrations and tend to bend towards *x*-axis at high concentrations. This deviation from linearity is only to a slight extent in 185.7 keV photons, to a considerable extent in 93 keV photons and highly pronounced in the case of 63 keV photons. In the latter case, a prominent plateau region running parallel to the *x*-axis is observed to start at lower concentration itself, i.e., 50 g l^{-1}. The curves follow a near linear path only up to 250 g l^{-1} of uranium in 63 and 93 keV photons. This phenomenon is explainable on the basis of the existence of self-absorption of these low energy gamma rays at higher uranium concentrations. In the case of 63 keV, there is no appreciable change in the counts above 250 g l^{-1} indicating the complete self-absorption, whereas in the case of 185.7 keV photons, the curve follows reasonable linearity even up to 450 g l^{-1}. The quadratic curves, however, are highly reproducible and hence can be used for the routine determination of concentrations of uranium in process stream samples. Using the counts of 185.7 keV gamma photons the concentration of uranium from 100 to 450 g l^{-1} could be determined without the need of dilution of the sample.

The concentrations of uranium in the samples can be read from a calibration curve as given in Fig. 3. But, the deviation from linearity causes negative bias in counts at higher concentrations. In order to overcome this constraint, the calibration curves were plotted in segments of concentration ranges of 0–50, 50–100, 100–200, 200–300 and 300–450 g l^{-1} and the values of concentrations can be read from them. The linear equations and the correlation coefficient r^2 values obtained are presented in Table 1. It can be seen from this table that the correlation coefficients are close to unity indicating the excellent linearity in all the concentration ranges in the case of 185.7 keV photons. Slight deviation from unity is observed in concentration range 200–300 g l^{-1} and above in the case of 93 keV photons. This deviation is much more pronounced in the case of 63 keV due to enhanced self-absorption of these low energy photons as anticipated. The choice of the appropriate linear equation dealing with different concentration ranges of uranium for the determination of concentrations of uranium in unknown samples is made with the help of the highly reproducible quadratic curves of Fig. 2.

Table 1
Linear equations for the quadratic curves obtained when the concentrations of uranium is plotted against counts in segments of various concentration ranges

S. no.	Gamma energy (keV)	Concentration range (g l^{-1})	Linear equations for the quadratic curves	Correlation coefficients, r^2
1	63	0–50	$Y = 282.57X + 305.75$	0.9976
2	63	50–100	$Y = 188.16X + 4787.9$	0.995
3	63	100–200	$Y = 144.22X + 12794$	0.9919
4	63	200–300	$Y = 27.652X + 3409$	0.6073
5	63	300–450	$Y = 33.961X + 28235$	0.7591
6	93	0–50	$Y = 475.4X + 108.48$	0.9999
7	93	50–100	$Y = 418.67X + 2745$	0.9993
8	93	100–200	$Y = 370.36X + 7914.8$	0.9993
9	93	200–300	$Y = 244.18X + 34238$	0.9594
10	93	300–450	$Y = 267.05X + 27241$	0.9689
11	185.7	0–50	$Y = 230.32X + 62.013$	0.9999
12	185.7	50–100	$Y = 206.24X + 1231.6$	1.0000
13	185.7	100–200	$Y = 180.24X + 4066.8$	0.9993
14	185.7	200–300	$Y = 153.06X + 9378.8$	0.9981
15	185.7	300–450	$Y = 123.41X + 18469$	0.9985

Table 2
Comparison of concentration of uranium obtained by gamma spectrometry with other analytical techniques

A	B	C	D	E	F	G	H	I	J	K	L	M	N
UNFS/UNS	721	336	42,462	419	+24	123,303	360	+7	58,833	327	−3	345	+3
	706	333	43,092	437	+31	124,601	365	+10	59,349	331	−1	323	−3
	703	276	42,264	413	+50	109,443	308	+12	50,940	272	−1	276	0
	690	329	42,748	427	+30	123,874	362	+10	59,382	331	+1	340	+3
	683	286	43,457	448	+57	114,819	328	+15	51,064	272	−5	297	+4
UNE	547	105	25,030	107	−2	47,968	108	+3	23,402	107	−2	96	−9
	566	107	25,376	110	+3	49,307	112	+5	23,858	110	+3	103	−4
	589	103	25,530	112	+9	49,515	112	+9	24,207	112	+9	105	+2
	625	112	23,938	98	−13	47,090	106	+5	23,952	110	−2	107	−5
	629	110	26,533	120	+9	52,594	121	+10	25,088	117	−6	***	**
UNPS/UNPE	723	116	25,780	114	+2	50,093	114	+2	24,569	114	+2	116	0
	684	113	24,888	106	−6	46,595	104	−8	23,198	106	−6	100	−12
	674	113	25,609	112	−1	48,953	111	−2	23,515	108	−4	108	−4
	648	121	26,108	117	−3	50,562	115	−5	24,966	116	−4	112	−7
	573	119	25,213	109	−8	49,340	112	−6	24,238	112	−6	105	−12
LS	658	10.2	7,989	10.2	0	12,150	10.0	−2	6,096	10.3	+1	7.9	−29
	677	9.6	7,650	9.7	+1	11,682	9.6	0	5,849	9.9	+3	7.5	−28
	678	10.9	8,460	10.9	0	13,059	10.8	−1	6,502	11.0	+1	8.5	−22
	728	9.8	7,912	10.1	+3	11,977	9.8	0	6,064	10.3	+5	7.4	−24
	729	9.0	7,443	9.5	+2	11,300	9.3	−3	5,641	9.5	+6	7.3	−19

(A) Sample category; (B) sample code number; (C) concentration of uranium in $g\,l^{-1}$ by potentiometry; (D, G and J) counts obtained for 63, 93 and 185.7 keV gamma photons, respectively; (E, H and K) concentration of uranium in $g\,l^{-1}$ obtained by gamma spectrometry using 63, 93 and 185.7 keV photons, respectively, and (M) by WD-XRF; (F, I, L and N) relative percentage error in the values compared to potentiometric values.

Table 2 provides the concentrations of uranium in UNF/UNS samples determined by the present method and those obtained by potentiometry and WD-XRF. It may be noted from this table that the concentrations of uranium in UNF/UNS determined using 63 and 93 keV photons are much higher than those obtained using 185.7 keV photons and other techniques. This is the outcome of self-attenuation effect both in sample as well as standards. Hence, it is impossible to use these lines for UNF/UNS samples without dilution. Yet, there is consistency in counts observed even for 63 and 93 keV photons for all the process stream samples including freshly extracted uranium, such as UNE, UNPS/UNPE, LS, etc. although these measurements were carried out on 40 different days in a span of 4–5 months. This shows that ^{234}Th($t_{1/2}$ 24 days) is already in secular equilibrium with ^{238}U. This could have been due to the complete co-extraction of uranium and thorium in TBP/HNO_3 system from MDU, the starting material for the production of uranium dioxide (Fig. 1), which might be older than 120 days, i.e., approximately greater than five half-lives of ^{234}Th—the time required for the attainment of secular equilibrium between ^{234}Th and ^{238}U. However, for the freshly extracted uranium, 185.7 keV photons are the suitable choice as it is emitted from ^{235}U itself.

It can be seen from Table 2 that the attenuation of gamma photons by the matrix, however, is not pronounced in samples, such as UNPS/UNPE, UNE and LS, where the concentration of uranium is between 10 and 120 $g\,l^{-1}$, for all energies of gamma photons. The values obtained for these samples using all the energies compare well with those obtained by potentiometry. Especially, the values obtained using 185.7 keV photons are relatively much closer to the values obtained by potentiometry for all the samples including UNF/UNS also. Based on the observations discussed above, the 185.7 keV photons are most suitable for the routine determination of concentrations of uranium of all the three gamma photons.

The measurements by WD-XRF require the samples need be diluted to the concentration range of 0–20 $g\,l^{-1}$ where there is a linear relationship between signal and the concentrations. In the case of UNE samples, the dilution must be done using TBP–kerosene mixture of matrix composition identical to both the sample as well as calibration standards. Such sample dilution is not required in gamma spectrometric measurements nor does the technique warrant the preparation of calibration standards in organic matrix in order to carry out determinations in UNE and LS samples. It is note worthy that the values obtained for LS by WD-XRF considerably deviate towards negative bias. This may be attributed to the imperfect matching of the matrix composition between samples and calibration standards. This situation arises since lean solvent, the organic extractant remains back when uranium values are stripped-off from UNE, may contain the degradation products of TBP viz. DBP, MBP, etc. Therefore, the resulting matrix composition does not match with that of calibration standards. The negative bias in the concentrations of uranium amounting to about 20% may be explainable based on this reason. The values obtained for lean solvent samples using gamma spectrometry for all the three photons are in excellent agreement with that obtained by potentiometry.

Though the 1001 keV photons, free from self-absorption owing to its higher energy, may be useful for the present application, it is very much limited by certain constraints. First of all, the concept of attainment of secular equilibrium arises even in

Table 3
Concentrations of uranium (in gl^{-1}) in uranyl nitrate raffinate samples

S. no.	Sample code number	By gamma ray spectrometry (direct counting)	By gamma ray spectrometry (through spiking)	By potentiometry	By WD-XRF	By voltametry	By spectrophotometry
1	1338	0.36	0.25	0.31	0.25	0.33	0.30
2	1372	0.34	0.19	0.15	0.10	0.14	0.18
3	1348	0.33	0.41	0.41	0.34	0.40	0.36
4	1253	0.41	0.55	0.45	0.37	0.44	0.39
5	1254	0.49	0.51	0.45	0.40	0.45	0.42
6	1381	0.49	0.33	0.48	0.40	0.50	0.45
7	1325	0.42	0.33	0.34	0.27	0.28	0.33
8	1433	0.36	0.42	0.44	0.35	0.44	0.41
9	1388	0.94	1.19	1.06	0.84	0.95	0.94
10	1402	0.84	0.72	0.88	0.66	0.93	0.77

this case since 1001 keV gamma photons emanates from ^{234m}Pa the daughter of ^{234}Th, and is second-generation daughter of ^{238}U photons. In addition, the photon yield is very low. Secondly, low photon yield entails the longer accumulation times for obtaining good counting statistics. Therefore, this line is not preferable for routine analysis. Ultimately, use of 185.7 keV photons only is found to be ideal in all respects for the routine determination of concentrations of uranium in process stream samples.

Table 3 provides the comparison of results in UNR samples obtained in the present method performed in direct and spiked mode with those obtained by potentiometry, WD-XRF, UV–vis spectrophotometry and differential pulse voltametry. This exercise had been undertaken to demonstrate the feasibility of gamma spectrometry for the determination of concentration of uranium as low as 0.1–1 $g\,l^{-1}$ that might be present in UNR samples.

However, this procedure is not recommended for routine process control work since the counting time is 1800 s. In addition, at such low levels of uranium concentration, discontinued peaks appear at times and the software could not evaluate the counts leading to the samples to be counted again for another half-an-hour. This results in wastage of time and is disadvantageous. The experimental results are presented here only to demonstrate the technical feasibility of the determination of uranium even at such low level using passive gamma spectrometry and this information may find application elsewhere.

Another valuable advantage of gamma spectrometry is that it is free from any kind of matrix effect, such as free acidity and slight density variation of the medium. This fact has been verified in this present investigation by choosing a standard containing 82 $g\,l^{-1}$ since it lies in the rectilinear part of the calibration curve in all the three gamma photons viz. 63, 93 and 185.7 keV. This observation is substantiated by the results presented in Table 4 in which the counts of 63, 93 and 185.7 keV gamma photons for the same amount of uranium present in various mineral acids at different free acidities are observed to be in the same range. The concentration of uranium present in the sample obtained in all the mineral acids with concentration ranging from 1 to 6N is $82 \pm 1\,g\,l^{-1}$. This is of greatest advantage in an industrial analytical laboratory where stan-

Table 4
Comparison of counts of 63, 93 and 185.7 keV gamma photons obtained for the uranium standard solution in various mineral acids of different acidities

Mineral acid	Strength of the acid (N)	Peak area of 63 keV peak	Peak area of 93 keV peak	Peak area of 185.7 keV peak	Concentration of uranium ($g\,l^{-1}$)[a]
HNO_3	1	20,337	36,596	17,398	83
	2	20,623	35,991	17,487	83
	4	20,078	36,155	17,409	82
	6	20,734	35,671	17,255	82
HCl	1	20,172	35,902	17,101	82
	2	20,381	34,900	17,147	82
	4	19,608	36,453	16,973	81
	6	20,558	36,726	16,726	80
H_2SO_4	1	20,943	37,167	17,654	84
	2	20,498	36,247	17,152	82
	4	20,786	37,312	17,027	81
	6	19,663	35,238	17,172	82
$HClO_4$	1	20,216	36,421	17,161	82
	2	20,385	36,601	16,972	81
	4	19,895	36,490	16,930	81
	6	19,224	34,990	16,626	79

[a] Values calculated using peak area values obtained for 185.7 keV gamma photons.

dards prepared in one kind of mineral acid of any free acid concentration can be directly used to determine the concentration of uranium present in a sample with unknown free acid concentration.

4. Conclusion

Passive gamma spectrometry is a versatile analytical technique for the determination of concentrations of uranium in process stream samples of a natural uranium extraction plant. Among the photo peaks, 185.7 keV from ^{235}U isotope has been found to be an ideal tool to measure total uranium concentration. Due to the limitations imposed by such problems like self-absorption and secular equilibrium use of the low energy gamma photons viz. 63 and 93 keV for the determination of concentrations of uranium is not preferable for routine analysis. This method is rapid, nondestructive and cost-effective, well suited for an industrial analytical laboratory.

Acknowledgements

The authors are thankful to Shri R.N. Jayaraj, Chief Executive, Nuclear Fuel Complex, for his kind support and encouragement and also to Shri B. Laxminarayana, Project Director, NFC, Zirconium Complex, Pazhayakayal and Shri A.V. Ramana Rao, Deputy General Manager, Quality Assurance, NFC, for the useful discussions during the course of this investigartion. The authors are also grateful to the staff, X-ray Fluorescence Spectrometry group for their analytical support.

References

[1] G. Boutonnet, Nucl. Eng. Int. 20 (1975) 100.
[2] R.C. Merrit, The Extractive Metallurgy of Uranium, Colorado School of Mines Research Institute, USAEC, Golden, CO, 1971.
[3] H.A.C. McKay, Proceedings of the International Conference on Peaceful Uses of Atomic Energy, vol. 7, Geneva, 1956, p. 314.
[4] W.T. Bourns, L.C. Watson, Report CRCE-716, Part I, Atomic Energy of Canada, Chalk River, Ontario, 1958.
[5] P.L. Lopez-de-Alba, S. Gonzalez, J. Gomez Lara, J. Radioanal. Nucl. Chem. 136 (1989).
[6] W. Davis, W. Grey, Talanta 11 (1964) 1203.
[7] M. Mlakar, M. Branica, Anal. Chim. Acta 221 (1989) 279.
[8] G.L. Booman, W.B. Holbook, J.E. Rein, Anal. Chem. 29 (1957) 219.
[9] A.W. McMohan, Sci. Total Environ. 130 (1993) 285.
[10] J.L. Perez Pavon, B. Moreno Cordero, E. Rodriguez Garcia, J. Hernandez Mendez, Anal. Chim. Acta 230 (1990) 217.
[11] W. Jianhua, H. Ronghuan, Chem. Anal. (Warsaw) 38 (1993) 497.
[12] B. Narasimha Murty, Y.V.S. Jagannath, R.B. Yadav, C.K. Ramamurty, S. Syamsundar, Talanta 44 (1997) 283.
[13] C.J. Sharland, M.E.A. Robertson, P.J. Brandt, Report IAEA-SM-239/42, p. 309.
[14] R.J.S. Harry, J.K. Aaldijk, J.P. Braak, Report IAEA-SM-201/66, p. 235.
[15] H. Ottmar, P. Matussek, Report IAEA-SR-7/29, p. 191.
[16] P. Matussek, H. Ottmar, Report IAEA-SM-201/46, p. 223.
[17] H.J.V. Wachtendonk, R. Baumann, J. Nucl. Mater. 153 (1988) 91.
[18] G.H. Morrison, J.F. Cosgrove, Anal. Chem. 29 (1957) 1771.
[19] P. Colsman, Report BNL-SM-67/47, p. 677.
[20] R.B. Walton, E.I. Whitted, R.A. Forster, Nucl. Technol. 24 (1974) 81.
[21] R.K. Singh, A.D. Moorthy, R.K. Babbar, S.V. Udagati, Report BARC-1478, p. 10.
[22] G.R. Reddy, M. Sankar Das, Report BARC-I-41, 2005, p. 2.
[23] R.O. Korob, D. Otero, J. Radioanal. Nucl. Chem. Lett. 186 (1994) 157.
[24] Y. Nir-El, Radiochim. Acta 88 (2000) 83.

Available online at www.sciencedirect.com
ScienceDirect
Talanta 73 (2007) 438–443
Talanta
www.elsevier.com/locate/talanta

Amperometric glutamate biosensor based on self-assembling glutamate dehydrogenase and dendrimer-encapsulated platinum nanoparticles onto carbon nanotubes

Longhua Tang, Yihua Zhu *, Lihuan Xu, Xiaoling Yang, Chunzhong Li

Key Laboratory for Ultrafine Materials of Ministry of Education, School of Materials Science and Engineering, East China University of Science and Technology, Shanghai 200237, China

Received 22 December 2006; received in revised form 6 April 2007; accepted 6 April 2007
Available online 22 April 2007

Abstract

A novel amperometric biosensor based on self-assembling glutamate dehydrogenase (GLDH) and poly(amidoamine) dendrimer-encapsulated platinum nanoparticles (Pt-PAMAM) onto multiwall carbon nanotubes (CNTs) has been developed for the determination of glutamate. The formation of the self-assembled $(GLDH/Pt\text{-}PAMAM)_n$/CNTs construction was investigated by ζ-potential and high resolution transmission electron microscopy (HRTEM). The results indicated the uniform growth of the layer-by-layer nanostructures onto carboxyl-functionalized CNTs. The electrocatalytic property of the $(GLDH/Pt\text{-}PAMAM)_n$/CNTs modified electrode to glutamate in presence of NAD^+ (β-nicotinamide adenine dinucleotide, 0.1 mM) was investigated at a low overpotential 0.2 V by electrochemical measurements. The results showed it had series of attractive characteristics, such as a large determination range (0.2–250 μM), a short response time (within 3 s), a high sensitivity (433 $\mu A/mM^{-1}\,cm^2$) and good stability (85% remains after 4 weeks).

Keywords: Multiwall carbon nanotubes; Poly(amidoamine)-encapsulated platinum nanoparticles; Glutamate dehydrogenase; Self-assembly; Biosensor

1. Introduction

Glutamate is an important neurotransmitter in the mammalian central nervous system and neuronal pathways in the brain which is related to several neurological disorders, such as schizophrenia, Parkinson's disease, epilepsy and stroke [1–3]. It also has widespread use in food as a flavour enhancing food additive. Thus, glutamate is an important analyte in medicine and food analysis which involves neurotransmission and protein metabolism.

Many spectrophotometric, fluorimetric and chromatographic methods have developed for the assay glutamate concentration, but they are considered to be time-consuming and laborious [4,5]. Several types of amperometric biosensors for glutamate have been reported. More recently, glutamate oxidase incorporated into modified electrode has been used for rapid estimation. Mesophilic and thermophilic glutamate dehydrogenase has also been used for the analysis of glutamate [6–9].

For achieving a rapid and high sensitive measurement of substrate, development of immobilization strategy and implementation of novel materials for the construction of desirable biosensor have been the subjects of intensive research.

Enzymes are immobilized on transducer or support matrices by physical and chemical methods [9,10], such as covalent binding, direct adsorption, cross-linking or entrapment, which often denature the enzymes and alter their conformations considerably. Recently, layer-by-layer (LbL) technique for constructing multilayer films has attracted much attention since it can provide a favorable microenvironment to keep the bioactivity of enzyme and prevent enzyme molecule leakage. This technique involves an alternate adsorption of enzyme and another electrolyte onto an electrode surface through electrostatic force and covalent bonding [11–15]. In addition, the efficient immobilization materials can prolong the use of the sensor and extend storage and working stability. They have recently been extended to a variety

* Corresponding author. Fax: +86 21 64250624.
E-mail address: yhzhu@ecust.edu.cn (Y. Zhu).

0039-9140/$ – see front matter © 2007 Elsevier B.V. All rights reserved.
doi:10.1016/j.talanta.2007.04.008

of materials, including redox mediators, conducting polymers, nanomaterials, dendrimers and so on [16,17].

A wide variety of nanomaterials with unique chemical and physical properties have found broad application in the construction of novel and improved biosensor. Metal nanoparticles have been intensively studied for the electrode modification owing to their extraordinary catalytic activity, especially Pt, Au nanoparticles [18–20]. Carbon nanotubes [21], another class of promising nanomaterials, have been drawn to considerable attention due to their unique electronic, chemical and mechanical properties [22]. Recent studies have demonstrated that carbon nanotubes can enhance the electrochemical reactivity of biomolecules and promote the electron transfer reactions of proteins [23–28].

Highly branched dendritic macromolecules poly(amidoamine) (PAMAM) could also be used to modify electrode surface due to their good biocompatibility and adequate functional groups for chemical fixation. It was reported that the material was capable of increasing the concentration of hydrophobic molecules at the electrode–solution interface, improving the sensitivity as well as the selectivity of certain specific electrochemical reactions [29,30,34].

Considering their truly enormous potential and unique properties, in this context, poly(amidoamine) dendrimer-encapsulated platinum nanoparticles (Pt-PAMAM) self-assembled onto multiwall carbon nanotubes (CNTs) were applied to the immobilization of glutamate dehydrogenase in biosensors for the first time (Fig. 1). The modification of CNTs and Pt-PAMAM not only increased the effective area of the electrode, but also may act as an efficient promoter used to enhance the electrochemical reaction, thereby increasing the rate of heterogeneous electron transfer.

2. Experimental

2.1. Chemicals and materials

Glutamate dehydrogenase (GLDH, EC 1.4.1.3, MW 300,000, from bovine liver, suspension in 2.0 M $(NH_4)_2SO_4$ solution, 48 units/mg prot.), L-glutamate (monosodium salt, 99%) and β-nicotinamide adenine dinucleotide (NAD^+) were purchased from Sigma–Aldrich. Multiwall CNTs were from UNILAB, State Key Laboratory of Chemical Engineering, East China University of Science and Technology. Pt-PAMAM was synthesized according to the previous literature [29–32]. Phosphate buffer was used for immobilization and electrochemical measurements 0.1 M potassium phosphate (PBS), pH 7.4. The other chemicals were of analytical grade. Doubly-distilled and deionized water was used through this work.

2.2. Instruments

Electrochemical measurements were performed by using a CHI 660C (CH Instruments, Chenhua Inc., Shanghai, China) connected to a personal computer. A three-electrode configuration was employed, consisting of a multilayer modified glassy carbon (GC) electrode (3 mm diameter) serving as a working electrode, whereas Ag/AgCl (3 M KCl) and platinum wire served as the reference and counter electrodes, respectively. Batch electrochemical experiments were carried out in a 10 mL voltammetric cell at room temperature (25 °C).

The HRTEM images were recorded on a JEOL-2100 transmission electron microscope. The electrophoretic mobilities of the adsorbed CNT suspension were measured using a Malvern Zetasizer 3000HS.

2.3. Synthesis of CNTs/Pt-PAMAM heterostructures

The CNTs were first shortened and functionalized by sonicating in a mixture of concentrated HNO_3 and H_2SO_4 (v/v, 1/3) for 6 h followed by extensive washing in deionized water several times and finally dried under vacuum, dispersed in double-distilled water in a concentration 5 mg/mL. After the acid treatment, the CNTs were shorter and left with the carboxylic groups that impart a hydrophilic nature and facilitate further functionalization by Pt-PAMAM. The Pt-PAMAM/CNTs heterostructures were attached covalently by 1-ethyl-3-(3-dimethylaminopropyl)carbodiimide (EDC), which yield stable conjugates, since they form amide linkages between them (Fig. 1a). The EDC reaction was carried out for 8 h at 50 °C under continuous mixing. The heterostructures were characterized by HRTEM.

2.4. Preparation of $(GLDH/Pt\text{-}PAMAM)_n$/CNTs nanocomposites

The isoelectric point (Ip) of GLDH lies around pH 4.83, and therefore at pH > Ip, it is net negatively charged, while at pH < Ip, it is positively charged. So GLDH can be used as polyanionic material for preparing LbL films around pH 7.4. Here, GLDH was immobilized on the positive charged Pt-PAMAM/CNTs surface by alternatively assembling a GLDH layer and a Pt-PAMAM layer (Fig. 1b). First, GLDH/Pt-PAMAM/CNTs film was attained by mixing the Pt-PAMAM/CNTs heterostructures with the negatively charged GLDH (0.2 unit/mL) in a PBS (pH 7.4) for 20 min, centrifuged at 7000 rpm for 10 min, and then washed with distilled water twice to remove the supernatant. Using the same procedure, positively Pt-PAMAM and negatively GLDH were alternately absorbed onto the CNTs until suitable layer was obtained. The resulting structures were characterized by ζ-potential measurement, HRTEM. Finally, the resulting nanocomposite was thoroughly washed with PBS (pH 7.4) and stored in PBS below 4 °C for future use.

2.5. Electrode preparation

Glass carbon (GC, 3 mm diameter, Model CHI 104, CH Instruments) electrodes were polished with 1.0, 0.3 and 0.05 μm alumina powder cleaned in a piranha solution (a 1:3 mixture of 30% H_2O_2 and concentrated H_2SO_4) and finally sonicated thoroughly in double-distilled water. After that, the electrode was cycled 10 times between −0.800 and 0.800 V in a phosphate buffer solution (pH 7.4) at 50 mV/s. The biosensors were prepared by casting the GCE with 20 μL of the resulted nanocomposite solution dispersion by sonicating for 5 min. The

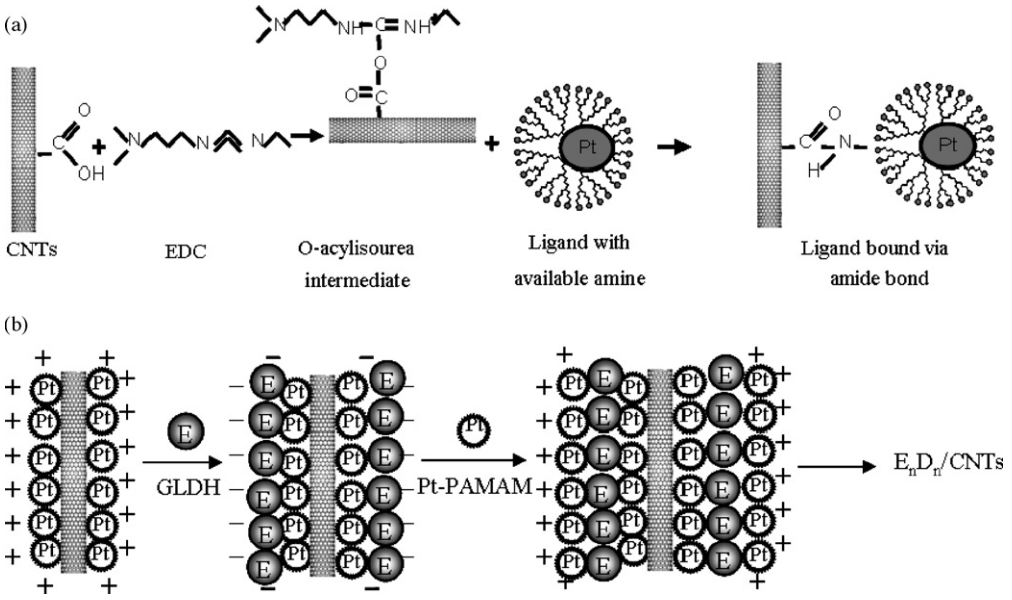

Fig. 1. Schematic showing the procedure of immobilizing Pt-PAMAM onto CNTs (a) and the layer-by-layer self-assembly of GLDH and Pt-PAMAM onto CNTs (b). Pt-PAMAM/CNTs heterostructures were attached covalently via EDC, Pt-PAMAM and GLDH were alternately deposited until suitable layers were obtained.

coated electrode was dried at room temperature and then kept under dry conditions at 4 °C before use.

3. Results and discussion

3.1. Electron micrographs of the Pt-PAMAM/CNTs heterostructures

A key element for the exploration of the nanoparticles–CNTs composites as sensing or catalyst materials is the ability in effective and controllable assembly of nanoparticles on the surface of CNTs, which is the focus of the present work. As demonstrated previously, the oxidation procedure used for treating carbon nanotubes, mainly to remove metal catalyst and amorphous carbon, also results in partial oxidation of the carbon atoms to produce oxygen-containing groups (such as carboxylic acid groups) especially in the open ends of the nanotubes. These groups electrostatically and covalently interact with the Pt-PAMAM. TEM (Fig. 2a) showed well-organized nanosized platinum nanoparticles, with a particle diameter of approximately 3 nm and a narrow distribution on the surface of CNTs. This demonstrates the assembly route linked via EDC is effective and controllable for the assembly of the monolayer-caped platinum nanoparticles on CNTs. Similar results have been reported in the literature [33,34].

3.2. Multilayers assembling and characterization

Microelectrophoresis measurements were conducted to qualitatively follow adsorption of the layers on the CNTs templates. The ζ-potentials of the hybrid layer were calculated from the mobilities that were measured after deposition of each layer. Fig. 3 shows the ζ-potentials change regularly and alternately as the outmost layer is adsorbed via a layer-by-layer approach. Weak positively charged Pt-PAMAM/CNTs showed a ζ-potential of 3.09 mV. Subsequent adsorption of GLDH enzyme resulted in ζ-potential of about −14.55 mV. Further depositions cause the ζ-potentials to alternate in sign from positive to negative, depending on whether the outmost layer is GLDH or Pt-PAMAM. Alternate adsorption of Pt-PAMAM and GLDH finally got a reversal cyclic change. This provides qualitative evidence for the successful adsorption of Pt-PAMAM (positive values) and GLDH (negative values).

HRTEM confirmed the success of the attachment of $(GLDH/Pt\text{-}PAMAM)_n$ multilayers onto the CNTs. As shown in Fig. 2(b), it can be seen that almost all of the tubes were evenly coated with $(GLDH/Pt\text{-}PAMAM)_n$ layers, and the thickness of the $(GLDH/Pt\text{-}PAMAM)_n$ layers is about 10 nm. HRTEM images provide strong evidence for the formation of LbL nanocomposite.

3.3. Electrochemical study of the $(GLDH/Pt\text{-}PAMAM)_3$/CNTs/GCE biosensor

To demonstrate the function of CNTs and Pt-PAMAM in the process of electrocatalytic process, different electrode has been prepared. Fig. 4 depicts the oxidation of glutamate at the GLDH/Pt-PAMAM/CNTs/GC (curve 4), Pt-PAMAM/CNTs/GC (curve 3), CNTs modified (curve 2) and bare GC (curve 1) electrodes in the PBS (pH 7.4) containing 0.1 M NAD^+. Glutamate dehydrogenase occurs irreversibly with a large overpotential at the bare electrode (curve 1), indicating the slow electron transfer rate at bare GC electrode. The CNTs or/and Pt nanoparticles modified electrodes show low overpotential and high current density (curves 2–4), suggesting that CNTs and Pt nanoparticles have promotion effect on the electrocatalytic activity of GLDH to the oxidation of glutamate [17]. The superior promotional effect of CNTs and Pt-PAMAM to the electrocatalytic activity of GLDH, when compared with other forms of carbon, such as GC and ACP, may be due to their small dimen-

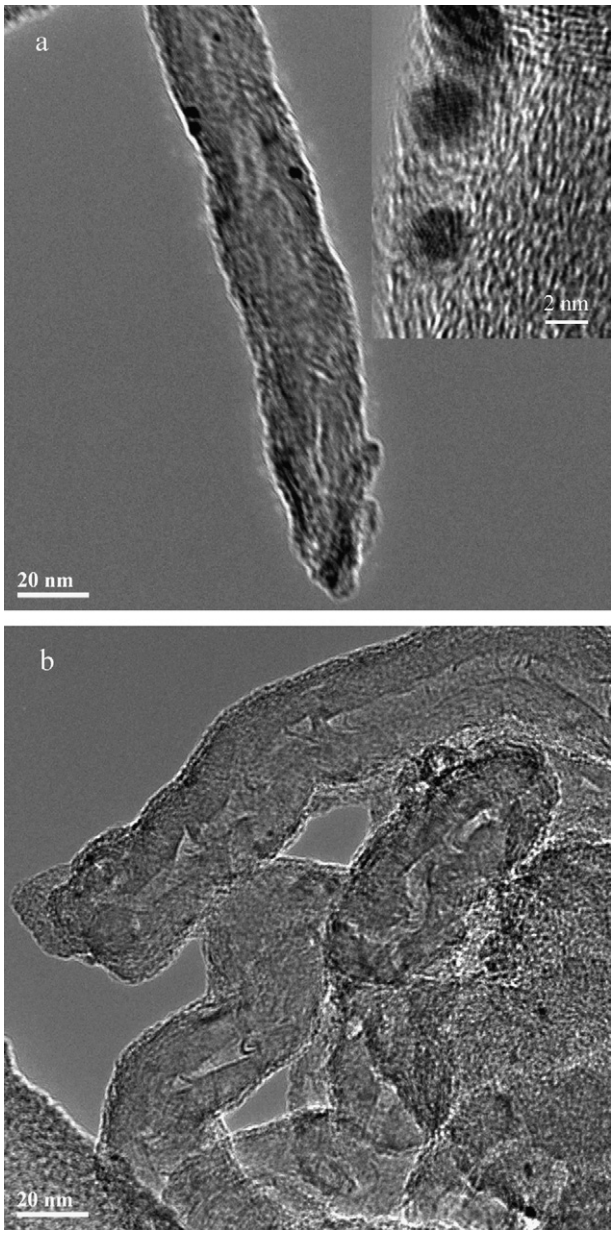

Fig. 2. HRTEM image of CNTs incorporated with Pt-PAMAM (a), and $(GLDH/Pt\text{-}DENs)_3$/CNTs hybrid nanocomposite (b). *Inset*: A magnified image of the Pt-PAMAM/CNTs heterostructure.

sion, their unique chemical structure, their distinctive electronic characteristics, and their high electrical conductivity, and importantly, also to some oxygen-contained groups present on their surface [35], even though the exact reason is not fully understood at the present time [36].

The layer number of the self-assembled nanocomposite had an important effect on sensitivity of the sensor. In this experiment, we found that with the increasing of layer numbers of enzyme, the oxidation peak potential stayed at 0.2 V and the current response increased gradually, but the response time would also be increased. So the $(Pt\text{-}PAMAM/GLDH)_3$/CNTs/GC electrodes were selected for the electrochemical measurements.

Fig. 5 shows the electrocatalytic behavior of the $(Pt\text{-}PAMAM/GLDH)_3$/CNTs nanocomposite modified GC elec-

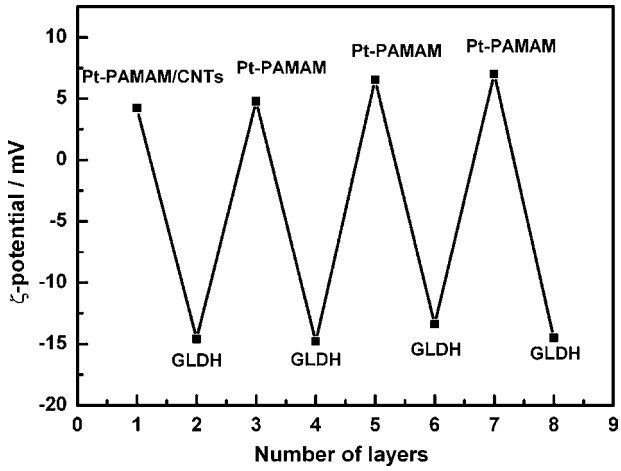

Fig. 3. ζ-Potentials changed as the multilayers were alternatively adsorbed via a layer-by-layer approach.

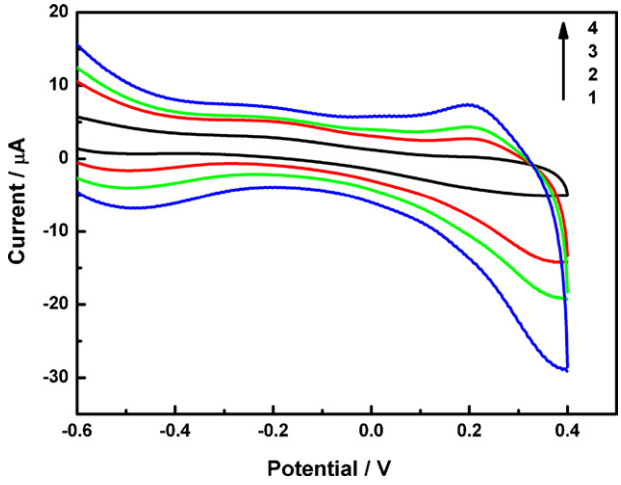

Fig. 4. The cycle voltammograms of $(GLDH/Pt\text{-}PAMAM)_n$/CNTs nanostructure assembled onto GC electrode in pH 7.4 PBS 0.1 mM NAD^+ and 0.1 mM glutamate. The numbers (1, 2, 3, 4) refer to the bare GCE, CNTs/GCE, Pt-PAMAM/CNTs/GCE, GLDH/Pt-PAMAM/CNTs/GCE, respectively.

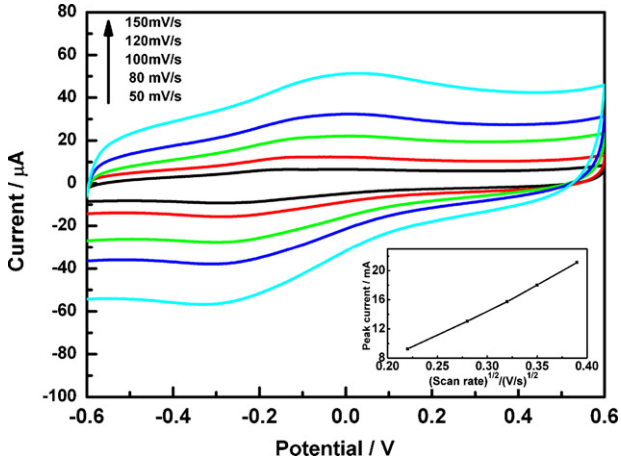

Fig. 5. The cycle voltammograms for oxidation of glutamate at $(GLDH/Pt\text{-}PAMAM)_3$/CNTs nanocomposite modified GC electrode in pH 7.4 PBS containing 0.1 mM NADH at different scan rates: 50, 80, 100, 120 and 150 mV/s. *Inset*: The relationship between the peak currents and square root of potential scan rate.

trode that changes with the scan rate. With the scan rate increasing from 50 to 150 mV/s, the peak current increased, while the peak potential shifted positively slightly. To confirm the anodic current response is coming from the enzymatic reaction between GLDH and the substrate glutamate, a comparison experiment was performed with the Pt-PAMAM/CNTs/GC electrode and GLDH/Pt-PAMAM/CNTs/GC electrode to glutamate at the working potential 0.2 V in the presence of NAD^+. We found that no response was obtained with the Pt-PAMAM/CNTs GC electrode on adding the substrate glutamate, while a very good response was obtained with GLDH/Pt-PAMAM/CNTs GC electrode. In Fig. 5, one notices that the peak current was linear with the square root of potential scan rate in a rage from 50 to 150 mV/s (shown in the inset), demonstrating that the electrochemical oxidation of glutamate is a diffusion-controlled process at the assembled CNTs.

The effect of pH value on the performance of the $(GLDH/Pt\text{-}PAMAM)_3$/CNTs/GCE biosensor has been investigated using 0.1 M PBS. It is found that the response of the resulting electrode is pH dependent. The maximum current response of the enzyme electrode was obtained at pH 7.4. To avoid the interference from other electroactive species, obtain the maximum current response and keep the good activity, a 0.2 V working potential and a pH 7.4 were used in the flowing.

The amperometric responses of the $(GLDH/Pt\text{-}PAMAM)_3$/CNTs modified biosensor were investigated by successively adding glutamate at an applied potential of 0.2 V versus Ag/AgCl, in a PBS (pH 7.4) supported electrolyte containing 0.1 mM NAD^+. It indicates that the $(GLDH/Pt\text{-}PAMAM)_3$/CNTs modified biosensor showed an increase in measured currents with the addition of glutamate. The resulting calibration curve plot displays linearly from 0.2 up to 250 μM with a correlation coefficient of 0.9992. The lowest detectable concentration of this biosensor was 10 nM, when the signal-to-noise characteristics of these data (S/N ratio) were 3. Also the time required to reach the 95% steady-state response of this biosensor was only 3 s.

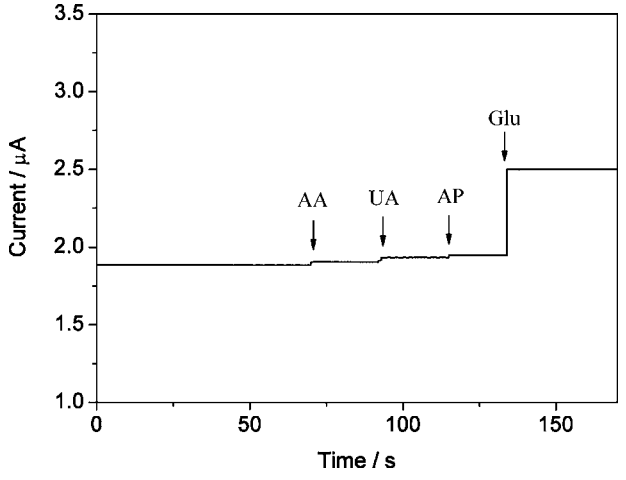

Fig. 6. Amperometric responses of the biosensors upon subsequent additions of 0.1 mM L-ascorbic acid (AA), 0.1 mM uric acid (UA), 0.1 mM acetaminophen (AP) and 0.1 mM glutamate (Glu) in PBS (pH 7.4) at 0.2 V vs. Ag/AgCl.

In real samples, some co-existing electroactive species might affect the biosensor response, for example, ascorbic acid (AA), uric acid (UA), acetaminophen (AP), L-cysteine (L-Cys), etc. The selectivity and anti-interference advantages are demonstrated in Fig. 6, which compares amperometric responses for three relevant electroactive species (UA, AA, AP, 0.1 mM, respectively) and L-glutamate (0.1 mM) at a modified GC electrode at a working potential of 0.2 V. The successive addition of each interfering species brought out fairly discernible current response and a well-defined L-glutamate response was obtained, which is largely attributed to the low working potential of 0.2 V used in the determination of glutamate. Reproducibility of the biosensor system was evaluated from the response for 10 μM glutamate at 10 different biosensors and an acceptable R.S.D. value of 4.8% was observed. We stored the enzyme electrode under 4 °C for 4 weeks, and the sensitivity of electrode was reduced to 85% of our former assay. These results indicate the suitability of the nanocomposite modified glutamate biosensor to practical applications.

4. Conclusion

In this work, we presented a novel amperometric glutamate biosensor based on functionalized carbon nanotubes by alternatively electrostatic or/and covalently self-assembling Pt-PAMAM and GLDH layers on CNTs surface. The LbL film-modified enzyme sensors have been shown to exhibit a good reproducibility, stability and high sensitivity, which can efficiently preserve the activity of enzyme molecules and prevent enzyme leaking. The fabrication method of biosensor opens a new opportunity for the development of simple and reliable other enzymes. Moreover, the film is expected to have potential applications in the construction of screen-printed biosensor, in virtue of many advantages such as ease of fabrication, enhanced electrocatalysis, etc.

Acknowledgements

The authors gratefully acknowledge National Natural Science Foundation of China (20236020, 20676038), Key Project of Science and Technology for Ministry of Education (107045), and the Special Projects for Key Laboratories in Shanghai (05DZ22302, 06DZ22008) for financial supports.

References

[1] R.L. Villarta, D.D. Cunningham, G.G. Guilbauil, Talanta 38 (1991) 49.
[2] M.E. Wolf, Prog. Neurobiol. 54 (1998) 679.
[3] C. Xue, Y. Li, M.E. Wolf, J. Neurochem. 67 (1996) 352.
[4] T. Gunduz, N. Gunduz, E. Kilic, F. Koseoglu, S. Guloztas, Analyst 113 (1998) 715.
[5] C. Jeffries, N. Pasco, K. Baronian, L. Gorton, Biosens. Bioelectron. 12 (1997) 225.
[6] Z. Liu, O. Niwa, T. Horiuchi, R. Kurita, K. Torimitsu, Biosens. Bioelectron. 14 (1999) 631.
[7] E. Mikeladze, A. Collins, M. Sukhacheva, A. Netrusov, E. Csöregi, Electroanalysis 14 (2002) 1052.
[8] B. Prieto-Simón, J. Macanás, M. Muñoz, E. Fàbregas, Talanta 71 (2007) 1893–1900.

[9] A.A. Karyakin, E.E. Karyakina, L. Gorton, Anal. Chem. 72 (2000) 1720.
[10] T.Y. You, O. Niwa, R. Kurita, Y. Iwasaki, K. Hayashi, K. Suzuki, S. Hirono, Electroanalysis 16 (2004) 54.
[11] H. Shi, Y. Yang, J. Huang, Z. Zhao, Talanta 70 (2006) 852.
[12] H. Zheng, H. Xue, Y. Zhang, Z. Shen, Biosens. Bioelectron. 17 (2002) 541.
[13] J. Huang, Y. Yang, H. Shi, Mater. Sci. Eng. C 26 (2006) 113.
[14] D. Trau, R. Renneberg, Biosens. Bioelectron. 18 (2003) 1491.
[15] S. Campuzano, M. Pedrero, J.M. Pingarrón, Talanta 66 (2005) 1310.
[16] X. Luo, A.M. Anthony, K.M. Smith, Electroanalysis 18 (2006) 319.
[17] A. Guiseppi-Elie, C.H. Lei, R.H. Baughman, Nanotechnology 13 (2002) 559.
[18] S.G. Penn, L. He, M.J. Natan, Curr. Opin. Chem. Biol. 7 (2003) 609.
[19] S. Iijima, Nature 354 (1991) 56.
[20] G.L. Luque, N.F. Ferreyra, G.A. Rivas, Talanta 71 (2007) 1282.
[21] W. Joseph, Electroanalysis 17 (2005) 7.
[22] C.V. Nguyen, L. Delzeit, A.M. Cassell, J. Li, Nano Lett. 2 (2002) 1079.
[23] X. Yu, D. Chattopadhyay, I. Galeska, F. Papadimitrakopoulos, Electrochem. Commun. 5 (2003) 408.
[24] S. Sotiropoulou, N.A. Chaniotakis, Anal. Bioanal. Chem. 375 (2003) 103.
[25] M. Zhang, K. Gong, H. Zhang, L. Mao, Biosens. Bioelectron. 20 (2005) 1270.
[26] J.L. Garcia, J. Manriquez, S.G. Granados, L.A. Godinez, Electroanalysis 7 (2003) 657.
[27] X. Chu, D.X. Duan, G.L. Shen, R.Q. Yu, Talanta (2007) 2040.
[28] L. Qian, X.R. Yang, Talanta 68 (2006) 721.
[29] H.C. Yoon, M.Y. Cox, Electrochem. Commun. 3 (2001) 285.
[30] L. Svobodova, M.Š. Nejdárkova, K. Tóth, R.E. Gyurcsanyi, T. Hianik, Bioelectrochemistry 63 (2004) 285.
[31] M. Zhao, R.M. Crooks, Angew. Chem. Int. Ed. Engl. 38 (1999) 364.
[32] H.C. Yoon, H.S. Kim, Anal. Chem. 72 (2000) 922.
[33] F.N. Crespilho, V. Zucoloto, C.M. Brett, O.N. Oliveira, J. Phys. Chem. B 110 (2006) 17478.
[34] H. Zhu, Y. Zhu, X. Yang, C. Li, Chem. Lett. 35 (2006) 326.
[35] C.X. Cai, J. Chen, Anal. Biochem. 325 (2004) 285.
[36] S.N. Liu, C.X. Cai, Electroanal. Chem. 602 (2007) 103.

Available online at www.sciencedirect.com
ScienceDirect
Talanta 73 (2007) 471–475
Talanta
www.elsevier.com/locate/talanta

New tetrazolium method for phosphatase assay using ascorbic acid 2-phosphate as a substrate

Tadayuki Tsukatani [a,*], Seiji Ide [a], Masashi Ono [a], Kiyoshi Matsumoto [b]

[a] *Biotechnology and Food Research Institute, Fukuoka Industrial Technology Center, Kurume 839-0861, Japan*
[b] *Division of Food Biotechnology, Department of Bioscience and Biotechnology, Faculty of Agriculture, Graduate School Kyushu University, Fukuoka 812-8581, Japan*

Received 19 January 2007; received in revised form 10 April 2007; accepted 10 April 2007
Available online 24 April 2007

Abstract

A new method to assay alkaline and acid phosphatases assay using ascorbic acid 2-phosphate (AsA-P) and ditetrazolium salt nitroblue tetrazolium chloride (NBT) was developed. AsA-P is hydrolyzed in the presence of phosphatase to yield ascorbic acid. In turn, the ascorbic acid reduces NBT directly or indirectly, opening the tetrazole ring to produce an insoluble formazan as a colored precipitate. The proposed method for alkaline phosphatase was compared with a conventional method in which 5-bromo-4-chloro-3-indolyl phosphate (BCIP) is used in combination with NBT in the dot blots of a dilution series of β-lactoglobulin. AsA-P reduced NBT more effectively than BCIP in the presence of alkaline phosphatase. AsA-P could be also used as the chromogenic substrate for an acid phosphatase assay in the presence of phenazinium methylsulfate and NBT.

Keywords: Ascorbic acid 2-phosphate; Alkaline phosphatase; Acid phosphatase; Immunostaining; Tetrazolium salt

1. Introduction

Phosphatase is an enzyme that catalyzes the removal of phosphate ions from aliphatic and aromatic phosphate esters. There are two main groups of phosphatases, acid and alkaline depending on their optimum pH. It was reported that potent acid phosphatase (ACP) activity is found in osteoclasts, and alkaline phosphatase (ALP) activity is found in osteoblasts [1]. Following this report, various studies of phosphatase activities associated with osteocytes have been reported, and the ACP activity of osteoclasts was shown to be of the type that retains phosphatase activity in the presence of tartrate [2,3]. The tartrate-resistant ACP activity is now a requisite for osteoclasts. ALP is bound to the membrane of the osteoblast and functions to enhance osteogenesis by degrading pyrophosphate, which inhibits crystallization at the calcification site, and by degrading organic phosphate esters to increase the inorganic phosphate concentration. Therefore, ALP is known as a specific marker of osteogenesis in the cycle of bone metabolism. Because bone metabolism is composed of mutually balanced osteogenesis and bone resorption, simultaneous estimation with two enzyme makers is deemed useful [4,5].

In addition, ALP is intensively used as active label in immunohistology, immunoblotting and enzyme immunoassay [6,7]. The popularity of ALP assays is based on its high turnover-rate, good stability, and the large number of commercially available ALP-conjugated immunoreagents. The broad substrate specificity of ALP accounts for the large variety of these assays. Chromogenic substrates for ALP include halogenated indolyl phosphates, which are hydrolyzed in the presence of ALP to yield an indigo dye. In turn, the indigo dye reduces a tetrazolium salt, opening the tetrazole ring to produce an insoluble formazan that combines with the indigo dye to form a colored precipitate [8]. The ditetrazolium salt nitroblue tetrazolium chloride (NBT) and 5-bromo-4-chloro-3-indolyl phosphate (BCIP) are the most widely used chromophores for localizing phosphatase activity [9,10].

We replaced BCIP by ascorbic acid 2-phosphate (AsA-P) for ALP assay. Although AsA-P is used for ALP assays electrochemically and chemiluminescently [11–13], AsA-P has not been applied to the staining method. In this paper, we report several advantages of the staining method using the combination of

* Corresponding author. Fax: +81 942 30 7244.
E-mail address: tukatani@fitc.pref.fukuoka.jp (T. Tsukatani).

0039-9140/$ – see front matter © 2007 Elsevier B.V. All rights reserved.
doi:10.1016/j.talanta.2007.04.017

AsA-P and NBT. The proposed method was applied to the dot blots of a dilution series of β-lactoglobulin and compared with the BCIP/NBT method. In addition, AsA-P could be also used as the chromogenic substrate for ACP assay in the presence of phenazinium methylsulfate (PMS) and NBT.

2. Experimental

2.1. Reagents

Alkaline phosphatase (ALP, EC 3.1.3.1, from calf intestine) was obtained from Roche (Basel, Switzerland). Acid phosphatase (ACP, EC 3.1.3.2, from potato), 2,3-bis(2-methoxy-4-nitro-5-sulfophenyl)-2*H*-tetrazolium-5-carboxanilide (XTT) and phenazinium methylsulfate (PMS) were bought from Sigma (St. Louis, MO, USA). Ascorbic acid 2-phosphate (AsA-P) and *N*,*N*,*N*′,*N*′-tetramethylethylenediamine (TEMED) were purchased from Wako Pure Chemicals Industries, Ltd. (Osaka, Japan). 3,3′-[3,3′-Dimethoxy-(1,1′-biphenyl)-4,4′-diyl]-bis[2-(4-nitrophenyl)-5-phenyl-2*H*-tetrazolium chloride] (NBT), 5-bromo-4-chloro-3-indolyl phosphate (BCIP), 3-(4,5-dimethylthiazol-2-yl)-2,5-diphenyltetrazolium bromide (MTT), and *N*-cyclohexyl-2-hydroxy-3-aminopropanesulfonic acid (CAPSO) were bought from Dojindo (Kumamoto, Japan). Nitrocellulose membrane (Hybond-P®) was obtained from GE Healthcare Bio-Sciences (Piscataway, NJ, USA). A milk protein Western blot kit (β-lactoglobulin) was purchased from Morinaga Institute of Biological Science (Yokohama, Japan). The kit consists of β-lactoglobulin and the primary rabbit antibody. A VECTASTAIN® ABC-AP Rabbit IgG kit was bought from Vector Laboratories Inc. (Burlingame, CA, USA). The VECTASTAIN® ABC system can be used to detect antigens bound to the nitrocellulose membrane after they have been dot-blotted. All other chemicals were of analytical reagent grade and were used without further purification.

2.2. Microtiter plate assay for ALP and ACP activity

In the ALP assay, the buffer solution containing 0.45 mM tetrazolium salt, ALP (0–4.6 μg), and TEMED (0–100 mM) as a final concentration in a total volume of 45 μl was added to each well of a 96-well microtiter plate. Then, 5 μl of AsA-P solution (0.4–70.0 mM) was added to the well and incubated at 30 °C for 7 min. Tris–HCl buffer (0.1 M, pH 8.0–9.0) and CAPSO buffer (0.1 M, pH 9.5–10.0) were used as the reaction buffer. NBT and XTT were used as the tetrazolium salt to form the insoluble and soluble formazans, respectively. The formation of formazan was measured as absorbance at 530 nm for NBT or 470 nm for XTT with a microplate reader (VersaMax, Molecular Devices Co., Sunnyvale, CA, USA).

In the ACP assay, 0.1 M tartrate buffer (pH 4.5) containing 0.45 mM tetrazolium salt, ACP (0–2.7 mg), and PMS (0–200 μM) as a final concentration in a total volume of 45 μl was added to each well of a 96-well microtiter plate. Then, 5 μl of AsA-P solution (70 mM) was added to the well and incubated at 37 °C for 20 min. NBT, MTT, and XTT were used as the tetrazolium salt to form the insoluble and soluble formazan, respectively. The formation of formazan was measured as absorbance at 530 nm for NBT, 570 nm for MTT, or 470 nm for XTT.

2.3. Staining procedure for ALP and ACP activity

Serial dilutions of ALP and ACP were adsorbed onto the nitrocellulose membranes. The membranes were dried at 5 °C, and then incubated with the substrate solution for the enzyme (AsA-P/NBT or AsA-P/PMS/NBT solution) for 2 min. Finally, the membranes were washed three times for 5 min and allowed to dry.

2.4. Dot blot of β-lactoglobulin

Serial dilutions of β-lactoglobulin were adsorbed onto the nitrocellulose membranes. The membrane were dried, rehydrated, and blocked for 1 h in 20 mM Tris–HCl buffer (pH 7.4) containing 500 mM NaCl, 1% casein, 0.05% Tween-20 and 0.1% bovine serum albumin. Then, the membranes were incubated for 1 h in primary rabbit antibody (0.5 μg/ml) diluted with the blocking solution. Finally, the membrane was washed three times for 5 min each.

The following procedure is suggested as a guideline for the use of VECTASTAIN® ABC-AP kit. The membranes were incubated for 30 min in a biotin-labeled secondary antibody, which was biotinylated anti-rabbit IgG, and then washed three times for 5 min each. This introduces many biotins into the section at the location of the primary antibody. The membranes were incubated in the avidin:biotinylated ALP complex for 20 min and then washed three times for 5 min each. In the last step of the procedure, the membranes were incubated with the substrate solution (AsA-P/NBT or BCIP/NBT solution) after immersion in 0.1 M CAPSO buffer (pH 10.0). Color development was halted after exactly 5 min by removing the substrate solution and washing the membranes with copious distilled water.

3. Results and discussion

3.1. Optimization of ALP assay

Although the tetrazolium method for ALP activity using AsA-P and NBT gives insoluble formazan on the nitrocellulose membranes, it is thought that the precipitate formed in the solution and its adsorption to the surface of a microplate at the initial reaction process (within 20 min) can be ignored in a relative comparison of AsA-P and BCIP. Therefore, the spectrophotometric measurement for ALP activity can be performed in the microtiter plate to determine the optimum condition of the AsA-P/NBT staining procedure. First, in order to obtain the maximum sensitivity of the AsA-P/NBT staining procedure for ALP activity, the effect of pH on the reduction rate of NBT was studied using 0.1 M Tris–HCl buffer (pH 8.0–9.0) and 0.1 M CAPSO buffer (pH 9.5–10.0). As shown in Fig. 1, the rate of NBT reduction was promoted by increasing the pH, and the reaction was finished in about 5 min at pH 10.0 in the presence

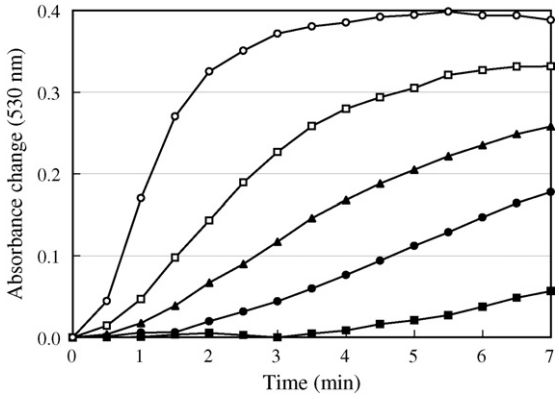

Fig. 1. Effect of pH on the reduction rate of NBT in ALP assay. 0.1 M Tris–HCl buffer: (■) pH 8.0; (●) pH 8.5; (▲.) pH 9.0. 0.1 M CAPSO buffer: (□) pH 9.5; (◯) pH 10.0.

of ALP at 2.3 μg/well, 0.7 mM AsA-P, and 0.4 mM NBT. We selected 0.1 M CAPSO buffer (pH 10.0) in consideration of the optimum pH (8.5–10.0) of ALP activity.

It was reported that dehydroascorbic acid is reduced to ascorbic acid by TEMED [14,15]. Thus, it was thought that the rate of NBT reduction might be promoted by the addition of TEMED. The effects of the concentration of TEMED on the reduction rate of NBT at pH 8.0 and 10.0 were investigated (Fig. 2). The amount of formazan formed from NBT increased sharply with increasing concentration of TEMED at pH 8.0, although the reduction rate was hardly promoted at pH 10.0. NBT can be reduced directly by ascorbic acid, provided that the stoichiometric ratio is above 40:1 in favor of ascorbic acid at pH 7.8 [14]. However, in the presence of TEMED, much lower concentrations of ascorbic acid are able to reduce NBT. These results show that the reduction of NBT can be done effectively in the presence of TEMED at weakly alkaline conditions. Therefore, the addition of TEMED is effective when the reaction must be done under weakly alkaline conditions.

In Fig. 3(A) and (B), the proposed method is compared with the BCIP/NBT method. The reduction rate of NBT was measured in the presence of AsA-P or BCIP in the range of

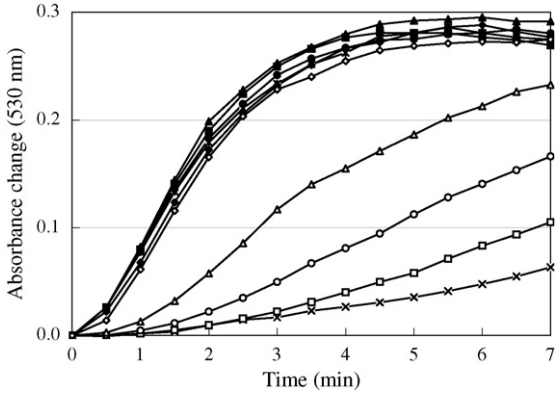

Fig. 2. Effect of concentration of TEMED on the reduction rate of NBT in ALP assay. TEMED concentration (mM) at pH 8.0: (×) 0; (□) 9; (◯) 27; (△) 45; (◇) 90. TEMED concentration (mM) at pH 10.0: (*) 0; (■) 9; (●) 27; (▲) 45; (◆) 90.

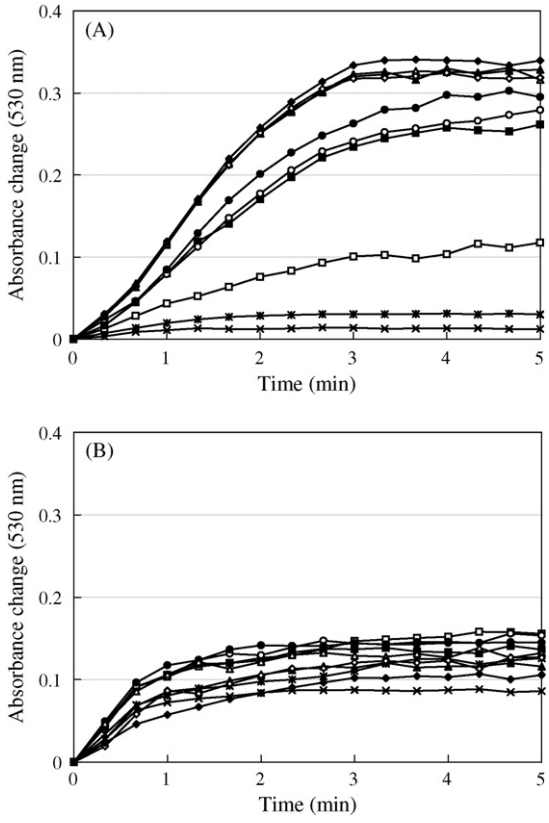

Fig. 3. Effect of concentrations of AsA-P (A) and BCIP (B) on the reduction rate of NBT in ALP assay. AsA-P and BCIP concentration (mM): (×) 0.04; (*) 0.07; (□) 0.18; (■) 0.35; (◯) 0.53; (●) 0.70; (△) 1.75; (▲) 3.50; (◇) 5.25; (◆) 7.00.

0.04–7.0 mM. At low concentrations, the initial rate of NBT reduction with BCIP was higher than that with AsA-P. The K_m values were 2.3×10^{-4} and 2.1×10^{-5} M for AsA-P and BCIP, respectively. The yielded absorbance, however, was considerably higher with the proposed method at higher concentrations (>0.35 mM). In addition, the initial rate of NBT reduction increased with increasing concentration of AsA-P. In contrast, both the initial rate and the yielded absorbance decreased with increasing concentration of BCIP (>0.7 mM). From these results, it appears that AsA-P is superior to BCIP in the reduction of NBT above a certain concentration (>0.35 mM). This reaction depends on the hydrolyzation reaction of substrate by ALP and the reduction reaction of NBT with the hydrolysates. Although the hydrolyzation rate of AsA-P is lower than that of BCIP, it is thought that the reduction efficiency of NBT with the hydrolysate of AsA-P is much higher than that with BCIP. The suitability of AsA-P for ALP assay mainly reflects a difference in the reduction efficiency of NBT with the hydrolysate between AsA-P and BCIP.

Instead of NBT, XTT and MTT were used as the tetrazolium salt to form the soluble formazan to accomplish the spectrophotometric measurement for ALP activity (data not shown). XTT could react with AsA-P more effectively than MTT in the presence of ALP. A linear relationship between the absorbance (XTT-formazan) and the amount of ALP was observed between 0.02 and 4.60 μg/well with a correlation coefficient of 0.9979

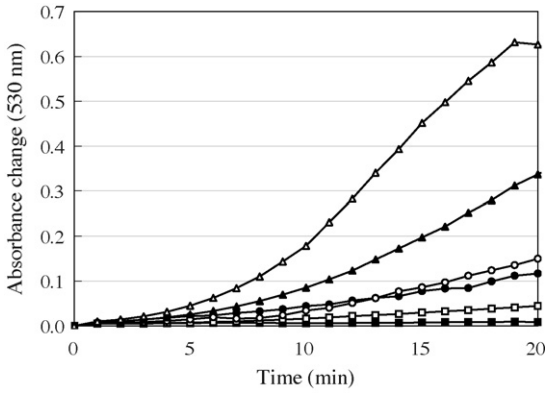

Fig. 4. Effect of concentration of PMS on the reduction rate of NBT in ACP assay. PMS concentration (μM): (■) 0; (□) 9; (●) 27; (○) 45; (▲) 90; (△) 180.

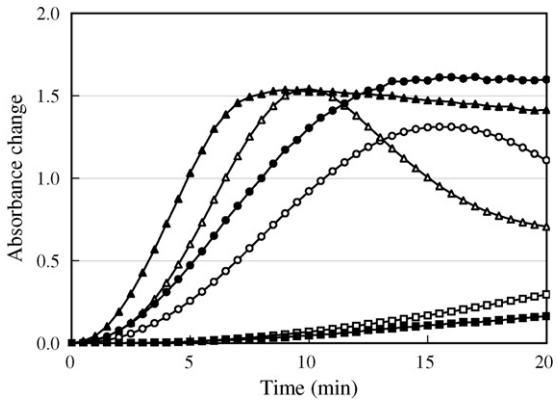

Fig. 5. Effect of concentration of PMS on the reduction rate of MTT and XTT in ACP assay. PMS concentration (μM) with MTT: (■) 0; (●) 45; (▲) 180. PMS concentration (μM) with XTT: (□) 0; (○) 45; (△) 180. Absorbance: MTT, 570 nm; XTT, 470 nm.

($n = 10$). Therefore, the utilization of XTT is effective when ALP activity is measured spectrophotometrically.

3.2. Optimization of ACP assay

We tried to apply the AsA-P/NBT method to the measurement of ACP activity. However, the reduction of NBT by AsA hardly occurs under acidic conditions. Although the effect of TEMED on the reduction rate of NBT in the presence of AsA-P and ACP at pH 4.5 was investigated like the ALP assay, the addition of TEMED slightly promoted NBT reduction under acidic conditions (data not shown). It is reported that NBT in the presence of PMS reacts with the NADPH produced by dehydrogenases to produce an insoluble formazan [16]. Therefore, the effect of PMS as an electron-coupling agent on the reduction of NBT by AsA was studied. As shown in Fig. 4, the reduction rate of NBT was markedly promoted by increasing the concentration of PMS in 0.1 M tartrate buffer (pH 4.5) containing ACP (2.7 mg/well), 7.0 mM AsA-P and 0.4 mM NBT. Because the reactivity of the ascorbic acid with NBT is relatively low under acidic conditions, it is thought that PMS functions effectively as the electron-coupling agent in the reduction of NBT. On the other hand, TEMED functions as an electron donor on the reduction of dehydroascorbic acid to reproduce ascorbic acid in the NBT reduction under weakly alkaline conditions. We decided to add PMS at the final concentration of 180 μM for the ACP assay. 1-Methoxy-PMS also could be applied to the reduction reaction of NBT by AsA as the electron-coupling agent, although the rate of NBT reduction was lower than that obtained by PMS (data not shown).

Instead of NBT, MTT or XTT was used as the tetrazolium salt to form the soluble formazan for the spectrophotometric measurement for ACP activity (Fig. 5). Although the formation of formazan was hardly promoted in the absence of PMS, the addition of PMS potentiated the reduction of XTT or MTT. However, the formazan produced from XTT was unstable under acidic conditions. On the other hand, the formazan generated from MTT was stable. The PMS/MTT system is widely used for the enzymatic determination of ascorbic acid under acidic conditions [17]. A linear relationship between the absorbance and the amount of ACP was obtained between 0.27 and 2.70 mg/well with a correlation coefficient of 0.9968 ($n = 8$) when MTT was used as the tetrazolium salt.

3.3. Dot blot of ALP and ACP activity

The activities of serial dilutions of ALP and ACP adsorbed onto the nitrocellulose membranes were visualized with the substrate solution (AsA-P/NBT or AsA-P/PMS/NBT solution). Fig. 6 shows dot blots of a dilution series ranging from 0.022 to 2.20 ng of ALP and 0.015 to 1.50 μg of ACP. The intensity of color development increased with increasing amount of enzymes. These results showed that the activities of ALP and ACP could be visualized semi-quantitatively with the proposed method. The color of the formazan obtained in the presence of AsA-P, NBT, and ALP was blue-purple. On the other hand, the color of the formazan produced in the presence of AsA-P, PMS, NBT, and ACP was red-purple.

Because bone metabolism is composed of balanced osteogenesis and bone resorption, simultaneous estimation for ALP, an enzyme marker of osteoblasts, and tartrate-resistant ACP, an enzyme marker of osteoclasts, is deemed useful [4,5]. Recently, a double staining method for ALP and tartrate-resistant ACP was developed [18], allowing both ALP and ACP activities in cells to be stained simultaneously for comparison. In this method, the BCIP/NBT solution for ALP activity is used. On the other hand, the combination of 6-bromo-2-phosphohydroxy-3-naphthoic acid-*o*-anisidide (naphthol-AS-BI-phosphate) and diazomium salt (Fast Red Violet LB) is used for the ACP stain-

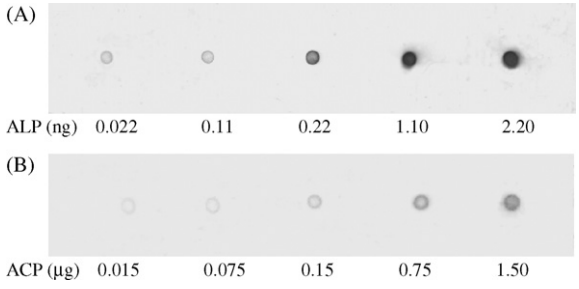

Fig. 6. Dot blots of a dilution series of ALP (A) and ACP (B).

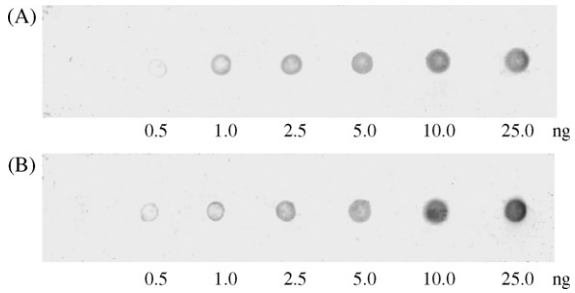

Fig. 7. Comparison of BCIP/NBT method (A) and AsA-P/NBT method (B) in dot blots of a dilution series of β-lactoglobulin.

ing method. In the proposed method, both ALP and ACP activity can be measured by the combination of AsA-P and NBT.

3.4. Dot blot of β-lactoglobulin

In Fig. 7, the staining intensity obtained with the BCIP/NBT method is compared with that obtained by the AsA-P/NBT method. The figure shows dot blots of a dilution series ranging from 0.5 to 25.0 ng of β-lactoglobulin. Two series of dots were hybridized in the same bag with the primary rabbit antibody, the biotin-labeled secondary antibody, which was biotinylated anti-rabbit IgG, and the avidin:biotinylated enzyme complex, and subsequently detected separately with the conventional method or the proposed method. Fig. 7 shows that color development with the proposed method is faster than with the BCIP/NBT method. The detection limit in the detection time of 5 min was 0.02 ng for β-lactoglobulin. It took only about 30 s to visualize a blotted dot containing 25.0 ng of β-lactoglobulin.

4. Conclusions

A new method for phosphatase assay using AsA-P and NBT was developed and its efficiency was demonstrated. For the ALP assay, the proposed method was compared with a traditional method (BCIP/NBT) in the dot blots of a dilution series of β-lactoglobulin. The color development with the AsA-P/NBT method was faster than that with the BCIP/NBT method. The detection limit in the detection time of 5 min was 0.02 ng for β-lactoglobulin.

In addition to sensitivity, the AsA-P/NBT reaction for ALP-conjugated antibodies offers other several advantages in comparison with the BCIP/NBT method. BCIP is relatively expensive, whereas AsA-P is very cheap. Furthermore, BCIP is slightly hazardous in case of skin contact (irritant), eye contact (irritant), or ingestion, whereas AsA-P is harmless to human. The stability of AsA-P may be very high because it is reported that the introduction of the phosphoric group in the 2-position protects the molecule from a break-up of the enediol system [19]. Therefore, AsA-P is widely used in various types of cosmetic products. Although the solubility of BCIP in water is relatively low, AsA-P has a high solubility in water. Thus, organic solvents such as DMF need not be used to dissolve the reagents in the case of AsA-P. It is thought that AsA-P has advantages from the viewpoint of the users.

Furthermore, AsA-P could be also used as the chromogenic substrate in the presence of PMS for the ACP assay. PMS functions effectively as the electron-coupling agent in the reduction of NBT under acidic conditions. The proposed method may be applied for the staining of ALP and ACP in bone-related cells, and the detection of proteins, DNA, and RNA on Western, Southern and Northern blots, respectively.

References

[1] M.S. Burstone, J. Histochem. Cytochem. 7 (1959) 39.
[2] F.R. van de Wijngaert, E.H. Burger, J. Histochem. Cytochem. 34 (1986) 1317.
[3] M.H. Helfrich, C.W. Thesingh, R.H. Mieremet, A.S. van Iperen-van Gent, Cell Tissue Res. 249 (1987) 125.
[4] R.H. Christenson, Clin. Biochem. 30 (1997) 573.
[5] E. Bonucci, A. Nanci, Ital. J. Anat. Embryol. 106 (2001) 129.
[6] S. West, J. Schröder, W. Kunz, Anal. Biochem. 190 (1990) 254.
[7] D.A. Knecht, R.L. Dimond, Anal. Biochem. 136 (1984) 180.
[8] F.P. Altman, Prog. Histochem. Cytochem. 9 (1976) 1.
[9] E.E. Kim, H.W. Wyckoff, J. Mol. Biol. 218 (1991) 449.
[10] G.B. Smejkal, C.A. Kaul, J. Histochem. Cytochem. 49 (2001) 1189.
[11] M. Kitamura, M. Maeda, A. Tsuji, J. Biolumin. Chemilumin. 10 (1995) 1.
[12] A. Kokado, H. Arakawa, M. Maeda, Anal. Chim. Acta 407 (2000) 119.
[13] R.E. Gyuresányi, A. Bereczki, G. Nagy, M.R. Neuman, E. Lindner, Analyst 127 (2002) 235.
[14] M. Maccarrone, A. Rossi, G. D'Andrea, G. Amicosante, L. Avigliano, Anal. Biochem. 188 (1990) 101.
[15] R. Mittler, B.A. Zilinskas, Anal. Biochem. 212 (1993) 540.
[16] K.M. Mayer, J. Biomol. Screen. 7 (2002) 135.
[17] U. Deneke, G. Michal, H.O. Beutler, Dtsch. Lebensmittel-Rundsch. 74 (1978) 400.
[18] E. Harlow, D. Lane, Antibodies: A Laboratory Manual, Cold Spring Harbor Laboratory, New York, 1988, p. 406.
[19] R. Austria, A. Semenzato, A. Bettero, J. Pharm. Biomed. Anal. 15 (1997) 795.

Available online at www.sciencedirect.com
ScienceDirect
Talanta 73 (2007) 490–497
Talanta
www.elsevier.com/locate/talanta

Optimization of GC–ICPMS system parameters for the determination of butyltin compounds in Hungarian freshwater origin sediment and mussel samples

Márta Üveges *, László Abrankó, Péter Fodor

Corvinus University of Budapest, Department of Applied Chemistry, 1118 Budapest, 29–33 Villányi út, Hungary

Received 12 December 2006; received in revised form 5 April 2007; accepted 11 April 2007
Available online 4 May 2007

Abstract

The optimization and application of gas chromatograph coupled with inductively coupled plasma mass spectrometer (GC–ICPMS) (equipped with a commercially available interface) for the speciation of butyltin compounds in freshwater origin sediment and mussel samples is described. Optimization focused on the system parameters that have the greatest effect on signal intensity such as plasma power, ion lenses and make up gas flow (in the interface). Xenon (Xe) containing argon gas (Ar) was applied as tuning gas providing continuous Xe signal for the optimization of system parameters. It was found that plasma power and make up gas are interrelated variables and provide a set of paired optimum values at each power settings. The absolute optimum values obtained at 800 W plasma power and 1.2 L min^{-1} make up gas flow rate when 7 mm sample depth was adjusted. The optimum settings obtained were then checked by means of a test solution (tetraethyltin dissolved in hexane). Same optimum conditions were found when tin (Sn) transient signals were monitored. Detection limits were calculated for the three species using the optimized system parameters. Detection limits are the following: for monobutyltin (MBT) 5.6 ng Sn kg^{-1}, for dibutyltin (DBT) 6.6 ng Sn kg^{-1} and for tributyltin (TBT) 3.4 ng Sn kg^{-1} obtained. Determination of the butyltin compounds were carried out by means of species-specific isotope dilution analysis. The spike solution contained all species investigated but with altered isotopic composition. Each species were enriched in their ^{119}Sn isotope. Concentrations found in Hungarian freshwater origin mussel and sediment samples ranged between 19 and 39 ng g^{-1} for MBT, between 1.2 and 6.3 ng g^{-1} for DBT and between 1.2 and 3.2 ng g^{-1} for TBT indicated as Sn in dry weight. Validation of the method was done by means of certified reference materials (BCR CRM 646 and 477). Good agreement was found between certified and experimental values. Normalized deviation (E_n) was also computed in order to validate the method used. E_n values obtained ranged between 0.07 and 0.11 for mussel samples and between 0.26 and 0.72 for sediment samples. These values show that isotope dilution–GC–ICPMS methodology is valid for the determination of MBT, DBT and TBT from both types of matrices.

Keywords: Freshwater origin samples; Xe as tuning gas; Butyltin compounds; IDA–GC–ICP–MS

1. Introduction

Organotins are widespread as pesticides, additives in antifouling paints, preservatives in wood, textile, paper and leather and commonly used as heat and light stabilizer in PVC production [1,2]. Tributyltin (TBT) and its degradation products (dibutyltin and monobutyltin) persist in the environment (in water and particularly in sediments) where they are concentrated. Toxic effects of organotin compounds on aquatic organisms and mammals are well known and also have great concern on humans [3,4]. Due to the fact that organotin compounds have high bioaccumulation potential control of contamination levels in environmental samples is necessary. As a consequence, different water quality criteria and several legislative restrictions have been adopted in order to control the usage of especially TBT. Directives have been also adopted in the EU in order to eliminate several toxic substances from the environment including TBT and its degradation products. Commission Directive 2002/62/EC prohibited the use of organotin compounds as biocides in antifouling paints in all craft, and in marine, costal, estuarine and inland waterways and lakes [5]. A priority list of pollutants has been established in Decision 2455/200/EC in

* Corresponding author. Tel.: +36 1 4826164; fax: +36 1 4664272.
E-mail address: marta.uveges@uni-corvinus.hu (M. Üveges).

0039-9140/$ – see front matter © 2007 Elsevier B.V. All rights reserved.
doi:10.1016/j.talanta.2007.04.032

order to eliminate within twenty years the emission of toxic anthropogenic pollutants to the aquatic environment [6].

Researchers have studied for many years the determination of such compounds in different kinds of matrices. Quantification of organotin compounds in environmental samples has been considered a complex task, since they show instability and have low concentration levels in environmental matrices. Therefore, highly sensitive hyphenated techniques are demanded for the determination of these species. Nowadays, the most commonly used hyphenated techniques involve gas chromatography (GC) or high performance liquid chromatography (HPLC) for the separation of the species and an element selective detector such as AED [7–9], AAS [10] or ICPMS [11–15,24–29].

Within the analysis initial sample preparation procedure was considered to be one of the most critical steps. Several limitations regarding efficiency of recovery and quality in species preservation remain at this level. Different extraction and derivatization techniques have been developed for the determination of organotin compounds in environmental samples. These techniques were developed taking into account more efficient recovery of the species, amount of solvent used, time consumption [16–22,35] and/or simultaneous determination of organometallic species [23,24]. Furthermore, recent studies show that possible species degradation and/or interconversion may occur during the initial sample preparation procedure that can be followed up and corrected with the help of isotope dilution analysis [25–27].

In recent years, the number of reports on the use of GC–ICPMS for the determination of organotin species has been continuously growing [28]. This refers to the fact that GC–ICPMS hyphenation is one of the most adequate techniques able to fulfil the above-mentioned requirements. Indeed, it provides sensitivity that few other techniques can offer and allows simultaneous multi-isotopic detection in a single run. Due to the isotopic information of the element of interest isotope dilution techniques may be applied as calibration method providing reliable results with good precision [29].

Optimization of ICP–MS parameters is indispensable in order to make efficient experiments. During common multielemental measurements system parameters that affect the most the signal of an element, are optimized with the help of a tuning solution (containing the corresponding elements in a given concentration). The system can be also specifically tuned in order to make it more sensitive to a given element. For instance, for the optimization of selenium detection Etxebarria et al. [30] applied an experimental design (full factorial design) to obtain such instrumental conditions that define the maximum response. They concluded that all the variables (e.g. power supply, sample depth, auxiliary flow rates) show significant effect on the response.

In spite the relevancy and good capability of GC–ICPMS hyphenation system parameters must also be optimized purposely to obtain the advantages this system provides. Since the way of sample introduction is different in the case of GC–ICPMS compared to common solution nebulization–ICPMS the optimal operating conditions are also proven to be very different [31]. It is due to the fact that in the latter case dry plasma is generated as gaseous samples are introduced to the plasma. Since GC–ICPMS coupling provides transient signals optimization procedures based on these signals would be time consuming. A continuous signal is required in order to manage optimization of system parameters. For this purpose Kim et al. [32] applied vapour mercury as continuous signal. Beside the fact that careful treatment is necessary working with Hg, memory effect might take place if mercury itself is the analyte.

Argon dimers (Ar_2^+) can also be monitored in ICPMS application in order to correct for long-term instrumental drift and to use it as instrumental standard [33]. Moreover, Encinar et al. [14] have applied $^{40}Ar_2^+$ for optimization of ion lens in GC–ICPMS application. They concluded that the optimum plasma and ion lens conditions obtained with nebulization differed greatly from the optimum conditions achieved with a dry plasma set-up.

A more widely used continuous signal in dry plasma applications is xenon (Xe) that can be mixed into the GC carrier gas [34,35], introduced to the system with the make up gas [36] or can be found as a trace contaminant gas in the Ar supply [37]. In the referred research works Xe was applied as an internal standard for peak area correction (corrected for instrumental drift) and for the optimization of instrumental operating conditions.

This paper reports the results of the optimization of GC–ICPMS as a detection system for the speciation analysis of butyltin compounds applying isotope dilution analysis for quantification. Furthermore, the application of the method is shown for the analysis of Hungarian environmental sediment and mussel samples. To the best of our knowledge data are first reported on butyltin determination in Hungarian freshwater environmental samples in present study.

2. Experimental

2.1. Chemicals and reagents

All solvents and reagents were of analytical-reagent grade. For the optimization of system parameters 1% xenon (Xe) in argon (Ar) gas was obtained from Messer (Budapest, Hungary). Analytical standards such as monobutyltin trichloride (MBT, 95%), dibutyltin dichloride (DBT, 96%), tributyltin chloride (TBT, 96%) and tetraethyltin (TeEtT, 97%) were obtained from Sigma–Aldrich (Budapest, Hungary). The spike solution containing a mixture of MBT, DBT and TBT enriched in ^{119}Sn was supplied by ISC-Science (Gijon, Spain). This spike solution is certified both in isotopic composition and concentration. The isotopic composition for the three main isotopes is as follows: Sn-118 14.33%, Sn-119 82.40% and Sn-120 3.13%. The certified concentrations of the three species were $0.121 \pm 0.005\ \mu g\ g^{-1}$ as tin for MBT, $0.748 \pm 0.009\ \mu g\ g^{-1}$ as tin for DBT and $1.02 \pm 0.02\ \mu g\ g^{-1}$ as tin for TBT, respectively. This enriched butyltin mix was diluted in acetic acid: methanol 3:1 (g:g) to the appropriate concentration. Glacial acetic acid and methanol was obtained from Merck and Carlo Erba (Milano, Italy). The ethylation of the butyltin species was performed

using 2% (w/v) sodium tetraethyl borate (Galab, Geesthacht, Germany) in 0.2 M NaOH aqueous solution (Merck, Budapest, Hungary). The optimum pH for derivatization was adjusted with acetic acid (Merck) and sodium acetate (Merck) buffer. Derivatized analytes were extracted into hexane (Merck). Deionised water, $R > 10\,M\Omega$ (Elgacan Ultrapure, Vivendi Water Systems Ltd., High Wycombe Bucks, England), was used for preparing the buffer solution. Amber chromatographic vials with screw caps (Sigma–Aldrich) were applied for the sample preparation procedure.

2.2. CRMs and matrices

Certified reference materials BCR CRM 646 and BCR CRM 477 freshwater sediment and mussel tissues were purchased from Institute for Reference Materials and Measurements, IRMM (Geel, Belgium). These materials are certified among others their butyltin contents. The certified butyltin concentrations for BCR CRM 646 sediment tissue indicated in ng g^{-1} as tin are the following: MBT 410 ± 69, DBT 394 ± 36 and TBT 195 ± 18 (dry weight, respectively). For the same species the certified concentrations expressed in ng Sn g^{-1} in BCR CRM 477 mussel tissue are as follows: MBT 1013 ± 189, DBT 785 ± 61 and TBT 900 ± 78 (dry weight, respectively).

Since Hungary has become a member of the European Union environmental samples have to be examined for their butyltin (especially TBT) contents. Real freshwater origin environmental samples were analyzed in this manner. These samples were collected from the river Danube in Hungary around the area of the city Paks. Mussel samples (Unio pictorum) are from the main channel and from a by-channel of the Danube. Sediment sample originates from the stagnant water of the river Danube from the same location.

2.3. Sample preparation

Extraction and derivatization of organotin compounds from freshwater origin sediment and mussel samples were performed in the following way. Weights of 0.25 g of the freeze-dried samples were accurately measured in a pre-cleaned microwave vessel (in course of sediment) and glass vial (in course of mussel). Then, they were spiked with an appropriate amount of the ^{119}Sn-enriched spike solution in order to result approximately equal concentrations of the spike and the authentic Sn. In each case the amounts of sample and spike added were controlled gravimetrically in order to avoid volumetric errors. Then, immediately 4 mL of an acetic acid and methanol 3:1 mixture was added as extraction solution. The final slurries were exposed to microwaves at 90 W for 4 min in case of sediment samples, and to thermostatic bath in case of mussel samples at 37 °C for at least two hours under mechanical shaking. Both extracts were left to elutriate and to cool down to ambient temperature at the end of the extraction procedure. Previous works [25,27,38] have shown that this procedure assured quantitative extraction of the butyltin compounds from the sediment and mussel without degradation of the species. Then 300 μL of the liquid phase was ethylated in a 7-mL vial using 4 mL of buffer pH 5.4 and 0.5 mL of 2% (w/v) sodium tetraethyl borate diluted in 0.2 M NaOH. The resulted slurry was shaken for 10 min manually. The organic layer was transferred to a 2-mL vial and stored at −18 °C in the dark until measurement, in both cases. The hexane phase was evaporated before injection under a gentle stream of argon in order to obtain higher intensities.

A standard mixture solution was prepared from stock solutions of the three species (MBT, DBT and TBT) containing naturally abundant tin isotopes. It was applied for the determination of mass bias during isotope dilution analysis. The stock solutions were mixed and diluted in the mixture of acetic acid and methanol (3:1). It was followed by a derivatization procedure in the way mentioned before. After 10 min shaking the organic layer was then skimmed and transported to a 2-mL dark vial. Concentrations in the final mixture were obtained about 20 ng g^{-1} (as Sn) for each species.

A 100 ng g^{-1} (as Sn) tetraethyl tin (TeEtT) was also prepared by dissolving it in hexane. It was applied as a test solution for the optimization of the system parameters.

2.4. Instrumentation set-up

An Agilent gas chromatograph Model 6890 (Agilent Technologies Inc., Tokyo, Japan) equipped with a split/splitless capillary injector, and a HP-5 capillary column (cross linked 5% phenyl-methyl siloxane, 30 m × 0.32 mm × 0.25 μm thickness) was used for the separation of the organotin species.

The gas chromatograph was coupled with an Agilent 7500ce ICPMS (equipped with a shielded torch, Agilent Technologies Inc., Waldbronn, Germany) via a commercially available (Agilent) interface. A fused silica capillary is connected to the GC column through a glass connector. The fused silica capillary is inserted into a silcosteel tube via a metallic T-piece. The eluted compounds are transported from the GC column to the ion source through this assemblage. Make up gas surrounds the fused silica capillary inside the silcosteel tube in order to get optimal central gas flow rate. In this system one of the gas channels of the ICPMS was chosen to supply and control the above-mentioned make up gas flow. An insulator material covers the transfer line part of the interface (starts from the top of the oven ends at the injector part) to keep it at a convenient temperature. The second part of the interface is the so-called injector. This is a cast-iron metallic assemblage. A demountable torch is used for this set-up in which the injector is inserted providing the central channel of the torch. Both parts (transfer line and injector) are electrically heated and controlled by the GC in order to avoid condensation of the eluted species.

The GC carrier gas supply line is divided in two parts by a switching valve. In this way switching between two types of carrier gases can be worked out. One percent xenon containing argon gas was used for the optimization of system parameters while the chromatographic separation was carried out by means of 100% argon gas.

Sediments and biota samples were freeze-dried using a Christ Alpha 1–4 lyophiliser (Christ, Germany). A digitally controlled immersion thermostat model GFL Type 1031 (Burgwedel, Germany) was used for the extraction of the organotin compounds

Table 1
Operating conditions of GC–ICP–MS

Gas chromatograph	
Column	HP-5 (30 m × 0.32 mm × 0.25 μm)
Carrier gas	Ar (15 psi)
GC program	50 °C (1 min) to 250 °C (1 min) at 30 °C min^{-1}
Injector mode	Split/splitless
Split time	1 min
Injection temperature	250 °C
Interface	Fused silica capillary i.d. 0.32 mm
Transferline temperature	250 °C
Injector temperature	250 °C
Make up gas flow rate	1.2 L min^{-1}
ICP–MS parameters	
RF power	800 W
Plasma gas flow rate	15.0 L min^{-1}
Sample depth	7 mm
Extract 1	−180 V (Hard extraction)
Extract 2	−168 V
Omega Bias-ce	−40 V
Omega Lens-ce	8.8 V
Cell Entrance	−50 V
QP Focus	10 V
Cell Exit	−70 V
Octp. Bias	−6 V
QP Bias	−3 V
Isotopes monitored	^{118}Sn, ^{119}Sn, ^{120}Sn and ^{126}Xe

from the biological materials, whereas the extraction from the sediment was carried out by a microwave oven model MDS-81D (CEM Corporation, Matthews, NC, USA) equipped with PTFE-PFA vessels.

Operating conditions used for the gas chromatographic separation and the ICP–MS detection of butyltin compounds is shown in Table 1. Separation conditions were optimized in a previous study [14]. In brief, a linear gradient between 50 °C and 250 °C was used at 30 °C min^{-1} with 1 min as initial and final time of isotherm conditions. The injector temperature was maintained at 250 °C using split/splitless mode. That means in splitless mode the valves are closed for 1 min, then the valves open and it splits for 2 min. After 2 min it switches to a gas saver mode. Chromatograms were recorded in time resolved analysis mode (measuring 1 point per mass) at 66 ms dwell time per mass.

A primary method, species-specific isotope dilution (technique worked out by Encinar et al. [44]) was applied in this work for the quantitative determination of organotin compounds due to the high precision capabilities. Isotope ratios in the mixture were calculated from the integrated peak areas of the isotopes. Factors (e.g. mass bias and detector dead time) affecting the accuracy of the measurement of isotope ratios must be under control. The only factor influencing the accuracy of tin isotope ratio measurements was found to be mass bias. The correction of mass bias was fulfilled by external correction procedure based on the evaluation of the isotope ratio 118/119, 120/119 and 120/118 in a standard mixed solution containing natural isotope abundant species. This solution was analyzed after every triplicate injections of the sample.

3. Results and discussion

3.1. Optimization of GC–ICPMS conditions

As it was already mentioned, the operating conditions of GC–ICPMS coupled system have to be optimized previous to the measurement. Since no desolvation is taking place with the introduction of gaseous samples dry plasma is generated. The optimal system conditions are expected to be different for this type of plasma compared to wet plasma conditions. The parameters chosen were conditions which affecting the most the signal intensity. These were found to be plasma power, make up gas flow (surrounds the inert capillary in the interface) and sampling depth [34–36,39]. Ion lens were also optimized to get optimal and high intensity signals. Therefore, to study the different parameters affecting the response of an analyte two different signals were monitored: a continuous Xe signal provided by the optional carrier gas and the area of TeEtT (test solution).

3.2. Plasma power and make up gas flow

These two parameters are considered to be interrelated variables. At each plasma power settings, series of measurements were performed at make up gas flow rates ranging from 0.5 L min^{-1} to 1.9 L min^{-1}. The profile of the ^{126}Xe signal intensity as a function of make up gas and plasma power at 7 mm sampling depth is shown in Fig. 1. The 3-D column chart clearly shows that the optimum setting was found to be 800 W at 1.2 L min^{-1} make up gas flow. It was observed that local optimums were also obtained at each plasma power settings. Going from low plasma power settings to high ones the local optimums have higher and higher make up gas flow rates (e.g. at 600 W 1.0 L min^{-1}, at 700 W 1.1 L min^{-1}, at 800 W 1.2 L min^{-1}, etc.). This phenomenon may be discussed with the assumption that the plasma temperature is changing by adjusting these values. If the power is increased the gas flow must also be increased in order to prevent the resulting plasma to be too 'hot' [31]. Especially in the case when dry plasma is applied. If one of the investigated parameters is altered the other one must be resettled in order to reach the optimal performance again. The absolute optimum values were chosen (800 W and 1.2 L min^{-1}) for further investigation. The same investigation was also carried out at 5 and 6 mm sampling depths. Diagrams with the same shapes were obtained but with less ion intensity. Thus, 7 mm was chosen for further investigations. During the optimization procedure background was monitored at m/z 8 and m/z 210. No significant changes were observed; it continuously stayed 0–1 counts (at 0.1 integration time).

Investigation of the mentioned system parameters was also carrier out by analysing 100 ng Sn g^{-1} TeEtT as test solution. The optimal sample depth (7 mm) was fixed while make up gas flow rate ranged between 1.1 and 1.3 L min^{-1} at each plasma power settings. Isotopes ^{120}Sn, ^{119}Sn and ^{118}Sn were monitored during data acquisition then chromatographic peaks obtained were integrated (total ion current, TIC). It was observed that make up gas flow rate and plasma power affected the

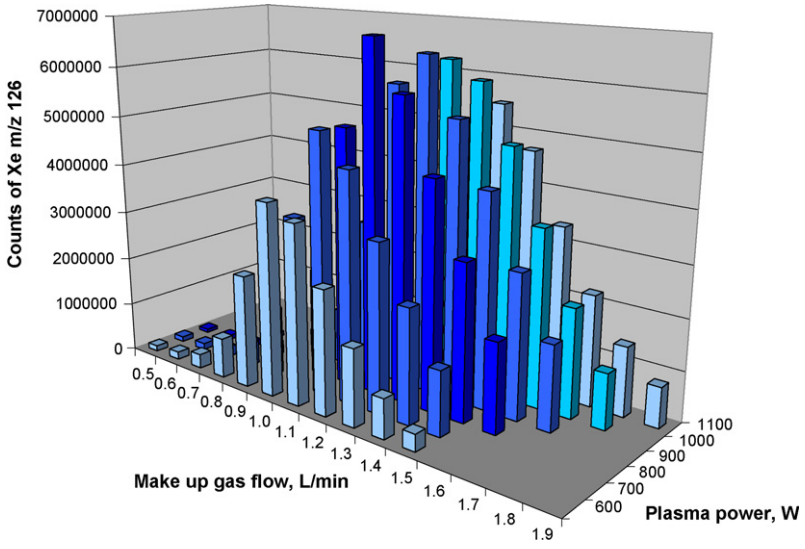

Fig. 1. Dependency of Xe ion on make up gas flow rate and plasma power at constant 7 mm sample depth.

TeEtT (Sn) signal in the same way resulted congruous optimum values (800 W, 1.2 L min^{-1}). Same phenomenon was found by other researchers [34,36,40–42] proving the statement that ^{126}Xe isotope can be used for optimization. In this way time-consuming transient signal measurements for the Sn isotopes at different system parameters may be avoided. For further analysis these optimal parameters were applied (see Table 1).

Difference in sensitivity was observed when Xe containing Ar gas was applied as carrier gas. It caused high suppression on chromatographic signals. The rate of reduction is more than 60% on peak area of TeEtT. Because of the drastic decrease of signal intensity, Xe containing Ar gas was only used for optimization procedure of system parameters. For the investigation of real samples and CRMs 100% Ar carrier was solely used.

3.3. Ion lenses

In Agilent 7500ce ICPMS extraction lenses (Extract 1 and Extract 2) are the first lenses in the assembly and they extract ions from the plasma. The efficiency of the extraction depends on the applied voltage on these lenses. If on the first lens (Extraction 1) low negative potential is set the extraction procedure is called 'hard extraction', if small positive potential is adjusted on it is called 'soft extraction' [43]. When the tuning procedure was performed manually monitoring ^{126}Xe as analyte ion it was found that hard extraction settings yielded five times higher ion intensity than obtained with soft extraction settings. Therefore, optimum values (−180 V in case of Extraction 1 lens and −168 V in case of Extraction 2 lens) were applied during the measurements.

An initial evaluation on the ion lenses monitoring Xe signal showed that among the other lenses Omega Bias-ce seems to have the greatest effect on signal intensity. It is situated behind the skimmer cone serving the off-axis section of the ion optics. It bends the trajectory of the ion beam in order to eliminate photons and neutrals from passing through. Data was collected by monitoring ^{126}Xe signal (0.1 s integration time) at different Omega Bias-ce voltages. In Fig. 2 the contour of Xe signal intensity shows a plateau from −40 V to −50 V and drops off with 10 V change by 40% on both sides of the scale.

The relationship between the Xe signal intensities and the chromatographic peak areas of TeEtT was also examined in the case of Omega Bias-ce lens. For this purpose 1 μL of the 100 ng Sn g^{-1} TeEtT test solution was injected at each Omega Bias-ce lens setting. It can be seen that TeEtT gave maximum intensities between −50 and −40 V and drops off with 10 V change by 40% on the more positive side of the scale. The optimum range of settings obtained in this experiment differs from recommended optimum range for Omega Bias-ce when wet plasma measurements are carried out. It is recommended to choose a value between −15 and −40 V [42] in order to obtain higher sensitivity. For further investigation −40 V was chosen for Omega Bias-ce settings.

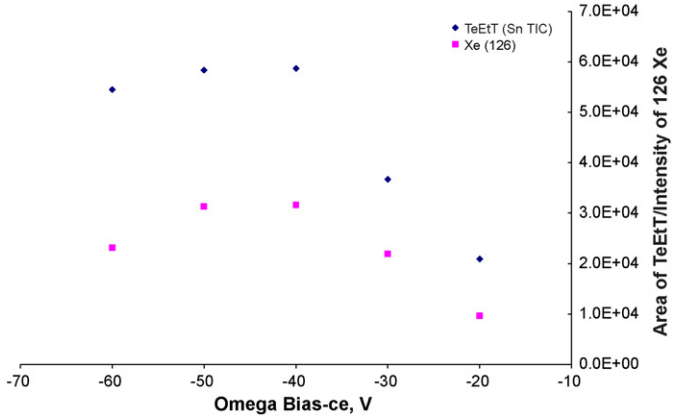

Fig. 2. Omega Bias-ce lens optimization curves for dry plasma monitoring ^{120}Sn and ^{129}Xe isotopes.

3.4. Analytical performance of isotope dilution–GC–ICPMS

The quantification of the three species (MBT, DBT and TBT) was carried out with isotope dilution of the species of interest. Therefore, peak area ratios between the tin isotopes (118/119 and 120/119) were computed, as indicated above. Isotope ratio precision was obtained by injecting each samples and standards three times to the gas chromatograph. Typical relative standard deviations occurred to be less then 1%, which is in accordance with precisions reported by other authors [23,42].

The only factor influencing the accuracy of tin isotope ratio measurements was found to be mass bias. The correction of mass bias was fulfilled by external correction procedure based on the evaluation of the isotope ratios 118/119, 120/119 and 120/118 (using 66 ms integration time) in a standard mixed solution containing natural isotope abundant species as mentioned before. The mixture was analyzed after every triplicate injections of the sample. The isotope ratios were computed as peak area ratios. Differences to the theoretical natural ratios were observed only in the second digits of the decimal places in the measured values. That means the standard deviations caused by mass bias are less than the standard deviation of the measurements.

The detection limit (LOD) of each species was estimated as the concentration corresponding to the peak that has the height of three times the standard deviation of the base line noise. The detection limits obtained for the three different species are the following: for MBT 5.6 ng Sn kg^{-1}, for DBT 6.6 ng Sn kg^{-1} and for TBT 3.4 ng Sn kg^{-1} was found. Lower LODs can be worked out by the application of solid phase micro extraction (SPME) as a well known matrixless extraction technique [19] or with stir bar sorptive extraction (SBSE) that provide 2–3 orders of magnitude LODs than SPME [18]. LOD values obtained in this work are acceptable for the determination of butyltin species in sediment and mussel samples but in case of seawater or freshwater environmental samples the current limit of detections should be decreased with the help of the above mentioned techniques.

3.5. Accuracy of the measurement

Since environmental samples with freshwater origin were intended to be analyzed CRMs with the same matrix were chosen for accuracy determination. BCR CRM 477 mussel tissue and BCR CRM 646 sediment tissue were analyzed prior to the real sample measurements. Sample preparation procedures were discussed before. For the quantification of the three species isotope dilution analysis was used as calibration procedure. Mean values of triplicate measurements with uncertainties for each CRMs are given in Table 2. Referring to the work of Nogueira et al. [16] verification of the applied method was carried out calculating the normalized deviations (E_n) according to the European Co-operation for Accreditation of Laboratories Guidance (EA2/03) [45]. It is established in the guidance that absolute value of E_n should be less than a unit in order to accept the measurement. Taking into account the reference values of the CRMs and the measured values obtained in our laboratory with the corresponding uncertainties for each species, E_n values obtained are ranging between 0.07 and 0.11 for mussel samples and between 0.26 and 0.72 for sediment samples. These values show that isotope dilution–GC–ICPMS methodology is valid for the determination of MBT, DBT and TBT from both types of matrices.

Table 2
Determination of MBT, DBT and TBT in BCR CRM 477 (mussel tissue), BCR CRM 646 (sediment tissue) and real environmental samples by isotope dilution analysis–GC–ICPMS

Sample	MBT	DBT	TBT
BCR CRM 477			
Average ($n=3$)	1027 ± 41	790 ± 19	891 ± 17
Certified	1013 ± 192	785 ± 62	901 ± 82
BCR CRM 646			
Average ($n=3$)	366 ± 23	422 ± 7	200 ± 3
Certified	410 ± 69	394 ± 36	195 ± 18
Sediment (stagnant water)	19.2 ± 0.6	6.26 ± 0.09	1.22 ± 0.02
Mussel (by channel)	38.6 ± 1.6	1.87 ± 0.05	3.17 ± 0.05
Mussel (main channel)	34.9 ± 1.5	1.25 ± 0.03	2.24 ± 0.03

Concentrations are expressed in ng Sn g^{-1} dry weight.

3.6. Analysis of real samples

Determination of the three butyltin species were carried out in Hungarian freshwater origin sediment and mussel samples collected from the river Danube. Results obtained in this preliminary study are presented in Table 2. With respect to the site they derive comparison resulted insignificant differences in the concentrations of the three butyltin species in the case of mussel samples. Slightly higher concentration values occurred (for each species) in mussel sample collected from the by-channel of the river. It may be due to the assumption that in by-channel area there is less water renewal activity providing higher availability of butyltin compounds for living organisms. In both type of mussel samples (collected in by-channel and main channel) higher MBT content was observed compared to DBT and TBT values. Also in sediment samples (collected from the stagnant water of the river) MBT concentration occurred to be the highest within the species analyzed. No potential industrial activity is known at that area. Therefore, higher MBT concentrations may be provided by the possible higher MBT content of the surrounding water (Danube) deriving from other sources (needs revision) or it can be due to degradation/species conversion takes place in aquatic environment in order to eliminate the toxic effect of TBT. In mussel samples higher MBT and TBT concentrations are observed due to the bioaccumulation potential of aquatic organisms. Few reports exist on freshwater environmental samples with respect to their butyltin content. Concentration values (lower ppb range) obtained in this work are in good agreement with values are reported by other authors [46]. It is worth stressing that all of the concentrations obtained exceeded the concentration of 0.4 ng Sn L^{-1} which is the toxic level of many marine species [47]. Rel-

ative standard deviations are ranging between 1.4 and 4.3%. No homogenization studies were carried out during this experiment. Further investigation of butyltin species is necessary since no data exists on Hungarian freshwater environmental samples.

4. Conclusion

In the light of the results it can be concluded that 1% Xe in Ar is an acceptable tuning gas for the optimization of GC–ICPMS conditions measuring Sn containing compounds. This study shows that Xe is a good indicator of Sn and provides effective optimization of the investigated system parameters such as plasma power, the ion lenses (Extraction 1,2 and Omega Bias-ce) and make up gas flow in the interface. Compromised optimization procedure seems to be a helpful method for the determination of the most suitable system parameters that produce maximum analyst ion intensity. Among the commonly optimized ion lenses Omega Bias-ce had the greatest effect on signal intensities. Since Xe containing Ar gas caused high suppression on chromatographic signals it is not recommended to apply it as GC carrier gas. It can also be concluded that species-specific isotope dilution analysis in combination with GC–ICPMS is a powerful and precise method for the determination of MBT, DBT and TBT in freshwater sediment and mussel samples. Although, results obtained do not represent the average concentration of butyltin species in real samples derive from the Danube in Hungary but are informative to consider further investigations. It is also worth stressing that in all samples analyzed in this study concentrations obtained were found to be higher than 0.4 ng Sn L^{-1} exceeding the toxic level for many marine species. Since Hungary has joint to the European Union further investigation is needed to estimate the presence of organotin compounds in the Hungarian environment not only in the case of sediment and biota but in presumably freshwater origin samples.

Acknowledgements

The authors are grateful to Jose Ignacio Garcia Alonso and Pablo Rodriguez-Gonzalez from the group of Oviedo, Spain for the kind offer of the spike solution and for the valuable scientific help for Alfredo Sanz-Medel. We would like to also acknowledge the real samples for Csilla Soeroes and Richard Shaffer.

References

[1] K. Fent, Crit. Rev. Toxicol. 26 (1996) 3–117.
[2] M. Hoch, Appl. Geochem. 16 (2001) 719–743.
[3] P.E. Gibbs, G.W. Bryan, P.L. Pascoe, G.R. Burt, J. Mar. Biol. Assoc. UK 67 (1987) 507–523.
[4] H. Yamada, K. Takayanagi, M. Tatushi, H. Tataga, Environ. Pollut. 96 (1997) 217–226.
[5] Directive 2000/60/EC of the European Parliament and the Council of the European Union, 23 October 2000.
[6] Decision 2455/2001/CE of the European Parliament and the Council of the European Union, 20 November 2001.
[7] M. Crnoja, C. Haberhauer-Troyer, E. Rosenberg, M. Grasserbauer, J. Anal. At. Spectrom. 16 (2001) 1160–1166.
[8] M. Ceulemans, S. Slaets, F. Adams, Talanta 46 (1998) 395–405.
[9] Y.K. Chau, F. Yang, M. Brown, Anal. Chim. Acta 338 (1997) 51–55.
[10] K. Bergmann, B. Neidhart, J. Sep. Sci. 24 (2001) 221–225.
[11] T. De Smaele, L. Moens, P. Sandra, R. Dams, Microchim. Acta 130 (1999) 241–251.
[12] J. Szpunar, S. McSheehy, K. Polec, V. Vacchina, S. Mounicou, I. Rodriguez, R. Lobinski, Spectrochim. Acta 55B (2000) 779–793.
[13] R. Wahlen, LC GC Eur. 15 (2002) 670–677.
[14] J.R. Encinar, J.I. Garcia Alonso, A. Sanz-Medel, J. Anal. At. Spectrom. 15 (2000) 1233–1239.
[15] P. Rodriguez-Gonzalez, J. Ruiz Encinar, J.I. Garcia Alonso, A. Sanz-Medel, J. Anal. At. Spectrom. 17 (2002) 824–830.
[16] J.M.F. Nogueira, P. Teixeira, M.H. Florencio, J. Microcolumn Sep. 13 (2001) 48–53.
[17] R. Morabito, P. Massanisso, P. Quevauviller, Trends Anal. Chem. 19 (2000) 113–119.
[18] J. Vercauteren, C. Peres, C. Devos, P. Sandra, F. Vanhaecke, L. Moens, Anal. Chem. 73 (2001) 1509–1514.
[19] Z. Mester, R. Sturgeon, J. Pawliszyn, Spectrochim. Acta 56B (2001) 233–260.
[20] K.C. Bowles, M.D. Tiltman, S.C. Apte, L.T. Hales, J. Kalman, Anal. Chim. Acta 509 (2004) 127–135.
[21] J. Darrouzes, M. Bueno, C. Pecheyran, M. Holeman, M. Potin-Gautier, J. Chromatogr. A 1072 (2005) 19–27.
[22] K. Inagaki, A. Takatsu, T. Watanabe, T. Koruiwa, Y. Aoyagi, K. Okamoto, Anal. Bioanal. Chem. 378 (2004) 1265–1270.
[23] M. Monperrus, R.C. Rodriguez Martin-Doimeadios, J. Scancar, D. Amouroux, O.F.X. Donard, Anal. Chem. 75 (2003) 4095–4102.
[24] R. Wahlen, T. Catterick, Rapid Commun. Mass Spectrom. 18 (2004) 211–217.
[25] J.R. Encinar, P. Rodriguez Gonzalez, J.I. Garcia Alonso, A. Sanz-Medel, Anal. Chem. 74 (2002) 270–281.
[26] P. Rodriguez-Gonzalez, J. Ruiz Encinar, J.I. Garcia Alonso, A. Sanz-Medel, J. Anal. At. Spectrom. 5 (2004) 685–691.
[27] P. Rodriguez-Gonzalez, J.I. Garcia Alonso, A. Sanz-Medel, J. Anal. At. Spectrom. 6 (2004) 767–772.
[28] B. Bouyssiere, J. Szpunar, R. Lobinski, Spectrochim. Acta 57B (2002) 805–828.
[29] P. Rodriguez-Gonzalez, J.M. Marchante-Gayon, J.I. Garcia Alonso, A. Sanz-Medel, Spectrochim. Acta 60B (2005) 151–207.
[30] N. Etxebarria, R. Antolin, G. Borge, T. Posada, J.C. Raposo, Talanta 65 (2005) 1209–1214.
[31] A. Montaser, D.W. Golightly, Induktively Coupled Plasmas in Analytical Atomic Spectrometry, VCH Publishers Inc., USA, 1987, p. 518.
[32] A.W. Kim, M.E. Foulkes, L. Ebdon, S.J. Hill, R.L. Patience, A.G. Barwise, S.J. Rowland, J. Anal. At. Spectrom. 7 (1992) 1147–1149.
[33] M. Krachler, J. Zheng, D. Fisher, W. Shotyk, J. Anal. At. Spectrom. 19 (2004) 1017–1019.
[34] M. Heisterkamp, T. De Smaele, J.P. Candelone, L. Moens, R. Dams, F.C. Adams, J. Anal. At. Spectrom. 12 (1997) 1077–1081.
[35] L. Moens, T. De Smaele, R. Dams, Anal. Chem. 69 (1997) 1604–1611.
[36] H. Tao, T. Murakami, M. Tominaga, A. Miyazaki, J. Anal. At. Spectrom. 13 (1998) 1085–1093.
[37] J. Meija, M. Montes-Bayon, D.L. Le Duc, N. Terry, J.A. Caruso, Anal. Chem. 74 (2002) 5837–5844.
[38] P. Rodríguez-González, J.I. Garcia Alonso, A. Sanz-Medel, J. Anal. At. Spectrom. 20 (2005) 1076–1084.
[39] G. Horlick, S.H. Tan, M.A. Vaughan, C.A. Rose, Spectrochim. Acta 40B (1985) 1555–1572.
[40] P.A. Gallagher, O. Evans, A.N. Park, C.A. Schwegel, Speciation of non-pesticidal organotin compounds using gas chromatography with inductively coupled plasma-mass spectrometry, in: European Winter Conference on Plasma Spectrochemistry, 2003.
[41] R. Wahlen, Agilent Publication, Number 5988-0336E.
[42] M. Yamanak, O.F.X. Donard, Agilent Publication, Number 5988-6697EN.

[43] Agilent, Quick Guide to Tuning the Agilent 7500c and 7500ce ORS ICP–MS Instruments for Environmental and Other High Matrix Applications, A tuning supplement, Version 6.
[44] J.R. Encinar, M.I. Monterde Villar, V.G. Santamaria, J.I. Garcia Alonso, A. Sanz-Medel, Anal. Chem. 73 (2001) 3174–3180.
[45] Europen Co-operation for Accreditation of Laboratories guidance (EA2/03), Interlaboratory Comparision, 1996.
[46] J. Szpunar, J. Falandysz, V.O. Schmitt, E. Obrebska, Bull. Environ. Contam. Toxicol. 58 (1997) 859–864.
[47] C. Alzieu, Ecotoxicology 9 (2000) 71–76.

Available online at www.sciencedirect.com
ScienceDirect
Talanta 73 (2007) 534–539
Talanta
www.elsevier.com/locate/talanta

Electroosmotic flow-switchable poly(dimethylsiloxane) microfluidic channel modified with cysteine based on gold nanoparticles

Wei Wang [a,b], Liang Zhao [a], Fang Zhou [a], Jun-Jie Zhu [a,*], Jian-Rong Zhang [a,**]

[a] *Key Lab of Analytical Chemistry for Life Science (MOE), School of Chemistry & Chemical Engineering, Nanjing University, Nanjing 210093, China*
[b] *School of Chemical and Biological Engineering, Yancheng Institute of Technology, Yancheng 224003, China*

Received 14 January 2007; received in revised form 11 April 2007; accepted 13 April 2007
Available online 25 April 2007

Abstract

An electroosmotic flow (EOF)-switchable poly(dimethylsiloxane) (PDMS) microfluidic channel modified with cysteine has been developed. The native PDMS channel was coated with poly(diallyldimethylammonium chloride) (PDDA), and then gold nanoparticles by layer-by-layer technique was assembled on PDDA to immobilize cysteine. The assembly was followed by infrared spectroscopy/attenuated total reflection method, contact angle, EOF measurements and electrophoretic separation methods. EOF of this channel can be reversibly switched by varying the pH of running buffer. At low pH, the surface of channels is positively charged, EOF is from cathode to anode. At high pH, the surface is negatively charged, EOF is from anode to cathode. At pH 5.0, near the isoelectric point of the chemisorbed cysteine, the surfaces of channels show neutral. When pH is above 6.0 or below 4.0, the magnitude of EOF varies in a narrow range. And the modified channel surface displayed high reproducibility and good stability, a good reversibility of cathodic–anodic EOF transition under the different pH conditions was observed. Separation of dopamine and epinephrine as well as arginine and histidine were performed on the modified chip.

Keywords: EOF-switchable; Poly(dimethylsiloxane) (PDMS); Gold nanoparticles; Cysteine; Microchip capillary electrophoresis

1. Introduction

The manipulation of fluids in channels with dimensions of tens of micrometres – microfluidics – has emerged as a distinct new field. Micrometre-scale analytical devices are more attractive than their macroscale counterparts for various reasons [1–4]. The fundamental benefits associated with miniaturizing analytical systems are well understood and recognized. In particular, chip-based microfluidic systems show many advantages over their conventional analogues. These include improved efficiency with regard to sample size, response times, cost, analytical performance, process control, integration, throughput and automation.

Poly(dimethylsiloxane) (PDMS) is one of the most utilized polymeric material employed in fabricating microfluidic devices [5]. One common problem with polymer devices, including PDMS, is poorly defined electroosmotic flow (EOF) [6]. To meet the specific requirements in application, the surface of PDMS can be chemically modified or physically masked by adsorption [7–17]. Anionic, neutral, and cationic surface can be generated in this way and are useful for controlling EOF direction and magnitude.

The dispersions with nanoparticles have attracted extensive attention in various fields such as physics, biology, and chemistry [18–21]. However, very little research has been devoted to the application of nanoparticles in chemical separation [22–32]. Gold nanoparticles were used both as additive and modifier in capillary electrophoresis (CE) and microchip CE [33–39].

In this study, we developed an EOF-switchable PDMS microfluidic channel dependent on pH of running buffer. Gold nanoparticles were employed as bifunctional linkers to immobilize cysteine on the surface. The native PDMS channel was coated with poly(diallyldimethylammonium chloride) (PDDA) and gold nanoparticles were immobilized to chemisorbed cysteine via its −SH functionality. The unique feature of the chemisorbed amino acid is that, depending on the solution pH,

* Corresponding author. Tel.: +86 25 83594976; fax: +86 25 83594976.
** Corresponding author. Tel.: +86 25 83686130.
E-mail addresses: jjzhu@netra.nju.edu.cn (J.-J. Zhu), jrzhang@nju.edu.cn (J.-R. Zhang).

0039-9140/$ – see front matter © 2007 Elsevier B.V. All rights reserved.
doi:10.1016/j.talanta.2007.04.024

the surface can have excess positive charge (low pH), no net charge (isoelectric point), or excess negative charge (high pH). As a result, the EOF can be switched by running buffer with different pH, and the magnitude of EOF vary in a narrow range when pH above 6.0 or below 4.0. To the best of our knowledge, it was the first time that cysteine was employed as modifier to manipulate EOF on PDMS microchip. The assembly was followed by infrared spectroscopy/attenuated total reflection method, contact angle and electrophoretic separation methods. The channel surface displayed high reproducibility and good stability.

2. Experimental

2.1. Reagents and solutions

All reagents were of analytical grade. Sylgard 184 (PDMS) silicone elastomer and curing agent were obtained from Dow Corning (Midland, MI, USA). Poly(diallyldimethylammonium chloride) (PDDA, 20%, w/w in water, M_w = 200 000–350 000), dopamine and epinephrine were purchased from Sigma–Aldrich, L-arginine, L-histidine, L-cysteine, disodium hydrogen phosphate(Na_2HPO_4), potassium dihydrogen phosphate (KH_2PO_4), sodium hydroxide (NaOH) were obtained from Nanjing Chemical Reagents Factory (China). PDDA solution (0.04%, w/w in water), L-cysteine (2 mM), phosphate buffer saline (PBS) (25 mM pH range from 3.0 to 12.0, 10 mM pH 7.0), 0.5 mM dopamine, 0.5 mM epinephrine, 1 mM L-arginine and 0.5 mM L-histidine were prepared with doubly distilled water and passed through a 0.22 μm cellulose acetate filter (Shanghai Bandao Factory, Shanghai, China).

2.2. Fabrication of PDMS microchips

The master with a positive relief structure of GaAs for the channels was made using microphotolithographic technique. A cross-type channel of PDMS chip with a 3.8 cm long separation channel (effective separation length, 3.5 cm) and 1.0 cm long injection channel and a flat substrate were fabricated from PDMS as the described procedure elsewhere [16,17]. Briefly, A mixture of elastomer precursor and its curing agent (ratio of 10:1) (sylgard 184) were degassed, poured over the GaAs master, and cured for 150 min at 80 °C. After the replica was peeled from the mold, holes (3 mm diameter) were punched. A flat PDMS substrate (0.3 mm thick) was obtained via casting and curing the prepolymer mixture in a large flat glass box (5 cm × 5 cm). The PDMS layer with microchannels and the PDMS flat were ultrasonically cleaned subsequently with acetone, ethanol, and water, then dried under infrared lamp. Finally, they were sealed together to form a reversible PDMS microchip. The sampling channel's width and depth were 30 and 18 μm, the separation channel's width and depth were 50 and 18 μm, respectively.

2.3. Preparation of coated PDMS channels

2.3.1. Preparation of gold nanoparticles (AuNPs)

Gold nanoparticles (AuNPs) were prepared according to the literature [40], 0.5 mL of 100 mM $HAuCl_4$ rapidly added to a 50 mL 4 mM boiling trisodium citrate. The solution was boiled for another 3 min, the solution changed color from pale yellow to purple and then to deep red. The solution was set aside while cooling to room temperature. The particle sizes were about 15 nm, which were measured by transmission electron microscopy (TEM). The prepared AuNPs were stored in brown glass bottle at 4 °C.

2.3.2. Modification of PDMS channels

PDMS channels were coated with PDDA and AuNPs according to the conventional CE procedures developed by Katayama et al [8]. Briefly described, the channels were rinsed with 0.1 M NaOH and deionized water, respectively, for 10 min each. Once preconditioned, the channels were sequentially filled with PDDA solution (0.04%, w/w), citrate stabilized AuNPs solution and 2 mM cysteine solution for 30 min each, after each step, the channel was washed with deionized water for 3 min. This procedure of successive coating resulted in AuNPs functionalized with cysteine on the channel walls. All rinsing was performed by applying a vacuum to the buffer waste reservoir with the other three reservoirs filled with the respective rinsing solution.

2.4. Contact angle measurements

A flat piece of PDMS was immersed in 0.1 M NaOH solution for 10 min, PDDA solution (0.04%, w/w) for 30 min, gold nanoparticle solution for 30 min with stirring intermittently, respectively. After each step, the flat piece was washed with deionized water for 3 min.

A static contact angle measurement was performed on the plate using a CAM2000 optical contact angle analyzer (KSV Instruments, Finland). Five microliters of water droplet was placed on the material and allowed to rest on the surface for 1 min, and then an image was taken. The contact angle was recorded automatically.

2.5. Fourier transformed infrared absorption by total attenuated reflection (ATR–FT-IR)

A flat piece of PDMS was coated as the same procedure in section 2.4. ATR–FT-IR was performed for cysteine coated surface of PDMS piece using a Perkin-Elmer PE-1800 FT-IR spectrometer.

2.6. Capillary electrophoresis arrangement and electrochemical detection

2.6.1. Microchip capillary electrophoresis

The microchip was fixed on a plexiglass holder that integrated a precise three-dimensional system (Shanghai Lianyi Instrument Factory of Optical Fiber and Laser, Shanghai, China) with the precision of 1 μm in each direction. A clip of optical fiber that can be fastened in the three-dimensional system was used to clip the working electrode. The amperometric detector was located in the detection reservoir (at the channel outlet side) and consisted of a Ag/AgCl wire reference electrode, a Pt wire counter electrode and a homemade in-channel carbon

fiber working electrode (i.d. 7 μm). The fabrication processes for the carbon fiber working electrode were described in the reference [41]. The working electrode was placed in the channel, the distance between its surface and the channel outlet (40 μm) was controlled by a stereoscopic microscope with micro-ruler (XTB-1; Jiangnan Optical Instrument Factory, Nanjing, China). Electrical contact with the solutions was achieved by placing platinum wires into each of the reservoirs. In a routine electrophoresis, sampling voltage is 600 V, sampling time is 3 s, separation voltage is 800 V and detection potential is 1.4 V.

2.6.2. High voltage supply

The laboratory-made power supply had a voltage ranging from 0 to 5000 V and 0 to −5000 V. Parameters such as sampling voltage, sampling time, separation voltage, and separation time can be set up and automatically switched by personal computer. The separation current can be monitored graphically in real time.

2.6.3. Electrochemical detection

Electrochemical detection was performed using "amperometric *i–t* curve" mode with a CHI 832b electrochemical workstation (CHI Co., Shanghai, China), which was used to provide a constant potential to the detection electrode and measure the output current. The electropherograms were recorded while applying 1.4 and 0 V detection potential for detecting neurotransmitters and amino acids, respectively. All experiments were performed at room temperature. (20 ± 5 °C)

2.7. EOF measurements

The EOF measurements were performed using current monitoring method [42]. Briefly, the waste buffer reservoir and the channel were filled with 25 mM PBS running buffer and the buffer reservoir was filled with 22.5 mM buffer. Upon application of the voltage (1000 V), electroosmosis took place and the lower concentration electrolyte solution from the running buffer reservoir gradually displaced the higher concentration buffer in channel, resulting in a decrease in the electrical current of the channel. Once a constant current was obtained, the potential was then applied to the reservoir with concentrated buffer and above procedure repeated. The time required to reach a current plateau was used to calculate EOF based on Eq. (1). Where L is the length of separation channel (3.8 cm), V is the total applied voltage (1000 V), and t is the time in seconds required to reach a new current plateau

$$\mu_{\mathrm{EOF}} = \frac{L^2}{Vt} \tag{1}$$

3. Results and discussion

3.1. Characterization of modified PDMS channel

According to the previous reports [7,8,43], the main interaction of successive multiple ionic layers was ionic interaction. The pH dependence of EOF in PDMS microchips is well-known, at low pH, EOF is at a minimum, while at high pH, it is at a maximum. This behavior is the result of titration of the surface-bound silanol groups. The surface of PDMS has negative charge at pH 7.0. PDDA is a quaternary ammonium polyelectrolyte, this structure is easily protonated and retains positive charge. In this case, hydrophobic interaction must be taken into account [44]. Both ionic and hydrophobic interactions result in combination of PDDA on PDMS surface. PDDA covers the surface with positive quaternary ammonium groups to produce a much more homogeneous inner wall. EOF changes its direction from cathodic to anodic. Absolute value of EOF (anodic) -1.3×10^{-4} cm^2/V s was measured in PBS solution (25 mM, pH 7.0) [25]. Gold nanoparticles in solution are negative charged because of they were citrate stabilized. The gold nanoparticles were strongly adsorbed on the surface of PDDA [33,34]. Then cysteine was chemisorbed on the gold nanoparticles via its −SH functionality.

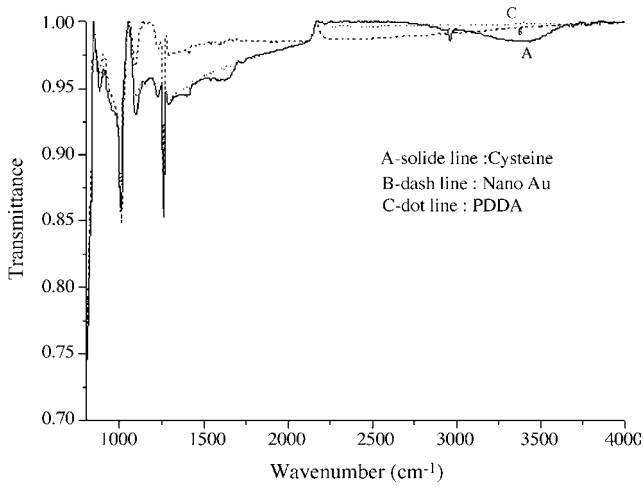

Fig. 1. ATR–FT-IR spectrograms (A) Cysteine chemisorbed on gold nanoparticles; (B) Gold nanoparticles absorbed on PDDA surface; (C) PDDA coated on PDMS surface.

ATR–FT-IR spectra were employed to characterize the coating. Fig. 1 shows the spectrograms. The band in cysteine at 1650 and 1380 cm^{-1} corresponds to the asymmetric and symmetric stretching of COO^-. A very broad band of NH_3^+ stretch was observed in the 3100–3650 cm^{-1} range. A shift in the position of COO^- and NH_3^+ stretching is likely due to a change in their dipole moment when cysteine binds on metal surface with high electron density [45]. We could conclude that cysteine was intensively combined on the surface from the ATR-FT-IR data.

The hydrophilicity of the cysteine coated PDMS wall was assessed using water contact angle measurement. The initial water contact angles measured on the native PDMS was 112°. The value for the coated PDMS was 86°. The difference of 26° between native PDMS and coated PDMS chips indicated the coated surface was more hydrophilic than native PDMS.

3.2. EOF on cysteine modified chip

EOF on the coated PDMS over pH range of 3–12 was investigated. The unique feature of the channel chemisorbed cysteine is that EOF can be reversibly switched by varying pH of the run-

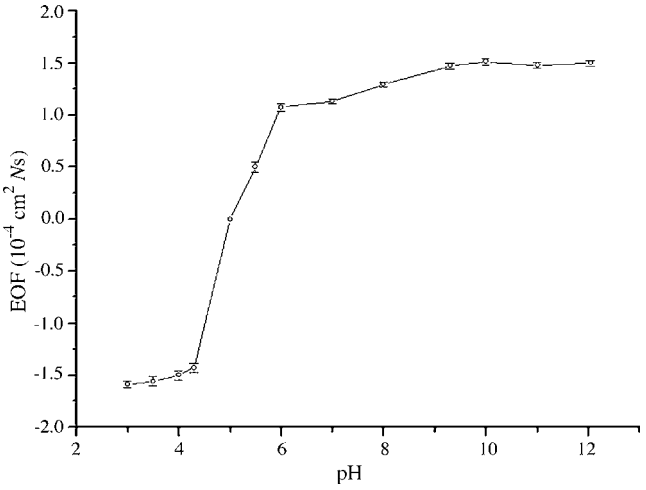

Fig. 2. EOF values on modified microchannels with cysteine in the solution of different pH conditions: total applied voltage, 1000 V; running buffers, 25 mM PBS at pH 7.0. The data points are the average ± standard deviation of six measurements.

ning buffer. The results are shown in Fig. 2. When pH of running buffer is below 4.0, EOF is in anodic direction, and pH is above 6.0, it is in cathodic direction, and the magnitude of EOF values varied in a narrow range in both anodic and cathodic direction. It is a significant benefit for electrophoresis. When EOF measurement was performed at pH 5.0, the dilute solution was added to the reservoir, we could not observe current change in 15 min both positive and negative polarities of the power supply, then EOF at this pH is assumed to be zero.

We inferred the mechanism of EOF generation in modified channels. Since amino and carboxyl groups are involved in cysteines, at low pH, where both amino and carboxyl groups of cysteine are protonated, the surface has positive charge. At high pH, where both amino and carboxyl groups are deprotonated, the surface possesses negative charge. At pH 5.0, near the isoelectric point of the chemisorbed cysteine, the surface of channels is neutral. Fig. 3 shows the states.

It is necessary to point out that the isoelectric point for the chemisorbed cysteine is different from the material in solution [46], because the isoelectric point for cysteine in solution includes the influence of −SH group which is not available when the molecule is chemisorbed to gold nanoparticles. The isoelectric point of the chemisorbed cysteine is near pH 6.0, which is higher than that for cysteine in solution pH 5.0. In this study, the isoelectric point for the coated surface is pH 5.0, we speculated that the cysteines did not completely displace the citrates on the gold nanoparticle surface, the surface charge of modified channel was determined by cysteines and residue citrates. Hence the isoelectric point for surface is lower than that only for chemisorbed cysteine.

The reversibility of cathodic–anodic EOF transition under different pH conditions was also investigated. When the channel was filled with PBS solution pH 8.0, EOF was cathodic, after the solution was displaced by PBS pH 4.0, EOF changes from cathodic to anodic. This process was repeated several times, and good reversibility was observed. The result was shown is Fig. 4.

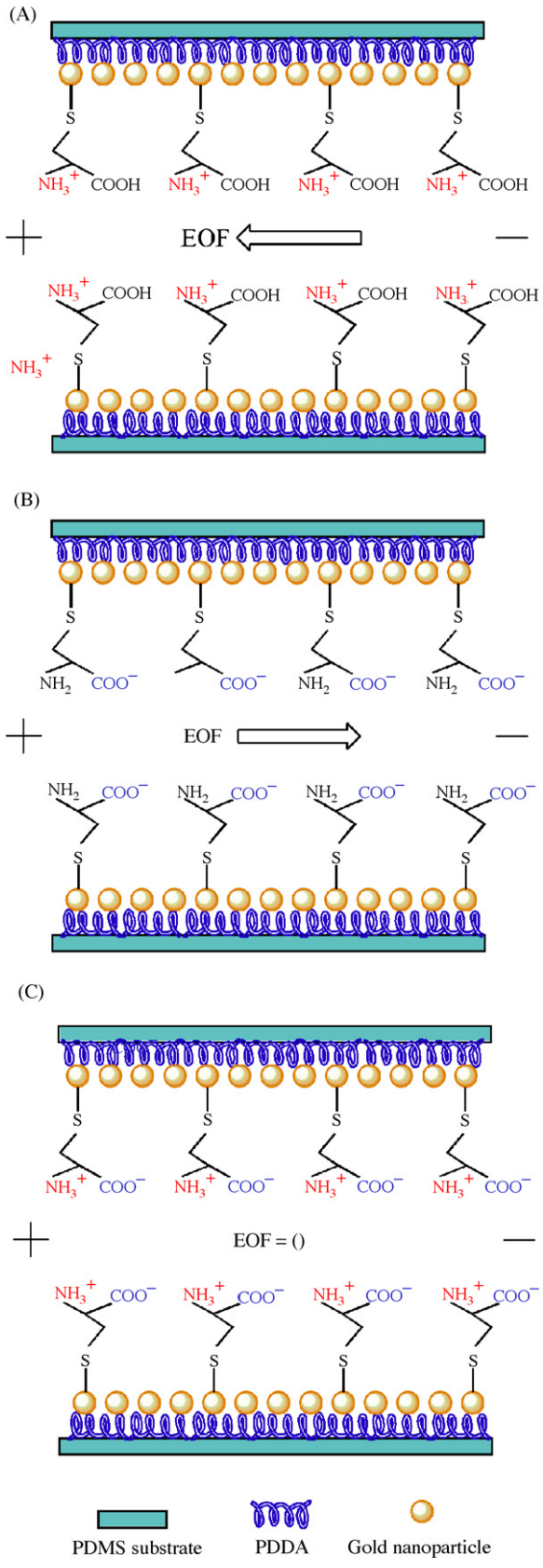

Fig. 3. Schematic representation showing the three states of the chemisorbed cysteine. (A) At low pH, both the amino and carboxyl groups of the cysteine are protonated. (B) At high pH, both the amino and carboxyl groups are deprotonated. (C) At pH 5.0, near the isoelectric point of the chemisorbed cysteine.

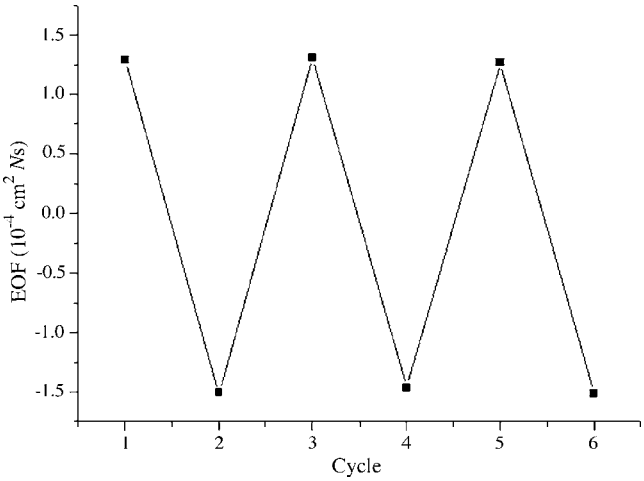

Fig. 4. Reversible cathodic–anodic EOF transition under the conditions with PBS solutions pH 8.0 and 4.0. One, 3 and 5 state the channels filled with PBS solution pH 8.0; 2, 4 and 6 state channels filled with PBS solution pH 4.0.

Table 1
Stability of PDMS channel modified with cysteine

	EOF_1[a] ($n=6$) ($\times10^{-4}$ cm^2/V s)	EOF_2[b] ($n=6$) ($\times10^{-4}$ cm^2/V s)	Change ratio[c] (%)
pH 3.00 PBS	1.13	1.12	0.96
pH 12.00 PBS	1.09	1.07	2.11
Store for 2 weeks	1.15	1.12	2.93

Conditions: total applied voltage, 1000 V; running buffers, 25 mM PBS at pH 7.0; length of channel, 3.8 cm.

[a] EOF_1 was measured before rinsing with the solvents or before store.

[b] EOF_2 was measured after rinsing with the solvents or after store.

[c] Change ratio = $(EOF_1 - EOF_2)/EOF_1 \times 100$ (%).

3.3. Stability and reproducibility of coated chips

One concern with dynamic coating procedure is stability of the coating. The stability was evaluated on the basis of change of EOF, which was expressed as the change ratio defined in Table 1. Measuring EOF with PBS solution (pH 7.0) after the channel was rinsed with solutions of pH 3.0 and 12.0, where EOF would vary evidently if the coating was detached. Thirty runs (2 min duration in a run) were performed with PBS solution of pH 3.0 and 12.0 in 5 min intervals, and the results showed there was no evident variation in the magnitude of EOF. The microchip coated with cysteines functionalized gold nanoparticles displayed longtime stability in mild condition. It could be used for more than 2 weeks, while the channels were filled with PBS solution (pH 7.0) and stored at 4 °C. Good stability of the coating results from that PDDA is strongly combined with PDMS and gold NPs, and then cysteine on it intensively.

Table 2
Reproducibility of PDMS chips modified with cysteine ($n=6$)

	EOF ($n=6$) ($\times10^{-4}$ cm^2/V s)	R.S.D. (%)
Run-to-run	1.14	0.84
Chip-to-chip	1.20	2.75
Day-to-day	1.18	2.26

Conditions: total applied voltage, 1000 V; running buffer, 25 mM PBS at pH 7.0; length of channel, 3.8 cm.

The relative standard deviation (R.S.D.) of EOF was 1.65% for runs made on native PDMS chip and 0.84% on cysteine coated PDMS chip ($n=6$). The values of R.S.D. indicated more stable EOF on the coated chip than that on native one. The reproducibilities of cysteine coatings were investigated by evaluating the R.S.D. of EOF. R.S.D. of EOF for six replicate analyses on the same chip was employed for estimating run-to-run reproducibility, on five replicate chips for chip-to-chip reproducibility, and average R.S.D. of EOF detected on the same chip with an interval of 1 day for day-to-day reproducibility. Table 2 shows the results. R.S.D. of the EOF was less than 2.8%, and excellent reproducibility was obtained.

3.4. Electrophoretic separation

To determine separation characteristics of the cysteine coated PDMS chip, two categories of biomolecules were performed. Fig. 5A shows the electrophoregram of separation of dopamine and epinephrine. Due to low EOF, the excellent separation efficiency could be seen from the electrophoregram, high resolution of 1.5 was achieved on the coated chip. The plate numbers of dopamine and epinephrine at 800 V separation voltage on 3.5 cm

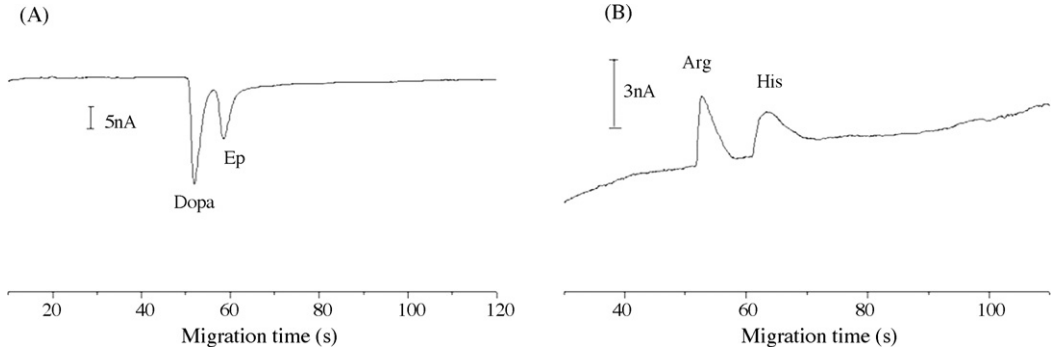

Fig. 5. (A) Electrophoregram of 500 μM dopamine (Dopa) and epinephrine (Ep) on cysteine coated PDMS microchip. Experimental parameters: running buffer 10 mM PBS, pH 7.00, sampling voltage 600 V; sampling time 3 s; separation voltage 800 V; detection potential +1.4 V (vs. Ag/AgCl wire). (B) Electrophoregram of 1 mM arginine (Arg) and histidine (His) on cysteine modified PDMS microchip. Experimental parameters: running buffer 10 mM PBS, pH 7.00, sampling voltage 600 V; sampling time 3 s; separation voltage 1000 V; detection potential 0 V.

cysteines modified PDMS channel were 3383 and 3307 (corresponding 9.7×10^4, 9.5×10^4 number of plates per meter). Fig. 5B shows the electrophoregram of separation of arginine and histidine on the modified PDMS chip. Arginine and histidine could be separated on the coated chip and detected by in-channel electrochemical method [41].

4. Conclusions

We have reported on EOF-switchable PDMS channel dependent on pH of running buffer. The microchip channel was prepared by chemisorbing cysteine to gold nanoparticles that were attached on the channel surface by layer-by-layer technique. The EOF can be reversibly switched between cathodic direction (high pH) and anodic direction (low pH). This pH-dependent selectivity can be divided into three surface charge states: positive charged, neutral, negative charged with the protonated degree of amino and carboxyl groups of the cysteine. Additionally, the "On/Off" responsiveness of the channel is stable and reversible. The modified microchip could also be used for capillary electrophoresis separation. This study shows the potential that the microchip could be used as microsensor to detect chemical identity and other parameters including pH. And due to the advantages of micro total analysis systems (μTAS), the technology should find use in the analysis of biological and homeland security applications.

Acknowledgements

This work was supported by the National Natural Science Foundation of China (NSFC) (no. 20635020, 20575026) and Jiansu Natural Science Foundation (no. BK2006114).

References

[1] G.M. Whitesides, Nature 442 (2006) 368.
[2] P. Yager, T. Edwards, E. Fu, K. Helton, et al., Nature 442 (2006) 412.
[3] D. Janasek, J. Franzke, A. Manz, Nature 442 (2006) 374.
[4] P.S. Dittrich, K. Tachikawa, A. Manz, Anal. Chem. 78 (2006) 3887.
[5] J.C. McDonald, G.M. Whitesides, Acc. Chem. Res. 35 (2002) 491.
[6] G. Ocvirk, M. Munroe, T. Tang, R. Oleschuk, et al., Electrophoresis 21 (2000) 107.
[7] H. Katayama, Y. Ishihama, N. Asakawa, Anal. Chem. 70 (1998) 2254.
[8] H. Katayama, Y. Ishihama, N. Asakawa, Anal. Chem. 70 (1998) 5272.
[9] H. Makamba, J.H. Kim, L.K. wanseop, N. Park, et al., Electrophoresis 24 (2003) 3607.
[10] S. Hu, X. Ren, M. Bachman, C.E. Sims, et al., Anal. Chem. 74 (2002) 4117.
[11] S. Hu, X. Ren, M. Bachman, C.E. Sims, et al., Anal. Chem. 76 (2004) 1865.
[12] D. Xiao, T.V. Le, M.J. Wirth, Anal. Chem. 76 (2004) 2055.
[13] G.T. Roman, T. Hlaus, K.J. Bass, T.G. Seelhammer, et al., Anal. Chem. 77 (2005) 1414.
[14] G.D. Sui, J. Wang, C.C. Lee, W. Lu, et al., Anal. Chem. 78 (2006) 5543.
[15] Y. Luo, B. Huang, H. Wu, R.N. Zare, et al., Anal. Chem. 78 (2006) 4588.
[16] Y.H. Dou, N. Bao, J.J. Xu, H.Y. Chen, Electrophoresis 23 (2002) 3558.
[17] Y.H. Dou, N. Bao, J.J. Xu, F. Meng, et al., Electrophoresis 25 (2004) 3024.
[18] G. Schmid, Chem. Rev. 92 (1992) 1709.
[19] C.R. Martin, D.T. Mitchell, Anal. Chem. 70 (1998) 322A.
[20] L. He, C.S. Toh, Anal. Chim. Acta 556 (2006) 1.
[21] D.Y. Godovsky, Adv. Polym. Sci. 153 (2000) 163.
[22] G. Kleindienst, C.G. Huber, D.T. Gjerde, L. Yengoyan, et al., Electrophoresis 19 (1998) 262.
[23] C.G. Huber, A. Premstaller, G. Kleindienst, J. Chromatogr. A 849 (1999) 175.
[24] S.A. Rodriguez, L.A. Colon, Anal. Chim. Acta 397 (1999) 207.
[25] W. Wang, L. Zhao, J.R. Zhang, X.M. Wang, et al., J. Chromatogr. A 1136 (2006) 111.
[26] N. Na, Y.P. Hu, J. Ouyang, W.R.G. Baeyens, et al., Anal. Chim. Acta 527 (2004) 139.
[27] P. Viberg, M. Jornten-Karlsson, P. Petersson, P. Spegel, et al., Anal. Chem. 74 (2002) 4595.
[28] C. Fujimoto, Y.J. Muranaka, High Resolut. Chromatogr. 20 (1997) 400.
[29] I.T. Kuo, Y.F. Huang, H.T. Chang, Electrophoresis 26 (2005) 2643.
[30] B. Neiman, E. Grushka, J. Gun, O. Lev, Anal. Chem. 74 (2002) 3484.
[31] Z.H. Wang, G.A. Luo, J.F. Chen, S.F. Xiao, et al., Electrophoresis 24 (2003) 4181.
[32] G.T. Roman, T. Hlaus, K.J. Bass, T.G. Seelhammer, C.T. Culbertson, Anal. Chem. 77 (2005) 1414.
[33] B. Neiman, E. Grushka, O. Lev, Anal. Chem. 73 (2001) 5220.
[34] M. Pumera, J. Wang, E. Grushka, R. Polsky, Anal. Chem. 73 (2001) 5625.
[35] L. Yang, E. Guihen, J.D. Holmes, M. Loughran, et al., Anal. Chem. 77 (2005) 1840.
[36] M.F. Huang, Y.C. Kuo, C.C. Huang, H.T. Chang, Anal. Chem. 76 (2004) 192.
[37] T. O'Mahony, V.P. Owens, J.P. Murrihy, E. Guihen, et al., J. Chromatogr. A 1004 (2003) 181.
[38] Y.W. Lin, M.J. Huang, H.T. Chang, J. Chromatogr. A 1014 (2003) 47.
[39] Y.W. Lin, H.T. Chang, J. Chromatogr. A 1073 (2005) 191.
[40] M.F. Huang, C.C. Huang, H.T. Chang, Electrophoresis 24 (2003) 2896.
[41] J.J. Xu, N. Bao, X.H. Xia, Y. Peng, et al., Anal. Chem. 76 (2004) 6902.
[42] X.H. Huang, M.H. Gordon, R.N. Zare, Anal. Chem. 60 (1988) 1837.
[43] Y. Liu, J.C. Fanguy, J.M. Bledsoe, C.S. Henry, Anal. Chem. 72 (2000) 5939.
[44] N.A. Kotov, Nanostruct. Mater. 12 (1999) 789.
[45] S. Aryal, B.K.C. Remant, N. Dharmaraj, N. Bhattarai, et al., Spectrochim. Acta, Part A 63 (2006) 160.
[46] S.B. Lee, C.R. Martin, Anal. Chem. 73 (2001) 768.

Available online at www.sciencedirect.com
ScienceDirect
Talanta 73 (2007) 431–437
Talanta
www.elsevier.com/locate/talanta

Fabrication of layer-by-layer modified multilayer films containing choline and gold nanoparticles and its sensing application for electrochemical determination of dopamine and uric acid

Po Wang, Yongxin Li *, Xue Huang, Lun Wang *

Anhui Key Laboratory of Functional Molecular Solids, College of Chemistry and Materials Science, Anhui Normal University, Wuhu 241000, PR China

Received 12 December 2006; received in revised form 5 April 2007; accepted 6 April 2007
Available online 25 April 2007

Abstract

A novel electrochemical sensor has been constructed by use of a glassy carbon electrode (GCE) coated with a gold nanoparticle/choline (GNP/Ch). Electrochemical impedance spectroscopy (EIS), field emission scanning electron microscope (SEM) and X-ray photoelectron spectroscopy (XPS) were used to characterize the properties of this modified electrode. It was demonstrated that choline was covalently bounded on the surface of glassy carbon electrode, and deposited gold nanoparticles with average size of about 100 nm uniformly distributed on the surface of Ch. Moreover, the modified electrode exhibits strong electrochemical catalytic activity toward the oxidation of dopamine (DA), ascorbic acid (AA) and uric acid (UA) with obviously reduction of overpotentials. For the ternary mixture containing DA, AA and UA, these three compounds can be well separated from each other, allowing simultaneously determination of DA and UA under coexistence of AA. The proposed method can be applied to detect DA and UA in real samples with satisfactory results.

Keywords: Choline; Gold nanoparticles; Glassy carbon electrode; Ascorbic acid; Dopamine; Uric acid

1. Introduction

Dopamine (DA), the most significant among the class of catecholamines, plays an important role in the function of the central nervous, cardiovascular, renal and hormonal systems [1,2]. The determination of DA is a subject of great importance for investigating its physiological functions and diagnosing nervous diseases resulting from DA abnormal metabolism, such as epilepsy, senile dementia, Parkinsonism, schizophrenia and HIV infection [3,4]. However, a major problem in its determination is the interference from ascorbic acid (AA), which largely coexists with DA in brain issue. At traditional solid electrodes, AA is oxidized at potentials close to that of DA, which result in overlapped voltammetric responses making their discrimination highly difficult [5]. Moreover, the solid electrodes very often suffer from the fouling effort due to the accumulation of oxidized products on the electrode surface, which results in rather poor selectivity and sensitivity. Therefore, the development of new electrochemical sensors for DA has received much interest in the last decades [6].

As we known, uric acid (UA) is the principal final product of purine metabolism in the human body [7]. It has been shown that extreme abnormalities of UA levels are symptoms of several diseases (e.g. gout, hyperuricaemia and Lesch–Nyhan syndrome) [8,9]. Other diseases, such as leukemia and pneumonia are also associated with enhanced urate levels [9]. In general, electroactive UA can be irreversibly oxidized in aqueous solution and the major product is allantoin [10]. Since UA, AA and DA usually coexist in physiological samples, it is essential to develop simple and rapid methods for their determination in routine analysis. Simultaneous detection of UA and neurotransmitters, especially DA is a problem of critical importance not only in the field of biomedical chemistry and neurochemistry but also for diagnostic and pathological research. Among many methods for determination of DA and UA in biological samples, electrochemical techniques with modified electrodes have been shown to be powerful tools

* Corresponding authors. Fax: +86 553 3869303.
E-mail addresses: yongli@mail.ahnu.edu.cn (Y. Li), wanglun@mail.ahnu.edu.cn (L. Wang).

0039-9140/$ – see front matter © 2007 Elsevier B.V. All rights reserved.
doi:10.1016/j.talanta.2007.04.022

due to their advantages of simple, inexpensive and fast analysis in combination with high sensitivity and selectivity [11]. Thus, different kinds of modified electrodes have been fabricated for detection of DA and UA [12–16]. All the modified electrodes, they have some advantages and limitations. Up to now, still there is an expanding demand for the development of simple, reliable and efficient sensors with enhanced characteristics for effective sensing of DA and UA simultaneously.

Choline (Ch) is an essential nutrient required by the body for healthy cell membrane function [17]. In most living cells, Ch plays an important role for the production of phosphatidylcholine, which is an important constituent of lipid membranes in the cell [18]. Thus, it has been received much attention for the quantitative analysis of Ch with a simple analytical method, several methods for the detection of choline have been reported [19,20]. Although Ch and its derivatives modified electrodes have been developed for electrochemical sensors [21], layer-by-layer modified multilayer films containing Ch and other species that used to enhance its characteristics have not been reported yet.

In recent years, nanoparticles of noble metals have provoked much more attention in electroanalysis because of their novel physical and chemical properties [15]. In particular, the catalytic properties of some nanoparticles cause a decrease in the overpotential needed for a redox reaction to become kinetically viable, producing voltammetry which appears more reversible than that displayed by the same material in a macroelectrode form [22]. Moreover, the use of nanoparticle-modified electrodes presents some other advantages as: high effective mass transport catalyzes and controls the local environment [23]. Among some noble metal-nanoparticles, gold nanoparticles (GNPs), in particular, have been the focus of numerous investigations in recent years because of their unique properties [24,25]. The use of GNPs superstructures for the creation of electrochemical devices is an extremely promising prospect. Therefore, further studying on the application of GNPs is valuable to extend its application fields.

In this report, a novel biosensor has been fabricated by using a glassy carbon electrode (GCE) coated with Ch and GNPs. As we known, Ch has a hydroxy group, which could be covalently bound to the edge plane sites of the carbon surface through the oxygen atom [21]. The significance of Ch modified layer might provide a monolayer containing positively charged $–N^+(CH_3)_3$ polar head group, which could facilitate the modification of GNPs through the electrostatic interaction between $–N^+(CH_3)_3$ and $AuCl_4-$. Several techniques were used for characterization of the electrode, it can be observed that Ch was grafted on the surface of electrode forming a monolayer modification, and deposited GNPs with average size of about 100 nm uniformly distributed on the surface of Ch. This paper describes the preparation, characterization and application of GNP/Ch film modified GCE. It was found that DA, AA and UA could be electrocatalytic oxidized at the GNP/Ch film modified GCE, and the proposed electrode could be used as a sensitive sensor for the assessment of DA and UA simultaneously.

2. Experimental

2.1. Chemicals and solutions

Choline was purchased from Chemical Reagent Factory of Beijing (Beijing, China). Dopamine hydrochloride (DA) and $HAuCl_4·4H_2O$ were obtained from Sigma (USA). Ascorbic acid and uric acid were purchased from Shanghai Chemical Co. Ltd. (Shanghai, China). They were used as received without further purification. All other chemicals were of analytical grade. Solution of Ch was freshly prepared in 10 mM KCl. UA was prepared by dissolving it in a small volume of 0.1 mol L^{-1} NaOH solution and diluted to desired concentration. Phosphate-buffered saline (PBS; 1/15 mol L^{-1}) solutions of different pH (varies from 3 to 10) were prepared by mixing four stock solutions of 1/15 mol/L H_3PO_4, KH_2PO_4, K_2HPO_4 and KOH.

All aqueous solutions were prepared in doubly distilled, deionized water. High purity nitrogen was used for deaeration of the prepared aqueous solutions.

2.2. Apparatus

Electrochemical experiments including cyclic voltammetry (CV), differential pulse voltammetry (DPV) and amperometric i–t curve were performed on CHI 440A electrochemical workstation (ChenHua, Shanghai, China). Electrochemical impedance spectroscopy (EIS) was carried out at CHI 660C electrochemical workstation (ChenHua). A conventional three-electrode electrochemical system was used for all electrochemical experiments, which consisted of a working electrode, a Pt foil auxiliary electrode and a saturated calomel electrode (SCE). A glassy carbon disk electrode was used as the basal working electrode. All potentials given in this paper were reported versus SCE. All experiments were performed at ambient temperature. The electrochemical solutions were thoroughly deoxygenated by N_2 before sampling and a N_2 atmosphere was maintained throughout the experiments.

X-ray photoelectron spectroscopy (XPS) was performed on ESCALAB MKα spectrometer (VG Co., UK). Field emission scanning electron microscope (FE-SEM) images were obtained on a JSM-6700F field emission scanning electron microanalyser (JEOL, Japan).

2.3. Electrode preparation

Glassy carbon electrode was carefully polished successively with 6, 1 and 0.05 μm alumina slurries. Then it was rinsed with water, and sonicated in ethanol and water for 5 min, successively. After cleaning, the electrode was performed in PBS (pH 7.0) containing 1 mM Ch and 10 mM KCl by scanning between −1.7 and 1.8 V at 20 mV/s for six cycles for surface modification. Then the electrode was rinsed with distilled water and sonicated for 5 min to remove any physically adsorbed materials. The Ch modified electrode, denoted as Ch/GCE.

The deposition of GNPs on the Ch/GCE was carried out according to the previous report [26]. A Ch/GCE was immersed in 0.2 mg/mL $HAuCl_4$ solution, and performed by applying

−0.2 V for 5 min for deposition of gold nanoparticles (The obtained electrode was described as GNP/Ch/GCE).

For the sake of comparison, a Ch/GCE and a gold nanoparticles-modified GCE (denoted as GNP/GCE) were also prepared under the same conditions.

3. Results and discussion

3.1. Characterization of modified electrode

Impedance spectroscopy is an effective method for probing the features of a surface-modified electrode using the redox probe $Fe(CN)_6^{4-/3-}$ [27]. Fig. 1 illustrates the results of impedance spectroscopy on bare GCE (a), Ch/GCE (b) and GNP/Ch/GCE (c) in the presence of equivalent 10 mM $Fe(CN)_6^{4-/3-}$ + 0.1 M KCl, which are measured at the formal potential of $Fe(CN)_6^{4-/3-}$. It can be seen at the bare GCE, a semicircle of about 1050 Ω diameter with an almost straight tail line are present, implying very low electron transfer resistance to the redox-probe dissolved in the electrolyte solution. The diameter of the high frequency semicircle was obviously reduce to 750 Ω by the surface modification of the Ch layer (b), suggesting that a significant acceleration of the $Fe(CN)_6^{3-/4-}$ redox reaction occurred due to the presence of Ch assembly. Interestingly, the diameter of the high frequency semicircle was still reduced by the further deposition of GNPs on the Ch layer (c), a charge transfer resistance value of about 450 Ω can be estimated, which indicates a decreased resistance to the anion redox reaction at the GNP/Ch/GCE. This may be attributed to the well conductivity of the surface deposited GNPs. The impedance change of the modification process indicated that Ch and GNPs had been modified to the GCE surface.

XPS is a powerful tool to examine the elemental distribution on the electrode surfaces. To verify that Ch and GNPs have been immobilized on the surface of GCE, an XPS experiment was performed, and the result is shown in Fig. 2. As shown in Fig. 2A, two XPS bands appeared at 84.1 and 87.9 eV, corresponding to the $Au4f_{7/2}$ and $Au4f_{5/2}$ signal, respectively. The appearance of these two bands is demonstration of the presence of gold particles in the modified layer on the electrode. From Fig. 2B, we can see that the N (1s) is appeared at 399.8 eV, showing the evidence that the Ch has been immobilized on the surface. It was noted that the peak remained constant after the electrode was subjected to a treatment of sonication in PBS for 10 min, demonstrating that Ch has been strongly immobilized on the surface by covalent linkages, not attached to the electrode surface by adsorption. The result is consistent with the previous reports [21].

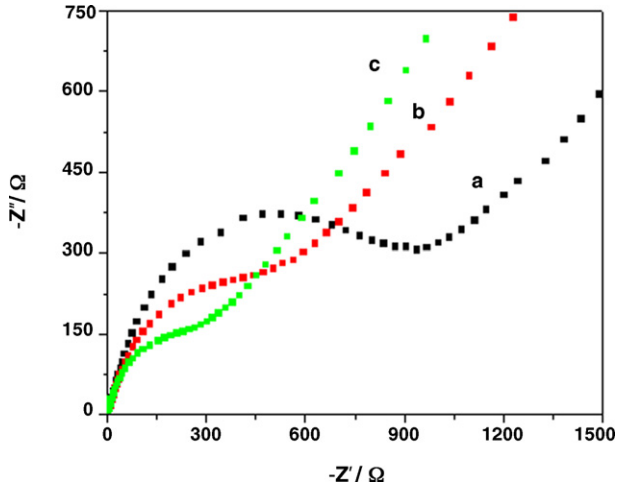

Fig. 1. Complex plane impedance plots in 10 mM $K_3[Fe(CN)_6]$:$K_4[Fe(CN)_6]$ (1:1) mixture containing 0.1 M KCl at bare GCE (a); Ch/GCE (b) and GNP/Ch/GCE (c), respectively.

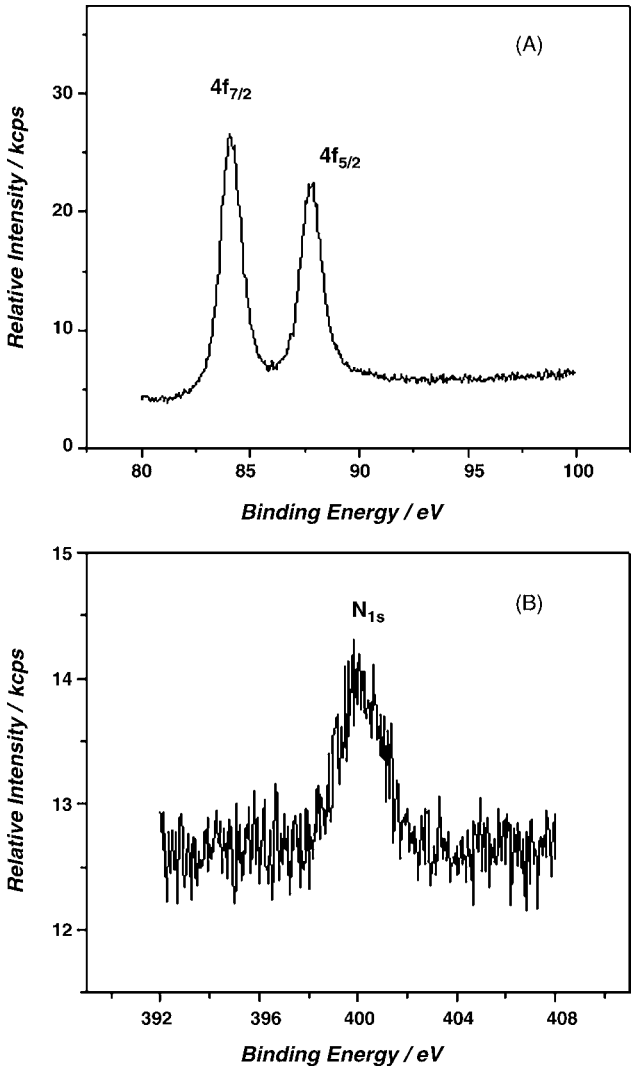

Fig. 2. XPS spectrum of Au4f (A) and N1s (B) regions of GNP/Ch/GCE.

The prepared electrode was further characterized by FE-SEM. The FE-SEM image of the GNP/Ch/GCE is shown in Fig. 3. It can be seen that the gold particles was formed by uniformly distributed on the surface of electrode. The GNPs was assembled to form a flowers like structure if look at carefully, and they were uniformly cast on the electrode surface forming a porous and three-dimensional film structure. The size of the deposited GNPs varied from 100 to 200 nm can be estimated, and the inside particles are relative smaller than the outside ones. The larger GNPs might be an aggregation of much finer nanopar-

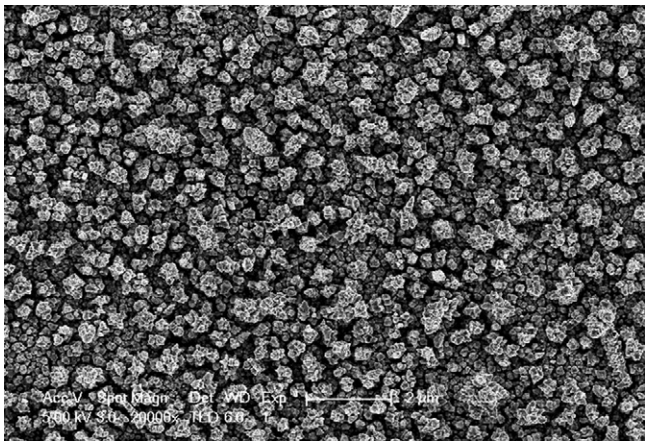

Fig. 3. FE-SEM image of the GNP/Ch/GCE.

ticles due to the acceleration of the positively charged Ch layer to the $AuCl_4^-$ oxidation.

3.2. Electrochemical behavior of DA, AA and UA

The preliminary study showed that the GNP/Ch/GCE had a significant electrocatalytic activity toward the oxidation reactions of DA, AA and UA. The CV curves of these compounds at different electrodes are presented in Fig. 4.

As shown in Fig. 4A, AA shows a broad and irreversible oxidation peak at 0.35 V at the bare GCE. However, a sharp peak appeared at 0.12, 0.09 and 0.09 V at GNP/GCE, Ch/GCE and GNP/Ch/GCE, respectively (curves 2–4), showing all the three electrodes had strong electrocatalytic activity toward the AA oxidation. And about 2.5-fold peak current at the GNP/GCE, 5-fold increase at the Ch/GCE and 7-fold increase at the GNP/Ch/GCE were observed in comparison with that at GCE. Interestingly, a small re-reduction peak at about 0.01 V could be seen at the GNP/Ch/GCE. The 260 mV negative shift and enhanced current of the anodic peak indicates that the GNP/Ch/GCE plays an excellent catalytic effect on the AA oxidation.

Fig. 4B depicts the CVs of DA at bare GCE, GNP/GCE, Ch/GCE and GNP/Ch/GCE. The oxidation of DA has been documented to be a two-proton and two-electron process [28]. As can be seen, DA presents a very weak CV peak response with a ΔE_p of 71 mV at bare GCE. But at the GNP/Ch/GCE, the peak current increased greatly and the peak potential shifted negatively. The voltammograms shows a couple of reversible and well behaved redox peaks with a ΔE_p of only 32 mV, and the anodic peak current obviously is enhanced and is about 14 times higher than that at the bare GCE. The reason for the higher peak current may originate in the multilayer films's larger surface area and very high electron transfer rate. The above results suggested that the GNP/Ch/GCE plays a strong catalytic effect on the DA oxidation. Similarly, compared with GNP/Ch/GCE, GNP/GCE and Ch/GCE can also exhibit an electrocatalytic response to DA.

Fig. 4C illustrates the CVs of UA with pH 7.0 PBS at different electrodes. It can be seen that voltammetric peak of UA in the neutral PBS appeared at about 0.41 V at the bare GCE; the peak

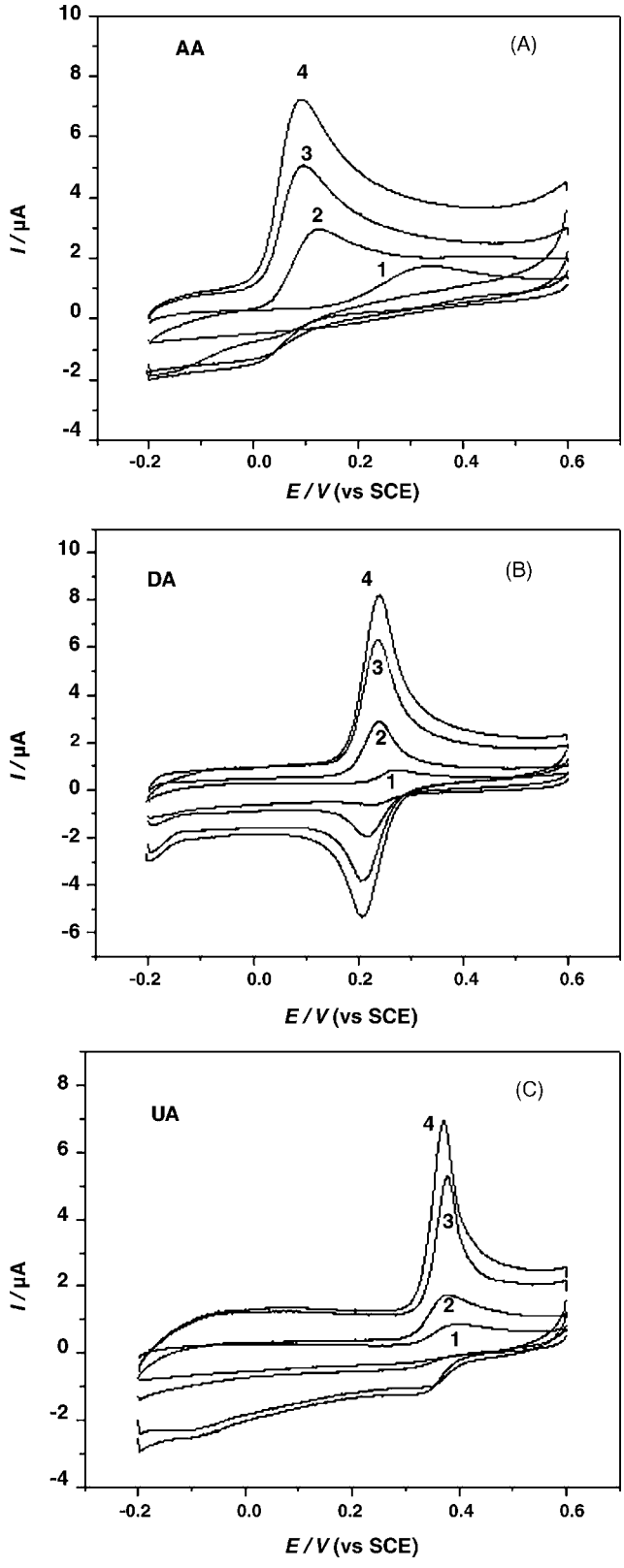

Fig. 4. CVs of 0.05 mmol L^{-1} AA, 0.01 mmol L^{-1} DA and 0.01 mmol L^{-1} UA at bare GCE (1); GNP/GCE (2); Ch/GCE (3) and GNP/Ch/GCE (4) in 1/15 mol L^{-1} PBS (pH 7.0). Scan rate: 50 mV s^{-1}.

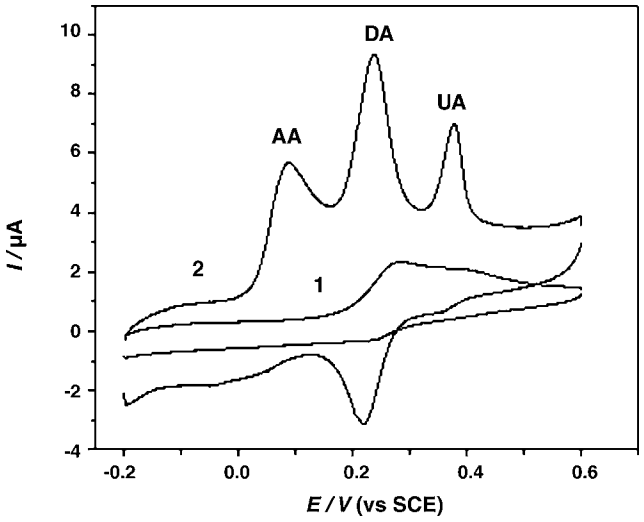

Fig. 5. CVs of a bare GCE (1) and GNP/Ch/GCE (2) in 1/15 PBS (pH 7.0) containing 0.05 mmol L^{-1} AA, 0.01 mmol L^{-1} DA and 0.01 mmol L^{-1} UA. Scan rate: 50 mV s^{-1}.

was rather broad, indicating a slow electron transfer kinetic. However, a well-defined oxidation peak at 0.37 V and a small re-reduction peak at 0.33 V were obtained at the GNP/Ch/GCE. The 40 mV negative shift with much enhanced peak current suggests a strong catalytic effect of GNP/Ch/GCE. Moreover, it can be seen that there have appeared an obviously re-reduction peak of UA, showing the increased reaction reversibility and reduced rate of following reactions at the GNP/Ch/GCE. Furthermore, it can be easily seen that the anodic current enhanced in different extent due to the modification of Ch or GNPs, indicating that both GNP/GCE and Ch/GCE were able to accelerate the rate of UA electron transfer. However, GNP/Ch/GCE obviously is the best one for high potential resolution, high sensitivity and suitable for the following study.

As we known, DA, AA and UA coexist in the extra cellular fluid of the central nervous system and serum. Since they have similar oxidation potentials at most solid electrodes, separate determination of these species is a great problem due to their overlapped signals. In order to establish a sensitive and selective method for the quantification of DA, AA and UA, the GNP/Ch/GCE was used to simultaneously detect the mixtures of above three molecules. Fig. 5 presents the cyclic voltammograms in the potential range from −0.2 to 0.6 V for the mixture of DA, AA and UA at the GNP/Ch/GCE and bare GCE in pH 7.0 PBS. As can be seen, the CV of the ternary mixture shows two broad and overlapped anodic peaks at 0.29 and 0.42 V at bare GCE (curve 1). So the peak potentials for DA, AA and UA are indistinguishable at a bare GCE. Therefore, it is impossible to deduce any information from the broad and overlapped voltammetric peak. But when the GNP/Ch/GCE was used, the overlapped voltammetric peak is resolved into three well-defined CV peaks (curve 2) at about 0.09, 0.23 and 0.37 V, corresponding to the oxidation of AA, DA and UA, respectively. The separations of peaks were 140, 140 and 280 mV in CV between DA and AA, DA and UA and AA and UA, respectively, which were large enough to determine DA and UA simultaneously in the presence of high concentration of AA. When the concentration of AA was 1000 times that of DA or UA, simultaneous detection can still be obtained. This result also illustrated that the GNP/Ch/GCE had a good catalytic activity for the oxidation of AA, DA and UA.

For investigation of reaction mechanism, scan rate dependent experiments were carried out for the DA and UA oxidation at the GNP/Ch/GCE. The obtained results showed that both the anodic and cathodic peak currents of DA at the modified electrode were proportional to the scan rate in the range of 25–350 mV/s, which indicated that the electrode reaction was typical of the adsorption-controlled process. The linear regression equations were obtained as: $I_{pa}(\mu A) = 2.800 + 0.039v\,(mV/s)$, $R = 0.9986$; $I_{pc}(\mu A) = -1.532 - 0.038v\,(mV/s)$, $R = 0.9984$. The redox peak currents that increase linearly with scan rates were expected as a thin layer electrochemical property [29]. In addition, the modified electrode was immersed in a solution of 10 μM DA for 5 min, then rinsed with water and taken into a blank buffer solution, subsequently a pair of redox peak of DA could be clearly observed. This is another evidence for the adsorption behavior. Considered above facts and the adsorptive properties of multilayer films for DA, we assume the mechanism of DA oxidation at the GNP/Ch/GCE as following: DA is adsorbed by multilayer films firstly, then loses electron to electrode and DA itself is oxidized. Similar experiment was also done for UA, and the results showed that the oxidation process of UA at the GNP/Ch/GCE is also a surface-controlled process.

3.3. Effect of pH on the oxidation of single DA and UA

In most case, the solution pH is an important influence factor to the electrochemical reaction. For DA determination, the pH effect on DPV signals at the GNP/Ch/GCE was examined. From the DPV results, it can be obtained that the peak potentials shifted towards negative potential with increasing pH of the solution. The relationship of E_{pa} and pH could be described by the following equation: E_{pa} (V) = 0.6448–0.05717 pH ($r = 0.9999$), which showed that the uptake of electrons is accompanied by an equal number of protons. Increasing the pH from 3.0 to 8.0 would lead to a sharp increase of peak current. But, further increase of pH beyond 8.0 will cause the peak current to decrease. In these experiments, pH 7.0 PBS was chosen as supporting electrolyte since it is close to the pH value of physiological condition.

The effect of solution pH on the response of UA was also investigated in the range 3.0–10.0. The DPV peak potential of UA oxidation shifted also negatively at a slope of 64.8 mV per pH unit (close to the anticipated Nernstian theoretical value of 59 mV), which is in agreement with the $2e^-/2H^+$ reaction. The linear regression equation was obtained as: E_{pa} (V) = 0.8289–0.06476 pH with the correlation coefficient 0.9993. In addition, the peak current shows a maximal i_{pa} of UA is appeared at pH 4.0, and a slow decrease for pH >5.0. It is obvious that lower pH value is favorable to UA determination for having higher sensitivity. However, in order to mimic the physiological environment, pH 7.0 was still chosen in the following experiments.

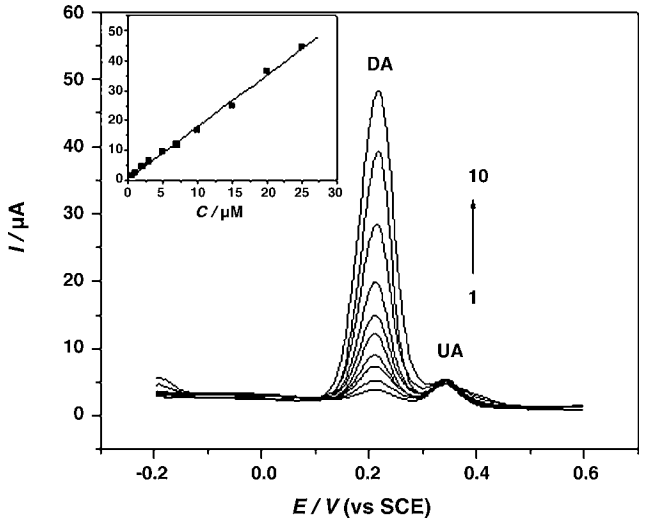

Fig. 6. DPVs of DA at GNP/Ch/GCE in the presence of 5 μmol L^{-1} UA in pH 7.0 PBS. DA concentrations (from 1 to 10): 0.5, 1, 2, 3, 5, 7, 10, 15, 20 and 25 μmol L^{-1}. Inset is the linear relationship between peak currents and the concentration of DA.

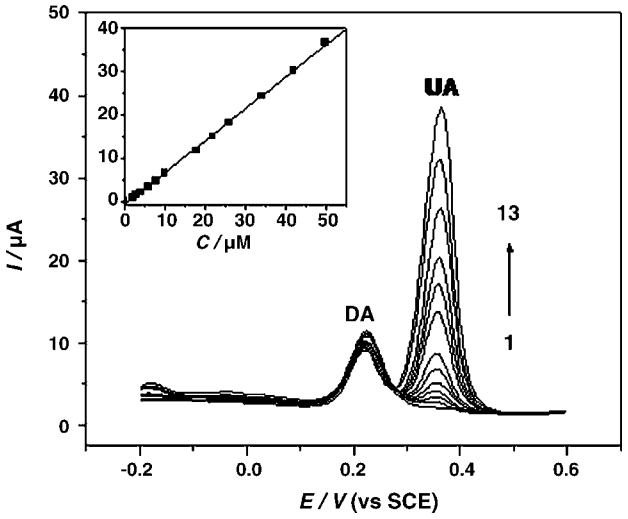

Fig. 7. DPVs of UA at GNP/Ch/GCE in the presence of 5 μmol L^{-1} DA in pH 7.0 PBS. UA concentrations (from 1 to 13): 0, 2, 3, 4, 6, 8, 10, 18, 22, 26, 34, 42 and 50 μmol L^{-1}. Inset is the linear relationship between peak currents and the concentration of UA.

3.4. Analytical application for simultaneous determination of DA and UA

In order to improve the sensitivity for the simultaneous determination of DA and UA, DPV has been adopted to record anodic peak current on the GNP/Ch/GCE. The electro-oxidation processes of DA and UA in the mixture have been investigated when the concentration of one species changed, whereas the other is kept constant. Fig. 6 gives the DPV recordings at various DA concentrations at the GNP/Ch/GCE in the presence of 5 μM UA. From Fig. 6, it could be seen that the location of the peak current for UA was almost constant during the oxidation of DA. The peak current of DA ($i_{p,DA}$) was linear to the concentration (C_{DA}) in the range 0.2–80 μM with a linear function $i_{p,DA}$ (μA) = 0.4319 + 1.741C_{DA} (μM) (r = 0.9982), and the detection limit was 0.12 μM.

Similarly as shown in Fig. 7, the voltammetric currents corresponding to the oxidation of UA increased linearly with the increase of UA concentrations while the peak current of DA remained unchanged. The results showed that $i_{p,UA}$ was proportional to concentration of UA in the range of 1.2–100 μM. The linear regression equation was expressed as: $i_{p,UA}$ (μA) = −0.8665 + 0.7360C_{UA} (μM) (r = 0.9994). The lower detection limit was 0.6 μM. It could also be noted from these results that the responses to DA and UA at the GNP/Ch/GCE were relatively independent.

Under the optimum conditions, using the DPV mode, the relative standard deviation (R.S.D.) for eight successive determinations of 10 μM DA and 10 μM UA were 2.9 and 3.7%, respectively, indicating the excellent reproducibility of the present system.

3.5. Interference

As demonstrated above, such an intrinsic property of the modified electrode could substantially differentiate DA, AA and UA. Therefore, the interference from AA can be neglected. Other influences from common co-existing substances were also investigated. It was found that no significant interference for the detection of 10 μM UA or DA was observed for these compounds: NaCl (500), $CaCl_2$ (200), citric acid (1000), glucose (200), tryptophan (100), cysteine (100) and tyrosine (200), where the data in the brackets were the concentration ratios.

3.6. Real samples analysis

In order to verify the performance and feasibility of the method for analysis of DA in pharmaceutical product, the proposed electrode was applied to the determination of DA in dopamine hydrochloride injection (standard concentration of DA 10 mg/mL, 2 mL per injection). The injection solution was diluted to 100 mL with water. Twenty microliters of this diluted solution or some amount of standard DA solution was injected into each of a series of 10 mL volume flasks and made up to volume with 1/15 M PBS (pH 7.0). An aliquot of 2.0 mL of this test solution was placed in an electrochemical cell for the determi-

Table 1
Determination results of DA in injections (n = 5)

Samples	Labeled (mg mL^{-1})	Found (mg mL^{-1})	R.S.D (%)	Added (mg mL^{-1})	Found (mg mL^{-1})	Recovery (%)
1	10	10.08	2.2	2	12.04	98
2	10	9.81	3.1	2	11.75.	97
3	10	10.11	1.8	2	12.20	104

Table 2
Determination of UA in urine samples ($n = 5$)

Urine samples	Detected (μM)	Added (μM)	Found (μM)	Recovery (%)
1	5.38	5	10.25	97.4
2	5.94	5	11.18	104.8
3	5.77	5	10.90	102.6
4	5.62	5	10.44	96.4

nation of DA using above DPV method. The results were listed in Table 1. The recovery and R.S.D. were acceptable, showing that the proposed methods could be efficiently used for the determination of DA in commercial samples.

In addition, the utilization of the proposed electrode in real samples was also investigated by direct analysis of UA in healthy human urine. In order to fit into the linear range of UA, all the urine samples were diluted 500 times with PBS (pH 7.0) before the measurement. The proposed methods were performed after dilution. The standard addition method was used for testing recovery. Table 2 presented the results obtained for four parallel measurements. The results were satisfied, indicating that this method was reliable and reproducible.

4. Conclusions

A novel nanoparticle thin film electrochemical sensor has been developed by using GCE coated with Ch and GNPs. The present study demonstrated that the electrochemical sensor not only improved the electrochemical catalytic oxidation of DA, UA and AA, but also resolved the overlapping anodic DA, UA and AA peaks into three well-defined peaks in neutral solutions, illustrating that the determination of DA and UA can be conducted in the presence of large amounts of AA. The electrochemical sensor showed excellent selectivity, good sensitivity and high stability. Moreover, this proposed method has been applied to the determination of DA and UA in pharmaceutical product and urine samples with satisfactory results. The reliability and utilization of the electrochemical sensor offer a good possibility for applying the technique to routine analysis of DA and UA in clinical use.

Acknowledgements

This work was supported by Natural Science Foundation of Educational Department of Anhui Province (No. 2006kj039a), National Natural Science Foundation of China (No. 20575001) and a key teacher project of High School of Anhui.

References

[1] X.L. Wen, Y.H. Jia, Z.L. Liu, Talanta 50 (1999) 1027.
[2] K. Wu, J. Fei, S. Hu, Anal. Biochem. 318 (2003) 100.
[3] J.W. Mo, B. Ogorevc, Anal. Chem. 73 (2001) 1196.
[4] R.M. Wightman, L.J. May, A.C. Michael, Anal. Chem. 60 (1988) 769A.
[5] A. Salimi, H. MamKhezri, R. Hallaj, Talanta 70 (2006) 823.
[6] J.A. Stamford, J.B. Justice, Anal. Chem. 68 (1996) 359A.
[7] S.H. Huang, Y.C. Shih, C.Y. Wu, C.J. Yuan, Biosens. Bioelectron. 19 (2004) 1627.
[8] D.V.S. Gswara, H.A. Mottola, Anal. Chem. 46 (1974) 1777.
[9] E. Miland, A.J. Miranda Ordieres, Talanta 43 (1996) 785.
[10] L. Zhang, X. Lin, Analyst 126 (2001) 367.
[11] R.P. Baldwin, K.N. Thomsen, Talanta 38 (1991) 1.
[12] M. Zhang, K. Gong, H. Zhang, L. Mao, Biosens. Bioelectron. 20 (2004) 1270.
[13] Y. Zhao, Y. Gao, D. Zhan, H. Liu, Q. Zhao, Y. Kou, Y. Shao, M. Li, Talanta 66 (2005) 51.
[14] F. Xu, M.N. Gao, L. Wang, G. Shi, W. Zhang, L. Jin, J. Jin, Talanta 55 (2001) 329.
[15] T. Liu, M. Li, Q. Li, Talanta 63 (2004) 1053.
[16] T. Hoshi, H. Saiki, J.I. Anzai, Talanta 61 (2003) 363.
[17] K.M. Mitchell, Anal. Chem. 76 (2004) 1098.
[18] J.K. Blusztajn, R.J. Wurtman, Science 221 (1983) 614.
[19] S. Serradilla Razola, S. Pochet, K. Grosfils, Biosens. Bioelectron. 18 (2003) 185.
[20] L.Q. Mao, K. Yamamoto, Talanta 51 (2000) 187.
[21] G.P. Jin, X.Q. Lin, Electrochem. Commun. 6 (2004) 454.
[22] M. Christine, Welch, G. Richard, Compton, Anal. Bioanal. Chem. 384 (2006) 601.
[23] E. Katz, I. Willner, J. Wang, Electroanalysis 16 (2004) 19.
[24] N.T.K. Thanh, Z. Rosenaweig, Anal. Chem. 74 (2002) 1624.
[25] N. Levit-Binnun, A.B. Lindner, O. Zik, Z. Eshhar, E. Moses, Anal. Chem. 75 (2003) 1436.
[26] L.P. Lu, X.Q. Lin, Anal. Sci. 20 (2004) 527.
[27] C. Saby, B. Ortiz, G.Y. Champagne, D. Belanger, Langmuir 13 (1997) 6805.
[28] C.R. Raj, T. Ohsaka, J. Electroanal. Chem. 496 (2001) 44.
[29] X. Chen, X. Peng, J. King, J. Deng, J. Electroanal. Chem. 480 (2000) 26.

Available online at www.sciencedirect.com
ScienceDirect
Talanta 73 (2007) 540–545
Talanta
www.elsevier.com/locate/talanta

A new hydride generation system applied in determination of arsenic species with ion chromatography–hydride generation-atomic fluorescence spectrometry (IC–HG-AFS)

Changjin Wei, Jixin Liu *

Beijing Titan Instruments Co. Ltd., Beijing 100016, China

Received 14 October 2006; received in revised form 9 February 2007; accepted 15 April 2007
Available online 4 May 2007

Abstract

A novel procedure was developed for the determination of arsenite (As(III)), arsenate (As(V)), monomethylarsonic (MMA) and dimethylarsinic acid (DMA) with ion chromatography–hydride generation-atomic fluorescence spectrometry (IC–HG-AFS) by employing a new gas–liquid separator (GLS). The effective separation of the four arsenic species was achieved in about 12 min. With a sample loading volume of 20 μl, the measurable minimum for As(III), DMA, MMA and As(V) were 0.02, 0.045, 0.043 and 0.166 ng, respectively, along with relative standard deviations of 1.1, 1.1, 1.7 and 2.2% at the 100 $\mu g\,l^{-1}$ level ($n=6$) for As(III), DMA, MMA and As(V), respectively. The present procedure was applied for the speciation of arsenic in underground water and in urine samples, and the sum of the four arsenic species by IC–HG-AFS was in good agreement with the total value by HG-AFS.

Keywords: Arsenic speciation; Ion chromatography; Hydride generation-atomic fluorescence spectrometry; Gas–liquid separator

1. Introduction

Arsenic exists in both organic and inorganic forms in nature, and the differentiation of arsenic species has acquired great importance in recent years, since the toxicity of As differs dramatically with its forms. Inorganic arsenical compounds, such as arsenite (As(III)) and arsenate (As(V)) are highly toxic [1]; the methylated organic arsenicals, specifically monomethylarsonic (MMA) and dimethylarsinic acid (DMA), are less toxic than the inorganic forms; while other forms such as arsenobetaine (AsB) and arsenocholine (AsC) are generally considered non-toxic [1,2]. Consequently, it is necessary to develop analytical techniques not only capable of determining the total arsenic concentration, but distinguishing between arsenic species as well. To attain this purpose, chromatography separation coupled to atomic spectrometry is most frequently used.

As regard to the chromatography separation, the most widely employed methods reported in the literatures are cation-exchange [3,4], anion-exchange [5–9] and reversed-phase chromatography [10,11] or combination of these techniques [12–14], among which the anion-exchange chromatography can separate inorganic and mono- and dimethylated species, which have an anionic character.

Inductively coupled plasma mass spectrometry (ICP-MS) has been chosen by many authors as a chromatographic detector system, because of the rapidity and very high sensitivity of measurements [14–16]. However, both the cost of ICP-MS instrumentation as well as its maintenance are quite high that limits its' applications for routine analysis. In recent years, hydride generation-atomic fluorescence spectrometry (HG-AFS) has been well developed as a hyphenated detection means with sensitivities comparable to those of ICP-MS based procedures [5–12,17–20]. While the cost for acquiring the instrument and its maintenance is much more less than ICP-MS, HG-AFS involves the use of tetrahydroborate to convert the hydride forming elements into hydride, which is separated from the reaction mixture by using a gas–liquid separator, followed by directing into the atomizer with carrier gas. In HG system, the gas–liquid separator (GLS) had influence on separation effect of hydride gas, the background noise, and the

* Corresponding author. Tel.: +86 10 64377759; fax: +86 10 64379929.
E-mail address: ljx2117@mail.china.com (J. Liu).

0039-9140/$ – see front matter © 2007 Elsevier B.V. All rights reserved.
doi:10.1016/j.talanta.2007.04.026

interference and so on [21–23]. In AFS, during gas–liquid procedure, the excessive moisture can be transported to the atomizer or lodged in the transfer line, and would cause problems such as the loss of sensitivity and even a blockage of the transfer line. In addition, water vapor carried by carrier gas cause quenching of fluorescence, Furthermore, in atomizer water vapor would generate •OH which may interference determination [24]. Therefore the capability for moisture removing of gas–liquid separating system is important. A Nafion drying tube or a second GLS is inserted between the primary GLS and the atomizer to dehydrate. Unfortunately, neither the expensive 1-year-lived Nafion drying tube nor the complicated second GLS is proved to be good enough. The aim of this work is to develop a new GLS and find a simple yet effective method for the analysis of As(III), DMA, MMA and As(V) by coupling an anion-exchange chromatographic separation system with HG-AFS. For this purpose, the chromatographic parameters were optimized and the characteristics of the two GLS were evaluated.

2. Experimental

2.1. Apparatus

The schematic diagram of the IC–HG-AFS operation system is shown in Fig. 1(A). The IC separation was achieved using an anion-exchange PRP-X100 analytical column (250 mm × 4.1 mm i.d., 10 μm) protected by a guard column (25 mm × 2.3 mm i.d., 12–20 μm) (Hamilton, Reno, NV). A Rheodyne Model 7725i injection valve with a 20 μl sample loop (Rheodyne, Cotati, CA, USA) was used for the introduction of the sample. The mobile phase was delivered by a Labtech P600 (Labtech Inc.) pump. The LC effluent was delivered to a T-cross and mixed with HCl firstly and then reacted with KBH_4. A peristaltic pump was used to introduce HCl and KBH_4. The produced hydrides were separated in a gas–liquid separator and carried by argon to the atomizer.

GLS system 1 and GLS system 2 were applied in IC–HG-AFS system. Fig. 1(B) was the diagram of GLS system 1. It was a

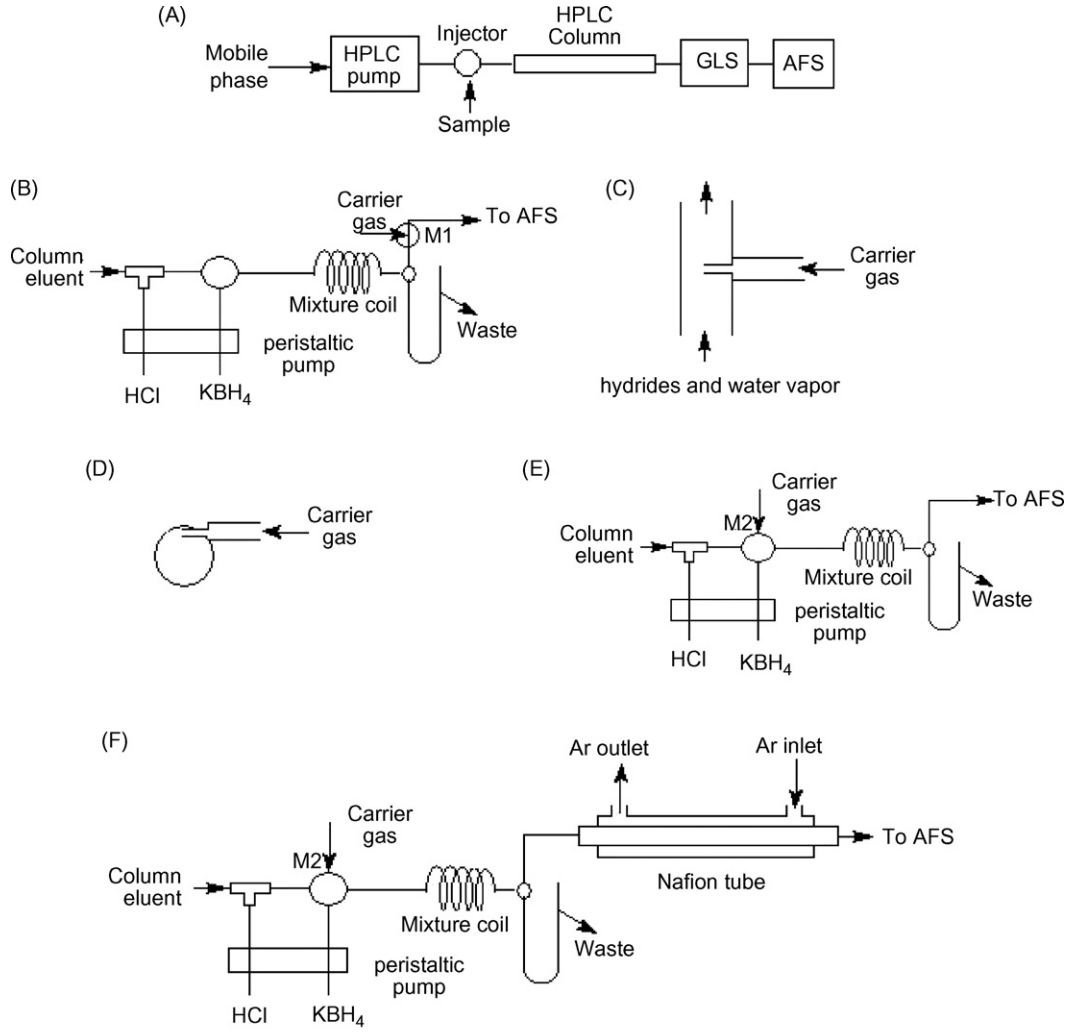

Fig. 1. The schematic diagram of IC–HG-AFS operation system and different gas–liquid separators. (A) The schematic diagram of IC–HG-AFS operation system. (B) GLS system 1. (C) Amplificatory diagram of M1. (D) Planform of M1. (E) GLS system 2. (F) GLS system 3.

Table 1
Optimized experimental conditions for the IC–hydride generation-AFS system

IC		
Column	Hamilton PRP-X100 (250 mm × 4.1 mm i.d., 10 μm)	
Mobile phase	15 mmol l^{-1} $(NH_4)_2HPO_4$ (pH 6.0)	
Flow rate	1.0 ml/min	
Injection volume	20 μl	
	GLS system 1	GLS system 2
HG-AFS		
KBH_4	1.5% in 0.5% KOH, 6.0 ml/min	
HCl	7%, 6.0 ml/min	7%, 6.0 ml/min
Mixture coil	1.5 m (Ø1.4mm)	0.25 m (Ø4.0 mm)
PMT voltage	270 V	
Hcl current	50 mA (primary)/50 mA (boosted)	
Carrier gas	Argon, 400 ml/min	Argon, 300 ml/min

U-type GLS, in which carrier gas was added from M1. Fig. 1(C) was amplificatory diagram of M1. As shown in Fig. 1(C), M1 was a special three channel mixing module, through which the hydrides and water vapor pass, and carrier gas was added along tangent direction, as shown in Fig. 1(D). The carrier gas inlet mode would bring swirling action on the stream to remove water vapor.

As shown in Fig. 1(E), carrier gas was added in M2 in the GLS system 2. M2 was a three channel mixing module through which carrier gas and KBH_4 were added simultaneously. GLS system 3 combined with GLS system 2 and Nafion drying tube, as shown in Fig. 1(F). The Nafion drying tube was equipped between GLS system 2 and AFS.

Determinations were performed by using an AFS-820 atomic fluorescence spectrophotometer (Beijing Titan Instruments Co. Ltd., Beijing, China). The excitation source used in the instrument was a high intensity arsenic hollow cathode lamp (Beijing Research Institute of Nonferrous Metals) operated with a primary current of 50 mA with boosted current of 50 mA. A personal computer fitted with the modified software of AFS820 was required for the control of the instrument. Peak heights were employed for evaluation. Details of the chromatographic and instrumental parameters are summarized in Table 1.

2.2. Standards and reagents

All reagents were at least of analytical reagent grade, and deionized water was used throughout. Arsenite stock solution (1 mg ml^{-1} as As) was purchased from National Standard Substance Center in China. Aqueous standard stock solution of arsenate, MMA and DMA were prepared by dissolving appropriate amounts of disodium hydrogen arsenate, disodium methyl arsenate (Sigma–Aldrich Chemical Company, USA) and cacodylic acid (Acros, USA) in deionized water. Working solutions were prepared daily by step-wise dilution of the stock solutions.

LC mobile phases were prepared using $(NH_4)_2HPO_4$ and the corresponding pHs were adjusted by using 4% formic acid. All these solutions were filtered through a 0.45 μm membrane filter prior to use. Potassium tetrahydroborate (KBH_4) solutions were prepared daily by dissolving KBH_4 in 0.5% potassium hydroxide (KOH).

2.3. Sample preparation

2.3.1. The determination of total arsenic

After water samples were filtered through a 0.45 μm membrane, an aliquot of 10 ml of each sample was added into a 50-ml flask, followed by adding 10 ml of a mixed solution of thiourea and ascorbic acid where both components were at 50 g/l, and filled to mark with water. Total arsenic was determined by HG-AFS after 30 min.

To urine samples, 10 ml of each of the samples was added to a 50-ml Erlenmeyer flask. Eight milliliters of nitric acid and 2 ml perchloric acid and 2 ml sulphuric acid were added. The 50-ml Erlenmeyer flasks were heated on hot plate until the residual solutions were only 2 ml. Then the residual solutions were cooled down and were diluted to with a little deionized water, followed by adding 5 ml thiourea and ascorbic acid (50 g/l, respectively), and filled to mark with water. Total arsenic was determined by HG-AFS after 30 min.

2.3.2. Arsenic speciation

Before injection into the loop of the IC valve, water samples were filtered through a 0.45 μm membrane and further pretreatment procedures were not required. For urine samples, firstly, 4 ml portion was poured into a 5 ml centrifuge tube, then ultrasonicated for 15 min and centrifuged at 12,000 rpm for 10 min. Secondly, the supernatant was filtered through a 0.45 μm membrane and the sample was diluted from two to five times with deionized water before analysis.

The sample solution was injected into the LC system, with the mobile phases pumped at a flow of 1 ml min^{-1}. Separation was achieved at pH 6.0 with a 15 mmol l^{-1} $(NH_4)_2HPO_4$. Arsenic species in the samples were identified by matching the retention time of the samples with those of spiked standards. The eluate was mixed with HCl at a T-cross, then reacted with KBH_4 to generate hydrides. After that, the hydrides were separated from the solution in a gas–liquid separator and carried by an argon flow to the AFS detector.

3. Results and discussion

3.1. Optimization of the chromatographic parameters

Because As(III), DMA, MMA and As(V) can exist in anionic form in water, the isocratic chromatographic separation for the four arsenic species was carried out on an anion-exchange column (Hamilton PRP X-100) using phosphate buffer as mobile phase. In order to optimize the separation conditions, the influence of the concentration and pHs of $(NH_4)_2HPO_4$ in the mobile phase on the separation were investigated. The effect of phosphate buffer on the retention time was studied by varying its concentration within the range of 9–18 mmol l^{-1}. In ion-exchange chromatographic systems, an increase of the buffer concentration in the eluent results

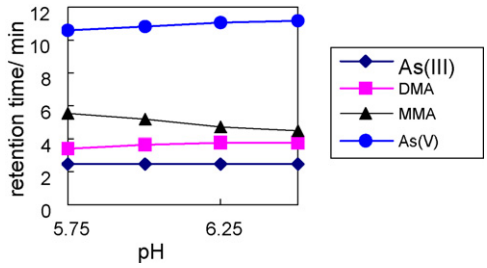

Fig. 2. The effect of pH on the separation of arsenic species.

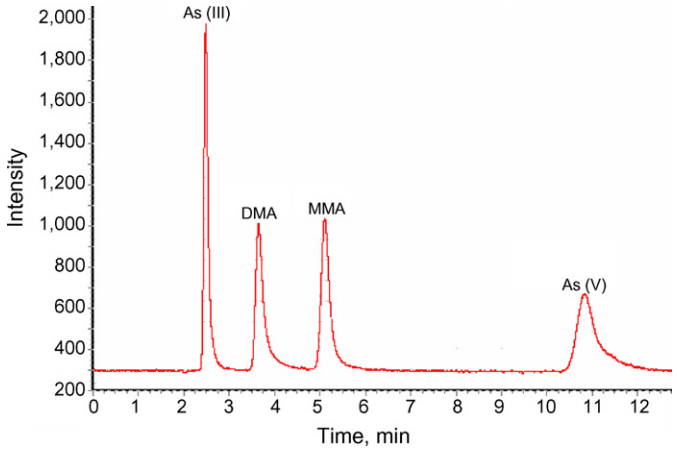

Fig. 3. Typical chromatogram of a standard solution, in which the concentrations of all arsenic species were 100 μg l^{-1}, analytical conditions were given in Table 1 with GLS system 1.

in a decrease in retention time. Though low mobile phase concentration produced well-separated peaks, the last-eluting species, As(V), showed peak broadening due to the long retention time. Thus it is preferable to use 15 mmol l^{-1} phosphate as mobile phase. As shown in Fig. 2, the peaks of DMA and MMA overlapped at pH 6.5. There was no overlap of peaks at pH 6. Therefore, this was selected for further experiments.

Under these conditions, a good separation of arsenic species was obtained in about 12 min. The retention times were 2.5, 3.7, 5.1 and 10.9 min for As(III), DMA, MMA and As(V), respectively. A typical chromatogram indicating the separation of As(III), DMA, MMA and As(V) is shown in Fig. 3.

Table 3
Dew points of different GLS system

	GLS system 1	GLS system 2	GLS system 3[a]
Partial pressure of water (mmHg)	6.4	16.2	4.0
Dew point (°C)	4.8	18.7	-2.0

[a] Inner gas flow to outer dry gas flow for Nafion drying tube was about 1:2.

3.2. Optimization of the GLS system

GLS system 1 and GLS system 2 were applied in IC–HG-AFS system. As shown in Fig. 1, carrier gas was added in M2 in the GLS system 2; in the GLS system 1, carrier gas was added through M1 to quickly draw out and mix evenly with the hydrides generated in GLS. To obtain the maximum sensitivity, the influences of various parameters were investigated using standard mixture of arsenic species independently for the two GLS systems on the optimum chromatographic conditions. The optimized conditions for both GLS systems were summarized in Table 1. In Table 2, several obtained parameters were evaluated to compare the performance using the two GLS systems: Sensitivities were expressed as peak height; measurable minimums were calculated as indicated in the notes. Relative standard deviation was calculated after six consecutive injections of the same standard solution. Results in Table 2 showed that measurable minimums as low as 0.02–0.17 ng for arsenic species were obtained with IC–HG (GLS system 1)-AFS, which was two to four times lower than that of IC–HG (GLS system 2)-AFS. A better relative standard deviation was gained with IC–HG (GLS system 1)-AFS compared to IC–HG (GLS system 2)-AFS. The high signal to noise ratio of IC–HG (GLS system 1)-AFS are attributed to several factors, such as the improvement of the gas–liquid separation efficiency, carrier gas inlet mode, partial dryness of the hydrides by the carrier gas and a decrease of water vapor introduced to the detector. This was consistent to the reports of Fang [25] and Chen et al. [26]. They pointed out that the proper carrier gas inlet mode would improve the sensitivity and stability of the system.

Furthermore, in order to evaluate the efficiency of dryness of GLS system 1, dew points of different GLS systems were measured and the intensity of As(III) determinated with the three GLS systems separately was evaluated in the simulative fashion of continuous HG-AFS. The results were shown in Table 3 and Fig. 4. It was indicated that the dew point gained with GLS sys-

Table 2
Comparison of the IC–HG (GLS system 1)-AFS and IC–HG (GLS system 2)-AFS

	IC–HG (GLS system 1)-AFS				IC–HG (GLS system 2)-AFS			
	As(III)	DMA	MMA	As(V)	As(III)	DMA	MMA	As(V)
Sensitivity[a]	16.14	6.86	7.26	1.94	7.81	2.77	3.28	1.10
Measurable minimum[b] (ng)	0.020	0.045	0.043	0.17	0.068	0.19	0.16	0.49
R.S.D.[c] (%) (n = 6)	1.1	1.1	1.7	2.2	3.7	1.5	2.1	4.3

[a] Sensitivity, expressed as the ratio of peak height to concentration.
[b] Measurable minimum, calculated as $3H_N cv/H$; H_N = baseline noise; c = concentration of arsenic species; H = peak height of arsenic species in the corresponding concentration; v = injection volume.
[c] Relative standard deviation at 100 ng/ml (n = 6).

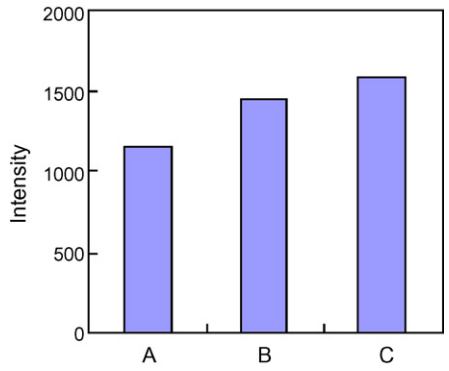

Fig. 4. Intensity with different GLS systems. (A) GLS system 2; (B) GLS system 3 (the inner gas flow to outer dry gas flow of Nafion drying tube was about 1:2.); (C) GLS system 1.

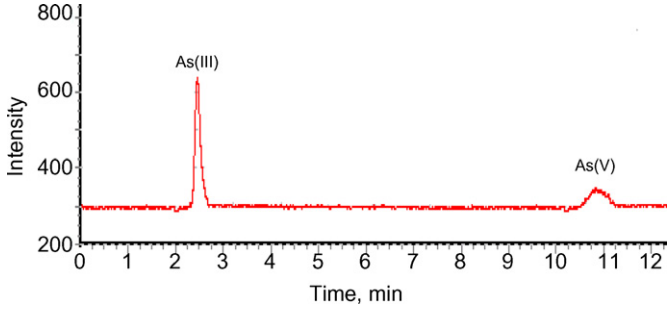

Fig. 5. The chromatogram of arsenic species in water sample W7.

tem 1 was much lower than that with GLS system 2, but close to that with GLS system3. Fig. 4 indicated that the intensity acquired with GLS system 2 was the lowest. There was little difference between the intensity gained with GLS system 1 and GLS system 3. It showed that simultaneous gas–liquid separation and partial dryness was only achieved by GLS system 1. This was perhaps attributed to the fashion that the carrier gas was added along tangent direction in M1 in the GLS system 1. In the carrier gas inlet mode, although there were visible liquid drops found in the underside of M1, they were not found in the upper of M1, which meant that the water vapor had been entrapped with hydride gas by carrier gas into the M1, but were condensed and separated from the hydride gas by rotational flow cooling effect. Liquid drops which were cooled from water vapor flowed into the GLS. Considering the high cost of Nafion drying tube, it was preferable to use GLS system 1 alone in our IC–HG-AFS system. Therefore, GLS system 1 was used in further experiments.

Table 4
Species and total of arsenic in underground water samples (concentration in ng/ml as As)

Water sample	As(III)	DMA	MMA	As(V)	Total by IC–HG-AFS	Total by HG-AFS
W1	n.d.[a]	n.d.	n.d.	n.d.	n.d.	2.1
W2	7	n.d.	n.d.	n.d.	7	9.9
W3	19	n.d.	n.d.	n.d.	19	22.4
W4	29	n.d.	n.d.	12	41	44.2
W5	n.d.	n.d.	n.d.	n.d.	n.d.	2.1
W6	n.d.	n.d.	n.d.	n.d.	n.d.	2.5
W7	24	n.d.	n.d.	17	41	46.0

[a] n.d.: not detected.

Table 5
Species and total of arsenic in urine samples (concentration in ng/ml as As)

Urine sample	As(III)	DMA	MMA	As(V)	Total by IC–HG-AFS	Total by HG-AFS
U1	7	36	5	n.d.	48	52.6
U2	3	24	6	n.d.	33	36.5
U3	9	32	9	n.d.	50	52.1
U4	12	96	22	n.d.	130	130.0
U5	n.d.	39	5	8	52	55.9

3.3. Analysis of samples

The four arsenic species in some underground water samples in Henan province in China were determined under the above optimal conditions. Since there were few certified values of species and total available, we also determined the total arsenic by HG-AFS after pre-reduction by a mixed solution of thiourea and ascorbic acid where both components were at 10 g/l. The results listed in Table 4 indicated that arsenic species in the water samples were mainly As(III) and As(V). But no As species were detected in some water samples. The chromatogram of arsenic species in water sample W7, which contained As(III) and As(V), was shown in Fig. 5. Table 5 shows DMA was the predominant species in most urine samples, but As(III) and MMA were found in most of them. As(V) was found in U5 of the urine samples. Fig. 6 shows the chromatogram of arsenic species in urine sample U4. When it was diluted five times with deion-

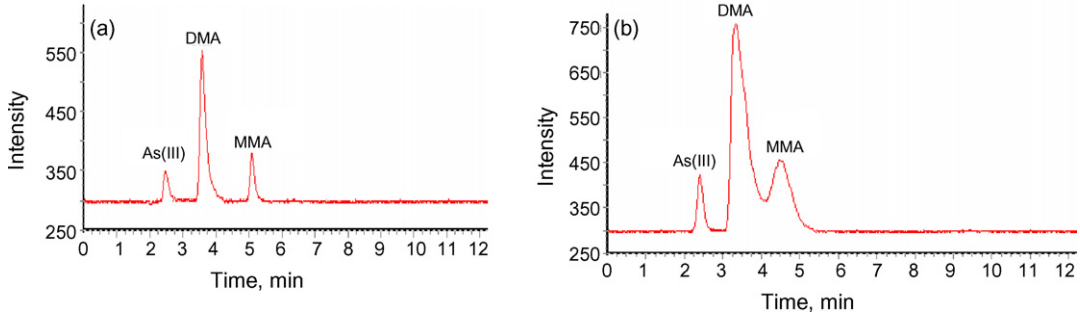

Fig. 6. The chromatogram of arsenic species in urine sample U4: (a) diluted to five times and (b) diluted to two times.

ized water prior to analysis, As(III) and DMA and MMA were well separated in Fig. 6(a). But in Fig. 6(b), DMA and MMA were overlapped partially when the sample was only diluted two times with deionized water. Because there were some salts in urine samples, which resulted that the retention time of arsenic species in urine samples were shortened, moreover, DMA and MMA would be overlapped partially when urine samples were injected without diluting with water. Diluted multiples depended on the concentrations and separation of arsenic species in urine samples. In general, urine samples were diluted from two to five times with deionized water to be made good separation between arsenic species and to be determined quantitatively. Therefore to avoid interferences of salts, it was preferable that the urine samples were diluted from two to five times with deionized water prior to analysis.

For water samples and urine samples, the sum of the four arsenic species by IC–HG (GLS system 1)-AFS was in good agreement with the total value by HG-AFS.

4. Conclusion

A new gas–liquid separator system in which simultaneous gas–liquid separation and partial dryness can be achieved was used in IC–HG-AFS. It was special in carrier gas inlet mode which can improve the sensitivity and stability for analysis of arsenic species. It needs no other complicated apparatus, such as hygroscopic membrane or second GLS. Measurable minimum (20 μl injected) for As(III), DMA, MMA and As(V) is 0.02, 0.045, 0.043 and 0.166 ng, respectively. To water samples and urine samples, the sum of the four arsenic species by IC–HG-AFS was in good agreement with the total value by HG-AFS. This simple and robust system is very suitable for the detection of arsenic species.

References

[1] M.O. Andrea, in: P.J. Craig (Ed.), Organometallic Compounds in the Environment, Longman, London, 1986.
[2] R. Ritsema, L. Dukan, T.R.I. Navarro, W. van Leeuwen, N. Oliveira, P. Wolfs, E. Lebret, Appl. Organomet. Chem. 12 (1998) 591.
[3] A.D. Madsen, W. Goessler, S.N. Pedersen, K.A. Francesconi, J. Anal. At. Spectrom. 15 (2000) 657.
[4] J. Feldmann, K. John, P. Pengprecha, Fresenius J. Anal. Chem. 368 (2000) 116.
[5] Y. Bohari, A. Astruc, M. Astrucb, J. Cloudc, J. Anal. At. Spectrom. 16 (2001) 774.
[6] Z Šlejkovec, J.T. van Elteren, A.R Byrne, Anal. Chim. Acta 358 (1998) 51.
[7] B. He, G.-B. Jiang, X.-B. Xu, Fresenius J. Anal. Chem. 368 (2000) 803.
[8] M. Segura, J. Muñoz, Y. Madrid, C. Cámara, Anal. Bioanal. Chem. 374 (2002) 513.
[9] S. Simon, H. Tran, F. Pannier, M. Potin-Gautier, J. Chromatogr. A 1024 (2004) 105.
[10] Z. Mester, P. Fodor, J. Chromatogr. A 756 (1996) 292.
[11] X.C. Le, M. Ma, Anal. Chem. 70 (1998) 1926.
[12] M. Vilanó, A. Padró, R. Rubio, Anal. Chim. Acta 411 (2000) 71.
[13] M.A. Suñer, V. Devesa, O. Muñoz, D. Vélez, R. Montoro, J. Anal. At. Spectrom. 16 (2001) 390.
[14] M. Van Hulle, C. Zhang, B. Schotte, L. Mees, F. Vanhaecke, R. Vanholder, X. Zhang, R. Cornelis, J. Anal. At. Spectrom. 19 (2004) 58.
[15] S. Londesborough, J. Mattusch, R. Wennrich, Fresenius J. Anal. Chem. 363 (1999) 577.
[16] W. Li, C. Wei, C. Zhang, M. Van Hulle, R. Cornelis, X. Zhang, Food Chem. Toxicol. 41 (2003) 1103.
[17] M. Vilanó, R. Rubio, Appl. Organomet. Chem. 15 (2001) 658.
[18] A.M. Featherstone, P.R. Boult, B.V. O'Grady, E.C.V. Butler, Anal. Chim. Acta 409 (2000) 215.
[19] J.L. Gómez-Ariza, D. Sánchez-Rodas, I. Giráldez, E. Morales, Talanta 51 (2000) 257.
[20] L.O. Leal, R. Forteza, V. Cerdà, Talanta 69 (2006) 500.
[21] M.L. Magnuson, J.T. Creed, C.A. Brockhoff, J. Anal. At. Spectrom. 11 (1996) 893.
[22] X.D. Tian, Z.X. Zhuang, B. Chen, X.R. Wang, Analyst 123 (1998) 627.
[23] T. Matousek, J. Dedina, M. Johansson, W. Frech, Spectrochim. Acta 55B (2000) 151.
[24] W.T. Corns, P.B. Stockwell, J. Anal. At. Spectrom. 8 (1993) 71.
[25] Z.L. Fang, Flow Injection Analysis, Science Press, Beijing, 1999, p. 201.
[26] S. Chen, Z. Zhang, H. Yu, W. Liu, M. Sun, Anal. Chim. Acta 463 (2002) 177.

Available online at www.sciencedirect.com
ScienceDirect
Talanta 73 (2007) 529–533
Talanta
www.elsevier.com/locate/talanta

Studies on the effects of Al(III) on the lactate dehydrogenase activity by differential pulse voltammetry

Kaian Yao [a,b], Na Wang [a,b], Jingyue Zhuang [a,b], Zhengbiao Yang [a,b], Haiyan Ni [a,b], Quan Xu [a,b], Cheng Sun [a,b], Shuping Bi [a,b,*]

[a] *State Key Laboratory of Pollution Control and Resource Reuse, School of Chemistry and Chemical Engineering, Nanjing University, Nanjing 210093, China*

[b] *Key Laboratory of MOE for Life Science, School of Chemistry and Chemical Engineering, Nanjing University, Nanjing 210093, China*

Received 4 January 2007; received in revised form 10 April 2007; accepted 13 April 2007
Available online 25 April 2007

Abstract

In this paper, differential-pulse voltammetry (DPV) was applied to study the effects of aluminum (Al(III)) on the lactate dehydrogenase (LDH) activity, K_m^{NADH} and v_{max} in the enzyme promoting catalytic reaction of "Pyruvate + NADH + $H^+ \overset{LDH}{\rightleftarrows}$ Lactate + NAD^+" by monitoring DPV reduction current of NAD^+. The changes of Al's influence on the LDH activities caused by the concentration of LDH, pH, temperature as well as Al speciation including Al hydroxide (Al-OH), Al fluoride (Al-F) and organically complexing Al (Al-Org) compounds have been investigated. The results showed that the effects of Al on the LDH activity exhibited two kinds of behaviors under different conditions, i.e. inhibitory effects or slightly increased LDH activity at low concentrations and inhibited at high concentrations. To analyze the values of K_m^{NADH} and v_{max} of LDH reaction system in the absence and presence of 0.04 mmol/L Al(III), it was found that the types of the inhibition of Al(III) varied with experimental conditions. The comparisons of effects of Al(III) with Pb(II), Cd(II) and Cr(III) on the LDH activities were also inspected.

Keywords: Al(III); DPV; Lactate dehydrogenase; Activity of enzyme; Metal ions

1. Introduction

Aluminum (Al), the most abundant metal and the third most abundant element in the earth's crust, has been proposed as an important factor that may contribute to several diseases, such as dialysis encephalopathy, Alzheimer' disease, Parkinson's disease, osteomalacia and anemia [1–5]. In recent years, considerable researches have demonstrated that Al(III) can interact with biological systems and interfere with biological functions, e.g. alter the cell membrane stability by interacting directly with the membrane phospholipids to modify the blood–brain barrier [6–9] and change some enzymatic activities in key metabolic pathways, central nervous system and antioxidant enzyme systems [10–16]. It is recognized that the metal's speciation can have an important influence on its toxicity, fate and behavior [17]. Al occurs as many different species with varying toxicity towards organisms in natural waters. Generally, the inorganic monomeric forms of Al(III) are thought to be the most toxic species [18–20], whereas Al fluoride complexes (Al-F) may mitigate toxicity and organically complexing Al (Al-Org) are non-toxic [21]. Furthermore, some recent studies have shown that polymeric forms of soluble Al(III) were significantly more toxic than monomeric forms [20]. Previous investigations had revealed that the species of Al that were in the dominant were showed to vary with pH, temperature, ionic strength and ligands [19,22]. Therefore, it is important to study the impact of various environmental factors on the Al(III)'s toxicity.

Lactate dehydrogenase (LDH) is one of the most important enzymes in the biological systems. Employing NADH as coenzyme, LDH catalyzed the reversible reaction of conversion the NADH and pyruvate to NAD^+ and lactate.

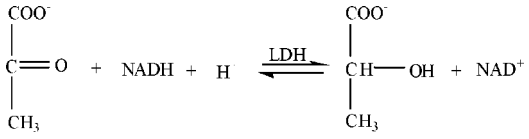

* Corresponding author. Tel.: +86 25 83594255/86205840; fax: +86 25 83317761.
E-mail address: Bisp@nju.edu.cn (S. Bi).

0039-9140/$ – see front matter © 2007 Elsevier B.V. All rights reserved.
doi:10.1016/j.talanta.2007.04.025

The activity of LDH has been considered as a biomarker and used in clinical analysis, pollution monitoring and impairment assessing after pollution exposure [23,24]. In recent years, the effects of the metal ions on LDH reaction processes have received much attention. According to the previous researches, Zn(II) and Ca(II) did not affect LDH activity whereas Mn(II) exerted inhibitory effect and Mg (II) slightly increased LDH activity. At low concentrations, Cu(II) slightly stimulated LDH activity, but showed inhibitory effects in high concentrations [25]. Similarly, rare earth ions (La(III), Ce(III), Eu(III), Dy(III) and Yb(III)) showed a minor activation effects on LDH when their concentrations were less than 3 μmol/L, but indicated some strong inhibitory effects on LDH activity when concentrations were above 5 μmol/L [26,27].

Due to large molecular weight, it is quite difficult to investigate the alteration of enzymatic properties and structure when in the presence of metal ions. Compared to the other analytical methods, the electrochemical technique offers a number of remarkable advantages, e.g. rapidity, high sensitivity, cheap instrumentation and a simple operation procedure. It could satisfy many requirements to analyze different biological systems and be widely applied. In this article, based on our previous works [28–30], we reported the effects of Al(III) on the LDH activities under different conditions. Moreover, the influences of Pb(II), Cd(II) and Cr(III) on the LDH activities were also investigated. This study may help to understand not only the effects of Al(III) on enzyme reaction processes but also the impacts of conditions on the actions of Al(III).

2. Experimental

2.1. Materials and instrumentation

A three-electrode system was used, which consisted of a hanging mercury drop electrode (Jiangsu Electroanalytical Instrument Factory), a platinum foil counter electrode, and a saturated calomel reference electrode. All electrochemical experiments were performed with a CHI660B electrochemical system (CH Instruments Inc., Shanghai, China). The DPV parameters were: scan rate 20 mV/s, pulse amplitude = 50 mV, pulse width = 50 ms.

Most chemicals were obtained from Shanghai Chemical Reagent Factory and used as received unless otherwise noted. All chemicals were of analytical reagent grades. Bovine heart lactate dehydrogenase was obtained from Sigma Co. (St. Louis, MO, USA) which was diluted 100 times when used. β-NAD^+ and NADH (purity 90%) were purchased from Shanghai Bio Life Science & Technology Co., Ltd. (China). Pyruvic acid (Pyr, 98.50%) was of biological-reagent grade, purchased from Shanghai Chemical Reagent Factory. Al stock solution (0.01 mol/L) was prepared by dissolving super-purity Al powder (99.99%) in concentrated HCl solution and was diluted to the proper volume. The pH of Al stock solution was under 2, which could prevent the hydrolysis of the metal ion. The 0.01 mol/L Tris–HCl buffer solutions with different pH were prepared as the description in handbook. The supporting electrolyte is KCl (0.15 mol/L). All dilute solutions were prepared by diluting this solution with double-distilled water.

2.2. Procedures

2.2.1. Effects of Al(III) on lactate dehydrogenase activity in LDH reaction system

Twenty-five millilitres of Tris–HCl buffer solution was transferred into the electrolytic cell. The solution was degassed for 10 min by bubbling of nitrogen gas through it and kept in the ambient of nitrogen as well as at a constant temperature all through the experiment. After injecting LDH, the solution was stirred for 5 min (with or without Al(III)). Then Pyr (0.8 mmol/L) and NADH (0.2mmol/L) were added. The reduction currents of NAD^+ (i_{p,NAD^+}) and Pyr ($i_{p,\,Pyr}$) were recorded in DPV mode at regular time intervals. The effects of other metal ions were determined following the preceding procedures.

2.2.2. Determination of michaelis constant K_m and maximum velocity v_{max} for NADH

Twenty-five millilitres of Tris–HCl buffer solution was treated as Section 2.2.1. After injecting LDH, the solution was stirred for 5 min (with or without 0.04 mmol/L Al(III)). Then added Pyr (0.8 mmol/L) and NADH (the concentration was varied). The reduction currents of NAD^+ (i_{p,NAD^+}) were recorded in DPV mode. K_m and v_{max} for NADH were calculated by using the formula: $1/v = K_m/(v_{max}C_{NADH}) + (1/v_{max})$. The model of competitive inhibition means the substrate and inhibitor compete for the free enzyme. The model of non-competitive inhibition means the inhibitor not bound at the substrate-binding site and may complex both the free enzyme and enzyme–substrate complex. The model of uncompetitive inhibition means the inhibitor may combine only with the enzyme–substrate complex. Mixed inhibition type: If the intersection of Lineweaver-Burk plots lies in the upper x axis and left y axis, the inhibition contain both competitive and non-competitive character. The intersection of Lineweaver-Burk plots lies in the lower x axis and left y axis, the inhibition contains both non-competitive and uncompetitive character [31].

3. Results and discussion

3.1. The DPV response of LDH enzyme reaction system

In the LDH, NADH, Pyr system, only the substrates Pyr and NAD^+ yield electrochemical responses at hanging mercury drop electrode [32,33]. Without the addition of NADH, only the substrate Pyr produces the electrochemical response peak, whose potential is −1.38 V (versus SCE, pH 7.5). When NADH is added, the peak current of NAD^+ whose potential is −0.89 V (versus SCE, pH 7.5) is increasing continually while the peak current of Pyr is decreasing constantly along with the time (Fig. 1). The peak current of NAD^+ is increasing until it reaches at the platform after 18 min. Within the first 3 min of the enzyme reaction progress, there were positive linear relationships between the peak currents i_{p,NAD^+} and the time. According

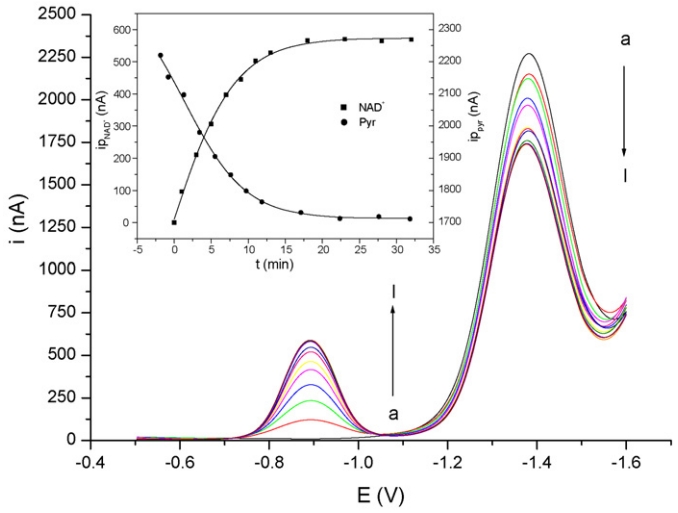

Fig. 1. The DPV responses of LDH reaction system changed with time, $T = 25 \pm 1$ °C. 0.10 mol/L Tris–HCl buffer solution (pH 7.5) + 0.15 mol/L KCl, 8.0×10^{-4} mol/L Pyr, 2.0×10^{-4} mol/L NADH and 30 μL LDH. a → l: $t = 0$, 1, 3, 5, 7, 9, 11, 13, 18, 23, 28, 32 min.

to that, the initial velocity (ν_0) is calculated and used to describe the enzymatic activity.

3.2. Effects of Al(III) on LDH activity

3.2.1. Effects of Al(III) on LDH enzyme reaction system with different use level of LDH

Effects of Al(III) on LDH activity with different use level of LDH are shown in Fig. 2. It can be seen that at low concentrations, Al(III) slightly stimulates LDH activity but inhibits the activity at high concentrations while adding 20 and 30 μL LDH in reaction system. Whereas, when adding 40 μL LDH, the influence of Al(III) on LDH activity only shows the inhibitory effect. Obviously, the levels of inhibition of LDH activity increase with elevating the concentration of LDH.

Table 1
The effects of Al(III) on K_m^{NADH} and ν_{max} of LDH with different use level of LDH ($T = 25 \pm 1$ °C, pH 7.5)

	Use level of LDH (μL)		
	20	30	40
$C_{Al(III)} = 0$ mol/L			
ν_{max} (μmol/(L min))	29.2	38.8	57.5
K_m^{NADH} (μmol/L)	87.7	85.7	86.8
$C_{Al(III)} = 4 \times 10^{-5}$ mol/L			
ν_{max} (μmol/(L min))	25.4	28.8	31.5
K_m^{NADH} (μmol/L)	161	107	99.1

In contrast to the values of K_m^{NADH} and ν_{max} in the absence and presence of 0.04 mmol/L Al(III) with different concentrations of LDH (Table 1), it is noted that the inhibitory type of Al(III) are all of a competitive–non-competitive mixed type [34] with different concentrations of LDH.

3.2.2. Effects of Al(III) on LDH enzyme reaction system at different pH values

Fig. 3 indicates that the influences of Al(III) on LDH activity changed with the solution pH values. When pH is 7.5 and 8.5, LDH activities show a trend to increase at low Al(III) concentrations and decrease at higher ones. However, only the decline in the activity of LDH is observed at pH 6.7. It is worth noting that the levels of inhibition of LDH activity increase with the decrease of pH, especially at pH 6.7, the inhibitory effect of Al(III) enhances greatly. This difference caused by pH is probably due to the fact that the dominant species of Al vary with pH. When pH descends, the cation species of Al increase and become dominant [17,19,22]. These cation species have more effective interaction with the ionization enzyme at low pH. This pH dependence of metal ions inhibition was similar to the results observed in previous research [35].

The values of K_m^{NADH} and ν_{max} in the absence and presence of 0.04 mmol/L Al(III) at different pH are given in Table 2,

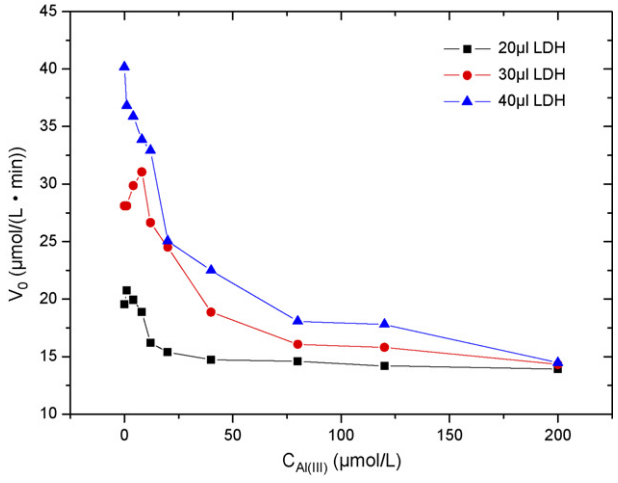

Fig. 2. The effects of Al(III) on the LDH activity with different use level of LDH. $C_{Al(III)} = (0, 0.10, 0.40, 0.80, 1.2, 2.0, 4.0, 8.0, 12, 20) \times 10^{-5}$ mol/L. Other experimental conditions are the same as in Fig. 1.

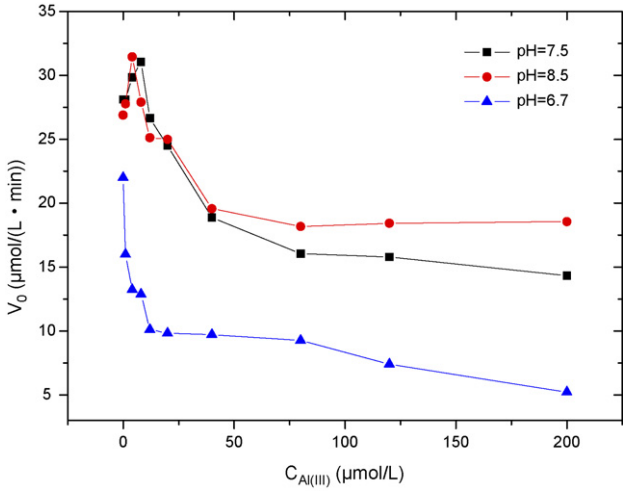

Fig. 3. The effects of Al(III) on the LDH activity at different pH. $C_{Al(III)} = (0, 0.10, 0.40, 0.80, 1.2, 2.0, 4.0, 8.0, 12, 20) \times 10^{-5}$ mol/L Al(III). Other experimental conditions are the same as in Fig. 1.

Table 2
The effects of Al(III) on K_m^{NADH} and ν_{max} of LDH at different pH (30 μL LDH, $T = 25 \pm 1$ °C)

	pH		
	6.7	7.5	8.5
$C_{Al(III)} = 0$ mol/L			
ν_{max} (μmol/(L min))	37	38.8	37.7
K_m^{NADH} (μmol/L)	129	85.7	94.3
$C_{Al(III)} = 4 \times 10^{-5}$ mol/L			
ν_{max} (μmol/(L min))	12.9	28.8	30.1
K_m^{NADH} (μmol/L)	86.6	107	77.1

Table 3
The effects of Al(III) on K_m^{NADH} and ν_{max} of LDH at different temperatures (30 μL LDH, pH 7.5)

	Temperature (°C)		
	15	25	37
$C_{Al(III)} = 0$ mol/L			
ν_{max} (μmol/(L min))	33.8	38.8	221
K_m^{NADH} (μmol/L)	75.6	85.7	500
$C_{Al(III)} = 4 \times 10^{-5}$ mol/L			
ν_{max} (μmol/(L min))	22.1	28.8	64.5
K_m^{NADH} (μmol/L)	70.5	107	207

indicating that the inhibitions caused by Al(III) are all of mixed type [34]. However, it is a competitive–non-competitive mixed type at pH 7.5 and a non-competitive–uncompetitive mixed type at pH 6.7 and 8.5 [34], respectively.

3.2.3. Effects of Al(III) on LDH enzyme reaction system at different temperatures

As shown in Fig. 4, temperature also plays an important role in the effects of Al(III) on LDH activity. The influences of Al(III) on the LDH activity exhibit two kinds of behaviors at different temperatures, i.e. only show inhibitory effect at 15 and 37 °C and slightly increase LDH activity at low concentrations and inhibits at high concentrations at 25 °C. The levels of inhibition of LDH almost do not change from 15 to 25 °C, but at a higher temperature, it increases rapidly. The reason for this probably is that the high temperature not only makes the reaction rate of enzyme reaction increase but also enhances the interaction between Al(III) and LDH. Moreover, it is widely accepted that enzyme is unstable at high temperature, which may promote the Al(III) to affect LDH.

The values of K_m^{NADH} and ν_{max} in the absence and presence of 0.04 mmol/L Al(III) at different temperature are displayed in Table 3. The types of the inhibition of Al(III) vary with temperature: a competitive–non-competitive mixed type [32] at 25 °C and a non-competitive–uncompetitive mixed type [34] at 15 and 37 °C.

3.2.4. Effects of Al speciation on LDH activities

Speciation is important because not all chemical forms of Al are equally toxic. In our researches, the effects of different Al speciation on molecular level are carried out. Fig. 5 shows that the Al-fluoride complexes and Al-citrate complexes almost have no effects on LDH activities (the citrate and F^- have weak activate effects on the activity of LDH under the same condition), whereas Al-OH complexes have much more influences. This result was similar to conclusions coming out from the effects of Al speciation on animals, plants, methanotroph and cell mechanisms [22,36,37]. Those reports shown that Al-F and Al-Org complexes may greatly reduce the Al's toxicity whereas the Al-OH complexes induce the most damaging influences and have changeful toxicity.

3.3. Comparison of effects of Al(III) with Pb(II), Cd(II) and Cr(III) on the LDH activities

The alteration of the LDH activities with the addition of Pb(II), Cd(II) and Cr(III) are also inspected. Fig. 6 indicates that the Pb(II) and Cd(II) have weak inhibitory effects on LDH activities, while Cr(III) can activate the activity of LDH when

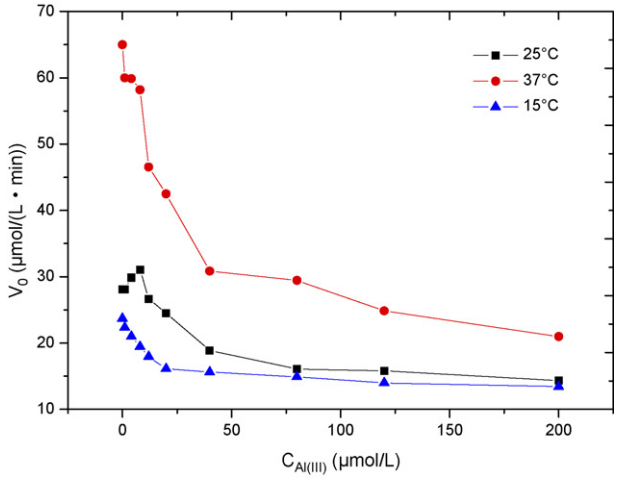

Fig. 4. The effects of Al(III) on the LDH activity at different temperature. $C_{Al(III)} = (0, 0.10, 0.40, 0.80, 1.2, 2.0, 4.0, 8.0, 12, 20) \times 10^{-5}$ mol/L. Other experimental conditions are the same as in Fig. 1.

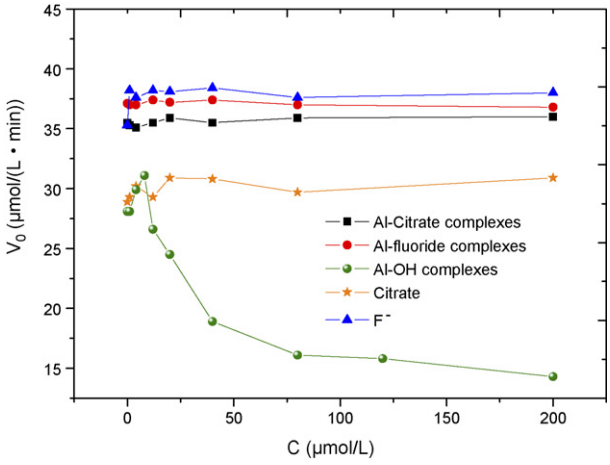

Fig. 5. The effects of Al species on LDH activities. $C = (0, 0.10, 0.40, 0.80, 1.2, 2.0, 4.0, 8.0, 12, 20) \times 10^{-5}$ mol/L. Other experimental conditions are the same as in Fig. 1.

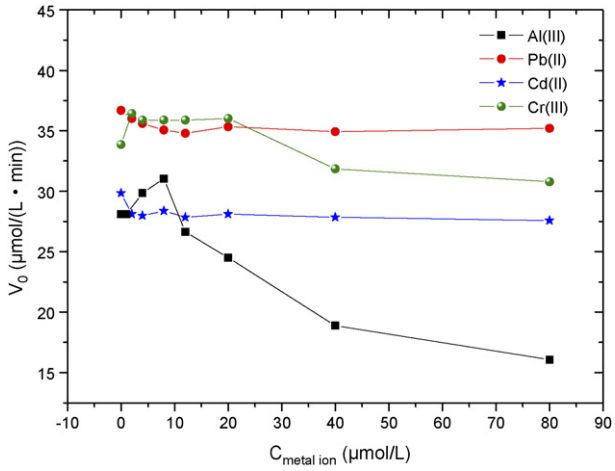

Fig. 6. The effects of four metal ions (Al(III), Pb(II), Cd(II) and Cr(III)) on the LDH activities. $C_{\text{metal ions}} = (0, 0.10, 0.40, 0.80, 1.2, 2.0, 4.0, 8.0) \times 10^{-5}$ mol/L. Other experimental conditions are the same as in Fig. 1.

the concentrations are under 40 μmol/L and then restrain when concentrations are over 40 μmol/L. Under the same condition, Al(III) has stronger influence on the LDH activity than Pb(II), Cd(II) and Cr(III). The mechanism for the different influence on the LDH caused by those metal ions might be due to the distinct chemical property of each metal ion, which may make them have varying binding sites on the enzyme and dissimilar interact with enzyme [35,36].

Acknowledgements

This project supported by the Natural Science Foundation of Jiangsu Province (BK 2005083), Grant of analytical Measurements of Nanjing University, National Science Foundation of China (No. 20575025) and Research Funding for the Doctoral Program of Higher Education (No. 20050284030).

References

[1] S. Polizzi, E. Pira, M. Ferrara, M. Bugiani, A. Papaleo, R. Albera, S. Palmi, Neurotoxicology 23 (2002) 761.
[2] A. Campbell, Nephrol. Dial. Transpl. 17 (Suppl.) (2002) 17.
[3] T.P. Flaten, Brain Res. Bull. 55 (2001) 187.
[4] H.H. Malluche, Nephrol. Dial. Transpl. 17 (Suppl.) (2002) 21.
[5] D. Orihuela, V. Meichtry, M. Pizarro, J. Inorg. Biochem. 99 (2005) 1879.
[6] P. Zatta, T. Kiss, M. Suwalsky, G. Berthon, Coord. Chem. Rev. 228 (2002) 271.
[7] M. Suwalsky, B. Ungerer, F. Villena, B. Norris, H. Cardenas, P. Zatta, Brain Res. Bull. 55 (2001) 205.
[8] Z. Rengel, Biometals 17 (2004) 669.
[9] P.F. Zatta, D. Cervellin, P. Zambenedetti, Toxicol. in Vitro 12 (1998) 287.
[10] V.S. Silva, A.I. Duarte, A.C. Rego, C.R. Oliveira, P.P. Goncalves, Toxicol. Sci. 88 (2005) 485.
[11] R. Dua, K.D. Gill, BBA-Gen. Subjects 1674 (2004) 4.
[12] V.S. Silva, P.P. Goncalves, J. Inorg. Biochem. 97 (2003) 143.
[13] D. Orihuela, V. Meichtry, N. Pregi, M. Pizarro, J. Inorg. Biochem. 99 (2005) 1871.
[14] M.I. Yousef, Toxicology 199 (2004) 47.
[15] P. Zatta, E. Lain, C. Cagnolini, Eur. Biochem. J. 267 (2000) 3049.
[16] P. Zatta, A. Taylor, P. Zambenedetti, R. Milacic, P. dell' Antone, Life Sci. 66 (2000) 2261.
[17] M.J. Gardner, E. Dixon, I. Sims, P. Whitehouse, Bull. Environ. Contam. Toxicol. 68 (2002) 195.
[18] R.W. Gensemer, R.C. Playle, Crit. Rev. Environ. Sci. Technol. 29 (1999) 315.
[19] G. Guibaud, C. Gauthier, J. Inorg. Biochem. 99 (2005) 1817.
[20] J.E. Amonette, C.K. Russell, K.A. Carosino, N.L. Robinson, J.T. Ho, Appl. Environ. Microb. 69 (2003) 4057.
[21] S.P. Bi, Environ. Geol. 40 (2001) 300.
[22] G. Sposito, The Environmental Chemistry of Aluminium, 2nd ed., CRC Press/Lewis Publishers, 1996, p. 464.
[23] M. Monteiro, C. Quintaneiro, M. Pastorinho, M.L. Pereira, F. Morgado, L. Guilhermino, A.M.V.M. Soares, Chemosphere 62 (2006) 1333.
[24] J.A. Almeida, Y.S. Diniz, S.F.G. Marques, L.A. Faine, B.O. Ribas, R.C. Burneiko, E.L.B. Novelli, Environ. Int. 27 (2002) 673.
[25] X.X. Gao, X.Q. Wang, Chin. J. Anal. Chem. 26 (1998) 757.
[26] X.Q. Wang, X.X. Gao, Chem. J. Chin. Univ. 19 (1998) 543.
[27] X.Q. Wang, X.X. Gao, Chem. J. Chin. Univ. 18 (1997) 1027.
[28] F.P. Zhang, S.P. Bi, H.Z. Li, Y.J. Chen, L.M. Dai, Electroanalysis 13 (2001) 1054.
[29] J.W. Di, F. Zhang, M. Zhang, S.P. Bi, Electroanalysis 16 (2004) 644.
[30] L. Yang, Z.B. Yang, M. Zhang, H.Y. Ni, M. Ji, Y.Z. Tang, X.D. Yang, X.F. Long, S.P. Bi, Electroanalysis 16 (2004) 1051.
[31] Y.Z. Li, W.B. Chang, Biochemical Analysis, Higher Education Press, Beijing, 2003, pp. 6–14.
[32] C.O. Schmakel, K.S.V. Santhanam, P.J. Elving, J. Am. Chem. Soc. 97 (1975) 5083.
[33] W.T. Bresnahan, P.J. Elving, J. Am. Chem. Soc. 103 (1981) 2379.
[34] Q.S. Yuan, Modern Enzymology, East China University of Science and Technology Press, Shanghai, 2001, pp. 31–44.
[35] K.S. Larsen, D.S. Auld, Biochemistry 28 (1989) 9620.
[36] T.N.C. Wells, F. Coulin, M.A. Payton, A.E.I. Proudfoot, Biochemistry 32 (1993) 1294.
[37] M. Suwalsky, B. Norris, T. Kiss, P. Zatta, Coord. Chem. Rev. 228 (2002) 285.

Available online at www.sciencedirect.com
ScienceDirect
Talanta 73 (2007) 523–528
Talanta
www.elsevier.com/locate/talanta

Preparation of photocatalytic nano-ZnO/TiO_2 film and application for determination of chemical oxygen demand

Zhonghai Zhang, Yuan Yuan, Yanju Fang, Linhong Liang, Hongchun Ding, Litong Jin *

Department of Chemistry, East China Normal University, Zhongshan Road North 3663, Shanghai 200062, China

Received 21 December 2006; received in revised form 10 April 2007; accepted 13 April 2007
Available online 22 April 2007

Abstract

A composite nano-ZnO/TiO_2 film as photocatalyst was fabricated with vacuum vaporized and sol–gel methods. The nano-ZnO/TiO_2 film improved the separate efficiency of the charge and extended the range of spectrum, which showed a higher efficiency of photocatalytic than the pure nano-TiO_2 and nano-ZnO film. The photocatalytic mechanism of nano-ZnO/TiO_2 film was discussed, too. A new method for determination of low chemical oxidation demand (COD) value in ground water based on nano-ZnO/TiO_2 film using the photocatalytic oxidation technology was founded. This method was originated from the direct determination of the Mn(VII) concentration change resulting from photocatalytic oxidation of organic compounds on the nano-ZnO/TiO_2 film, and the COD values were calculated from the absorbance of Mn(VII). Under the optimal operation conditions, the detection limit of 0.1 mg l^{-1}, COD values with the linear range of 0.3–10.0 mg l^{-1} were achieved. The results were in good agreement with those from the conventional COD methods.

Keywords: Chemical oxygen demand; Photocatalytic oxidation; Nano-ZnO/TiO_2 film; $KMnO_4$

1. Introduction

Over past few decades, there have been significant advances in the development of photocatalyst based on the immobilization of the metal oxide semiconductor thin film [1–4]. TiO_2, because of its excellent chemical and photochemical stability, non-toxic, and capable of photooxidative destruction of most organic pollutants [5–7], has a wide range of technologically relevant applications such as gas sensors, photo and thermal catalysis, photoelectrocatalysis [8–10]. Unfortunately, the low degradation efficiency of nano-TiO_2 film limited the application of the TiO_2 as photocatalyst because of the easily recombination of photogenerated electrons and holes. It is an available way of the composite of nano-semiconductor to improve the photocatalytic efficiency [11–15].

The composite nano-semiconductor promoted the separate efficiency of photogenerated charge and extended the range of excite spectrum, which improved the photocatalytic efficiency. In this work, the nano-TiO_2 film and nano-ZnO film formed a new composite nanofilm, nano-ZnO/TiO_2 film, which fabricated with vacuum vaporized and sol–gel methods. The nano-ZnO/TiO_2 film as photocatalyst degraded the organic pollution in water would show higher photocatalytic efficiency than the efficiency of pure nano-ZnO film and nano-TiO_2 film.

Chemical oxygen demand (COD) is one of the most important parameters and has been widely employed for water quality assessment. Because the degradation of organic compounds requires oxygen, the quantity that they are present in a water sample can be estimated by the amount of oxygen necessary for their oxidation [16–21]. Thus, COD was preferred for estimating organic pollution of water. The conventional method for COD determination was based on a measure of the oxygen consumed in the oxidation of organic compounds by strong oxidizing agents such as dichromate or permanganate [22]. Despite widely spread application, the traditional method had several drawbacks: 2 h degradation process under high pressure and temperature, requirement of expensive (Ag_2SO_4), highly corrosive (H_2SO_4), and toxic ($HgSO_4$ and $Cr_2O_7^{2-}$). Consequently, the secondary pollution is unavoidable when the conventional method is employed. In addition, the conventional method with the sensitivity of approximately 10 mg l^{-1}, which has large error when determining the low COD values, not suitable for

* Corresponding author. Tel.: +86 21 62232627; fax: +86 21 62232627.
E-mail address: ltjin@chem.ecnu.edu.cn (L. Jin).

0039-9140/$ – see front matter © 2007 Elsevier B.V. All rights reserved.
doi:10.1016/j.talanta.2007.04.011

the determination of the tap water, spring water and reservoir water.

Many articles have reported that the photocatalytic technology have been applied to detect the COD value, while because of the above mentioned reason of easily recombination of photogenerated electrons and holes caused the low photocatalytic efficiency [23–27]. So, the composite nano-ZnO/TiO_2 was fabricated to improve the photocatalytic efficiency. Furthermore, the immobilization of ZnO/TiO_2 film is more convenient than the suspension of the nanoparticles.

In this paper, we attempt to introduce Mn(VII) into ZnO/TiO_2 photocatalytic system as an electron scavenger, thus, a new COD measurement method using a nano-ZnO/TiO_2–Mn(VII) coexisted system is proposed. The measurement principle is based on the direct determination of concentration change of Mn(VII) during photocatalytic oxidation of organic compounds in ground water.

2. Experimental

2.1. Reagents

Titanium isopropoxide (Shandong Qilu Plasticizers Co. Ltd., China) was used to prepare the sol–gel for TiO_2 film preparation. Pure Zn powder (Shanghai Chemical Reagent Company) was used to prepare the Zn film. D-Glucose (analytical reagent, TorLin Chemicals Co., China) was used as a standard compound to study the photocatalytic characteristics of the sensor. All other chemicals were of analytical reagent grade (Shanghai Chemical Reagent Company) without further purification. Doubly distilled deionized water was used for all solution. KOH and H_2SO_4 were used to adjust pH value of the reaction solution. All real samples used for this study were collected from river and tap water, in Shanghai, China. All samples were preserved according to the guideline of the conventional method. The same sample was subject to the analysis by both the conventional permanganate COD method and this proposed method.

2.2. Preparation of nano-ZnO/TiO_2 film photocatalyst

The quartz tube (height: 6 cm, inner radius: 2.5 cm) was thoroughly cleaned in hot sulfuric acid overnight, and then it was ultrasonicated thoroughly with acetone, finally rinsed with distilled water and dried under ambient conditions. A thin symmetrical film of zinc was vaporized in the high vacuum film plating table (Shanghai Electron Optical Technology Institute, Model: DM 220) and was covered on the inner and outer surface of quartz tube. The nano-ZnO film was fabricated that the quartz tube with a film of zinc calcined at 500 °C for 1 h in a muffle furnace.

The TiO_2 sol was prepared according to the method described by Takahashi et al. [28], where Ti(i-OC_3H_7)$_4$ was first diluted with absolute ethanol, nitric acid and ethanol were mixed together and used as the acidic catalyst for hydrolysis of Ti(i-OC_3H_7)$_4$. The acidic solution was added dropwise to the Ti(i-OC_3H_7)$_4$-ethanol solution, then the solution was stirred for 30 min at 0 °C. The final compositions of coating solution was Ti(i-OC_3H_7)$_4$:H_2O:C_2H_5OH:HNO_3 = 1:1:10:0.2. The TiO_2 film was prepared by dip-coating of the quartz tube coved with ZnO film support into the TiO_2 sol and aged for *ca.* 5 min. The film was calcined at 500 °C for 1 h at muffle furnace, and the composite nano-ZnO/TiO_2 film was prepared.

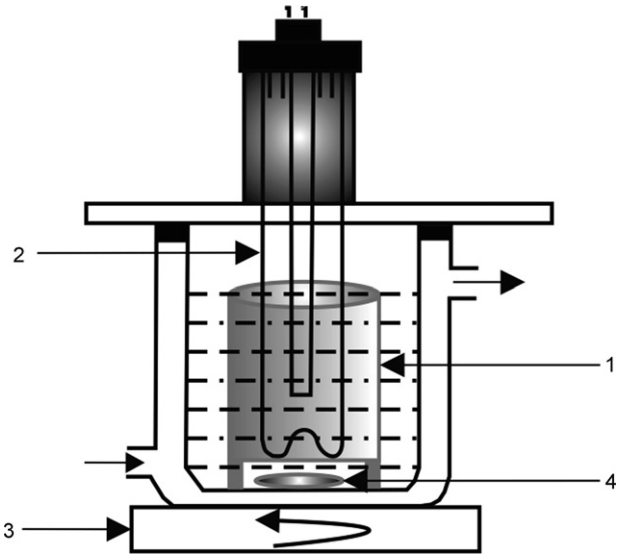

Fig. 1. Schematic diagram of the photocatalytic reactor. 1: quartz tube with nano-ZnO/TiO_2 film, 2: UV lamp, 3: magnetic stirrer, 4: stirrer.

2.3. Device

A bath reactor system was used to perform the photocatalytic reaction. As shown in Fig. 1, a quartz tube with nano-ZnO/TiO_2 film was placed at the center of the reactor. The reaction mixture inside the reactor was maintained by means of a magnetic stirrer. A UV irradiator with an 11 W lamp (Shanghai Jinguang Lamps Factory) at the center of the quartz tube was used as the UV source and the reactor was equipped with a water jacket to maintain constant temperature.

The absorbance change caused by a decrease in potassium permanganate ($KMnO_4$) concentration was measured by a UV spectrophotometric detector (Varian Corp., Model Cary 50) and operated at 525 nm, and the initial concentration of Mn(VII) with 5×10^{-4} mol l^{-1} was selected.

2.4. Experimental procedure

The sample solution and $KMnO_4$ solution were added to the reactor. The reactor was water-jacket to maintain constant temperature and magnetic stirring was used throughout the experiment. The pH value of the solution was maintained at a desired level with KOH and H_2SO_4 and monitored by a Kyoto AT-400 autotitrator. The total volume of reaction system was maintained at 40 ml for each experiment. When the UV lamp was turned on (λ_{max} = 253.7 nm), photocatalytic oxidation of the organic compounds began to occur, accompanying an decrease of Mn(VII) concentration. The absorbance of Mn(VII) was determined at 525 nm with a UV spec-

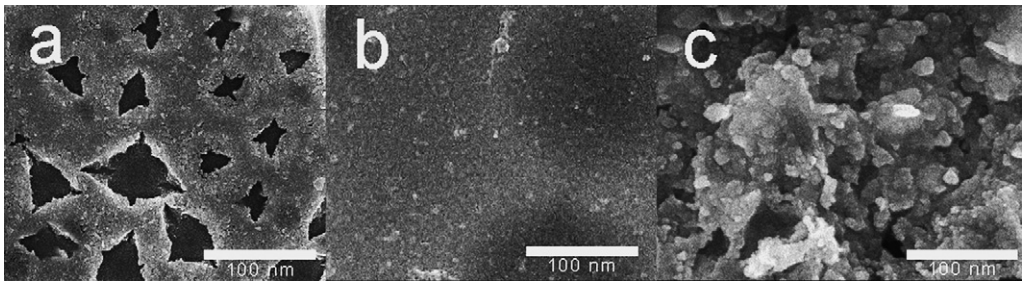

Fig. 2. SEM images of nano-ZnO/TiO_2 film: (a) TiO_2 film, (b) ZnO film, (c) ZnO/TiO_2 film.

trophotometric detector. All measurements were repeated three times.

For preparing a COD calibration, different volume of glucose was stepwise added to the reactor and the corresponding absorbance of Mn(VII) was determined. Then, the COD calibration graph of the absorbance of Mn(VII) versus COD was obtained.

3. Results and discussion

3.1. Characteristics of nano-ZnO/TiO_2 film

3.1.1. Morphology of ZnO/TiO_2 film

The morphology of ZnO/TiO_2 film was characterized using scanning electron microscopy (SEM, JEOL FE-SEM JSM-6700F) with an accelerating voltage of 20 KV. Fig. 2a–c were the SEM images of nano-TiO_2 film, nano-ZnO film and nano-ZnO/TiO_2 film, respectively. We can see more nanoparticles appeared in the ZnO/TiO2 film, and the average nanoparticles diameter of nano-ZnO/TiO_2 was 30 nm. The surface area of nano-ZnO/TiO_2 film was obvious larger than that of nano-ZnO film and nano-TiO_2 film.

3.1.2. XRD analysis

The crystallinity of ZnO/TiO_2 film was determined by X-ray diffraction (XRD) using a diffractometer with Cu K_α radiation (Model, D/max 2550 V). Fig. 3 was the XRD profiles of the TiO_2 film, ZnO film and ZnO/TiO_2 film prepared in this work, respectively. As shown in figure, the anatase phase was dominant corresponding to 25.3°, there was no rutile or any other phase in Fig. 3. The ZnO was main appeared with hexagonal crystal system.

3.1.3. UV–vis analysis

Light absorption properties were measured using a UV–vis spectrophotometer (Varian Corp., Model Cary 50) with a wavelength range of 200–600 nm. As shown in Fig. 4, the UV–vis adsorption spectrum indicated the maximum adsorption wavelengths of TiO_2 film, ZnO film and ZnO/TiO_2 film were 280, 360 and 380 nm, respectively. The significant red-shift with lower band energy of ZnO/TiO_2 film comparing with the ZnO film and TiO_2 film may be owing to the differences in the surface state. The ZnO/TiO_2 film need lower energy to be excited than the ZnO film and TiO_2 film, which improve the using efficiency of irradiation energy.

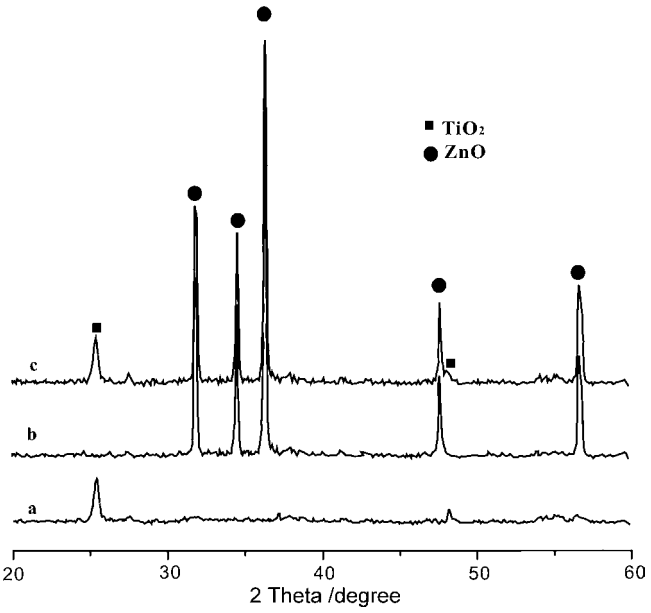

Fig. 3. X-ray diffraction patterns of nano-ZnO/TiO_2 film. (a) TiO_2 film; (b) ZnO film; (c) ZnO/TiO_2 film.

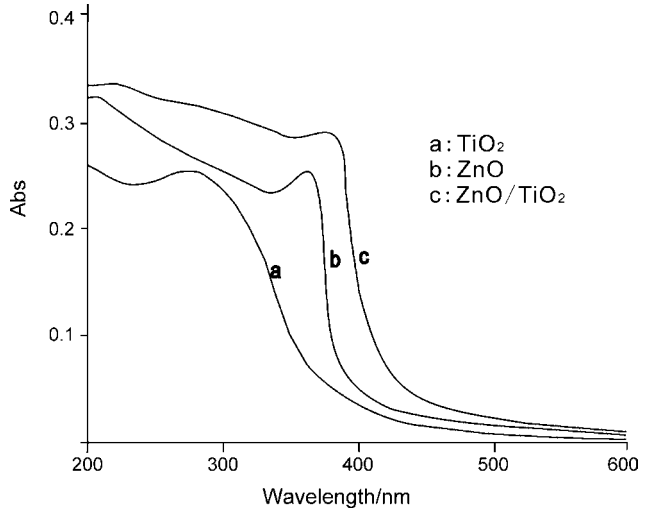

Fig. 4. UV–vis spectra of (a) nano-TiO_2 film, (b) nano-ZnO film, (c) nano-ZnO/TiO_2 film.

3.2. Photocatalytic mechanism of nano-ZnO/TiO_2 photocatalyst

The composite of nano-semiconductor is an alternative way to improve the photocatalytic efficiency. In essentially, the composite of nano-semiconductor is looked as the modification of one particle to another particle. The ZnO/TiO_2 film excited by photons with energy higher than the gap energy (E_g), a great number of electrons are promoted from valence band (VB) to the conduction band (CB) of ZnO and TiO_2, leading to the generation of electron/hole (e^-/h^+) pairs. The electrons transfer from the CB of TiO_2 to the CB of ZnO, and conversely, the holes transfer from the VB of ZnO to the VB of TiO_2 give rise to decrease the pairs' recombination rate [29]. The charge transport in the ZnO/TiO_2 film is no doubt a key step for further increasing the photocatalytic efficiency. Though the ZnO possesses an energy band similar to that of TiO_2, it still plays an important role in electron transport. The flatband potential (V_{fb}) is positively shifted by 0.12 V after the ZnO modified the TiO_2 film [30]. Obviously, the energy level for electron injection is decreased after TiO_2 film cover the surface of ZnO film, which increases the driving force for electron injection and hence reduce recombination between electrons and holes. On the other hand, ZnO can increase concentration of free electrons in the CB of TiO_2, this result implies that the charge recombination is reduced in the process of electron transport. All above of results increase the availability of the pairs on the surface of the photocatalyst and consequently an improvement of the occurrence of redox processes can be expected.

Fig. 5 demonstrated the oxidative ability of the different photocatalysts. Under the settled conditions, glucose oxidation efficiency of the no photocatalyst just UV irradiation, ZnO film, TiO_2 film and ZnO/TiO_2 film were studied, respectively. From Fig. 5, the ZnO/TiO_2 film was shown a higher oxidation efficiency of glucose than that of pure ZnO film and TiO_2 film. Therefore, it can be concluded that the nano-ZnO/TiO_2 film can largely enhance the photcatalytic efficiency of degradation the organic compounds, and thus, the determination time is shortened and the sensitivity is increased.

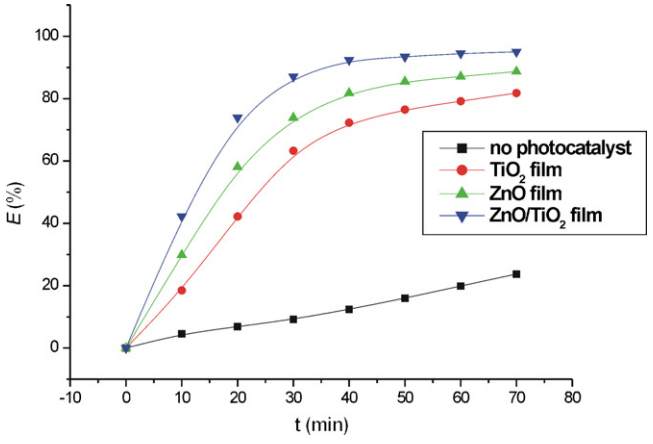

Fig. 5. Glucose oxidation efficiency (E) with different photocatalysts. Conditions: pH, 5.6; Mn(VII), 5×10^{-4} mol l^{-1}; T, 50 °C; COD, 5 mg l^{-1}.

3.3. Optimization of operation conditions

3.3.1. Selection of the electron scavenger and its initial concentration

Suitable oxidizing agent should be selected as the electron scavenger to prevent the recombination of the photogenerated electrons and holes. In this work, potassium permanganate was chose as a suitable candidate and appeared to have a great promise. According to the redox potential of Mn(VII), $E^{\theta} = 1.33$ V, Mn(VII) was strong enough as an oxidizing agent. Therefore, it was faster for the nano-ZnO/TiO_2–$KMnO_4$ synergic system to degrade the organic compounds, which only take 20 min for photocatalytic oxidization.

The effect of the initial concentration of Mn(VII) on the photocatalytic determination of COD by the UV–ZnO/TiO_2 process was studied. The results were shown in Fig. 6. The absorbance of Mn(VII) increases with the increasing concentration of Mn(VII) up to, the increase seemed to change more slowly for higher Mn(VII) concentration. So 5×10^{-4} mol l^{-1} was selected as the initial concentration of Mn(VII).

3.3.2. Selection of pH value

The effect of pH on the photocatalytic oxidation of organic compounds using nano-ZnO/TiO_2 film as photocatalyst was investigated and the results have been shown in Fig. 7. The absorbance of Mn(VII) increases with decreasing pH at a fixed COD value of 5 mg l^{-1}, which shows that the photocatalytic oxidation of organic compounds increases with the lowering of the pH value. The point of zero charge (PZC) of ZnO and TiO_2 are about 6–9 and 5.8–6.3 [31–33], respectively, so, at pH < 6, the surface is electropositive, which favors the adsorption of Mn(VII) anions. Hence, the oxidation rate of organic compounds increases with decreasing pH. But if the acidity of solution becomes too great, the ZnO as an amphoteric metal oxide cannot exist, and the homogeneous catalysis reaction where organic compounds are directly oxidized by $KMnO_4$ will become evident. Consequently, pH 5.6 was selected for further experiments.

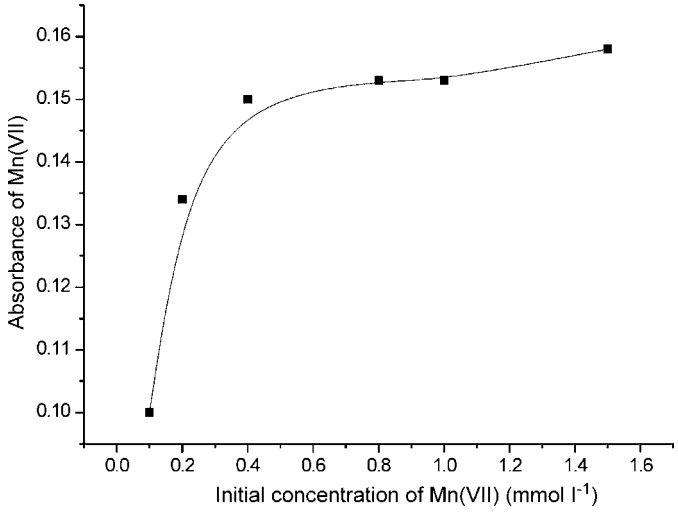

Fig. 6. Effect of initial of Mn(VII) concentration on the absorbance. Conditions: pH, 5.6; T, 50 °C; t, 20 min; COD, 5 mg l^{-1}.

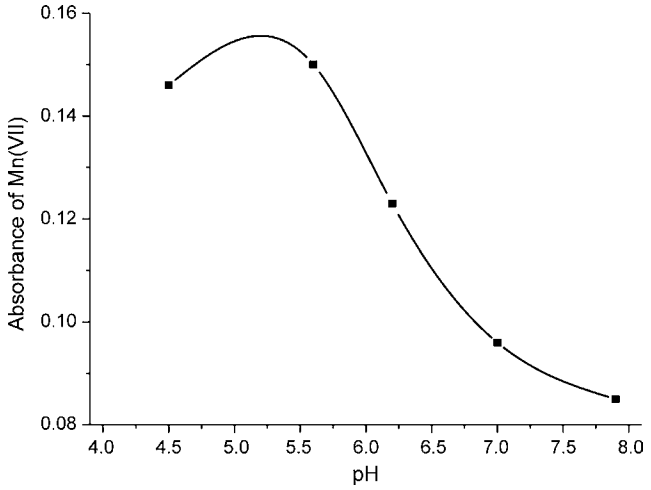

Fig. 7. Effect of the value of pH on the photocatalytic oxidation reaction. Conditions: Mn(VII), 5×10^{-4} mol l^{-1}; T, 50 °C; t, 20 min; COD, 5 mg l^{-1}.

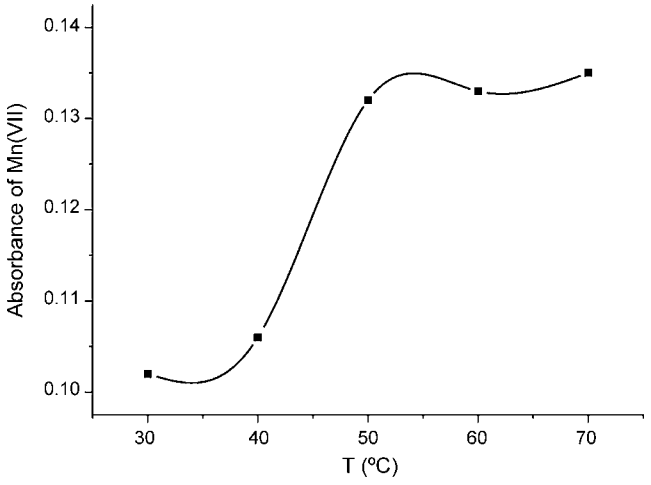

Fig. 8. Effect of temperature on absorbance. Conditions: pH, 5.6; Mn(VII), 5×10^{-4} mol l^{-1}; t, 20 min; COD, 5 mg l^{-1}.

3.3.3. Selection of temperature

The effect of temperature on the photocatalytic determination of COD was studied and the results have been shown in Fig. 8. The absorbance of Mn(VII) increased with increasing temperature in the range of 30–70 °C. Because of the increase of the collision frequency between ZnO/TiO_2 film and the substrates, the oxidative rate increase with increasing temperature. When the temperature exceeded 50 °C, the absorbance was increased slowly, and the reproducibility was decreased under very high temperature due to the evaporation. Hence, 50 °C was selected for further experiments.

3.3.4. Influence of chloride

The most significant interference with the determination of COD is duo to chlorides, since the mercury (II) sulfate and/or silver sulfate is added to avoid the determination error. Here, the inference from chloride was investigated under the optimum operation conditions using the standard solution (5 mg l^{-1} COD) containing chloride levels between 0 and 1000 mg l^{-1}. It is found that up to 1000 mg l^{-1} Cl^- does not show any influence on the results without the need for the addition of mercury (II) sulfate and silver sulfate, when Mn(VII) is used as an oxidant.

3.4. Reproducibility and stability of the nano-ZnO/TiO_2 film

It is desirable for the photocatalyst to have good reproducibility and stability. The reproducibility of the nano-ZnO/TiO_2 film to 5.26 mg l^{-1} (COD_{Mn}) of D-Glucose solution was studied using repeated determination ($n = 10$), and evaluated by the relative standard deviation of absorbance changes. This gave a relative standard derivation of 2.81%, indicating that the photocatalyst has a good reproducibility. The stability, that is the life of the composite film on the determination of the glucose solution (COD_{Mn} 5.26 mg l^{-1}) was also investigated during a period of 15 days. The absorbance change of the film to 15 samples did not show any apparent change with a relative standard deviation of 2.35%. Between measurements, the electrodes were stored in deionized water at room temperature.

3.5. Calibration graphs for COD and the limit of detection

Calibration graph of COD was produced by using glucose at various concentrations. Under the optimum experimental conditions described above, the calibration graph of the absorbance of Mn(VII) versus the concentration of the standard solution was linear in the range of 0.25–10.0 mg l^{-1}. The linear regression equations and correlation coefficient were $A = 0.0318$ COD + 0.3046 and 0.9979. According to IUPAC, the limit of detection (LOD) was determined from three times the standard deviation of the blank signal (3σ, $n = 10$) as 0.1 mg l^{-1}.

3.6. Determination of real samples

Real samples taken from various types of groundwater were analyzed by the proposed method. The real sample can be diluted

Table 1
Comparison between the permanganate index method and the proposed method for COD determination

Sample	COD determined by this method/(mg l^{-1})	R.S.D. (%) $n = 10$	COD determined by Permanganate index/(mg l^{-1})	R.S.D. (%) $n = 10$
Sample 1	8.52	2.1	8.47	1.6
Sample 2	1.43	3.0	1.54	2.2
Water of Huangpu River	6.75	3.2	6.87	3.6
Tap water of Pudong	3.56	2.5	3.69	4.7
Tap water of Puxi	2.12	3.4	2.23	3.8

before determination, if the COD value of the real sample is over $10\,mg\,l^{-1}$. The compared result for five groundwater samples obtained by the proposed method and those obtained by the conventional method (permanganate index method) [22] were given in Table 1 and the correlation was satisfactory. The regression equation and correlation coefficient were $y = 1.0173x - 0.1627$ and $r = 0.999$ ($n = 10$), respectively, where y and x denoted the results obtained using the proposed method and the conventional method, respectively. The comparison indicated that the two methods were agreed very well.

4. Conclusions

A simple and rapid analytical method for the evaluation of low COD has been proposed, based on composite nano-ZnO/TiO_2 film photocatalytic oxidation organic compounds in water. The composite nano-ZnO/TiO_2 film as photocatalyst was fabricated with vacuum vaporized and sol–gel methods, and the characteristic of the nano-ZnO/TiO2 film was performed with SEM, XRD and UV–vis adsorption spectrum. The photocatalytic mechanism of nano-ZnO/TiO_2 film was discussed, which seemed that the ZnO in the nano-ZnO/TiO_2 film played an important role in the electrons transport, enhanced the separation of the photogenerated electrons and the holes, which improved the photocatatic oxidation efficiency to the organic compounds. The optimization of operation conditions was studied. Under the mild conditions, a good calibration graph for COD values between 0.3 and $10\,mg\,l^{-1}$ was obtained. This method was sensitive, capable of detecting as low as $0.1\,mg\,l^{-1}$ COD. When using this method to determine the real samples, it displayed some advantages, such as short analysis time, simplicity, and no requirement of expensive and toxic reagents. Additionally, results obtained by the method were in good agreement with the values obtained by the conventional method. Thus, it showed a promising prospect for determining the low COD values of the ground waters.

Acknowledgement

This work is supported by the National Natural Science Foundation of the People's Republic of China (No. 20327001).

References

[1] W.J. Zhang, Y.Q. He, Q. Qi, Mater. Chem. Phys. 93 (2005) 508.
[2] N. Negishi, K. Takeuchi, T. Ibusuki, Appl. Surf. Sci. 121 (1997) 417.
[3] R.S. Sonawane, S.G. Hegde, M.K. Dongare, Mater. Chem. Phys. 77 (2002) 744.
[4] M.C. Yang, T.S. Yang, M.S. Wong, Thin Solid Films 469 (2004) 1.
[5] J.A. Navio, C. Cerrillos, M.A. Pradera, E. Morales, J.L. Gomez-Ariza, Langmuir 14 (1998) 388.
[6] K.T. Ranjit, I. Willner, J. Phys. Chem. B 102 (1998) 9397.
[7] I. Poulios, M. Kositzi, A. Kouras, J. Photochem. Photobiol. A: Chem. 115 (1998) 175.
[8] C.P. Chang, J.N. Chen, M.C. Lu, H.Y. Yang, Chemosphere 58 (2005) 1071.
[9] S.B. Kim, S.C. Hong, Appl. Catal. B 35 (2002) 305.
[10] X.Z. Li, H.S. Liu, Environ. Sci. Technol. 39 (2005) 4614.
[11] M. Noorjahan, V.D. Kumari, M. Subrahmanyam, P. Boule, Appl. Catal. B 47 (2004) 209.
[12] M.R. Dhananjeyan, E. Mielczarski, K.R. Thampi, P. Buffat, M. Bensimon, A. Kulik, J. Mielczarski, J. Kiwi, J. Phys. Chem. B 105 (2001) 12046.
[13] M. Takeuchi, S. Dohshi, T. Eura, M. Anpo, J. Phys. Chem. B 107 (2003) 14278.
[14] G. Marci, V. Augugliaro, M.J. Lopez-Munoz, C. Martin, L. Palmisano, V. Rives, M. Schiavello, R.J.D. Tilley, A.M. Venezia, J. Phys. Chem. B 105 (2001) 1026.
[15] R.S. Mane, W.J. Lee, H.M. Pathan, S.H. Han, J. Phys. Chem. B 109 (2005) 24254.
[16] Y.C. Kim, S. Sasaki, K. Yano, K. Ikebukuro, K. Hashimoto, I. Karube, Anal. Chem. 74 (2002) 3858.
[17] H.J. Zhao, D.L. Jing, S.Q. Zhang, K. Catterall, R. John, Anal. Chem. 76 (2004) 155.
[18] J.S. Chen, J.D. Zhang, Y.Z. Xian, X.Y. Ying, M.C. Liu, L.T. Jin, Water Res. 39 (2005) 1340.
[19] Y.H. Chai, H.C. Ding, Z.H. Zhang, Y.Z. Xian, Z.S. Pan, L.T. Jin, Talanta 68 (2006) 610.
[20] K.H. Lee, T. Ishikawa, S. McNiven, Y. Nomura, S. Sasaki, Y. Arikawa, I. Karube, Anal. Chim. Acta 386 (1999) 211.
[21] H.C. Ding, Y.H. Chai, Z.H. Zhang, M.C. Liu, Y.Z. Xian, Z.S. Pan, L.T. Jin, Chin. J. Chem. 23 (2005) 1425.
[22] China State Environment Protection Agency, 1998. Monitoring methods for water and wastewater, 3rd ed. CESP, Beijing, pp. 354–361.
[23] Y.C. Kim, S. Sasaki, K. Yano, K. Ikebukuro, K. Hashimoto, I. Karube, Anal. Chim. Acta 432 (2001) 59.
[24] S.Y. Ai, J.Q. Li, Y. Yang, M.N. Gao, Z.S. Pan, L.T. Jin, Anal. Chim. Acta 509 (2004) 237.
[25] S.Q. Zhang, D.L. Jiang, H.J. Zhao, Environ. Sci. Technol. 40 (2006) 2363.
[26] J.Q. Li, L.P. Li, L. Zheng, Y.Z. Xian, L.T. Jin, Talanta 68 (2006) 765.
[27] K.H. Lee, Y.C. Kim, H. Suzuki, K. Ikebukuro, K. Hashimoto, I. Karube, Electroanalysis 12 (2000) 1334.
[28] M. Takahashi, K. Tsukigi, T. Uchino, T. Yoko, Thin Solid Films 388 (2001) 231.
[29] G. Marci, V. Augugliaro, M.J. Lopez-Munoz, C. Martin, L. Palmisano, V. Rives, M. Schiavello, R.J.D. Tilley, A.M. Venezia, J. Phys. Chem. B 105 (2001) 1033.
[30] Z.S. Wang, C.H. Huang, Y.Y. Huang, Y.J. Hou, P.H. Xie, B.W. Zhang, H.M. Cheng, Chem. Mater. 13 (2001) 678.
[31] G.E. Brown, V.E. Henrich, W.H. Casey, D.L. Clark, C. Eggleston, A. Felmy, D.W. Goodman, M. Gratzel, G. Maciel, M.I. McCarthy, K.H. Nealson, D.A. Sverjensky, M.F. Toney, J.M. Zachara, Chem. Rev. 99 (1999) 77.
[32] M. Kosmulski, Langmuir 13 (1997) 6315.
[33] K. Keis, J. Lindgren, S.E. Lindquist, A. Hagfeldt, Langmuir 16 (2000) 4688.